WJSA-92-01
DOE/ER/54100-1

OSIRIS and SOMBRERO
Inertial Fusion Power Plant Designs

Volume 2
Designs, Assessments, and Comparisons

Final Report
March 1992

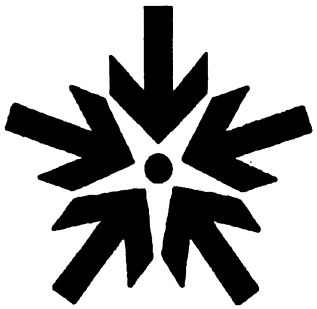

WJSA-92-01
DOE/ER/54100-1

OSIRIS and SOMBRERO
Inertial Confinement Fusion Power Plant Designs

Volume 2
Designs, Assessments, and Comparisons

W. J. Schafer Associates
Wayne R. Meier, Robert L. Bieri, Michael J. Monsler,
Charles D. Hendricks, Paul Laybourne, Keith R. Shillito

Bechtel
Sunil K. Ghose, Lenard M. Goldman, Kim D. Auclair, Chan Y. Pang

General Atomics
Robert F. Bourque, Larry D. Stewart, Edward E. Bowles, Edward L. Hubbard

Textron Defense Systems
Chas. W. von Rosenberg, Jr., Malcolm W. McGeoch

University of Wisconsin
Igor N. Sviatoslavsky, Robert R. Peterson, Mohamed E. Sawan, Hesham Y. Khater,
Layton J. Wittenberg, Gerry L. Kulcinski, Gregory A. Moses, ElSayed A. Mogahed,
Joseph J. MacFarlane, Sean Rutledge

Accelerator Consultants
Stanley Humphries, Jr.

TSI Research
Edward T. Cheng

March 1992

Disclaimer

This report was prepared as an account of work sponsored by an agency of the United States Government. Neither the United States Government nor any agency thereof, nor any of their employees, make any warranty, expressed or implied, or assumes any legal liability or responsibility for the accuracy, completeness, or usefulness of any information, apparatus, product or process disclosed, or represents that its use would not infringe on privately owned rights. Reference herein to any specific commercial product, process, or service by trade name, trademark, manufacturer, or otherwise, does not necessarily constitute or imply its endorsement, recommendation, or favoring by the United States Government or any agency thereof. The views and opinions of the authors expressed herein do not necessarily state or reflect those of the United States Government or any agency thereof.

Acknowledgments

The authors would like to acknowledge the help in the form of briefings and discussions with individuals in the Inertial Confinement Fusion Programs at the Laboratory for Laser Energetics, Lawrence Livermore National Laboratory, Los Alamos National Laboratory, and the Navy Research Laboratory, and individuals in the Heavy Ion Fusion Program at Lawrence Berkeley Laboratory. We also thank the members of the Oversight Committee for assembling the Study Guidelines and for providing feedback at our progress review meetings. We thank the secretaries at our institutions for their assistance in preparing this report with special thanks to Barbara Lane at W.J. Schafer Associates for editing the final report. Finally, we thank the Department of Energy, Office of Fusion Energy for supporting this study under contract No. DE-AC02-90ER54100.

CONTENTS

VOLUME 1 – EXECUTIVE SUMMARY AND OVERVIEW

EXECUTIVE SUMMARY

OVERVIEW

1.0 INTRODUCTION 1
1.1 BACKGROUND 1
1.2 ORGANIZATION OF THE OVERVIEW 1

2.0 OSIRIS HIB-DRIVEN POWER PLANT 3
2.1 SUMMARY OF OSIRIS PLANT PARAMETERS 3
2.2 OSIRIS CHAMBER DESIGN 3
2.3 OSIRIS POWER CONVERSION AND PLANT FACILITIES 7
2.4 HEAVY-ION DRIVER DESIGN 8

3.0 SOMBRERO LASER-DRIVEN POWER PLANT 17
3.1 SUMMARY OF SOMBRERO PLANT PARAMETERS 17
3.2 SOMBRERO CHAMBER DESIGN 17
3.3 SOMBRERO POWER CONVERSION AND PLANT FACILITIES 20
3.4 KrF DRIVER DESIGN 24

4.0 TARGET SYSTEMS 32
4.1 TARGET PRODUCTION 32
4.2 TARGET INJECTION, TRACKING, AND POINTING 39
4.3 TARGET HEATING DURING INJECTION 43

5.0 ENVIRONMENTAL AND SAFETY ASSESSMENT 45
5.1 INTRODUCTION 45
5.2 SAFETY DESIGN GOALS 45
5.3 RESULTS 46

6.0 RELIABILITY, AVAILABILITY, & MAINTAINABILITY ASSESSMENT 48
6.1 INTRODUCTION 48
6.2 AVAILABILITY ASSESSMENT 48
6.3 MAINTAINABILITY OF THE OSIRIS PLANT 50
6.4 MAINTAINABILITY OF THE SOMBRERO PLANT 52

7.0 TECHNOLOGY ASSESSMENTS 54
7.1 INTRODUCTION 54
7.2 SUMMARY OF DEVELOPMENT PRIORITIES FOR OSIRIS 54
7.3 SUMMARY OF DEVELOPMENT PRIORITIES FOR SOMBRERO 56
7.3 GENERIC IFE ISSUES 567

8.0 ECONOMIC ASSESSMENT 58
8.1 INTRODUCTION 58
8.2 RESULTS FOR REFERENCE DESIGNS 58
8.3 RESULTS OF PARAMETRIC STUDIES FOR OSIRIS AND SOMBRERO 58
8.4 CONCLUSIONS 61

9.0 COMPARISON OF OSIRIS AND SOMBRERO DESIGNS 62
9.1 INTRODUCTION 62
9.2 DRIVERS 62
9.3 TARGETS 62
9.4 CHAMBER DESIGNS 62
9.5 POWER CONVERSION SYSTEMS 64
9.6 RESULTS OF ASSESSMENT STUDIES 64

10.0 CONCLUSIONS AND RECOMMENDATIONS 65
10.1 INTRODUCTION 65
10.2 OSIRIS POWER PLANT 65
10.3 SOMBRERO POWER PLANT 68
10.4 TARGET SYSTEMS 71
10.5 ENVIRONMENTAL AND SAFETY ASSESSMENT 72
10.6 RELIABILITY, AVAILABILITY, AND MAINTAINABILITY 72
10.7 ECONOMIC ASSESSMENTS 73

11.0 REFERENCES 74

VOLUME 2 – DESIGNS, ASSESSMENTS, AND COMPARISONS

1.0 INTRODUCTION

1.1 BACKGROUND 1-1
1.2 OBJECTIVES AND SCOPE OF THE STUDIES 1-1
1.3 DESIGN PHILOSOPHY 1-1
1.4 STUDY GUIDELINES 1-2
1.5 ORGANIZATION OF THE REPORT 1-3
1.6 REFERENCES FOR CHAPTER 1 1-4

2.0 OSIRIS HIB-DRIVEN POWER PLANT

2.1 OVERVIEW OF OSIRIS POWER PLANT DESIGN 2-1
2.2 OSIRIS CHAMBER DESIGN AND ANALYSIS 2-5
2.3 OSIRIS POWER CONVERSION AND PLANT FACILITIES 2-52
2.4 HEAVY-ION DRIVER DESIGN AND SCALING 2-69
2.5 REFERENCES FOR CHAPTER 2 2-136

3.0 SOMBRERO LASER-DRIVEN POWER PLANT

3.1 OVERVIEW OF SOMBRERO POWER PLANT DESIGN 3-1
3.2 SOMBRERO CHAMBER DESIGN AND ANALYSIS 3-6
3.3 SOMBRERO POWER CONVERSION AND PLANT FACILITIES 3-89
3.4 KrF DRIVER 3-107
3.5 REFERENCES FOR CHAPTER 3 3-146

4.0 TARGET SYSTEMS

4.1 TARGET PRODUCTION 4-1
4.2 TARGET INJECTION, TRACKING, AND POINTING 4-24
4.3 TARGET HEATING DURING INJECTION 4-39
4.4 REFERENCES FOR CHAPTER 4 4-52

5.0 ENVIRONMENTAL AND SAFETY ASSESSMENT

5.1 INTRODUCTION 5-1
5.2 SAFETY DESIGN GOALS 5-1
5.3 OFF-SITE DOSE DEFINITIONS 5-2
5.4 CALCULATIONAL PROCEDURE 5-3
5.5 SOMBRERO SAFETY ANALYSIS 5-4
5.6 OSIRIS SAFETY ANALYSIS 5-19
5.7 TARGET FACTORY ANALYSIS 5-32

5.8 FUEL REPROCESSING FACILITIES 5-33
5.9 NUCLEAR GRADE COMPONENTS 5-33
5.10 COMPARISON OF SOMBRERO AND OSIRIS 5-35
5.11 REFERENCES FOR CHAPTER 5 5-36

6.0 RELIABILITY, AVAILABILITY, AND MAINTAINABILITY ASSESSMENT
6.1 INTRODUCTION 6-1
6.2 AVAILABILITY ASSESSMENT 6-1
6.3 MAINTAINABILITY OF THE OSIRIS PLANT 6-5
6.4 MAINTAINABILITY OF THE SOMBRERO PLANT 6-9
6.5 REMOTE HANDLING CAPABILITY & UTILIZATION CONSIDERATIONS . 6-10
6.6 REFERENCES FOR CHAPTER 6 6-14

7.0 TECHNOLOGY ASSESSMENTS
7.1 APPROACH AND METHODOLOGY 7-1
7.2 OSIRIS ISSUES AND DEVELOPMENT NEEDS 7-2
7.3 TECHNOLOGY ASSESSMENT RATINGS FOR OSIRIS 7-9
7.4 SUMMARY OF DEVELOPMENT PRIORITIES FOR OSIRIS 7-19
7.5 SOMBRERO ISSUES AND DEVELOPMENT NEEDS 7-21
7.6 TECHNOLOGY ASSESSMENT RATINGS FOR SOMBRERO 7-28
7.7 SUMMARY OF DEVELOPMENT PRIORITIES FOR SOMBRERO 7-37
7.8 GENERIC IFE ISSUES 7-39
7.9 TECHNOLOGY ASSESSMENT RATINGS FOR GENERIC ISSUES 7-43
7.10 SUMMARY 7-46
7.11 REFERENCES FOR CHAPTER 7 7-46

8.0 ECONOMIC ASSESSMENT
8.1 INTRODUCTION 8-1
8.2 COST OF ELECTRICITY 8-2
8.3 CALCULATING PLANT OPERATING PARAMETERS 8-4
8.4 COST MODELING FOR OSIRIS 8-12
8.5 COST MODELING FOR SOMBRERO 8-25
8.6 COMPARISON OF OSIRIS AND SOMBRERO 8-42
8.7 SUMMARY 8-44
8.8 REFERENCES FOR CHAPTER 8 8-45

9.0 COMPARISON OF OSIRIS AND SOMBRERO DESIGNS
9.1 INTRODUCTION 9-1
9.2 CHAMBER AND VACUUM SYSTEMS 9-1
9.3 POWER CONVERSION SYSTEMS 9-5
9.4 BUILDING VOLUME COMPARISON 9-6
9.5 DRIVER SYSTEMS 9-7
9.6 TARGET SYSTEMS 9-8
9.7 OPERATION AND MAINTENANCE COMPARISON 9-9
9.8 ENVIRONMENTAL AND SAFETY COMPARISON 9-10
9.9 ECONOMIC COMPARISON 9-11
9.10 REFERENCES FOR CHAPTER 9 9-12

10.0 CONCLUSIONS AND RECOMMENDATIONS
10.1 INTRODUCTION 10-1
10.2 OSIRIS POWER PLANT 10-1
10.3 SOMBRERO POWER PLANT 10-4
10.4 TARGET SYSTEMS 10-7
10.5 ENVIRONMENTAL AND SAFETY ASSESSMENT 10-8
10.6 RELIABILITY, AVAILABILITY, AND MAINTAINABILITY 10-9
10.7 ECONOMIC ASSESSMENT 10-9

APPENDICES
A STUDY GUIDELINES
B REACTOR CONCEPT SELECTION PROCESS
C THE ONION IFE REACTOR CONCEPT
D THE LIFE IFE REACTOR CONCEPT
E REMOTE MAINTENANCE EQUIPMENT CONFIGURATION CONCEPTS
F ADDITIONAL COMPARISONS OF OSIRIS AND SOMBRERO

Chapter 1

Introduction

CONTENTS

1.1 BACKGROUND 1-1
1.2 OBJECTIVES AND SCOPE OF THE STUDIES 1-1
1.3 DESIGN PHILOSOPHY 1-1
1.4 STUDY GUIDELINES 1-2
1.5 ORGANIZATION OF THE REPORT 1-3
1.6 REFERENCES FOR CHAPTER 1 1-4

1.0 INTRODUCTION

1.1 BACKGROUND

In the fall of 1990, the Department of Energy's Office of Fusion Energy funded two industrial/university teams of fusion scientists and engineers to conduct parallel studies on a project entitled "Inertial Fusion Energy (IFE) Reactor Design Studies." The studies concluded in March 1992, and the results of the W. J. Schafer Associates (WJSA) team, which consisted of Bechtel, General Atomics (GA), Textron Defense Systems (formerly Avco Research Lab), and the University of Wisconsin, are reported here.

1.2 OBJECTIVES AND SCOPE OF THE STUDIES

The primary objective of the of the IFE Reactor Design Studies was to provide the Office of Fusion Energy with an evaluation of the potential of inertial fusion for electric power production. The term *reactor* studies is somewhat of a misnomer since these studies included the conceptual design and analysis of all aspects of the IFE power plants: the chambers, heat transport and power conversion systems, other balance of plant facilities, target systems (including the target production, injection, and tracking systems), and the two drivers.

The scope of the IFE Reactor Design Studies was quite ambitious. The majority of our effort was spent on the conceptual design of two IFE electric power plants, one using an induction linac heavy ion beam (HIB) driver and the other using a Krypton Fluoride (KrF) laser driver. After the two point designs were developed, they were assessed in terms of their 1) environmental and safety aspects; 2) reliability, availability, and maintainability; 3) technical issues and technology development requirements; and 4) economics. Finally, we compared the design features and the results of the assessments for the two designs.

1.3 DESIGN PHILOSOPHY

Early in the project, our team developed several new ideas for chamber concepts to a preliminary level. The downselection to the two designs described in this report was based on a set of weighted selection criteria established by our team. After screening out obviously unfeasible or uneconomical concepts, the following criteria and weightings were used:

Technical Issues	50%
Environmental and Safety	30%
Economics	20%

The two designs that we selected are the HIB-driven Osiris reactor, and the KrF laser-driven SOMBRERO reactor. (SOMBRERO is an acronym for **SO**lid **M**oving **BRE**eder **R**eactor.)

Technical Issues. Our judgments on technical issues were based on our assessment of credibility that the physics, engineering, technologies, materials, and processes needed for the concepts to function as conceived would be available by the time the systems are commercialized, 40 years or so from now. Clearly, the current state of the art for some of the key subsystems is far from what is required for a commercial power plant. We have, however, identified technology development programs or design alternatives to address the critical issues associated with each design. Many of the issues can be addressed with analyses or non-nuclear experiments of modest duration and cost.

Environmental and Safety. As the reader will discover, both of these designs have very attractive environmental and safety features (see Chapter 5). This is the result of using only low activation materials for the first walls, vacuum chambers, and breeding blankets, and minimizing the tritium inventory and controlling its leakage.

Economics. The economic characteristics, although not given a high priority in the selection process, have turned out to be attractive in comparison to previous IFE and MFE designs (see Chapter 8). This is largely due to two factors: 1) the high safety ratings of the designs allowed us to cost the power conversion and plant facilities on a non-nuclear basis and 2) innovation in the design of the drivers led to a higher efficiency (and thus lower operating cost) for the KrF driver and lower capital cost for the HI driver than previous design concepts.

For the most part, we feel that we have met the goals we set for ourselves at the start of the study and have developed IFE power plant design concepts that are technically credible and have attractive safety and economic features.

1.4 STUDY GUIDELINES

The DOE provided a set of study guidelines at the start of the project.[1.1*] These guidelines are reproduced in Appendix A for completeness. Some of the key ground rules are listed here.

Net Electric Power. The base case designs were to have a net electric power of 1000 MWe, typical of large central station electric power plants built today. In the economic evaluation, we examined the impact on cost of electricity of 500 MWe and 1500 MWe plants (i.e., ± 50% from the base case).

Target Gain. Target performance was given in terms of target gain as a function of incident driver energy for direct and indirect drive targets. Based on the information supplied, we selected direct drive targets for the laser system and indirect drive for the HIB-driven plant.

* References are given at the end of each chapter.

We did not attempt to evaluate the credibility of the information that was supplied by the Target Working Group of the Study Oversight Committee, which was made up of distinguished members of the fusion community. We accepted this as input information to the study. We are aware of the honest difference of scientific opinion on the credibility of some of the gain curves and assumptions associated with driver irradiation geometry, beam uniformity, etc. It was not within the scope of our work to judge or debate this information.

Economic Assumptions. The economic assumptions listed in the study guidelines were modified to correct some inconsistencies and errors. The economic assumptions given in Chapter 8 were agreed to by the Oversight Committee.

1.5 ORGANIZATION OF THE REPORT

This report contains two volumes: Volume 1 – Executive Summary and Overview, and Volume 2 – Designs, Assessments, and Comparisons.

VOLUME 1 – EXECUTIVE SUMMARY AND OVERVIEW

Volume 1 contains a brief executive summary and an overview of the two designs. The main sections of the overview correspond to the chapters of Volume 2, which are described below.

VOLUME 2 – DESIGNS, ASSESSMENTS, AND COMPARISONS

Volume 2 is organized along the same lines as the study was itself.

Description of the Designs. Chapters 2 to 4 contain the detailed descriptions of the designs. Chapter 2 is devoted to the Osiris HIB-driven power plant. It begins with an overview of the design (Section 2.1) and then proceeds with more detailed descriptions of the chamber (2.2), power conversion and plant facilities (2.3), and concludes with a description of the HIB driver (2.4). Chapter 3 provides a description of the SOMBRERO laser-driven power plant. The organization of Chapter 3 parallels Chapter 2, beginning with an overview (3.1), description of the chamber (3.2), power conversion and plant facilities (3.3), and concludes with the KrF laser design (3.4). Chapter 4 describes the target systems for both plants. This chapter describes target production (4.1); target injection, tracking, and beam pointing (4.2); and target heating during injection (4.3).

Assessments of the Designs. Chapters 5 to 8 are assessments of the designs. Chapter 5 covers the environmental and safety assessment for SOMBRERO and Osiris and

provides a detailed comparison of the results. Chapter 6 contains the reliability, availability, and maintainability (RAM) assessments. Chapter 7 identifies technical issues and makes an assessment of technology development needs and priorities. Chapter 8 contains our economic assessment of the two designs and a detailed comparison of the results.

Comparison of the Designs. Chapter 9 compares the operating characteristics of the two designs and the results of the assessment studies.

Conclusions and Recommendations. Chapter 10 contains a summary of our conclusions and recommendations.

Appendices. The appendices contain supporting information relative to the design studies including the study guidelines (Appendix A), information on the procedure used to select the two reactor concepts (Appendix B), more detailed descriptions of two reactor concepts that were considered in the preliminary phases of the study but were not selected for the detailed conceptual design and assessment phases (Appendices C and D), additional detail on remote maintenance (Appendix E), and the results of a survey of study participants comparing various aspects of the two designs (Appendix F).

1.6 REFERENCE FOR CHAPTER 1

1.1 R.C. Davidson, C.C. Baker, R.O. Bangerter, E.C. Brolin, D.R. Cohn, D.L. Cook, D.J. Dudziak, D.B. Harris, R.A. Krakowski, T.E. Shannon, W.E. Stacey, C.P. Verdon, "Inertial Confinement Fusion Reactor Design Studies Recommended Guidelines," (Sept. 1990).

Chapter 2

Osiris

HIB-Driven Power Plant

CONTENTS

2.1 OVERVIEW OF OSIRIS POWER PLANT DESIGN 2-1
2.1.1 Chamber Design 2-1
2.1.2 Heavy Ion Beam Driver 2-1
2.1.3 Final Focusing and Beam Transport 2-3
2.1.4 Balance of Plant 2-3
2.2 OSIRIS CHAMBER DESIGN AND ANALYSIS 2-5
2.2.1 Evolution of Design 2-5
2.2.2 First Wall Protection 2-9
2.2.3 First Wall Design 2-22
2.2.4 Blanket Design 2-25
2.2.5 Vacuum Vessel Design 2-28
2.2.6 Neutronics Analysis 2-29
2.2.7 Tritium Recovery and Containment 2-41
2.3 OSIRIS POWER CONVERSION AND PLANT FACILITIES 2-52
2.3.1 Introduction 2-52
2.3.2 Heat Transport System 2-52
2.3.3 Power Conversion 2-57
2.3.4 Plant Facilities 2-59
2.4 HEAVY-ION DRIVER DESIGN AND SCALING 2-69
2.4.1 Introduction 2-69
2.4.2 Heavy-Ion Driver Description 2-70
2.4.3 Design Strategy 2-72
2.4.4 Accelerator Modeling 2-74
2.4.5 Driver Efficiency 2-90
2.4.6 Final Compression and Focus Modeling 2-91
2.4.7 Reactor Chamber Transport 2-97
2.4.8 Parametric Studies 2-109
2.4.9 Description of the Base 5 MJ Driver Design 2-115
2.4.10 Potential Reductions in Driver Cost 2-131
2.4.11 Results and Conclusions 2-134
2.5 REFERENCES FOR CHAPTER 2 2-136

2.0 OSIRIS HIB-DRIVEN POWER PLANT

2.1 OVERVIEW OF OSIRIS POWER PLANT DESIGN

2.1.1 Chamber Design

The reactor chamber for the heavy ion beam-driven power plant employs low activation ceramic materials and a drainable liquid coolant/breeder. The ceramics are used as woven cloth panels stitched together. This avoids many of the problems caused by flexing and stress concentration in large solid ceramic structures, which are still in the developmental stages of production. The cloth supports a liquid lithium-bearing coolant, and coolant bleeding through the cloth provides a sacrificial protective film on the first wall. A pool of coolant and coolant sprays at the bottom condenses blowoff vapor. The pool also provides hot storage of the coolant during changeouts.

Figure 2.1 shows the final Osiris configuration. (Section 2.2.1.1 reviews the evolution of the final design.) A three-layer carbon cloth blanket is suspended from the cover of the vacuum chamber, which is made of carbon composite. Flibe flows from the top of the reactor, makes a quick pass along the backside of the first wall, and returns more slowly through the wider channels between the second and third cloth layers. It then cascades down the outside of the blanket, releasing some of the bred tritium and other gases. It then falls into the annular cascade flow blanket and dumps into the pool at the bottom. In a second inlet flow path, Flibe at high pressure enters an annular manifold at the bottom of the blanket and sprays into the pool. Blowoff vapor from the first wall is condensed by this spray. The entire blanket/manifold assembly is replaced periodically by lifting it from the reactor along with the reactor cover.

2.1.2 Heavy Ion Beam Driver

We used conservative driver design assumptions and created an optimized design for a 5 MJ driver that has a total direct capital cost of only $120/J and produces a target gain of 86. The base driver design has lower cost and better performance than was anticipated at the beginning of this study, primarily because the driver parameters were determined from an extensive examination of the large parameter space available for heavy-ion accelerators. These parameters are the number of beams, type of superconductor used in the quadrupole focusing

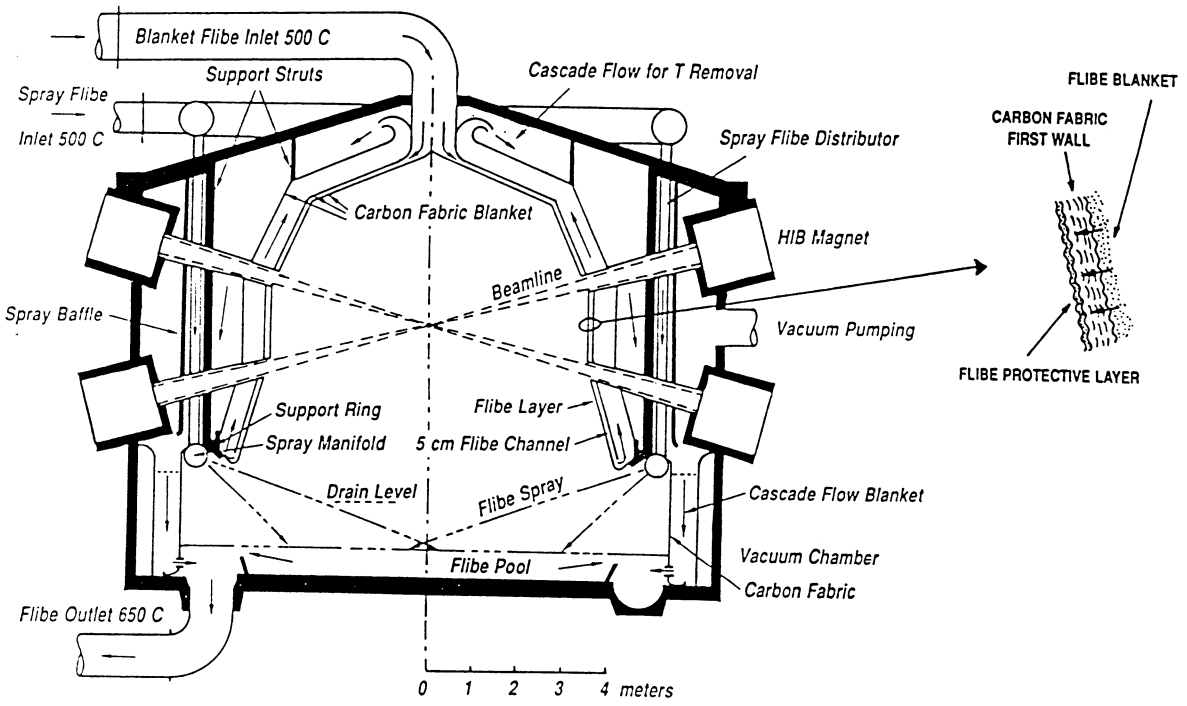

Fig. 2.1. Osiris heavy-ion-beam reactor chamber concept showing carbon fabric blanket structure with Flibe spray and pool.

magnets, maximum magnetic field allowed at the superconducting windings, the axial packing fraction occupied by the focusing fields, the ion mass, and the ion charge state.

We used conservative design choices to create a credible driver design. We chose not to use beam combination, beam separation, or recirculation. All of these options have the potential to reduce the cost of the driver, but they do it at the expense of added complexity and uncertainty and (with the possible exception of beam separation) at the expense of beam quality and anticipated driver performance. Driver designs using these design options will require results from future experiments or development programs before they can be certain of their performance scaling.

The only aggressive design feature is the use of compact Nb_3Sn quadrupole arrays. The high current densities of Nb_3Sn allow for smaller quadrupole windings and smaller quadrupole arrays. Reducing the size of the arrays also reduces the required bore radius for the induction cells. Because Nb_3Sn quadrupoles have been built and operated at fields approaching 10 T, their use in our designs at 10 T relies on minimal extrapolation from present technology.

Although we found small cost savings from the use of ions with charge states greater than 1, our base design uses singly-charged ions. The cost saving with higher charge states were achievable only by using designs with more beams and larger spot sizes. These designs introduce more complicated final focusing and beam combination requirements and give slightly lower anticipated gain even if the effects of beam combination on spot size are ignored. Higher charge states may be less prone to additional electron stripping, but they require much more complicated sources and may require higher vacuums to prevent electron capture from residual gas in the accelerator.

2.1.3 Final Focusing and Beam Transport

Target gain was improved by using an autoneutralized final focusing scheme. In this scheme, electrons are injected with the converging heavy-ion beams after they leave the final focusing magnets. The co-injected electrons provide charge neutralization to the beams by forming an autoneutralized plasma with the heavy-ions. Models for the autoneutralized beams differ from those based on a fraction of charge neutralization, but provide similar reductions in the achievable spot size.

2.1.4 Balance of Plant

The Osiris reactor building provides biological shielding. A sliding shield block separates the reactor building from the maintenance building. The latter building is used to build up and tear down replacement blankets. Intermediate heat exchangers are used with liquid lead as the intermediate coolant. A double reheat supercritical steam cycle is used giving 45% gross conversion efficiency. After subtracting the recirculating power to the driver, net plant efficiency is 40%. This cycle is chosen over advanced cycles in order to meet the requirements of moderate Flibe vapor temperature in the chamber. Flibe, lead, and steam peak temperatures are 650°C, 600°C, and 538°C, respectively. The lead temperature is compatible with type 347 stainless steel. Table 2.1 shows the basic parameters of the power plant. All plant parameters seem quite reasonable, and none of the power systems require great modifications to existing systems.

Table 2.1. Major Osiris Plant Parameters

Target Yield	432 MJ
Rep-Rate	4.6 Hz
Fusion Power	1987 MW
Surface Power	596 MW
Blanket Power	1908 MW
Total Thermal Power	2504 MW
Power Conversion Efficiency	45%
Gross Electrical Power	1127 MWe
Net Electric Power	1000 MWe
Flibe Inlet Temperature	500°C
Flibe Outlet Temperature	650°C
Spray Flow Rate	2265 kg/s
Blanket Flow Rate	4598 kg/s
Max First Wall Channel Velocity	5 m/s
Flibe Upflow Average Velocity	0.2 m/s
Spray Velocity	46 m/s
Spray Manifold Pressure	2.1 MPa
Spray Ideal Pumping Power	3 MW
Total Flibe Mass in Chamber	456,000 kg
Total Supported Mass	274,000 kg
Main Support Hangers Diameter	10 - 24 cm
Hanger Tensile Stress	14 MPa
Total Flibe Inventory	940,000 kg
Flibe Vaporized per Shot	4.3 kg
Peak Vaporization Pressure on First Wall	36.9 GPa
Impulse on First Wall	89.5 Pa-s
Surface Heat Load per Pulse at Target Plane	0.84 MJ/m^2
Neutron Wall Loading at Target Plane	9.0 mW/m^2

2.2 OSIRIS CHAMBER DESIGN AND ANALYSIS

2.2.1 Evolution of Design

2.2.1.1 Design Goals

The primary goal of the Osiris concept is to devise a low activation chamber design that is innovative, but requires no great leaps in technology. Other goals are leak tolerance, low pressure operation, low tritium inventory, rapid changeout of neutron-damaged parts, low vapor density in the chamber, and high power conversion efficiency.

2.2.1.2 Earlier Concepts

First Version. Figure 2.2 shows the first embodiment of Osiris. There are two pools of liquid coolant (originally lithium-lead), one each above and below the target chamber. The coolant flows by gravity through an annular carbon fabric "sock" from one pool to the other. It also weeps to the surface of the first wall, providing a sacrificial film that protects the fabric from damaging x-ray and debris energy from the target. The similarities to the HYLIFE[2.1] and HIBALL[2.2] designs are readily apparent. The primary advantages over HYLIFE are the greater control of flow rate and the reduced impact of isochoric heating.

The system is very leak tolerant with everything dropping to the lower pool. At changeout time, the liquid is completely drained to the lower pool, and the empty carbon sock is lifted out the top.

The key issue that arose from this design centered around heat removal. Most of the vaporized coolant was expected to condense on the first wall; a smaller fraction condensed in the pool. Because heat fluxes were so high, a great deal of coolant turbulence was needed to prevent overheating, which would ultimately create excess vapor in the chamber which would interfere with HIB propagation.

Second Version. The next version, shown in Fig. 2.3, attempted to solve the heat flux problem by using baffles placed at a shallow angle to the target. In addition to providing a large surface area, the back side of the baffles could be used for vapor condensation. The baffles would also shield the rear blankets, which would receive neutron heating only.

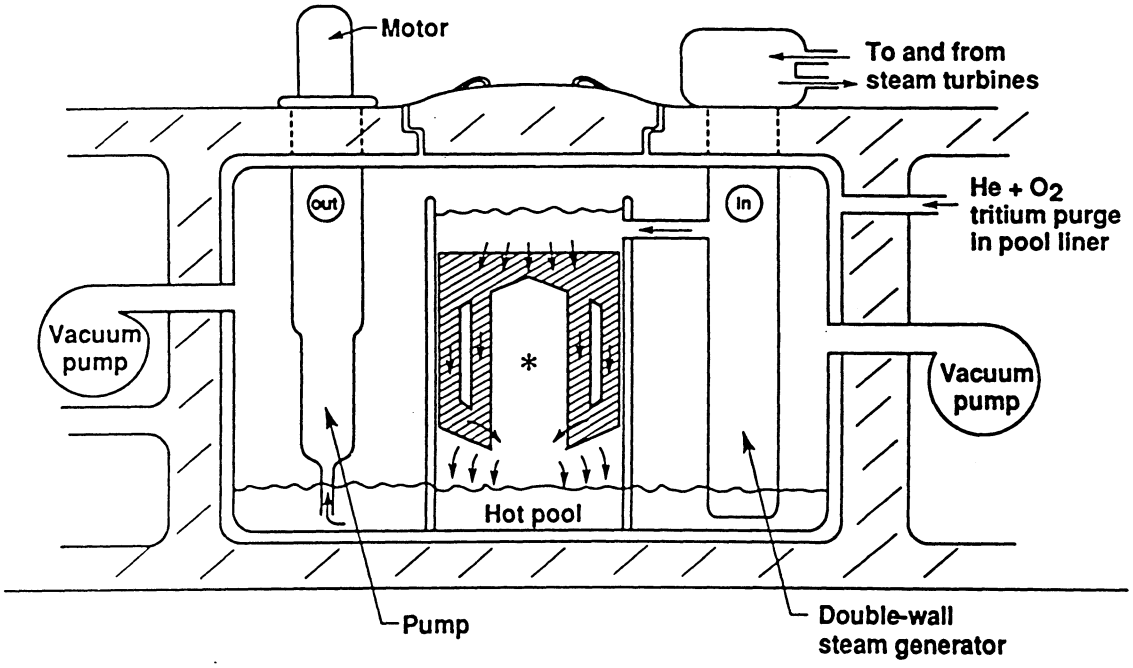

Fig. 2.2. The original version of Osiris using lithium lead.

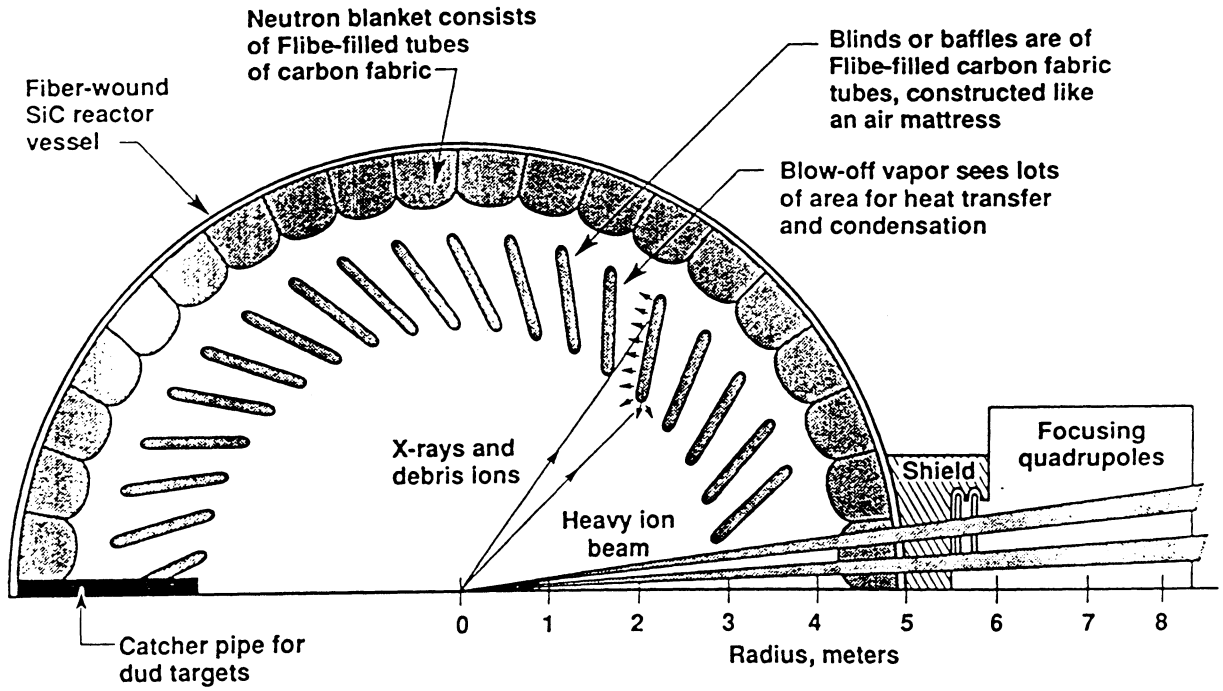

Fig. 2.3. The second version of Osiris using Flibe. The thin panels are intended to compensate for the poor thermal conductivity of Flibe.

Because the baffles were fairly thin, impulse loading created structural problems that were difficult to assess. Also, while the heat flux issue was largely resolved over most of the surface area, the curved sides of the baffles nearest the target still received the full impact. Lastly, while the concept resolved some problems for the chamber walls, the issue of the chamber roof was left unresolved.

Third Version. A fundamental design change occurred in the next version, shown in Fig. 2.4. Rather than attempt to condense the blowoff vapor back on the wall, it was directed toward the pool where it was condensed. This greatly relieved the heat flux and overheating problems on the wall, which became especially serious when the blanket coolant was switched from LiPb to the lower activation, but poorly conducting, Flibe (2 LiF + BeF_2 molten salt). In this version, the blanket took on a tepee-like shape, and the angled panels were eliminated. With this geometry, the blowoff vapor was directed downward toward the pool. The pool was far enough from the target that it did not generate a counterflow blowoff vapor. A perforated plate in the pool generated jets that churned the surface, creating enough turbulence to condense the vapor. With the exception of energy radiated to the first wall by the hot vapor, little heat transfer took place along the wall. The primary heat transfer for condensation was by direct contact of the vapor with the pool.

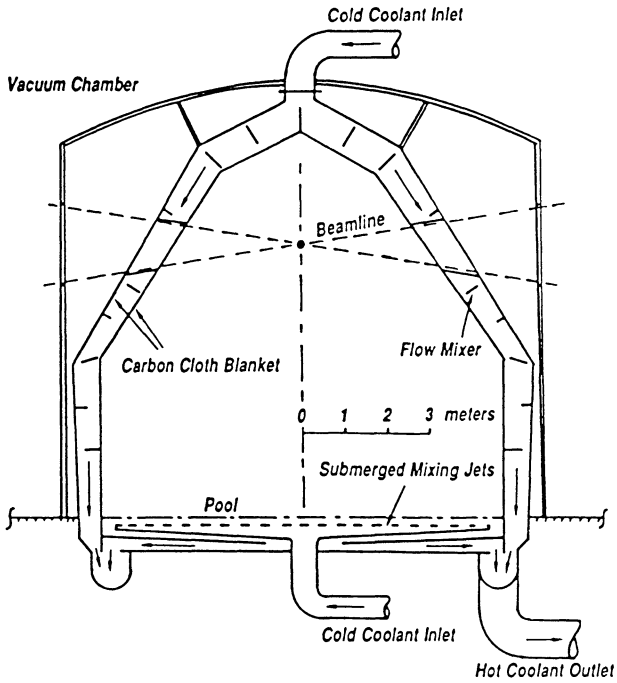

Fig. 2.4. The third version of Osiris where the Flibe vapor condenses in the pool rather than on the first wall.

2.2.1.3 Final Design

The final design evolved from the third design to the one shown in Fig. 2.5. It retains the essential elements of the previous version with small but significant changes. The pool is closer to the target reducing the height of the chamber and volume of blanket, but the pool contribution to blowoff vapor remains small. It was not that necessary to direct the blowoff toward the pool. Even a quiescent gas filling the volume will condense quickly if the pool can absorb the heat without overheating. The perforated plates in the pool are replaced with spray nozzles around the blanket. (The plates, being closer now to the target, would have had to be replaced periodically.) The nozzles are shielded from direct exposure to fusion neutrons.

The coolant now makes two passes through the blanket. The first is at high speed, and the temperature rise is only 20°C. The coolant then makes a U-turn and goes up the outer channel collecting the bulk of the neutron heat. It then tumbles down the outside of the blanket, releasing some of the bred tritium to the vacuum system. At the bottom of the reactor, the coolant dumps into an annular blanket and mixes with the pool flow at the exit.

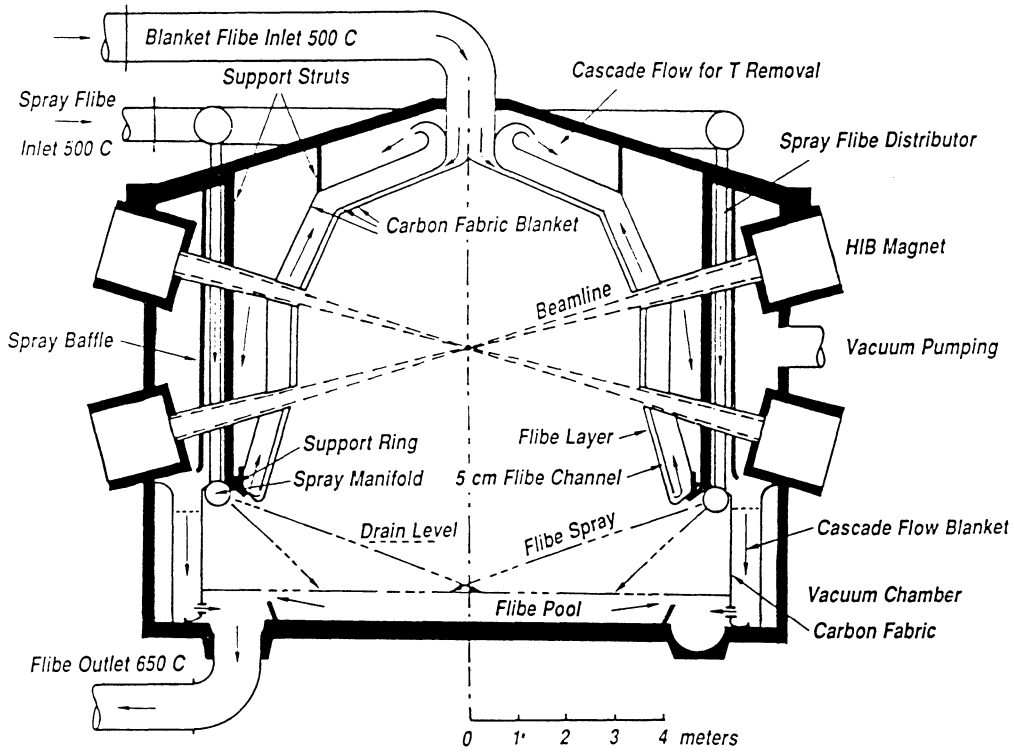

Fig. 2.5. The final version of Osiris with sprays to ensure vapor condensation. Shown for two-sided illumination using final beam geometry.

This arrangement is fairly simple to implement and assures a low vapor temperature in the chamber. The design reflects an improved understanding of the vaporization process. The Flibe coating on the first wall boils off down to a depth and temperature where the boiling point of the Flibe corresponds to the vapor pressure in the chamber. The temperature distribution in the Flibe, which is created by the X-ray deposition from the target, must at some point fall below this boiling point, or the Flibe will be a continuous source of vapor. By providing a high-speed, low-temperature flow channel behind the first wall, the temperature distribution of the Flibe coating the first wall is controlled and the layer boiled off is very thin. A Flibe vapor density of about $5 \cdot 10^{18}$ m^{-3} will strip an extra electron each from about 30% of the ions in the beam over a 5 m propagation distance (see Section 2.4). This amount of stripping has little effect on the beam spot size. This Flibe density corresponds to a temperature of 570°C. The bulk Flibe temperature near the wall must be kept below this limit. To allow some margin, the Flibe enters at 500°C, 40° above the melting point, and leaves the first wall region at 520°C. While the spray does heat up to 607°C, the average in transit is 554°C, so excess vapor generation should not occur.

2.2.2 First Wall Protection

Because ballistic focusing of heavy ion beams requires a low chamber fill gas density (we have allowed a number density of 5×10^{18} molecules m^{-3}) and limited focusing distances, the first wall of the reactor is exposed to high intensities of x-ray radiation from the target. As discussed above, we protect the first wall fabric with continuous coating of liquid Flibe. Vaporized Flibe is replaced by liquid Flibe seeping through the woven graphite that supports the film. This section examines the vaporization process and the resulting stresses on the first wall.

2.2.2.1 Target Emanations

The Osiris targets emit x-rays, neutrons, and ions. The assumed target parameters are given in Table 2.2. The calculations presented in this section were based on a preliminary estimate for the target gain. The assumed target gain was increased by 18% as the driver design improved, so the results presented here should be scaled with target yield.

The interaction between target emissions and reactor gases and surfaces is dependent upon the spectra and timing of the target radiation. The x-ray spectrum assumed in this study was

taken from the HIBALL-II report.[2.3] The target debris ion species and energies used in these calculations are given in Table 2.3.

Table 2.2. Target Parameters for Osiris

	Assumed	Base Case
Energy on Target (MJ)	5	5
Target Gain	73	86.5
Target Yield (MJ)	365	432
Neutron Yield (MJ)	256	303
X-ray and Debris Yield (MJ)	109	129

Table 2.3. Target Debris Ion Energies

Normalized Energy (keV/amu)	0.85
Deuterium Energy (keV)	1.70
Tritium Energy (keV)	2.55
Helium-4 (keV)	3.40
Lithium-7 (keV)	5.90
Lead 207 (keV)	176.0

2.2.2.2 CONRAD Computer Code

The CONRAD[2.4] computer code was used to analyze reactor chamber designs for Osiris. CONRAD is a one-dimensional Lagrangian finite difference computer code that calculates hydrodynamic motion, radiation transport, and vaporization and condensation in planar, cylindrical, or spherical geometries. Radiation transport is calculated with flux limited multi-

group diffusion. Time dependent target x-ray and ion deposition are calculated in the fill gas and walls. Heat transfer calculations are performed by CONRAD to get wall surface temperatures and temperature profiles in the wall at all times. These temperature profiles are used to calculate vaporization and condensation rates.

Equation-of-state and opacity data are read by CONRAD from tables. The properties of the materials are assumed to be quasi-static. The data tables are created with equation-of-state results from the IONMIX[2.5] computer code or from the SESAME[2.6] library. IONMIX is better suited to materials much less dense than solids or liquids, while SESAME is preferred at higher densities. Opacity tables are constructed with results from IONMIX. Twenty energy group opacities are used in these calculations.

CONRAD calculates the amount of material vaporized by the target x-rays when the x-rays volumetrically heat the absorbing material to above the energy required to vaporize the material. The x-rays arrive at the material in a pulse applying a time-dependent power to the surface. The x-rays are divided into photon energy groups, and each group has a separately calculated deposition length in the material. An example deposition profile in the material is shown in Fig. 2.6 The energy density profiles are time-dependent since the x-ray fluence is spread over a finite pulse width and because heat is conducted away from the heated inner surfaces.

Figure 2.6 illustrates how the thickness of the vaporized material is calculated; the vaporization energy density and sensible heat at the vaporization temperature are shown. The vaporization temperature is calculated as a function of the local vapor pressure. Three regions are defined in the material. Region A is where material gains an energy density above that required for vaporization and is vaporized. In Region C, the material remains below the sensible heat of the material, and none of the material is vaporized. Because the material in Region B gains energy beyond the sensible energy but below the vaporization energy, the extent of vaporization in Region B is uncertain. We have estimated vaporization in Region B by using the total energy deposited in the region and calculating the corresponding amount of material that could be raised to its vaporization energy; this amount of material is assumed to be vaporized.

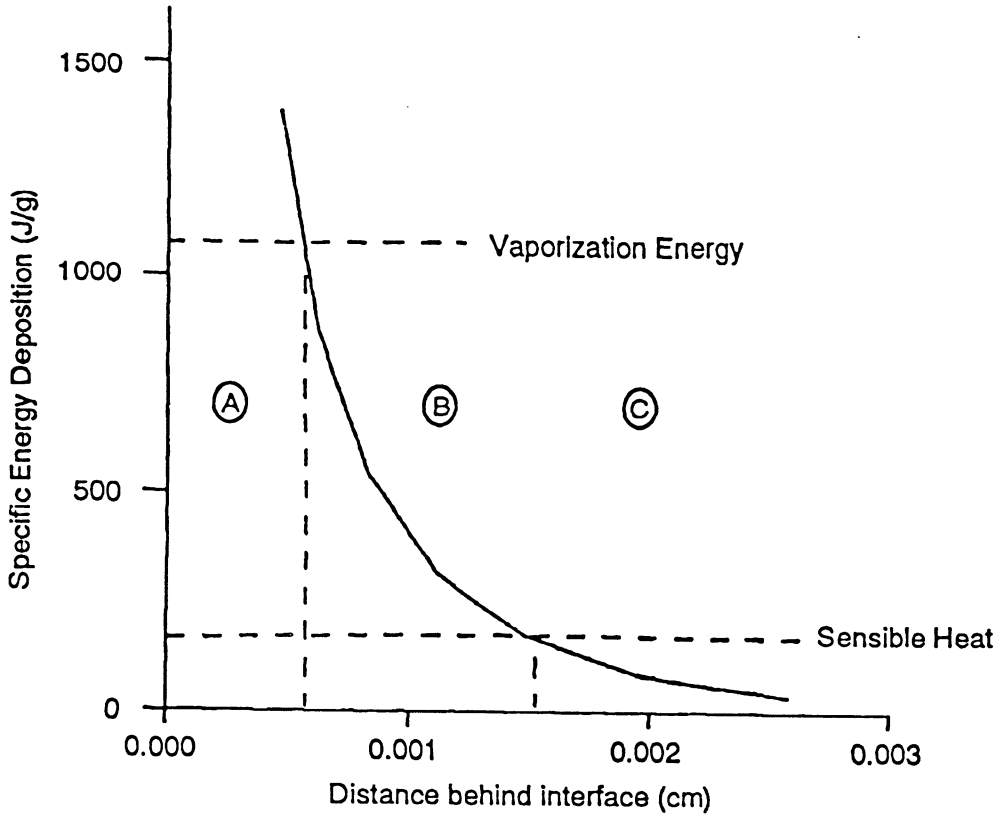

Fig. 2.6. Sample time-dependent energy profile from deposited X-rays.

2.2.2.3 Vaporization

A CONRAD simulation for Osiris was performed using a yield of 365 MJ. The essential calculated parameters for Osiris are given in Table 2.4. These results are proportional to the target yield for yields within 20% of the 365 MJ assumed yield. The results for the base case yield of 432 MJ are also shown. The smallest separation of a Flibe-coated wall from the target is 3.5 m, so the maximum x-ray fluence and intensity at the liquid Flibe surface are 46.7 J/cm^2 and 46.7 GW/cm^2, respectively. The x-rays vaporize 2.35 mg/cm^2 or 11.9 μm of Flibe from the wall. The base case results are all 18% higher. The x-rays also create a high pressure gradient in the vapor that drives a shock wave into the vapor. This shock can be seen in Fig. 2.7, where Lagrangian zone boundaries that are fixed in the material are plotted against time. The shock propagates through the vapor, which is at or slightly above the liquid density of the liquid, and eventually reaches the vapor/liquid interface in the Flibe. In Fig. 2.8, we have added pressure contours to Fig. 2.7. This figure shows that pressures of several tens of GPa are generated in the material.

Table 2.4. Parameters on the Closest Wall of the Osiris Target Chamber

	Assumed	Base Case
Wall Material	Flibe	Flibe
Distance From Target (m)	3.5	3.5
Yield (MJ)	365	432
X-Ray Fluence on Wall (J/cm^2)	46.7	55.3
X-Ray Intensity on Wall (GW/cm^2)	46.7	55.3
Vaporized Mass / unit area (mg/cm^2)	2.35	2.78
Vaporized Thickness (μm)	11.9	14.1
Total Vaporized Mass (kg)	3.6	4.3
Impulse on Wall (Pa-s)	75.6	89.5
Peak Pressure (GPa)	31.2	36.9

The issue of where the vapor flows has yet to be analyzed in detail. The Osiris chamber has been designed to direct the flow of the vapor downward into the condensing spray and pool. The spray provides a very large surface area of Flibe at the cold leg temperature. The condensation of material onto spray droplets can be analyzed, but it was outside the scope of the current study. We must assume that the spray injection system can be adjusted to provide enough droplet surface area to reduce the vapor density to the proper level before the next shot. We must design the system to condense ~ 4 kg per shot, so we must inject a least a few kg of spray per shot to absorb all of the latent heat of vaporization.

Another concern is the flow of vapor into the beam ports. Condensed liquid in the beam tubes could drip into the path of the heavy-ion beams and prevent them from reaching the target. We are relying on the shape of the reactor chamber to direct the flow of vapor away from the beam ports, but some material transport down the beam tubes is unavoidable. An estimate of how much material will flow into the ports will require a three dimensional simulation of the vapor flow and condensation in the target chamber. One can imagine several solutions to this problem. Condensation of the vapor onto particular surfaces could be achieved by controlling the temperatures on the port walls. Surfaces above the beams could be heated to prevent condensation in critical areas.

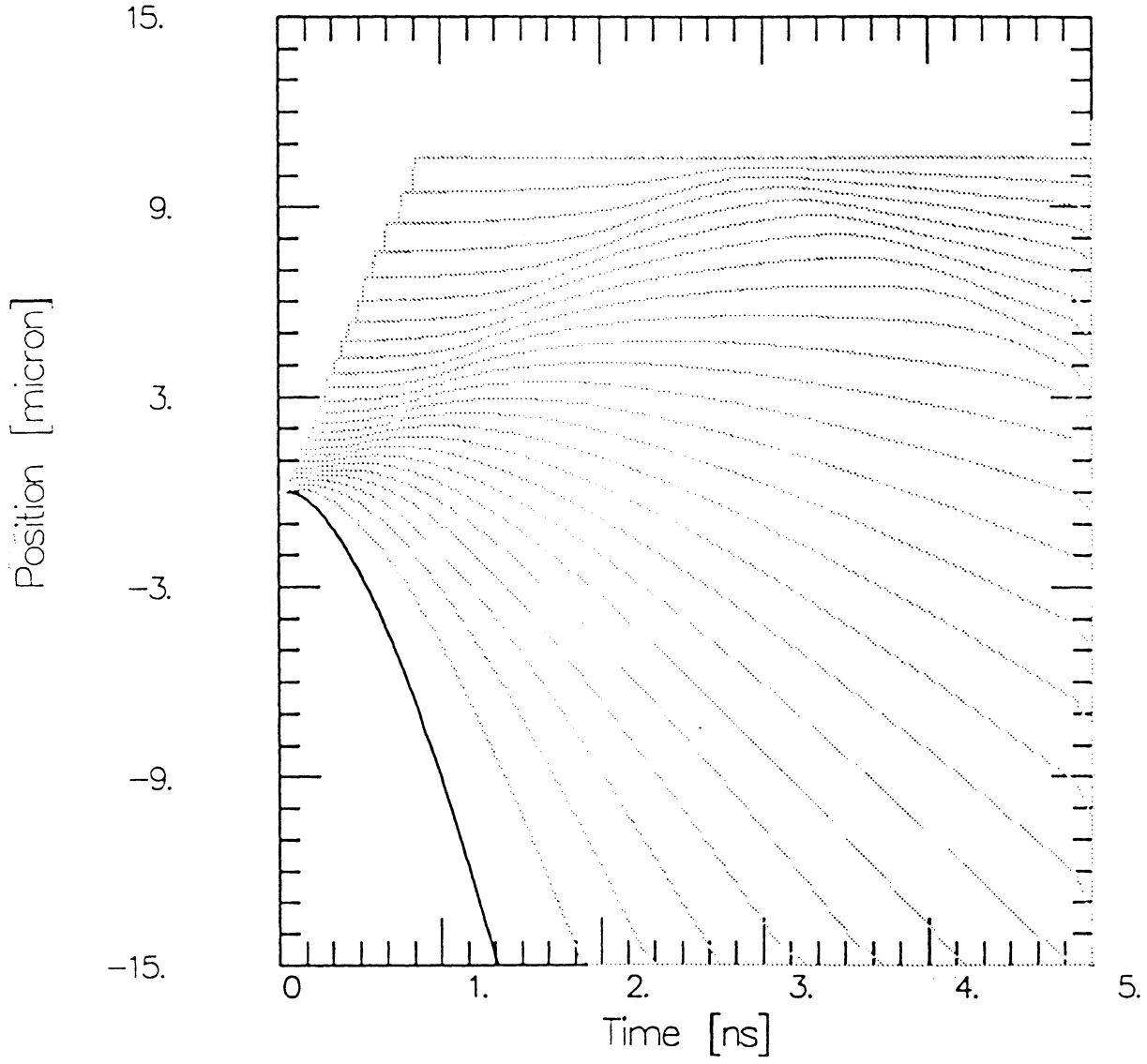

Fig. 2.7. **Positions of Lagrangian Zone boundaries vs. time for vaporization from the Osiris first wall. Position equals 0 is the original position of the liquid surface of the Flibe. All other positions are in μm.**

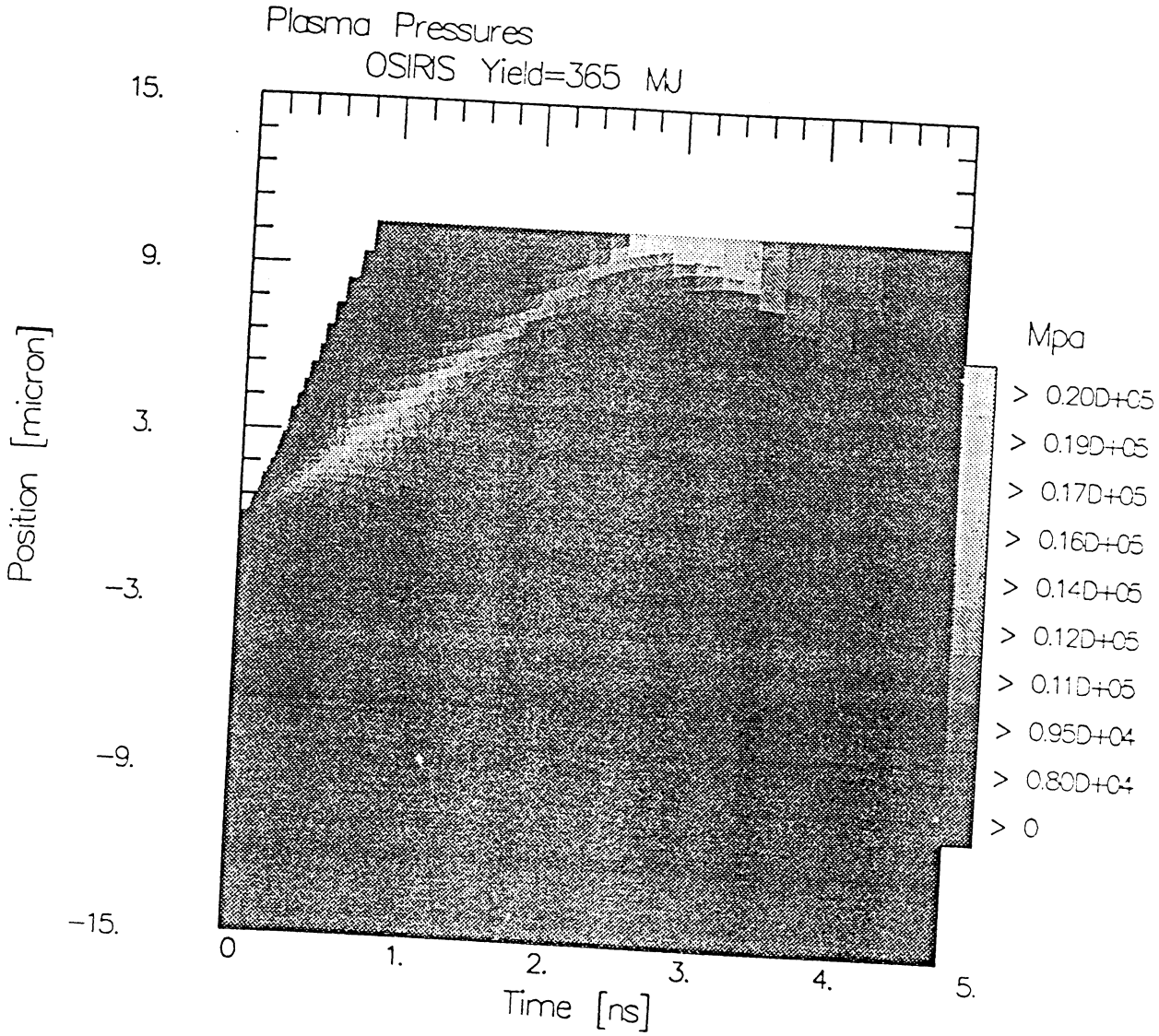

Fig. 2.8. **Pressure contours for Osiris assumed conditions overlayed on Fig. 2.7. Position equals 0 is the original position of the liquid surface of the Flibe. All other positions are in μm.**

2.2.2.4 Wall Mechanical Loading

The pressure at the interface is shown as a function of time in Fig. 2.9. The peak pressure at the interface is 31.2 GPa, which is enough to launch a shock into the liquid Flibe. The impulse at the interface is 75.6 Pa-s, so the effective pulse width is 2.4 ns. This impulse is smaller than that used in several IFE reactor designs. Since the impulse and peak pressure are proportional to the target yield, the "Base Case" impulse is estimated to be 89.5 Pa-s, and the corresponding peak pressure is 36.9 GPa.

The propagation of shocks deeper into the liquid Flibe has yet to be analyzed. Computational tools are available to analyze this, and the work has been proposed as a follow-on task. Issues to consider are the splashing of liquid Flibe from the surface and propagation to the shock into the substrate material. The splashing of Flibe could leave the substrate material unprotected from the next shot. It could also generate slow-moving droplets to interfere with the next burst of heavy-ion beams. The imparting of shock to the substrate material could damage the material over time and shorten its lifetime.

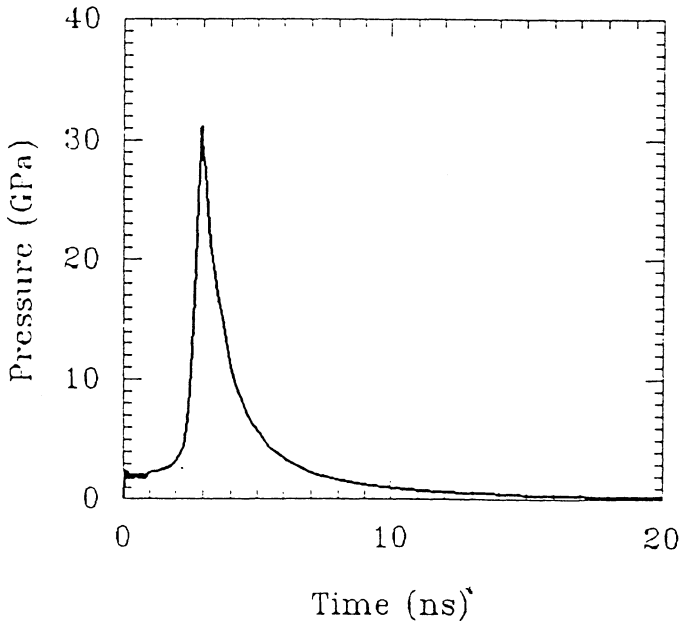

Fig. 2.9. Pressure at the vapor/liquid interface on the closest Flibe-coated wall of the Osiris target chamber.

2.2.2.5 Flibe Flow Through Fabric

The Flibe weeps through the carbon fabric to the first wall surface, as seen in Fig. 2.1, providing a protective layer. The weep rate controls the buildup of Flibe on the surface. This rate must closely match the vaporization rate from target x-ray and debris energy. Too high a weep rate will produce a thick film of Flibe, which will run down vertical surfaces and drip off horizontal ones. Too low a weep rate could leave the carbon exposed to damage.

It may actually be preferable to have too little Flibe than too much. The Flibe absorbs the softest portion of the X-ray spectrum, leaving the x-rays which pass into the lower-Z carbon harder (having higher average energy) as well as reduced in intensity. Some volumetric heating in the carbon should be acceptable, provided this heat is low enough to be conducted to the coolant without excess thermal stresses. This approach was discovered toward the end of this study, and there has not been time for any analysis; however, it seems worth pursuing.

Wetting. Flibe does not wet carbon; therefore, it would bead up on a flat plate of carbon since its surface tension, 0.2 N/m, is quite high even at 600°C. (It is about half the surface tension of mercury at 20°C.) The pore spacing in the carbon fabric can be very fine, so the Flibe may wet itself and form a uniform surface film held in place by the Flibe strands in the pores. This mode of attaching the film is critical because stress waves due to blowoff can otherwise knock the film off the carbon. While it would be quickly replaced, free-falling Flibe would be vaporized, increasing chamber density to excessive levels for beam propagation. Simple experiments using pulsed lasers could address a number of these issues.

If wetting is required to maintain the Flibe film on the carbon, a monolayer film of metal may be needed on the first wall surface. Tungsten, tantalum, and molybdenum have thermal expansion coefficients close to carbon. While this would induce some radioactivity, the volume of activated material would be small because the film is so thin. For example, with a first wall surface area of 150 m^2, a monolayer film 5Å thick would have a volume of only about 0.08 cc. How this high-Z film responds to x-ray shine-through needs to be investigated.

Flow Control. The Flibe weep rate is governed by the Flibe pressure and surface tension, and the fabric thickness and permeability. The flibe pressure ranges from 70 kPa at the top to 140 kPa at the bottom of the blanket. As mentioned, surface tension is quite high. The capillary pressure drop due to surface tension is[2.7]

$$\Delta P = \frac{4\gamma}{d}$$

where γ is the surface tension in N/m and d is the pore diameter. If d is below 10 μm, ΔP reaches the 100 kPa range and the surface tension could block the flow.

The other control variable is carbon permeability. For Reynolds numbers less than 10, which is typical, the bulk flow velocity u (= volume flow/wall area) is given by Darcy's Law[2.8]

$$u = -\frac{k}{\mu}\frac{dP}{dx}$$

where k is the permeability in m^2, μ the viscosity in newton-sec/m^2, and dP/dx the pressure gradient through the cloth in N/m^3. Permeability is often expressed in darcies (1.0 darcy = $9.875 \cdot 10^{-13}$ m^2). Note that permeability is <u>not</u> the same as porosity. Porosity ε is related to permeability k by the relation:[2.9]

$$k = \frac{\varepsilon^3 d^2}{150}.$$

A small change in porosity has a large effect on permeability. This equation is approximate and used for rough estimates only. More accurate calculations involve other features, such as connectivity and tortuosity.[2.10] The best action is to measure permeability experimentally.

As discussed in the next section, about 14 μm of Flibe are vaporized each shot, giving a recession rate at 4.6 Hz of $6.5 \cdot 10^{-5}$ m/sec (assuming no film is knocked loose by the shock waves in the Flibe). This must equal the flow velocity u above. Given a nominal pressure gradient over a 0.01 m thick wall of 10^7 N/m^3 and a Flibe viscosity of $8 \cdot 10^{-3}$ N-sec/m^2, then a cloth permeability of about $5 \cdot 10^{-14}$ m^2 (50 millidarcies) is needed. Note that this is actually 50 millidarcies per cm fabric thickness. A thicker fabric can have higher permeability.

Estimates of required fabric porosity and pore size can be made by combining the above equations, which gives a quadratic in $1/d$:

$$\frac{150\ u\ \mu\ t}{\varepsilon^3}\left[\frac{1}{d}\right]^2 + 4\ \gamma\left[\frac{1}{d}\right] - \Delta P = 0$$

Figure 2.10 shows solutions to the last equation for 2 and 10 mm fabric thicknesses. The curves

asymptote to d = 8 μm, which is the point at which capillary action blocks the flow for a nominal 100 kPa pressure drop across the fabric. Woven cloths generally have porosities of at least 10-20%. Contemporary carbon fabrics tend to be much higher, over 50%, because they are woven with the intention of being infiltrated with a matrix material like epoxy. But there is no reason why carbon can't be woven very tightly, like a seatbelt. Then porosities would be in the 10-30% range, and pore sizes could be in the 15-100 μm range, depending on fabric thickness. For example, with 2 mm thickness and 30% porosity, mean pore size must be around 15 μm. With tightly woven fabric, individual yarns are several times the pore size. In this case, yarn diameter might be in the 100 μm (.004") range, or about the thickness of ordinary sewing thread.

Considering the above, it appears likely that the proper range of Flibe weeping can be achieved with carbon cloth that is tightly woven using techniques commonly used for other cloth materials. Considerable fine tuning would be required to account for differences in pressure drop and vaporization depth at different points on the first wall. But the concept appears feasible, especially when one exploits the combined effects of permeability and surface tension.

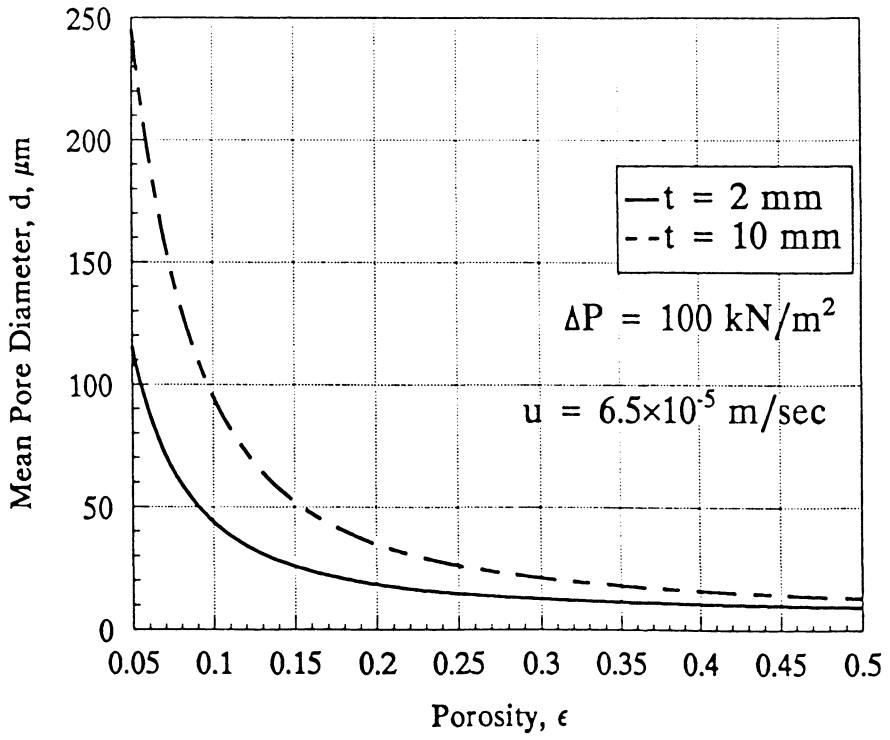

Fig. 2.10. **Allowable cloth porosity vs. pore size for two cloth thicknesses. With the nominal head of the Flibe in the blanket, flow is just sufficient to maintain a protective surface of liquid Flibe.**

2.2.2.6 Condensation of Vaporized Flibe

There are two issues relating to vapor condensation: (1) pumping of the vapor so that it contacts the cold liquid spray and pool and (2) the ability of this liquid to condense the vapor without overheating. In this section we examine these issues.

Vapor Pumping. The pumping speed, s, of the vapor through an area A just above the spray is given by[2.11]

$$S = \frac{62.5\ A_{cm^2}}{\sqrt{M}} \sqrt{\frac{T_K}{298}} \quad l/s$$

where M≈14 is the average molecular weight of dissociated Flibe, and T is the vapor temperature, about 2 eV (23,000 K). The pumpdown time, τ, is given by

$$\tau = 2.3\ \frac{V}{S} \log \left[\frac{n_1}{n_2}\right]^{1.67} \quad \text{sec}$$

where V is the vapor volume in liters, and n_1 and n_2 are the initial and final vapor densities, respectively, in m^{-3}.

With 129 MJ fusion surface energy per shot (as discussed in Section 2.2.2.3), about 4.3 kg of Flibe is vaporized. With a nominal 300 m^3 vapor volume, n_1 (of undissociated Flibe) is $6 \cdot 10^{23}$ m^{-3}. This must be brought down to $4.8 \cdot 10^{18}$ m^{-3} in the 220 msec available between shots. Using the two equations above gives τ = 60 msec, allowing plenty of margin.

Vapor Condensing. The Flibe vapor is condensed by direct contact with the spray and the pool. A number of processes are occurring here simultaneously: (1) High turbulence levels provide mixing, which reduces the liquid surface temperature; (2) The spray, pool, and the interaction between them increase the surface area available for condensation. (3) The expansion of the vapor cools it to the point of condensation into high speed droplets, which impact the pool and distribute their considerable kinetic energy to some depth. We estimate the ability of each of these processes to condense the vapor acting alone, knowing full well that there are complementary synergistic effects.

As seen above, the vapor may impact the liquid pool so quickly that condensation does not occur. If this happens, some liquid will be vaporized and condensed at a later time, thus spreading out the heating of the liquid with time.

The degree of turbulence needed in the pool depends on the heat flux and the allowable temperature rise. The target nonneutron energy is 129 MJ, all of which is assumed to go into Flibe vapor. The interpulse time is 0.22 sec. The pool disc area (ignoring the sprays for the moment) is about 95 m^2. Therefore, the needed condensing power is q_s = 6.3 MW/m^2. If the pool were quiescent, heat would be removed by thermal conduction alone, and the surface temperature rise, ΔT_s, in time, τ, would be[2.12]

$$\Delta T_s = 2\, q_s \sqrt{\frac{\tau}{\pi\ \rho\ K\ C_p}}$$

where ρ, K, and C_p are the Flibe density (2000 kg/m^3), thermal conductivity (1.0 W/m-K), and heat capacity (2380 J/kg-K), respectively. For τ = 0.22 sec, ΔT = 1520 K, an unacceptably high temperature rise. Turbulent mixing is clearly required.

A measure of turbulence is the Nusselt number Nu = hD/K, where h is the convection heat transfer coefficient and D is a characteristic dimension. This number is essentially a ratio of the apparent thermal conductivity during turbulent flow to thermal conductivity with a static liquid. Since Flibe has such a poor thermal conductivity, but has a fairly low viscosity, turbulence can greatly improve heat flow.

As seen in the above equation, surface $\Delta T \sim \sqrt{1/K}$. The Nusselt number needed to reduce the liquid surface temperature rise from 1520 K to an acceptable 50 K is then

$$Nu = \left[\frac{\Delta T_1}{\Delta T_2}\right]^2 = \left[\frac{1520}{50}\right]^2 = 900$$

This value is not difficult to achieve with Flibe. The Nusselt number is related to fluid flow by[2.13]

$$Nu = 0.036\ Pr^{0.33}\ Re^{0.8}$$

where $Pr = \mu C_p / K$ is the Prandtl number (19 for Flibe), and $Re = \rho u D/\mu$ is the flow Reynolds number with D as the channel characteristic dimension. Because of the complexity of the flow, the choice of D is not clear; but it is taken here to be 50 cm, beyond which one would expect the flow to be fully developed. The required Reynolds number for $Nu = 900$ is $Re = 95000$.

the choice of D is not clear; but it is taken here to be 50 cm, beyond which one would expect the flow to be fully developed. The required Reynolds number for *Nu = 900* is *Re = 95000.* The required characteristic velocity is only 0.8 m/sec, which would be readily exceeded. Therefore, pool turbulence alone is sufficient to condense the vapor.

The second process aiding condensation is the multiplication of the pool area by the sprays and the impact of the sprays on the pool. The relationship between temperature rise and heat flux given earlier can be used to calculate the required surface area. To reduce the surface ΔT from 1520 to 50 K, would require a heat flux reduction of about 30 to 1. This is the increase in surface area from the sprays and splashing required relative to a flat pool surface. This intuitively appears a little high, and it is unlikely that area multiplication alone can condense the vapor. It should, however, assist the other mechanisms.

The third condensation mechanism deals with the observed fact[2.14] that expanding blowoff vapor cools adiabatically and condenses to form high-speed droplets. These can impact the pool and distribute their energy to a considerable depth. The depth δ required to limit temperature rise to 50 K is

$$\delta = \frac{E_{surf}}{\rho\, A_{pool}\, C_p\, \Delta T}$$

which, for 129 MJ target surface energy, is about 6 mm. This depth is small enough that it appears to be achievable.

The combination of mechanisms discussed above appear likely to provide condensation of the vaporized Flibe within the interpulse time. In fact, droplet impact alone may be enough, which would eliminate the need for high pressure sprays. Simple experiments would provide much of the necessary data to determine which of the mechanisms discussed above are required.

2.2.3 First Wall Design

2.2.3.1 Fabrication and Assembly

The first wall is integral with the blanket support and consists of tightly-woven carbon cloth. Three cloth layers are used to make up the two Flibe flow channels, and front and back are stitched together with cloth radial cross members. This is shown in Fig. 2.11. Note that it resembles an air mattress in cross section. It looks externally like a peeled orange. This arrangement minimizes tensile stresses in the cloth from the Flibe pressure.

The critical radius for tensile stress is the radius of curvature for the individual blanket cells, and this varies with azimuthal angle reaching a maximum at the equator. If the radius of curvature is 2 m there, then a 5 mm thick cloth is stressed in tension to about 100 MPa with a Flibe pressure of 250 kPa. The flow contribution is negligible compared to the static pressure. This assumes an inlet duct pressure of 70 kPa. This is only about 5% of the strength of the P-100 fiber that is discussed below.

2.2.3.2 Expected Neutron Lifetime

An example carbon fiber that would work here is P-100, made by Union Carbide. It has shown very good resistance to fast neutrons to a fluence of $5 \cdot 10^{21}$ n/cm^2. As shown in Table 2.5, irradiation leads to little dimensional or modulus change, and actually increases strength. This is just one of many types of carbon fibers that may be suitable. Another is vapor-grown carbon fiber, developed by Endo in Japan and General Motors.[2.15] Versions of this fiber have also been tested under neutron irradiation[2.16] and perform even better than P-100.

Table 2.5. Neutron Irradiation Data for P-100 Carbon Fibers

Maker	Union Carbide
Type fiber	P-100
Annealing temperature	3100°C
Exposure temperature	620°C
Total neutron dose	$5 \cdot 10^{21}$ n/cm^2
Neutron energy	> 50 keV
Length change	-1.1%
Diameter change	+1.5%
Modulus before irradiation	586 GPa
Modulus after irradiation	565 GPa
Tensile strength before irradiation	2.0 GPa
Tensile strength after irradiation	2.4 GPa

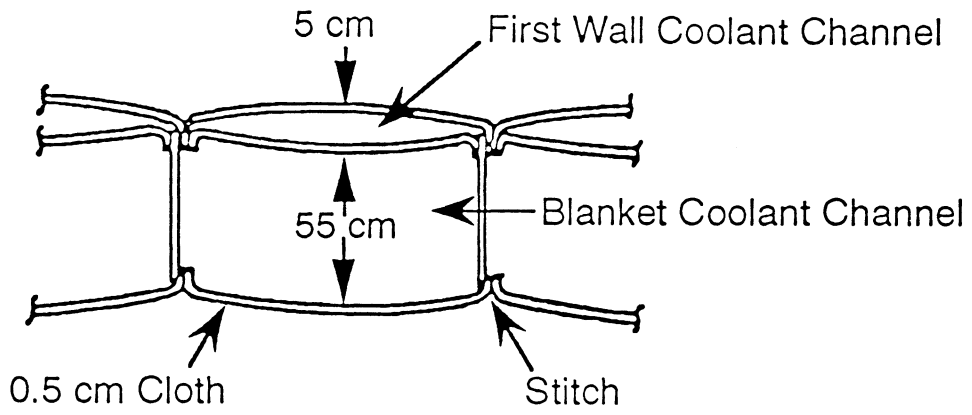

Fig. 2.11. Air mattress cross section of the blanket used to minimize hoop stresses.

2.2.3.3 Changeout Procedure

As discussed above, it is expected that the Osiris blanket will have to be changed out about once a year. An advantage of this concept is that the entire lightweight assembly, drained of Flibe, can be removed from the top. Routine in-chamber access is not required. The steps in this process are listed below.

1. After reactor shutdown, the Flibe is automatically drained through small holes in the blanket into the pool. Some recirculation of the Flibe may initially be required until the short-term afterheat has dissipated from the blanket fabric. Heaters in the bottom of the pool keep that Flibe molten, but any Flibe remaining in the blanket fabric is allowed to solidify. Since Flibe does not wet carbon, little will remain anyway. (5 days effort)

2. The low and high pressure Flibe inlet pipes at the top of the reactor are disconnected. To avoid interference, the break point in the upper pipe must be further from the reactor centerline than the lower, and both must clear the vacuum chamber cover. (2 days)

3. The vacuum chamber cover is unbolted from the vacuum chamber. (3 days)

4. The vacuum chamber cover is lifted out and the attached drained blanket fabric, supports, and high pressure manifold are transported to the hot cell. Note that all the interior

hardware clears the driver focussing magnets. After cooldown, the fabric structure along the first wall can be removed and prepared for shallow burial storage. The remaining hardware that was shielded from the primary neutrons, including the high pressure manifold, can probably be reused after refurbishing. (3 days)

5. The new blanket assembly and vacuum chamber cover are installed simply by lowering it into place, reversing the steps above. To avoid cold-trapping, the Flibe in the pool is heated to at least 100° above melting before circulating. (5 days)

The total elapsed time is estimated at 18 days, giving an availability loss of 5%. During that time, other non-interfering maintenance can also be performed. In addition to the reactor hall, a hot cell room, a spare blanket storage room, and a new blanket assembly room are needed. The first three rooms will each be 16 by 16 meters, and the new blanket assembly room will be 16 by 32 meters. The increased size of the assembly room allows for large component laydown space prior to assembly. Some of these activities can take place in the same area at different times.

2.2.4 Blanket Design

2.2.4.1 Use of Flibe

Two great advantages of flowing lithium-bearing coolants are the simplicity of the blanket and the fact that only an empty shell needs to be periodically changed out. For the pulsed loadings inherent in IFE, a further advantage is the ability of the coolant to carry damaging shocks away from the first wall and dissipate them. This occurs because shocks from x-ray blowoff are very short in duration. As they propagate, they automatically spread out and diminish in amplitude. Because Flibe and graphite have comparable acoustic impedances, relections at interfaces are minimal.

There are three coolant choices: pure lithium, lithium-lead ($Li_{17}Pb_{83}$) or Flibe (Li_2BeF_4). The first two could certainly be considered, but lithium is very reactive and is very combustible in air, and lithium-lead has high density and a problem with activation of the lead. Flibe, on the other hand, is quite inert; the activation of fluorine is much less than that of lead. Flibe also makes a good coating material for the first wall because its combination of low atomic number and low vapor pressure allows its use at high temperatures and low chamber pressures needed for heavy-ion beam transport.

Table 2.6 shows pertinent properties of Flibe. It has a high melting point, 460°C, but a low thermal conductivity, 1.0 W/m-K. While it will be necessary to keep pools of it molten during down periods, the heat that must be supplied should not be great. In the event of loss of flow, the system should be designed to automatically drain Flibe out of the ducting into the pool or a separate hotwell. This can be done for ducts above the reactor by having small permanent drain holes in the bottom of the blanket. During operation, the Flibe flowing through these holes would be negligible compared to the volume of Flibe flowing through the blanket. To drain all of the ducting and the IHX to the pool would require the reactor to be the lowest point, which would be rather inconvenient. Alternately, ducts can be jacketed to accept hot gas or liquid heating. in any case, with good insulation and the poor Flibe conductivity, the amount of heating needed should be small.

Table 2.6. Properties of Liquid Flibe[2.17]

Percent LiF	67
Percent BeF_2	33
Melting Temperature	459°C
Density	2000 kg/m^2
Specific Heat	2380 J/kg-K
Thermal Conductivity	1.0 W/m-K
Viscosity at 600°C	$8 \cdot 10^{-3}$ Pa-s
Prandtl Number at 600°C	19
Heat of Fusion	448 kJ/kg
Heat of Vaporization	5.54 MJ/kg
Surface Tension at 600°C	0.2 N/m
Approx Cost for Large Quantities	$84/kg

The viscosity of Flibe is about that of liquid water at room temperature. The high Prandtl number is due to the low thermal conductivity. Convective heat transfer coefficients can be quite high, and Flibe is actually a fairly good convector of heat although it is a poor conductor.

The surface tension is quite high, about half that of mercury at room temperature. This feature was exploited to limit the weep rate through the first wall fabric. Because Flibe does not wet carbon, a thin metal coating may be needed to get a uniform film on the surface, as discussed earlier in this chapter.

2.2.4.2 Flibe Flow Issues

Low Pressure Flibe. After the initial vaporization of surface Flibe, further vaporization occurs until an equilibrium pressure is reached where the saturation temperature at the liquid Flibe surface corresponds to the Flibe vapor pressure in the chamber. As discussed above, the acceptable density for beam propagation corresponds to a Flibe saturation temperature of 570°C. The bulk Flibe temperature below the surface must be below this or equilibrium will be reached at a higher temperature. This is the reason for the two flow channels in the blanket. The Flibe in the first, very thin channel, is moving very quickly, picks up little neutron heating, and increases to only 520°C. Most of the neutron heat is picked up by the Flibe in the second, much slower, pass up the back of the blanket.

The Flibe in the high-speed channel has a nominal Reynolds number of 66,000, making it quite turbulent. Heat transfer to the first wall channel is low, because most of the nonneutron energy goes to the pool. The hydrostatic head from top to bottom of the blanket is 137 kPa, compared to 49 kPa flow pressure drop in the first channel. The second figure is then the required inlet pressure to the blanket. After the second turn, the flow pressure drop is nil, and with the 49 KPa inlet pressure, the Flibe exits into vacuum at zero pressure. There would be no difficulty in increasing the Flibe pressure in the blanket to have some residual pressure so that the Flibe exiting the blanket can be sprayed into the vacuum, enhancing tritium release.

High Pressure Flibe. Flibe enters the reactor chamber in two flow streams: the low pressure blanket stream discussed above and the high pressure stream that sprays into the pool. The high pressure is due to the short in-flight time needed to keep the spray from overheating. This time is taken to be 0.13 sec, about half the dwell time between shots. Since it must traverse about 6 m, the spray velocity is 46 m/sec. The nozzle pressure is $\rho u^2/2$ = 2.1 MPa.

The spray supplies all of the pool flow; the side blanket is dumped directly to the exit manifold. The pool absorbs all of the nonneutron energy plus about 12% of the neutron energy, for a total power of ~950 MW. The desired exit temperature is 650°C. But another 5.5% of the neutron power is absorbed in the annular exit manifold. The design exit temperature from the pool should then be about 640°C. For this 140° temperature rise, the mass flow in the spray must be ~2300 kg/sec. The ideal pumping power for the spray is 3.0 MW. Note that this power is also counted as heat addition.

2.2.4.3 Blanket Changeouts

The key blanket issues during changeout are draining of the Flibe in the blanket and upper ducting, and preventing solidification of Flibe remaining in the pump and IHX. Fortunately, Flibe is such a poor conductor that solidification takes a long time. For example, it can be shown[2.9] that, in an uninsulated 1.0 m diameter duct carrying Flibe at 500°C, at least one week would be needed to cool the Flibe half way through to the solidification temperature. Adding insulation and accounting for the latent heat of fusion should increase this time several fold. At the worst, insulated ducts wrapped in heater tape will keep the Flibe liquid. With 20-cm-thick pipe insulation, heater tape must supply a modest 200 W/m^2.

The Flibe in the pool can be maintained liquid by heating elements at the bottom. Even if the top surface solidifies, solid particles will sink and provide circulation for the heater. Because hot Flibe vapor can get into the building atmosphere while the cover is off, some sort of filtration system will be needed.

2.2.5 Vacuum Vessel Design

2.2.5.1 Description of Vacuum Vessel

The vacuum vessel is 13 m diameter by 11 m high. It consists of a 5 cm thick cylinder 8.5 m high, a 13 m diameter base 7 cm thick, and a 13 m diameter conical cover 2 m high that is also 7 cm thick. Loads from the one atmosphere overpressure are compressive and quite low, about 14 MPa. It is shielded from both primary and secondary neutrons by the main and cascade flow blankets. It should, therefore, last the life of the plant.

2.2.5.2 Vacuum Vessel Materials

There is a wide variety of acceptable materials for the vacuum vessel, although there will be enough neutron fluence that low activation materials are preferred. Because it is in contact with the Flibe, the chamber will run quite hot. One material that will work is carbon or silicon carbide composite with the inevitable porosity sealed by infusing it with Flibe. As long as the outside of the vessel remains below 460°C, the Flibe will stay solid and provide a vacuum seal. The total chamber mass is about 80,000 kg. Assuming a unit cost of the composite to be $100/kg, the total vacuum vessel cost is about $8 million.

There are certainly other material choices, such as austenitic or ferritic stainless steels, which are less expensive and easier to fabricate. While they will last the life of the plant, they will introduce a substantial gamma ray source that will require additional shielding. There are a number of possible vessel design options, so the choice of vessel material is not an important feasibility issue for the Osiris design.

2.2.6 Neutronics Analysis

2.2.6.1 Neutronics Model and Assumptions

Neutronics analysis was performed using a spherical geometry model to simulate the Osiris fusion power reactor. The compressed DT target was included in the neutronics calculations with the DT source neutrons uniformly distributed in a 0.1 mm radius region of DT at 300 g/cm^3 density. Target materials surrounding the DT core are not included in the model due to their small impact on neutronic parameters. Neutronics calculations were performed with the one-dimensional discrete ordinates transport code ANISN.[2.18] A coupled 30 neutron - 12 gamma group nuclear data library, MATXS5, based on ENDF/B-V cross section files was employed.[2.19] All calculations were performed with P_3S_8 approximations.

Table 2.7 shows the regional dimensions and materials in a spherical geometry model used for scoping and optimization analyses.

2.2.6.2 Blanket Design Optimization

Neutronics calculations were performed parametically (varying the blanket thickness x) for the scoping model shown in Table 2.7. The results are presented in Figs. 2.12 - 2.15 and discussed below.

Figure 2.12 depicts the tritium breeding ratio (TBR) and overall energy multiplication of the scoping Osiris system as a function of total Flibe zone thickness. Note that the overall energy multiplication, M_o, here is defined as the total energy deposited per DT reaction divided by 17.6 MeV. The total energy includes neutron energy deposited in the target, blanket, and other structures, and the alpha particle energy. In these calculations, natural lithium (7.42% in^{6}Li) is employed. (Enriching in ^{6}Li to 20% would probably give bettter results when the Flibe zone thickness is less than 0.5 m.)

Two observations can be made for TBR and M_o: (1) In addition to the graphite vessel, which is 0.2 m thick, a graphite reflector/shield would be helpful in enhancing both TBR and M_o, particularly when the total Flibe zone thickness is less than 0.5 m, and (2) the TBR and M_o are near their asymtotic values when the total Flibe zone thickness is >0.5 m.

Table 2.7. Osiris Neutronics Problem Description

Geometry: 1-D spherical

Region	Description	Material	Inner radius (cm)	Outer radius (cm)	Thickness (cm)
1	Target	DT	0.0	0.01	0.01
2	Inner vacuum	Flibe Vapor	0.01	350.0	350.0
3	Surface Film	Liquid Flibe	350.0	350.2	0.2
4	Panel inner wall	Carbon Fabric	350.2	350.5	0.3
5	Panel coolant	Liquid Flibe	350.5	365.5	15.0
6	Panel outer wall	C-fabric	365.5	365.8	0.3
7	Spray zone	Flibe vapor	365.8	450.0	84.2
8	Neutron blanket wall	C-fabric	450.0	450.3	0.3
9	Neutron blanket	Liquid Flibe	450.3	450.3 + x	x
10	Vessel wall	Carbon	450.3 + x	470.3 + x	20.0

Materials Compositions

Material	Density (g/cm^3)	Element	Atom Fraction
Target	300.0	D	0.5
		T	0.5
Flibe	2.0	^6Li	0.0211
($2LiF + BeF_2$)		^7Li	0.2646
		F	0.5714
		Be	0.1429
Carbon fabric	1.7	C	1.00
Carbon vessel	1.7	C	1.00

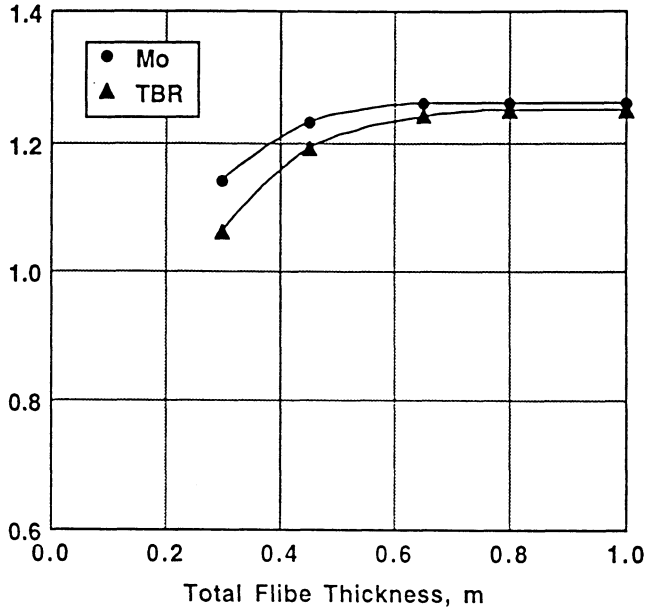

Fig. 2.12. Tritium breeding ratio and overall energy multiplication factor as a function of Flibe thickness.

Figure 2.13 gives the nuclear energy deposited in the graphite vessel and total energy leakage as a function of total Flibe zone thickness. The total energy leakage converges to the energy deposited in the vessel when the total Flibe zone thickness is thick enough.

Observations obtained from the analysis shown in Fig. 2.13 are (1) the energy leakage decreases as the total Flibe zone thickness increases, and (2) the nuclear energy deposited in the vessel is 20 MW when the total Flibe zone thickness is 0.5 m (0.35 m neutron blanket, Region 9). Note that here we assume the total fusion power in the scoping Osiris is 2200 MW; after further analysis, the reference fusion power level was reduced to ~2000 MW. The energy deposited in the vessel represents only 0.75% of the total thermal energy when the total Flibe zone thickness is 0.5 m.

Figure 2.14 displays the spatial power density distribution in the scoping Osiris reactor components. The total fusion power assumed is 2200 MW, and the total Flibe zone thickness is 0.45 m. The maximum power densities in the carbon fabric, Flibe, and the graphite vessel are ~ 34, 70, and 1 w/cm^3, respectively. Maximum neutron wall looking at the first wall is 9 MW/m^2.

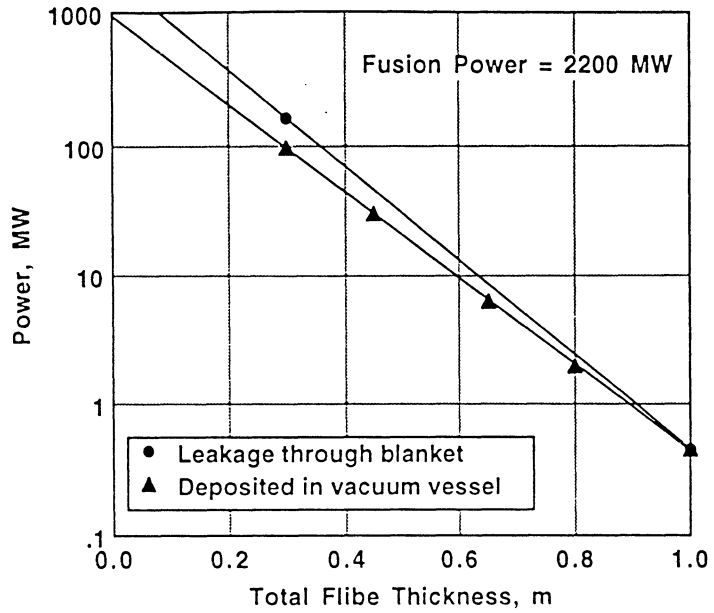

Fig. 2.13. Nuclear power leakage and the vacuum vessel heating as a function of Flibe thickness.

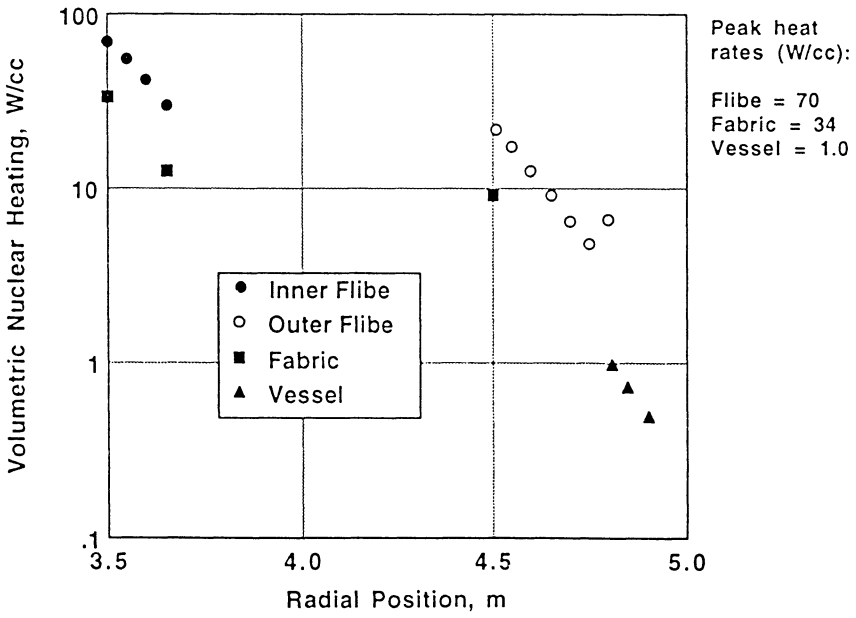

Fig. 2.14. Power density distribution for a 0.45m-thick Flibe blanket.

Figure 2.15 shows the radiation damage parameters in the vessel (maximum numbers) as a function of total Flibe zone thickness. We may conclude that, based on the scoping and optimization design analysis, a design with 0.5 m total Flibe zone thickness is adequate for Osiris.

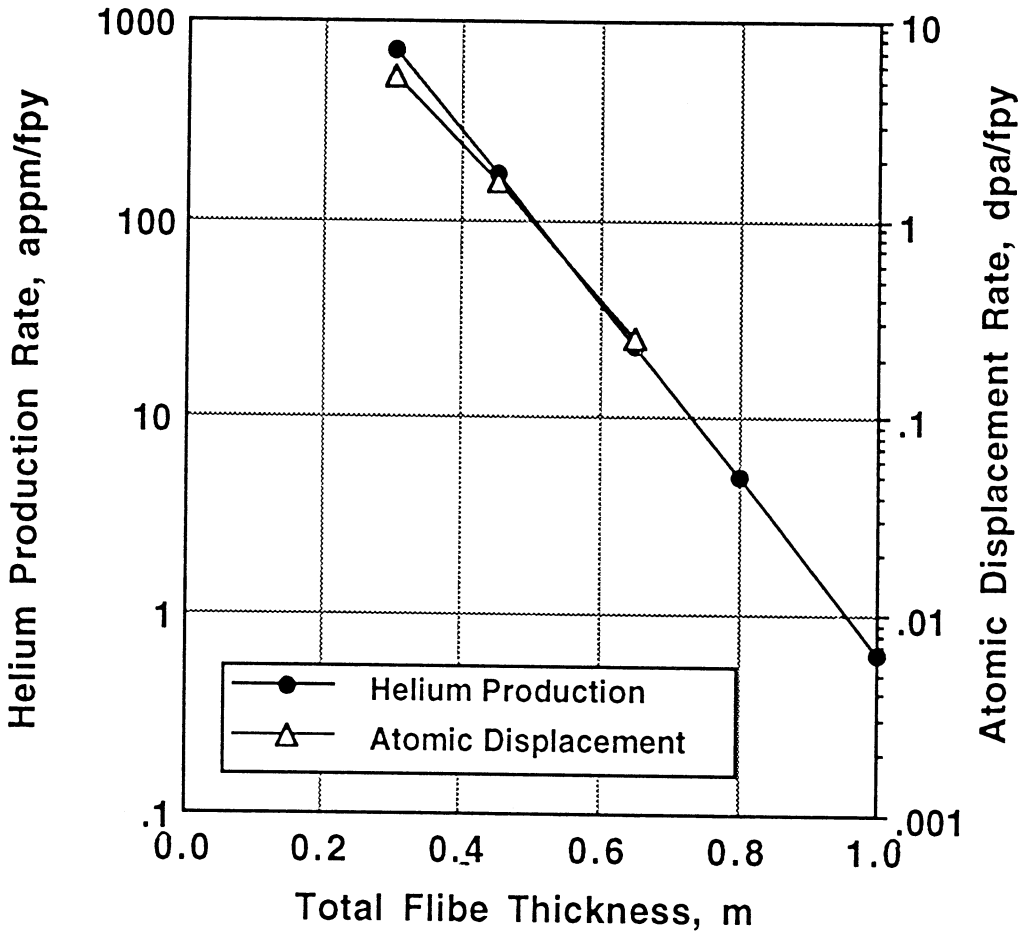

Fig. 2.15. Radiation damage parameters in the vessel as a function of total Flibe zone thickness.

2.2.6.3 Neutronics Parameters for Reference Design

Based on the scoping and optimization design analysis performed in Section 2.2.6.2, and other design requirements, the reference Osiris design was determined. Table 2.8 shows the regional dimensions and materials for the reference design. Note that the total Flibe zone thickness in the reference design is 70 cm, more than enough to optimize the nuclear performance of the blanket and provide attenuation protection of the vacuum vessel. Table 2.9 summarizes the tritium breeding and nuclear heating rates in the reference Osiris design.

As shown in Table 2.9, the total tritium breeding ratio is 1.24 tritons/DT neutron, which is more than adequate. The tritium production rate from $^{6}Li(n,\alpha)T$ reaction (T6) is 1.099, while it is 0.137 from $^{7}Li(n,n'\alpha)T$ reaction (T7). The total nuclear heating rate in the Flibe coolant and carbon-carbon composite structure (including the vacuum vessel) is 17 MeV/DT neutron. The nuclear energy deposited in the DT target is 1.75 MeV/DT neutron which will be carried by the target debris to the Flibe first wall film. The sum of the neutron energy deposited in the target is 18.75 MeV/DT neutron. (This results in a target/blanket energy multiplication of 1.33.) If alpha particles are accounted for, the total thermal energy to be removed by the Flibe coolant will be 22.25 MeV per DT neutron (or per fusion reaction). The total energy multiplication M_o, is 1.26, as shown in Table 2.9. Figure 2.15 displays spatially the volumetric nuclear heating rates in the various reactor components.

Table 2.10 gives the maximum helium production and atomic displacement rates in the carbon-carbon composite fabric and vacuum vessel components. for the Osiris reference design. As shown, the maximum atomic displacement rates in the carbon-fabric first wall and vacuum vessel are 42 and 0.14 dpa per full power year, respectively, while the corresponding helium production rates are 10,600 and 6.1 ppm per full power year, respectively.

2.2.6.4 Biological Shielding

The biological shielding is an important component to protect the working personnel outside of the reactor chamber, where the biological dose rate during reactor operation should not exceed 2.5 mR per hour. In the Osiris reference design, a steel- reinforced concrete shield (20% mild steel, 70% concrete, and 10% void for gas coolant) of 3 m thick is considered as the biological shield. It is located at 10 m from the target location. Using the concrete and steel compositions given in Table 2.11 we have estimated the operating dose rates outside the concrete shield, as well as behind the carbon vacuum vessel (reactor chamber).

The operating biological dose rate behind the concrete wall is estimated to be about 1.7 mR/h at a fusion power level of 2000 MW. Most of which, about 94%, is due to neutrons. This level of dose rate is lower than the limit, 2.5 mR/h. The biological dose rate behind the chamber, however, is about 55 MR/h which is more than 10 orders of magnitude higher than acceptable.

2.2.6.5 Lifetime of Chamber

The radiation damage parameters are shown in Table 2.10, Sec. 2.2.6.3. The atomic displacement and helium production rates in the carbon vacuum vessel are 0.14 dpa and 6.1 ppm per full power year, respectively. The vacuum vessel will last the entire lifetime of the Osiris reactor, since the accumulated displacements per atom there (5.6 for 40 full power years) is more than a factor of 10 lower than the estimated limit, 75 dpa. However, the layers of carbon fabrics inside the vacuum vessel will have to be frequently replaced (every 1.8 full power year) because the maximum atomic displacement rate is 42 per full power year.

Table 2.8. Neutronics Model for the Reference Osiris Design
Geometry: 1-D spherical

Region	Description	Material*	Inner radius (cm)	Outer radius (cm)	Thickness (cm)
1	Target	DT	0	0.01	0.01
2	Inner vacuum	Flibe vapor	0.01	350.0	350.0
3	Surface film	Liquid Flibe	350.0	350.2	0.2
4	First inner wall	Carbon fabric	350.2	350.7	0.5
5	First wall coolant	Liquid Flibe	350.7	355.7	5.0
6	Neutron blanket wall	Carbon-fabric	355.7	356.2	0.5
7	Neutron blanket	Liquid Flibe	356.2	411.2	55.0
8	Neutron blanket wall	Carbon-fabric	411.2	411.7	0.5
9	Cascade repair	Liquid Flibe	411.7	421.7	10.0
10	Spray zone	Flibe vapor	421.7	680.0	258.3
11	Vacuum vessel	Carbon	680.0	700.0	20.0

*Material compositions are the same as in Table 2.7.

Table 2.9. Tritium Breeding and Nuclear Heating Rates in the Reference Design (Natural Lithium in Flibe)

Tritium Production Rate (T/DT Neutron)	**T6**	**T7**	**TT**
Region 3 (Surface Film)	0.008	0.002	0.010
Region 5 (1st Wall Coolant)	0.197	0.042	0.239
Region 7 (Neutron Blanket)	0.873	0.093	0.966
Region 9 (Cascade Repair)	0.021	< 0.001	0.021
Tritium Breeding Rates	1.099	0.137	1.236

Nuclear Heating Rate	**(MeV/DT Neutron)**
Region 1 (DT Target)	1.753
Region 3 (Flibe)	0.181
Region 4 (C-Fabric)	0.210
Region 5 (Flibe)	4.215
Region 6 (C-Fabric)	0.168
Region 7 (Flibe)	12.03
Region 8 (C-Fabric)	0.0032
Region 9 (Flibe)	0.156
Region 11 (Carbon Vessel)	0.0349
Total Energy due to DT Neutrons	18.75
M_b (Blanket + Target Energy)/14.1	1.33
Total Thermal Energy (with α particles)	22.25
M_o (Total System Energy)/17.6	1.26

Table 2.10. Radiation Damage Parameters in Carbon Fabric and Vacuum Vessel (2000 MW Fusion Power; Osiris Reference Design)

Region	Helium Production Rate (ppm/FPY)	Atomic Displacement Rate (dpa/FPY)
4 Carbon Fabric	10,600	42
11 Carbon Vacuum Vessel	6.1	0.14

[FPY = Full Power Year]

Table 2.11. Compositions of Steel and Concrete Shield Materials (atom densities, x 10^{24} atoms/cm^3)

Mild Steel (100%)			
C	7.85×10^{-4}	N	2.36×10^{-5}
Al	5.89×10^{-5}	Si	5.21×10^{-4}
Mn	4.46×10^{-4}	Fe	8.35×10^{-2}
Cu	1.19×10^{-4}		
Concrete (100%)			
H	1.04×10^{-2}	^{10}B	3.59×10^{-4}
^{11}B	1.44×10^{-3}	O	3.94×10^{-2}
F	2.26×10^{-4}	Na	9.83×10^{-4}
Mg	1.77×10^{-4}	Al	4.43×10^{-4}
Si	2.2×10^{-3}	S	5.33×10^{-3}
Ca	2.92×10^{-3}	Fe	7.32×10^{-4}

2.2.6.6 Shielding of the Final Focusing Magnets

Five superconducting quadrupoles are arranged along each beam line to focus the ion beam onto the target. Adequate shielding should be provided to protect the final focusing magnets from the streaming radiation. In a previous study,[2.20] it was shown that radiation effects in the magnets can be reduced significantly by tapering the inner surface of the shield along the direct line-of-sight of source neutrons in both the quadrupole and drift sections with all direct neutrons impinging on neutron dumps located in the drift sections between the quadrupoles. This results in increasing the minimum distance between the magnet and the point on the surface of the shield where the source neutrons have their first collision. It was shown that these modifications in the shield shape result in about three orders of magnitude reduction in peak magnet radiation effects compared to the traditional flat shield. A similar shield configuration is adopted to protect the final focusing magnets of Osiris.

The inner dimensions of the magnet shield along the beam lines were determined such that the shield does not interfere with the ion beams. The beam envelopes in the x and y directions have been utilized to determine the shield configuration. The shield is tapered along the direct line-of-sight of source neutrons generated in the target such that no direct source neutrons will impinge on the shield in the magnet sections. The shield configuration for the final focusing magnets is shown in Fig 2.16. The configuration is given for both the x and y directions. Notice that different scales are used for distances along the beam axis and in directions perpendicular to the beam axis. Three neutron dumps are utilized at distances of 25, 45, and 60 m from the target. Because of the relatively large beam envelope in the x direction, providing adequate shielding in this direction was given higher priority. A minimum shielding thickness of 0.3 m is maintained for the quadrupoles in this direction. In the y direction, the smaller beam envelope allows for thicker shield for the quadrupoles Q2, Q3, and Q4 as shown in Fig. 2.16. The inner bore radii and minimum shield thickness for the final focusing magnets are given in Table 2.12. Three-dimensional neutronics calculations have been performed for the HIBALL-II[2.3] final focusing magnets. A shield consisting of 63% 316 SS, 15% Pb, 17% B_4C, and 5% H_2O was used. 15 cm of this shield result in an order of magnitude radiation attenuation. Using the Osiris fusion power, magnet distances from target and minimum shield thicknesses, Table 2.13 gives the peak magnet radiation effects in the final focusing magnets of Osiris.

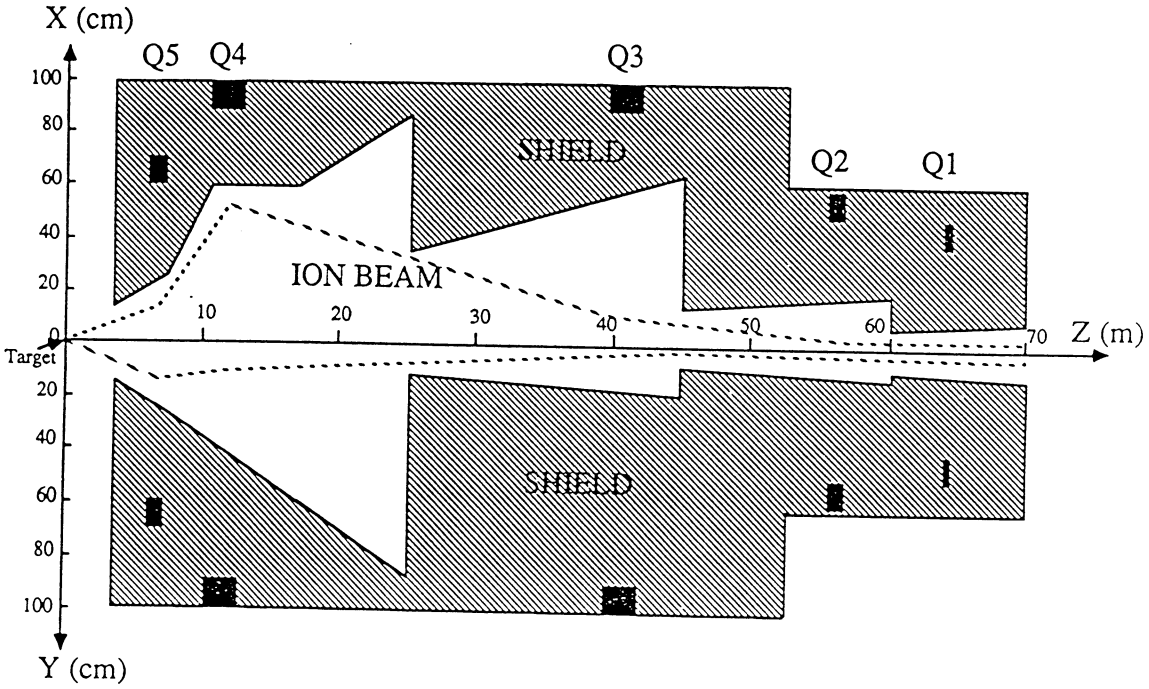

Fig. 2.16. Shield configuration for final focusing magnets of Osiris.

Table 2.12. Bore Radii and Shield Thicknesses for the Final Focusing Magnets

Magnet	Inner Bore Radius (m)	Minimum Shield Thickness in x Direction (m)	Minimum Shield Thickness in y Direction (m)
Q1	0.4	0.31	0.31
Q2	0.5	0.30	0.40
Q3	0.9	0.30	0.73
Q4	0.9	0.34	0.47
Q5	0.6	0.36	0.36

Table 2.13. Peak Radiation Effects in the Final Focusing Magnets

Magnet	Peak Cu dpa/FPY	Peak Magnet Power Density (mW/cm^3)	Peak Insulator Dose (rads @ 30 FPY)[a]	Peak Fast Neutron Fluence (n/cm^2 @ 30 FPY)[b]
Q1	1.1×10^{-7}	7.2×10^{-5}	7.7×10^{6}	6.0×10^{15}
Q2	1.9×10^{-7}	1.2×10^{-4}	1.2×10^{7}	9.2×10^{15}
Q3	3.4×10^{-7}	2.0×10^{-4}	2.1×10^{7}	1.7×10^{16}
Q4	2.1×10^{-6}	1.2×10^{-3}	1.3×10^{8}	1.0×10^{17}
Q5	5.0×10^{-6}	2.9×10^{-3}	3.0×10^{8}	2.4×10^{17}

[a] Limit ≈ 10^9 - 10^{10} rads
[b] Limit ≈ 10^{19} n/cm^2

The magnet radiation effects are the highest in the magnet closest to the target (Q5). The peak dpa rate in the copper stabilizer is only 5×10^{-6} dpa/FPY implying that radiation induced resistivity at end-of-life (30 FPY) is only 0.1 nΩ-m.[2.21] Hence, magnet annealing is not required during the reactor lifetime.[2.21] Experimental results with 5 K irradiation of epoxy and polyamide insulators indicated that the insulator retains 75% of its mechanical strength with doses up to 10^9 and 10^{10} rads, respectively.[2.22] The peak end-of-life insulator dose in Q5 is 3×10^8 rads implying that either epoxy or polyamide can be used for electric insulation. Currently available irradiation data indicate that end-of-life fast neutron fluences up to 10^{19} n/cm^2 ($E > 0.1$ MeV) will not result in significant degradation in the Nb_3Sn critical properties.[2.23] The results in Table 2.13 indicate that the peak fast neutron fluence levels in the magnets are well below the design limit. The peak winding pack nuclear heating is very small. The total nuclear heating in the five magnets along each beam line is estimated to be only about 1 W. Hence, the proposed magnet shield configuration will provide adequate protection for the final focusing magnets from streaming radiation.

2.2.7 Tritium Recovery and Containment

2.2.7.1 Potential Chemical Reactions of Flibe

Irradiated Liquid Flibe. The fused salt system LiF-BeF_2 was extensively studied at ORNL for use in the Molten Salt Breeder Experiment[2.24] because of its low activation, high thermal stability, and low vapor pressure. The phase diagram indicates[2.25] a eutectic composition at 53 mole % BeF_2 and 364°C; however, because of the high BeF_2 content, this composition has an extremely high viscosity. The compound Li_2BeF_4 (known as Flibe) melts at 459°C, has a lower viscosity, and was used in the experimental fission reactor studies to dissolve the fuel UF_4.

The Molten Salt Breeder Experiment noted only light corrosion of the Ni-base alloys and graphite in contact with the molten salt containing fissionable UF_4. The Flibe utilized Li7 so that tritium was produced only by the ternary fission of U-235 (1 atom/10,000 fissions). The neutronic reactions in an IFE reactor are different, however. An IFE breeder generates 1 atom T/fusion neutron by the nuclear reaction $^6Li(n,\alpha)T$ with thermal neutrons forming copious amounts of TF, which may react with the metallic, SiC, or carbon (graphite) structures. The potential corrosion reactions were assessed by use of the thermodynamic free-energy[2.25,2.26,2.27] changes from reactants to products tabulated at 1000 K, as follows, based upon the use of HF data for TF.

Potential reactions by TF:

1. $SiC + 4TF = SiF_4 + C + 2T_2$; ΔG = -660 kJ/mole

   This reaction is favored to go to completion.

2. $C + 4TF = CF_4 + 2T_2$; ΔG = +40 kJ/mole

   This reaction is slightly unfavorable but could progress if gaseous T_2 and CF_4 were less soluble in the salt than TF and were removed in the off-gas system.

3. $2\ TF + Fe = FeF_2 + T_2$; ΔG = -152 kJ/mole

   This reaction is favored to go to completion so that steel structures can not be used in the presence of TF. This reaction can be prevented by coating all the metallic structure with Mo or W. A technique was developed in which a Mo coating was formed in situ by dissolving a small amount of MoF_6 in the molten salt so that the MoF_6 was reduced as the Fe was oxidized to FeF_2. The reaction continued until all the surfaces were covered

with Mo and could be repaired as needed. This technique, however, introduces FeF_2 and Mo into the salt phase, which results in the irradiation of Mo forming undesirable radioactive products. In addition, providing a Mo coating in the presence of carbon fibers, as utilized in Osiris, is not possible.

It would be very desirable to prevent the corrosion of steel components which may be used in the heat transfer system and SiC or carbon which could be used as first-wall materials. In order to prevent this corrosion, the compound TF in solution needs to be destroyed before it comes in contact with the structural materials. This can be accomplished easily by placing sacrificial Be spheres in the exit flow of the molten salt from the reactor. As was demonstrated for the MSBRE, the Be reduces all species in solution except LiF. The accumulating concentration of BeF_2 would be adjusted in a fuel clean-up side-stream in which new LiF will need to be added at its burn-up rate.

Another type of nuclear transformations with 14 MeV neutrons can cause further chemical corrosion of the structure. For instance, in an IFE reactor, neutrons above the 2.2 MeV threshold energy react with Be (which is unlikely in a fission reactor) by the nuclear reaction,

$$BeF_{2(liq.)} + n = 2n + 2^4He(g) + F_2(g)$$

The free fluorine gas would react rapidly with SiC, carbon, or metallic structures to form the corresponding fluorides: SiF_4, CF_4 and metallic fluorides, as shown by the following free-energy changes @ 1000 K.

$$\begin{aligned} C + 2F_2 &= CF_4 && \Delta G = -774 \text{ kJ/mole} \\ SiC + 2F_2 &= SiF_4 + C && \Delta G = -1407 \text{ kJ/mole} \\ Fe + F_2 &= FeF_2 && \Delta G = -559 \text{ kJ/mole} \end{aligned}$$

This nuclear transformation would be enhanced closest to the first wall where the neutron energies are highest; consequently, the chemical attack would be greatest on the first wall materials.

Flibe Decomposition by Target X-rays. Potential chemical reactions may occur at an ablated first wall wetted with liquid Flibe. These reactions are caused by radiolytic products formed by the absorption of x-rays emitted from the burning target, which carry nearly 20% of the energy (~400 MW) at x-ray energies from 10 keV to 10 MeV. On the other hand, the chemical binding energy in the molecules of Flibe composition, 2 LiF + BeF_2, is only 20 ev. As

a result, many Flibe molecules completely decompose into their elementary atoms. The recombination of these atoms is difficult to predict without knowing the gaseous reaction rates at high temperature, but could lead to LiF, BeF, BeF_2, LiBe and F_2. The chemically reactive fluorine (F_2) formed near the first wall would react rapidly with any first wall material (SiC, C, or metallic fibers).

In order to appraise the potential impact of the chemical, neutronic, and radiolytic decomposition products upon the first-wall materials (SiC or C), the potential corrosive effects of these materials were calculated for a full-power year (FPY). The following assumptions were made: (a) 50% of the TF formed from (LiF + n) reacted with the SiC first wall, but none with the C; (b) all the F atoms produced by the nuclear reactions with Be reacted with the first wall; and (c) the absorption of the x-ray energy in the ablated salt was based upon the following assumptions: a 5 mm thickness of Flibe covered the first wall, the attenuation factor of Flibe, which is mostly F atoms would be similar to oxygen, 5.57 cm^2/g @ 10 keV x-rays,[2.28] and because the F atoms would react mostly with the vaporized salt atoms only 1% would react with the first wall.

The results of these preliminary calculations (Table 2.14) indicates that 8.5 mm thickness of SiC and 6.5 mm of C would be corroded per FPY. These calculations indicate that the useful lifetime of the first wall fabric could be < 1 FPY.

Table 2.14. Potential Corrosion of First-Wall by Flibe Due to Nuclear Transformations and X-ray Decomposition

Reactive Species	Carbon mm/yr	SiC mm/yr
TF[(a)]	-	0.5
F_2[(b)]	0.9	1.4
F_2[(c)]	5.6	6.6
Total	6.5	8.5

(a) Produced by neutronic absorption of ^6LiF and 50% of the TF reacts with the first-wall.
(b) Produced by neutronic absorption of BeF_2 and 100% reacts with the first-wall.
(c) Produced by x-ray decompositon of Flibe attenuated by 5 mm of Flibe and 1% of the F_2 reacts with the first wall.

The loss in the strength of these composites caused by the several corrosive effects noted will need to be experimentally determined because the corrosion may not be uniform, but may preferentially attack localized sites at high stress points, causing premature breakage of certain fibers without much overall corrosion. The following conclusions are drawn from the analysis of the potential chemical reactions in Flibe as used in the Osiris reactor.

1. The first wall fabric should be composed of carbon fibers not SiC.
2. The tritium in the molten salt will be adjusted to exist as T_2 which can permeate through the IHX into the steam cycle.
3. Conservative estimates of the radiolytic decomposition of the Flibe near the first wall indicates that the corrosion of the carbon fibers may be 6.5 mm/FPY. The loss in the strength of the fabric due to this corrosion needs to be evaluated.

2.2.7.2 Tritium Recovery

Chemical Form of Tritium. The neutron irradiation of Flibe causes the following nuclear reaction,

$$^6LiF + n = {}^4He + TF$$

Consequently, the reactive chemical species TF accumulates in the salt and, as previously noted can corrode SiC or a steel structure. It is desirable, therefore, to reduce TF by use of the chemical reaction,

$$2TF + Be = BeF_2 + T_2(g) .$$

Both the BeF_2 and the T_2 remain dissolved in the fused salt. It is desirable to reduce the TF as soon as it is formed; consequently, a bed of Be spherical particles is embedded at the bottom of the pool in the Osiris reactor chamber, because all the salt in the chamber must exit through this pool. The total flow of salt from the pool is 7000 kg/s, ~3.5 m^3/s, while the tritium addition is at the rate of 12.1 x 10^{-3} g T/s; consequently, the T_2 concentration is 5.8 x 10^{-4} moles T_2/m^3 (salt) or 1.7 x 10^{-3} wtppm.

The solubility of T_2 in the molten Flibe can be expressed by the Henry's Law constant,[2.25] K_H, obtained from measurements with H_2, i.e.

$$K_H = \frac{7 \times 10^{-7}\ moles\ T_2}{m^3\ (salt)\ Pa},$$

at 1000 K. Based upon this relationship and the value of the T_2 concentration in the salt, we

calculate a T_2 pressure of 820 Pa. At such a high pressure T_2 gas would permeate easily through the IHX and be lost to the environment. It is necessary, therefore, to reduce the T_2 concentration in the salt before it reaches the IHX to a level so that the tritium permeation rate is acceptable.

Tritium is removed from Flibe as it cascades down the back of the blanket and is then pumped out by the chamber vacuum systems. If the tritium concentration is not reduced enough by the cascade, a vacuum disengager will be needed.

Design of the Vacuum Disengager. In order to remove rapidly a dissolved gas from a liquid, it is necessary to create a large liquid to gas surface area. Recently, Dolan et al.,[2.29] have designed a vacuum disengager to remove T_2 from Flibe in HYLIFE-II. This disengager consists of a spray of 400 μm droplets of molten salt falling vertically downward at a height of 5 m while in a vacuum chamber. The pumping capacity of the vacuum chamber is sufficient to obtain a decontamination factor of 10^{-5} for a 2-stage system so that the T_2 concentration dissolved in the salt at the exit from the disengager is 5.8×10^{-9} moles T_2/m^3. An orifice plate where the droplets are formed is 4.2 m dia. (13.9 m^2) for a flow rate of 6.3 in HYLIFE-II, while for Osiris with a flow rate of 3.5 m^3/s, this plate would be only 3.2 m dia.

The vacuum disengager for Osiris would consist of two evacuated right-circular chamber, 3.2m dia. x 5 m high, with 10% of the orifice plate area containing holes for the formation of the droplets. These chambers must be well-insulated because all of the heat transfer fluid transits these chambers before the IHX.

Removal of Target Debris. In addition to unburned DT in the target debris, other constituents are the tamper materials, either Pb or Ta, and the ablator material, probably a polymer of $(CH_2)_n$ or $(CD_2)_n$. All these materials will be vaporized by the target explosion and become mixed with the Flibe vapors ablating from the first wall. The recombined carbon-hydrogen species will probably form methane, perhaps containing some fluorine; consequently, the methane should remain as a gas and exit from the reactor chamber via the vacuum system. The metals, Pb and Ta, would form their corresponding fluorides, PbF_2 and TaF_5, which would remain dissolved in the Flibe. Because both Pb and Ta form undesirable radioactive products upon neutron irradiation, it is necessary to control the quantities of these debris products in the Flibe.

Both PbF_2 and TaF_5 will react with the Be balls at the bottom of the reactor pool. For instance, the reaction with Ta is

$$Be + \frac{2}{5} TaF_5 = BeF_2 + \frac{2}{5} Ta.$$

Based upon the free-energy of formation of these compounds at 900 K, it has been shown[2.30] that the concentration of TaF_5 in the system should be,

$$Conc.\ TaF_5 = \frac{0.254 ppm \cdot moles(TaF_5)}{mole(BeF_2)}$$

One mole of BeF_2 exists in one mole of Li_2BeF_4 with a molecular wt of 99 g/mole, and one g·atom of Ta at 181 g/g·atom, so that the concentration of Ta in the Flibe would be 0.46 wtppm. Caution should be used in assessing this value because it assumes ideal thermodynamic efficiency and it also assumes that the reduced metallic Ta can be quantitatively removed from the salt. This separation may be difficult at such a small concentration because the Ta may form a colloidal suspension and be difficult to filter from the salt and may require special treatments, which need to be developed. A more reasonable value would be 1 wtppm (Ta) in the Flibe. Based upon this value and the total Flibe in the system, 940 Mg, the total Ta in the system would be 940 g(Ta). Also, all the Flibe flowing through the vacuum disengager should initially pass through the Ta separation device, or the colloidal Ta might interfere with the formation of the small droplets in the disengager.

Estimate of Tritium Permeation. The permeation of tritium at the IHX could represent a path for significant tritium release to the environment. The tritium concentration in the Flibe entering the IHX is 5.8 x 10^{-9} moles T_2/m^3 (salt) and based upon the Henry's law constant, a partial pressure of 8 x 10^{-3} Pa of T_2 supplies the driving force for permeation through the IHX tubes. The usual method to calculate this permeation has been to use the permeation constant for T_2 in the metallic tubes times the $(P_{T_2})^{1/2}$. Such a calculation is based upon the assumption that the tritium concentration is a constant value at the Flibe/tube interface which can be calculated from (P_{T_2}). Longhurst and Dolan[2.31] have analyzed these assumptions and determined that for Flibe solutions containing (T), the tritium near the salt/tube interface quickly becomes depleted due to permeation through the tube, and the diffusion of T_2 to this surface layer is slow,

becoming the rate determining step. Based upon these assumptions, they determined that the total tritrium permeation through the IHX was 7.3% of the total tritium per day which flows through the IHX for the HYLIFE-II system which is similar to that required for Osiris. Their results indicated that the tritium permeation increased slightly with the concentration of T_2 and increased directly with the length of the IHX tubes (e.g., surface area for the same dia. tubing). These results are directly scalable to Osiris, in which the Flibe flows through the disengager and subsequently carries 105 Ci/d of T_2 through the IHX. The amount of T_2 which permeates is 7.3% of this value times the length of tubes (surface area) of the Osiris IHX which is 4 times that of HYLIFE-II model.[2.31] Based upon these assumptions, the calculated permeation for Osiris would be 30 Ci/d of T_2. The total inventory of tritium in the Flibe is based upon the total inventory of ~470 m^3 (salt) in the reactor chamber and the heat transfer system. Approximately half of this total volume would be at the concentration existing at the exit from the reactor and half at the concentration subsequent to the disengager, giving a total inventory of ~1 g(T) for the entire Flibe system.

2.2.7.3 Tritium Inventory and Potential Loss Rate

In order to determine the steady-state and accidental tritium releases from the plant-site the tritium inventories and locations throughout the plant were assessed as shown in Table 2.15 Osiris has a fusion power of ~2000 MW and, therefore, must burn a ~300g of tritium per day. Assuming a typical burn fraction of 30%, ~1000 g of tritium must be injected each day since the tritium breeding ratio is 1.24, 1070 g of tritium must be recovered daily. The routine tritium releases were, then, based upon the daily flow rate of tritium through each piece of apparatus, based upon the TSTA experience[2.32] that ~1 Ci/d of tritium is released per 100 g of tritium processed in well-enclosed secondary containment systems.

Table 2.15. Tritium Locations, Inventories, Flow Rates, and Potential Release Rates

Location	Inventory g(T)	Flow Rate g/d	Routine Ci/d	Accidental g(T)
Reactor System				
Breeder	1	~1070	10	1
Graphite	4	-	-	2 (50%)
Steam generator to coolant water	-	-	30	-
Beam line	1	10	1	1
Containment Building				
Atmosphere	~0	-	-	-
Fuel Injector	1.2	~1000	10	1.2
Fuel Reprocessing				
Vacuum disengager	44	~1070	10	-
Cryo-distillation	9.5	~1070	10	-
Target factory	260	~1000	10	100

The Reactor and Heat Transfer System. This system consists of the total Flibe in the reactor, the vacuum disengager, the IHX and the connecting pipes for a total of 470 m^3 (940,000 kg). Approximately 50% of this molten salt, mostly in the reactor and vacuum disengager, is at a concentration of 5.8×10^{-4} moles $(T_2)/m^3$ while the other 50% is at a concentration of $\sim 10^{-8}$ moles $(T_2)/m^3$; consequently, the total tritium inventory in Flibe is ~1 g(T). In a severe accident, perhaps only 50% of the gaseous tritium would be released before the salt solidifies, because there is no major radioactive nuclides in this salt to prolong its heating. Based upon the flow rate of tritium in the breeder of 1070 g/d, a well-enclosed system would off-gas ~10 Ci/d.

The graphite fibers forming the first-wall (~3000 kg) are subjected to a T_2 pressure from the tritium dissolved in the Flibe and, also, subjected to the ion flux from the target debris. Under such circumstances, it has been observed that the H(T) atoms saturate along the grain-

boundaries at 5 atomic ppm T/C; consequently, the maximum tritium inventory in these fibers would be 4 g(T). The c/c composite forming the tank is subjected to only a low T_2 pressure; consequently, it absorbs <0.1 g(T).

The loss of tritium through the heavy-ion beam port could become a serious contamination in the accelerator facility unless it is well-managed. There are two sources of tritium which could enter the beam port: namely, (1) the continual evaporation of TF from the Flibe and (2) the unburned target fuel which is propelled throughout the chamber following each target ignition. These two sources were evaluated as follows:

Evaporation of TF from the Flibe. The unburned target fuel represents a tritium source of 8.2×10^{-3} g(T)/s; consequently, at the radial distance to the entrance of the beam port from the target, 5.5 m, the (T) flux is only 2.2×10^{-5} g(T)/m^2·s. For beam port entrance area of 1.4 m^2, ~10 g(T)/day effuses into the beam port; as a result, cryogenic adsorption traps must be installed along the internal surface of the beam tube. In addition, other vapors in the chamber, such as gaseous TF with a freezing point of 190 K and vaporized Flibe which solidifies at 732 K, will be swept into the beam ports. The cryo-fluid for the absorber plates could be liquid nitrogen at 77 K. These absorber traps could be placed along the flat surfaces constructed as neutron absorbers in the beam port nozzle. Two cryo-absorber plates would be installed back-to-back at each location selected so that one trap would be in use while the duplicate trap would be heated to evaporate the absorbed gases.

Some gases, such as DT, would not be absorbed on the nitrogen-cooled traps and would continue deeper into the beam tube, plus the vapors which are directly in-line with the center of the beam line. Both of these species would impinge upon the inner surface of the beam-line at the point where it begins to bend. At this bend and at locations deep into this bend, large cryo-adsorber surfaces would be installed using liquid He coolant which would adsorb the species DT and T_2 which solidify at ~20 K. All of these traps would accumulate the 10 g(T)/d. If they are recycled every two hours, their total inventory is only 1 g(T). If the adsorption and degassing of these absorbers are tightly controlled to prevent leakage, then the loss of tritium further into the beam facility would be much less than 1 Ci/d. Nearly all of this tritium would be deposited in the vacuum pumps installed along the beam line.

Tritium in the Containment Building. The containment building would contain the Osiris reactor and perhaps the vacuum disengager and the IHX. Because each of these systems

contains tritium at high temperature, the possibility of tritium loss by permeation or leakage exists; consequently, all these systems and connecting pipes would be within secondary enclosures. As a result, the atmosphere in the building should contain very little tritium or other radioactive gases.

The target delivery system located near the reactor contains tritium; however, the number of targets on hand is limited to ~1 min fueling time so that the quantity of tritium is only 1.2 g(T) which could be released in an accident. The target delivery system handles 1000 g(T)/d, which is projected to release ~10 Ci/d for a well-enclosed apparatus.

Fuel Reprocessing Facility. High tritium inventories exist in the fuel processing facility principally in two systems: namely, (1) the vacuum pumps from the vacuum disengager and (2) the cryo-distillation system. The vacuum disengager must separate T_2 from the molten Flibe at the rate which it exits the reactor chamber by the use of vacuum pumps capable of maintaining low pressures. Such pumps could be turbo-molecular or cryo-absorption pumps. Because of the possibility of Flibe vapors and TF contamination in the gas stream, cryo-absorption pumps are suggested. If these pumps are on stream for one-hour, their inventory would be 44 g(T). Such pumps would process 1070 g(T)/d and with secondary enclosures would be expected to release only 10 Ci/d of tritium. Most of the tritium from the cryo-absorption pump should be DT which would go directly to the distillation system. The cryo-distillation system must handle 1070 g(T)/d. Based upon the design of an advanced distillation system,[2.33] the constant inventory of tritium in the distillation system would be 9.5 g(T) and the loss of tritium would be ~10 Ci/d. Both the cryo-absorption pumps and the cryo-distillation systems operate at sub-atmospheric pressures. If such systems are accidentally heated and evaporate the cryogenic fluids, then a passive safety seal is ruptured and the tritium contents of the equipment is vented to a large, preexisting, evacuated tank; consequently, no accidental release of tritium is predicted.

Target Factory. The target factory must fill ~400,000 targets/d with a total of 1000 g(T). For well-enclosed processing apparatus, the total tritium loss out the stack is expected to be 10 Ci/d. The rate of target filling is maintained at the rate of usage so that no large quantities of tritium in targets are in storage. The total inventory along the production line is limited to 260 g(T); however, 160 g(T) is enclosed in two liquid cryogenic containers, surrounded by evacuated chambers. These chambers are connected to evacuated tanks; consequently, if the apparatus becomes overly pressurized, a passive seal breaks and vents the tritium to the tank

which has sufficient capacity to contain all the T_2 at a low pressure. The tank may also contain a tritium getter to immobilize the T_2. Because of this fail-safe system, the maximum T_2 release would be only 100 g(T) in auxiliary components.

2.3 OSIRIS POWER CONVERSION AND PLANT FACILITIES

2.3.1 Introduction

The balance-of-plant (BOP) includes heat transport and energy conversion systems, plant auxiliary systems, plant electrical systems, and structures and facilities. A conceptual BOP design has been developed for the Flibe-cooled Osiris chamber and is described in this section. The main objective of the BOP design study was to develop a preliminary understanding of the requirements of plant design. Of particular importance are the requirements imposed by the reactor and its auxiliaries on buildings and structures. These requirements have a significant impact on the economics of the plant. Thus, the main BOP systems and aspects considered in this study include the heat transport system, energy conversion system, reactor confinement building system, major equipment and plant facilities arrangement, and remote maintenance concept. The key issues addressed include the following:

- **Heat Transport System** - The basic issue is whether an intermediate coolant loop is needed to act as a barrier so that tritium permeation to the steam system is limited to acceptable levels.
- **Power Conversion System** - A high efficiency power conversion system is desirable due to the capital-intensive nature of the plant.
- **Reactor Building** - Reactor building size and cost are strongly influenced by the need to provide for remote maintainability for Osiris.
- **Reliability, Availability, and Maintainability (RAM)** - Since adequate design information is not available on major reactor and driver systems and components, the RAM analysis focused on developing a set of requirements that these systems needed in order to satisfy the plant availability goal of 75%.

2.3.2 Heat Transport System

Primary Coolant Loop. The heat transport system proposed for the Osiris reactor concept is shown schematically in Fig. 2.17. The primary coolant selected is liquid Flibe (lithium and beryllium fluoride) and operates between 500°C and 650°C. The primary loop consists of two coolant circuits including one heat exchanger in each circuit. The number of circuits was based on the size of the heat exchangers. A state-of-the-art heat exchanger design was assumed.

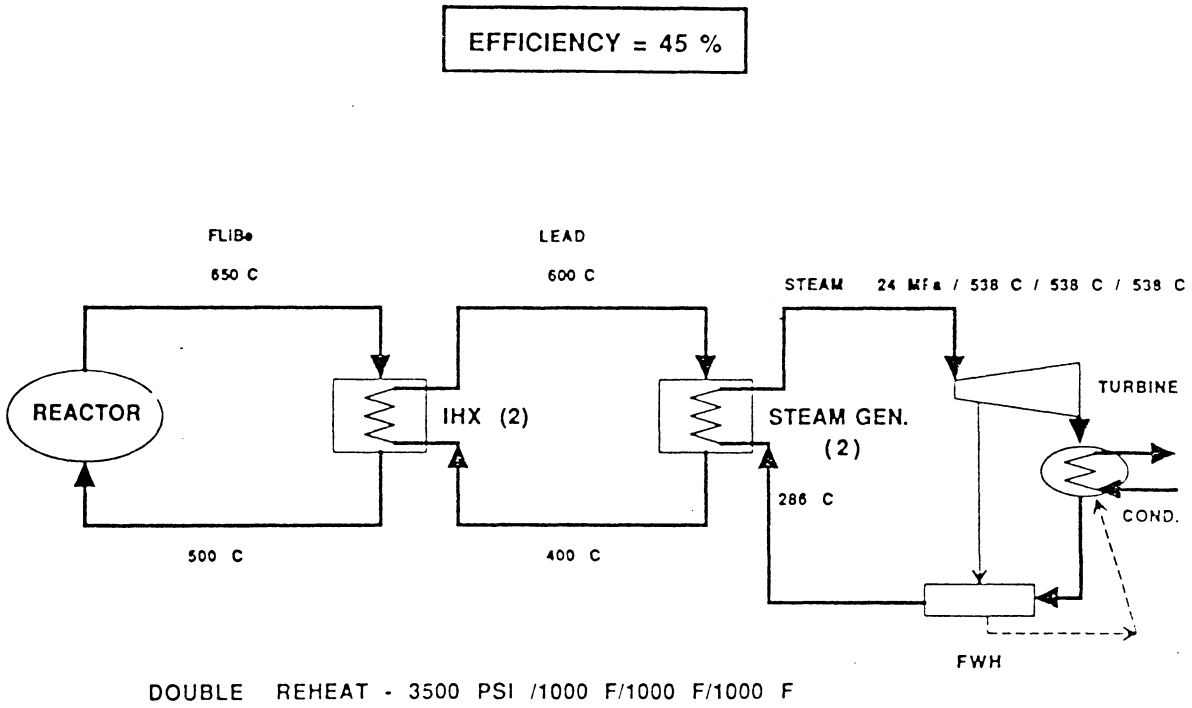

Fig. 2.17. Osiris power conversion cycle.

Intermediate Coolant Loop. The need for an intermediate loop was investigated to determine if tritium permeation to the environment is acceptable without this loop. The primary motivation is to reduce the plant complexity and cost and to improve plant reliability. With these considerations in mind, the following two cases were considered:

1) A heat transport system without an intermediate loop along with a simplex tube (single-walled) steam generator. Two alternative cases were looked at: a) Unoxidized tube surfaces result in unacceptable tritium permeation into the power conversion system; b) If the tube surfaces are oxidized, a reduction factor of approximately 30 in tritium permeation can be achieved. However, this reduction factor is not adequate to meet the off-site dose criteria.

2) A heat transport system without an intermediate loop along with a duplex tube (double-walled) steam generator. In a duplex tube steam generator, tubes are essentially made of two tubes fitted one on top of the other to form a single tube. Three duplex tube configurations were considered (Fig. 2.18): a) Mechanically-bonded, b) Metallurgically-bonded, and c) Oxidized tube surfaces with a gas space between the two walls of the tubes.

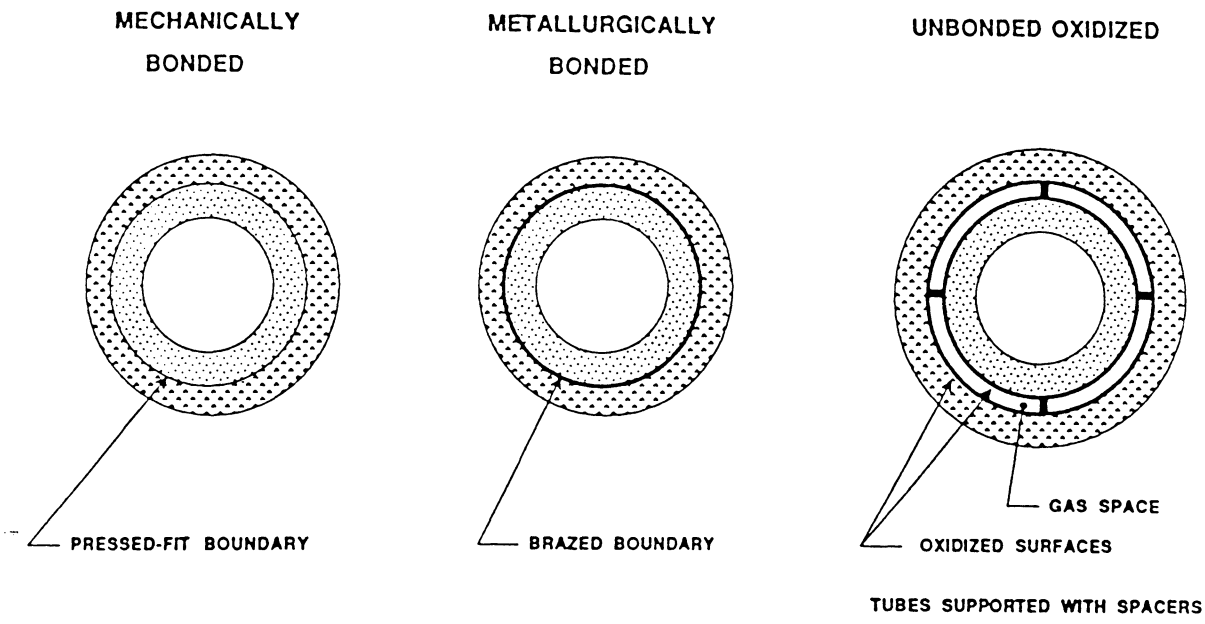

Fig. 2.18. Possible duplex tube configurations.

Mechanically- and metallurgically-bonded configurations without any surface oxidation can reduce tritium permeation by a factor of only two as a result of doubling the wall thickness. However, permeability can be reduced by two to three orders of magnitude[2.34] by oxidizing the tube surfaces (inside of the outer tube and outside of the inner tube) in case of the third duplex tube configuration. This configuration seems to offer the permeation reduction factor needed to maintain the off-site dose within acceptable levels. However, there are a number of uncertainties associated with this. Reliability and longevity of the oxide layers are quite uncertain as very little experimental evidence exists today. In addition, the cost effectiveness of using duplex tube steam generators has not yet been established. Several features of the simplex and duplex tubes are presented in Table 2.16.

Table 2.16. Duplex Tube Features

		DUPLEX TUBE	
	Simplex	**Mechanically- and Metallurgically-Bonded**	**Unbonded and Oxidized**
1. Tritium permeation rate	Highest	Reduced by a factor of 2	Reduced by factor of > 100
2. Heat flux	Highest	Reduced by a factor as high as 1.8	Reduced by orders of magnitude
3. Reliability/availability/ maintenance	Base	Much better than than Simplex	Can be same as bonded
4. Cost of heat exchanger	Base	> 2 x base	> N x Base
5. Is tritium permeation barrier adequate?	No	No (?)	Perhaps yes (?)

In light of these uncertainties and as a conservative approach, an intermediate loop is included in the heat transport system. The intermediate loop consists of two circuits including one steam generator in each circuit. This selection was based on the projected steam generator capacity. Each steam generator has a capacity of 1225 MWt. Although this capacity level has not been demonstrated to date, no show stoppers are anticipated in the development of steam generators of this power level.

Intermediate Coolant. Three alternative coolants (i.e., Flibe, sodium, and lead) were investigated to identify the most appropriate choice for the intermediate loop.

Flibe was considered as a candidate because it serves as the primary coolant, and thus its selection would simplify many of the coolant handling and processing systems. Sodium was considered because it has a large technology base and also it has good heat transfer characteristics. Lead was considered as a candidate because it is being developed as a fission reactor coolant in the Commonwealth of Independent Countries (Russia, Ukraine, etc.). Lead also appears to have good safety features.

The criteria used to select the coolant are

- Safety and health hazard impacts
- Heat transfer characteristics and impact on steam generator size and cost
- Required technology extrapolation.

The three coolants were qualitatively evaluated, and engineering judgement was used whenever needed to develop the following comparison:

Flibe. The composition of the two varieties of Flibe that were considered are

- Low viscosity: 66% LiF + 34% BeF2
- High viscosity: 47% LiF + 53% BeF2

The low viscosity Flibe was not considered since its melting point, 460°C, is above the cold leg temperature, 400°C, of the intermediate loop. The major important characteristics of Flibe as a coolant are

- Fluorine in Flibe is potentially a chemical hazard.
- Due to the poor heat transfer characteristics of Flibe, the size of the Flibe steam generator would be three to five times that of the sodium steam generator.
- Technology extrapolation is expected to be modest as significant development work has been done in connection with the Molten Salt Reactor Experiment at Oak Ridge National Laboratory (ORNL).

Sodium. The major important characteristics of sodium as a coolant are

- Exothermic sodium-water reactions are a potentially serious safety concern.
- Due to its very good heat transfer characteristics, sodium offers the smallest size steam generator.
- No technology extrapolation would be required. Much of the technology is being developed in the Advanced Liquid Metal Reactor (ALMR) program.

Lead. The major important characteristics of lead as a coolant are

- Lead offers a safety advantage as no safety hazard is identified.
- Due to its moderate heat transfer characteristics, the size of the lead steam generator appears to be reasonable.
- Modest technology extrapolation is expected. Lead is used as a reactor coolant in Russia and its neighboring countries. Thus, much of the know-how resides outside the United States.

Coolant Selection. Using the selection criteria listed above, the coolant selection for the intermediate loop was made as follows:

- Flibe was not selected primarily due to the high cost of steam generators, but also because of its high chemical hazard potential.
- Sodium was not selected because of its safety concern (exothermic sodium-water reaction).
- Lead was selected because of its minimal safety concern and moderate cost impact.

Intermediate Heat Exchanger. There are four intermediate heat exchangers (IHX), and each is sized for 25 percent thermal capacity of the plant. Thus each IHX has a rated capacity of ~613 MWt. The key parameters of each IHX are given in Table 2.17.

Table 2.17. IHX Design Parameters

Number of IHX	2
Duty	612.5 MW
Core height (along Flibe flow)	3.64 m
Core depth (along lead flow)	8.10 m
Core width	3.04 m
Tube outside diameter	2.54 cm
Tube inside diameter	2.22 cm
Heat transfer area	
- Outside	11,780 m^2
- Inside	10,300 m^2
Lead pressure drop	0.13 MPa

2.3.3 Power Conversion

Power Cycle. To achieve high efficiency power conversion, a high pressure/high temperature steam cycle was adopted for the Osiris reactor concept. The steam pressure and temperature conditions chosen are consistent with the intermediate coolant temperature. These

conditions also represent the state-of-the-art steam conditions used for fossil-fired steam power plants. A supercritical pressure double-reheat steam cycle is used with the following steam conditions:

24.2 MPa / 538°C / 538°C / 538°C

[3000 psig / 1000°F / 1000°F /1 000°F]

The above pressure and temperature conditions refer to the steam conditions at the high-pressure turbine inlet. The three temperature values stand for initial superheat, first reheat, and second reheat, respectively. These conditions provide a cycle efficiency of 45 percent. The heat transport and power cycle schematic was shown in Fig. 2.17.

The power conversion system chosen does not present any developmental, reliability, or availability concern. In fact, more advanced steam conditions (higher temperature and pressure) can be considered if the intermediate loop can be avoided because the primary loop allows a higher steam temperature. At the present time and without any further development, all U.S. manufacturers are prepared to offer equipment necessary to build double reheat units with steam conditions up to 31 Mpa/565°C/565°C/565°C.[2.35] There are about two dozen supercritical pressure double reheat fossil-fired units in the U.S. These units have proved to be at least as reliable and available as their subcritical non-reheat counterparts.

Steam Generator. There are two steam generators, each sized for 50 percent thermal capacity of the plant, or 1225 MWt. To accommodate the double reheat feature of the power cycle, each steam generator is made up of three stages, and each stage is provided with a separate vessel. These stages are superheater, first reheater, and second reheater. These steam generator vessels are supplied with liquid lead from the intermediate heat exchangers (IHXs). There are two IHXs consistent with the two circuits primary loop. The key parameters of each steam generator are given in Table 2.18.

Turbine-Generator. The Osiris reactor plant is provided with a turbine-generator capable of generating the required gross electrical power (1129 MWe). The turbine-generator is supplied with steam from the two steam generators. The turbine-generator consists of one high-pressure section, one intermediate-pressure section, and two low-pressure sections arranged in a cross-compound configuration. In a cross-compound configuration the low-pressure turbine sections are mounted on two parallel shafts. This is done to keep the shaft lengths to practical limits.

Table 2.18. Steam Generator Design Parameters

Parameter	Superheater	1st Reheater	2nd Reheater
Thermal Duty (MWt)	899	204	122
Shell Inside Diameter (m)	3.4	2.1	2.1
Tube Bundle Length (m)	19.5	16.8	18.0
Number of Tubes	9967	4634	4983
Tube Size (cm)	1.27	1.27	1.27
Tube O.D. (cm)	2.13	2.13	2.13
Tube Wall Thickness (cm)	6.37	0.28	0.28

The turbine-generator has a size limitation, however. The largest turbine which has been built for advanced steam conditions was a 325 MWe machine. Currently, all of the techniques needed to build much larger capacity turbines do not exist in the United States; they exist to a large extent in Europe. Thus, for units 800 MWe or larger, a cross-compound configuration may very well only be practical at a much higher cost.

2.3.4 Plant Facilities

The facilities for the Osiris plant are shown in Figs. 2.19 through 2.23. The plot plan, Fig. 2.19, shows the major structures of the plant. These structures include:

- Reactor Building
- Maintenance Building
- Auxiliary Buildings
- Target Fabrication Building
- Heavy Ion Beam Facility
- Steam Generator Building
- Turbine-Generator Building

The outline of the five-kilometer-long HIB tunnel is shown on Figs. 2.20a and b. Figure 2.21 shows an illustrative cross-sectional view of the tunnel.[2.36] The plan and cross-sectional views of the Fusion Island, primarily consisting of the reactor building, maintenance building, and steam generator building, are shown on Figs. 2.22 and 2.23.

2.3.4.1 Reactor Building

The reactor building has been designed as a Seismic Category I structure. The building provides housing for the reactor; shielding of the public from fusion neutrons; confinement barrier to the accidental release of tritium. In addition, the building also accommodates remote maintenance of the reactors. The remote maintenance requirements (discussed in Section 6.4) dictate the size of this building. The conceptual arrangement of the building is shown in Figs. 2.22 and 2.23. The reactor is located at the center of the reactor hall. The IHXs are located in a separate hall so that the area can be accessed for limited periods during normal power operation; the reactor hall is provided with requisite shielding for this purpose. The nearest shield wall is located at a distance of ten meters from the center of the reactor, and the shield thickness is 3.2 meters.

Another feature of the reactor building is that there is no direct piping penetration between the reactor and IHX halls. The primary coolant piping is routed via an underground piping tunnel; there is no direct neutron path from the reactor hall to the IHX hall. The shield wall between the IHX hall and the steam generator building is set at one meter to allow unlimited access to the steam generator building.

A second feature that determines the location of primary heat transport loop components is the hydraulic profile of the coolant circuit. Two alternative hydraulic profiles were considered (see Figs. 2.24 and 2.25).

The major difference between the two alternatives is the location of the primary coolant pump. In general, the preferred location of the coolant pump is the cold leg so that the pump is required to handle the lower- temperature coolant and thus avoid any pump materials concern. This arrangement is readily achievable in a pressurized closed-loop configuration without unduly complicating the equipment arrangement. In an open-loop configuration, such as in Osiris, the pump can be located in the cold leg if the IHX is located sufficiently below the Flibe pool to allow gravity-assisted flow. This requires longer piping lengths and a deeper reactor building. On the other hand, if the pump is located in the hot leg (Alternative 1), both the piping length and the building size are reduced. Although the pump is required to handle hotter coolant, it is assumed that at the time of IFE deployment, advanced materials will be developed to eliminate the materials concern. Thus, Alternative 1 is selected as the base case since it is judged that the additional cost of building and piping for Alternative 2 will more than offset the additional cost of the coolant pumps for Alternative 1.

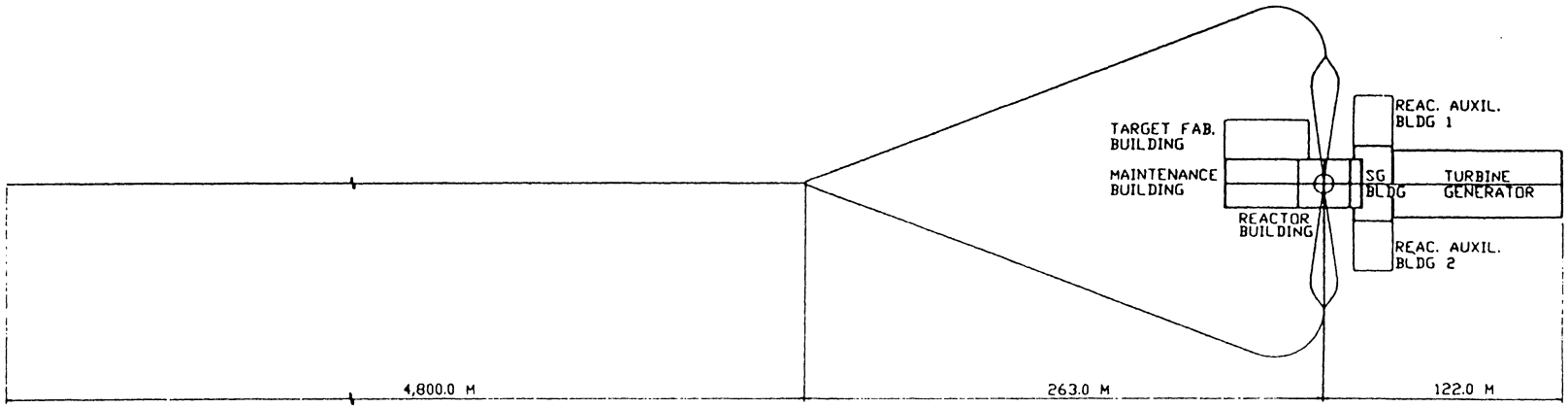

Fig. 2.19. Osiris power plant layout.

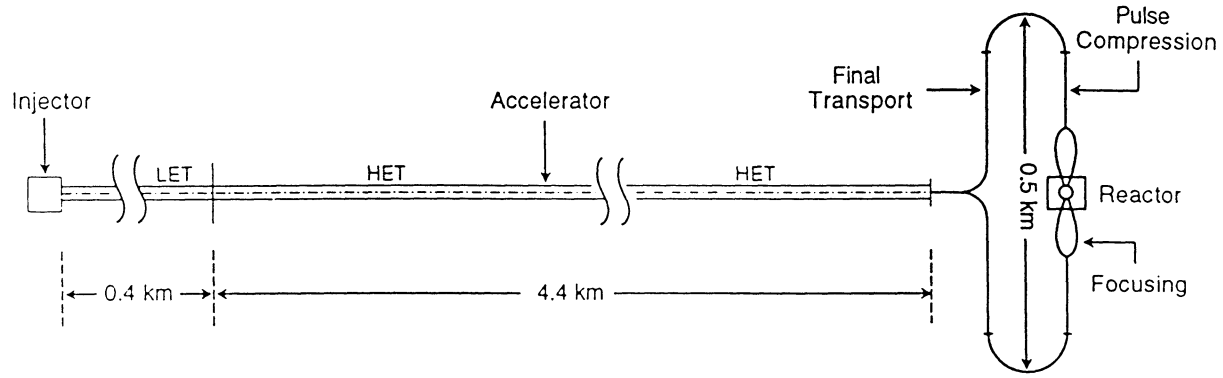

Fig. 2.20a. Heavy-ion driver tunnel layout.

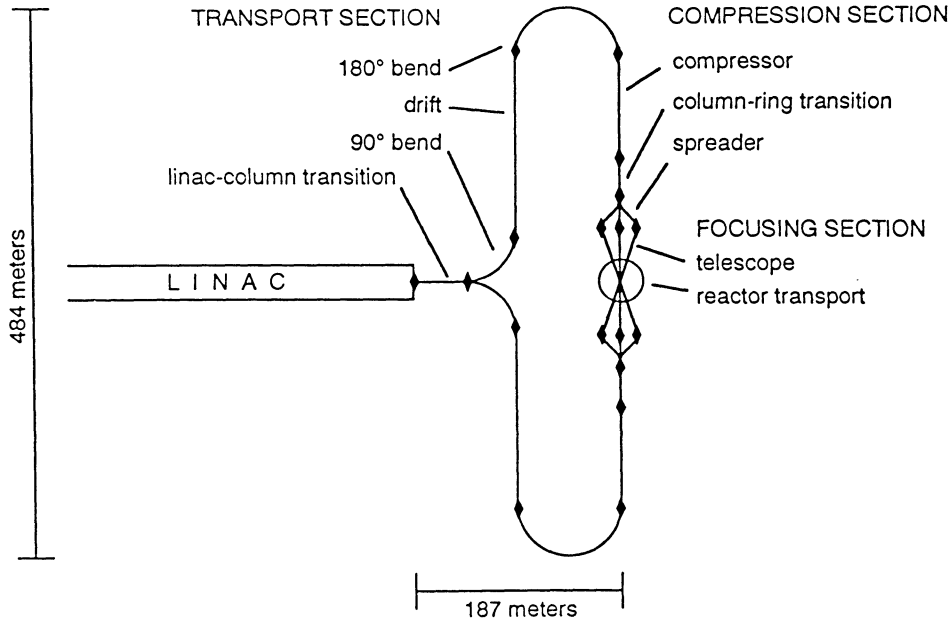

Fig. 2.20b. Final transport layout.

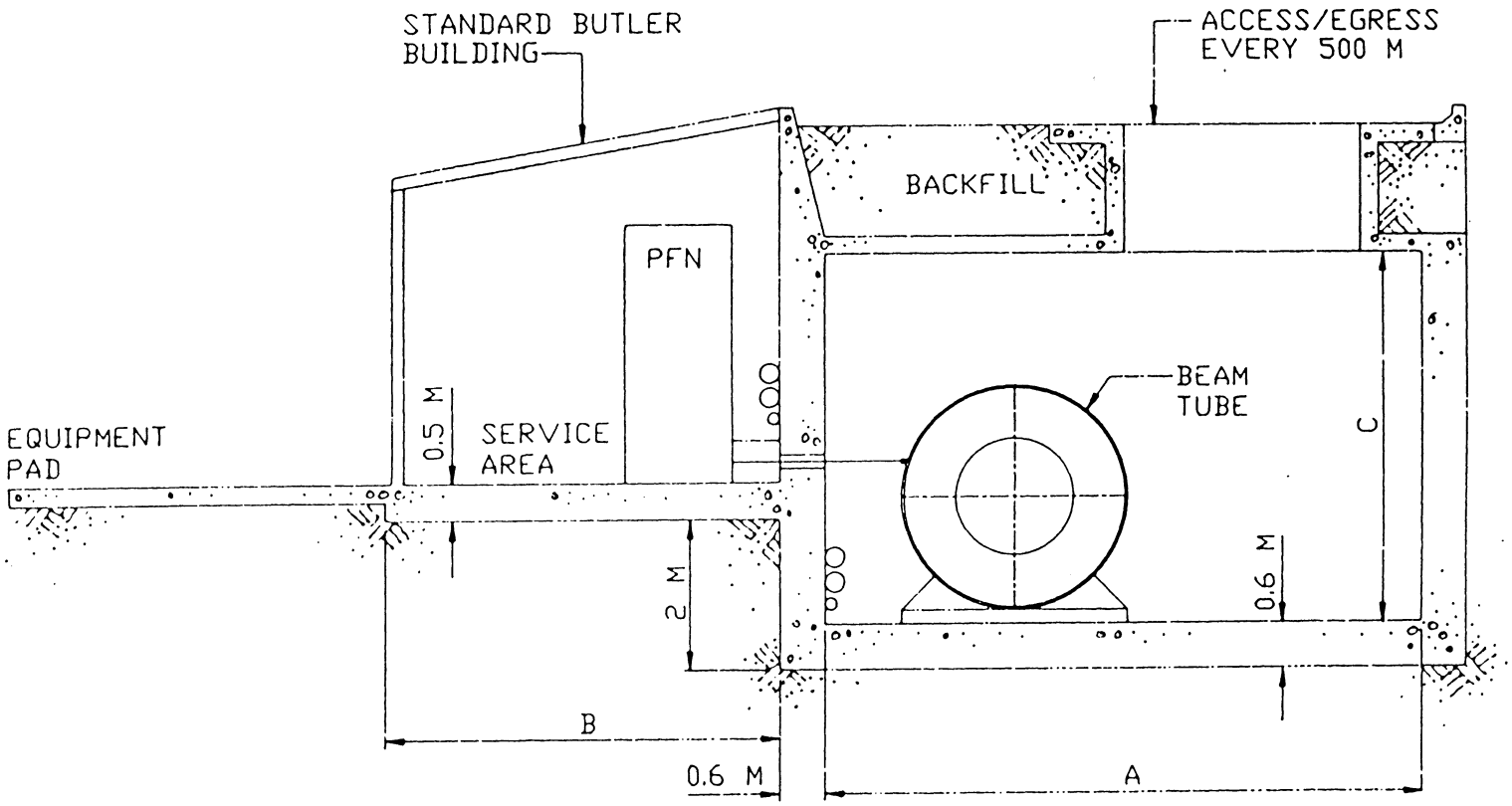

Fig. 2.21. Driver tunnel cross section.

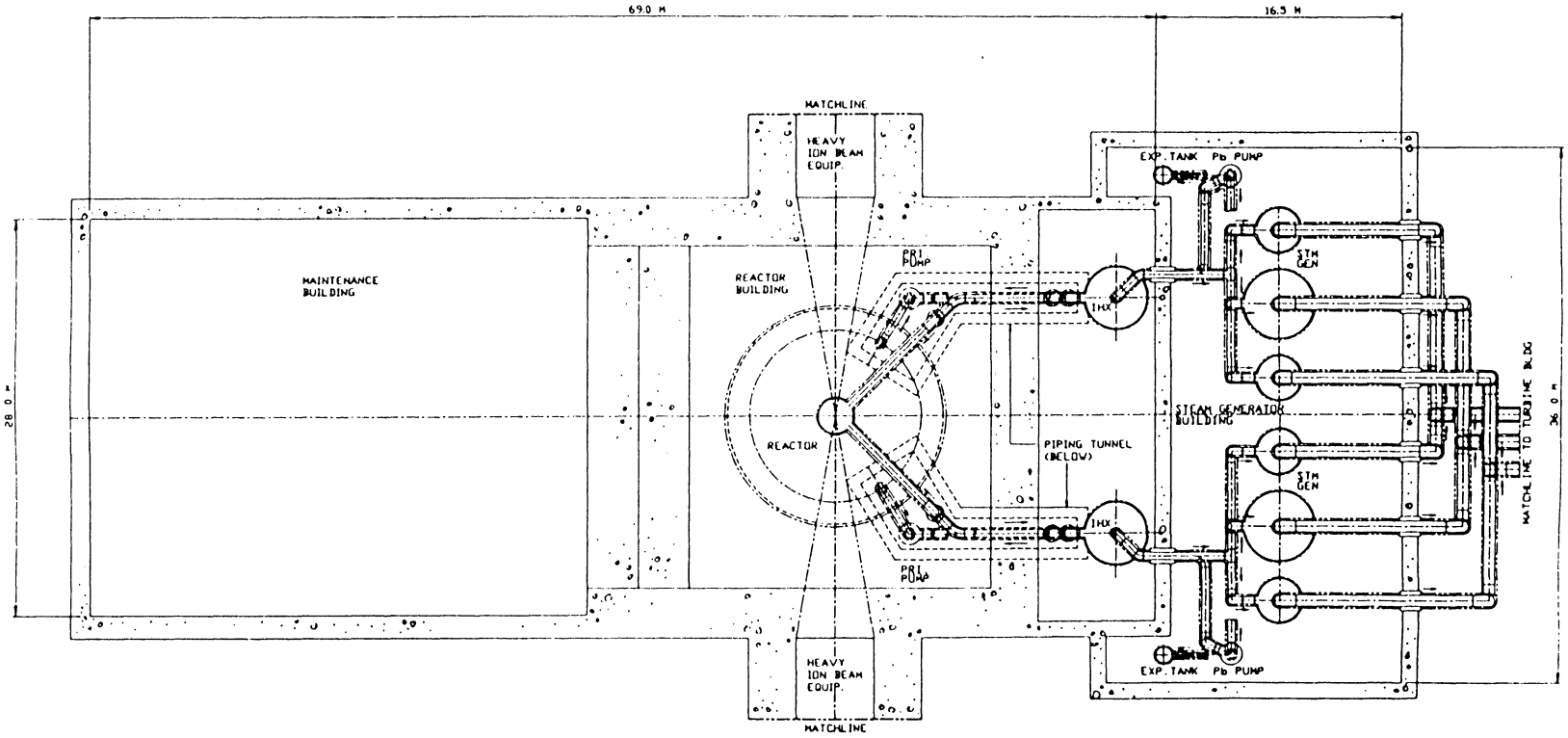

Fig. 2.22. Overhead view of Osiris reactor containment.

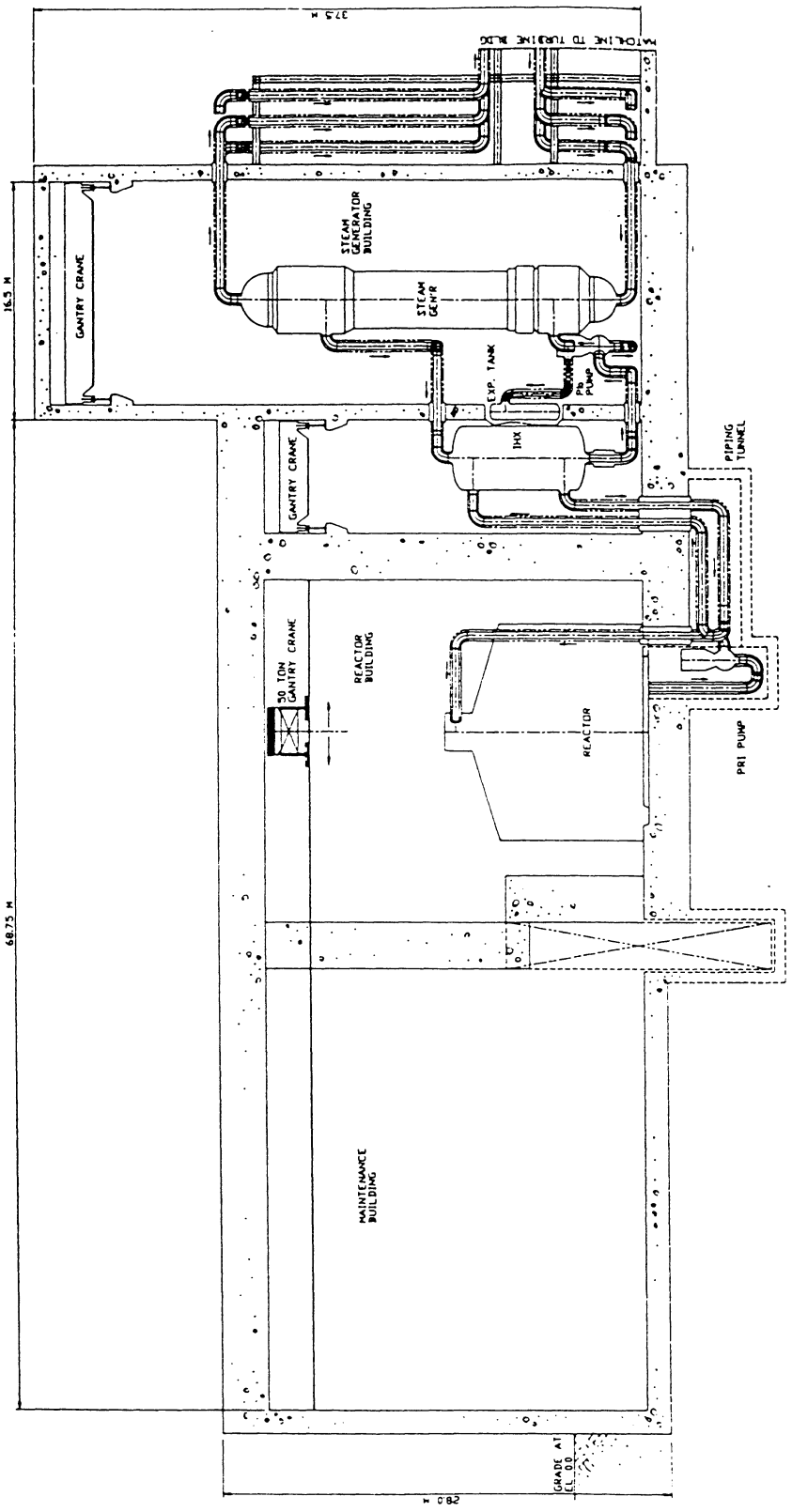

Fig. 2.23. Side view of Osiris reactor containment.

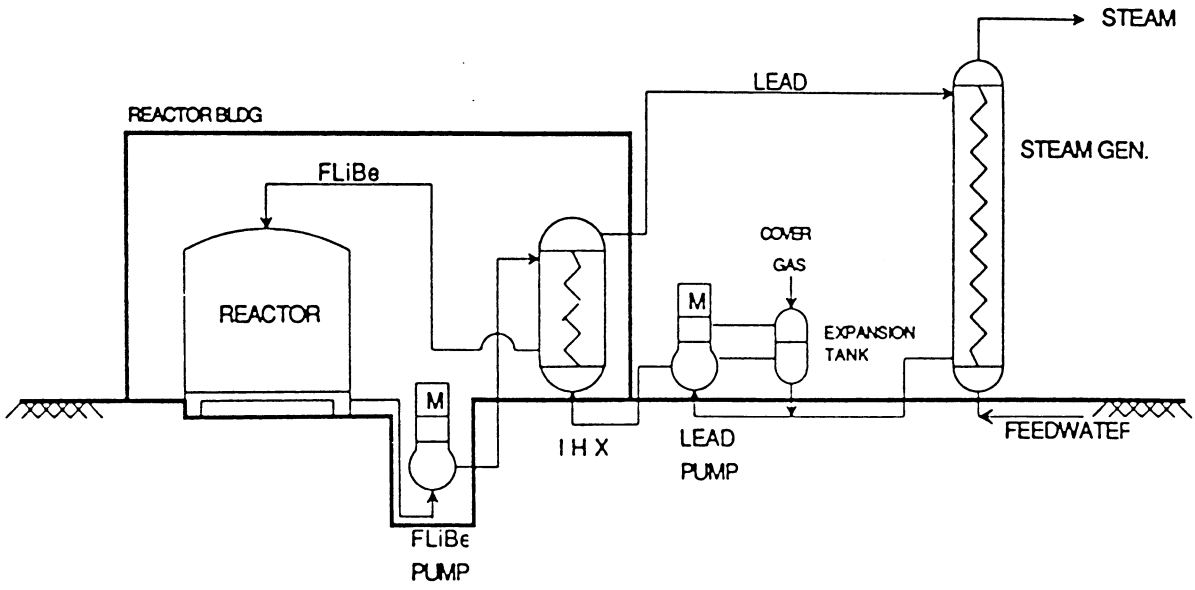

Fig. 2.24. Alternative 1 - Osiris HTS hydraulic profile.

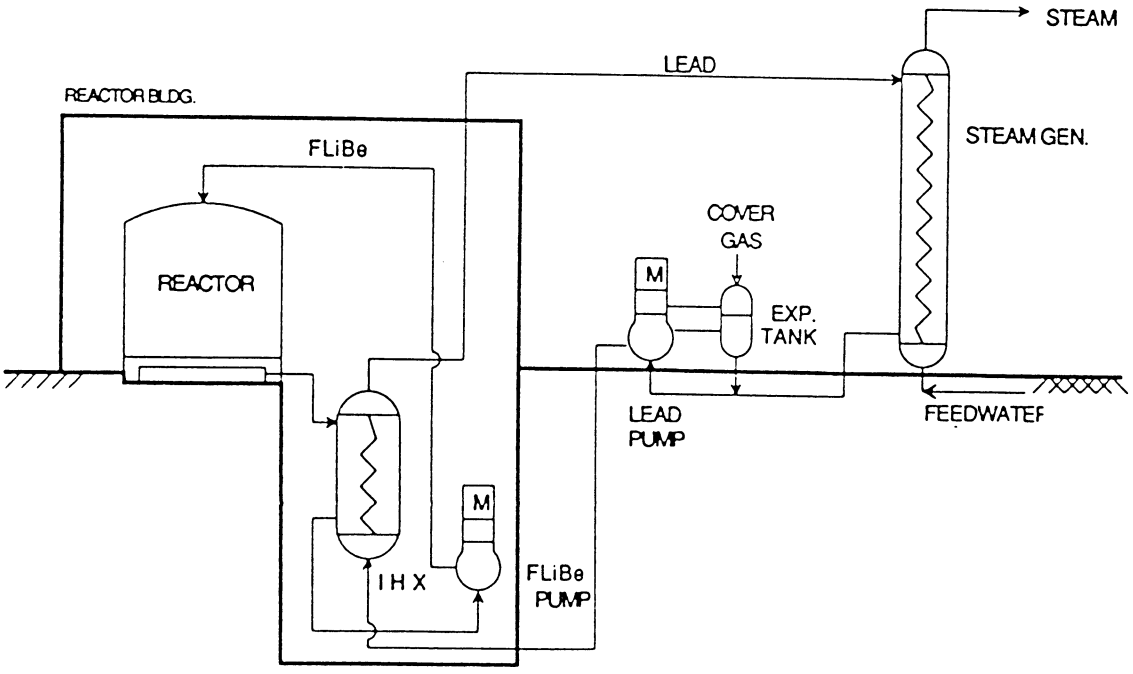

Fig. 2.25. Alternative 2 - Osiris HTS hydraulic profile.

Tritium Confinement Barrier. The reactor building provides a leak-tight barrier to tritium leakage into the environment. The leakage from the building can be reduced to limit the tritium leak rate to an acceptable level. The leakage from the building is generally controlled by properly sealing the penetrations, access doors, and equipment hatches. In addition to this, all the interior surfaces of the building walls, floors, and ceiling are coated with epoxy paint to minimize tritium permeation into the concrete. Similarly, all equipment surfaces are also painted with suitable coatings to minimize tritium permeation.

Vacuum Boundary. The external boundaries of the reactor and the beam lines serve as the vacuum boundary for Osiris. The vacuum pumping systems are included in the reactor and the heavy ion beam systems. The reactor building is maintained at near-atmospheric pressure with the help of an atmosphere cleanup system. A slightly negative pressure (approximately 0.5mm of mercury) is maintained in the building to avoid out-leakage of the potentially contaminated air.

Atmosphere Cleanup System. To maintain an equilibrium tritium concentration as well as to cleanup the tritium following an accidental leakage within the reactor building, an atmosphere cleanup system is provided. The system also maintains the tritium concentration within the building well below the maximum permissible level during maintenance operations. After processing by the system, the recovered tritium is pumped back into the tritum processing system provided to recover tritium from the blanket and coolant systems.

2.3.4.2 Other Facilities

A brief description of the other major facilities is given here and is shown in the Plot Plan (Fig. 2.19). Only an outline of these facilities is shown in the figure to indicate that facilities are needed to support the operation of the plant. No design has been developed for them at this stage.

Maintenance Building. This building is essentially an integral part of the reactor building. It is separated from the reactor hall during normal operation by a movable shield wall. The maintenance building houses the equipment for assembly and disassembly of the Osiris components and provides space for both irradiated and refurbished modules. The building is designed as an earthquake and tornado hardened structure.

Auxiliary Building. This building houses the reactor and heat transport system auxiliary equipment. These include auxiliary cooling system, plant electrical systems, heat tracing system,

coolant handling system, heating, ventilation, and air conditioning (HVAC) system, vacuum system as appropriate, etc. The building is designed as an earthquake and tornado hardened structure.

Target Fabrication Building. This building houses all the systems and components necessary for storage, fabrication, and delivery of the fuel pellets. The building is designed as an earthquake and tornado hardened structure.

Heavy Ion Beam Facility. This facility is shown in Figs. 2.19, 2.20, and 2.21. This facility is a five-kilometer-long tunnel to house the various stages (formation, acceleration, drift, etc.) of the heavy ion beams. A typical view of the tunnel is shown in Fig. 2.21. This was proposed by C. Fong of Lawrence Berkeley Laboratory.[2-36]

Steam Generator Building. A concept has been developed for this building as shown in Figs. 2.22 and 2.23. The tall structure of this building is dictated by the height of the steam generator. The building is designed as an earthquake and tornado hardened structure.

Turbine-Generator Building. The building is sized to house the 1129 MWe cross-compound turbine-generator and its auxiliaries, steam system components, feedwater heating and condensing system components, etc. The building is envisaged as a conventional building similar to those used in fossil-fired plants.

2.4 HEAVY-ION DRIVER DESIGN AND SCALING

2.4.1 Introduction

A driver for an inertial fusion energy (IFE) reactor must deliver sufficient energy and power density to ensure target ignition. Although the requirements on efficiency and cost are less absolute, higher efficiencies and lower costs lead to more attractive plant designs.

In order to produce target ignition and gain, the driver must deliver several MJ of energy to a small spot size (approximately 2 to 4 mm in radius) in a very short-duration shaped pulse. The total pulse duration may be several tens of nanoseconds, but most of the driver energy should be delivered at the end of the pulse. The duration of the high-power part of the pulse may be less than half of the total pulse duration.

The fraction of an IFE plant's gross electrical power that must be recirculated to operate the driver is given by

$$f_R = \frac{1}{\eta_D G M_0 \eta_{th}}$$

where

f_R = recirculating power fraction,

η_D = driver efficiency,

G = target gain,

M_0 = energy multiplication factor of the blanket, and

η_{th} = thermal conversion efficiency.

Plant designs attempt to make all of these power ratios as large as possible, since it is difficult to achieve economic power production if f_R exceeds 20 to 25%. For the Osiris power plant, $M_0 = 1.25$ and $\eta_{th} = 45\%$. As we will show in this chapter, the base-case heavy-ion driver has an efficiency of 28% and produces a target gain of 86.5. This gives a small recirculating power fraction of ~ 7%.

It is also desirable to minimize the cost of the driver in order to keep the plant capital costs and cost of electricity (COE) competitive with the costs for power plants using other energy sources. The estimated cost of the driver described in this chapter results in a economically attractive power plant (see Chapter 8).

2.4.2 Heavy-Ion Driver Description

A heavy-ion induction linac for use as a driver for an IFE power plant will consist of: an ion injector, a multiple beam induction accelerator to produce high beam energies and currents, a drift compression region for shortening the ion bunch lengths, and a final focussing system for reducing the beam radii to the small spot size required for target ignition. Figure 2.26 shows a schematic diagram of a heavy-ion driver.

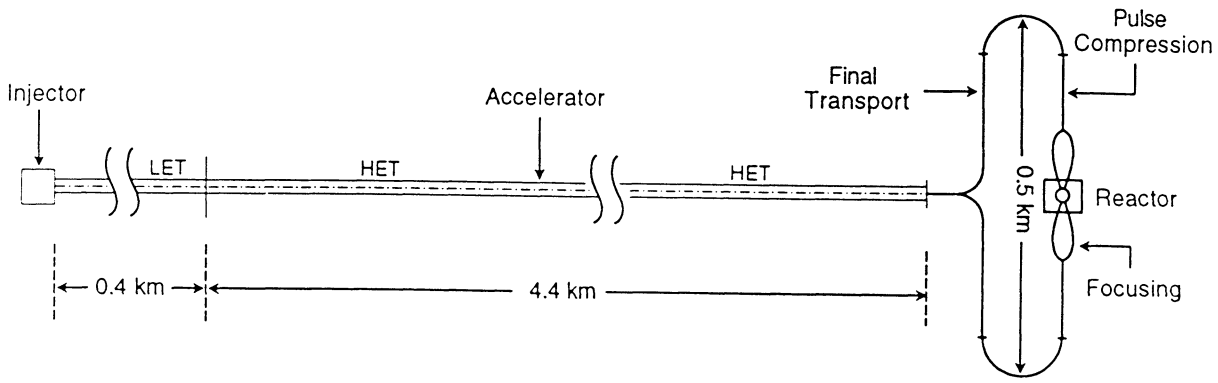

Fig. 2.26. Major elements of a heavy-ion driver.

The injector consists of a source of charged ions and a voltage gradient to accelerate the ions. The injector is followed by an injection matching section where the ion beam parameters (spot-size and undepressed tune) are adjusted to match those of the accelerator focusing lattice.

There are several types of sources and injectors. A simple injector could consist of a plasma-discharge ion source followed by a voltage grid. In this design, ions would be created from a gas or vapor by a discharge voltage and then accelerated between electrical voltage grids. The shape of the grids (anodes and cathodes) is designed to produce a source of ions with minimal angular divergence. We have not created a detailed design of the injector, but we have used common limits to scale the achievable injection currents with ion mass, ion charge state, and acceleration gap voltage.

The accelerator consists of a lattice of quadrupole arrays with induction cells located between the arrays. The quadrupole arrays contain a superconducting quadrupole winding around each beam tube. The quadrupole field of adjacent quadrupoles are offset by a 90° rotation to provide an alternating focusing lattice (which is described as a focusing-drift-defocusing-drift, or FODO, lattice). Each pair of quadrupoles in a repeating FODO lattice focuses the beam in two dimensions. Inductor cells are placed between quadrupoles as shown in Fig. 2.27 Each induction cell consists of a ferromagnetic core surrounding all of the beams as shown schematically in Fig. 2.28; the cores accelerate the beams through transformer action.

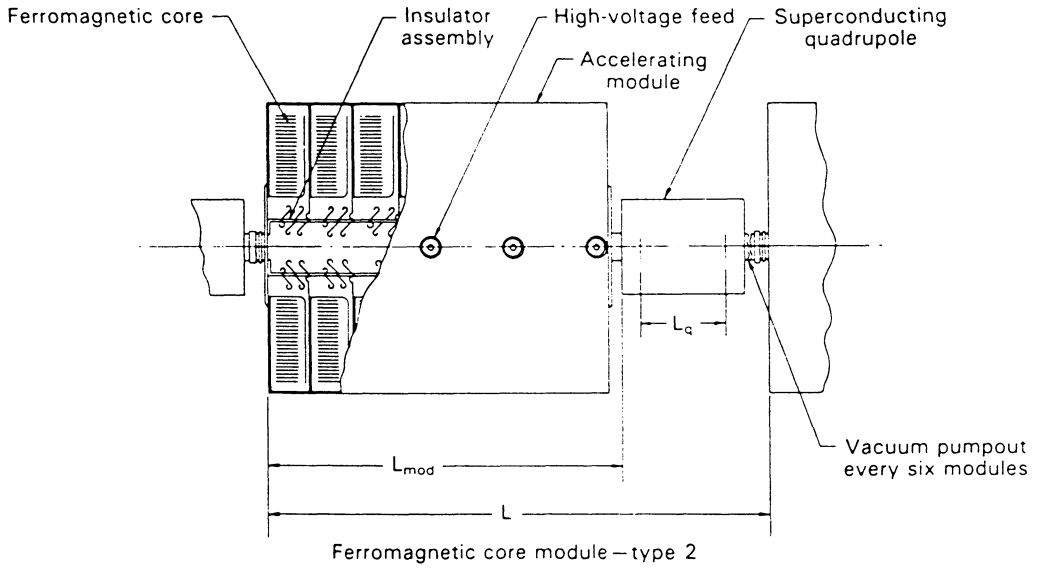

Fig. 2.27. Acceleration and focusing components in each half-lattice period.[2.37]

Because of the need for very short pulse durations at the target, the axial length of the pulse must be compressed after the beam leaves the accelerator. This is done by using a shaped pulse for the final induction cells to preferentially accelerate the end of the ion pulse and give the beams a velocity tilt. The drift compression region follows the final inductors and allows the velocity tilt to compress the beam's length.

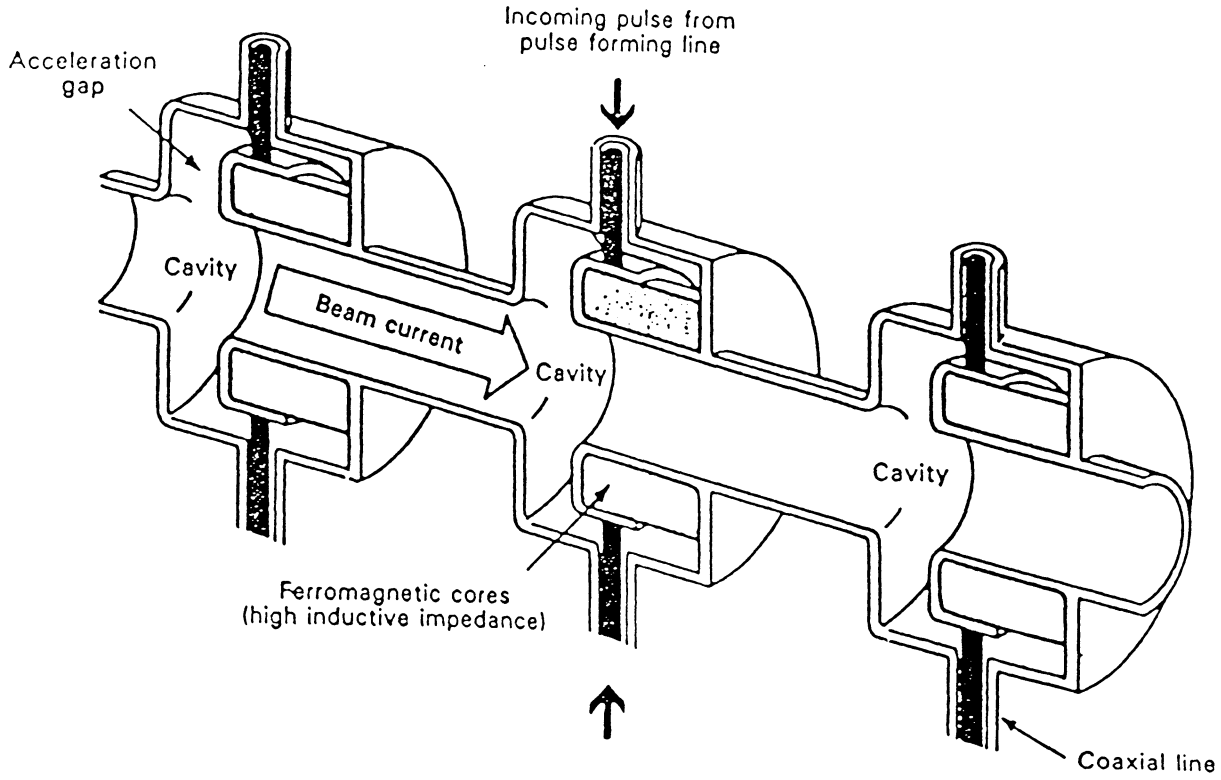

Fig. 2.28. Schematic cutaway of an induction linac.[2.38]

The final focusing system consists of quadrupole pairs or triplets which compress the beams to the final spot size. In order to attain the smallest possible spot sizes, the beams are separated and expanded before final focusing. The beams are also neutralized with co-injected electrons just after leaving the final focusing magnets in order to minimize space-charge effects during focusing.

2.4.3 Design Strategy

Our design strategy builds upon one described by Monsler[2.39] in 1987. The chosen high-energy propagation mode uses a constant effective focusing length for each quadrupole and a constant beam radius. This allows for a single quadrupole array design to be used for the entire length of the driver. The spacing of the quadrupole arrays (the linear quad packing fraction) is varied so that the beam carries the maximum allowable current at every point in the driver.

Two types of inductor cells are used. A large radial build is used in the beginning of the driver where cores and quad arrays are packed closely together, and a smaller radial build is used in the high-energy section of the driver where there are greater separations between quad arrays. The use of inductors with a smaller radial build in the longest section of the driver lowers the total required volume of core material (metglas).

The use of a single design for the quad arrays and only two designs for the inductors simplifies manufacturing requirements and allows for maximum economy of scale for producing driver components.

Our reference design is conservative in several respects. More aggressive driver designs use beam combination, beam separation, and/or recirculation to lower driver costs. All three modifications add performance uncertainties and design complexity, so we have chosen not to use these options in our base driver. We also chose a base design using singly charged, $q = 1$, ions. Higher charge states require more complicated sources and injectors, and highly charged ions may require better vacuums because of the increased potential for beam-gas charge exchange.

Beam combination could reduce the length and cost of the low-energy part of the driver. If beams can be combined, then high beam currents can be achieved early in the driver without large beams or unattainable rates of pulse compression. Unfortunately, even perfect theoretical beam combination leads to beam emittance growth which degrades target performance.

Beam separation before final focusing could theoretically lower the emittance per beam and reduce the achievable single-beam spot sizes. The beam separators would have to split beams with the high final ion energies and currents at the end of the accelerator with minimal beam loss. Even small amounts of ion loss may be disastrous at final beam energies. Any ions "lost" from the front of the pulse will impact the beam tube and scatter ion and electrons from the wall that may interfere with the following ions. While it is possible that the required beam separators could be developed, we have not assumed them in our base design.

Recirculation involves bending sections of the driver into a circle so that the beam may pass through each acceleration cell several times. Recirculation can greatly reduce the number and cost of driver components required, but the feasibility of recirculation has not yet been demonstrated. Critical issues include the effects of bending magnets on beam quality (emittance),

maintaining vacuum quality in the beam lines over several beam "laps", and the possibility for several modes of resonant instability growth.

2.4.4 Accelerator Modeling

Each driver is designed from both ends. The beam parameters in the majority of driver are set by the desired final beam energy and pulse duration. The beam parameters, required energy, and length of the low-energy transport stage are set by the injector beam parameters for a beam radius consistent with the beam radius and total charge used in the high-energy transport section of the driver. An intermediate pulse-matching stage is inserted between these two driver sections in order to shorten the pulse length (and thus increase the current) coming from the low-energy stage to that needed for the high-energy stage.

The three heavy-ion driver stages can be described as a low-energy transport stage, a pulse-matching stage, and a high energy transport stage. In the low-energy transport stage, initial beam currents and pulse lengths are determined by injector characteristics, and acceleration gradients and pulse compression are limited by the velocity tilt limit for the magnetic focusing lattice. The velocity tilt limit results from the fact that charged particles with different velocities in a given magnetic field experience different forces. Even though the single-particle trajectories in a quadrupole lattice are independent of velocity (since displacements in a constant magnetic field gradient are set by the charge-to-mass ratio), the head-to-tail relative velocity difference ($\Delta v/v$) for the beam must be limited to prevent serious mismatch oscillations of the beamlets in the focal system.

In the pulse-matching stage, the acceleration gradient is fixed at the insulator flash-over limit and pulse compression continues at the velocity tilt limit. The flash-over limit for a beam-tube is much lower than the hold-off voltage gradient for the beam-line vacuum. If the average acceleration gradient along the beam-tube is high enough, a charged particle released near the tube wall will accelerate, impact the wall, release more particles, and produce a discharge breakdown of the applied electric field. Because the allowable acceleration gradient at injection is well below the flash-over limit, the gradient is continuously increased in the low-energy transport stage. Once the flash-over limit is reached, the average acceleration gradient must remain constant, but head-to-tail acceleration differences can still be used for pulse compression.

The need for a pulse-matching stage could be removed if larger injector voltages, larger injector currents, or larger beam diameters for the low-energy stage were used.

The high-energy transport stage makes up most of the accelerator (roughly 90% of the total length). During the high-energy stage, the physical pulse length is kept constant and the voltage gradient remains fixed at the insulator flash-over limit; the scaling of beam parameters in this section was first described in Monsler's 1987 paper.

2.4.4.1 Scaling High-Energy Beam Parameters from Final Beam Requirements

The Maschke equations[2.40] can be used to determine the maximum transportable beam current, I_b, as a function of the cumulative acceleration voltage, V. The relationship between achievable final beam current and final driver voltages can then be used to determine the minimum driver voltage needed for a given driver power (driver energy / final accelerator pulse duration). The Maschke limits for beam current and beam radius can then be used with the constant voltage gradient to determine the beam parameters throughout the high-energy driver stage.

The Maschke equations derive the transportable current and beam size by equating the focusing force given by the continuous limit approximation for FODO focussing systems with the defocusing forces resulting from a given line charge density. The Maschke limit for the beam current is

$$I_b = (2.89\ \mathrm{MA}) \left(1 - \left(\frac{\sigma}{\sigma_0}\right)^2\right) \left(\sigma_0^4\, (\beta\gamma)^5\, \eta^2 \left(\frac{A}{q}\right) \left(\frac{\varepsilon_n}{\sigma}\right)^2 B_{be}^2\right)^{1/3}$$

where

A = the ion mass (amu),

q = the ion charge state,

B_{be} = the maximum magnetic field at the beam edge (T),

ε_n = the normalized emittance of the beam (m-radians),

η = the axial quad packing fraction (η_i is η at injection),

σ_0 = the undepressed tune (phase advance per lattice period in radians),

σ = the depressed tune (including space charge effects) (radians), and

$\beta\gamma$ = relativistic factor approximately given by

$$\beta\gamma = \left[\sqrt{\frac{2\,q\,e}{A\,m_p\,c^2}}\right]\sqrt{V}$$

In order to maintain a constant beam radius, the axial packing of the quadrupole fields must scale as $\eta = \eta_i\,(V_i / V)^{1/2}$. Using this relationship gives the desired equation for the maximum transportable beam current as a function of cumulative voltage

$$I_b(V) = 2.89 \times 10^6 \left(1 - \left(\frac{\sigma}{\sigma_0}\right)^2\right)\left(\sigma_0^4\,\eta_i^2\,V_i\,\frac{A}{q}\left(\frac{\varepsilon_n}{\sigma}\right)^2 B_{be}^2\right)^{1/3}\left(\frac{2\,q\,e}{m_p\,A\,c^2}\right)^{5/6}\sqrt{V}$$

or

$$I_b(V) = C_I(\eta_i,\ B_{max},\ A,\ q,\ \sigma,\ \sigma_0,\ \varepsilon_n,\ V_i)\ \sqrt{V}$$

where, in addition to the variables already defined,

C_I = constant that depends on the indicated parameters,

m_p = the mass of a proton (nucleon) in kg,

e = the charge of an electron in Coulombs,

V_i = the injection voltage in Volts, and

B_{max} = 1.5 B_{be} is the Max. field at the Superconductor.

The required accelerator voltage can then be found from the driver energy, E, and the post-acceleration pulse duration, τ_f by solving the following power equation for V:

$$V\,I_b(V) = \frac{E}{N\,\tau_f}$$

where N = number of beams and τ_f is the pulse duration of the beam as it leaves the accelerator. The required final voltage is thus:

$$V_f = \left(\frac{E}{N\,\tau_f\,C_I}\right)^{2/3}$$

and the required final beam current is given by: $I_{b,f} = I_b(V_f)$. The decision to fix the beam radius, the effective quadrupole length, and the undepressed tune also fixed the physical pulse length and the depressed tune as constant.

Figures 2.29a and 2.29b show the calculated accelerator voltages and beam currents as a function of driver energy for heavy-ion drivers using our base parameters. The chosen base-driver parameters were the result of a parametric study described in Section 2.4.8. The base driver parameter set was: N = 12 beams, τ_f = 100 ns, η_i = 0.8, B_{max} = 10 T, A = 131, q = 1, σ = 8°, σ_0 = 80°, and $\varepsilon_n = 10^{-5}$ meter - radians, for an assumed injection voltage of V_i = 3 MV.

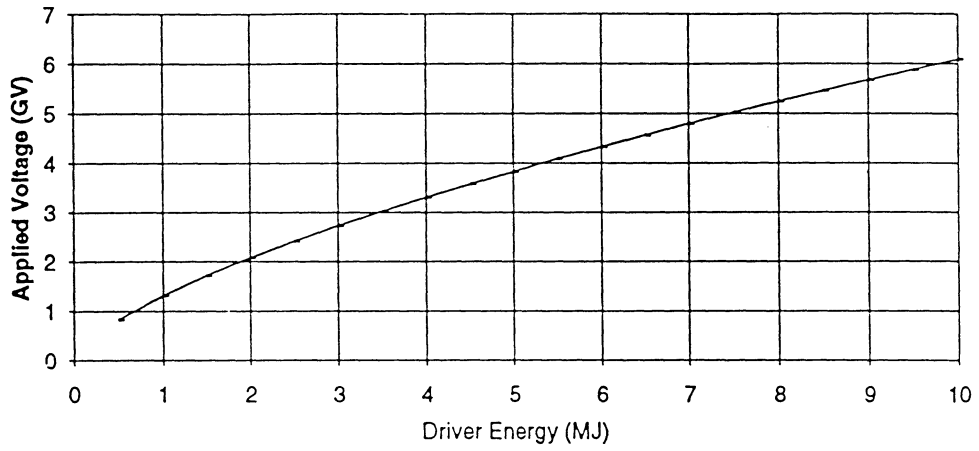

Fig. 2.29a. Cumulative voltage for base driver designs.

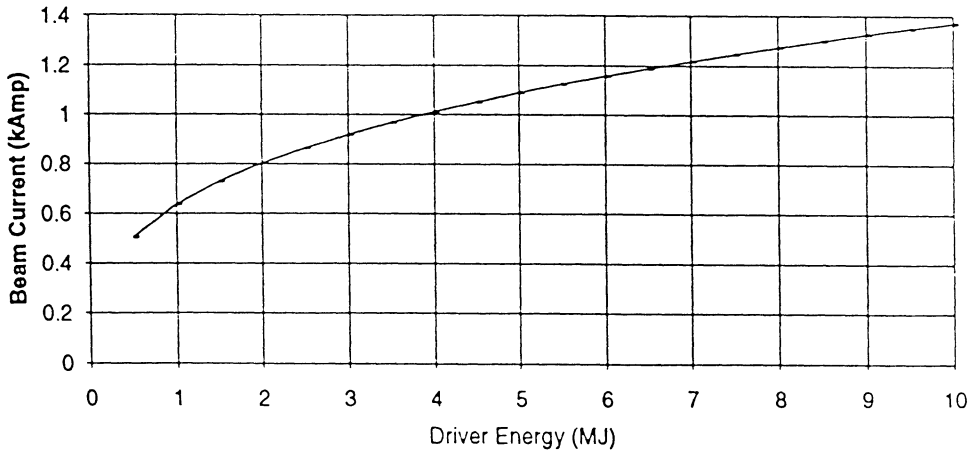

Fig. 2.29b. Final beam currents for base driver designs.

2.4.4.2 Ion Range, Spot Size, and Target Gain

Once the final beam voltage and current are determined, the gain and optimum final focusing half angle can be scaled from the corresponding ion range, R_{ion}, and spot size, r_s. For this study, we developed the following curve fit for cold ion ranges in terms of the ion mass, A, and cumulative accelerator voltage, V:

$$R_{ion} = \left(3.04 \times 10^{-5} A + 349\, A^{-2.21}\right) \left(\frac{qV}{10^9}\right)^{(1.72 - 0.00275A)} \text{ g/cm}^2.$$

Figure 2.30 shows the ion range as a function of energy for our base driver parameters.

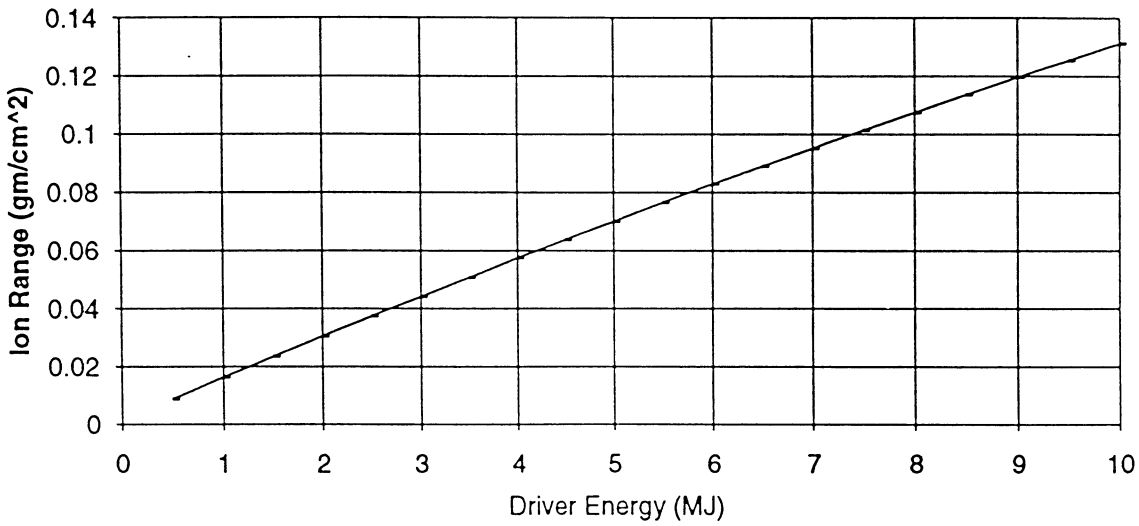

Fig. 2.30. Ion ranges for base driver designs.

The achievable spot size depends on the final focusing half angle, θ. We elected to specify θ for each driver as that value yielding the minimum spot size, r_s. The spot size, r_s, is determined as discussed in Section 2.4.7.2. Figure 2.31 shows the minimum spot size vs. energy for our base parameters, and Fig. 2.32 shows the dependence of spot size contributions on the final focusing half angle for a 5 MJ driver.

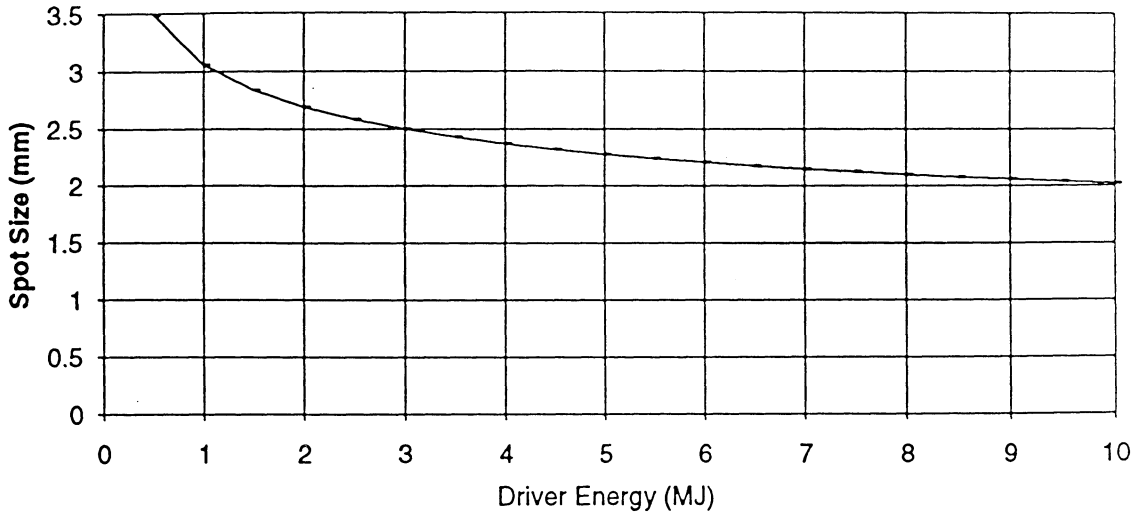

Fig. 2.31. Spot sizes for base driver designs.

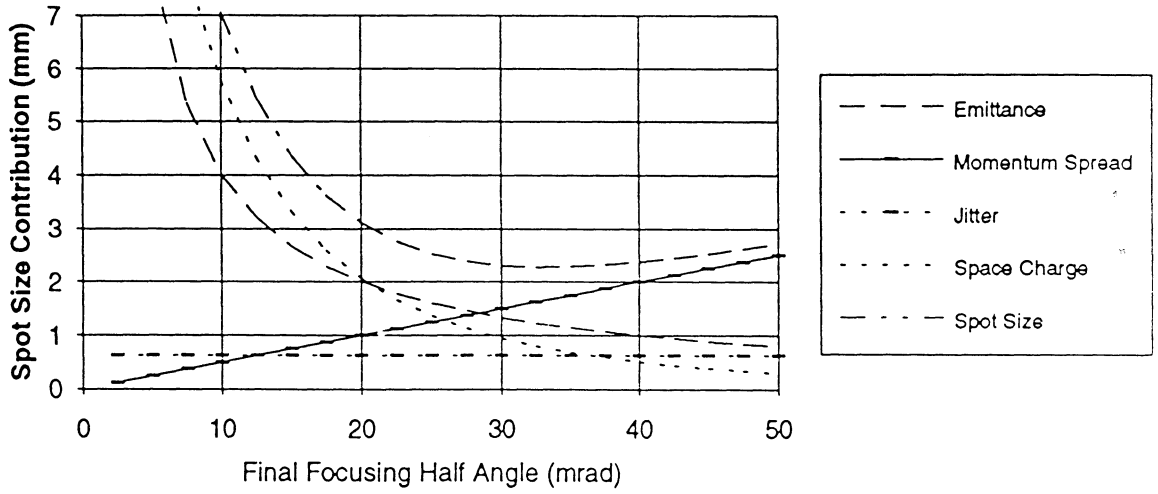

Fig. 2.32. Spot size contributions for a 5 MJ heavy-ion driver.

Gain curves for indirect drive targets provided by the study guidelines were fit to the functional form G = A + B ln(E), where A and B are functions of r_s and R_{ion}. The resulting gain calculations:

$$G = 62.6 - 142.3\, r_s^{1.25} R_{ion}^{0.633} + \left(32.8 + 82.1\, r_s\right)^{0.783} R_{ion}^{0.647} \ln(E)$$

(where E is given in MJ) are shown as a function of E for our base driver in Fig. 2.33.

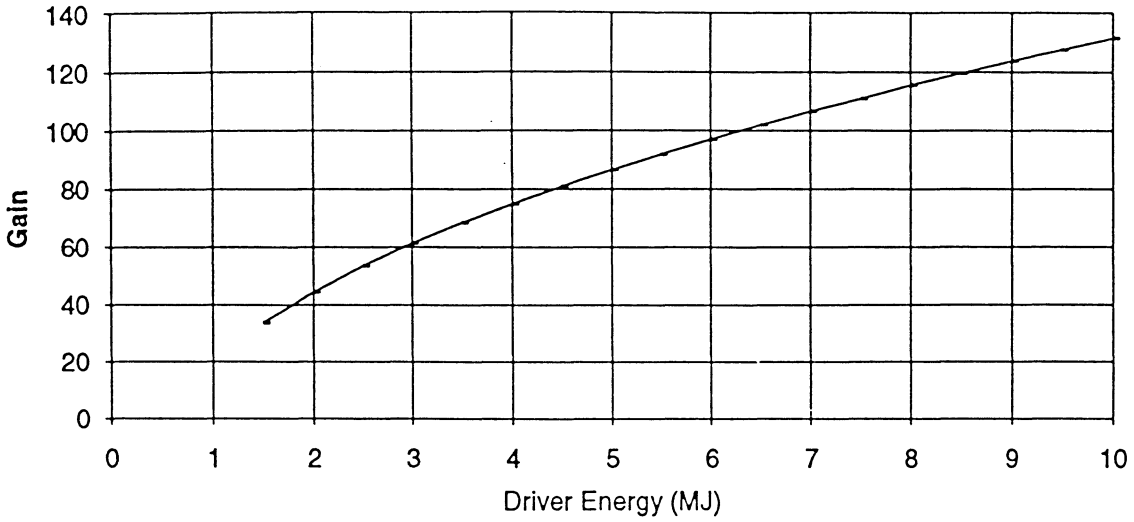

Fig. 2.33. Gain curve for base driver designs.

2.4.4.3 Injector Characteristics

A detailed injector design was beyond the scope of this study. The base injector design and scaling shown here were taken from the HIFSA study.[2.41] More advanced injector designs may be able to produce higher injection currents and/or higher energy ions.

The injected current density is assumed to be limited by the Child-Langmuir law:[2.42]

$$j = 5.46 \times 10^{-8} \sqrt{\left(\frac{q}{A}\frac{V_s^3}{d^4}\right)}$$

where

V_s = (4/3) V_i = the extractor voltage (assumed = 4 MeV for all drivers), and

d = the source extraction gap width (= 0.8 m for a 5 MV/m voltage gradient limit).

In order to increase the injection current, the source radius can be larger than the transport beam radius (a). Assuming focusing in the injector which allows a source radius of 2×a, gives an injected current per beam, $I_{b,inj}$, of:

$$I_{b,inj} = 4\pi a^2 \left[5.46 \times 10^{-8} \sqrt{\frac{q}{A}\frac{V_s^3}{d^4}}\right]$$

Where the transport beam radius is given by the Maschke approximation:

$$a = (2.32\ \mathrm{m}) \left[\left(\frac{\sigma_0}{\eta} \right) \left(\frac{1}{\beta\gamma} \right) \left(\frac{A}{q} \right) \left(\frac{\varepsilon_n}{\sigma} \right)^2 \left(\frac{1}{B_{be}} \right) \right]^{1/3}$$

which is a simplified version of the approximation:

$$a = \left[\frac{\varepsilon_n^2 \sigma_0 c^2}{\sigma^2 \left(\frac{B_{max}}{1.5} \right) \eta_i \sqrt{V_i}} \right]^{1/3} \left[\frac{2 A m_p}{q e} \right]^{1/2}$$

Assuming 8% of the beam is lost from the injector to the target (a somewhat arbitrary assumption allowing for 2% beam loss in the injector, 2% beam loss in the accelerator, 2% beam loss in final focussing, and 2% beam loss in the chamber), the pulse duration at injection will be:

$$\tau_i = \frac{Q_{inj}}{I_{b,inj}} = \frac{1}{0.92} \frac{\tau_f I_{b,f}}{I_{b,inj}}$$

where $I_{b,f}$ is the final beam current calculated earlier. The corresponding pulse length will be:

$$l_{p,inj} = \tau_i \sqrt{\frac{2 q e V_i}{A m p}}$$

Possible Improvements in Injector Performance. Both The cost and performance of a heavy-ion driver improve significantly with increases in the assumed injector voltage and current. The injected current limit from the Child-Langmuir law is a small fraction of the transportable current limit for the focusing lattice. In theory, an injector could be built with current densities much greater than those given by the Child-Langmuir law. High injected currents and injector voltages are not assumed in our designs because high voltage, high current density injectors require significant development.

An example of a high current injector would be a low-voltage, high-current, converging beam source followed by a long low-gradient (10 kV/cm) acceleration column with quadrupole

pairs for focusing the beam to the desired beam size. Advanced injectors such as this could provide currents and beam sizes closer to the transport limits of the quadrupole focusing array.

Producing a high-current, low-emittance beam and matching the beam parameters to those required by the accelerator is a complex problem. A source producing converging ions requires an acceleration gap with shaped electrodes.

If the injector current can be increased enough so that the initial current limit is set by the transport lattice, the limits on the transportable current will need to be examined more closely. The Maschke limit assumes step-like quadrupole fields which have constant strengths over an effective length. Actual magnets will have to be longer than their effective field lengths, and field cancellation from the end fields of adjacent magnets may further limit the maximum axial packing fraction for the quadrupole fields. These limits on η become less important at high energies where η is small, but both limits could reduce the allowable low-energy currents below our calculated currents.

Transportable currents at low ion energies may be increased by substituting electrostatic quadrupoles (such as those used at LBL in the MBE-4 experiment) for the magnetic quadrupoles. Short quadrupole designs and high axial packing fractions are much easier to achieve with electrostatic quadrupoles. However, because electrostatic quadrupoles use space-charge effects instead of magnetic fields, they are only effective for low line-charge density beams (i.e., at low beam currents).

2.4.4.4 Low-Energy Transport Modeling

Magnetic focusing requires a maximum velocity tilt,

$$\left(\frac{V_{tail} - V_{head}}{V_{ave}}\right)$$

of 0.3 . In order to prevent elongation of the pulse, the entire pulse is loaded into the accelerator before acceleration is begun; this gives a limit on the initial voltage gradient, Φ_i (Volt/m), of:

$$\Phi_i = 0.3 \frac{V_i}{I_{p,inj}}$$

The allowed voltage gradient will then increase as:

$$\Phi(V) = \Phi_i \left(\frac{V}{V_i} \right)^{3/2}$$

where V is the cumulative accelerator voltage, until the insulator flash-over limit is reached. Once the flash-over limit is reached, the acceleration gradient remains constant for the remainder of the driver.

2.4.4.5 Pulse Compression in the Pulse-Matching Driver Stage

The pulse length is fixed at injection by the injector current density limits and is fixed at the end of the accelerator by the choice of desired beam power (E and τ_f are set). Because we have chosen to keep the pulse length constant during high-energy transport, we need to adjust the pulse length at the end of the low-energy stage of the driver to the desired final value. In almost all cases, additional pulse compression is required after the low-energy stage. This pulse compression can be done by using a shaped pulse on the inductor cells which has an average voltage determined by the voltage flash-over limit and increasing voltage as the pulse passes through the inductor.

Because the pulse duration of the beam varies as the inverse of the cumulative voltage in the low-energy driver stage, the pulse duration at the end of the low-energy stage, τ_{fo} will be

$$\tau_{fo} = \tau_{inj} \frac{V_{inj}}{V_{fo}}$$

where V_{fo} is the voltage at which the voltage gradient (determined by the velocity tilt limit) reaches the insulator flash-over limit, Φ_{fo} = 0.85 MV/m (this limit is actually the product of the insulator limit of 1 MV/m and the fraction of the driver axial length lined with insulator = 0.85). V_{fo} can be calculated from the acceleration gradient limit given earlier as

$$V_{fo} = \left[\frac{\Phi_{fo}}{\Phi_i} \right]^{2/3} V_{inj}$$

so the pulse length at the end of the low-energy stage will be given by

$$l_{p,fo} = \tau_i \frac{V_i}{V_{fo}} \sqrt{\frac{2qeV_{fo}}{Am_p}}$$

The pulse length during the high-energy stage of the driver is equal to the final pulse length, $l_{p,f}$, which is determined by the final voltage of the accelerator, V_f, and the final pulse duration, τ, from the relationship

$$l_{p,f} = \tau_f \sqrt{\frac{2qeV_f}{Am_p}}$$

Because pulse compression is done at a velocity tilt limit of $\Delta v/v = 0.3$, the required length for the pulse compression region, X_{pc}, is then:

$$X_{pc} = \frac{1}{0.3} (l_{p,fo} - l_{p,f})$$

The total accelerating voltage of this section can be obtained by multiplying X_{pc} by Φ_{fo}.

2.4.4.6 Summary of Beam Parameter Scaling in the Three Driver Stages

Table 2.19 summarizes the dependencies described in the previous chapters for beam parameters variations in each driver stage with the cumulative accelerator voltage, V.

2.4.4.7 Requirements for Inductors and Quad Arrays

Quad Array Cross Section. Figure 2.34 shows the array and inductor cross sections, as well as a detailed cross section of the quadrupole insert. The required dimensions for quadrupole windings and the collar thickness are calculated from the quadrupole bore radius, the required magnetic field, and the properties of the superconductor and the collar material.[2.43] The compact arrays modeled allow some of magnetic field lines leaving one quadrupole to pass through adjacent quadrupoles. Designing high-field-quality windings for such an array is a complex problem, but the required dimensions will be similar to those of the simple windings modeled here. Parametric studies were done using steel collars around NbTi and Nb_3Sn superconducting windings with a 1:1 ratio of superconductor to copper.

Table 2.19. Scaling of Beam Parameters with Accelerator Voltage

	Low-Energy Stage	Pulse Matching Stage	High Energy Stage
Voltage	V_i to V_{fo}	V_{fo} to V_{HET}	V_{HET} to V_f
Voltage Gradient, Φ =	$\Phi_i \left(\frac{V}{V_i}\right)^{3/2}$	Φ_{fo}	Φ_{fo}
Beam Current, I_b =	$I_{b,inj}\left(\frac{V}{V_i}\right)$	$I_{b,fo}\left(\frac{l_{p,fo}}{l_p}\right)\sqrt{\frac{V}{V_{fo}}}$	$I_{b,f}\sqrt{\frac{V}{V_f}}$
Pulse Duration, τ =	$\tau_i\left(\frac{V_i}{V}\right)$	$\tau_{fo}\left(\frac{l_p}{l_{p,fo}}\right)\sqrt{\frac{V_{fo}}{V}}$	$\tau_f\sqrt{\frac{V_f}{V}}$
Pulse Length, l_p =	$l_{p,inj}\sqrt{\frac{V_i}{V}}$	$l_{p,fo} - \frac{0.3}{\Phi_{fo}}(V - V_{fo})$	$\tau_f\sqrt{\frac{2qeV_f}{(Am_p)}}$
Length of Stage in Base Driver	356 m	33.5 m	4.41 km

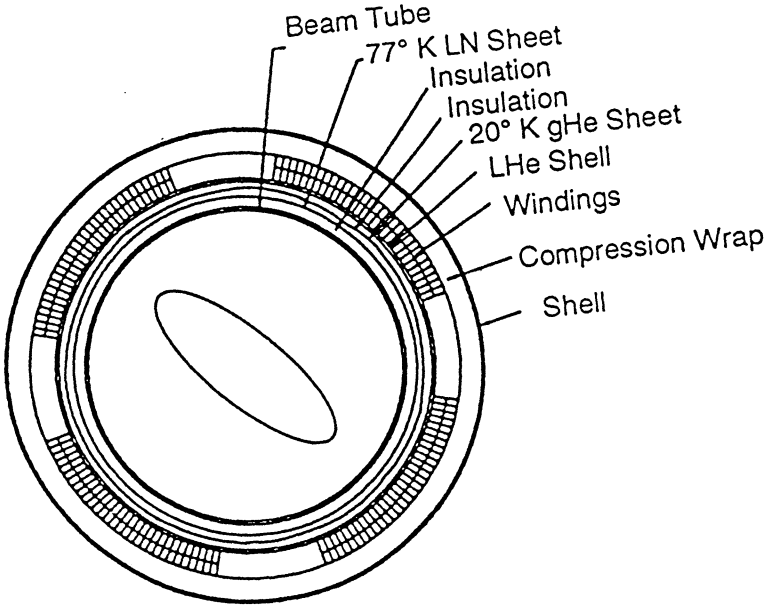

Quadrupole Insert

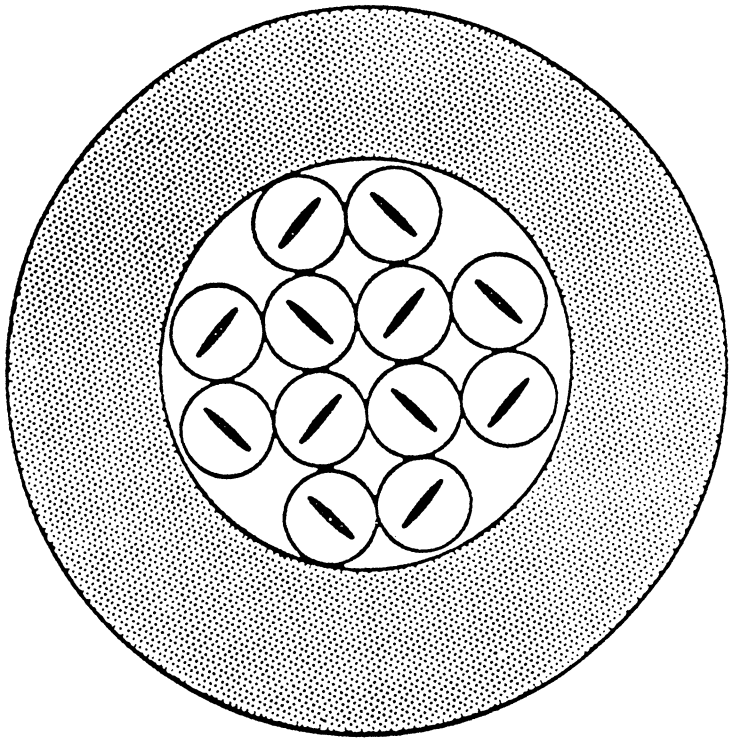

Fig. 2.34. Beam quad array and inductor cell cross sections.

Inner Winding Radius. The inner radius of the superconducting windings is set to 1.5 times the beam radius. This scaling allows for an inner beam tube radius roughly 1.3 times the beam radius surrounded by a 2 mm thick (warm bore) beam tube, 1 cm total thickness of superinsulation in three layers, two thin (mm) cooled Cu sheets at 77 K and 20 K, and a 2 mm thick support tube for the windings. These assumptions are based on the desire to keep the insulation and cooling dimension as small as possible while providing sufficient protection for the superconductors.

Winding and Collar Thickness. A quadrupole field requires a cos(2θ) current distribution, which may be approximated with four evenly spaced blocks of constant current (in alternating directions), each occupying a 60° arc with constant winding thickness. Actual windings will need to give better quality quadrupole fields and could consist of two or three radial layers each containing from one to three coils per quadrant, but the total required total thickness and conductor area will not differ greatly from the simpler model. The thickness is then given by:

$$\Delta R_w = R_{iw}\left[\exp\left(\frac{\pi}{\sqrt{3}}\,\frac{B}{\mu_0 \lambda J_c(B)}\,\frac{1}{R_{iw}}\right) - 1\right]$$

where:

- B = B_{max} = maximum magnetic quadrupole field (Tesla),
- R_{iw} = inner winding radius,
- λ = area fraction of the winding containing superconductor, and
- $J_c(B)$ = critical current of the superconductor.

The approximations used for $J_c(B)$ are:

$$J_c(B) = (3{,}520 - 339\,B)\left(\frac{MA}{m^2}\right)$$

for NbTi, and

$$J_c(B) = \frac{9.31 \times 10^4}{\sqrt{B_c}}\left(\left(1 - \left(\frac{T}{18.3}\right)^2\right)\left(1 - \frac{B}{B_c}\right)\right)^2\left(\frac{MA}{m^2}\right)$$

for Nb_3Sn,

where $B_c = 27.5\left(1 - (T/18.3)^2\right)(1 - T/54.9)$ is a function of the temperature, T (K).

The required collar thickness can then be determined from both the hoop stress if support from the array structure is assumed to cancel the bending moments. For a given collar thickness, t_c, the maximum hoop stress can be estimated by modeling the $\cos^2(2\theta)$ force distribution as four point loads on a ring.[2.44] This gives a maximum tensile load of

$$T = \frac{F}{2}\,\frac{1}{\sin(\pi/4)} = \frac{\left(B^2/(2\,\mu_0)\right)(\pi/4)\,R}{2\sin(\pi/4)}$$

The collar thickness is then set such that the tensile stress is less than half the yield stress of the collar material. The array is then scaled using trigonometric relationships for the radius of a circular "pile" of cylindrical quadrupoles with shaped iron inserts in the gaps, and a 2 cm thick steel collar around the entire array.

2.4.4.8 Required Length and Number of Driver Components

Core Requirements. The total magnetic flux, Φ_M (measured in Volt-seconds), required in each stage is obtained by integrating the pulse duration, $\tau(V)$, over V. Because the pulse duration, τ, continually decreases as the cumulative voltage, V, increases, the resulting requirements for each stage are:

$$\Phi_{M,\,LET} = \tau_i\,V_i\,\ln\left(\frac{V_{fo}}{V_i}\right)$$

for the low-energy stage,

$$\Phi_{M,\,PM} = 2\,\tau_f\sqrt{V_f}\left(\sqrt{V_{HET}} - \sqrt{V_{fo}}\right)$$

for the pulse-matching stage, and

$$\Phi_{M,\,HET} = 2\,\tau_f\,V_f\left(1 - \sqrt{V_{HET}/V_f}\right)$$

for the high-energy stage.

Each core can provide a volt-second impulse of: $\Phi_{M,\,core} = \Delta B\,\Delta r\,\Delta l$, where ΔB is the field swing of the core material (assumed = 2.4 T for metglas), Δr is the radial thickness of the core, and Δl is the axial width of the core. The number of cores needed in each section is then determined by the core dimensions, and the total volume of metglas can be calculated from these dimensions and the bore radius of the core. In the first two stages of the driver (LET and PM), the arrays intrude into the bores of the inductor cells, the bore radius is set to 1.05 times the outer quad array radius, Δr is set to 0.8 m, and Δl is set to 0.2 m. In the last stage of the driver, the arrays fit between adjacent inductor cells and the bore radius is set to 1.05 times the distance from the array center to the outermost beam tube, Δr is set to 0.4 m, and Δl is set to 0.1 m.

Quad Requirements. The total length needed for the quadrupole focusing fields, L_{focus}, can be obtained by integrating η/Φ with respect to V for each stage. The number of quadrupole arrays needed can then be obtained by dividing L_{focus} by the effective length of each quadrupole, L_q, where

$$L_q = \left(\frac{\varepsilon_n \eta_i \sigma_0^2 c \sqrt{V_i}}{\sigma B^2} \right)^{1/3} \sqrt{\frac{2 A m_p}{q e}}$$

In the low energy stage, the integral for L_{focus} gives:

$$L_{focus} = \eta_i V_i \left(1 - V_i/V_{fo}\right)/\Phi_i$$

The total focusing field length needed for the two higher-energy stages, where the voltage gradient is constant, is

$$L_{focus} = 2\,\eta_i \sqrt{V_i} \left(\sqrt{V_f} - \sqrt{V_{fo}}\right)/\Phi_{fo}$$

Total Driver Length. The total driver length can be obtained by integrating $1/\Phi$ from the injection voltage to the final voltage. This gives a driver length of:

$$L_{driver} = 2\,V_i \left(1 - \sqrt{V_i/V_{fo}}\right)/\Phi_i + \left(V_f - V_{fo}\right)/\Phi_{fo}$$

Quad Array and Inductor Costs. In choosing a base set of driver parameters, only the costs of the inductor cores and the quadrupole arrays were considered; total driver costs for our base driver are discussed in Chapter 8. Once the amount of materials needed in the arrays were calculated, the array components were priced using: \$300/(kg of superconductor in the windings), \$50/(kg of Cu in the windings), \$10/(kg of iron in the array), and \$25/(kg of steel in the collars). The inductor cores were priced using an assumed future unit cost of \$5/kg for metglas.

Because the inductor costs are larger than the quadrupole costs, minimizing material costs also implies minimizing the inductor core volumes. Minimizing the core volume also minimizes the energy lost in the cores and ensures that the chosen design is still optimal for more conservative assumptions on the price of metglas or the assumed cost/Joule of pulse forming networks (PFNs).

2.4.5 Driver Efficiency

Driver efficiency is calculated from energy losses in the pulse forming network and in the metglas inductor cells, and from energy given to the beam by each core. The voltage across a given cell is limited by the volt-seconds of the cell and the total time of pulse, this gives an energy gain per cell of $E_{beams}(V) = (N Q_{beam}) \frac{\Phi_{M,core}}{\tau(V)}$, or $E_{beams}(V) = N \Phi_{M,core} I_{beam}(V)$. The energy lost in the inductor core is scaled from the J/m^3 metglas losses,[2.45]

$$E_{loss}(V) = 140 \frac{(\Delta B)^{1.8}}{(\tau(V) \cdot 10^6)^{0.8}}$$

where τ is in seconds. The pulsed efficiency for a given inductor, η_p, is then given by

$$\eta_p(V) = \frac{E_{beams}(V)}{E_{beams}(V) + E_{loss}(V)}$$

and the average efficiency for the pulsed power is then

$$\langle \eta_p \rangle = \frac{1}{V_f - V_i} \int_{V_i}^{V_f} \eta_p (V)\, dV$$

The wall plug driver efficiency, η_{driver} , can be obtained from η_p, the pulse forming network efficiency (η_{pfn}), the driver energy (E), the driver repetition rate (ω), and the constant power load for cryogenic cooling and vacuum pumping (P_{fixed})

$$\eta_{driver}(E, V_f, \omega) = \frac{E\,\omega}{\frac{E\,\omega}{\eta_{pfn} \langle \eta_p (V_f) \rangle} + P_{fixed}}$$

This equation can then be used in plant system studies to give driver efficiencies as V_f, E, and ω are varied.

Our base driver uses: $\eta_{pfn} = 0.5$, E = 5 MJ, ω = 4.6 Hz, P_{fixed} = 5 MW, V_f = 3.83 GV, and V_i = 3 MV, and has a calculated wall plug efficiency of 28%.

2.4.6 Final Compression and Focus Modeling

For final compression and focus, three interrelated processes must be modeled: beam transport, beam compression (longitudinal focus), and beam transverse focus. Analysis and modeling of these processes is a current field of study and can be quite complex, particularly when space charge is important. Our approach, described in the following three sections, is a compromise between detail and study resources required. The analysis and modeling has been done in sufficient depth to give us confidence that the design concepts can be made to work. For the baseline design (Section 2.4.9), slightly different parameters were used in modeling different parts of the system. Development of a consistent set of parameters by further iteration of the design should be straight forward, and we would not expect it to require significant changes in the design concept.

2.4.6.1 Transport

Important constraints on transport include two-sided illumination of the target, simultaneous arrival at the target for all beam bunches, and beam-to-beam separation in the final

focusing quadrupoles. Section 2.4.9.2 describes the specific transport layout and transport system parameters.

Matching the transport line to the focusing system of the linac is simplified by using a FODO focusing lattice in the transport line which has the same period as the one in the linac. Dipole bending magnets are placed between the quadrupoles to make the bending sections. Precision controls will be required to avoid jitter in the position of the beam at the target.

The depressed tune in a FODO lattice is given approximately by:[2.46]

$$\cos(\sigma) - \cos(\sigma_0) = \frac{2KL^2}{(\bar{a})^2}$$

and the mean edge radius of the beam is given by:

$$(\bar{a})^2 = \frac{2\varepsilon L}{\sin(\sigma)}$$

The symbols used in the above equations are defined in Table 2.20. In the modeling, the simultaneous solution of these two equations provides values for the depressed tune and the mean edge radius of the beam.

Table 2.20. Definition of Terms and Symbols for Beam Radius and Tune equations.

SYMBOL	DESCRIPTION	EXPRESSION
σ	Depressed Tune	Given in 2.4.6.1
σ_o	Lattice Tune	
K	Generalized Perveance	$\frac{2I}{(\beta\gamma)^2[B\rho]}\left(\frac{1}{4\pi\varepsilon_o c^2}\right)$
I	Peak Current per Beam	
$[B\rho]$	Beam Stiffness	$\frac{\beta\gamma A m_p c}{qe}$
A	Ion Mass Number	
q	Ion Charge Number	
L	FODO Lattice Half-Period	
$\bar{a}$	Mean Edge Radius of Beam	Given in 2.4.6.1
ε	Emittance	$\varepsilon_n / \beta\gamma$
ε_n	Normalized Emittance	

2.4.6.2 Compression.

The pulse length is compressed by imparting a velocity tilt to the beam with a series of induction modules. The induction modules apply a linearly varying voltage pulse to the beam so that the head of the beam pulse is decelerated and the tail is accelerated. The tilting of the longitudinal phase space ellipse is illustrated in Fig. 2.35, which shows $\Delta p/p$ on the vertical axis and the bunch longitudinal half-width, a_z, on the horizontal axis. In the subsequent drift section the ellipse rotates until it comes to an upright position, and the bunch length is at a minimum. During the final stages of compression, the space charge forces become large and remove nearly all of the coherent velocity spread produced by the bunching voltage. Only the incoherent momentum spread remains, as illustrated in the figure. An example of ten-fold bunch compression, produced by compressor induction modules followed by a drift distance, is shown in Fig. 2.36,[2.47] which shows a_z and $\Delta p/p$ as a function of the drift distance, s.

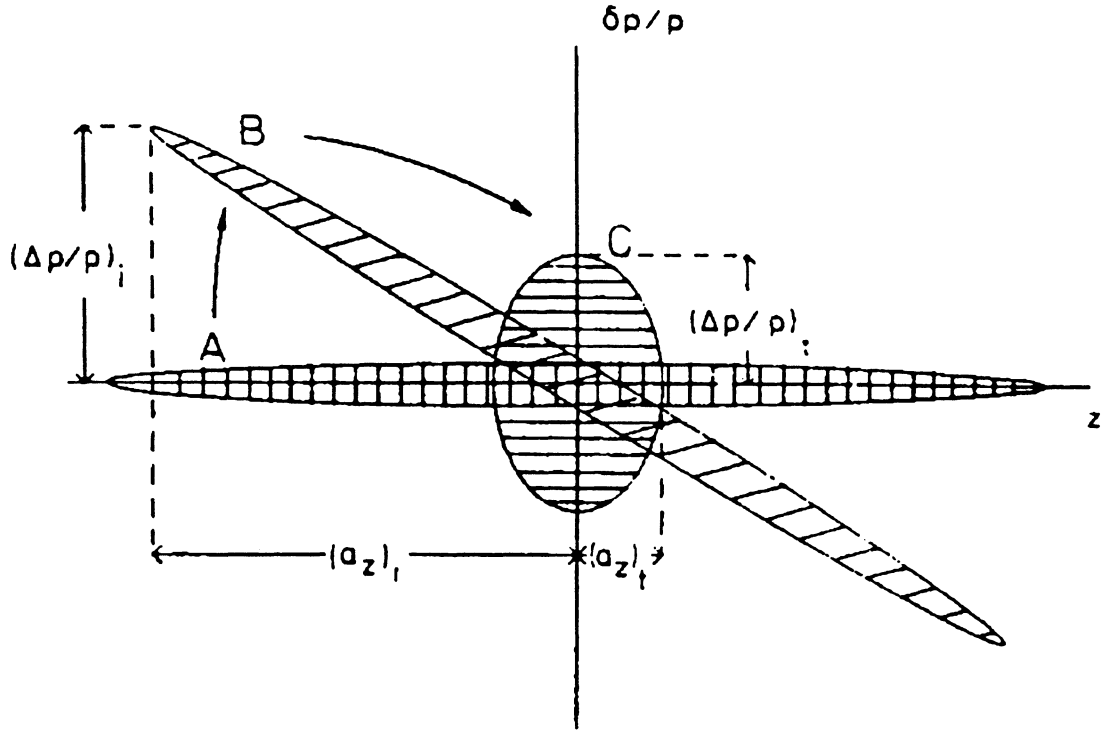

Fig. 2.35. Longitudinal bunch compression. An induction voltage pulse transforms ellipse A into ellipse B, with a large coherent momentum spread $(\Delta p/p)_i$. In a subsequent drift section the rotation is then completed (ellipse C), and $\Delta p/p$ decreases again because of space charge.

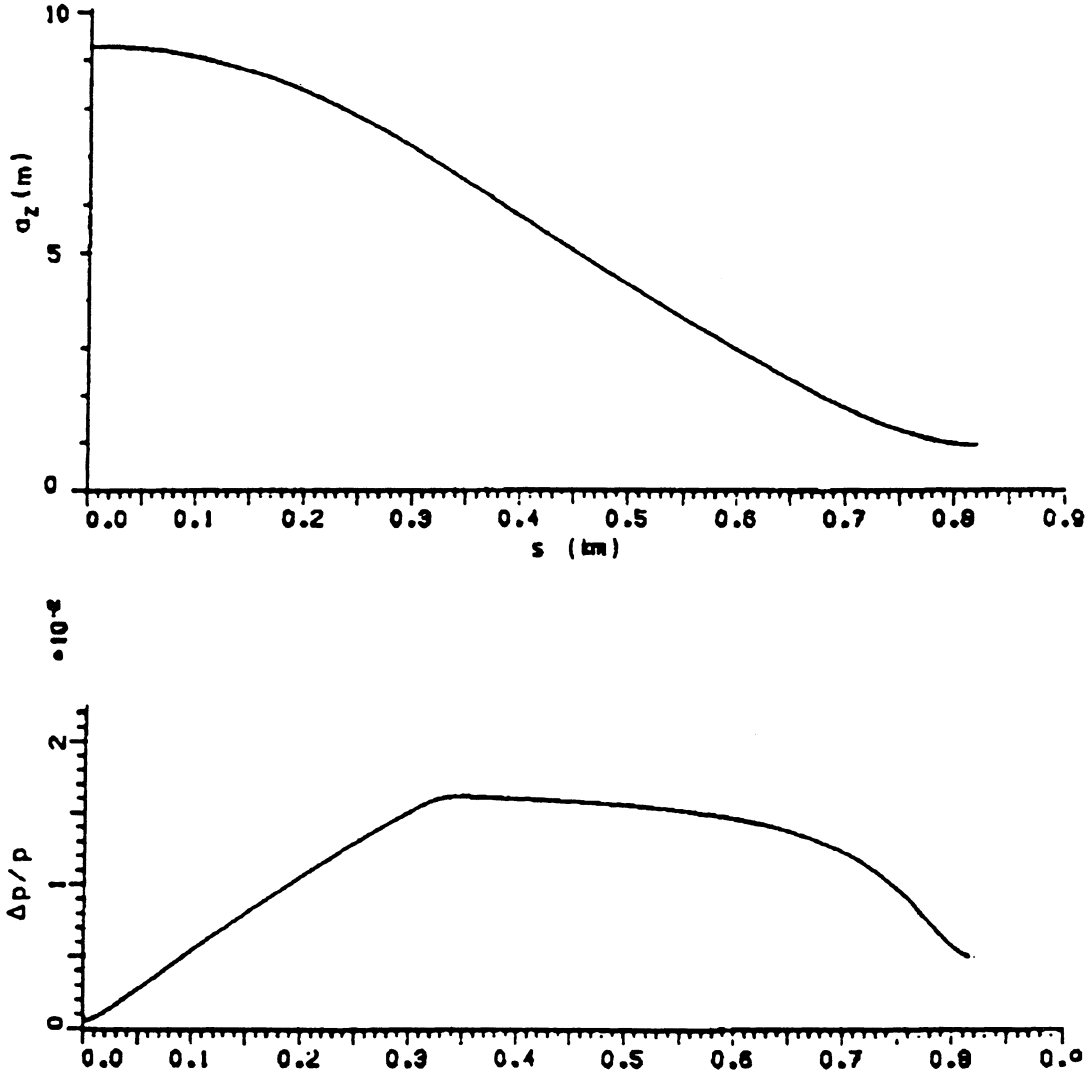

Fig. 2.36. Ten-fold bunch compression produced by 300 meters of compressor induction modules followed by a drift distance. Upper plot: the bunch longitudinal half-width, a_z, as a function of the drift distance, s. Lower plot: momentum spread, $\Delta p/p$, as a function of s.

The velocity tilt required to attain a specified compression is obtained from the equation:[2.48]

$$\text{compression ratio} = \frac{\ell_o}{\ell_f} = 1 + \frac{(\Delta\beta/\beta)^2}{\chi}$$

where ℓ_o is the initial bunch length, ℓ_f is the final compressed bunch length and χ is a dimensionless measure of space charge:

$$\chi = \frac{8\,e}{E_b}\,\frac{g\,\lambda_o}{4\,\pi\,\varepsilon_o}$$

where E_b is the kinetic energy, λ_o is the line charge density at the output of the accelerator, and g is a beam/beam tube geometry factor (which we estimate to be about 1.2 for our system).

The drift distance in a straight transport segment required to remove the tilt and compress the beam is given by:

$$s = \frac{\ell_0 - \ell_f}{\left(\frac{\Delta\beta}{\beta}\right)}$$

Although this equation doesn't apply near the end of the compression where the space charge forces are large, the total drift distance required to remove the tilt and obtain the minimum bunch width can be estimated by setting $\ell_f = 0$.

During compression, the peak beam current increases as the inverse of the bunch length, so the beam perveance K increases (see Table 2.20), and the radius of the beam increases according to the relationships for $\bar{a}$ and σ given earlier. System cost, transport magnet size, and final focus design difficulty all increase with beam size, so the half period of the focusing lattice is decreased gradually during compression to reduce beam radius growth.

2.4.6.3 Final Focus.

Focusing the beams onto the target requires the envelope of each beam to be converging with a half angle of ~ 10-30 mrad at the entrance to the reactor vessel. The simplest lens for making the convergent beam is a quadrupole doublet. At least two additional quadrupoles are

needed to match the beam going into the doublet with the beam emerging from the transport line. Our design for the resulting telescope is described in Section 2.4.9.2.

The upstream telescope quadrupoles are arranged to keep the beam from converging to a small waist within the telescope, in order to reduce the effect of space charge. However, the beam is small enough that our design would have to be modified to take more accurate space charge design calculations into account, and it may be advantageous to add more quadrupoles to the telescope. A final design would have to take into account chromatic corrections and also geometrical aberrations in the large diameter quadrupole lenses. The chromatic effects are minimized by designing the beam compression so that the coherent velocity tilt is a minimum in the center of the final focus system.

Space charge becomes very important as the beam converges to the very small size at the target. This problem is treated in Section 2.4.7.

2.4.7 Reactor Chamber Transport

2.4.7.1 Space Charge

Modeling. A traditional model for beam propagation in the reactor chamber is space charge neutralization (SCN),[2.49] wherein the beam envelope is calculated after specifying that an arbitrary fraction of the beam space charge has been neutralized. We have chosen an alternative model, auto-neutralization (AN),[2.50,2.51] wherein the beam envelope is determined by an auto-neutralizing cloud of hot electrons. By removing the subjective choice of the space charge neutralization fraction, the AN approach provides a higher degree of credibility and at the same time provides physics substance for parameter studies and design choices.

In the AN process, a plasma cloud or other electron source is put in contact with the individual beam bunches near the entrance to the reactor chamber. When the ion bunch separates from the electron source, it has captured an equal number of electrons, so it is macroscopically 100% space charge neutralized. With the traditional SCN modeling, this would mean a zero space charge contribution to the beam spot size. With the more realistic AN modeling, plasma effects within the bunch lead to defocusing of the beam.

Our analysis of AN begins with the trace equation for an ion on the beam envelope

$$\frac{d^2R}{dz^2} = \frac{q E_r(R)}{\gamma m_i \beta^2 c^2}$$

where R is the radial coordinate, z is the position along the beam axis, q is the ion charge state and m_i is the ion mass. $E_r(R)$ is the envelope defocusing electric field and is calculated from the Lemons formula[2.12]

$$E_r(R) = \frac{I_b}{\pi \varepsilon_o \beta c R} K_1\left[\frac{R}{\sqrt{2}\lambda_d}\right] I_1\left[\frac{R}{\sqrt{2}\lambda_d}\right]$$

where I_b is beam current per bunch, K_1 and I_1 are modified Bessel functions of the first and second kind, and λ_d is the electron Debye length

$$\lambda_d = \sqrt{\frac{kT_\perp \varepsilon_o}{e^2 n_e}}$$

where n_e is the bundle electron density and $T_\perp$ is the perpendicular electron temperature.

$T_\perp$ is determined as follows. With the ion bunch in thermal isolation, the electrons are assumed to have an isotropic Maxwell distribution with a temperature taken from previous analysis[2.13] as $T_e = 0.4(m_e/m_i)T_i$, where m_e is the electron mass and T_i is the directed kinetic energy of the beam ions. As the beam bunch converges to the target, the radial electron temperature increases due to radial spatial compression. Because of the high number of electron-boundary collisions during the transport time, electron energy sharing in all three dimensions is assumed. Due to a high axial electron thermal conductivity, the electron temperature is assumed to be approximately constant throughout the bunch at any given time, so the electron compression can be characterized by an average bunch radius, and the perpendicular electron temperature is

given by

$$T_\perp \approx \frac{2}{3} T_e = 0.27 \frac{m_e}{m_i} T_i$$

The defocusing process is terminated upon contact with the target, at which time hot electrons are rapidly replaced by cold electrons, canceling space-charge fields.

The one-dimensional analysis represented by the last four equations yields a beam halo radius but does not provide information on the beam density profile. In applying the analysis, we use the predicted beam halo radius at the target to represent the rms space charge contribution, r_{sc}, to the total beam spot size, r_{total}, thus implicitly assuming the beam density profile is Gaussian.

Figure 2.37a compares two beam envelopes resulting from the AN modeling, and Fig. 2.37b expands the final 1 meter of the representative 5 meter focus. The dotted curve of each figure illustrates a ballistic focus, which is the type of solution described in previous analyses. The solid curve shows a waist focus solution, analogous to the waist solutions of SCN modeling. To achieve the waist solution, the focusing half-angle θ has been increased from the ballistic value of 15 mrad to 16.5 mrad. For this representative case, the additional compression of the waist focus allowed more than 5 times as much ion current to be carried while still achieving the indicated 3 mm envelope spot size.

Because AN waist solutions have not been previously investigated, two concerns regarding their validity were addressed. First, λ_d should be much smaller than the envelope radius over most of the propagation distance so that the electrons provide good shielding of the beam core.[2.13] Although this constraint was found, in general, to be satisfied in AN ballistic solutions, beam compression is much higher for the waist solutions, so the n_e and $T_\perp$ to be used in the equation for the Debye length achieve much higher values. Figure 2.38 compares λ_d with the envelope radius for typical final focus parameters. For these representative parameters, the condition that the Debye length be much smaller than the envelope radius over most of the propagation distance is easily satisfied. For the AN waist solutions in general, we find the small-λ_d-constraint is violated only when r_{sc}^2 is small fraction of r_{total}^2, and in these cases any resulting error would be small.

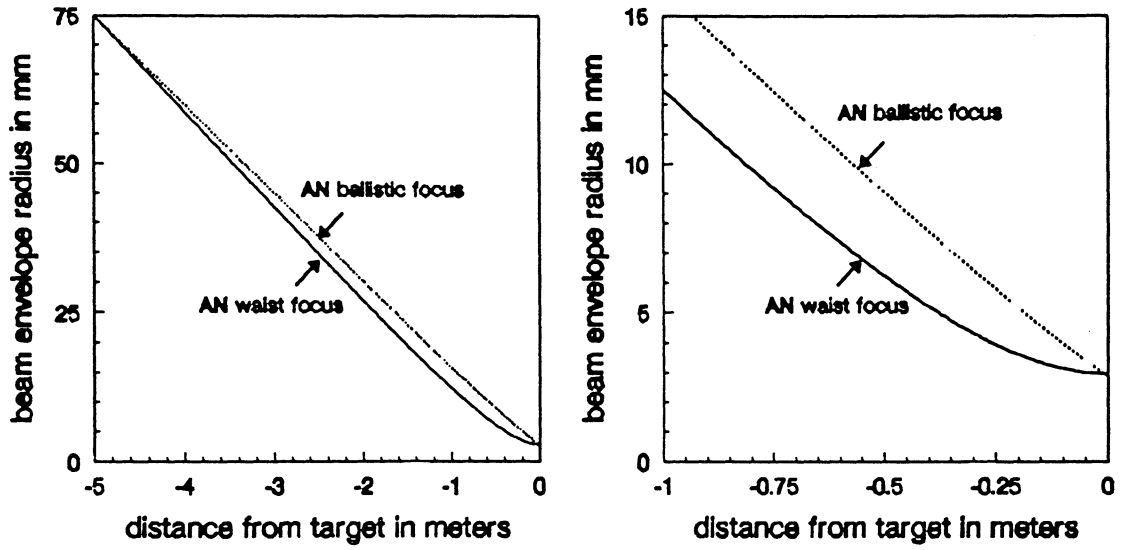

(a) View of Total Focal Length (b) Detail

Fig. 2.37. Beam envelopes from auto-neutralization model.

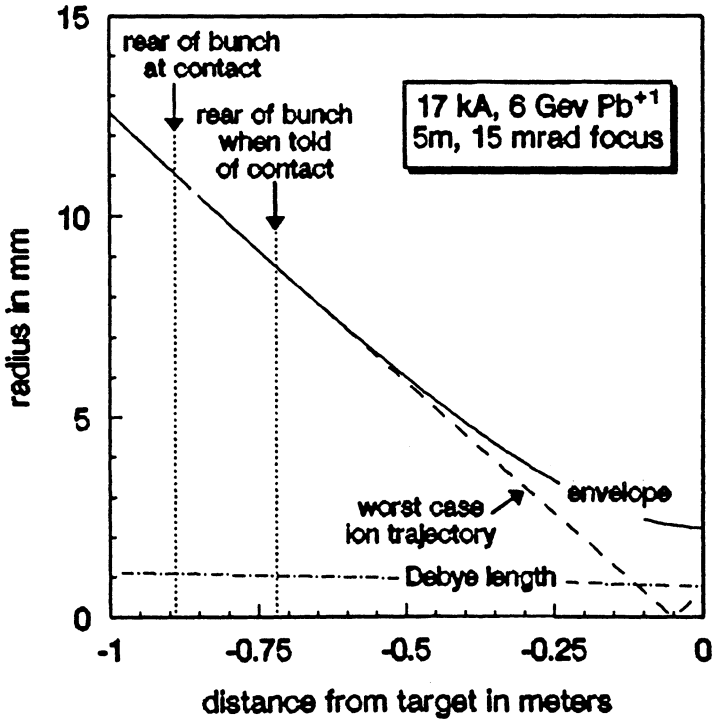

Fig. 2.38. Beam envelope, Debye length, and worst-case trajectory.

The second concern is whether all ions in the bunch will actually hit the target in the case of a waist focus. In the AN model, cold electrons cancel the space charge fields when the head of the beam contacts the target. Without space charge fields, ions proceed on ballistic trajectories. If we assume that the beam envelope trace represents the shape of the beam bunch, the AN modeling can be used to determine whether the worst-case trajectory (trajectory of the ion most likely to miss the target) intercepts the target.

This is illustrated in Fig. 2.38, which shows, as the left-most dotted vertical line, the position of the rear of the beam bunch at the instant the nose reaches the target. By inspection, it can be seen that the ions at the outside rear of the bunch are most likely to miss the target; with sufficient d^2R/dz^2 on the envelope, these ions might cross the axis and miss the target. Note, however, that cancellation of the electric fields within the bunch cannot occur throughout the bunch instantaneously, but rather will be communicated from the target at a velocity no faster than the velocity of light, c. Assuming a communication speed, v_{comm}, is equal to c, the right dotted vertical line shows the position of the rear of the bunch when the ion trajectories become ballistic. The dashed line is the extrapolation of the worst-case trajectory (crossing the axis is shown as a reflection), and for the representative parameters, these trajectories easily strike the target.

From Fig. 2.38, these worst-case trajectories become more favorable as v_{comm} is decreased from c. A good guess for v_{comm} might be the final electron thermal velocity, $\approx$ c/2. However, even when using the conservative value v_{comm} = c, we find that worst case trajectories begin to miss the target only when r_{sc}^2 is small fraction of r_{total}^2. Again, as with the small-λ_d-constraint, any resulting error in these cases would be small.

Parametric Algorithm. A fast and reasonably accurate algorithm for predicting r_{sc} as a function of principal driver parameters (e.g., kinetic energy E_b (= q V_f), focal length L_f, θ, q, and m_i) was needed to support the PC-based accelerator optimization code (see Sections 2.4.4 and 2.4.8). The AN analysis described in the previous section does not lead to closed-form equations, and the primary analysis was done with an large fortran code residing on a VAX.

The PC algorithm was created as follows: Because the initial (point of neutralization) electron Debye length, λ_{di}, is the key parameter which determines many of the dependencies on beam parameters[2.12] (in particular, λ_{di} carries the current-per-beam information), the equation for

λ_d was recast in terms of the driver parameters. The initial electron density, n_e, is equal to q times the initial ion density, n_i. n_i is calculated as the total ions in a bunch, $I_b t_b/qe$, divided by the bunch volume, $\pi \bar{R}^2 \beta L_b$, where t_b is the pulse width, $\bar{R}$ is a mean radius for the initial bunch volume, and $L_b = \beta c t_b$ is the bunch length. Combining gives:

$$n_e = q n_i = \frac{(I_b/e)}{\pi \bar{R}^2 \beta c}$$

In the Fortran code, the bunch volume is defined by the details of the beam envelope. A good approximation to the code value of $\bar{R}$ is given by assuming the bunch is a truncated cone converging at the geometric focusing half-angle, θ (as opposed to the slightly larger focusing angle actually used to provide the waist). The initial state of the bunch becomes fixed at the time when the trailing edge of the bunch loses contact with the electron source. This gives $\bar{R} = \theta \, (L_{inj} - L_b / 2)$, where L_{inj} is the distance from the target to the point of electron injection.

With these substitutions, the input electron Debye length can be calculated in terms of beam properties and focus geometry:

$$\lambda_{di} \approx 0.516 \, \theta \left(L_{inj} - \frac{L_b}{2} \right) \sqrt{\left(\frac{m_e}{m_i} \right) \frac{E_b \, \varepsilon_o \, \pi \, \beta \, c}{e \, I_b}}$$

Values calculated for the Debye length from the above equation are typically within a few percent of the values calculated by the fortran code.

With the simplified expression for λ_{di} in hand, the sequence for developing the $r_{sc}(\lambda_{di}, E_b, L_{inj}, \theta, q, m_i)$ algorithm was:

1. Define a base point parameter set.
2. Assume separability such that the fit will be:

$$r_{sc}(\lambda_{di}, E_b, L_{inj}, \theta, q, m_i) = C \, W_1(\lambda_{di}) \, W_2(E_b) \, W_3(L_{inj}) \, W_4(\theta) \, W_5(q) \, W_6(m_i)$$

As shown earlier, λ_{di} is a function of the parameters E_b, L_{inj}, θ, q and m_i, so

separability here means that the basic λ_{di} dependence, with these parameters fixed, is separated from additional dependencies observed when these parameters are varied individually.

3. Vary the current per beam at the base point in order to examine the code-predicted waist-size-vs-λ_{di} behavior with other parameters fixed; invent an algorithm, $W_1(\lambda_{di})$, to fit the behavior.
4. Vary E_b only, compare the code-predicted waist with $W_1(\lambda_d)$, and invent the fit $W_2(E_b)$ to provide the additional E_b dependence observed.
5. Repeat step 4 for L_{inj}, θ, q and m_i.

The algorithm resulting from this ad-hoc procedure, when using a base point of E_b = 5 GeV, L_{inj} = 5 m, θ = 30 mrad, q = +1, m_i = 207 (Pb), I_b = 76.8 kA and t_b = 11.1 nsec, is summarized in Table 2.21. The derived λ_{di} is 1.27 mm. Each of the fit factors W_n have been normalized to be 1.00 at the base point, so the coefficient C is equivalent to r_{sc} at the base point, 2.86 mm.

The code-predicted θ-dependence begins to change dramatically below about 13 mrad, as does the code-predicted mass dependence below 108 AMU (Ag). No attempt was made to fit this behavior, so algorithm errors at these extremes become larger, as shown in the table. If these regimes were of interest, it is likely that shifting of the base point towards these values would provide better agreement.

Our baseline driver parameters, which were selected after the algorithm was developed, turned out to differ substantially from the derivation base point in several respects: 3.83 GeV Xe^{+1} was chosen rather than 5 GeV Pb^{+1}, and the choice of 12 beams resulted in λ_{di} = 3.09 mm rather than 1.27 mm. (Note that the debye length decreases from this initial value as the beam approaches the target. For the baseline driver parameters, the debye length is always less than the beam envelope radius.) As indicated in the table, individually these changes do not result in large algorithm error. However, the combination was observed to result in a systematic error of 23%. As a quick fix, the constant C was reduced to 2.22 mm for use with the baseline design. For further work, a re-derivation with a base point equal to, or closer to, the baseline parameters is recommended.

Table 2.21. Description and Evaluation of the Fit:

$$r_{sc}(mm) = 2.86\ W_1(\lambda_{di})W_2(E_b)W_3(L_{inj})W_4(\theta)W_5(q)W_6(m_i)$$

PARAM (UNITS)	ALGORITHM W_n(PARAM)	BASE CASE VALUE	RANGE EXAMINED VALUES	RANGE EXAMINED ERROR
λ_{di}(mm)	$55.9(\lambda_{di}+2.2)^{-3.228}$	1.27 mm	0.80 mm 3.0 mm	-1.1% +0.2%
E_b(GeV)	$1.20-6.96\times10^{-2}E_b+8.69\times10^{-3}E_b^2$ $-5.35\times10^{-4}E_b^3$	5 GeV	2.44 GeV 14.9 GeV	+1.4% +4.5%
L_{inj}(m)	$0.398-0.233L_{inj}+0.131L_{inj}^2$ $-2.26\times10^{-2}L_{inj}^3+2.11\times10^{-3}L_{inj}^4$	5 m	3 m 10 m	-1.0% -0.1%
θ(mrad)	$1.66-4.372\times10^{-2}\theta+9.72\times10^{-4}\theta^2$ $-8.34\times10^{-6}\theta^3$	30 mrad	12.5 mrad 13.0 mrad 50 mrad	+27% +1.8% -0.1%
q(e)	$0.371+9.59\times10^{-2}q+0.533q^2$	1	1 7	0 +0.2%
m_i(AMU)	$2.47-7.07\times10^{-3}m_i$	207.2(Pb)	95.9 (Mo) 108.(Ag) 238.(U)	+53% +0.1% -9.7%

2.4.7.2 Beam Spot Size

The beam spot size, r_s, has contributions from effects in addition to space charge. We estimate r_s as the rms total of the contributions from AN (space charge), emittance, dispersion, and jitter/alignment:

$$r_s^2 = r_{sc}^2 + r_\varepsilon^2 + r_{\Delta p}^2 + r_{jitter}^2$$

By doing rms combining, we have implicitly assumed Gaussian beam profiles. The emittance spot size, r_ε is calculated as $\varepsilon_n / (\beta\gamma\theta)$, where ε_n is the normalized emittance. The

dispersion spot size, $r_{\Delta p}$, is calculated[2.52] as $8 L_f \theta \Delta p/p$, where $\Delta p/p$ is the incoherent beam momentum spread.

Figures 2.39 and 2.40 compare typical AN contributions (dashed) with typical contributions (dotted) from emittance, dispersion and jitter/alignment. Also shown on each of the figures is r_s (solid). An ε_n of 1 x 10^{-5} meter-radians was used for r_ε, and a $\Delta p/p$ of 1 x 10^{-3} was used for $r_{\Delta p}$. The jitter/alignment contribution was arbitrarily assumed to be 180 μrad. Figure 2.39 displays the spot contributions as a function of the beam kinetic energy, and shows, for these representative parameters, the AN component to be dominant at low energy and the emittance component to be dominant at high energy. Figure 2.40 uses focusing angle as a variable, and shows AN and emittance both contribute at small angles, while dispersion dominates at large angles. For the θ = 15 mrad used in the example, dispersion is not important. As a function of θ, a weak minimum in spot size is observed at 30 mrad. This minimum becomes more pronounced, and the optimum angle decreases, as the momentum spread increases from 1 x 10^{-3}.

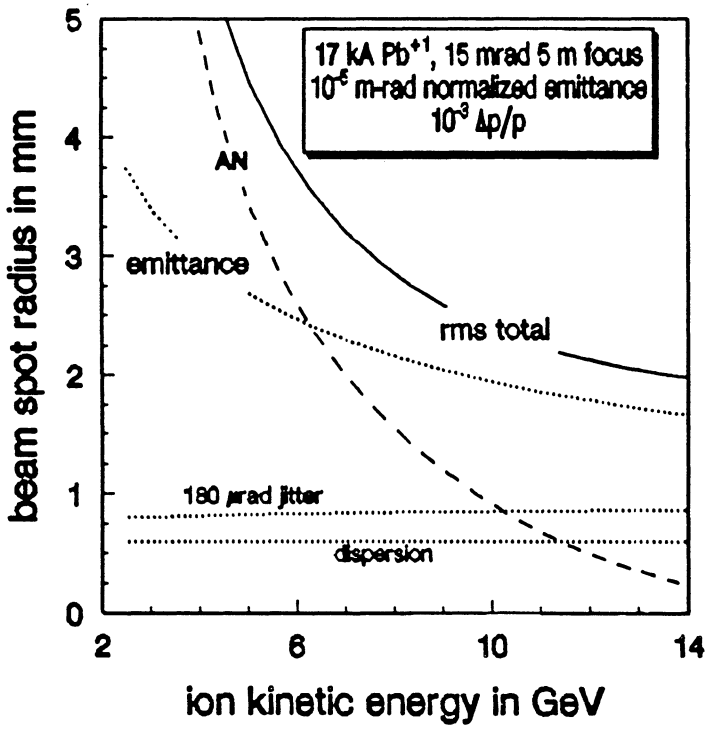

Fig. 2.39. Spot size composition vs. kinetic energy.

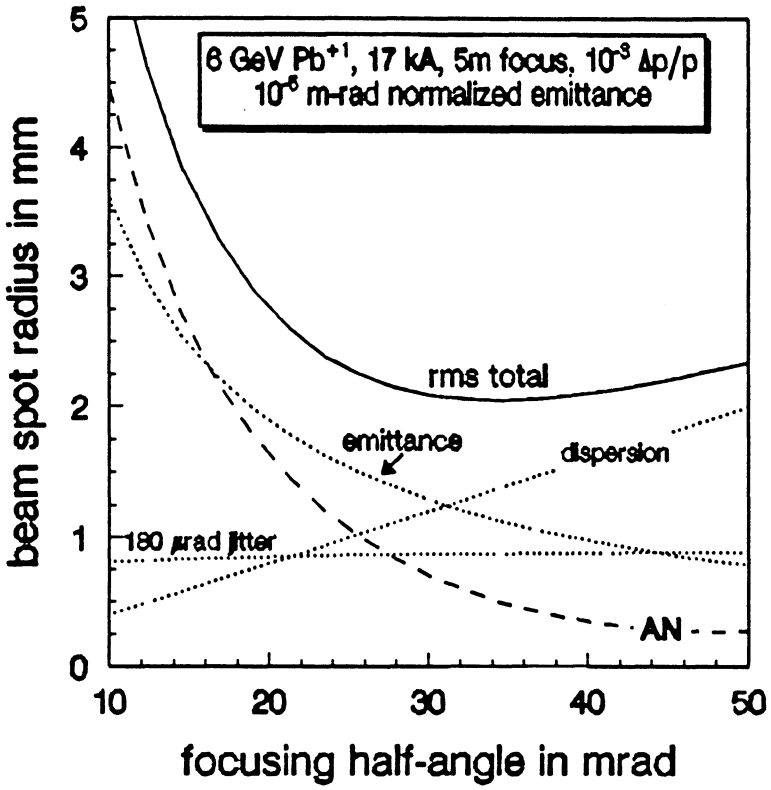

Fig. 2.40. Spot size composition vs. focusing angle.

Spot size predictions with AN modeling can be quite sensitive to the distance from the target at which the auto-neutralizing electrons are supplied. This is illustrated in Fig. 2.41, where it is assumed that the auto-neutralizing electrons are supplied at the beginning of the focus ($L_f = L_{inj}$). The figure shows that at constant θ, r_{sc} increases strongly with L_f (= L_{inj}), as does r_s for our example parameters wherein r_{sc} contributes significantly to r_s.

This dependence on length, which is much stronger than is seen with SCN modeling, occurs because more length results in more bunch compression, leading to higher electron temperatures and higher defocusing electric fields. So with the AN modeling, final focus performance improves significantly with decreasing distance between the point of electron injection and the target. In our baseline design, this is reflected in a relatively small chamber radius, allowing a smaller electron injection length, and in the choice of a sufficient number of paralleled beams such that the r_{sc} contribution to r_s is small, and the resulting r_s dependence on L_{inj} is not as pronounced.

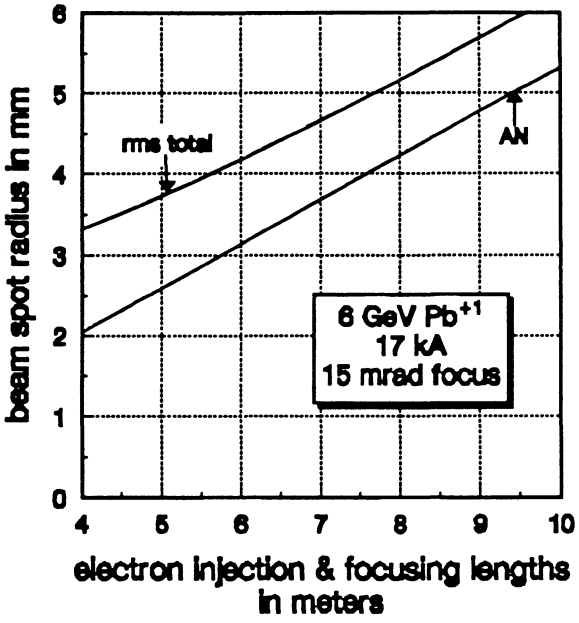

Fig. 2.41. Spot size vs. distance from electron injection.

2.4.7.3 Stripping

In contrast to SCN modeling, the AN model allows for chamber stripping without ambiguity. The essential effect of stripping is to add electrons and ion charge. For the < 100% fractional neutralization of the SCN model, this would change the neutralization fraction, thereby violating the model's basic assumption. Stripping is incorporated into the AN differential equation by incrementing the bunch electron density, incrementing the bunch average ion charge state, and diluting the bunch electron temperature for each stripping event. Stripping cross sections were estimated using the following parametric fit[2.53] to published calculations:[2.54]

$$\sigma_s \approx \frac{2.45\times10^{-18}\,\mathrm{cm}^2}{\beta^2}\left(\frac{Z_{gas}}{3}\right)\left(\frac{Z_i}{92}\right)\exp(-0.063\,q)$$

where Z_{gas} is the gas atomic number (x 2 for diatomic gases) and Z_i is the beam atomic number. The coefficients were picked to match U on Li data.

Typical stripping assessments are displayed in Fig. 2.42, which shows r_{spot} as a function of the cumulative fractional stripping attained when the beam bunch reaches the target. The solid

curves are for fixed focusing lengths L_f of 4, 5 and 6 meters, while the dotted curves are for the constant Li, Be, F or Pb vapor densities indicated. As inferred by Fig. 2.42, we find that stripping of tens-of-percent is not disastrous, and can be accommodated in system trades. Table 2.22 gives calculated densities along with the self-consistent vapor pressures and vapor temperatures which yield 20% stripping with our example parameters (i.e., 10 GeV Pb ions with L_f = 5 m).

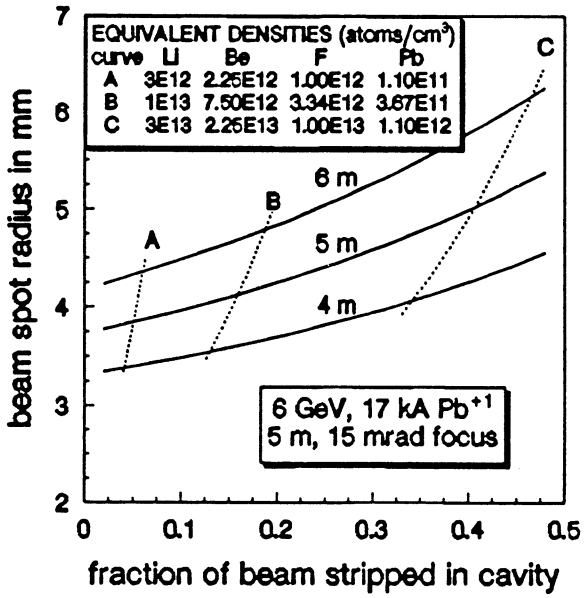

Fig. 2.42. Impact of beam stripping in reactor chamber.

Table 2.22. Vapor Densities, Pressures and Temperatures for 20% Stripping

VAPOR	DENSITY	PRESSURE	TEMPERATURE
Lithium	1.3×10^{13} cm^{-3}	9.9×10^{-4} torr	740 K
Lead	4.7×10^{11} cm^{-3}	4.0×10^{-5} torr	805 K
Flibe	2.5×10^{12} cm^{-3}	2.2×10^{-4} torr	824 K

2.4.8 Parametric Studies

2.4.8.1 Description of Parametric Studies

Parametric studies were done to choose a driver design with low cost and beam parameters which produce a high target gain. Scaling of target performance and driver cost was done for several driver parameters including:

- driver energy (E),
- number of ion beams (N),
- type of superconductor used in focusing magnets (NbTi or Nb_3Sn),
- maximum magnetic field allowed at the windings (B_{max}),
- axial packing fraction for the quadrupole fields (η),
- ion mass (A), and
- ion charge state (q).

Driver Assumptions Modeled. The goal of this study was to find the most affordable driver that does not require any aggressive design assumptions. Driver costs may be lowered if beam combination, beam separation, and recirculation can be used, but it is possible that some (or all) of these options will degrade or destroy beam quality and target performance. Beam combination and recirculation degrade target performance by increasing the beams emittance (crudely described as the product of the beam's radius and its angular divergence). Beam separation can theoretically produce two beams with lower emittance than the parent beam, but introduces other uncertainties. Beam separation requires complicated separation magnet designs which introduce the potential for ion loss or beam quality degradation, and increasing the number of beams at the reactor complicates the design for the final focussing systems and the reactor/driver interface.

For each set of driver parameters, we design the shortest possible driver and examine its cost. As discussed earlier in this chapter, we minimize the required driver voltage (and therefor the required length) by using the highest beam currents allowed for a given set of driver focusing parameters.

The Choice of a Base Driver Design. The base driver was chosen by examining the target gain and a driver cost contributions (a subset of the total direct costs) of 5 MJ drivers using a wide variety of driver parameters. The driver cost contributions used were the costs of

the quadrupole arrays and the inductor metglas cores. Limiting the cost figure of merit to the sum of these two elements was justified because the costs of other expensive components (support structures, the pulse forming network, the cryogenic cooling system, etc.) scale with core or quadrupole array requirements.

A true multivariable optimization was not done. While some design variables were optimized (e.g., the focusing angle was selected to give the minimum spot size for each design considered), other variable choices were made by picking a point from a parametric curve. A precise minimization of gain per unit cost was not done; rather, a sensible choice near the point of diminishing return is made for each parameter (usually the "knee" of the curve of target gain vs. parameter value). By adjusting the driver design one parameter at a time and then re-examining the choices of the other parameters (ion mass, number of beams, maximum magnet field at quadrupole windings, linear occupancy factor for the quadrupole fields, etc.), the cost and performance of the driver can be greatly improved.

The entire parametric search is not reproduced here, but several representative variations and chosen parameters are shown. The total costs for our base driver and plant are described in Chapter 8.

2.4.8.2 Cost and Gain Scaling

Parametric sensitivity studies were done for 5 MJ drivers. For all driver parameters, except the number of beams used, smooth curves can be created for the dependence of the driver cost and predicted target gain on the parameter value. Because the relationship between quadrupole magnet dimensions and the array radius is different for each choice for the number of beams, drivers were chosen for several possible values of N and these drivers were then compared. Five MJ driver designs with 4, 12, and 24 beams were compared. These values of N were chosen because they provide the highest packing fractions when the beams are stacked (with 4-fold symmetry to provide return paths for the magnetic fields) to fill a circle.

The axial packing fraction of quadrupole fields, η, is the fraction of the driver length occupied by the quadrupole fields. For a constant beam radius, the axial packing fractions for the entire driver will be limited by the maximum allowable initial packing fraction, η_i. Because greater focusing along the beam lines allows for greater beam currents larger values of η_i will give the shorter drivers. As shown in Figure 2.43, there can be a range of packing fractions with

comparable combined costs, but several cost which are not included (e.g., power distribution and tunnel construction) favor shorter systems.

When analyzing the effect of other driver variables on driver performance and cost, we fix the maximum field at the quadrupole superconductors at 10 Tesla. For drivers using singly charged ions (q = 1), we compared systems using the highest credible initial packing fraction which was taken as $\eta_i = 0.8$. For higher charge state ions (q = 2 or 3), high packing fraction were not as important and $\eta_i = 0.5$ was chosen.

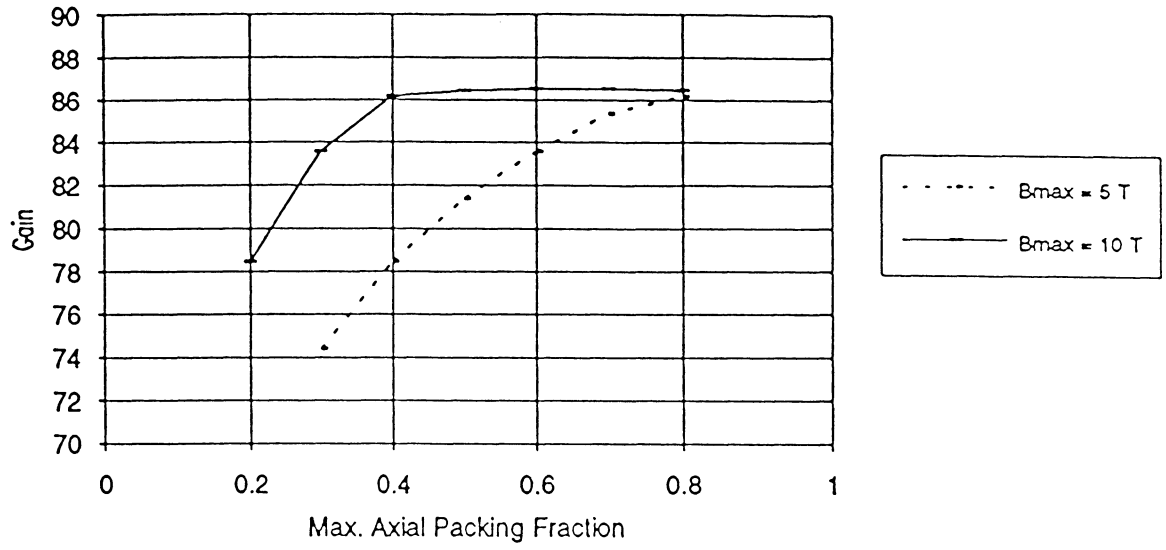

Fig. 2.43a. Gain vs. maximum quad packing fraction.

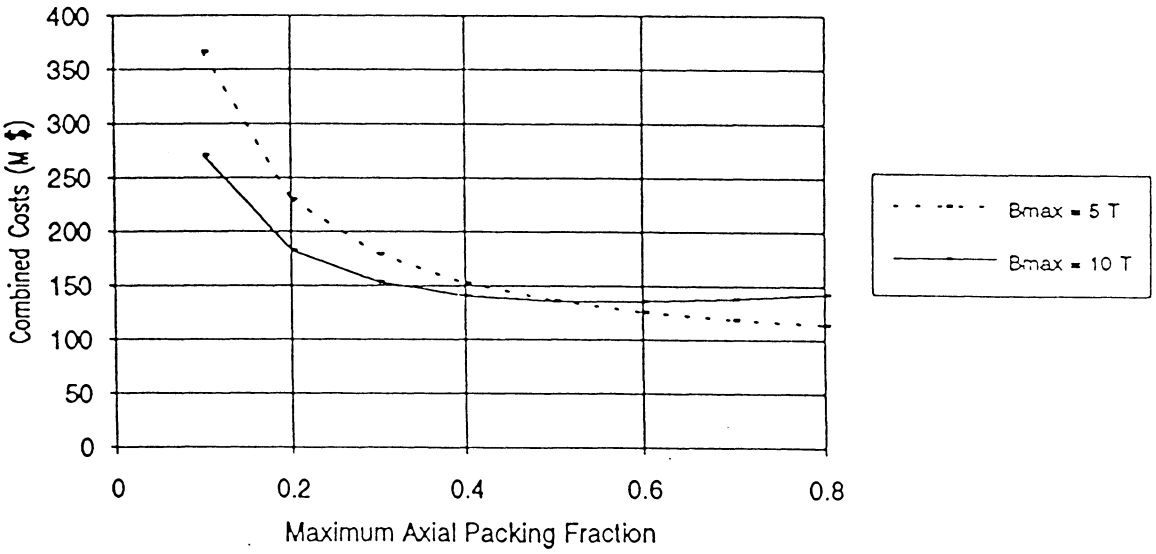

Fig. 2.43b. Combined costs vs. maximum quad packing fraction.

Figure 2.44a shows the achievable target gain for 12 beam 5 MJ drivers as a function of ion mass, A. Each point corresponds to a different driver designed to give the lowest required voltage for the chosen value of A. For a 12 beam driver, gain increases for drivers designed to use higher A and decreases for designs using higher values of q. (A driver designed for higher values of q will have a lower voltage, and hence a smaller range, but will have a larger spot size resulting from its higher beam currents.) For drivers using singly charge ions there is little benefit to using values of A higher than 150.

Figure 2.44b shows the combined costs for the same drivers. Although drivers using ions with higher charge states can have lower costs than those using singly charged ions, they also have lower gains. For our base driver, we selected ions with q = 1 and A = 131 (Xe) for a conservative design with costs slightly above those of the least expensive driver.

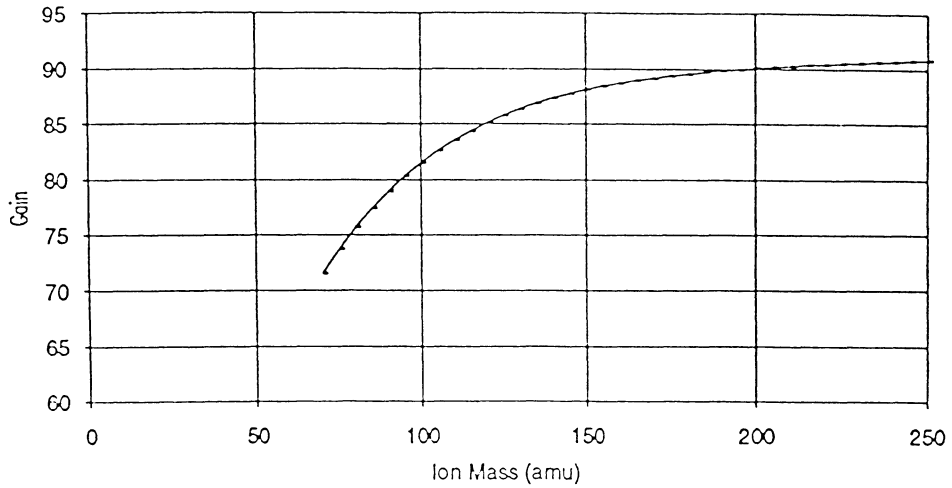

Fig. 2.44a. Gain vs. ion mass for base driver designs.

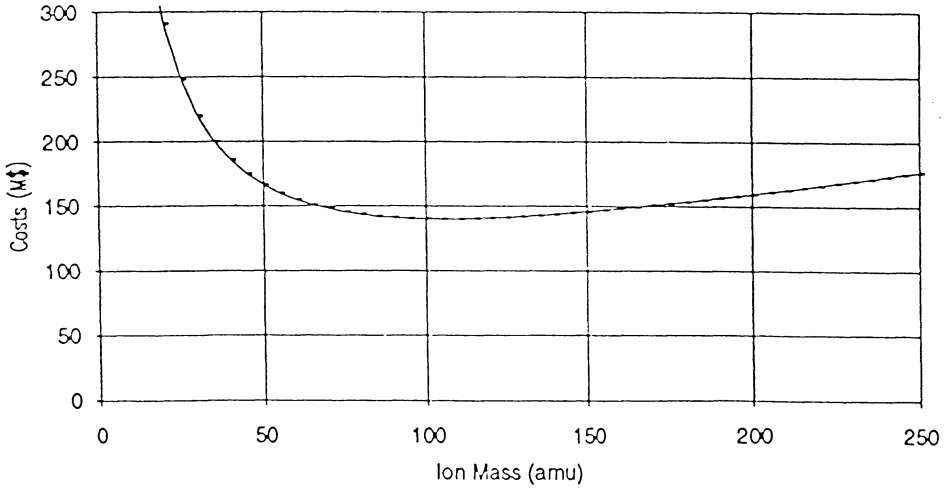

Fig. 2.44b. Combined cost vs. ion mass for base driver designs.

Although cost calculations were only done for a few values of N, the achievable gains were calculated for all possible values of N. (As mentioned earlier, costing depends on array designs which are unique for each value of N. Beam parameters needed for gain calculations, on the other hand, can be found without doing new array designs.) Figure 2.45 shows the dependence of target gain on N for 5 MJ drivers using A=131, η_i = 0.8, and B_{max} = 10 T.

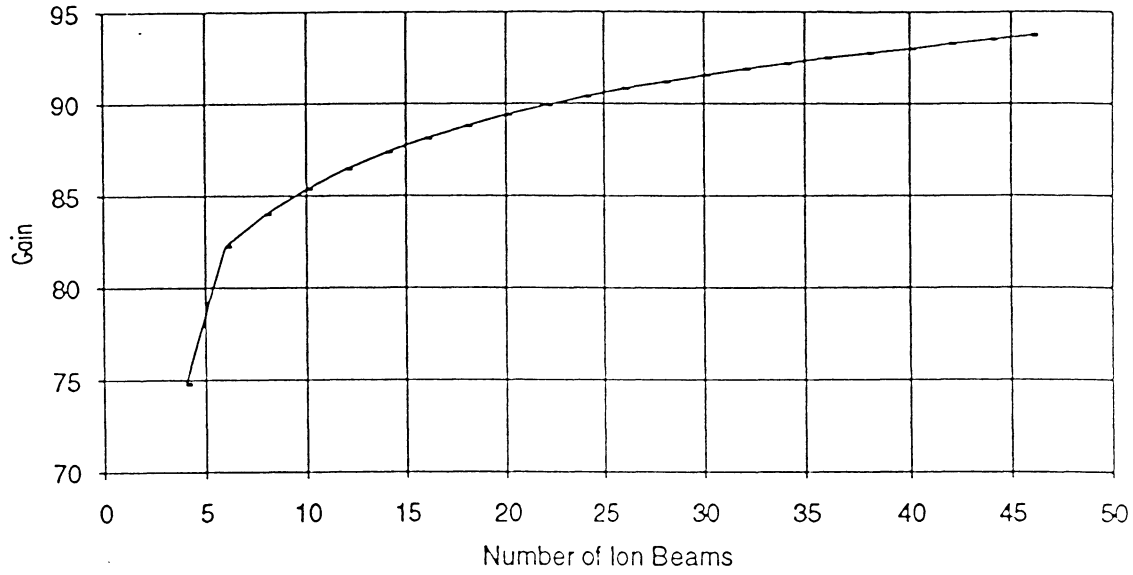

Fig. 2.45. Gain vs. number of beams for base driver designs.

We found that optimized 12 and 24 beam driver designs have similar cost and performance. The 12 beam driver was chosen for the base case because it allows for a simpler reactor interface. In addition, the difference between predicted and actual target performance is likely to be smaller for the 12 beam system. The spot sizes used in the gain calculations are those for a single beam. The physics of beam combination at the target will probably give a net spot size for all beams that will be slightly larger than the single-beam spot size. Degradation of net spot size will probably be worse for the 24 beam driver.

Higher charge state ions require complicated sources and have a higher potential for electron capture, but may have lower cross-sections for electron stripping. Because the cost saving from the use of high charge states are small and come at the expense of target performance, we chose a q = 1 driver as our base design.

Figure 2.46 and Table 2.23 show the cost savings resulting from driver parameter changes.

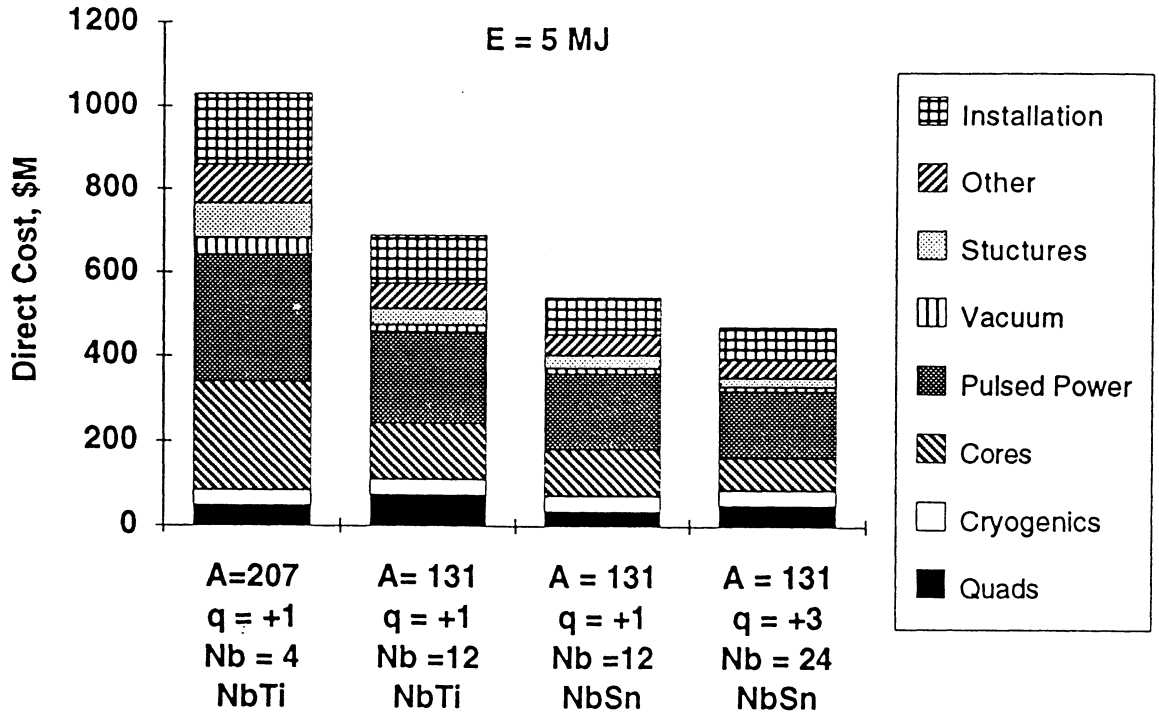

Fig. 2.46. Cost comparison of four possible heavy-ion driver designs.

Table 2.23. Parameters for Four Possible Heavy-Ion Driver Designs

Parameter	A = 207 q = 1 NbTi	A= 131 q = 1 NbTi	A = 131 q = 1 NbSn	A = 131 q = 3 NbSn
Energy, MJ	5	5	5	5
Number of Beams	4	12	12	24
B max at S/C, T	6	6	10	5
Initial Quad Occupancy	0.6	0.8	0.8	0.6
Final Voltage, GV	11.64	4.81	3.83	2.59
Current Per Beam, kA	1.07	0.87	1.09	0.81
Final Pulse Width, ns	100	100	100	100
Accelerator Length, km	13.8	5.8	4.8	3.4
Driver Efficiency, %	16.6	23.3	28.2	31.9
Spot Radius, mm	2.0	2.1	2.3	2.0
Ion Range, g/cm^2	0.15	0.10	0.07	0.18
Gain	80	86.4	86.4	73.8
Yield, MJ	400	430	430	370
Quad Arrays	1284	1202	1978	1741
Total Quads	5136	14424	23736	41784
Total Cores	23387	9446	7643	5001
Total Direct Cost, $B	1.03	0.69	0.54	0.47

2.4.9 Description of the Base 5 MJ Driver Design

2.4.9.1 Base Accelerator Design

The base design for a 5 MJ accelerator was chosen after several parametric variation studies. The optimum value for each driver parameter depends on the chosen value of all the other variables, so an iterative approach was used to set the base parameters. The chosen driver parameters led to a 4.81 km long driver shown in Fig. 2.47. The driver parameters for this base design are shown Table 2.24.

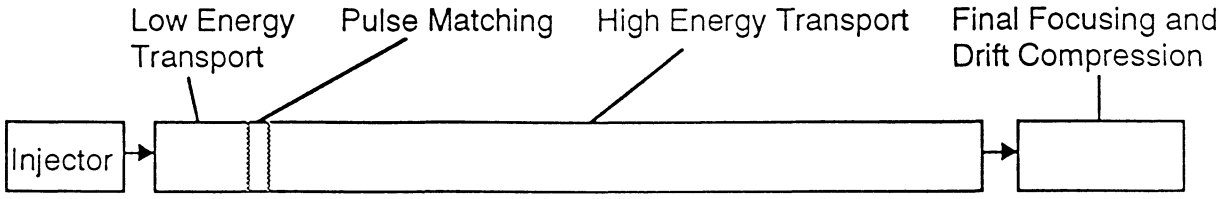

	Injection	Beginning of PM Stage	Beginning of HET Stage	End of Accelerator
X	0 m	359 m	392 m	4.81 km
Φ	12.6 kV/m	0.85 MV/m	0.85 MV/m	0.85 MV/m
V	3 MV	49.7 MV	78.1 MV	3.83 GV
I_b	3.46 A	57.4 A	168 A	1.09 kA
τ	34.1 μs	2.06 μs	703 ns	100 ns
I	71.4 m	17.5 m	7.49 m	7.49 m

Fig. 2.47. Base heavy-ion driver schematic.

Table 2.24. Base Case Heavy-Ion Parameters

Energy, MJ	5	Max. axial Quad. occupancy	0.8
Ion Mass, amu	131		
Charge State	1	Quads:	
Superconductor	NbSn	Number of Arrays	1978
Number of Beams	12	Number of Quads	23736
B max at S/C, T	10	Effective Field Length, cm	18.1
Driver Efficiency, %	28.2	Quad Length, cm	22.6
Beam Voltage		Beam Radius, cm	6.8
Initial, MV	3	Quad Bore, cm	8.9
Final, GV	3.83		
Current per Beam		LET Cores	
Initial, A	3.5	Number	804
Final, kA	1.09	Length, cm	20
Pulse Length		Radial Build, cm	80
Initial, microseconds	34	HET Cores	
Final, nanoseconds	100	Number	6840
Accelerator Length		Length, cm	10
Low Energy, m	359	Radial Build, cm	40
Pulse Compression, m	33		
High Energy, km	4.4	Total Metglass, MT	14.3
Total Length, km	4.8		
Final focus half-angle, mrad	33		
Spot radius, mm	2.3		
Ion Range, g/cm^2	0.07		
Gain	86.4		
Yield, MJ	430		

Once the base driver parameters were chosen, we investigated the effect of changing the chosen driver energy. The models presented in the previous sections were used to calculate driver sizes and cost contributions for drivers using our base driver assumptions at a variety of possible driver energies. Figures 2.48a and 2.48b shows how the target gain and combined costs vary with driver energy for our base driver assumptions.

By combining our base driver model with models for chamber and balance of plant costs, we can determine the effect of driver energy and repetition rate on the cost of electricity and total direct costs of a power plant. As discussed in Chapter 8, the minimum cost of electricity occurs at somewhat lower driver energy, but the savings are less than 5% of the total cost of the base driver design discussed here.

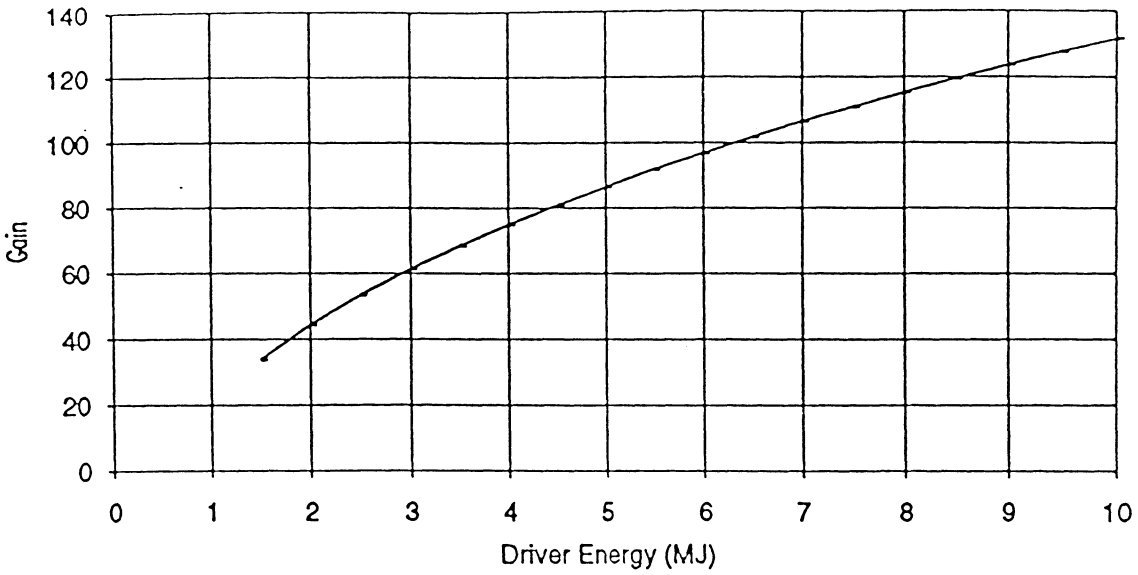

Fig. 2.48a. Gain curve for base driver assumptions.

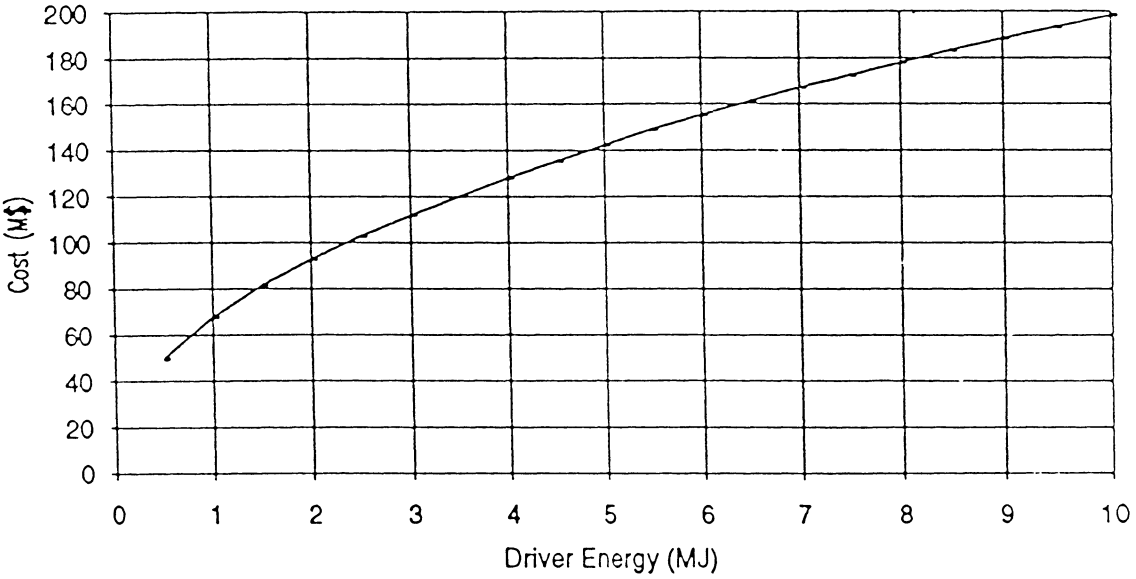

Fig. 2.48b. Cost subtotal for base driver assumptions.

2.4.9.2 Base Final Transport Design

The final compression and focus segment matches the 3.83 GeV Xe^{+1} linac output beam to the parameters specified at the target. Table 2.25 shows key input and output match-up parameters for the final compression and focus. Although there is no specification on pulse shape, we have constrained our design such that each of the individual beam tubes is the same length, and therefore each will deliver its respective beam bunch at the same time. Final gain optimization (see Section 2.4.4.2) resulted in an optimum focusing half angle of 33 mrad. We present here an earlier final transport design predicated on a 24 mrad optimum angle. We were able to design a 33 mrad final focus telescope prior to the end of the contract, but we did not have time to complete the integration of that design into the final drift, compression, and focus calculations. It is clear from this effort that the larger focusing angle stresses the final transport design: it increases the beam bundle size, the focusing quadrupole sizes, and the telescope length, and it decreases the spreader bend radius. We conclude that minimum beam spot size should not be the only criteria for determining the final focus angle.

Table 2.25. Input and Output Parameters for Final Compression and Focus

PARAMETER	INPUT FROM LINAC	SPECIFIED AT TARGET
Number of Beams	12	12
Bundle Geometry	Close-packed Rectilinear	Two 6-beam Hexagonal Rings
Current per Beam	1.09 kA	10.9 kA
Pulse Width	100 nsec	10 nsec
Beam Envelope Radius	6.8 cm	0.23 cm
Normalized Emittance	1×10^{-5} meter-radians	
Momentum Spread	1×10^{-3}	
Lattice Tune	80 degrees	
Depressed Tune	8 degrees	
Lattice Half-Period	8.1 meters	
Focusing Half Angle		33 mrad

Figure 2.49 shows the layout of the final compression and focus. There is a series of three functional sections: a transport section, a compression section, and a transverse focus section. In an alternative layout which we considered, the compression section was located at the end of the linac, so the beam was allowed to compress within the bends. However, with a feasible average bend radius, the tilt removal distance (from Section 2.4.6.2) was not long enough to accommodate bending, spreading, and final focus. The design illustrated in Fig. 2.49 allows the use of a conservative value (51.6 m) for the average bending radius. Also, the chosen layout eliminates the problem of dispersion in the bends due to the large coherent velocity tilt of the compression phase.

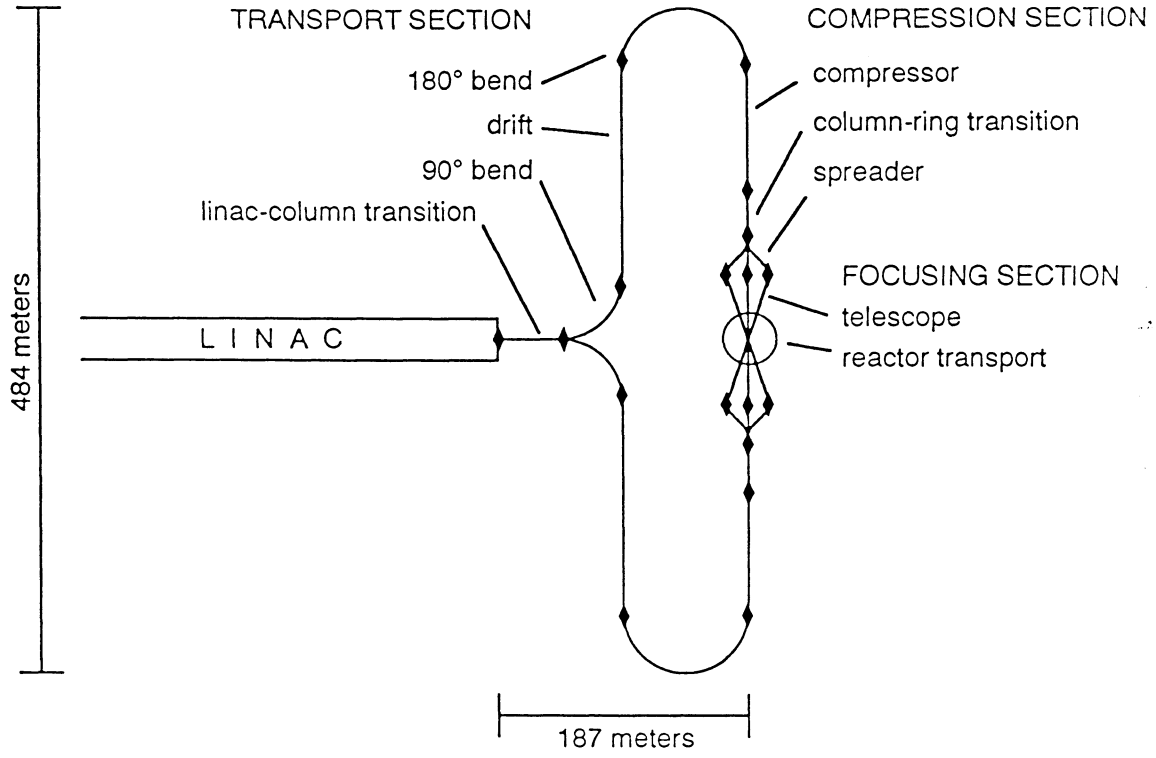

Fig. 2.49. Final compression and focus layout.

Overall design parameters for final compression and focus are listed in Table 2.26. Out of the total of 984 quadrupoles, 624 (from the linac to the compressor) can be made identical to the linac quadrupoles. The total of 528 dipoles includes 24 (2 per beam) which are very low field steering dipoles at the entrance to the reactor chamber. Each of the three functional sections of the final transport systems is now described.

Table 2.26. Overall Final Compression and Focus Design Parameters

PARAMETER	VALUE
Transport Length	611 meters
Linac-to-Target Distance	187 meters
Total Width (⊥ to linac)	484 meters
Number of Quadrupoles - per Beam	984 82
Number of Dipoles - per Beam	528 44

Transport Section. The transport section splits the 12-beam bundle from the linac into two 6-beam bundles, then transports each of the 6-beam bundles so that they are aimed at the target from a sufficient distance to accommodate compression and transverse focus. The transport section is composed of four elements: an initial transition element to transform the 12-beam bundle into two 6-beam columns, a 90 degree bend to direct the columns away from the linac axis, a straight section to carry the columns the required distance from the axis, and a 180 degree bend to direct the bundles back towards the target. Table 2.27 lists key design parameters for each of the transport section elements.

The linac-to-column transition is a translation sequence which is illustrated in Fig. 2.50 a through c. Equal transport lengths for all beams are maintained through this sequence by equalizing the individual lateral translations as indicated. Figure 2.50a shows the close-packed 12-beam rectilinear lattice at the exit to the linac. In Fig. 2.50b, each beam is translated using a dipole to initiate a 0.51 degree bend, followed by 32.1 m drift, then a second dipole, identical to the first but with reversed field, which restores the beam direction at a distance of one beam-lattice spacing from the original beam axis. In total, the transition encompasses two lattice periods (32.4 m).

The result, shown in Fig. 2.50c, is a column of six beams, with the total transport length for each beam exactly the same to this point. The column geometry, with the column

perpendicular to the bend plane, yields automatic equal-length transport through the subsequent major bends. Design parameters for the linac-to-column transition are given in Table 2.27.

Table 2.27. Transport Section Design Parameters.

Element	Linac-column transition	90 degree bend	Straight section	180 degree bend
Transport length	32.4 m	81.0 m	139.3 m	162.0 m
Length (∥ to linac)	32.4 m	51.6 m	139.3 m	103.1 m
Width (⊥ to linac)	0.26 m	51.6 m		51.6 m
Bending radius		51.6 m		51.6 m
Lattice half-period	8.1 m	8.1 m	8.1 m	8.1 m
Lattice tune	80 degrees	80 degrees	80 degrees	80 degrees
Depressed tune	7.0 degrees	7.0 degrees	7.0 degrees	7.0 degrees
Average beam radius	7.3 cm	7.3 cm	7.3 cm	7.3 cm
Dipoles per beam	2	10		20
Length (each)	14 cm	2.4 m		2.4 m
Field	6.7 T	6.7 T		6.7 T
Occupancy	0.8%	30%		30%
Quadrupoles per beam	4	10	18	20
Length (each)	18 cm	18 cm	18 cm	18 cm
Bore	10.9 cm	10.9 cm	10.9 cm	10.9 cm
Conductor field	10 T	10 T	10 T	10 T
Radial gradient	92 T/m	92 T/m	92 T/m	92 T/m
Occupancy	2.2%	2.2%	2.2%	2.2%

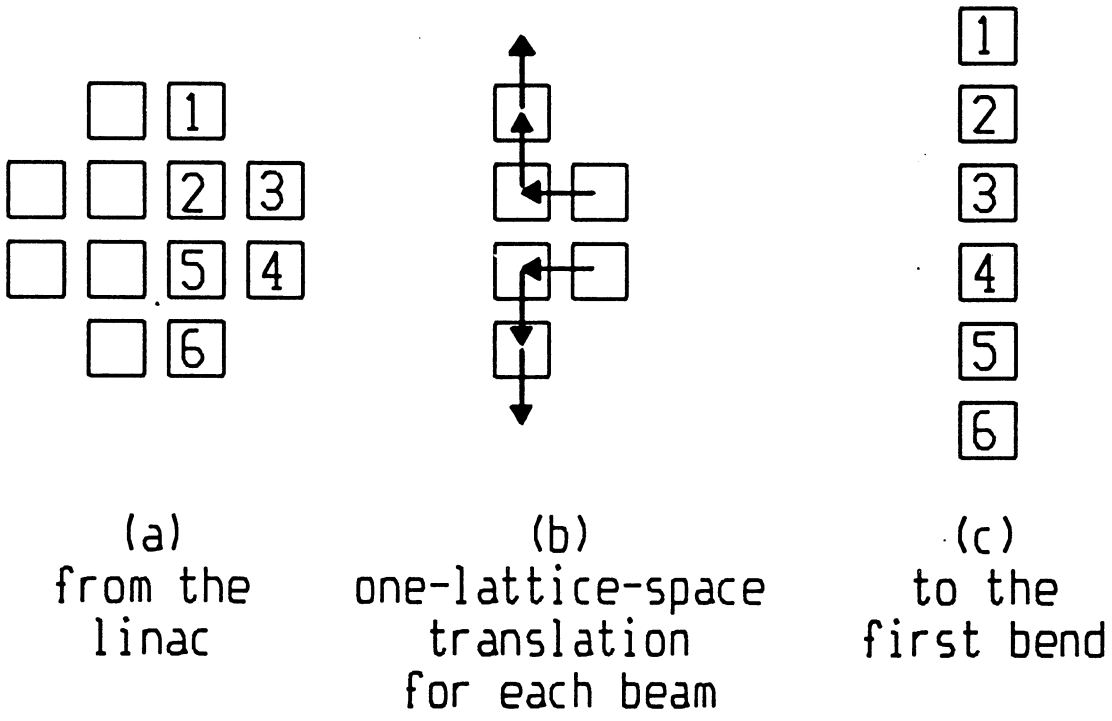

Fig 2.50. Linac-to-column transition.

The 90 degree bend is done by dipole magnets located between the quadrupoles of a FODO focusing lattice with parameters close to those used in the linac. Design parameters for this 5-lattice-period bend are given in Table 2.27. Figure 2.51 displays the calculated bend x and y beam envelopes. This calculation was done with approximate incorporation of space charge, but we would expect a similar result with a rigorous space charge treatment.

The straight section between the major bends is sized to provide the required compression, spreading, and focusing length between the 180 degree bend and the target. Straight section design parameters are given in the table.

The 180 degree bend is designed exactly as two consecutive 90 degree bends. Design parameters are given in Table 2.27. Beam envelopes for each half-bend are shown in Fig. 2.51.

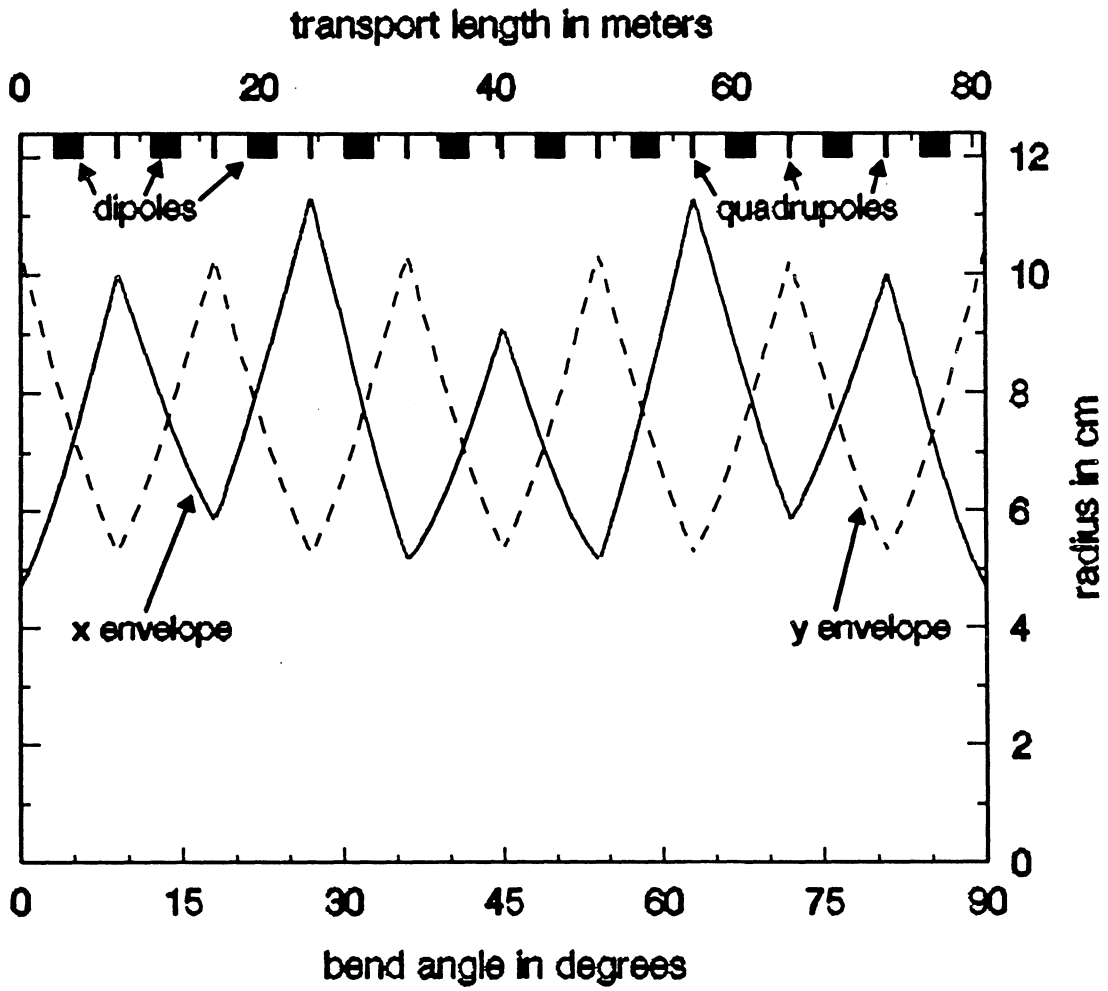

Fig. 2.51. 90 degree bend beam envelopes, quadrupoles and dipoles. (Note horizontal and top vertical scale are very different.)

Compression Section. The compression section provides the specified 10 nsec longitudinal focus in the middle of the final focusing quadrupole set. The compression section is comprised of three elements: the compressor element to provide the required velocity tilt, a transition element to transform the 6-beam column into a hexagonal ring, and a spreading element to provide sufficient clearance between the beams so that the final focusing quads of adjacent beams can be packaged. Table 2.28 lists key design parameters for the compression section elements.

Using the equations in Chapter 2.4.6, a compressor velocity tilt of 5.4% is required to provide the needed factor of 10 in compression. For 3.83 GeV Xe^{+1}, this is a head-to-tail pulse energy spread of 435 MeV. Because no beam acceleration is required from the compressor induction modules (in contrast to the linac), the applied voltage gradient can be relatively high. We chose a maximum of 2.5 MeV/m, which is near the sparking limit for the incoming 100 nsec pulse width. With the gradient ramped from -2.5 MeV/m at the head of the pulse to +2.5 MeV/m at the tail, the required compressor length is 87 meters.

Some beam compression occurs in the induction modules as illustrated in Fig. 2.36. For our baseline system, the equations of section 2.4.6 gave the beam bunch emerging from the compressor a pulse width of 68 nsec. The remaining effective transport length, to the center of the focusing telescope, was then calculated to be 91 meters. Design of the downstream transition element and spreader is constrained to achieve this total.

Pulse shaping to provide a pre-pulse at the target would be done by tailoring the applied voltage gradient waveform in the compressor. This approach allows an arbitrary fraction of the pulse energy to be in the pre-pulse, while preserving the equivalence of the individual beams. No specification on the pre-pulse was available. Additional design parameters for the compressor are given in Table 2.28.

Table 2.28. Compression Section Design Parameters.

Element		Compressor	Column-ring transition	Spreader
Transport length		87.1 m	24.2 m	49.2 m
Length ($\perp$ to linac)		87.1 m	24.2 m	45.2 m
Width ($\parallel$ to linac)				21.2 m
Bending radius				36.9 m
Lattice half-period	L	8.1 → 6.5 m	6.5 → 6.0 m	6.0 → 5.1 m
Bunch length	ℓ	7.3 → 4.9 m	4.9 → 3.0 m	3.0 → 1.6 m
Pulse width		100 → 68 nsec	68 → 41 nsec	41 → 21 nsec
Lattice tune	σ_o	80 degrees	80 degrees	80 degrees
Depressed tune	σ	7 → 6.3 deg	6.3 → 4.9 deg	4.9 → 3.9 deg
Average beam radius	$\bar{a}$	7.3 cm	7.3 → 8.5 cm	8.5→10 cm
Dipoles per beam			2	8
Length (each)			27 cm	2.4 m
Field			6.7 T	6.7 T
Occupancy			2.2%	42%
Quadrupoles per beam		12	4	8
Length (each)		18 → 22 cm	22 → 28 cm	28 → 112 cm
Bore		9.5 cm	9.5 → 10.9 cm	10.9 →15 cm
Conductor field		10 T	10 T	10 T
Radial gradient		92 T/m	92 → 79 T/m	79 →22 T/m
Occupancy		2.2 → 3.4%	3.4 → 4.6%	4.6 → 22%

The transition element that transforms the 6-beam column into a hexagonal ring is a translation sequence which is illustrated in Fig. 2.52 a through c. Equal transport lengths for all beams are maintained through this sequence by equalizing the individual lateral translations as indicated. Figure 2.52a shows the column of six beams emerging from the compressor. In Fig. 2.52b, each beam is translated using a dipole to initiate a 1.0 degree bend, followed by a drift, then a second dipole, identical to the first but with reversed field, which restores the beam direction. In total, the transition encompasses two lattice periods (24.2 m).

The 5.4% velocity tilt will cause the head and tail of the beam bunches to be deflected by different amounts unless the beam translation system is achromatic. Since the deflection of the centroid of the beam is not affected by space charge, designs similar to conventional low intensity achromatic systems can be used. In the column-to-hexagonal-ring transition, the dipole magnets are in the end half-periods of the two-period lattice. A D quadrupole is in the center, and symmetry is maintained about the center. The F quadrupoles adjacent to the bending magnets are tuned to make the translation achromatic.

The result, shown in Fig. 2.52c, is a ring of six beams, with the total transport length for each beam continuing to be exactly the same to this point. Design parameters for the column-to-hexagonal-ring transition are given in Table 2.28.

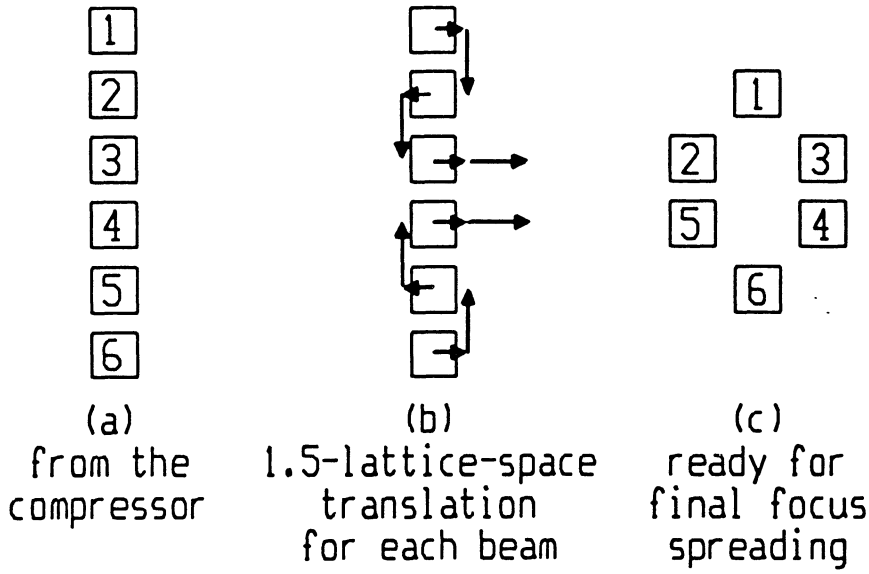

Fig. 2.52. Column-to-hexagonal-ring transition.

The spreader expands the 6-beam bundle to provide sufficient clearance between the beams so that there will be room for the final focusing quads of adjacent beams. The final quadrupoles of the spreader must provide matching to the initial quads of the focusing telescope. Spreader parameters were determined by starting with the required off-axis angle for each of the ring beams as they converge on the target (15.1 degrees), then determining the angles of the two consecutive (and oppositely directed) bends that would both match to the parallel beams emerging from the column-to-ring transition, and would yield the required compressor-to-mid-telescope transport distance to accomplish the longitudinal focus. Symmetry is used to make each of the bends achromatic. Figure 2.53 is a layout drawing of the 6-beam spreader and telescope.

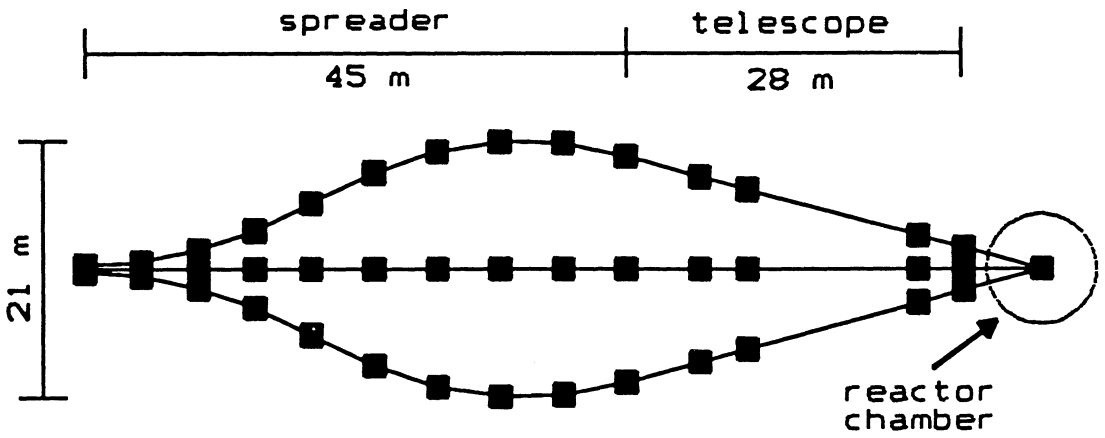

Fig. 2.53. Spreader and telescope layout.

In retrospect, placing the column-to-ring transition before the compression would result in a better design. More length would be allotted to the spreader, resulting in more gradual bending. In addition, smaller and/or fewer induction modules would be needed to surround the ring than would be needed for the 6-beam column.

Transverse Focus Section. The transverse focus section delivers the longitudinally-compressed beam to the target. It consists of two elements: a focusing telescope, which provides the required convergent angle to the beam bunches, and a reactor transport element,

which provides the final beam steering and the auto-neutralizing electrons immediately before the beam bunches enter the reactor chamber. Some combination of shielding, baffles, and shutters at the reactor interface must be included to protect the final focusing components from target radiation, target debris, and hot molten Flibe.

The focusing telescope consists of four quadrupoles. The layout for the 6-beam bundle is illustrated in Fig. 2.53. Figure 2.54 shows the calculated x and y beam envelopes along with the quadrupoles dimensions (shielding is not shown). This envelope calculation and the concurrent specification and placement of the four quadrupoles were done with approximate incorporation of space charge. Note that the horizontal and vertical scales of Fig. 2.54 are far different, so both the beams and quadrupoles are much longer or thinner than they appear in the figure.

The upstream telescope quadrupoles are arranged to keep the beam from converging to a small waist within the telescope, in order to reduce the effect of space charge. However, the beam is small enough that our design would have to be modified to take more accurate space charge design calculations into account, and it may be advantageous to add more quadrupoles to the telescope. A final design would have to take into account chromatic corrections, and also geometrical aberrations in the large diameter quadrupole lenses. This may require sextupole and octupole correction magnets. We would anticipate that incorporation of space charge effects would not lead to major modification of the design.

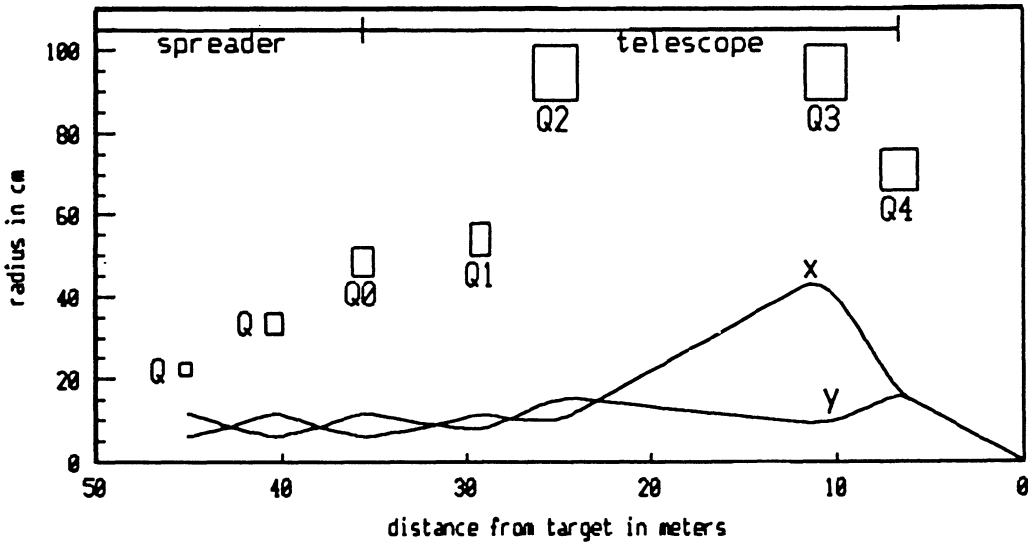

Fig. 2.54. Telescope beam envelopes and quadrupoles.
(Note horizontal and vertical scales are very different.)

Design parameters for the telescope quadrupoles are given in Table 2.29. Bore sizes are driven by radial shielding requirements. Shielding is analyzed and described in Section 2.2.6.6 and is illustrated in Fig. 2.16.

Table 2.29. Focusing Telescope Quadrupole Parameters.

beam →	Q0	Q1	Q2	Q3	Q4 *beam* →	
Distance from Target	35.6	29.2	25.1	10.5	6.6	m
Length	1.12	1.07	2.40	2.17	1.92	m
Shielding I.D.	0.30	0.40	1.12	1.12	0.52	m
Shielding O.D.	0.90	1.00	1.76	1.76	1.32	m
Gradient	-22.3	19.9	-9.5	11.4	-15.2	T/m
Superconductor Field	-10	10	-9.5	10	-10	T

The reactor transport segment is illustrated in Fig. 2.55. Table 2.30 lists geometrical design parameters and focusing performance parameters. The bundle size, as characterized by the bundle-center-to-beam-center angle, is determined in general by the close-packing of either telescope Quadrupole Set 3 or Quadrupole Set 4, depending on their distance from the target and their radial build. For the baseline design, this constraint is at Quadrupole Set 4, although Quadrupole Set 3 is also essentially packed to the limit.

A total of 1.1 m of longitudinal distance was allotted for electron injection and steering dipoles. No electron injector or steering dipole design was done. Although no steering dipole specification was developed, it is known that the beam displacement, and therefore the dipole field, is very small relative to the upstream bending dipoles. The turn-to-turn voltage insulation specification will be very modest, and it is likely that copper windings can be used (which is desirable for fast response). This reduces shielding requirements and allows a relatively small bore, as suggested in the figure. The x and y dipoles would be co-wound to reduce the longitudinal space required.

Because the steering field is very small and the shielding requirements are less than for the telescope quadrupoles, it may even be possible to locate the dipoles within the final quadrupole. The dipoles would displace radial shielding, while serving as shielding themselves. This arrangement provides a very compact, space-efficient layout, but neutronics and ion optics feasibility must be verified.

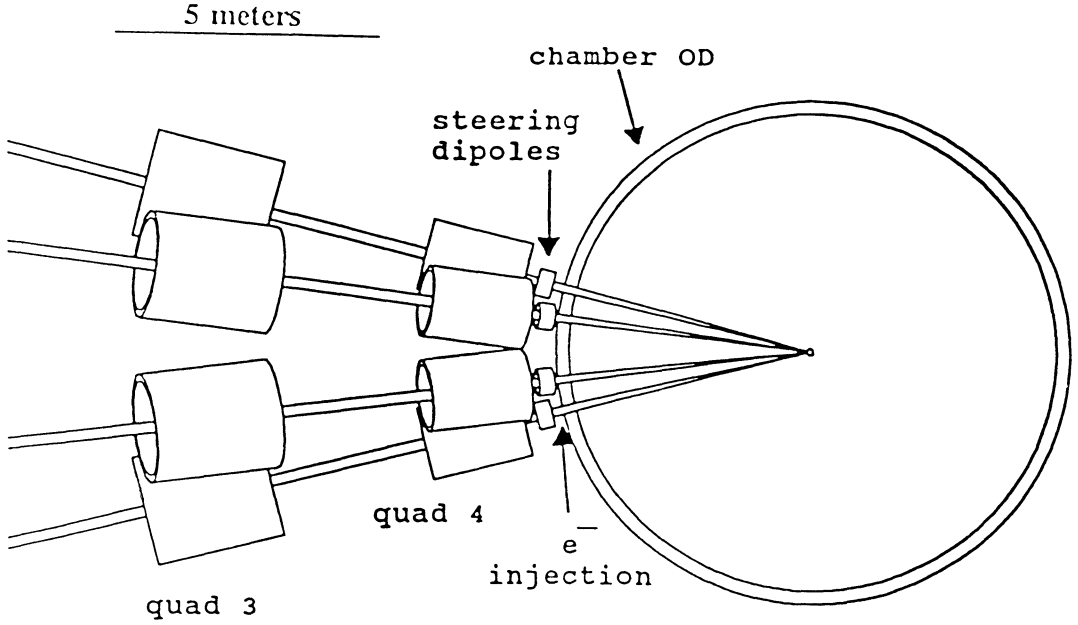

Fig. 2.55. Reactor transport layout.

Table 2.30. Reactor transport design and performance parameters

PARAMETER	VALUE
Vacuum vessel wall O.D.	9.0 meters
Beam geometric convergence half-angle	24.7 mrad
Beam port radius	14.2 cm
Area of beam ports (12 beams)	0.76 m^2
Bundle-center-to-beam-center angle	15.1 degrees
Bundle radius at wall O.D.	1.82 meters
Total wall area for bundles (12 beams)	20.1 m^2
Beam spot radius	2.3 mm
from space charge	1.5 mm
from emittance	1.6 mm
from dispersion	1.3 mm
from jitter/alignment	0.6 mm

2.4.10 Potential Reductions in Driver Cost

2.4.10.1 Low-Energy Transport Driver Savings

Because of the long initial pulse durations dictated by the Child-Langmuir injector limit, low-energy beams require large numbers of cores and quad arrays for small energy gains. Although the low-energy and pulse compression stages of our base driver make up only 8% of the driver length, they require 32% of the core volume and 50% of the quadrupole arrays.

Reducing the initial pulse length would:

- give greater voltage (and therefore energy) changes for a given core size (volt-seconds) and thus reduce the required total core mass, and

- increase the initial voltage gradient allowed by the velocity tilt limit and further reduce the length of the first two driver stages, the required number of quadrupoles, and the required core mass.

Cost/Benefit studies on methods of shortening the initial pulse should be done. An example of an improved base design is given in section 2.4.10.3. The improved driver shortens the initial pulse length by using larger beam sizes early in the driver. Other methods of reducing the initial pulse length could include:

- using higher injected current densities, and

- using beam combination so that more beams are used in the early driver stages than in the high-energy transport stage.

More aggressive source and injector assumptions decrease the estimated driver cost. Injector concepts exist that can provide currents densities above those given by the Child-Langmuir limit. High-performance injector development with more experimental results is needed to determine if savings from improved injectors can be realized.

Beam combination reduces the number of arrays and cores by increasing their sizes. In addition, beam combination leads to beam emittance growth (which degrades target performance as well as increasing bore sizes) and adds uncertainties to driver performance estimates. Further experiments and beam simulations could quantify the emittance growth effects needed to do a cost/benefit analysis for beam combination.

Beam separation before final focusing can lead to smaller spot sizes and higher gains. Beam separation could improve target performance, but improvements will be limited by spot growth resulting from beam combination at the target and by the performance of the beam-

separating magnets. Drivers which use both beam combination and beam separation will have both greater potentials for cost and performance improvements and greater uncertainties in the driver beam quality and achievable target performance.

2.4.10.2 Further Driver Savings

Recirculation. The number of driver components could be significantly lowered by using recirculation, so that the beams could pass through each component several times. Because dipoles used in a recirculating driver must be able to rapidly change the strength of the bending fields to accommodate the changing beam energies, this will require normal bending magnets which will have significant energy loss. Savings from "re-using" components will be offset by the fact that the bore sizes must be set from large initial beam sizes. Furthermore, the bending magnets needed for recirculation add momentum spread to the beams and thus degrade target performance.

Recirculation can be done at any point in the driver, and several recirculating loops may be used in a single driver. A cost/benefit analysis of recirculation should include experimental analysis of the effects of beam bending on beam growth.

Higher Average Voltage Gradients. The length and cost of linear drivers could be reduced if a higher average voltage gradient could be used. The required volt-seconds and core volumes will not change, but the number of quadrupoles and the length of the driver could be reduced. Although average voltage gradients much greater than 1 MV/m have been sustained for very short time periods, more experimental data on high-performance insulator designs is needed before higher average gradients can be assumed for a driver.

2.4.10.3 An Example of Driver Savings for a 5 MJ Driver

The decision to use a single beam radius and only one quadrupole array design allowed us to quickly examine the large available parameter space. The driver design can be improved by using two different quadrupole array designs. Using larger bore quadrupoles in the beginning of the driver will increase the initial beam current and decrease the initial pulse length. Beam compression during the low-energy stage of the driver will allow for smaller quadrupole bores to be used for the high-energy stage, which makes up the majority of the driver. Although the

maximum quad occupancy factor for the improved driver is low (0.5), the half periods early in the driver are short and the quadrupoles are short. The effect of limiting designs to those which use more credible quadrupoles with greater lengths relative to their bores is an area for further investigation.

Figure 2.56 shows how the cost of the quadrupoles and cores of this modified design compares with the same cost subset of drivers using our base-case assumptions. The savings for the quadrupoles and cores for a 5 MJ driver would be approximately $50 M, and the total driver savings (including savings in the pulse forming network, cryogenic system, etc.) would be larger.

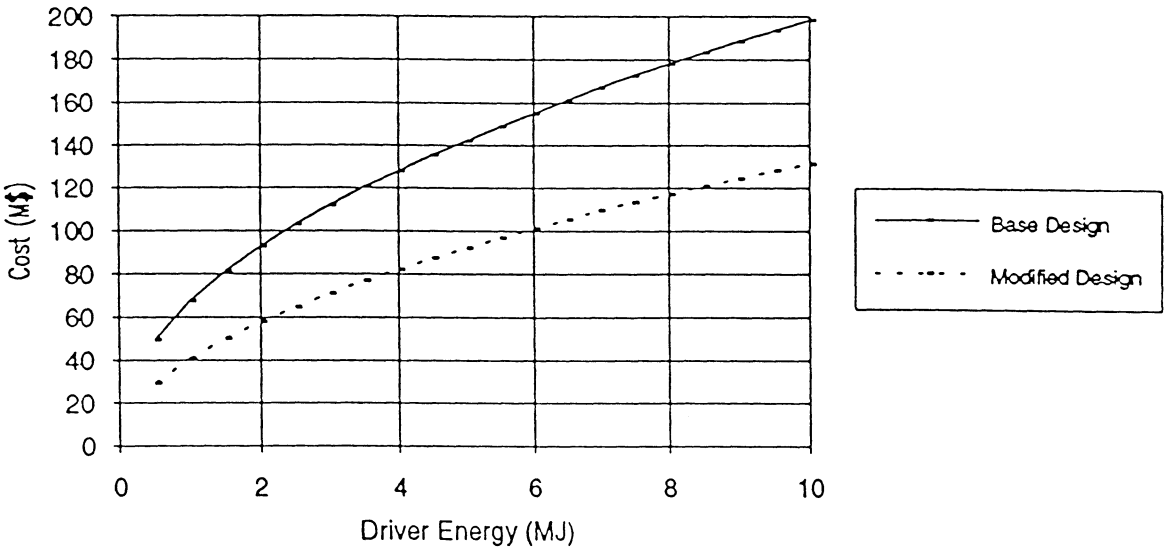

Fig. 2.56. Cost subtotals for modified and base driver assumptions.

2.4.11 Results and Conclusions

The base 5-MJ heavy-ion induction driver we have designed uses conservative design assumptions, has an efficiency of 28% and a cost of only $120/J. Combining the driver efficiency with an estimated target gain of 86.5 gives a recirculating power fraction for a 1,000 MW IFE plant of only ~ 7%. We created a high-performance, low-cost design by

- using an original design for compact arrays of high-performance, Nb_3Sn quadrupoles which leads to small sizes and costs for the inductor cells as well as the focusing arrays, and
- conducting a parametric search over a wide range of possible driver parameters to choose parameters which lead to an attractive design.

We use minimal extrapolation from existing accelerator technology and physics to create highly credible driver performance. We do not use any bends in the accelerator, beam combination, or beam separation. Although driver designs with bends, such as recirculating induction accelerators, offer the potential for cost savings by bending the beams in a circle and reducing the number of required driver elements, present performance uncertainties are large for high-current circular accelerators. Linear driver costs and projected target gains could be improved by combining beams early in the driver and separating them before final focusing; again we avoid performance uncertainties by not using beam combination or separation.

We found significant cost savings by choosing our driver parameters after an extensive search of the allowed driver design parameters. Driver parameters varied in our design sudy were

the number of beams in the driver,

the ion mass,

the ion charge state,

the quadrupole focusing field strength,

the quadrupole spacing, and

the type of superconductor used in the quadrupole windings (Nb-Ti or Nb_3Sn).

We examined the effect of variation in each of these driver parameters on both the driver cost and projected target gain.

By using larger beams early in the driver (and changing our design assumption from one quadrupole array design to two), we were able to further lower the driver cost. Further parametric studies with other design variations could give further savings.

We have developed powerful tools for modeling a wide variety of drivers and identified several areas where these tools could be used to quantify the benefits resulting from more aggressive design options.

2.5 REFERENCES FOR CHAPTER 2

2.1 R.W. Moir, "HYLIFE-II Inertial Confinement Fusion Reactor Design," Lawrence Livermore National Laboratory Report UCRL-JC-103816 (Oct. 1990).

2.2 B. Badger et al., "HIBALL - A Conceptual Heavy Ion Beam Driven Fusion Reactor Study," University of Wisconsin (Sept. 1981).

2.3 B. Badger et al., "HIBALL-II - An Improved Heavy-Ion Beam Driven Fusion Reactor Study," University of Wisconsin Fusion Technology Institute Report UWFDM-625 (Dec. 1984).

2.4 R.R. Peterson, J.J. MacFarlane, and G.A. Moses, "CONRAD - A Combined Hydrodynamic-Condensation/Vaporization Computer Code," University of Wisconsin Fusion Technology Institute Report UWFDM-670 (July 1988).

2.5 J.J. MacFarlane, "IONMIX - A Code for Computing the Equation of State and Radiative Properties of LTE and Non-LTE Plasmas," University of Wisconsin Fusion Technology Institute Report UWFDM-750 (Dec. 1987).

2.6 "T-4 Handbook of Material Properties Data, Vol. 1c: Equations of State," Los Alamos National Laboratory Report LA-10160-MS (Nov. 1984).

2.7 W.J. Moore, *Physical Chemistry*, 3rd ed., Prentice-Hall (NJ) (1965).

2.8 A.E. Scheidegger, *The Physics of Flow Through Porous Media*, 3rd ed., University of Toronto Press (1960).

2.9 R.D. Blevins, *Applied Fluid Dynamics Handbook*, Van Nostrand Reinhold (1984).

2.10 R.A. Greenkorn, *Flow Phenomena In Porous Media*, Marcel Dekker (NY) (1963).

2.11 A.E. Barrington, *High Vacuum Engineering*, Prentice-Hall (NJ) (1963).

2.12 H.S. Carslaw and J.C. Jaeger, *Conduction of Heat in Solids*, Oxford, Clarendon Press (1959).

2.13 F. Kreith, *Principles of Heat Transfer*, International Textbook (1966).

2.14 R.R. Peterson, J.J. MacFarlane, and G.A. Moses, "CONRAD, A Combined Hydrodynamics-Condensation/Vaporization Computer Code," University of Wisconsin Report UWFDM-670 (July 1988).

2.15 J. Heremans and C.P. Beetz, Jr., "Thermal Conductivity and Thermopower of Vapor Grown Graphite Fibers," *Physical Review* B, **32**, No. 4, 1981-1986 (15 Aug 1985).

2.16 R.J. Price, G.R. Hopkins, and G.B. Engle, "Effects of Fast Neutron Irradiation on Carbon Fibers," *Proc. 17th Carbon Conf.*, 348 (1981).

2.17 R.W. Moir et al., "HYLIFE-II Progress Report, Chapter 6," UCID-21816 (1991) and "Blanket Comparison and Selection Study Final Report," Argonne National Laboratory Report #ANL/FPP-84-1, **1** (Sept. 1984).

2.18 W.W. Eagle, Jr., "User's Manual for ANISN," K-1693, Oak Ridge Diffusion Plant (1967).

2.19 R.E. MacFarlane, "TRANSX-CTR): A Code for Interfacing MATXS Cross Section Libraries To Nuclear Transport Codes For Fusion System Analysis," Los Alamos National Laboratory Report LA-9863-MS (1984).

2.20 M. Sawan, W. Vogelsang, and D.K. Sze, "An Effective Penetration Shield Design for ICF Reactors,'' *Proc. 6th International Conf. on Radiation Shielding*, Tokyo, Japan, 675 (May 1983).

2.21 M. Sawan, "Charts for Specifying Limits on Copper Stabilizer Damage Rate," *J. Nucl. Mat.*, **122 & 123**, 1376 (1984).

2.22 W. Maurer, '"Neutron and Gamma Irradiation Effects on Organic Insulating Materials for Fusion Magnets," KfK-3974, Kernforschungszentrum, Karlsruhe (1985).

2.23 M. Sawan and P. Walstrom, "Superconducting Magnet Radiation Effects in Fusion Reactors," *Fusion Technology*, **10**, 741 (1986).

2.24 W.R. Grimes, "Molten Salt Reactor Chemistry," *Nuclear Applications and Technology*, **8**, 137 (1970).

2.25 W.R. Grimes and S. Cantor, "Molten Salts as Blanket Fluids in Controlled Fusion Reactors," in *The Chemistry of Fusion Technology*, D. M. Gruen, Ed., Plenum, New York, 161-190 (1972).

2.26 E.M. Larsen and L J. Wittenberg, "The Chemistry of Molten Li_2BeF_4," *Fusion Technology*, **10**, 990 (1986).

2.27 *J. Phys. Chem. Ref. Data.*, **14**, Suppl. 1 (1985).

2.28 A.B. Chilton, J.K. Schultis, and R.E. Few, *Principles of Radiation Shielding*, Prentice-Hall, Engelwood Cliffs, NJ, 429-431 (1984).

2.29 T.J. Dolan, G.R. Longhurst, and E. Garcia-Otero, "Vacuum Disengager Design for Tritium Removal from HYLIFE-II Reactor Flibe," *Fusion Technology*, **21**, 1947 (1992).

2.30 R.W. Moir et al., "HYLIFE-II Progress Report, Chapter 6," UCID-21816 (1991).

2.31 G.R. Longhurst and T.J. Dolan, "Tritium Permeation Loses in HYLIFE-II Heat Exchanger Tubes," *Fusion Tech.*, **19**, 820 (1991).

2.32 J.L. Anderson et al., "Experience with the TSTA Milestone Runs with 100 Gram-Levels of Tritium," *Fusion Tech.*, **14**, 438 (1988).

2.33 K.B. Woodall, S.K. Sood, and A. Busigin, "Conceptual Design of a Laboratory Scale Impurity Detritiation and Hydrogen Isotope Separation System," *Abstract 4th Topical Meeting on Tritium Technology*, Albuquerque, NM (1991).

2.34 S. Sinharoy, A.R. Keeton, W.J. Lange, "Permeation of Deuterium Through Double Walled Croloy Tubes," Westinghouse Research & Development, Report 86-7B6-HYPER-R1 (June 1986).

2.35 "Development Plan for Advanced Fossil Fuel Power Plants," Electric Power Research Institute, EPRI CS-4029, Final Report (May 1985).

2.36 Craig Fong, Lawrence Berkeley Laboratory, Private communication (October 1991).

2.37 J. Hovingh et al., "Heavy-Ion Linear Induction Accelerators as Drivers for Inertial Fusion Power Plants," *Fusion Technology*, **13**, No. 2, 262 (February 1988).

2.38 W. M. Polansky, "U.S. Accelerator Research Program for Heavy-Ion Fusion," Fusion Technology, **13**, No. 2, 202 (February 1988).

2.39 M. J. Monsler, "The Potential for Reducing the Cost of a Heavy-Ion Accelerator for ICF," Final Report PO #9056305, Submitted to Lawrence Livermore National Laboratory (Feb. 1987).

2.40 E. D. Courant, "Power Transport in Quadrupole or Solenoid-Focusing Systems," *Proc. ERDA Summer Study of Heavy Ions for Inertial Fusion*, LBL-5543, Lawrence Berkeley Laboratory, 72 (Dec. 1976).

2.41 *Fusion Technology*, **13**, No. 2, Special Issue on Heavy-Ion Fusion Systems and Their Assessment (Feb. 1988).

2.42 C.D. Child, *Phys. Rev.*, **32**, 492 (1911).

2.43 R. L. Bieri, "Inertial Confinement Fusion Driver Enhancements: Final Focusing Systems and Compact Heavy-Ion Driver Designs," MIT Nuclear Engineering Ph.D. thesis, Chapters 5 & 6, MIT Press (1991). Also published as Lawrence Livermore National Laboratory Report UCRL-LR-107986.

2.44 R. J. Roark, *Formulas for Stress and Strain*, 3rd Ed., N.Y. McGraw-Hill, 150 (1954).

2.45 S.S. Yu, H.D. Shay et al., "HIF Recirculating Induction Accelerator Report," Lawrence Livermore National Laboratory Report UCRL-LR-108095.

2.46 E. P. Lee, T. Fessenden, and Laslett, *Proc. 1985 Particle Accelerator Conf.*, IEEE Trans. Nucl. Sci., **NS-32**, No. 5, 2489 (1985).

2.47 I. Hoffman, *Applied Charged Particle Optics*, Part C, A. Septier, Ed., Academic Press, 124 (1983).

2.48 E. P. Lee, C. Fong, S. Mukherjee, and W. Thur, "Conceptual Design of Bend, Compression and Final Focus Components of ILSE," *Proc. 1989 IEEE Particle Accelerator Conf.*, Chicago, p. 971.

2.49 E.P. Lee, "Transport of Intense Ion Beams," LBL-21559 (June 1986).

2.50 D.S. Lemons and L.E. Thode, "Electron Temperature Requirements for Ballistically Focused Neutralized Ion Beams," *Nucl. Fusion*, **21**, 529 (1981).

2.51 S. Humphries, Jr., *Charged Particle Beams*, Chapter 11, Wiley, New York (1990).

2.52 J. Hovingh, V.O. Brady, A. Faltens, D. Keefe, and E.P. Lee, "Heavy-Ion Linear Induction Accelerators as Drivers for Inertial Fusion Power Plants," *Fusion Technology*, **13**, 255 (Feb. 1988).

2.53 Attributed to P. Stroud by E.P. Lee, Private communication (March 1990).

2.54 G.H. Gillespie, K. Cheng, and Y-K. Kim, *Proc. Heavy Ion Fusion Workshop*, Argonne National Laboratory Report ANL-79-41 (Sept. 1978).

Chapter 3

SOMBRERO

KrF-laser DrivenPower Plant

CONTENTS

3.1 OVERVIEW OF SOMBRERO POWER PLANT DESIGN 3-1
3.1.1 Introduction 3-1
3.1.2 General Description 3-2
3.1.3 Overall Reactor Layout 3-2
3.1.4 Tritium Considerations and Safety Assessment 3-4
3.2 SOMBRERO CHAMBER DESIGN AND ANALYSIS 3-6
3.2.1 Laser Propagation in Cavity Gas 3-6
3.2.2 First Wall Protection 3-12
3.2.3 First Wall and Blanket Design 3-24
3.2.4 Chamber Vacuum System 3-65
3.2.5 Neutronics Analysis 3-69
3.2.6 Tritium Considerations 3-81
3.3 SOMBRERO POWER CONVERSION AND PLANT FACILITIES 3-89
3.3.1 Heat Transport System 3-89
3.3.2 Power Conversion System 3-91
3.3.3 Plant Facilities 3-92
3.4 KrF DRIVER 3-107
3.4.1 KrF Driver System Requirements 3-107
3.4.2 Background 3-107
3.4.3 Amplifier Efficiency Optimization 3-111
3.4.4 Final Amplifier Technology 3-119
3.4.5 System Architecture 3-133
3.4.6 Grazing Incidence Metal Mirrors 3-139
3.4.7 Technology Development Requirements 3-145
3.5 REFERENCES FOR CHAPTER 3 3-146

3.0 SOMBRERO LASER-DRIVEN POWER PLANT

3.1 OVERVIEW OF SOMBRERO POWER PLANT DESIGN

3.1.1 Introduction

SOMBRERO (solid moving breeder reactor) is a conceptual design study of a 1000 MWe KrF laser-driven IFE power reactor utilizing direct drive targets in a near symmetric illumination configuration. Among the important goals of the study was the achievement of a safe and environmentally attractive reactor of relatively simple design. Thus, the chamber is constructed of a low activation carbon/carbon composite, and the blanket consists of a moving bed of solid Li_2O particles flowing through the chamber by gravity. The particles are transported through an intermediate heat exchanger (IHX) and around the loop in a fluidized state by He gas at 0.2 MPa. This very low pressure will exist in the blanket and thus distinguishes this breeding blanket from all other solid breeder schemes.

Solid breeding materials have always been considered front runners for use in fusion reactors with research and development programs in place investigating them in the U.S., Japan, and Europe. They offer the potential for high temperature capability, low activation, safety, no corrosion issues, and a good data base. Many of the recent tokamak studies both near term[3.1] and long term[3.2] have proposed static solid breeder blankets. Static solid breeder blankets, however, have some problems. Typically, they have to be cooled with a high pressure He gas at 5-8 MPa and require a separate loop of low pressure He gas for T_2 extraction. Temperature control in these blankets is difficult, because it depends on the effective thermal conductivity of the packed bed which can change with time and with radiation fluence in unpredictable ways. The operating temperature windows for solid breeders is relatively narrow. This tends to exacerbate temperature control. Further, static beds suffer from problems of Li burn-up, phase changes, swelling and hot spots. In the present design, the breeding material particles can be continuously reprocessed to insure size uniformity, to remove fractured particles, and to maintain the proper Li atom density. This can be done in a small side stream as is the practice in many liquid cooled systems. A moving bed of solid breeder particles retains all the advantages of static beds while eliminating the problems. This scheme has been proposed for tokamaks, but has not been taken seriously because of the geometric limitation due to the encumbering magnet systems.[3.3] A moving bed of solid Li_2O particles was used in the SOLASE CO_2 laser-driven conceptual reactor design (1977) at a time when relevant properties of Li_2O were not well characterized.[3.4] The issues that have to be dealt with in moving beds are the large inventory of solid breeder material, the large volumetric transport around the loop, break-up of particles, erosion of wall materials, and relatively poor heat transfer at the first wall, which also results in a large intermediate heat exchanger.

3.1.2 General Description

The SOMBRERO reactor a 1000 MWe commercial power plant utilizing inertial fusion energy (IFE) and driven with a KrF laser. The 3.4 MJ laser energy is divided into 60 beams to provide near symmetric illumination of direct drive targets giving a gain of 118 at a rep-rate of 6.7 Hz. The chamber is made of a 4D weave carbon/carbon composite and has a cylindrical central region with conical ends. The chamber has a minimum inner radius of 6.5 m at the midplane and a blanket/reflector thickness of 1.0 m at the midplane. Solid Li_2O particles 300-500 μm in size flow through the blanket by gravity from top to bottom. This blanket configuration gives a breeding ratio of 1.25 and an energy multiplication of 1.08. The coolant channel at the first wall (FW) has a constant flow area from top to bottom. Thus, it is wider at the conical extremities than at the midplane. This is done to insure a constantly high particle velocity at the FW where the surface heat load is high. The rear of the blanket/reflector region is divided into zones with increasing fraction of carbon. In this way, a reflector is incorporated into the blanket design and will not require a separate coolant. The particle velocity in the rear zones is progressively lower due to the reduced nuclear heating.

The Li_2O particles enter the chamber at 550°C and exit at an equilibrated temperature of 740°C. From the chamber, the particles go to the IHX where they exchange heat with liquid lead. The liquid lead at 600°C then goes to a steam generator and a double reheat power cycle, where the steam conditions are 538°C and 24 MPa. By recovering the laser waste heat, the efficiency is boosted by 2% giving an overall power cycle conversion efficiency of 47%. After going through the IHX, the particles are transported in a fluidized bed mode, using He gas, back to the chamber to start a new cycle.

3.1.3 Overall Reactor Layout

Figure 3.1 shows the layout of the reactor building with the reactor chamber shown in the middle. The target is illuminated by 60 beams in a near symmetric illumination configuration. There are beam ports lying on 10 horizontal planes with 6 beam ports in each plane forming a cone with the vertex at the chamber center. Such a configuration avoids the necessity of having beams at the north and south poles making the design simpler. The figure shows the upper manifold that feeds the solid breeder material through individual supply tubes to 12 wedge-shaped blanket modules. After going through the blanket, the breeding material exits from each module through individual tubes to a return manifold located below the chamber. From there the breeding material is transported in a fluidized bed mode to the IHX.

The chamber is surrounded by a 1.7 m thick shield wall at a radius of 10 m. This wall has several functions: it shields the area outside the wall such that it can have hands-on maintenance capability with 24 hours after shutdown in areas surrounded with an additional 1.0 m thick wall

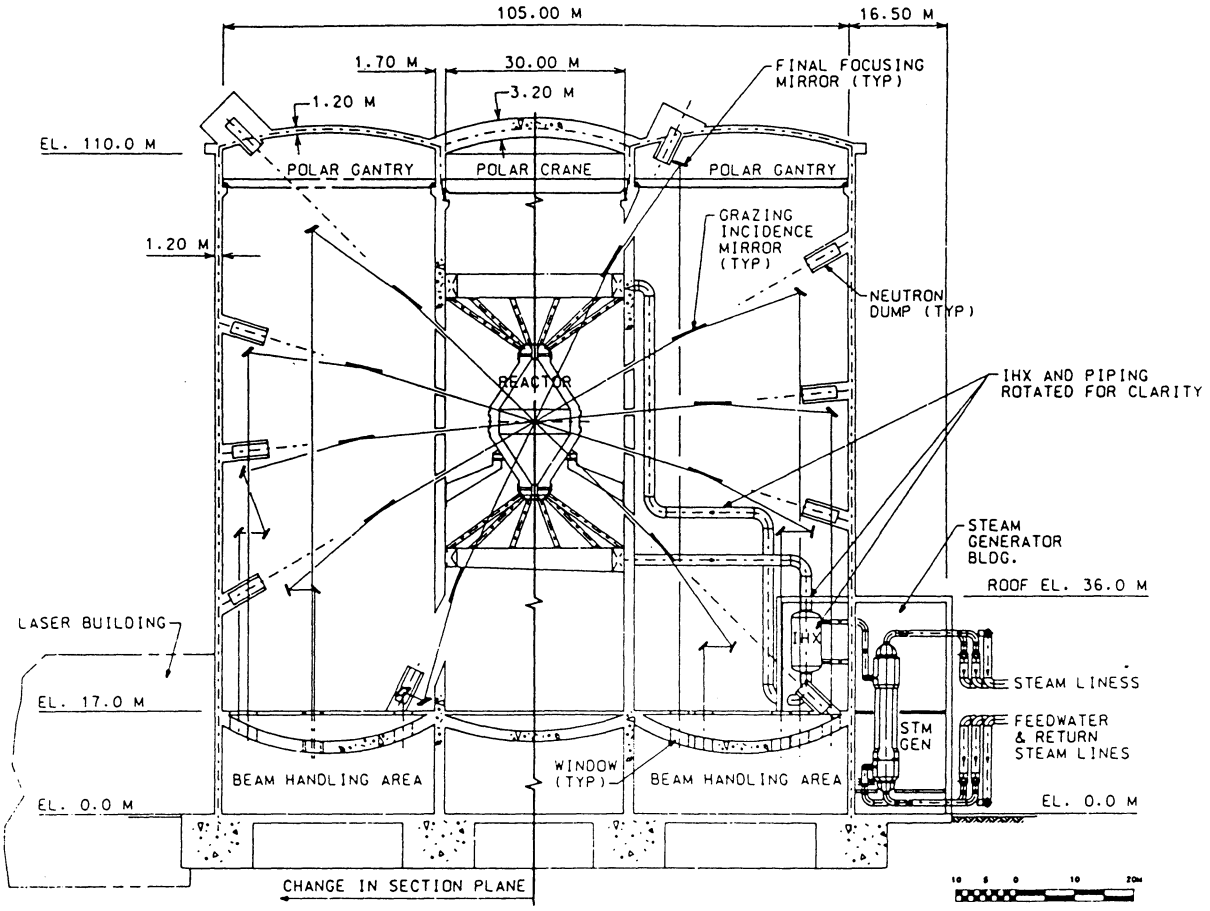

Fig. 3.1. Overall cross section of SOMBRERO reactor building.

such as the IHX area; it is the primary support for the chamber, and finally, it provides a central support column for the reactor building roof.

The laser beams are routed from the laser building to the reactor building through the lower level as shown in Fig. 3.1 and then reflected vertically through windows in the floor of the reactor building. These windows are the primary barriers against tritium diffusion into the laser building. Secondary windows located between the laser building and the lower level of the reactor building act as the back-up barriers. After going through the windows in the floor of the reactor building, the laser beams are incident onto the final focusing (FF) mirrors which focus the beam and direct them onto grazing incidence metal (GIM) mirrors which in turn deflect them into the chamber through ports in the shield wall and the chamber wall. The GIM mirrors are at a radius of 30 m and are subjected to primary neutrons coming through the beam ports. The lifetime of the GIM mirrors depends on the degree of damage recovery by annealing. The primary neutrons passing

through the thin metal of the GIM mirrors are directed into neutron traps located on the wall of the reactor building. These high aspect ratio neutron taps act as black holes for neutrons allowing only a very small fraction of low energy neutron to backscatter. The FF mirrors which are at a radius of 50 m are out of line-of-sight of primary neutrons. These dielectric-coated mirrors are very susceptible to neutron damage and cannot be annealed. According to present thinking, the limiting fluence to dielectric coatings is ~10^{18} n/cm^2. The estimated flux to these mirrors is 8.6×10^8 n/cm^2, which gives an approximate lifetime of 37 full-power-years. This is a significant development since up until now the FF optics has always been the Achilles heel in laser driven IFE reactors.

The reactor building which houses the chamber and beam optics is 110 m in diameter with an overall height of 115 m. Since there are no beam tubes, the building shares the same atmosphere as the chamber, namely ~0.5 torr of Xe gas. Roots type of pumps will be used to evacuate the building, and fresh Xe gas will be injected into the chamber continuously. Unburned tritium and target debris will be pumped through the vacuum system, and a side stream will be used for tritium recovery.

3.1.4 Tritium Considerations and Safety Assessment

Tritium extraction from the breeding material is accomplished by treating the He carrier gas. The predominant tritium species in the He carrier gas is maintained as HTO by the addition of H_2O such that the O_2 partial pressure of 10^{-5} Pa is achieved. Under these conditions the T_2 partial pressure will only be 2×10^{-6} Pa, and the T_2 permeation at the steam generator is manageable. Most of the carrier gas is disengaged from the breeder material, and only 10% of it goes through the IHX. Using this fact and taking credit for a tritium barrier of a factor of 100 due to the oxide layer on the steam generator tubes reduces the steady state T_2 permeation into the power cycle to only ~15 Ci/day. The amount of H_2O in the carrier gas has to be controlled carefully because of the danger of forming LiOH(T), which has a melting point of 417°C and could give problems with agglomeration. The required H_2O partial pressure of 64 Pa, however, is far below that needed to form LiOH(T), which is 3150 Pa. Tritiated water in the form of T_2O and HTO is recovered from the He carrier gas by adsorption on molecular sieves. The solubility of T_2 in Li_2O at 650°C is ~0.081 wppm and thus for the total 2000 tonnes of Li_2O in the reactor system, the T_2 inventory is ~162 g.

Activation and safety analysis has been performed for the chamber, shield, and breeder material. It is found that the total activities generated in the carbon/carbon composite of the chamber and in the steel-reinforced concrete shield are 0.054 and 10.12 MCi, respectively. Intermediate heat exchangers are located in the space between the reactor shield and the reactor building wall within circular enclosures which have a 1.0 m thick wall. Within these enclosures

the biological dose rate drops down to 1.6 mrem/h 24 hours after shutdown making it possible to do hand-on maintenance on the IHX and other components. Radwaste classification has shown that the chamber and the shield will easily qualify as Class A low level waste according to the waste disposal ratings defined by 10CFR61 guidelines. The Li_2O breeding material, however, only qualifies as Class C low level waste. The maximum public dose from atmospheric effluents is 0.73 mrem/y, occurring at the reactor site boundary, which is 1 km from the reactor building. The results of a loss of coolant accident (LOCA) have also been assessed. If the back of the FW will no longer be cooled as a result of LOCA, some of the FW carbon will be evaporated. It has been estimated that a loss of ~0.44% of the FW due to evaporation will generate a high enough C atom density in the chamber as to prevent the laser beams from reaching the target, in this way achieving a self regulating shutdown. The afterheat in the shield will only raise its temperature by a few degrees over a prolonged shutdown period; therefore, there is no danger of it releasing activation products. During a totally improbable accident which will cause the release of all 162 g tritium inventory in the Li_2O, the estimated off-site whole body dose to the surroundings is 2.11 rem. This low off-site dose eliminates the need for N-stamp components for the reactor thus reducing the cost and making it easier to license. Table 3.1 gives the relevant SOMBRERO parameters.

Table 3.1. SOMBRERO Plant Parameters

Driver	KrF Laser
Driver Energy (MJ)	3.4
Driver Efficiency (%)	7.5
Illumination	Near Symmetric
Type of Target	Direct Drive
Target Gain	118
Target Yield (MJ)	400
Rep-Rate (Hz)	6.7
Overall Energy Multiplication	1.08
Chamber Construction	C/C Composite
Breeding Material	Li_2O Particles
Breeding Ratio	1.25
Fusion Power (MW)	2677
Thermal Power (MW)	2891
Power Cycle Efficiency (%)	47
Gross Electric Power (MWe)	1359
Driver Power (MWe)	304
Auxiliary Power (MWe)	55
Net Electric Power (MWe)	1000

3.2 SOMBRERO CHAMBER DESIGN AND ANALYSIS

3.2.1 Laser Propagation in Cavity Gas

Primary to the SOMBRERO design is the choice of xenon gas density that fills the target chamber. Our approach in the target chamber design is to choose a target chamber fill gas that absorbs the target generated x rays and ions and re-radiates the energy to the target chamber first wall over the longest possible time while simultaneously allowing the propagation of the laser beams to the target. We have chosen xenon as a target chamber fill gas, because it has a high cross-section for stopping x rays and energetic ions and because it is chemically inert in its neutral state. Also, xenon is one of the few high atomic number elemental gases. We believe that breakdown of the gas by the laser places an upper limit on the density of the gas. In this section, we discuss laser-induced breakdown in the xenon chamber fill gas of SOMBRERO. We begin by discussing breakdown issues in laser fusion reactors. Here we also define the SOMBRERO target illumination conditions. We then review what laser-induced breakdown experimental results that we know to exist. Finally, we use these experimental results to extrapolate to the SOMBRERO conditions and choose a xenon density.

3.2.1.1 Laser-Induced Breakdown Issues

There is concern that laser-induced breakdown will affect the laser beams before they are absorbed in the target and will, therefore, reduce the target performance. If the uniformity of the laser illumination on the target is reduced, the implosion of the target will be less symmetric, and the thermonuclear burn of the DT fuel will be degraded. It is not clear to us how much breakdown is acceptable or where along the beam breakdown is allowed.

Breakdown very near to the surface of the target may not be detrimental to target performance. Even if there were no fill gas, the region near the target would be quickly filled with plasma because of blowoff from the target. So if the presence of ionized gas in the region near the target prevents proper implosion symmetry, then direct-drive laser fusion would not be possible under even vacuum conditions.

The laser intensity is much higher very close to the target than throughout most of the transport length. The illumination geometry for SOMBRERO is shown schematically in Fig. 3.2. Here, one sees the laser beams overlapping on the target. It is clear from this picture that it is only near the target that the beams overlap. The illumination parameters are given in Table 3.2. The peak intensity that the laser beams must jointly apply to the target is about 500 TW/cm^2. This is achieved with 60 beams with a peak intensity (over the beam cross-section) of 33 TW/cm^2. The radius at which the beams begin to overlap is ~1.2 cm. The average intensity rises quadratically from 33 TW/cm^2 at the overlap point to 500 TW/cm^2 at the target

surface. If breakdown within 1.2 cm of the target is acceptable, then laser-induced breakdown need only be considered at the lower intensity.

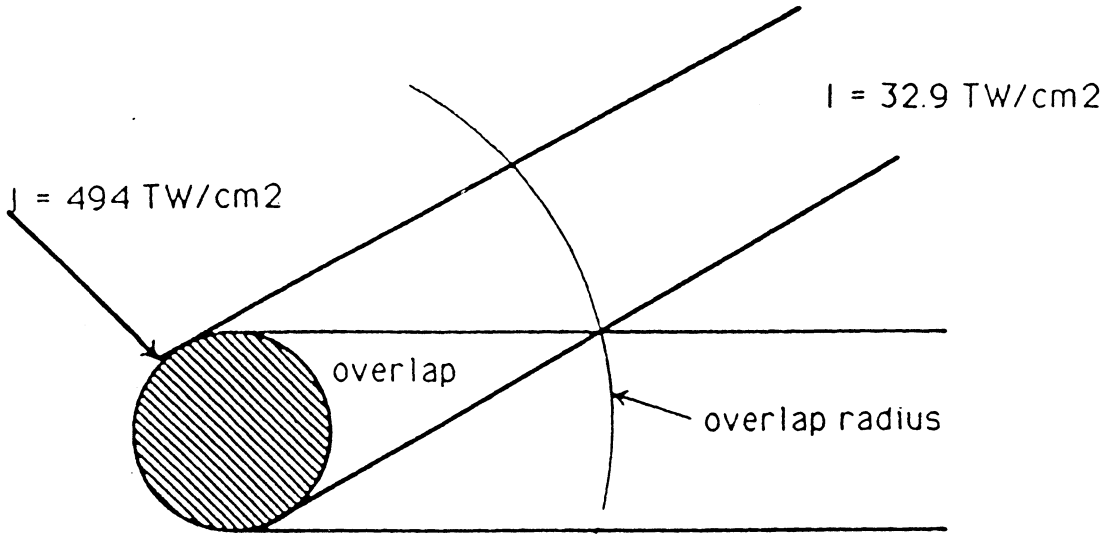

Fig. 3.2. Schematic picture of SOMBRERO target illumination geometry.

Table 3.2. SOMBRERO Target Illumination Parameters

Laser Pulse Width (ns)	6
Peak Total Intensity on Target ($TW/cm^{2)}$	500
Peak Beam Intensity ($TW/cm^{2)}$	33
Target Radius (cm)	0.3
Number of Beams	60
f # for Final Laser Optics	50
Overlap Radius (cm)	1.20
Fill Gas Species	Xenon
Fill Gas Density (cm^{-3})	1.8×10^{16} (0.5 Torr)

We are also curious as to the effects of incoherence on laser-induced breakdown. In the overlap region, the photons from separate laser beams are not coherent with each other. Their electric vectors are no longer in phase with each other so electron avalanche breakdown would be reduced compared to coherent light at the same intensity. However, KrF lasers produce light with photon energies of about 5 eV, so only three photons are needed to ionize a xenon atom, since xenon's ionization energy of 12.1 eV. Therefore, 3-photon absorption may be an important breakdown mechanism. There may be coherence effects with multi-photon absorption as well. If there are such effects, we may by able to use the single beam intensity even in the overlap region.

Breakdown is a process involving many effects and is not a simple threshold phenomenon. We choose to define breakdown in terms of free electron density, where the electron density is high enough to alter the passage laser light. We wish to know the xenon density allowed at SOMBRERO laser intensity, while not generating laser degrading electron density. This xenon density is a function of the laser intensity, the wavelength, the laser bandwidth, the laser coherence, the laser focal length, the spot size, the pulse width, and gas properties such as temperature and impurities. We have tried to rely on experimental results, but there are no experiments that meet all of the SOMBRERO conditions.

3.2.1.2 Breakdown Experimental Data

We have examined past experimental studies into laser induced breakdown and have found that the wavelength and density dependence is well documented.[3.5] Thresholds for four laser wavelengths were measured using ruby and neodymium lasers and their second harmonics, so the lowest wavelength used is 0.35 μm. This is still quite different from the KrF wavelength of 0.25 μm, so we have extrapolated. The spot radii varied and was 13 μm for the small wavelength, much smaller than the SOMBRERO value of 0.3 cm. The pulse width was 20 ns compared to 6 ns. The focal length was 18.4 mm compared with 30 m for SOMBRERO. Nothing is known about the smoothness of the laser profile. We can probably assume small bandwidths and high coherence. Breakdown was measured by observing visible emission at the focal spot. The threshold intensity as a function of gas pressure (or density) is shown in Fig. 3.3 for several wavelengths and for argon and xenon. The threshold intensity is seen to be a strong function of wavelength. One can also see that the threshold intensity for xenon is roughly the same at 1.06 μm as it would be at 0.25 μm . The measured breakdown threshold is plotted against wavelength for a number of densities for argon and xenon in Fig. 3.4. In these experiments, the breakdown threshold of xenon was measured above 1000 torr of gas pressure, three orders of magnitude higher than in SOMBRERO. Other experiments have measured the breakdown threshold near the SOMBRERO density for 1 μm laser light.[3.6, 3.7] The results of all

these experiments are shown in Fig. 3.5, where the quoted laser intensity thresholds for breakdown are plotted against gas density. One aspect of breakdown for which we have found no experimental studies is the effect of laser coherence.

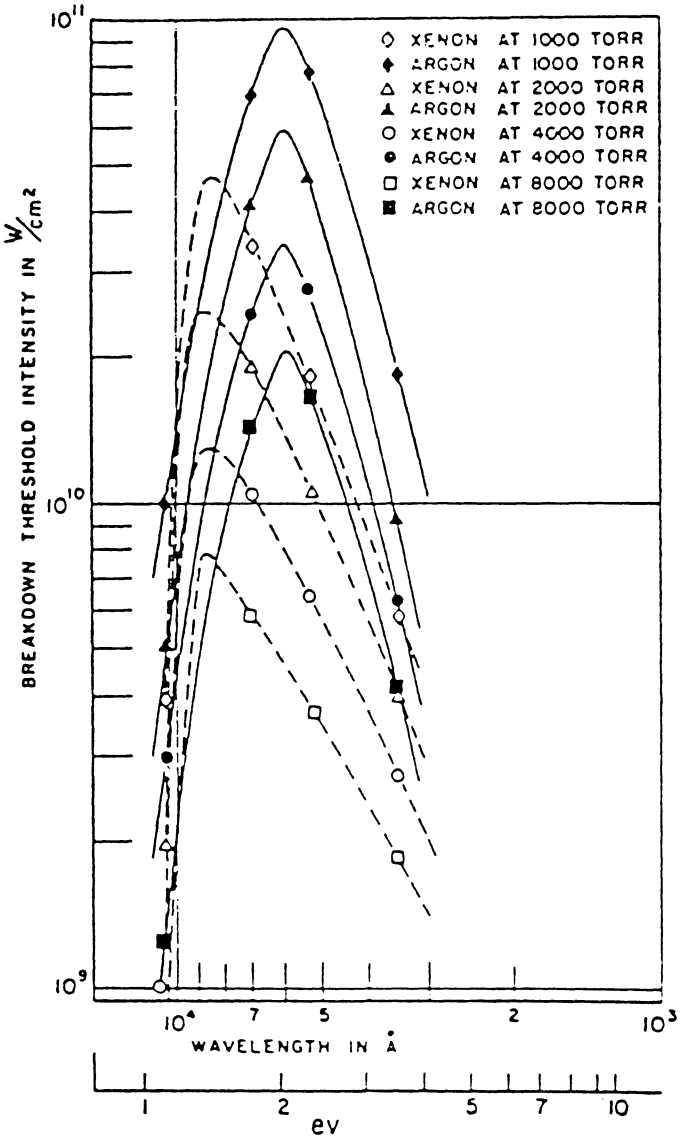

Fig. 3.3. Experimentally measured breakdown threshold intensities in xenon and argon versus wavelength for a number of densities. (Ref. 3.5)

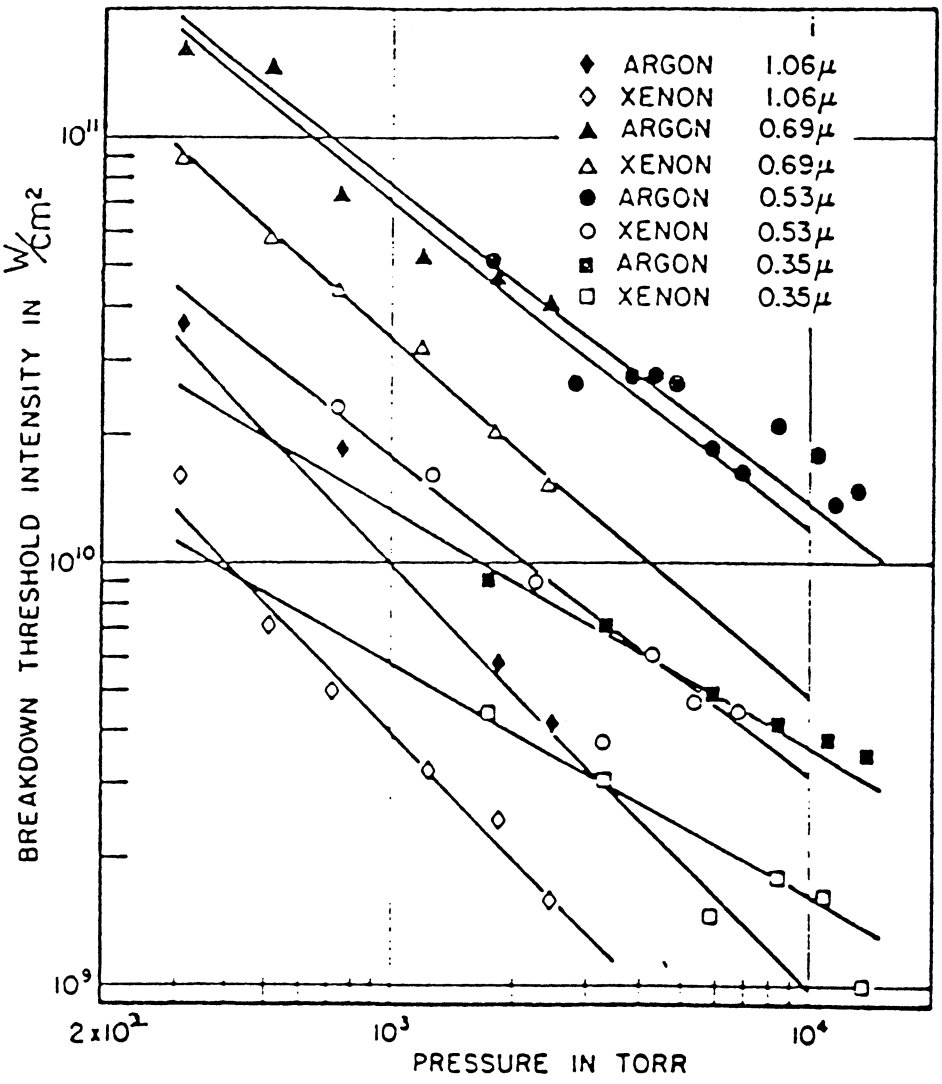

Fig. 3.4. Experimentally measured breakdown threshold intensities in xenon and argon versus density for a number of wavelengths. (Ref. 3.5)

3.2.1.3 Cavity Gas Density Limits

From Table 3.2 and Fig. 3.5, one sees that breakdown can be avoided with SOMBRERO parameters if we assume that the laser light must be coherent to breakdown and the density is 1.8×10^{16} cm^{-3} (0.5 Torr). The extrapolated line in Fig. 3.5 passes through 0.5 torr and 33 TW/cm^2. The experimental data at 1 μm wavelength is uncertain and could allow a higher gas pressure at 33 TW/cm^2. The Sandia National Laboratories results were that no breakdown was observed at this intensity in the gas density range of 0.1 to 0.5 torr. Therefore, we feel that 0.5 torr is a safe xenon gas density to avoid laser-induced breakdown at 33 TW/cm^2. Additionally, if breakdown within 1.2 cm of the target surface is acceptable, then we do not need to rely on increased breakdown threshold intensities due to the incoherence at adjacent beams or the incoherence induced in the beams to reduce parametric instabilities.

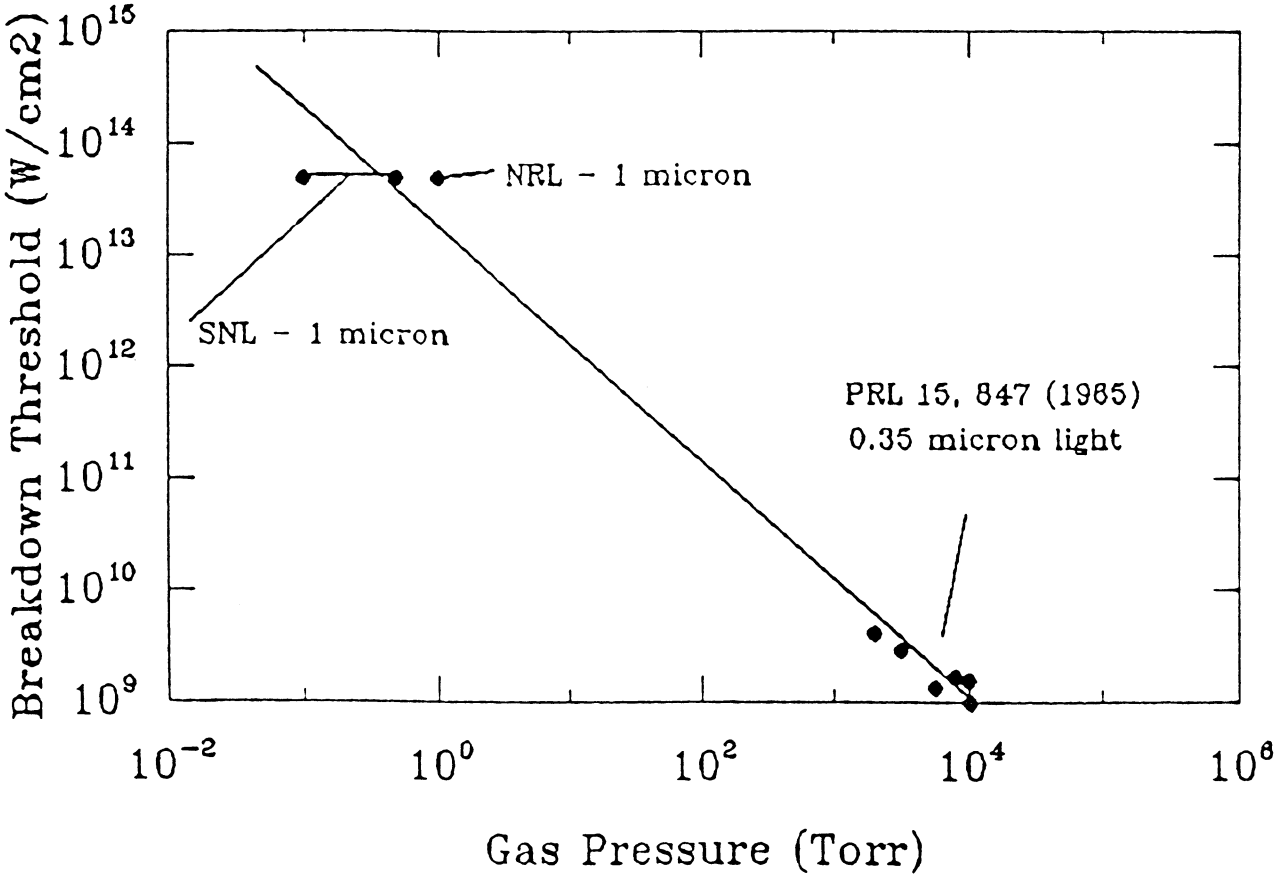

Fig. 3.5. Breakdown threshold intensities in xenon. Experimental values are shown as well as an extrapolated curve. (Refs. 3.5 - 3.7)

3.2.2 First Wall Protection

We propose to protect the graphite first wall of the SOMBRERO target chamber with 0.5 torr of xenon gas. The gas absorbs the target x rays and debris ions and re-radiates the energy to the wall over a long enough time that thermal conduction in the wall can keep the surface temperature low enough to avoid damage to the graphite. We will begin by describing the x rays and ions emitted from the target. We will then discuss the CONRAD computer code and how it calculates the re-radiation to the wall. We will also discuss the calculation of the wall surface temperatures. Finally, we will present the wall thermal and mechanical response.

3.2.2.1 Target Emanations

The SOMBRERO targets emit x rays, neutrons, and ions. The assumed target parameters are given in Table 3.3. The "Assumed" values were used in the calculations presented in this section. After these calculations were completed, the reference design point was changed to a slightly lower yield as shown under the "Base Case" column. Results will be scaled proportional to yield to generate "Base Case" results. The time-integrated x-ray spectrum is shown in Fig. 3.6. The intensity is shown in arbitrary units. The spectral shape is assumed to be independent of target yield, so the intensity is scaled uniformly in x-ray photon energy to reach the proper x-ray yield in Table 3.3. The debris ion energies are shown in Table 3.4. It is interesting to note the presence of very high energy carbon ions that are generated when the outer plastic shell is accelerated to a high velocity by the target micro-explosion. These carbon ions will have the longest range in the xenon gas of any of the target emanations except neutrons. The xenon gas must be thick enough to attenuate the carbon ions.

Table 3.3. Target Parameters for SOMBRERO

	Assumed	Base Case
Energy on Target (MJ)	3.6	3.4
Target Gain	118	118
Target Yield (MJ)	425	400
Neutron Yield (MJ)	317	298
X-ray Yield (MJ)	24	23
X-ray Pulse Width (ns)	0.1	0.1
Debris Yield (MJ)	84	79

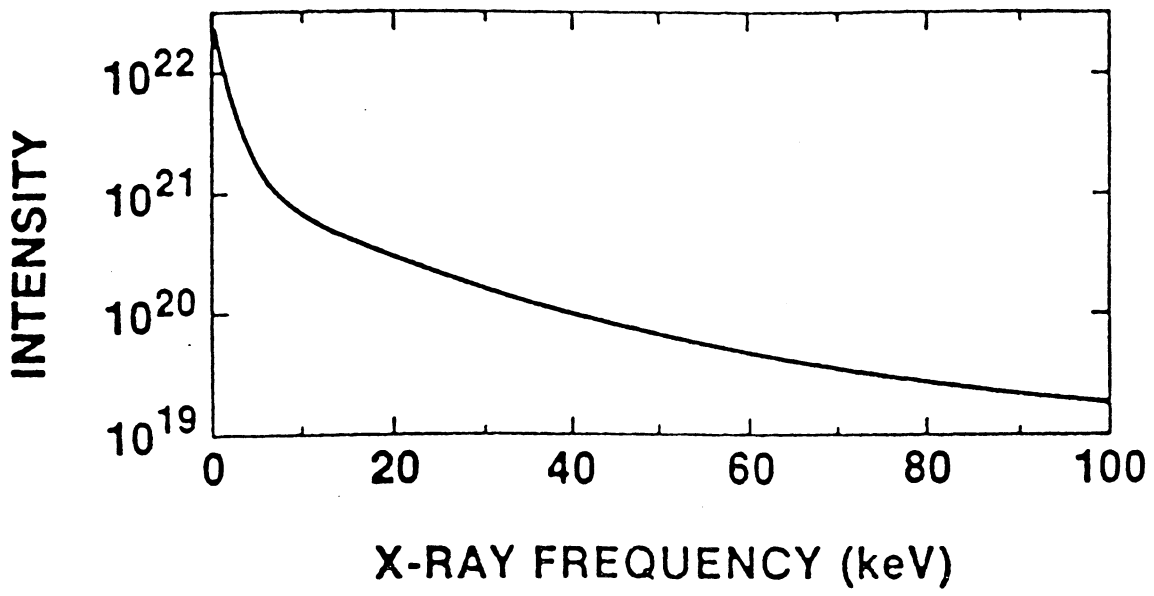

Fig. 3.6. Time-Integrated X-Ray Spectrum from SOMBRERO Target.

Table 3.4. Target Debris Spectra for SOMBRERO

Deuterium Energy (keV)	94
Protium Energy (keV)	138
Tritium Energy (keV)	141
Helium-4 Energy (keV)	188
Carbon-12 Energy (keV)	1650

3.2.2.2 CONRAD Computer Code

We have used the CONRAD computer code[3.8] to analyze the target chamber designs for SOMBRERO. CONRAD is a one-dimensional Lagrangian finite difference computer code that calculates hydrodynamic motion, radiation transport, and vaporization and condensation in slab, cylindrical, or spherical geometry. Radiation transport is calculated with flux limited multi-group diffusion. 180 group opacities are used in SOMBRERO calculations. Time-dependent target x-ray and ion deposition are calculated in the fill gas and walls. Heat transfer calculations are performed by CONRAD to get wall surface temperatures and temperature profiles in the wall at all times. Vaporization calculations can then be done.

Equation-of-state and opacity data is read by CONRAD from data tables. The properties of the materials are, therefore, assumed to be quasi-static. The data tables are created with equation-of-state results from the IONMIX[3.9] computer code or from the SESAME[3.10] library. IONMIX is better suited to materials much less dense than solids or liquids, while SESAME is preferred at higher density. Opacity tables are constructed with results from IONMIX.

3.2.2.3 First Wall Thermal Loading

The essential parameters for the SOMBRERO simulations are shown in Table 3.5. Parameters are shown for both assumed and "Base Case" conditions. The wall is taken to be 6.5 m in the simulation as this is the closest point in a non-spherical chamber. A steady state heat transfer calculation of the surface heat through the graphite leads to a steady state surface temperature of 1485°C. The results of the CONRAD simulation for the assumed conditions are plotted in Figs. 3.7 - 3.14. The radiation temperature is plotted over a radius versus time mesh in Fig. 3.7, where different shades of grade represent ranges of radiation temperature. The radiation temperature is that blackbody temperature that would provide the calculated radiation energy density. One can see the radiation burning through the xenon gas, finally reaching the wall some time near 0.1 ms. The radiation temperature is plotted against position for various times in Fig. 3.8. The surface heat flux on the wall of the SOMBRERO target chamber is shown in Fig. 3.9. The peak heat flux occurs at 86.8 μs. The CONRAD simulation predicts a peak surface temperature at the closest point on the wall of 2155°C, well below the sublimation temperature for graphite of 4100°C. Scaling this peak temperature to the "Base Case" conditions, the peak temperature would be 2116°C. CONRAD predicts that no graphite is vaporized. The xenon gas is very effective in slowing the transfer of energy from the target to the wall, which is why there is no vaporization. The surface temperature of the graphite is shown as a function of time in Fig. 3.10. The broad temperature pulse, which reaches a maximum at 0.134 ms, should be compared to the almost instantaneous target x-ray pulse and the target ion pulse width of a few ns. Based on this simulation, we believe that a 6.5 m radius graphite lined chamber filled with 0.5 torr of xenon will survive a 425 MJ target explosion. This situation for the "Base Case" is somewhat better because of the lower target yield.

3.2.2.4 First Wall Mechanical Loading

CONRAD calculations also predict the mechanical loading on the SOMBRERO target chamber first wall. The results of a CONRAD simulation for the assumed conditions is given in Table 3.5. The "Base Case" parameters are also shown in Table 3.5. The pressure profiles at various times are shown in Fig. 3.12. The gas density profiles are shown in Fig. 3.13. Comparing these with the radiation temperature profiles in Fig. 3.8, one may note that the gas

pressure moves with the radiation. This is also shown by comparing the gas pressure plotted over the time-position mesh of Fig. 3.12 with Fig. 3.7. There is very little hydrodynamic motion except near the target, which is shown in Fig. 3.13 and Fig. 3.14. The radiation diffuses through the gas, heating the gas as it goes. This is why the time of peak pressure and heat flux on the wall are the same. The peak pressure on the wall is very low, 0.0127 MPa. The impulse is also low. Neither should cause any major mechanical response in the first wall.

Table 3.5. SOMBRERO Gas and First Wall Parameters

	Assumed	**Base Case**
Gas Species	Xenon	
Gas Density (cm^{-3})	1.8×10^{16} (0.5 Torr)	
Distance to Wall (m)	6.5	
Wall Material	Woven Rigidized Graphite	
Steady State Wall Temperature (°C)	1485	
Peak Heat Flux on Wall (MW/cm^2)	0.138	0.130
Time of Peak Heat Flux (μs)	86.8	86.8
Peak Wall Temperature (°C)	2155	2116
Time of Peak Wall Temperature (ms)	0.134	0.134
Impulse on Wall (Pa-s)	2.21	2.08
Peak Pressure on Wall (MPa)	0.0127	0.0120
Time of Peak Pressure on Wall (μs)	88.7	88.7

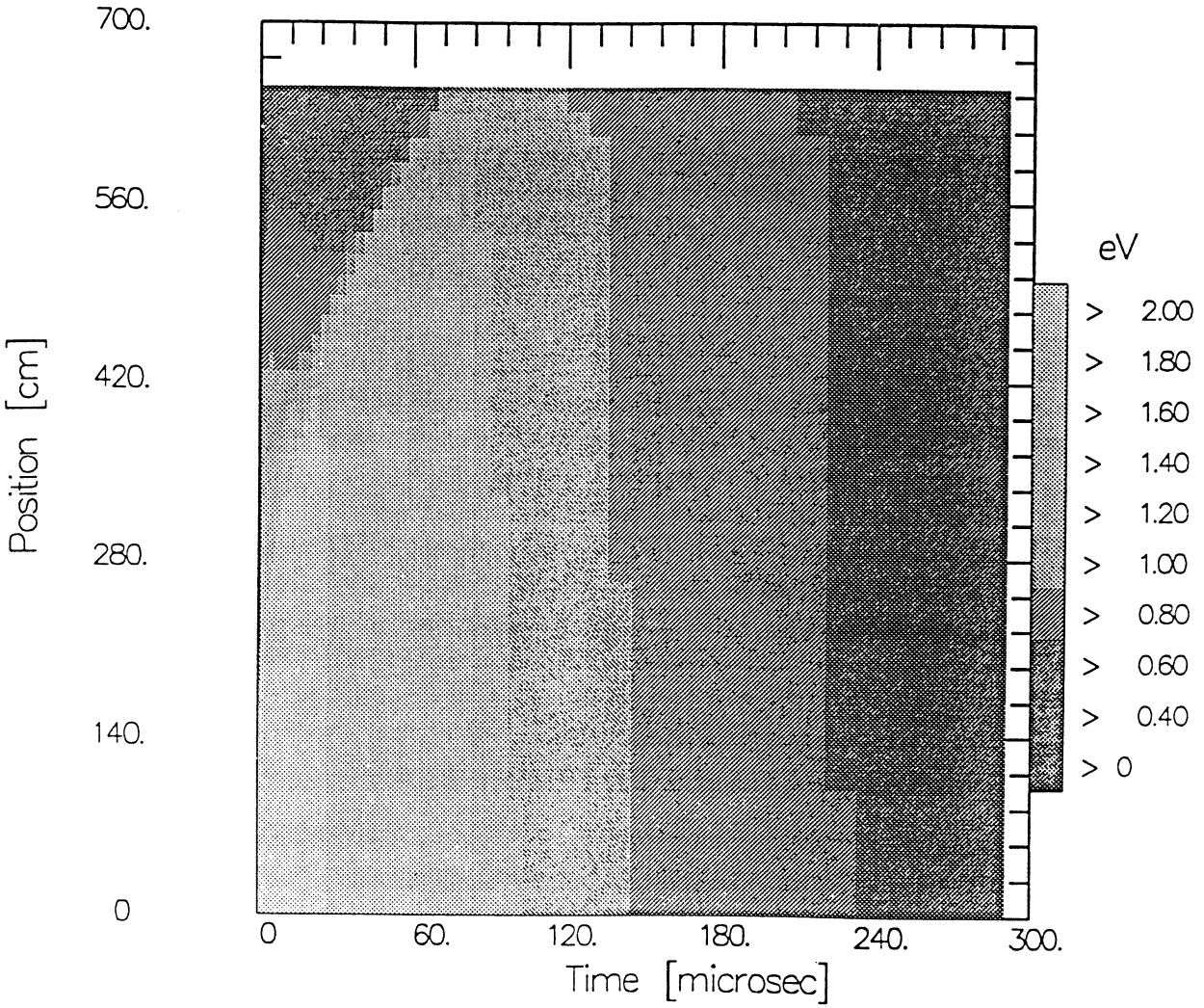

Fig. 3.7. Radiation temperatures in the SOMBRERO target chamber plotted over a time-position mesh. A 425 MJ yield, 0.5 torr Xenon fill gas, and a 650 cm radius chamber have been assumed. The target is positioned at the origin, the wall is at 650 cm.

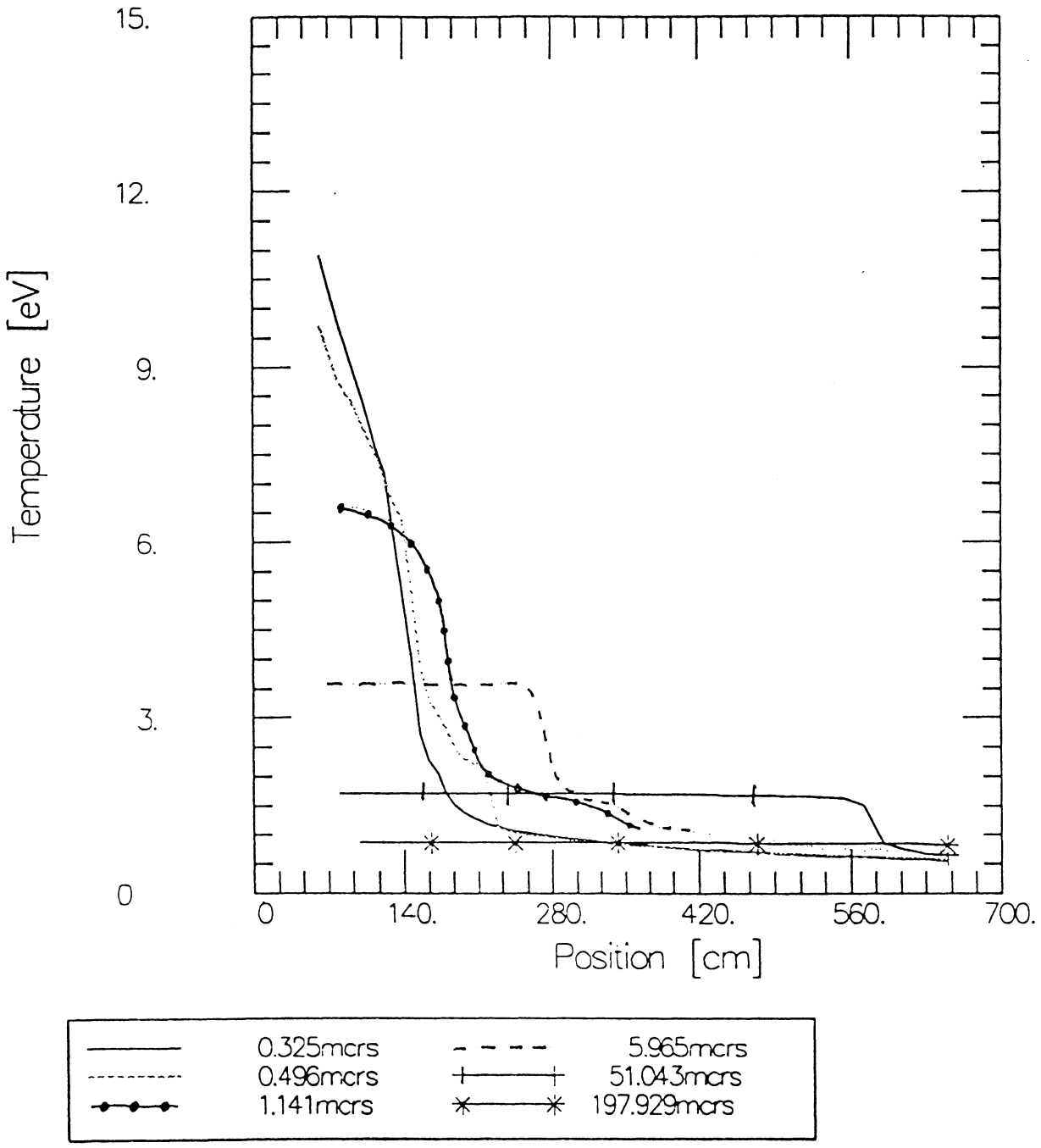

Fig. 3.8. Radiation temperature versus position for various times. A 425 MJ yield, 0.5 torr Xenon fill gas, and a 650 cm radius chamber have been assumed. The target is positioned at the origin, the wall is at 650 cm.

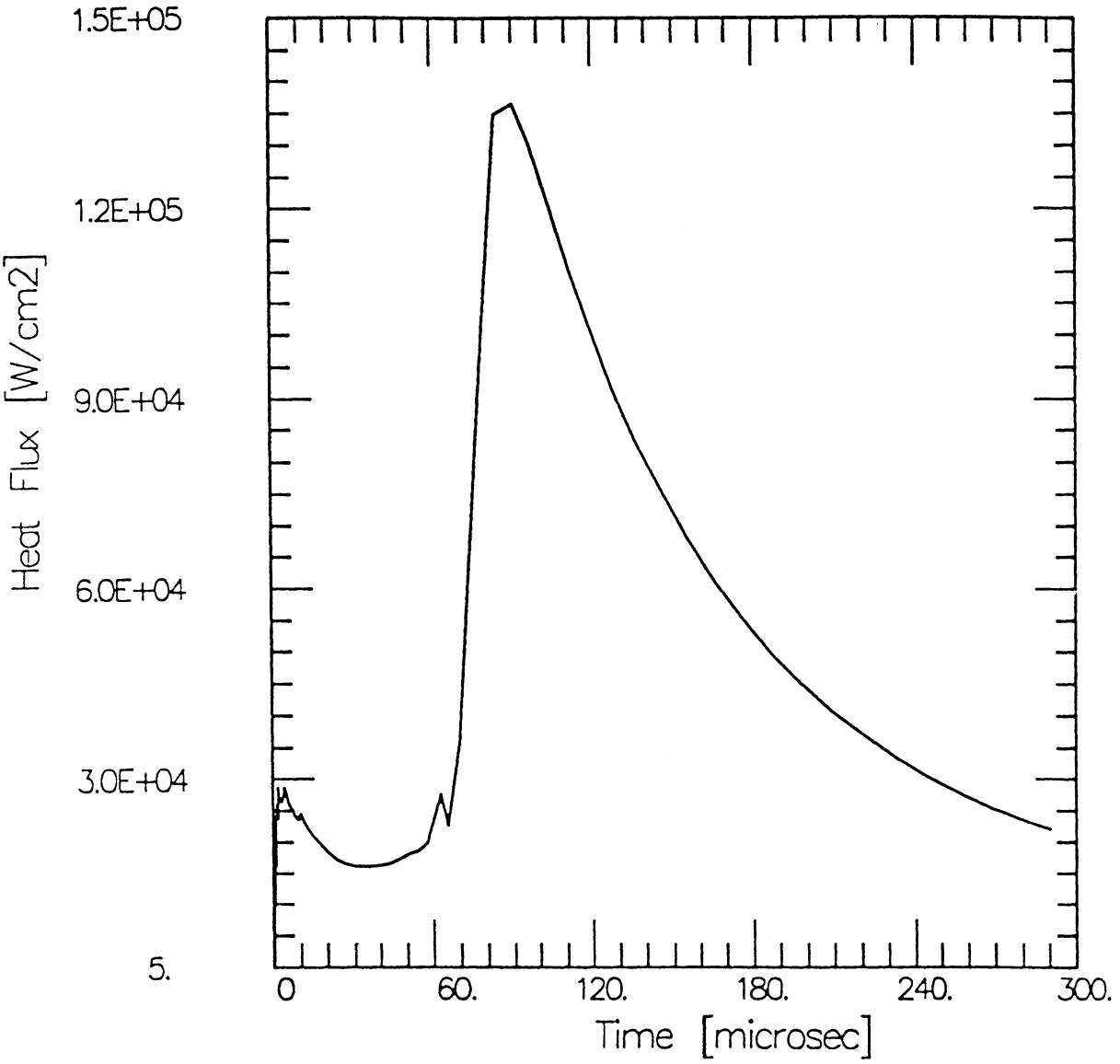

Fig. 3.9. Radiant heat flux on the surface of the SOMBRERO target chamber wall. A 425 MJ yield, 0.5 torr Xenon fill gas, and a 650 cm radius chamber have been assumed.

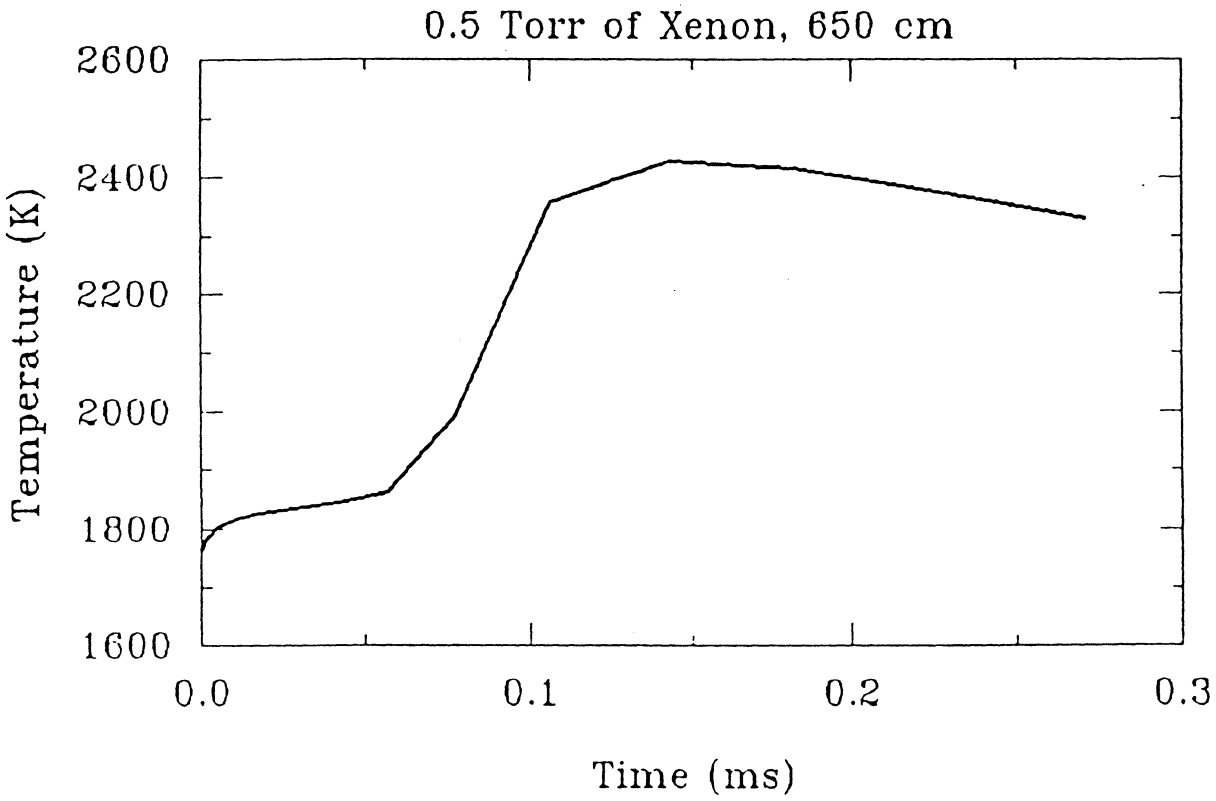

Fig. 3.10. Surface temperature on the graphite first wall of the SOMBRERO target chamber. A 425 MJ yield, 0.5 torr Xenon fill gas, and a 650 cm radius chamber have been assumed.

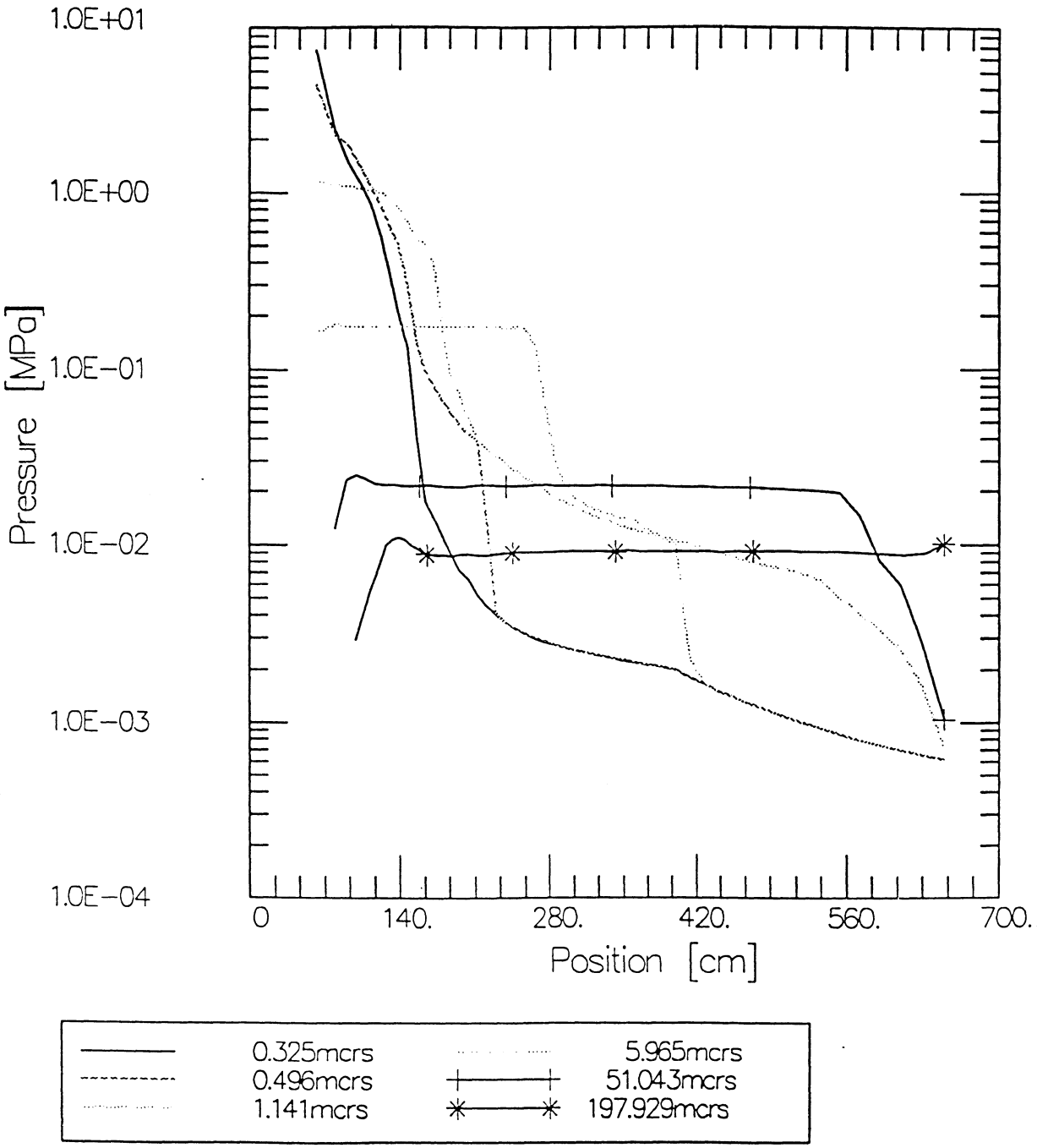

Fig. 3.11. **Gas pressure versus position for various times. A 425 MJ yield, 0.5 torr Xenon fill gas, and a 650 cm radius chamber have been assumed. The target is positioned at the origin, the wall is at 650 cm.**

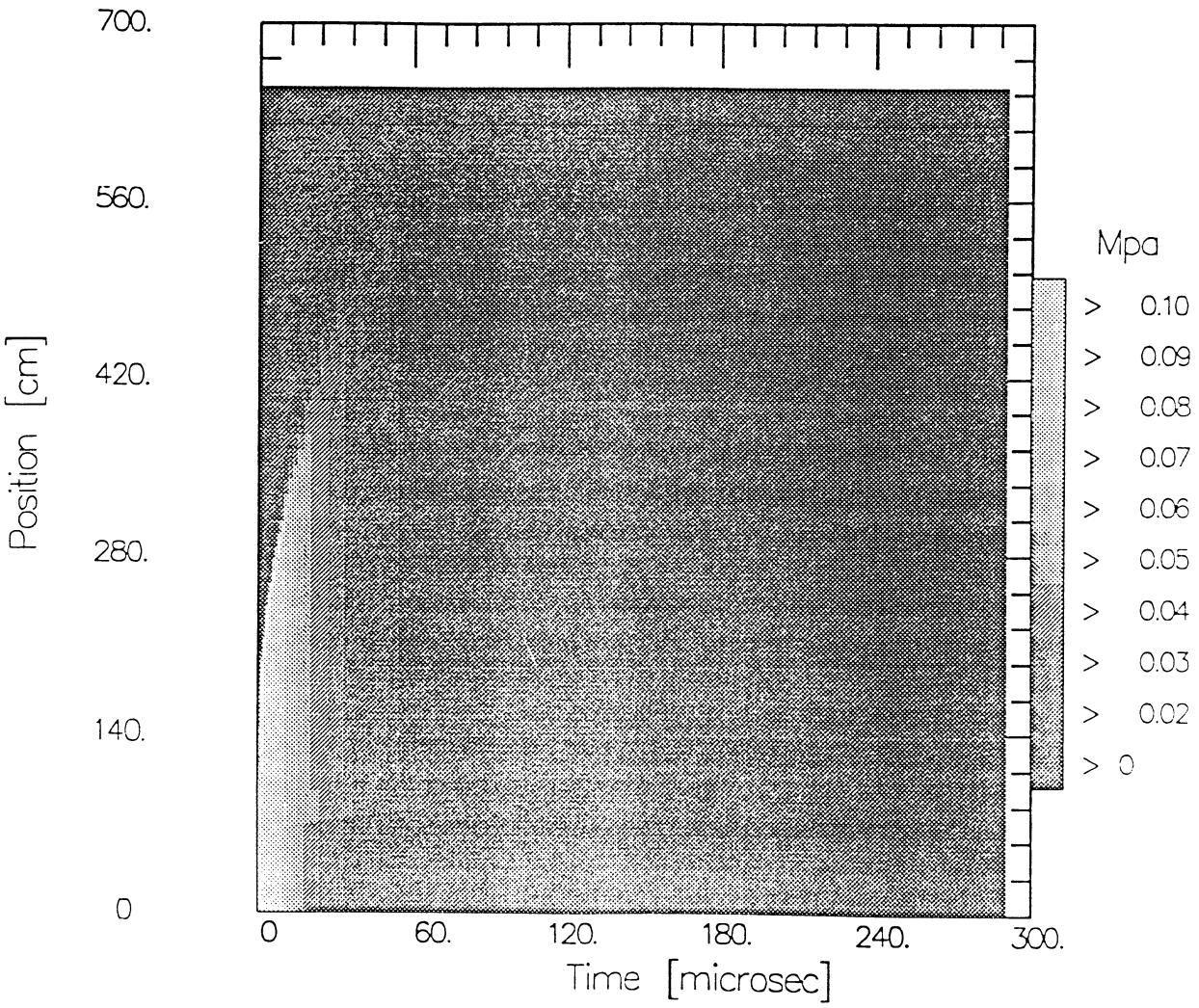

Fig. 3.12. **Gas pressure in the SOMBRERO target chamber plotted over a time-position mesh. A 425 MJ yield, 0.5 torr Xenon fill gas, and a 650 cm radius chamber have been assumed. The target is positioned at the origin, the wall is at 650 cm.**

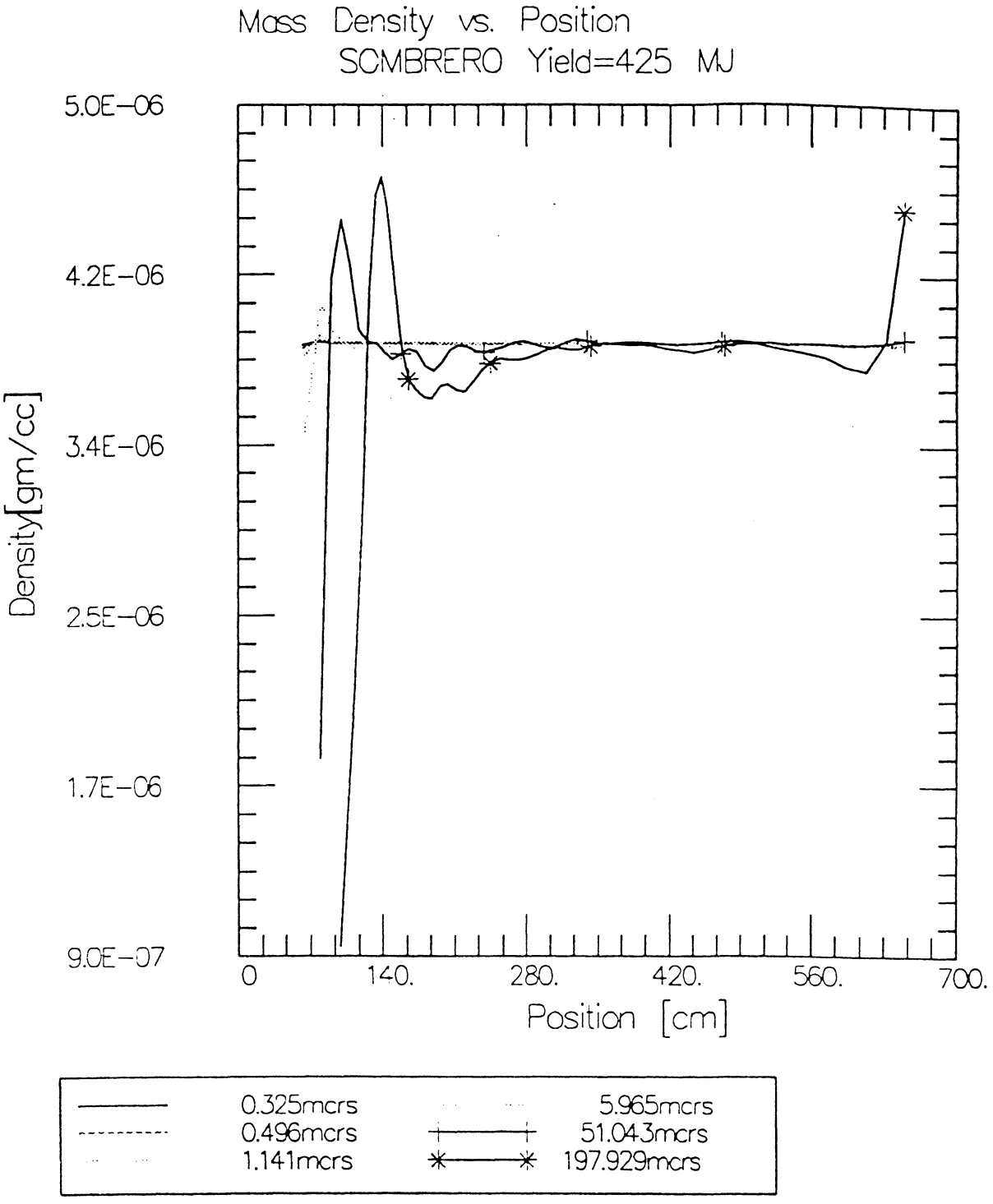

Fig. 3.13. **Gas density versus position for various times. A 425 MJ yield, 0.5 torr Xenon fill gas, and a 650 cm radius chamber have been assumed. The target is positioned at the origin, the wall is at 650 cm.**

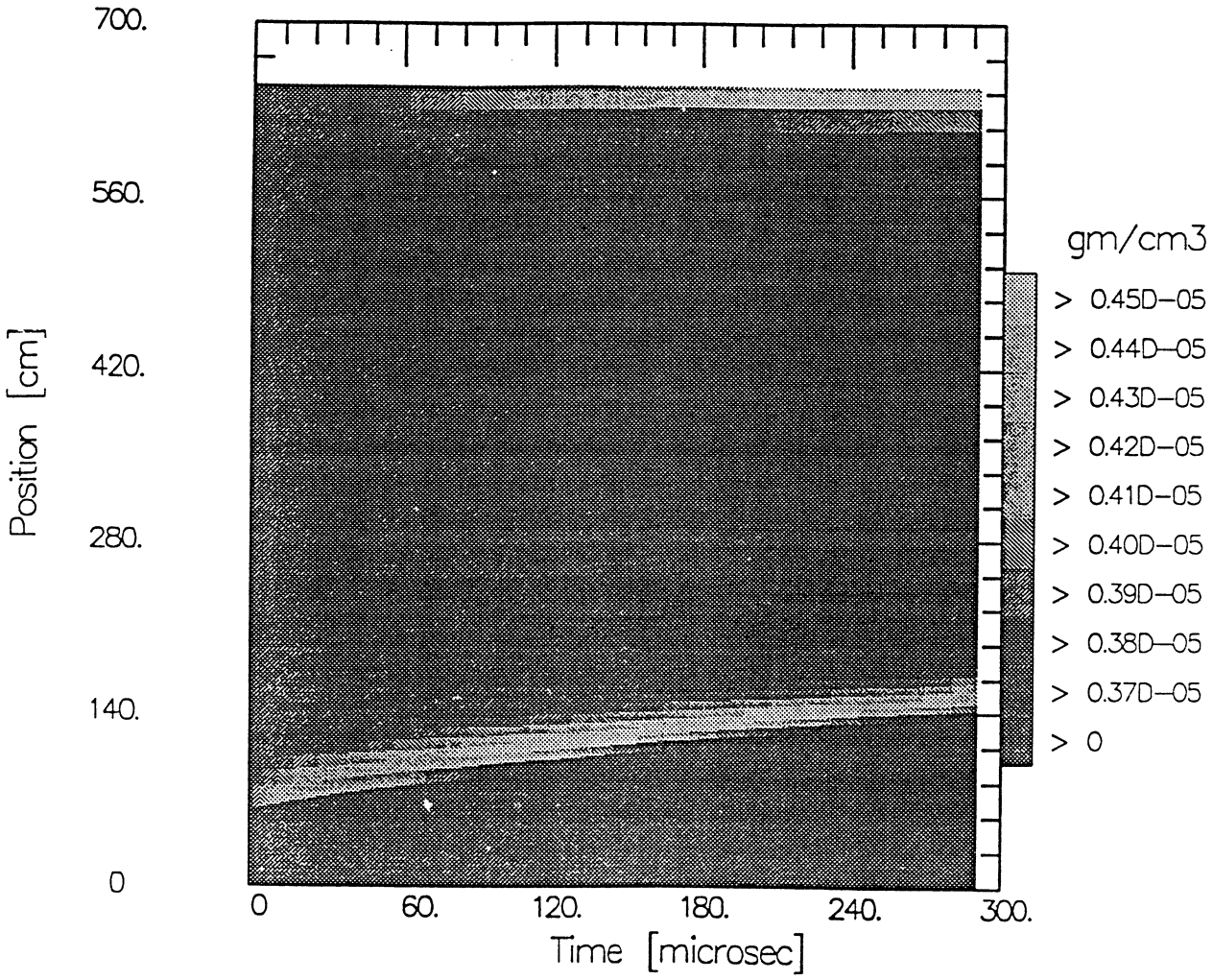

Fig. 3.14. **Gas density in the SOMBRERO target chamber plotted over a time-position mesh. A 425 MJ yield, 0.5 torr Xenon fill gas, and a 650 cm radius chamber have been assumed. The target is positioned at the origin, the wall is at 650 cm.**

3.2.3 First Wall and Blanket Design

3.2.3.1 Overall Chamber Description

The SOMBRERO chamber as shown in Fig. 3.15 is an upright cylinder with conical ends. In cross section on the inside of the chamber, the angle between the side of the cone and the side of the cylinder is 135°, which means the angle at the upper and lower vertices is 90°. Except for the location of the beam ports, the chamber is symmetric about the midplane. The cylindrical portion extends ±2.6 m, and each conical portion is 6.4 m high, making the overall internal vertical height of the chamber 18 m. At midplane the chamber radius is 6.5 m. In fact, if a 6.5 m radius sphere were to be placed at the center of the chamber, it would touch the first wall (FW) at midplane and at the conical surfaces located at a vertical height of ±4.6 m and a horizontal distance of 4.6 m from the chamber axis. These are the points on the FW at which the surface heat load will be the highest. Everywhere else, the surface heat load falls off by the ratio of $(6.5)^2/R^2$, where R is always >6.5 m.

The chamber is constructed from a 4D weave of a carbon/carbon composite. It is divided into 12 modules (i.e. every 30° on the horizontal plane). Each module extends vertically, the full height of the chamber. The modules are entirely independent of each other, having individual supply and return tubes connected to common supply and return manifolds. The target is imploded with 60 beams in a near symmetric configuration. All the beam ports lie along vertical planes at the interfaces between the modules. They also lie along ten horizontal planes with six beam ports in each plane forming a cone with the vertex at the chamber center. Five of the cones lie above midplane and have polar angles of 25.8°, 45.6°, 60°, 72.5°, and 84.3°, and there are five cones below the midplane with complimentary polar angles. Figures 3.16a and 3.16b give the horizontal distribution of the vertical planes and the five polar angles above midplane, respectively. Figure 3.17 shows the beam distribution in one octant. Note from Fig. 3.15 is that the beam ports do not face each other across from the target. Therefore, if a beam does not hit a target, it will not propagate through another beam port, but rather will hit the FW. The consequences of the beam impacting the FW are not serious, as will be shown in Section 3.2.3.3.

As mentioned earlier, the chamber is divided into 12 modules by vertical planes going through the chamber axis, rotated every 30°. The beam ports are built into the sides of the modules, half a beam port into each side. Mating the two sides of adjacent modules thus forms a single beam tube. This is done to minimize the beam obstruction on the particle flow side of the blanket. By streamlining the internal profile of the half beam port, the moving particles can flow past the beam port unobstructed. This is shown in Fig. 3.18. The twelve modules are identical in all respects except for the location of the beam ports. However, there are only two variations of beam port locations, meaning that there are two sets of six modules which are indentical in all

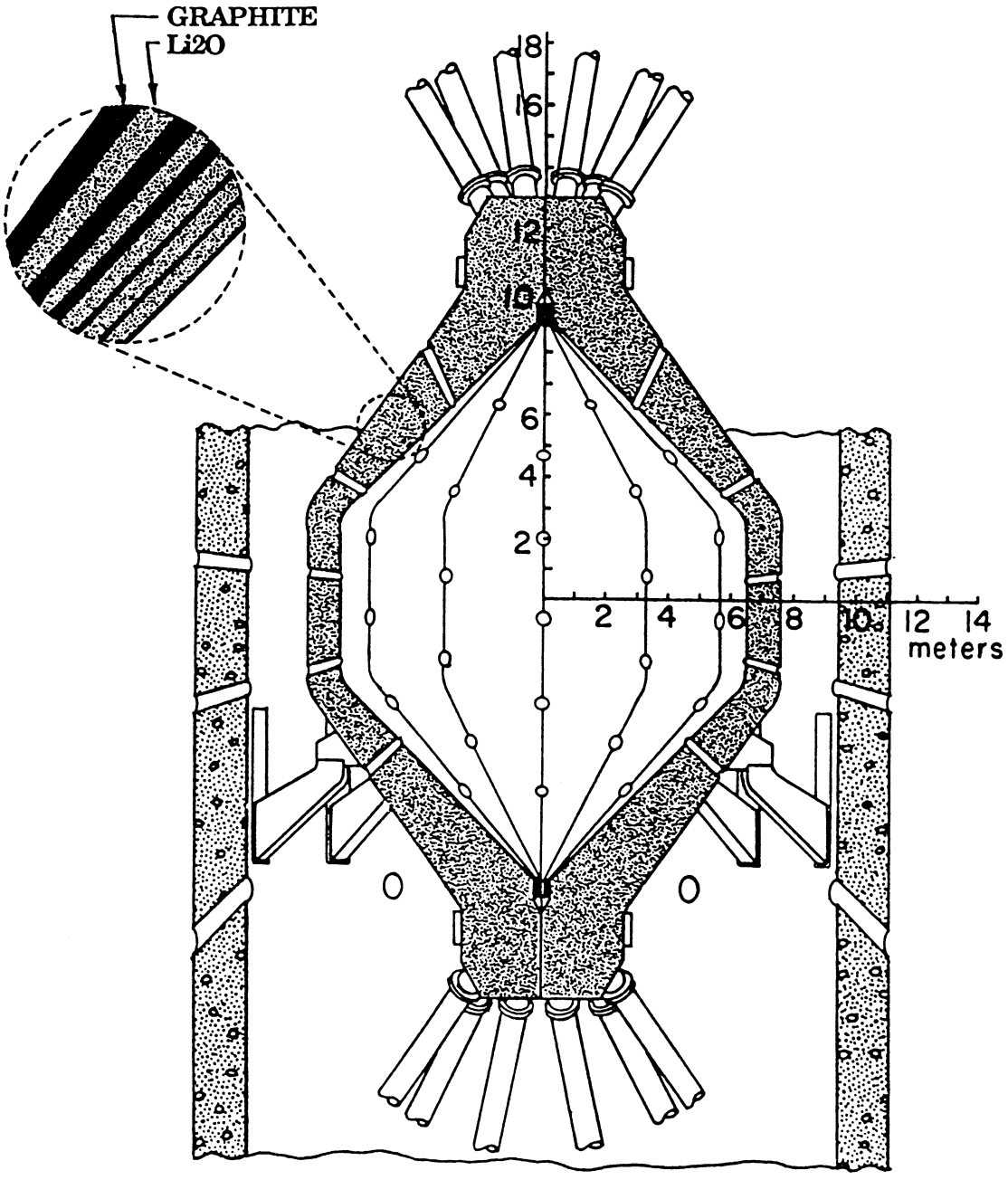

Fig. 3.15. Cross section of SOMBRERO chamber.

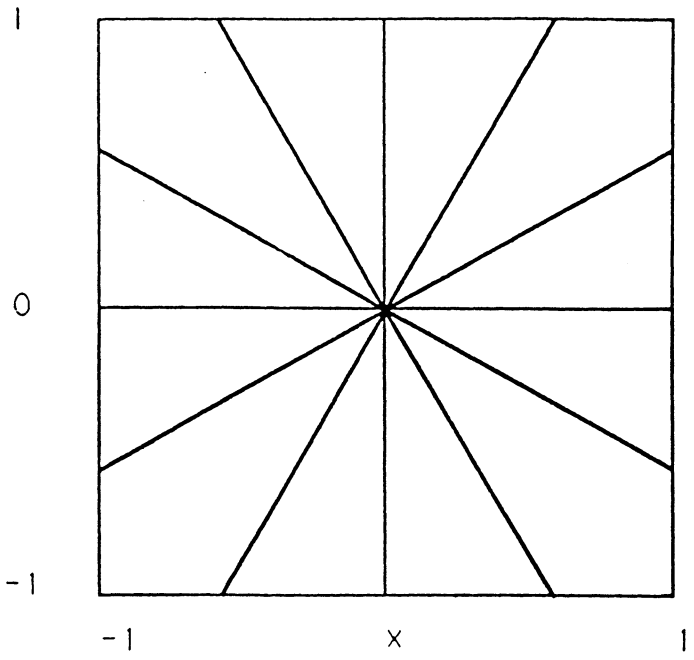

Fig. 3.16a. Azimuthal distribution of vertical planes separating modules.

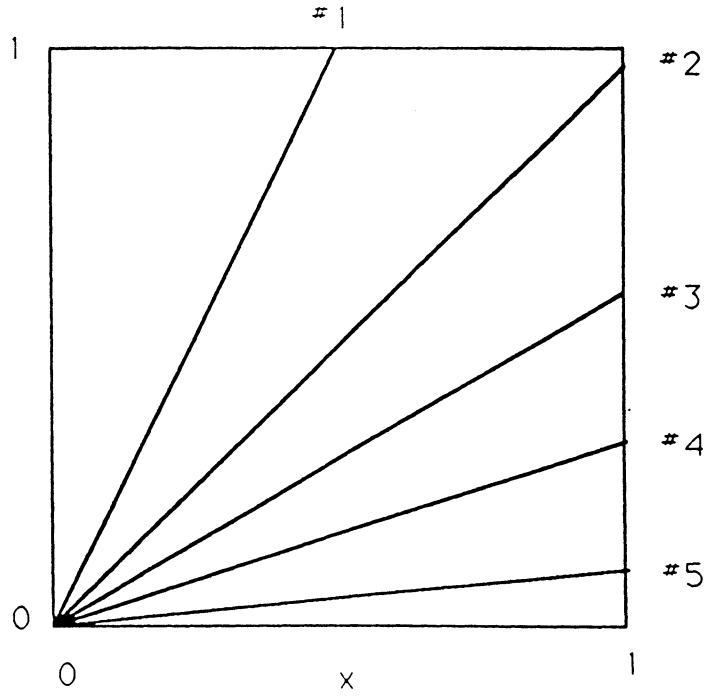

Fig. 3.16b. Five polar angles above midplane.

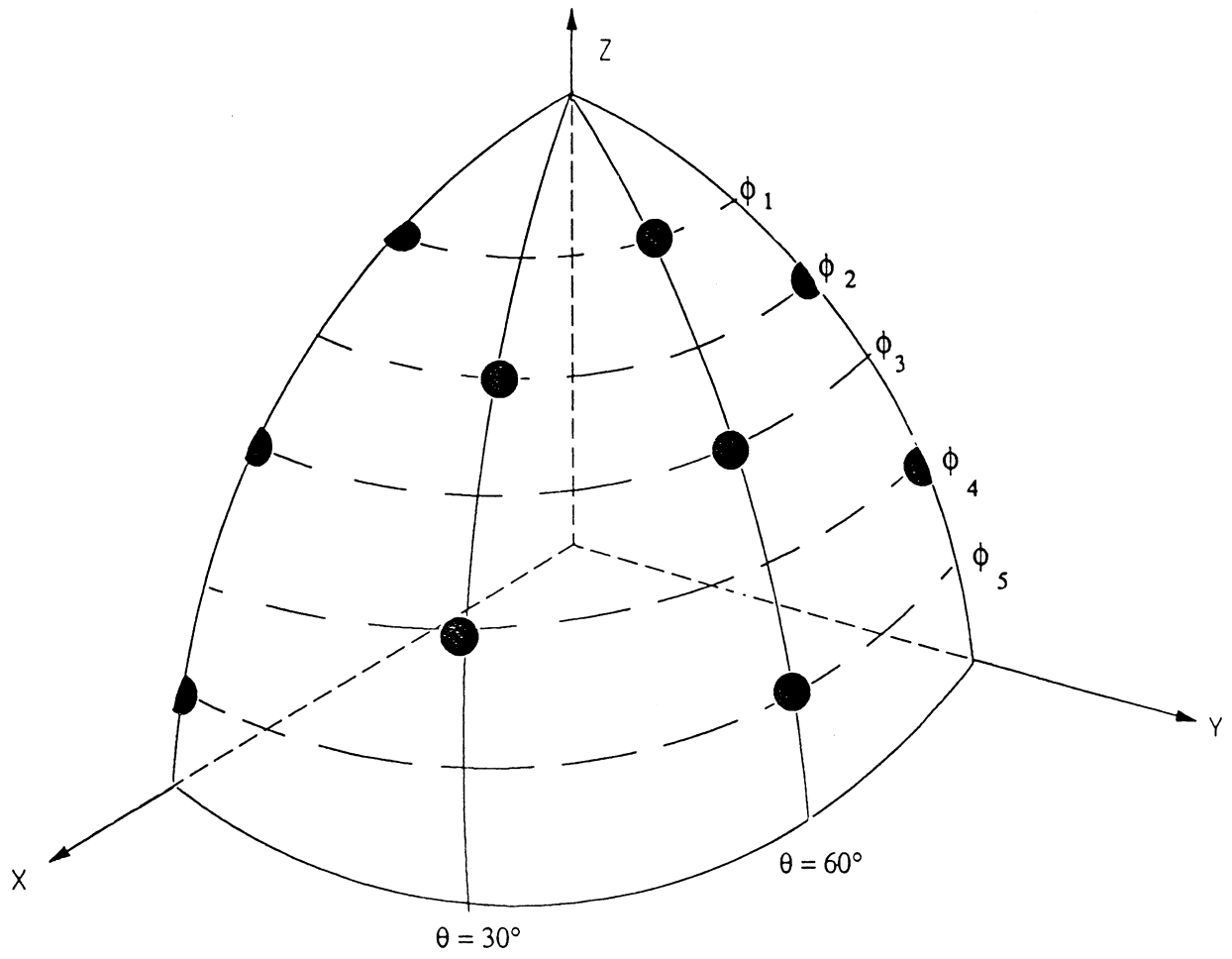

Fig. 3.17. Beam distribution in one octant of chamber.

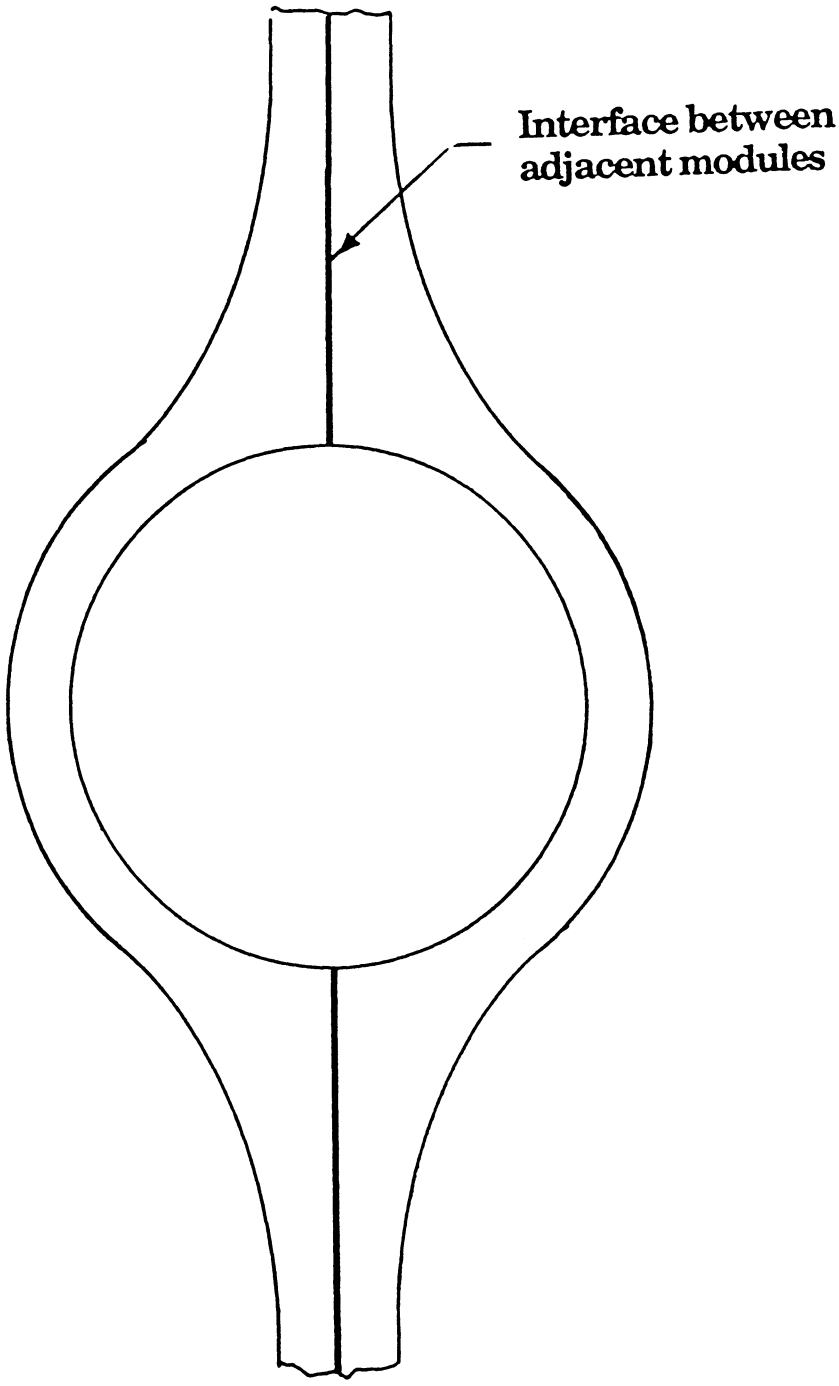

Fig. 3.18. Chamber wall profile around beam port.

respects. Figure 3.19 shows several views of the two types of modules. They are actually exact mirror images of each other. When assembled, the two types of modules are alternated such that the interface between them will form the proper beam port configuration.

Figure 3.20 is a cross section through a module at the midplane and at Z = ±5.8 m where the circumference of the FW is one half that at the midplane. Please note that in each case, the cut is taken normal to the FW, or in the case of the conical region, the cut is at 45° to the horizontal. The figure shows that the blanket/reflector is divided into five flow regions, which have a progressively higher carbon fraction from the FW to the rear. Figure 3.20 shows that the FW is attached to the back structure with radial ribs and from the target side has the appearance of an air mattress. It is curved toward the center of the chamber at a radius of 20 cm in order to minimize the stresses on the FW due to the 0.2 MPa internal pressure.

Figure 3.21 is a figure of the top half of a module with the FW removed to show how the radial ribs are arranged. At the midplane, the ribs are 21.3 cm center to center, but as they enter the conical part of the chamber, the ribs converge while the channel depth increases to make up for the decreased channel width. Finally, as the narrow region of the conical part is approached, alternate ribs are deleted altogether as shown in the figure.

Figure 3.22 shows the radial build of the blanket/reflector at the midplane as optimized by neutronic analysis. The overall thickness is 1.0 m. The FW is 1.0 cm thick and is followed by a 19 cm zone in which the carbon fraction is 3%. The second and third zones are each 40 cm thick and have 20% and 50% fraction of carbon, respectively. Increasing the carbon fraction toward the back of the blanket provides a built in reflector which gets cooled by the breeding material. The cross section at the conical region shows that the blanket/reflector was increased to a thickness of 1.75 m. It is important to note that the cumulative area of the flow channels at the FW is the same. The depth of the channels is increased to make up for the shorter circumferential extent. This is done to insure a constant high breeder material velocity of 115 cm/s at the FW where the surface heating is high. The second coolant channel also has a constant flow area from top to bottom since although this zone does not have any surface heating, it experiences a high nuclear heating. In the remaining three breeding material channels, the flow area at the extremities is reduced to 87%, 85%, and 83% relative to that at midplane, respectively. The velocity in these channels is very low, on the order of a few centimeters per second, thus, the flow area is not critical.

The breeding material chosen is granular Li_2O in the form of a moving bed. An attractive feature of Li_2O is its very high Li atom density, even higher than liquid Li, making it possible to breed without the benefit of neutron multipliers. In this design, the Li_2O particles of 300-500 μm flow through the blanket by gravity. Each module has dedicated supply and return tubes connected to common manifolds at the top and bottom. The velocity in the channel immediately behind the FW is ~115 cm/s while the average velocity in all the succeeding channels is ~12 cm/s, an order of

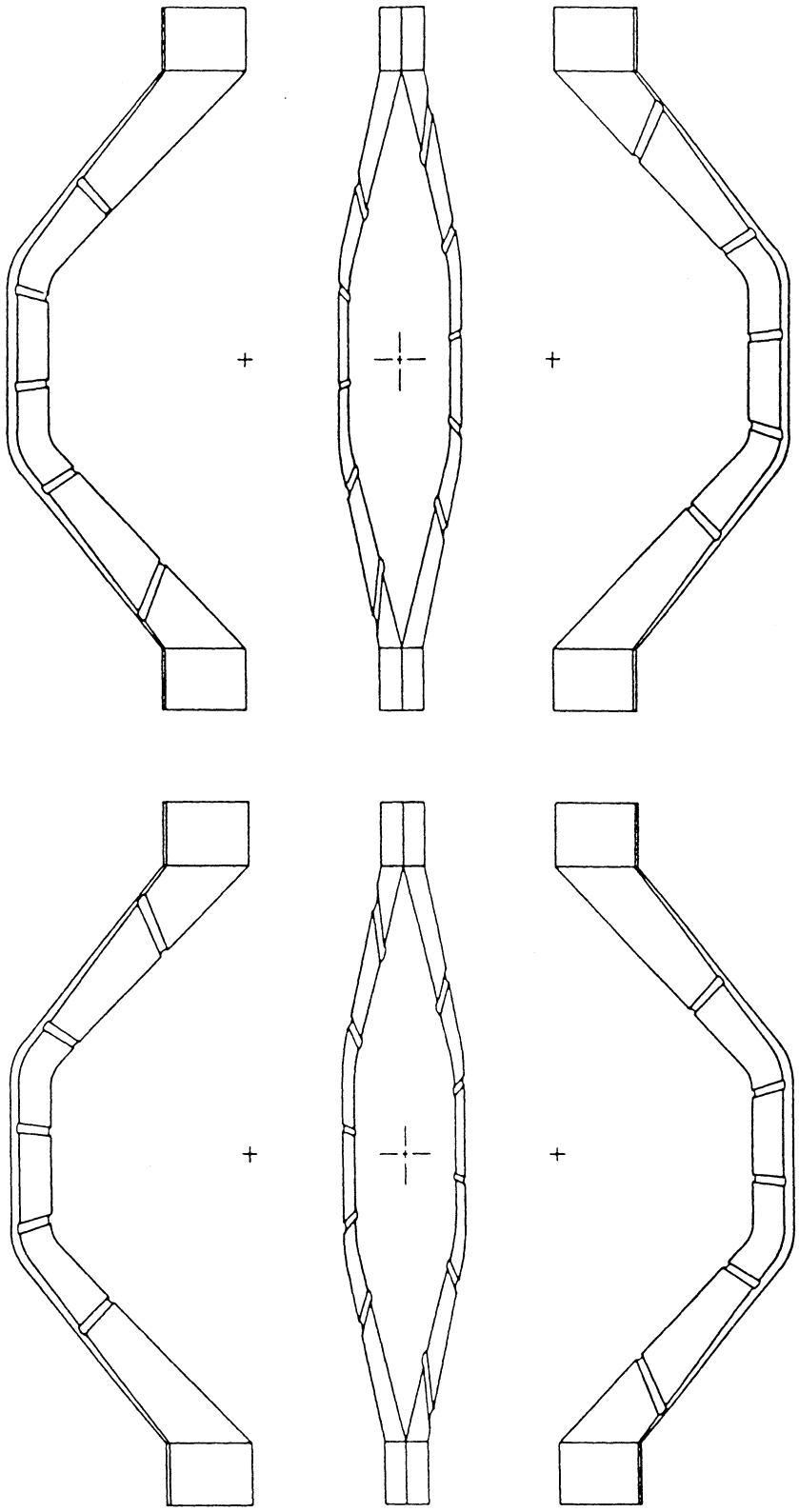

Fig. 3.19. Several views of the two types of modules.

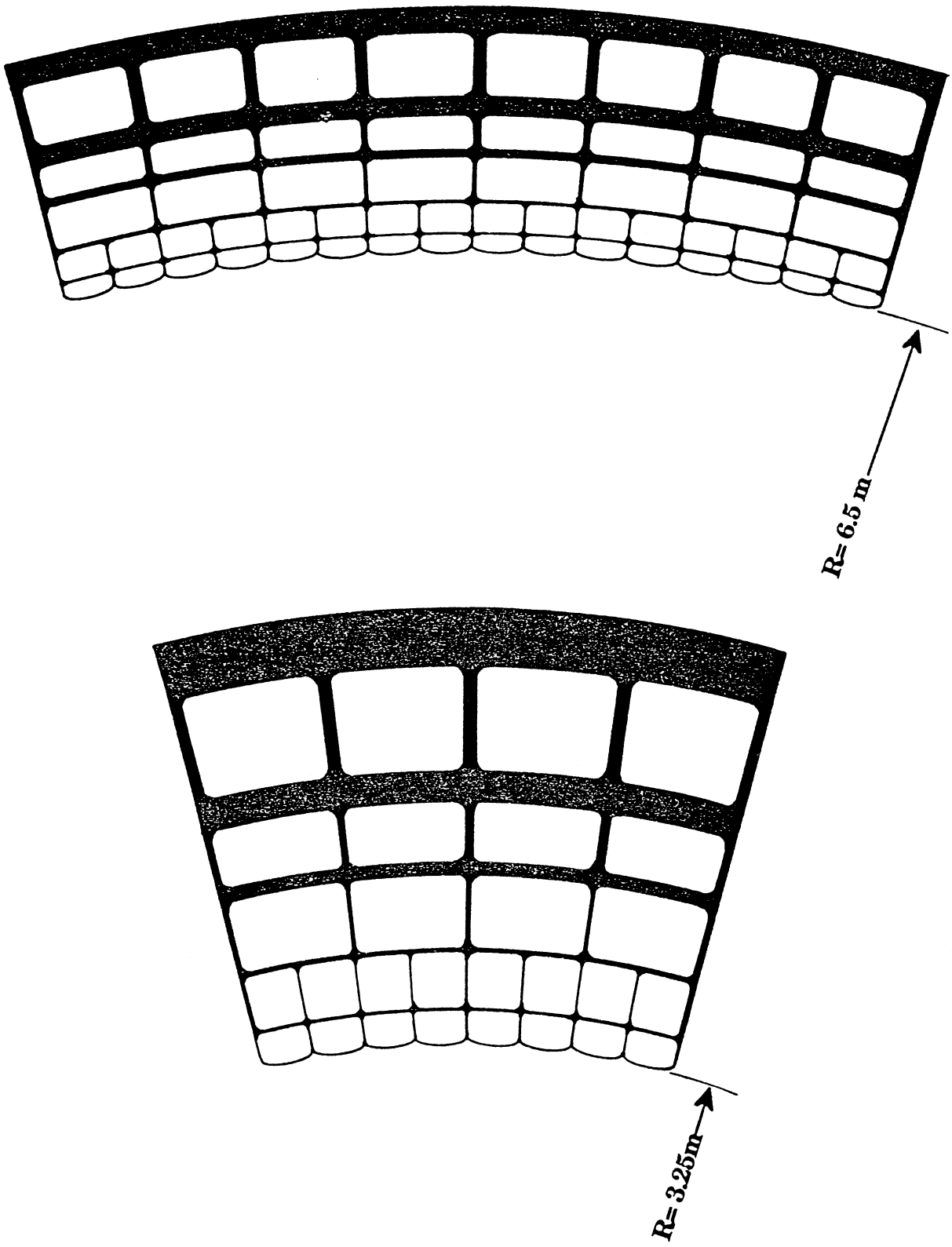

Fig. 3.20. Cross section through a module at midplane and at Z = 5.8 m.

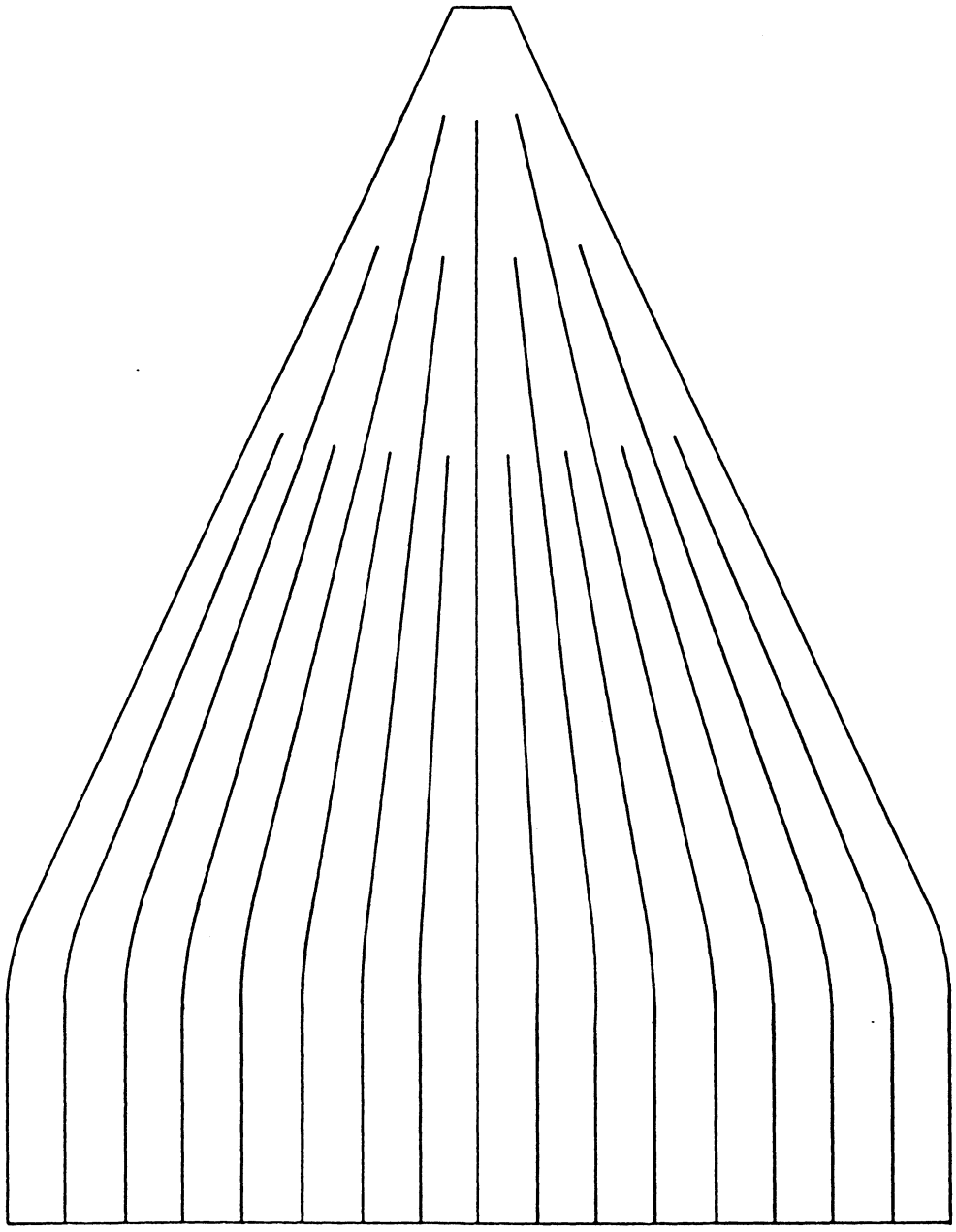

Fig. 3.21. Distribution of FW radial supports - upper half of module.

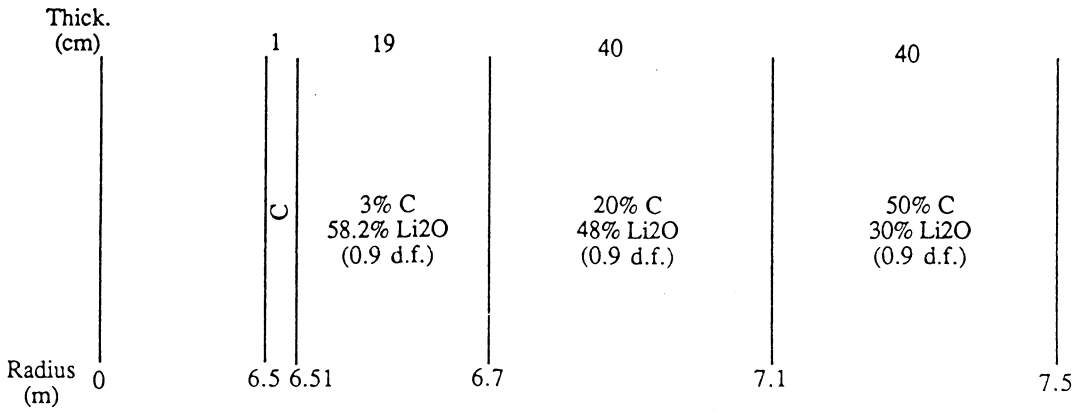

Fig. 3.22. Radial build of blanket at midplane.

magnitude lower. Of the total mass flow rate through the reactor of 5490 kg/s, 57% goes through the FW channel, while the remaining 43% goes through the rest of the channels. The theoretical density of Li_2O is 2.01 g/cm^3, but we assume that the material is 90% density, and the moving bed has a 60% Li_2O fraction, giving the effective density a value of 1.08 g/cm^3. The pressure of the He carrier gas in the blanket is 0.2 MPa and since the chamber is at 0.5 torr, the absolute pressure on the FW is 0.3 MPa. In the next section, finite element stress analysis of the FW is described.

The inlet temperature of the Li_2O into the chamber is 550°C. At the FW, the outlet temperature is 700°C and at the back, 800°C, but the equilibrated outlet temperature from the chamber is 743°C. Table 3.6 gives the physical parameters of the SOMBRERO chamber.

Table 3.6. Physical Parameter of SOMBRERO Chamber

Material of Construction	4D Weave C/C Composite
Chamber Radius at Midplane (m)	6.5
Overall Internal Chamber Height (m)	18
Number of Modules in Chamber	12
Number of Beam Ports in Chamber	60
Structural Mass Per Module (Tonnes)	37.8
First Wall Thickness (cm)	1.0
Radius of Curvature of FW Between Ribs (m)	0.2
Thickness of FW Ribs (cm)	1.0
Number of Ribs per Module at Midplane	17
Maximum Stress in FW (MPa)	42.9

Stress Analysis of the First Wall. The ANSYS finite element code was used for the first wall stress analysis. Material properties used in the analysis are given in Table 3.7[3.11] where the UVW directions are in one plane with the fibers laid 60° apart, and the Z direction is perpendicular to the primary fiber plane.

Table 3.7. Physical Properties of 4D Weave C/C Composites

	Z Direction	U,V,W Direction
Tensile Modulus (GPA)		48.3
Compressive Modulus (GPA)	110.3	41.4
Tensile Strain (%)		0.14
Compressive Strain (%)	1.3	0.12
Poissons Ratio	0.02 - 0.1	
Coefficient of Expansion (cm/cm °C)	5×10^{-7}	

The FW has a radius of curvature of 20 cm and a thickness of 1.0 cm. Figure 3.23 shows how the FW was modelled for ANSYS. Because of symmetry, only one half of a FW channel was modelled, showing one FW radial support and only one half of the FW in the channel attached to it. The location of the point of analysis is at Z = -4.6 m, where the FW surface heat load and temperature peak. This is the worst spot since the thermal stress will be lower everywhere else. Figure 3.23 shows that the radial support is fixed, but the FW is allowed to expand outward under the actions of the internal pressure and thermal stress.

Figures 3.24 and 3.25 show the FW stress distribution due to the internal pressure of 0.3 MPa in the X and Y directions, respectively. The X direction is perpendicular to the FW, and the Y direction is parallel to it. As expected, these stresses are very low, with the highest being 10.6 MPa in the Y direction at the corner between the radial support and the FW. At the FW midway between the supports, the maximum stress is ~6 MPa, or the value which is obtained from a simple $\sigma = pr/t$ for cylindrical geometry, where p is the pressure, r is the radius of curvature, and t the thickness.

Figures 3.26 and 3.27 show the stress distribution, again in the X and Y directions with the secondary thermal stress superimposed. Here the stress in the X direction is low, 8.5 MPa, but in the Y direction it is 42.9 MPa. The maximum stress again occurs at the corner between the radial support and the FW. In the actual case, there would be a rounded transition at this point, and the stress concentration would be reduced.

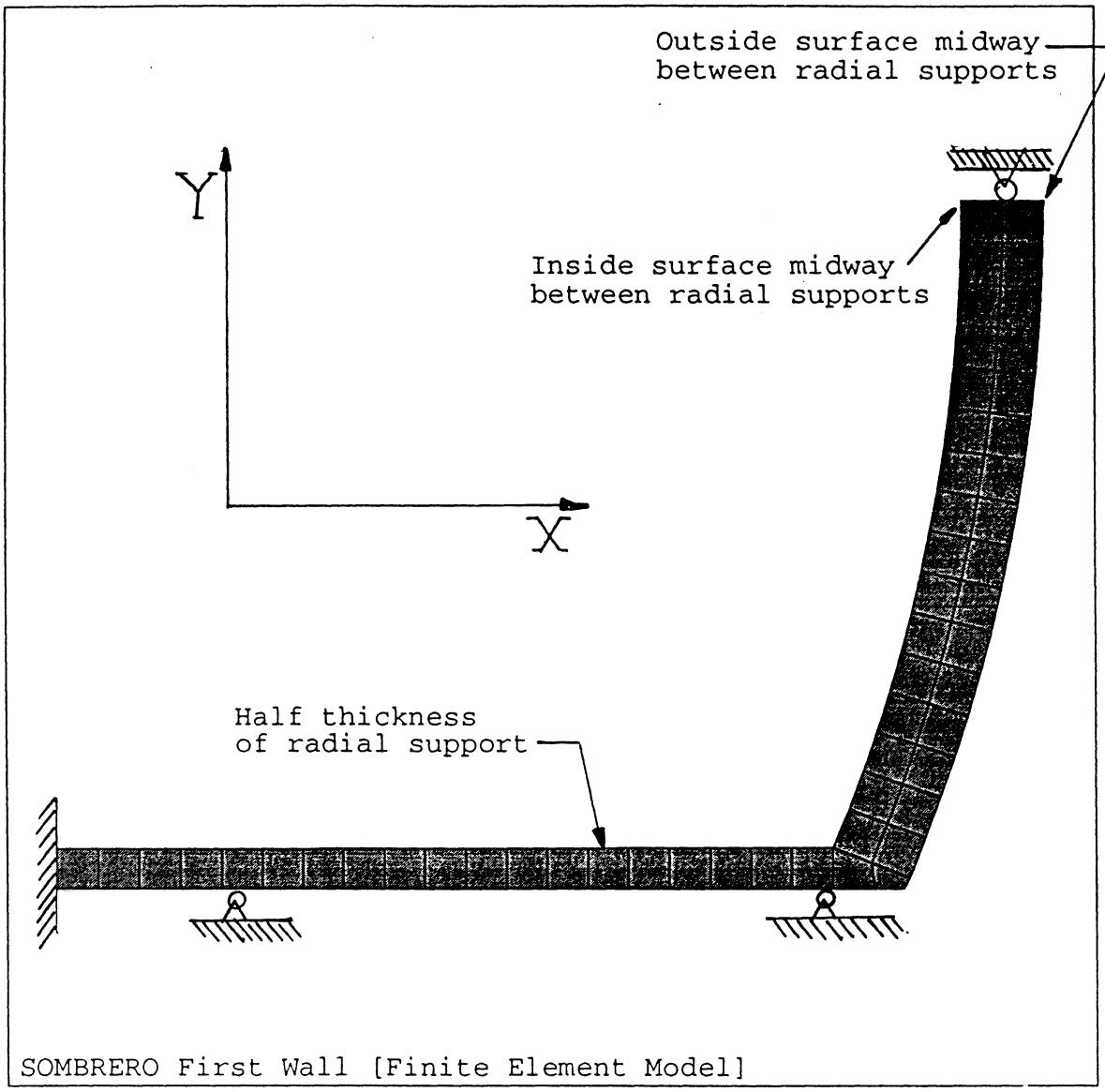

Fig. 3.23. First wall modeling for ANSYS.

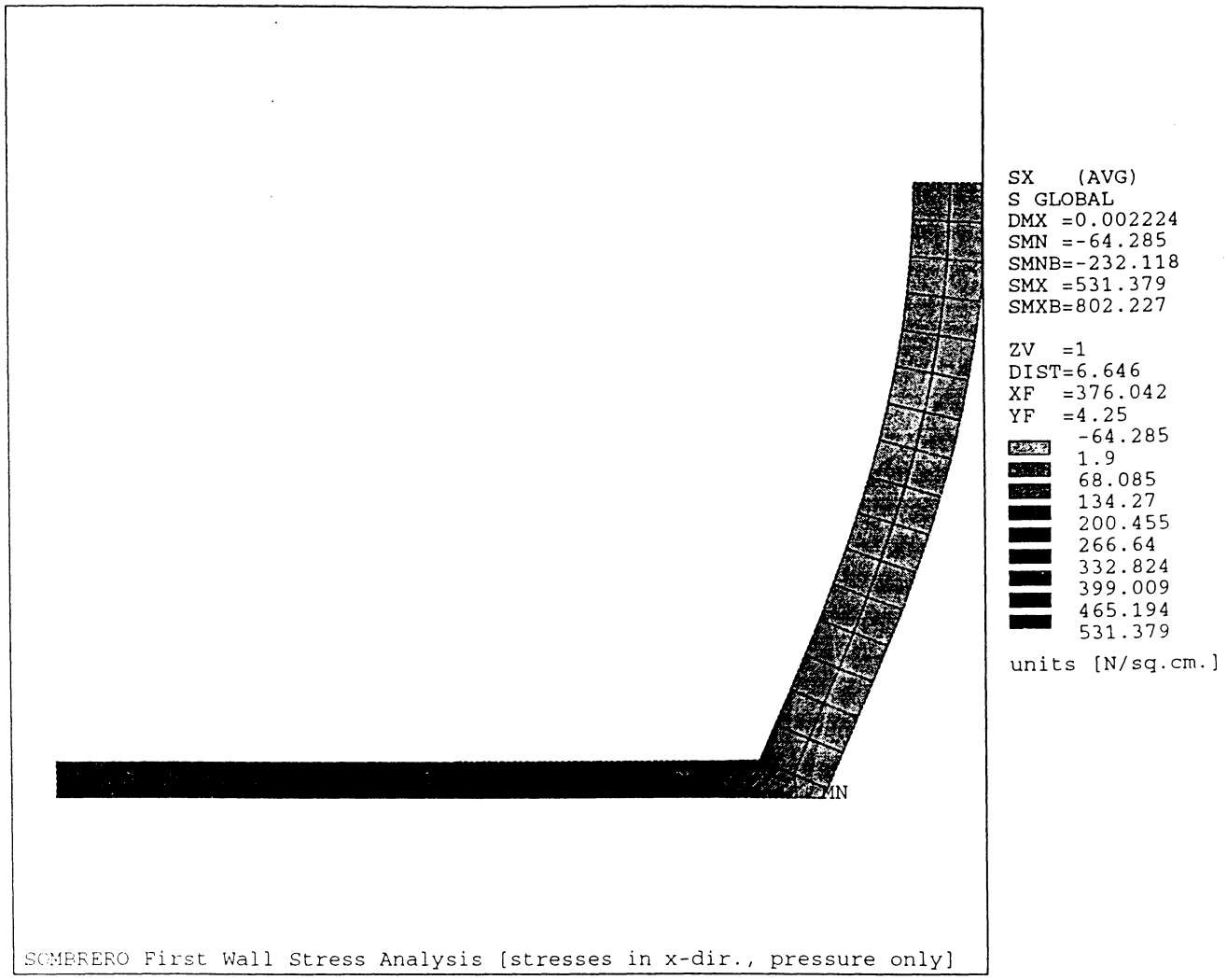

Fig. 3.24. First wall stress distribution in the X direction (perpendicular to FW) due to internal pressure of 0.3 MPa.

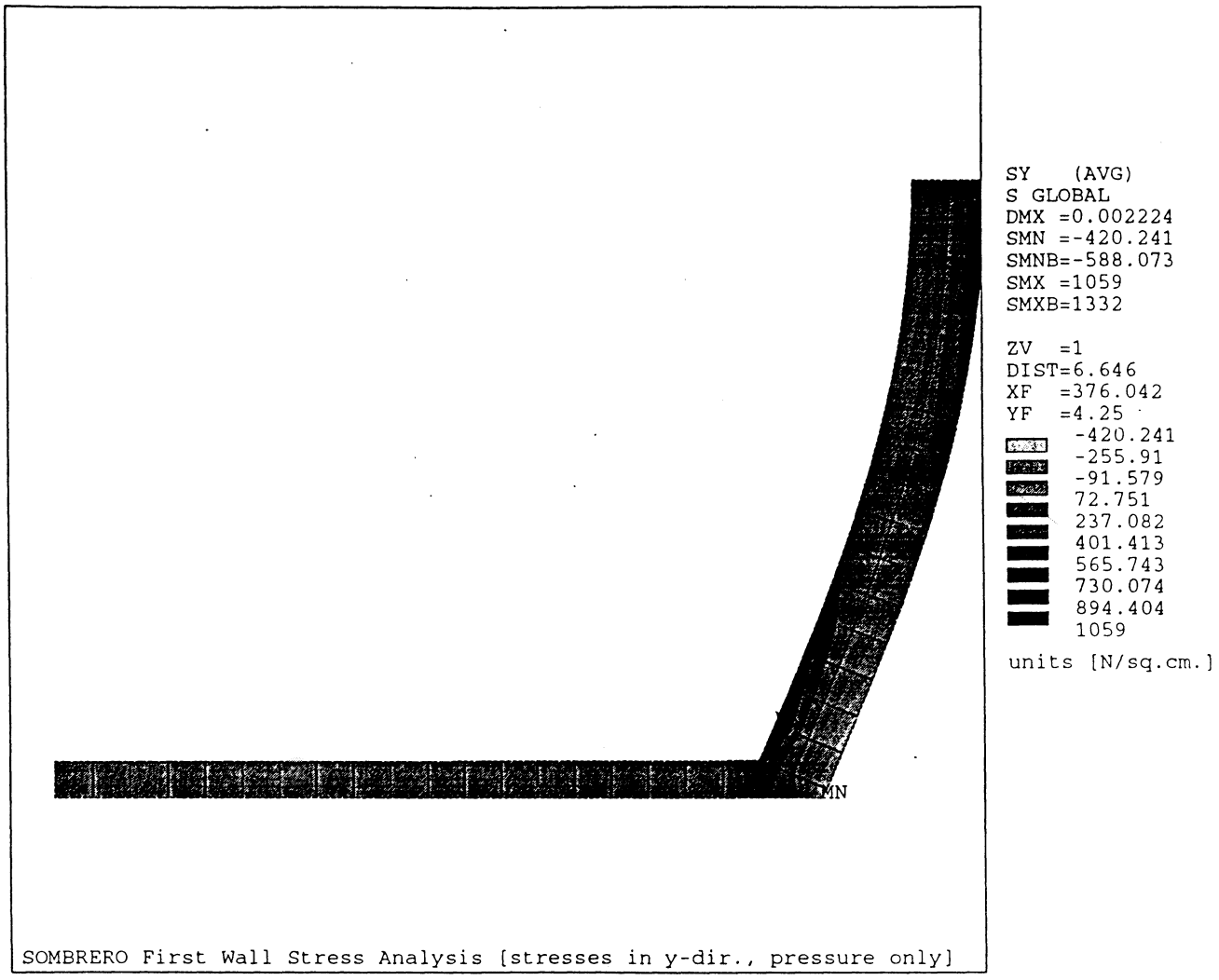

Fig. 3.25. First wall stress distribution in the Y direction (parallel to FW) due to internal pressure of 0.3 MPa.

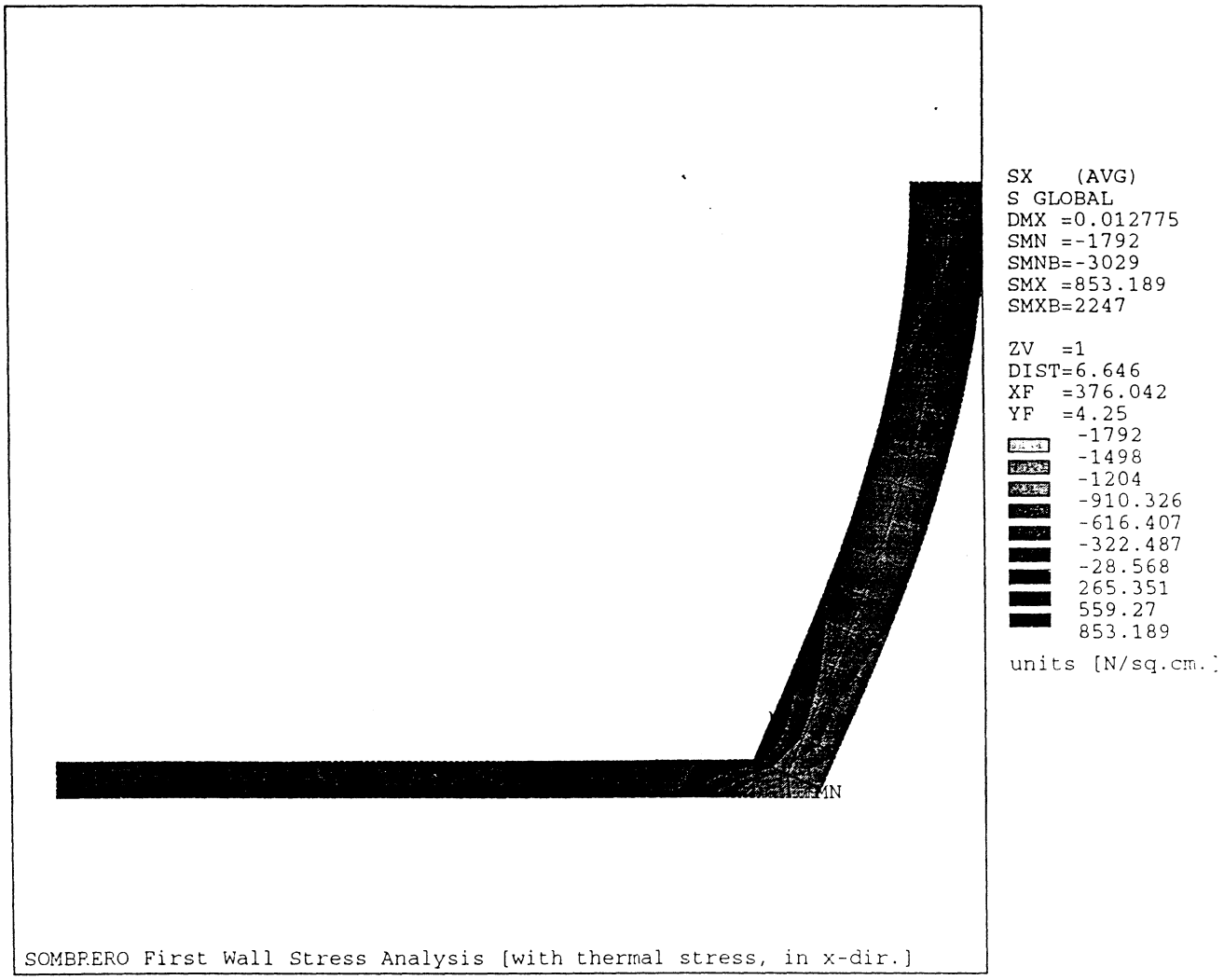

Fig. 3.26. First wall stress distribution in the X direction due to internal pressure and thermal stress.

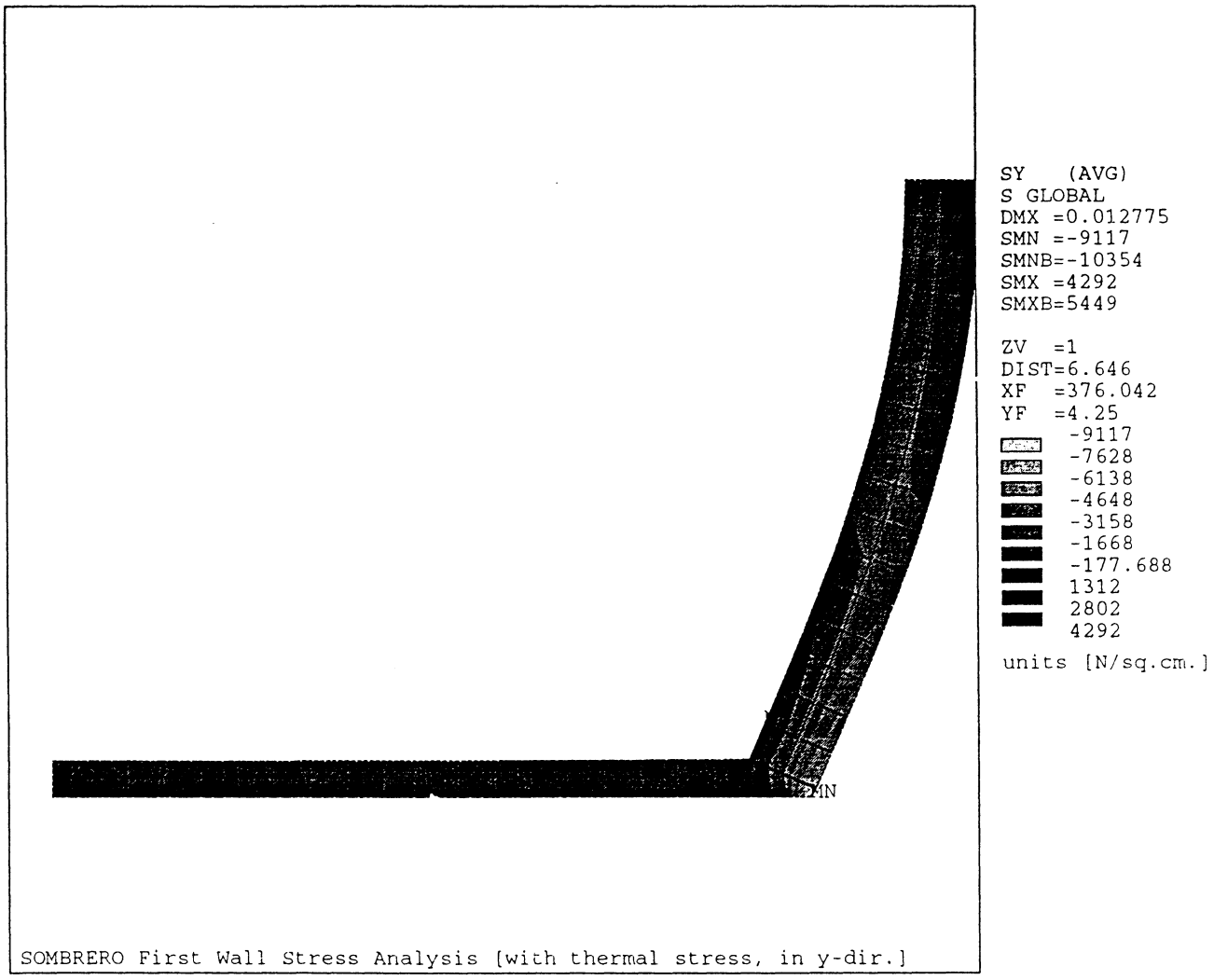

Fig. 3.27. First wall stress distribution in the Y direction due to internal pressure and thermal stress.

Structural characteristics of 3D and 4D weaves of C/C composites vary by quite a lot, depending on the manufacturer. Tensile strength can vary from 50-300 MPa and shear strength from 20-40 MPa[3.11]. The feature that distinguishes these materials from others is that they actually become stronger at higher temperatures. For example, some 3D and 4D C/C composites display a 25% increase in tensile strength at 2000°C as compared to room temperature strength. Thus, it would seem that a material with tensile strength of 100-150 MPa would be sufficient for use in the FW.

Finally, Fig. 3.28 gives the radial deflection of the FW under the combined action of pressure and thermal stress. The maximum displacement if the FW midway between radial supports is only 0.013 cm.

3.2.3.2 Materials and Fabrication

Structural Materials. The first wall in SOMBRERO is protected with a buffer gas of 0.5 torr Xe. This dry wall protection scheme puts stringent requirements on the FW materials. They should have high temperature capability, reasonably high thermal conductivity, and a combination of properties which will give a low thermal stress.

Figure 3.29 is a compilation[3.12] of the thermal stress figure of merit for various materials that have been considered for high heat flux plasma facing components. The thermal stress figure of merit is given by

$$\frac{2(1 - \nu)k\sigma_y}{E\alpha} \quad (W/cm)$$

where

ν = Poisson's ratio,
k = thermal conductivity,
σ_y = yield strength,
E = Young's modules, and
α = thermal expansion coefficient.

The C/C composites lead the way by a healthy margin over other ceramic and metallic materials. Carbon/carbon composites are attractive for high heat flux surfaces because of their high thermal conductivity of ~100 W/mK in a direction perpendicular to the fibers in 3D and 4D C/C composites.[3.13] In a direction parallel to the fibers, conductivity as high as 500 W/mK has been obtained. This compares favorably with copper, which has a conductivity of 400 W/mK at 25°C.

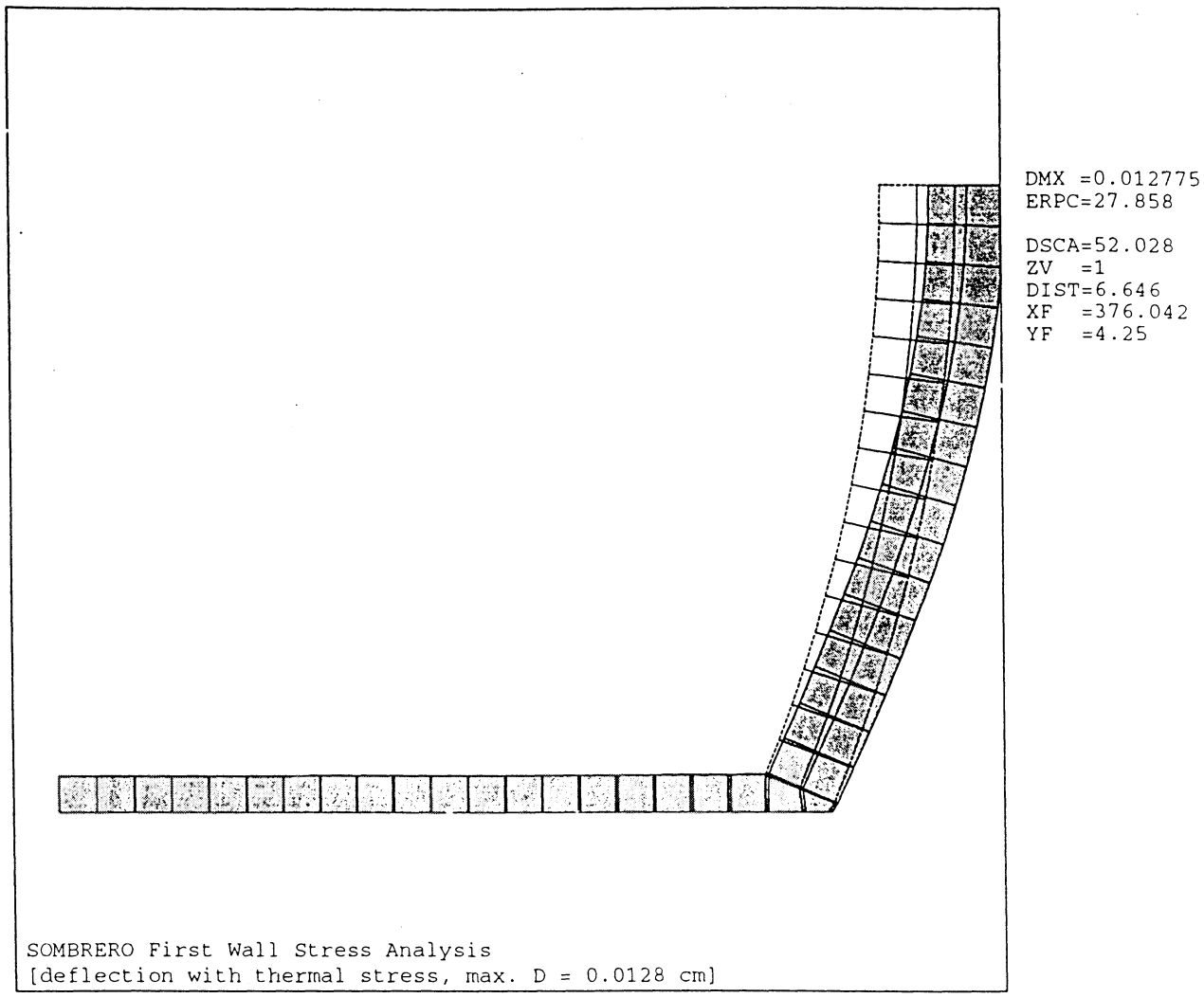

Fig. 3.28. First wall deflection under the combined action of internal pressure and thermal stress.

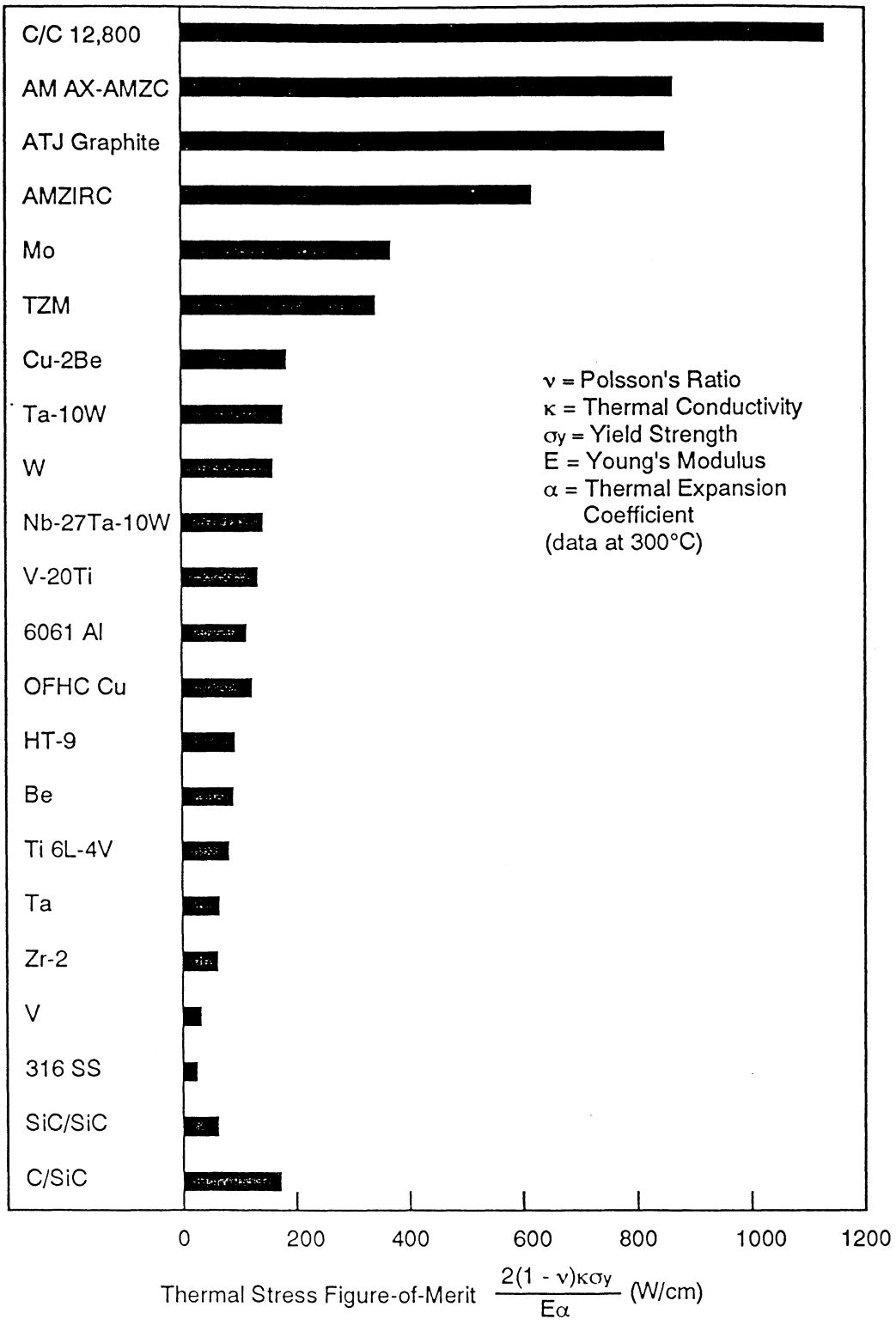

Fig. 3.29. Thermal stress figures of merit for several materials.

There are several other properties of C/C composites which make them attractive for such an application. They are

- High strength, tensile, compressive, and shear[3.11]
- They get stronger at high temperatures[3.11]
- Very low neutron activation

These are among the reasons a C/C composite material has been selected for the SOMBRERO chamber structure.

Although there is some information on radiation damage in pyrolytic graphite, there is none available on 3D and 4D C/C composites. During high temperature irradiation, graphites first experience shrinking or densification and then expand at a rapid rate. Figure 3.30 shows the results for GRAPHNOL N3M for example.[3.13] Useful lifetimes are usually determined when the dimensional change crosses the zero swelling line. The figure shows that for Graphnol N3M this value is 46 dpa at 1325°C. With improved material engineering, these values will go up, and for the present design we have assumed a limiting value of 75 dpa, which gives the FW a lifetime of 5 FPY.

Four dimensional C/C composites are constructed by running fibers in three directions in one plane, 60 degrees apart, commonly called the U,V, and W directions. The fourth direction, called Z, is perpendicular to this plane. When the weave is completed it undergoes a densification. It is first rigidized by chemical vapor deposition (CVD) or low pressure infiltration (LPI) by a hydrocarbon. The last step is called graphitization where the hydrogen is burned out of the hydrocarbon. This results in a composite weave with a density of 1.85-2.0 g/cm^3.

Some extremely complex shapes have been fabricated in these ways for the defense industry, such as very large reentry nose cones for rockets. Although the chamber modules are very large and fairly complex, it is felt that in 30-40 years, when such fusion reactors will be built, the manufacturing methods will have improved to the point where such items can be fabricated routinely.

Breeding Material. The breeding material selected for SOMBRERO is Li_2O in the form of flowing particles 300-500 μm in size. At a recent International Thermonuclear Engineering Reactor (ITER) specialists meeting on blanket materials data base, it was reported that with regard to baseline physical properties of ceramic breeders, the data base for Li_2O and $LiAlO_2$ is reasonably complete.[3.14] Tritium solubility and transport have been studied in significant detail for Li_2O, which is the only breeder material for which single-crystal tritium diffusion measurements have been made. Table 3.8 summarizes the data base assessment for Li_2O, and Table 3.9 is a summary of four recommended ceramic breeders.[3.14] Of these four, only Li_2O has a high enough Li atom density (even higher than Li) for adequate tritium breeding without neutron multiplication.

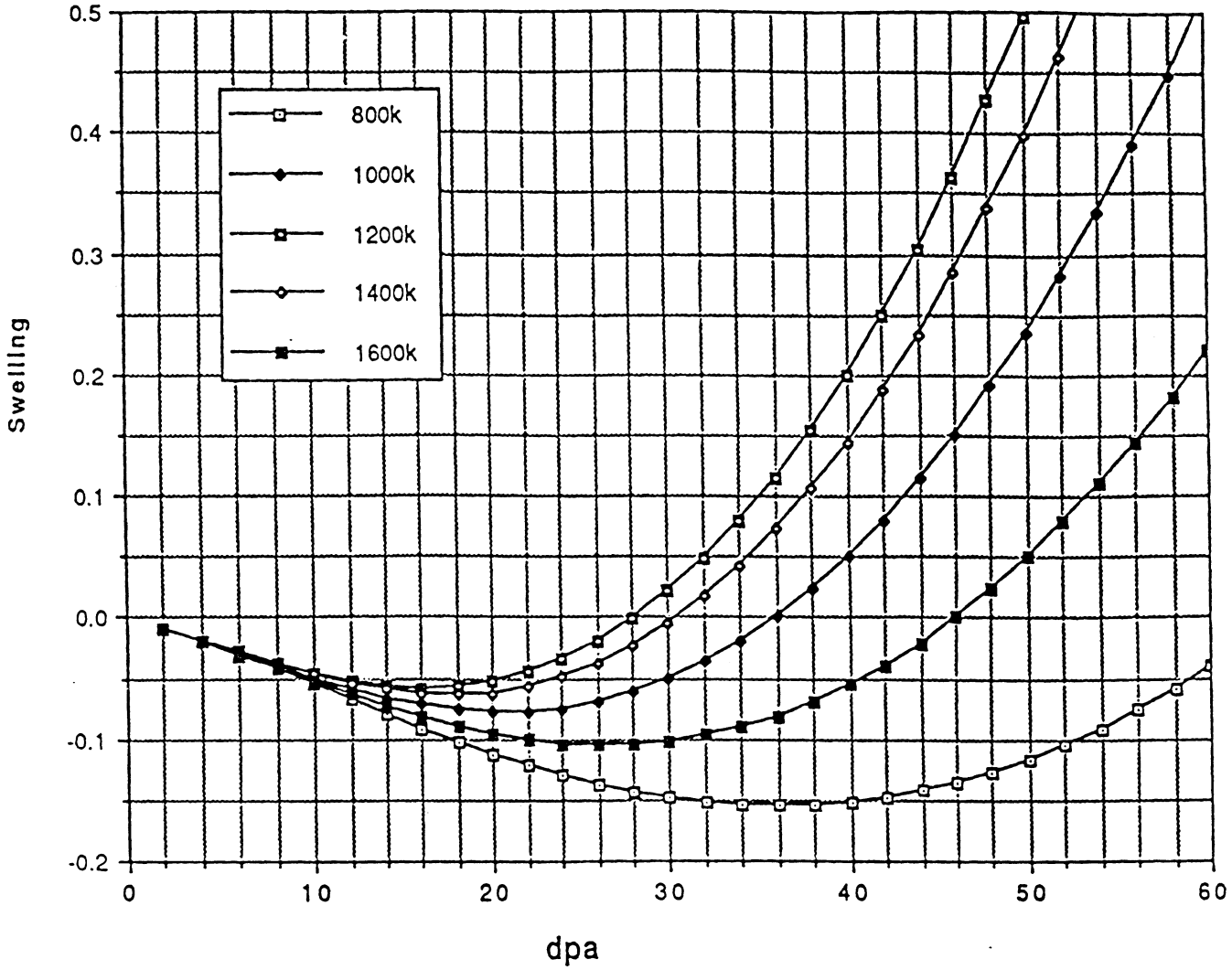

Fig. 3.30. Radiation swelling in Graphnol N3M as a function of temperature and fluence.

Table 3.8. Li_2O Data Base Assessment (Ref. 3.14)

Physical Properties	
Density	Adequate/good agreement
Melting temperature	Adequate/good agreement
Vapor pressure	Limited/general agreement
Thermal expansion	Adequate/good agreement
Thermal conductivity	Limited/general agreement
Specific heat	Adequate/good agreement
Mechanical Properties	
Elastic modulus	Limited/general agreement
Poisson's ratio	Limited/general agreement
Tensile strength	Very limited
Compressive strength	Single set of data
Bending strength	Single set of data
Chemical Stability / Compatibility	
Composition/purity	Adequate/good agreement
Stability	Adequate/good agreement
Vapor pressure/transport	Adequate/good agreement
Compatibility w/water	Limited/general agreement
Tritium Solubility / Transport	
Tritium solubility	Limited/some discrepancies
Tritium diffusivity	Adequate/good agreement
Adsorption/desorption	Limited/some discrepancies
Radiation Effects	
Swelling	Single set of date
Tritium trapping/transport	Limited/some discrepancies
Helium trapping/transport	Single set of data
Fracture properties	Single set of data

Table 3.9. Summary of Recommended Ceramic Breeders (Ref. 3.14)

	Li_2O	Li_4SiO_4	Li_2ZrO_3	$LiAlO_2$
Li Atom Density	G	F	F	F
Large Scale Production Feasibility	F	F	F	F
Activation	G	G	P	F
Thermal Conductivity	G	P	P	F
Melting Point/Phase Change	G	F	G	G
Thermal Expansion	F	F	G	G
Mechanical Strength	F	F	G	G
Creep/Ductility	F	P	P	P
Chemical Stability	F	F	G	G
Water Compatibility	P	F	F	G
Structural Compatibility	F	F	G	G
Li Mass Transfer	KI	G	G	G
Tritium Solubility	F	F	F	F
Tritium Release (Transport)	G	F	G	P
Irradiation Effects on Physical Properties	G	G	G	G
Irradiation Swelling	P	F	G	G
Irradiation Stability	F	P	G	F
Radiation Effects (T-transport, Compatibility)	KI	KI	KI	KI

G - Good, F - Fair, P - Poor, KI - Key Issue

From Table 3.8 it is obvious that for the application intended in this reactor, Li_2O has good credentials. Water compatibility and irradiation swelling were judged poor for Li_2O. For this reason we have opted for a Pb intermediate loop, to prevent water from coming in contact with Li_2O. As far as irradiation swelling, this is much less significant in a moving bed than in a static bed. The key issues listed are Li mass transfer and radiation effects on T_2 transport and compatibility. Here again, these issues have more relevance to static beds. A moving bed can have a continuous reprocessing side loop which can maintain the desired properties.

The melting temperature of Li_2O as listed in the *Handbook of Chemistry and Physics* is >1700°C. However, this somewhat depends on the purity of the material. A more typical value is 1432 ± 6°C for commercially produced material.[3.15]

The following correlations were used to evaluate the properties needed for thermal hydraulics calculations:

Specific Heat (kJ/kg K) for temprerature range of $306 \leq T \leq 1073$ K (Ref. 3.16)

$$C_p = 2.5179 + 3.328 \times 10^{-4} T - 8.382 \times 20^4 / T^4$$

Thermal Conductivity (W/mK) for temperature range of $473 \leq T \leq 1172$ K (Ref. 3.17)

$$k = (1 - P)^{1.96} [39.79 (1 + 7.067 \times 10^{-3} T)^{-1}]$$

where P is the porocity ($0.066 \leq P \leq 0.292$)

3.2.3.3 Thermal Hydraulics

Heat transfer in moving beds is dominated by the effective thermal conductivity of the solid and the interstitial gas instead of by the conductivity of the gas alone, as is the case in fluidized beds. For this reason, heat transfer coefficients in moving beds are higher than those for fluidized beds using the same material.[3.18]

The most critical cooling part in SOMBRERO is the FW. Figure 3.31 gives the nuclear heating distribution through the blanket at midplane. As can be seen, the nuclear heat generation in the front part is significantly higher than in the rear zones. In addition, the FW receives heat radiated to it by the Xe fill gas after the ions and soft x rays have been stopped. The front channel at the FW must, therefore, remove the nuclear heat generated in the graphite FW and the Li_2O in the channel, as well as all the surface heat incident on it from the fill gas. This amounts to 44% of the total thermal power in the reactor. Moreover, since the ΔT in the FW channel is only 150°C, and in the rear channels it is 250°C, the mass flow rate in the FW channel is 57% of the total mass flow rate. Figure 3.32 gives the mass flow rate in each blanket channel, and Fig. 3.33 gives the velocity in each channel at midplane (channel 1 is at the FW). These velocities are based on a void fraction of 40% and an equivalent Li_2O density of 1.08 g/cm^3. The Li_2O specific heat at the FW at an average temperature of 625°C was taken as 2713 J/kgK and in the rear zones at 675°C as 2740 J/kgK.

For determining the heat transfer coefficient at the FW, it was decided to treat the Li_2O moving bed as a continuum. This decision was taken after an extensive investigation into moving bed heat transfer research going back to 1955. It was found that most of the research gave formulations for heat transfer coefficients which depended on times or distances particles spent on the heated surface, parameters which are impossible to predict for SOMBRERO. Mickley and Fairbanks[3.19] derived a correlation for the local heat transfer coefficient based on particle residence time on the heated surface. Baskakov[3.20,3.21,3.22] introduced a contact resistance at the heated wall to allow for heat transfer impedance due to increased voidage at the wall. But their

correlations also depended on the mean residence time a particle spent on a heated surface. Gelperin[3.23,3.24] developed this approach further and derived expression for the overall heat transfer coefficient. Sullivan and Sabersky[3.25] made a series of experiments using flowing beds of glass beads, mustard seed and fine grained sand. They obtained Nusselt numbers based on a modified Peclet number which depended on L, the distance a particle stayed in contact with a heated surface:

$$N_{Pe} = N_{Re}\, N_{Pr}$$

$$N^{*}_{PeL} = \left(\frac{k}{k_g}\right)^2 \left(\frac{d}{L}\right)^2 N_{Pe}$$

where

N^{*}_{PeL} = modified Peclet number
k = effective bed thermal conductivity
k_g = gas thermal conductivity
d = particle diameter
L = distance a particle stays in contact with the heated surface.

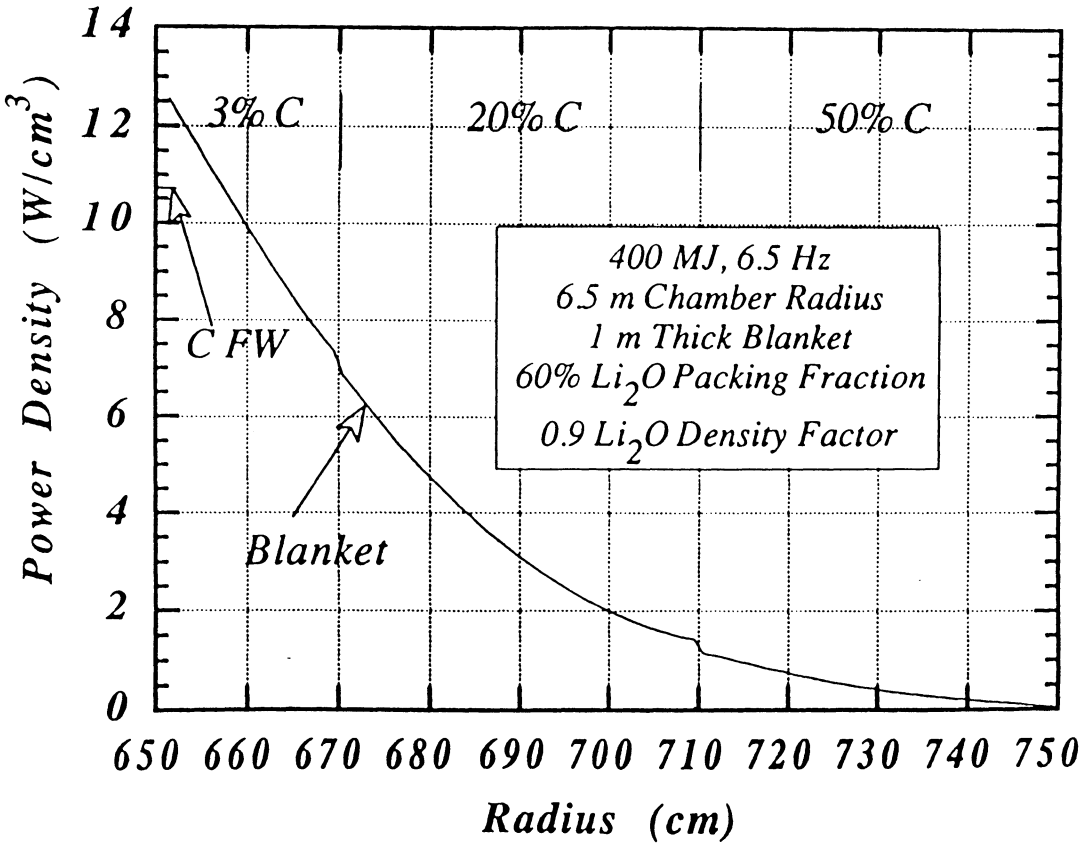

Fig. 3.31. Nuclear heating distribution at midplane.

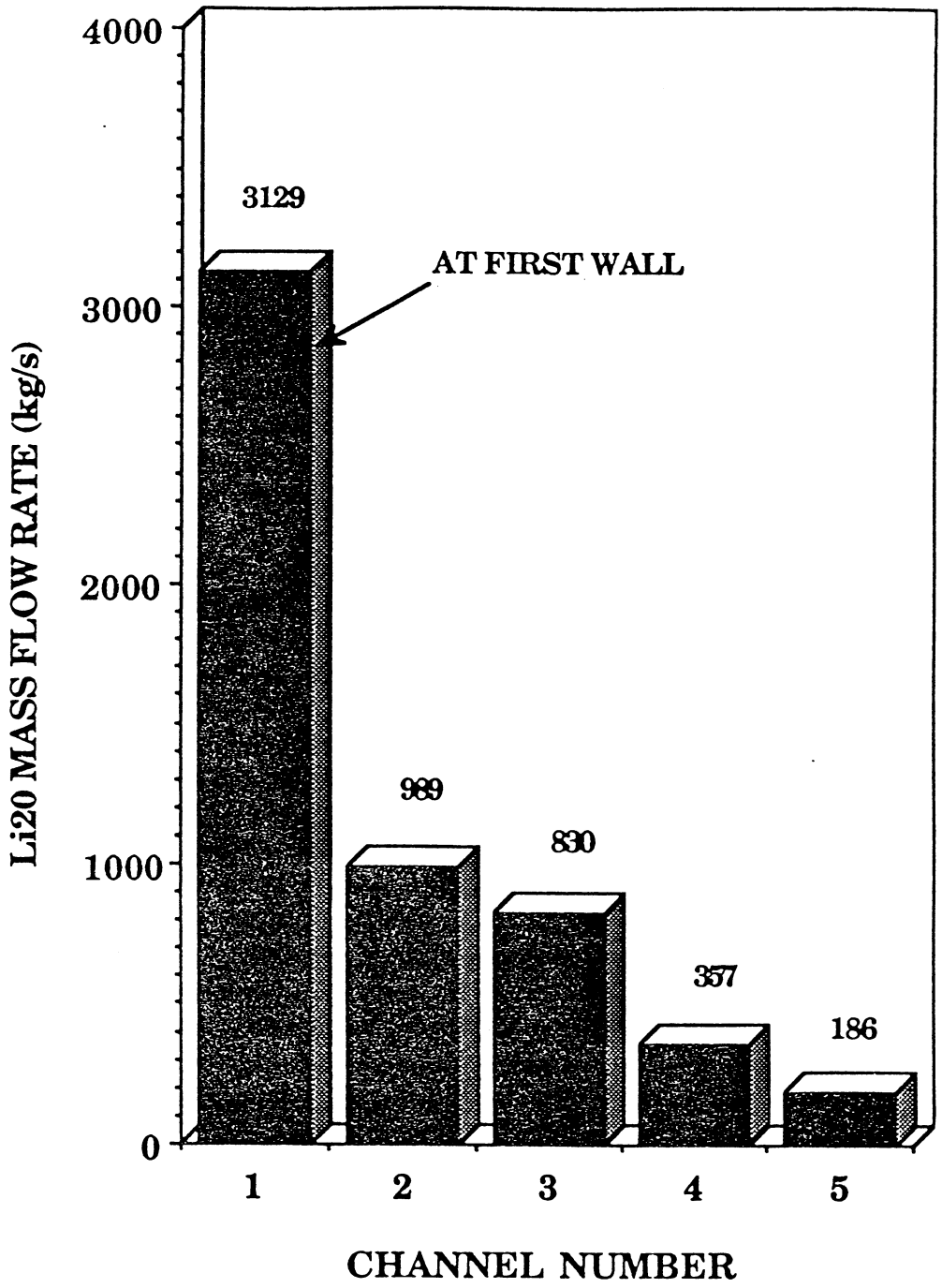

Fig. 3.32. Mass flow rate in the blanket channels.

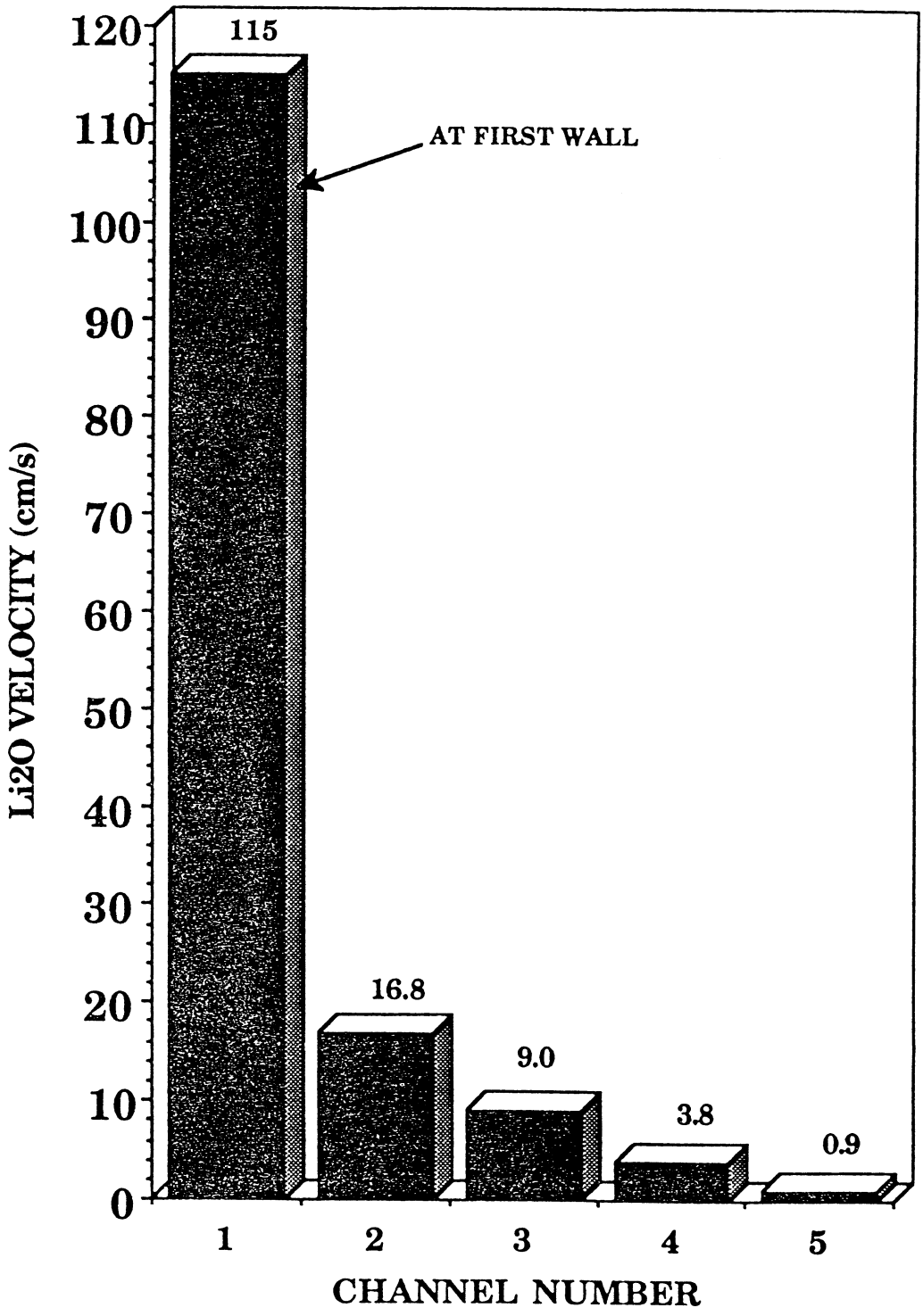

Fig. 3.33. Li_2O velocity at midplane in the blanket channels.

The Nusselt number is then:

$$N_{Nu} = \frac{h \cdot d}{k_g} = \frac{1}{\chi - \frac{\sqrt{\pi}}{2} \cdot \sqrt{\frac{1}{N^*_{PeL}}}}$$

where h is the heat transfer coefficient, and χ is a constant taken as 0.085 for the materials tested.

Figure 3.34 is a plot of local heat transfer coefficients as a function of moving bed velocity for sand particles of 500 μm and 1000 μm size at 400°C and 800°C using the Sullivan and Sabersky formulation for L = 1.0 cm. It can be seen that values of h approaching 2600 W/m^2K can be had for a velocity of 110 cm/s for particles of 500 μm size at 800°C. Since there is a lot of mixing going on at velocities greater than ~40 cm/s, an $L \leq 1$ cm is not unreasonable.

In order to be able to use the Li_2O stream as a continuum, the effective viscosity of the particles as a function of velocity has to be obtained. To obtain the effective viscosity, experiments performed by R. Nietert[3.26] at the University of Wisconsin in 1981 were used. The experiments involved flowing soda lime glass beads in electrically heated tubes. Nusselt numbers were obtained experimentally from three different particle size ranges in three different size tubes for a velocity range from 0.5-20 cm/s. The following parameters were known:

- Particle size
- Tube ID
- Inlet temperature
- Outlet temperature
- Velocity
- Density
- Void fraction
- Gas conductivity
- Solid conductivity
- Solid specific heat
- Heat flux

The Nusselt numbers were used to derive the effective viscosities for moving beds using the Dittus Boelter formulation. These effective viscosities for the same particle sizes and void fractions were plotted against velocity for the same heat flux and an analytic expression was obtained. There was a definite trend at the higher velocity values, thus, the curve was extrapolated to the velocity of interest. Since Li_2O is harder than soda lime glass, it is expected that the effective viscosities might be lower yet, making these values conservative. Figure 3.35 is a plot of the obtained effective viscosities for 500 μm size soda lime glass particles.

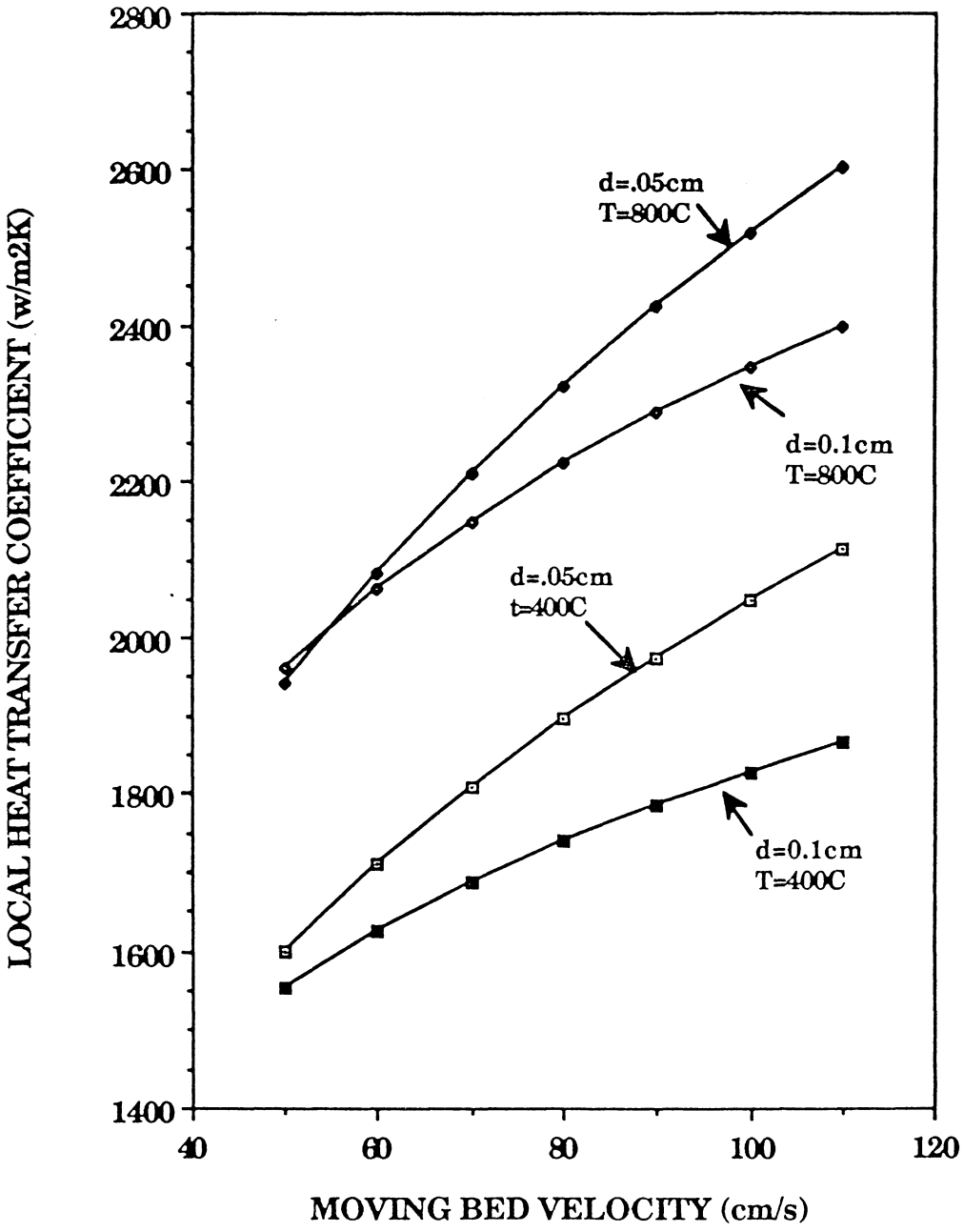

*L is the max. distance a particle stays in contact with the heated surface

Fig. 3.34. Local heat transfer coefficients as a function of velocity for sand particles using the Sullivan and Sabersky formulation for L=1 cm.

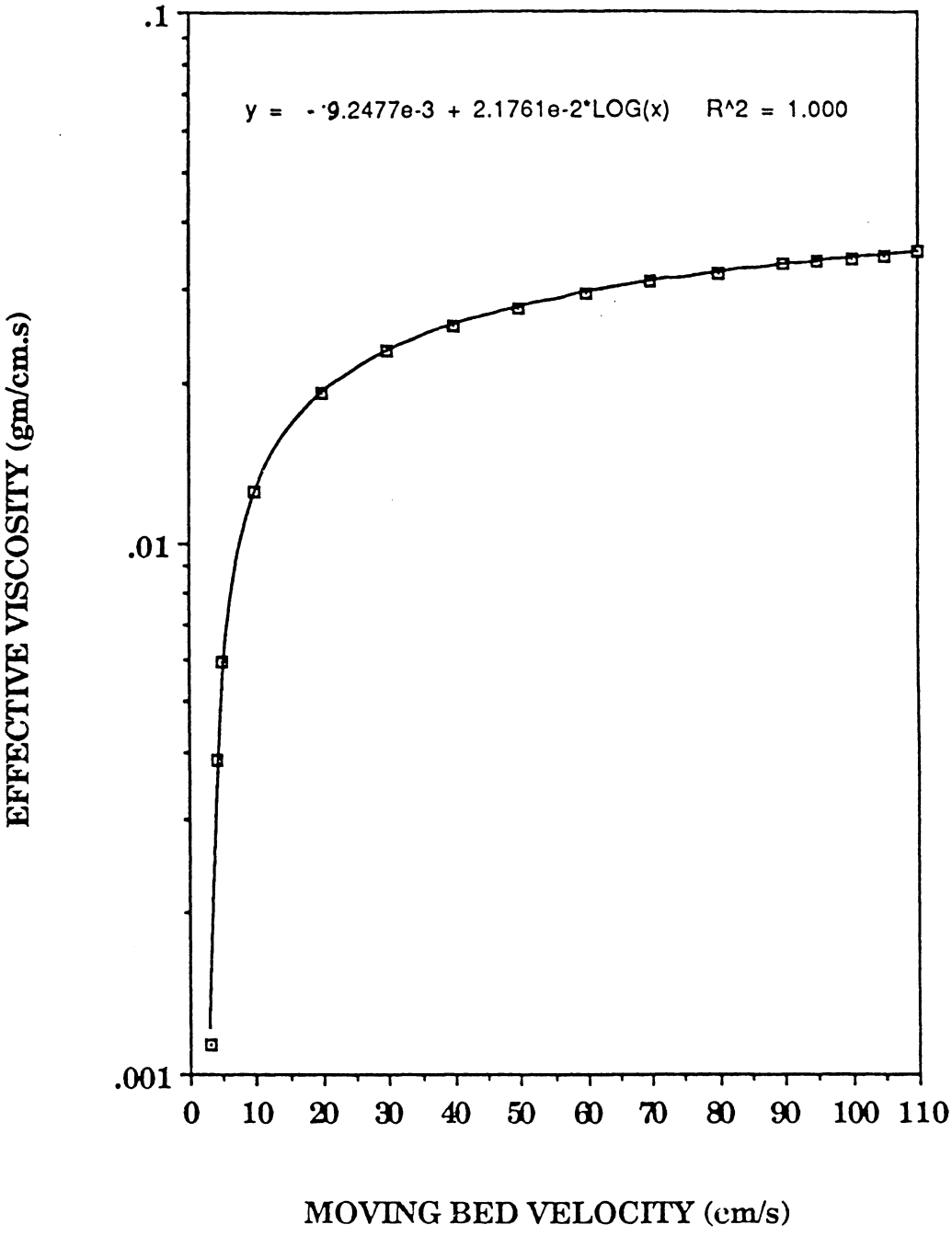

Fig. 3.35. Effective viscosity as a function of velocity for 500 μm soda lime glass particles.

To obtain the effective thermal conductivity of the moving bed, we made use of the method of Deissler and Boegli.[3.27] Figure 3.36 gives the static effective thermal conductivity for two phase systems as derived by Deissler and Boegli for materials separated by planes parallel to heat flow and perpendicular to heat flow. The thermal conductivity of Li_2O (90% density factor) was obtained using the expression given in Section 3.2.3.2. Thermal conductivity of He gas at 0.2 MPa is also well known.[3.28] The effective thermal conductivity for a bed with 40% He gas at 0.2 MPa is plotted in Fig. 3.37 as a function of temperature.

Figure 3.38 gives the specific heat for Li_2O as a function of temperature as obtained from the expression given in Section 3.2.3.2.

The Dittus-Boelter correlation is then used to determine the effective Nusselt number and hence the heat transfer coefficient in the different blanket zones. At the FW at midplane, this coefficient is 2758 W/m^2K, a value which is within 4% of that shown in Fig. 3.34 from the Sullivan and Sabersky formulation for L = 1.0 cm. In calculating FW temperatures a thermal conductivity for the 4D weave C/C composite of 70 W/mK has been used. There is still a lot unknown on how the thermal conductivity of C/C composites degrades as a result of radiation damage. In general for most graphites, the conductivity decreases to about 25% of its unirradiated value at high dose for an irradiation temperature of 500°C, and to 50% at 1200°C.[3.29] It was mentioned in Section 3.2.3.2 that C/C composites have been fabricated with conductivities up to 100 W/mK in a direction perpendicular to the fibers in 3D weaves. Parallel to the fibers it is as high as 500 W/mK. Since 4D weaves have a lot of fibers oriented parallel to the heat flow, we have assumed an initial conductivity of 140 W/mK, which degrades to 70 W/mK after irradiation. This is justified since the FW at midplane will have an average temperature of ~1300°C.

Table 3.10 gives the thermal hydraulics parameters for the SOMBRERO chamber. The temperature at the FW peaks at Z = -4.6 m where the surface heat load is equal to that at midplane and the Li_2O temperature is higher than at midplane. At Z = -4.6 m the FW internal surface temperature is 1242°C and the outside surface temperature is 1438°C.

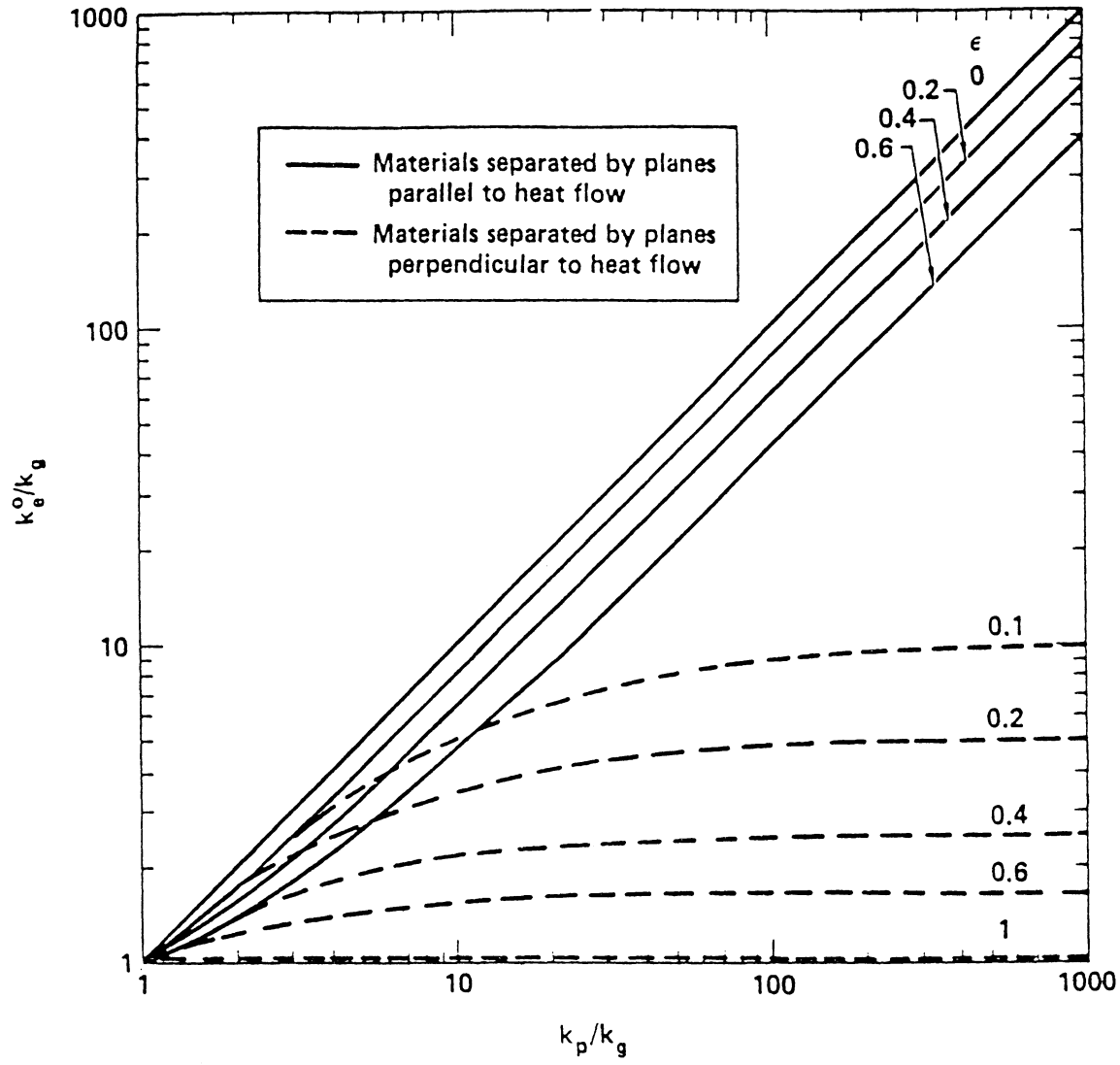

Fig. 3.36. Effective thermal conductivity for two phase system according to Deissler and Boegli.

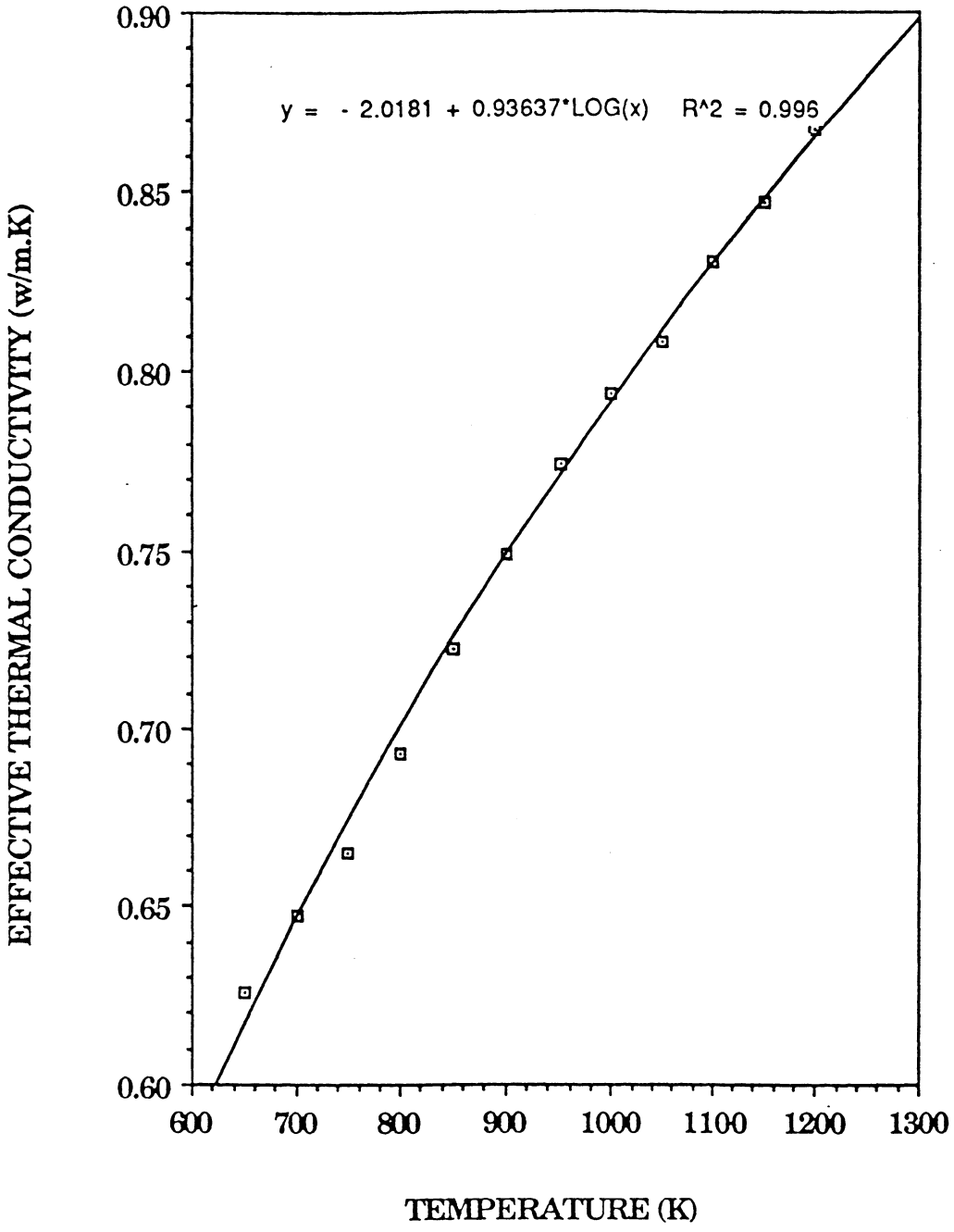

Fig. 3.37. Effective thermal conductivity of Li_2O (90% density) and 40% He gas at 0.2 MPa as a function of temperature.

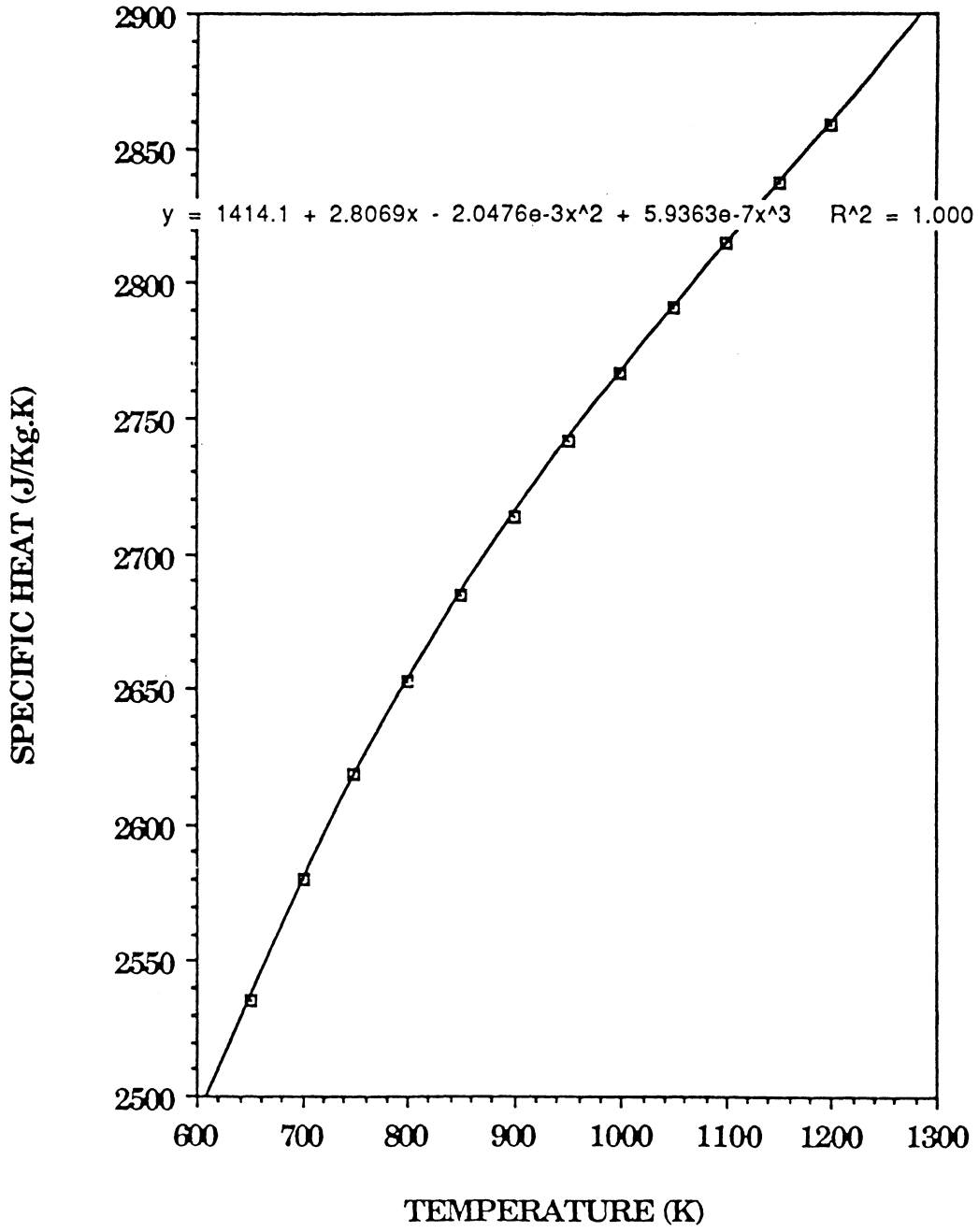

Fig. 3.38. Specific heat of Li_2O as a function of temperature.

Table 3.10. Thermal Hydraulics Parameters

Fusion Power (MW)	2677
Thermal Power (MW)	2891
Surface Power (MW)	801
Maximum Surface Heat Load (W/cm^2)	150.4
Maximum Nuclear Heat in FW (W/cm^3)	10.5
Inlet Li_2O Temperature (°C)	550
Outlet Temperature at FW (°C)	700
Outlet Temperature in Rear (°C)	800
Equilibrated Outlet Temperature (°C)	743
Li_2O Mass Flow Rate in 1st Channel (kg/s)	3129
Total Mass Flow Rate in Reactor (kg/s)	5491
Heat Transfer Coefficient at Midplane (W/m^2k)	2758
Inside FW Surface Temperature at Midplane (°C)	1149
Outside FW Surface Temperature at Midplane (°C)	1334
Heat Transfer Coefficient at Z = -4.6 (W/m^2k)	2573
Peak Inside FW Surface Temperature at Z = -4.6 m (°C)	1225
Peak Outside FW Surface Temperature at Z = -4.6 m (°C)	1438

The radial FW supports which are spaced every 21.3 cm act as fins and will reduce the FW temperature at the point where they are attached to it. Thermal conduction parallel to the fibers has been measured as high as 500 W/m^2K. If 50% of the conductivity is lost to radiation damage, then the remaining conductivity will still be very high at 250 W/mK. Figure 3.39 shows the model used and Fig. 3.40 the effect of the radial support on the peak FW temperature at Z = -4.6 m as modeled with a finite element code. Finally, Fig. 3.41 shows the temperature profiles at the FW on the inside and outside surfaces midway between radial supports as a function of the distance along the Z axis.

One of the concerns for the FW is in the event of a target misfire (i.e., the target does not get to the center of the chamber but the lasers fire because of a failure in the detection system). In this case the laser beams continue to the other side of the chamber and are incident on the FW. The worst case is close to the midplane where the beam diameter at the FW is ~18 cm. The laser energy per beam is 56.7 kJ, thus, the surface energy density is 222 J/cm^2. The latent heat of vaporization for graphite is 716 kJ/mole or 59.7 kJ/g. If we assume that all the energy goes into vaporizing the graphite, the amount vaporized is 3.7×10^{-3} g/cm^2. At a density of 1.8 g/cm^3, this amounts to ~20 μm. In the actual case there will be considerable vapor shielding, and the total deposited energy will be much less. For this reason, it is felt that a missed target does not present a serious problem for the FW.

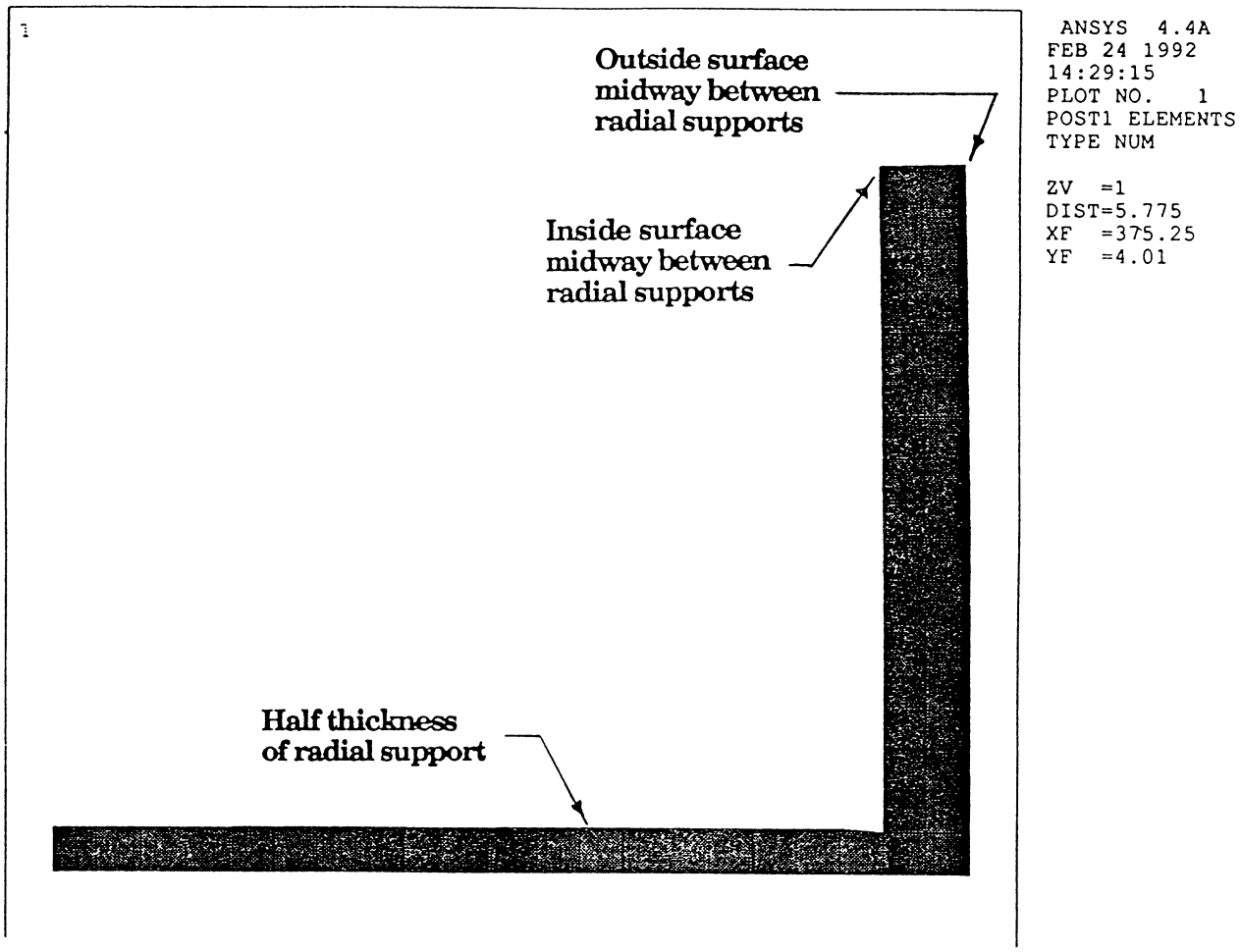

Fig. 3.39. Finite element model for determining the effect of the radial support on the FW temperature.

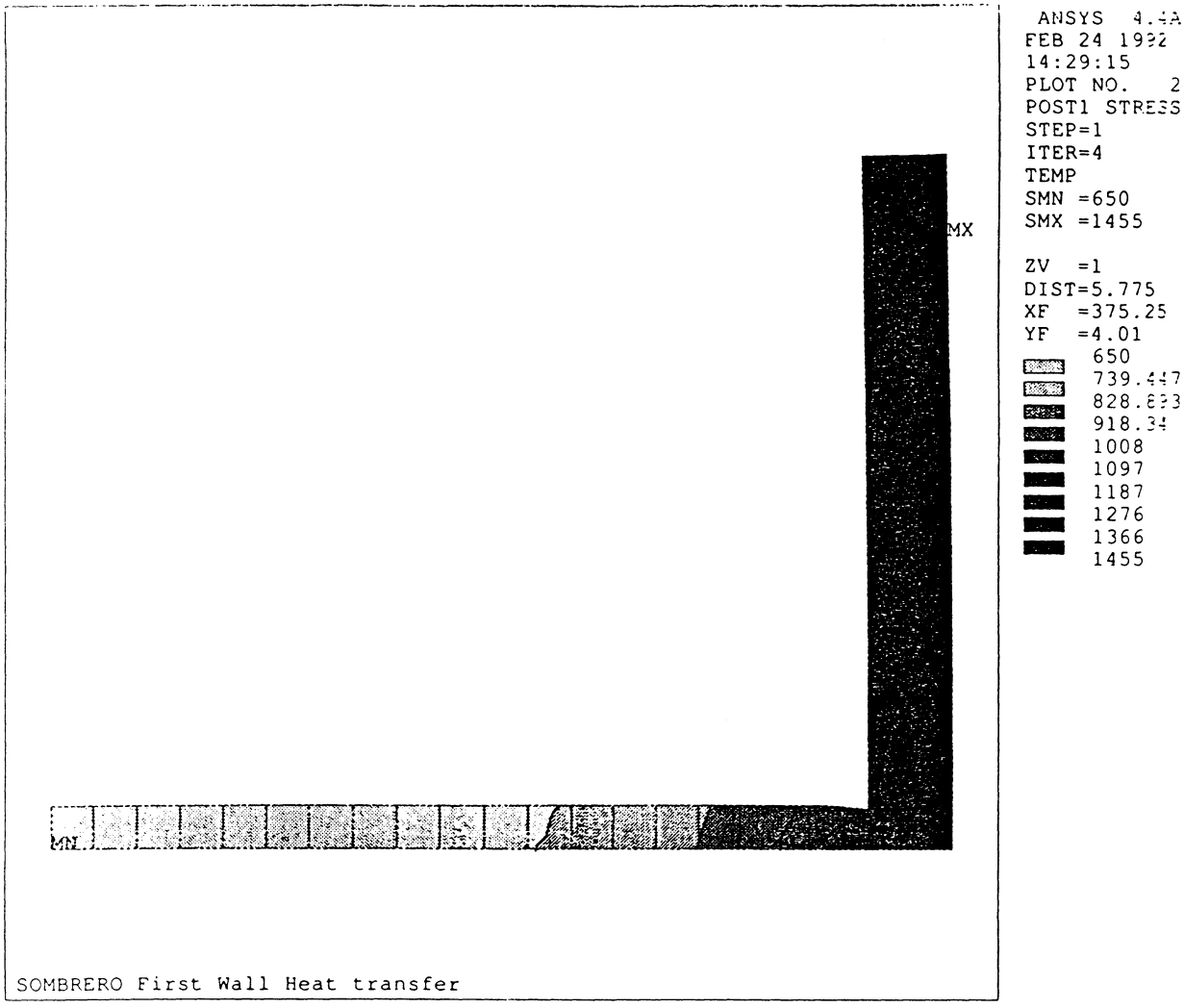

Fig. 3.40. Temperature variation at Z = -4.6 m as a result of the radial support.

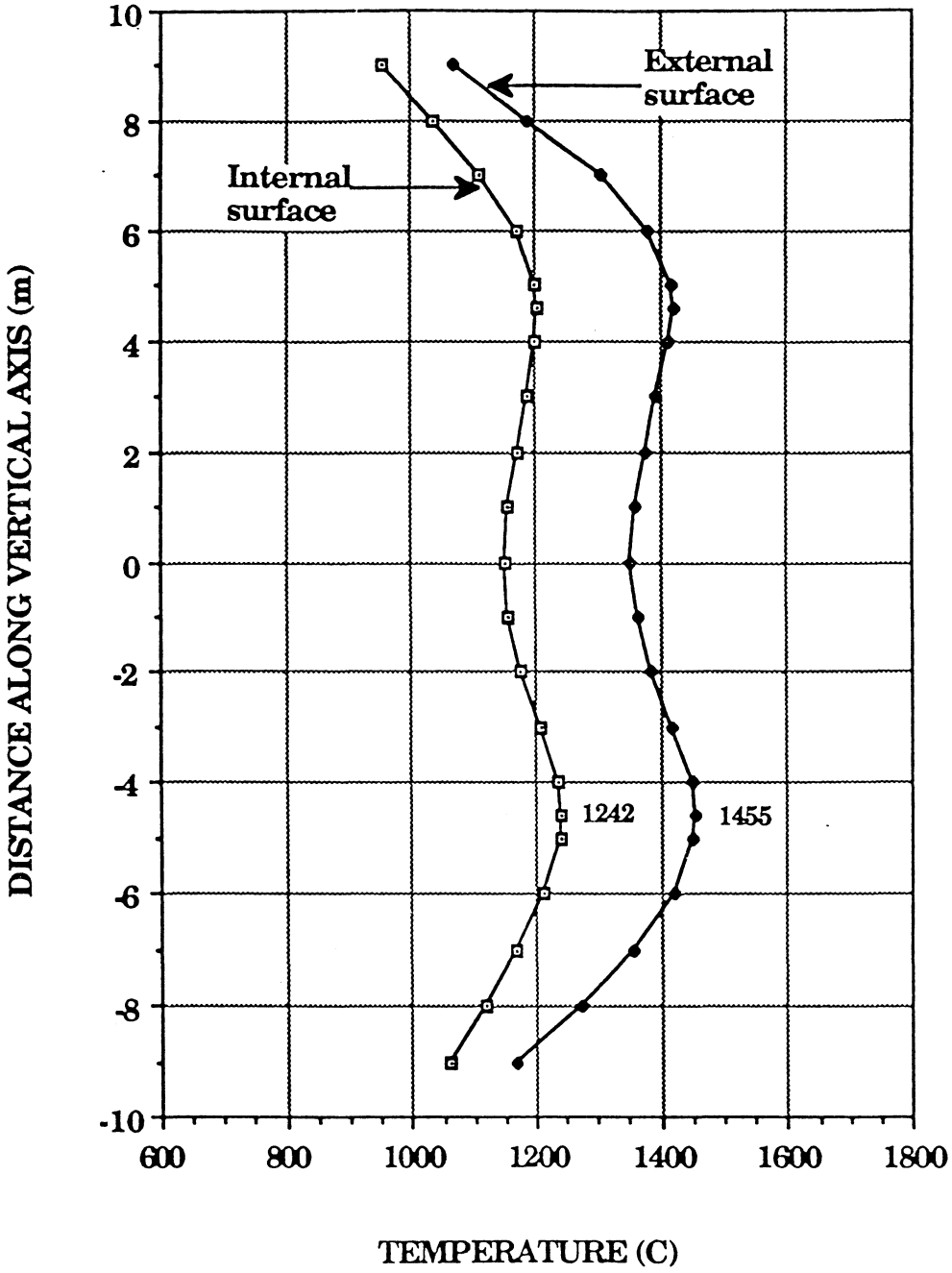

Fig. 3.41. Temperature profile on the inside and outside surfaces of the FW as a function of distance along the Z axis.

3.2.3.4 Chamber Support and Module Changeout

Figure 3.42 shows the chamber supported on the inner shield wall. There are 12 modules in the chamber and each module will have one support cantilevered from the shield wall. These modules have dedicated breeder material supply and return tubes. The supports are pivoted at the wall such that they can be retracted during module changeout.

This somewhat unique support and feed scheme was motivated by the desire to be able to remove a single module of the chamber due to a premature failure. Should any one module develop a problem, such as an excessive He leak, it would be possible to replace it with a new module without dismantling the whole chamber.

Figure 3.43 shows a schematic view of a chamber support. The side view indicates the arc the support executes during retraction. The top view shows that each support has a sector of a ring (1/12 of a circumference) attached to it. When all 12 supports are lowered into position, the sectors form a ring on which the chamber is supported. This scheme eliminates the bending moment on the cantilevered supports and puts the ring and the supports into compression. It also eliminates any concentrated loads on the chamber structure. The mass of the chamber is evenly distributed on the ring sectors.

Section 6.5 discusses the maintenance of the SOMBRERO chamber in detail. Briefly, to remove a module from the chamber, the following operations are needed:

- Li_2O breeder material drained from the reactor and supply/return manifolds.
- Supply and return tubes disconnected and removed.
- Tensioning bands at the upper and lower chamber extremities are released and removed.
- The polar crane attaches to the module in question and lifts it up ~0.5 m.
- The support retracts.
- A cage is lowered to the level of the module and the module is inserted into it and secured.
- The cage and module are lowered down into the pit below the chamber and laid down onto a polar carriage.
- The polar carriage then takes the module into a hot cell.

The procedure is reversed when a new module is replaced and inserted into the chamber.

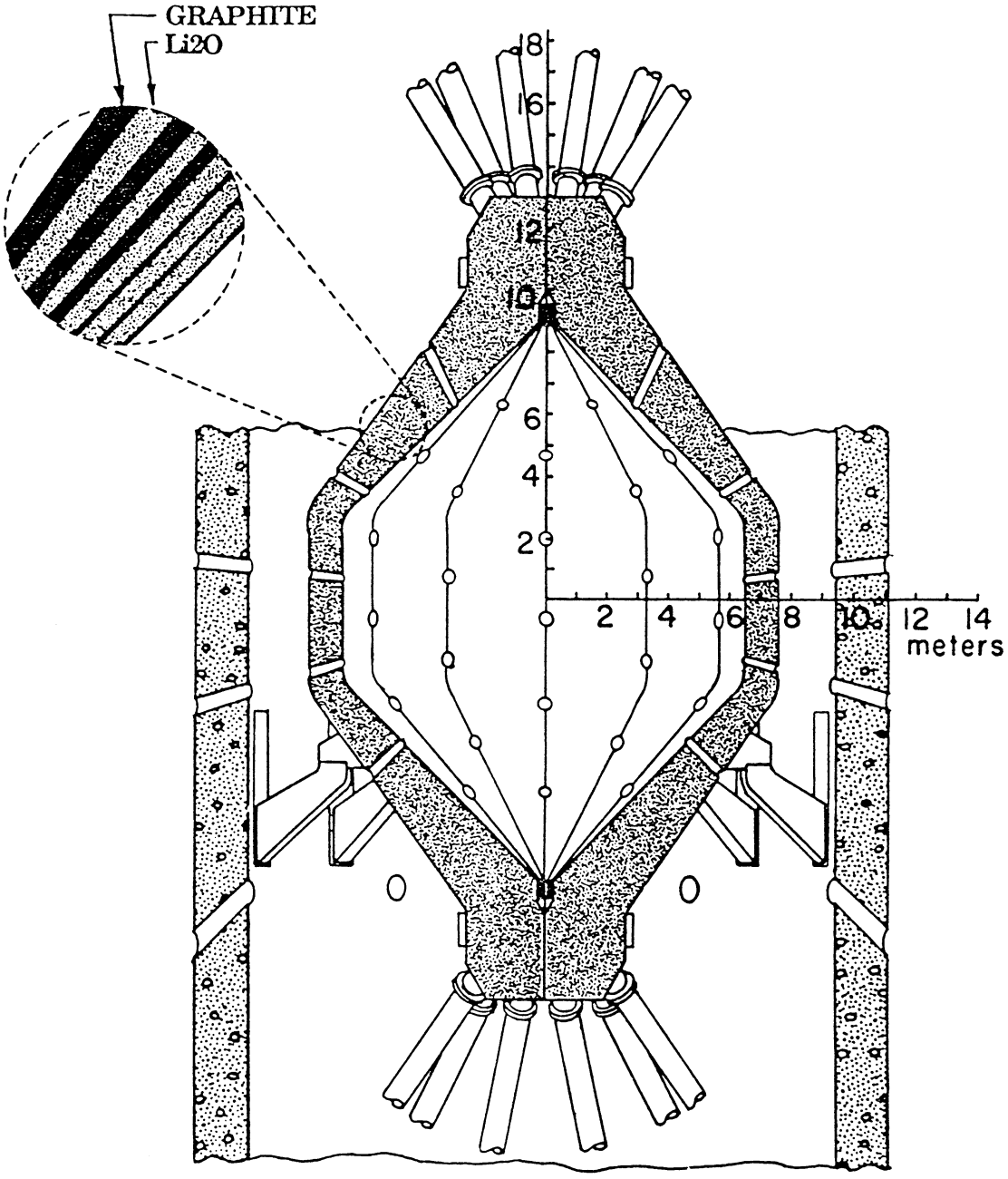

Fig. 3.42. Side view of the SOMBRERO chamber.

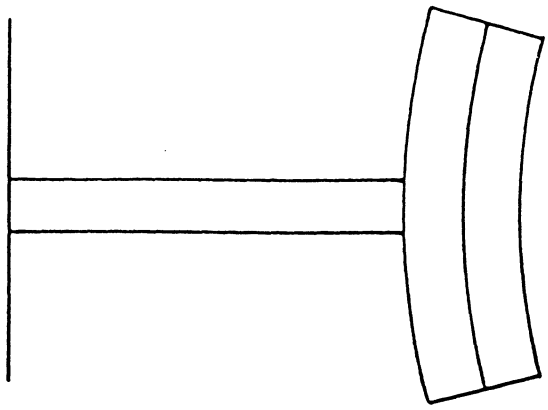

TOP VIEW

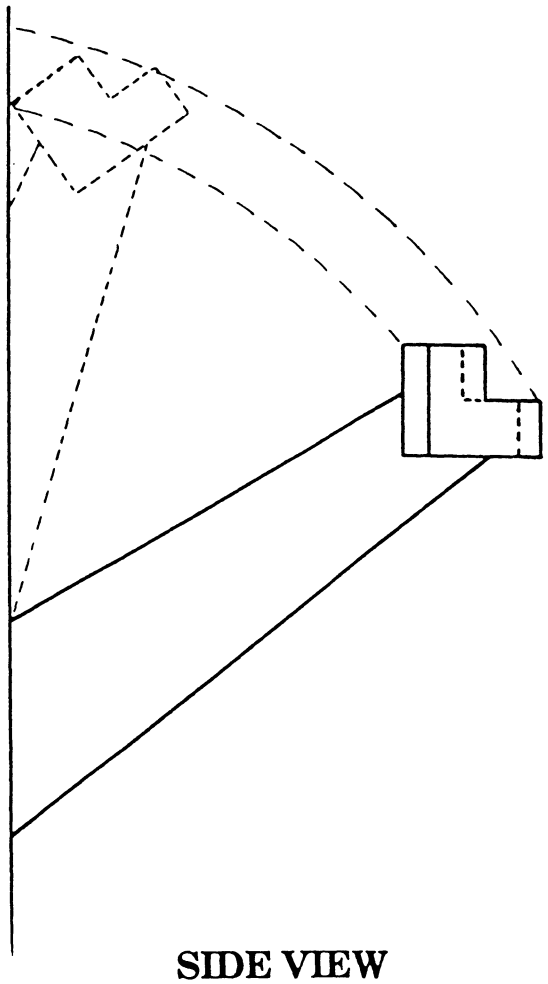

SIDE VIEW

Fig. 3.43. Schematic view of a chamber support.

3.2.4 Chamber Vacuum System

3.2.4.1 Vacuum Requirements

The atmosphere in the chamber is 0.5 torr of Xe gas. Since the beam ports in the chamber are open onto the reactor building, the atmosphere in the reactor building must be the same. The vacuum system must perform the following functions:

- Initial evacuation from atmospheric pressure to 0.1 torr.
- After Xe is injected up to a pressure of 0.5 torr, the vacuum system must recirculate it at some predetermined rate.
- Steady state evacuation of fusion products (unburned D, T and generated He).
- Steady state evacuation of leaks from the chamber and into the building.

The internal volume of the reaction chamber is 1.37×10^6 l. For the present it is felt that one gas changeover per second is appropriate which means a pumping speed of 1.4×10^6 torr l/s.

The volume of the building is 900,000 m^3. The time needed to evacuate this volume with a constant pumping speed of 1.4×10^6 l/s is:

$$t = \frac{V}{S} \ln\left(\frac{P_1}{P_2}\right)$$

where

V = volume (liters),
S = pumping speed (liters/s),
P_1 = initial pressure (760 torr), and
P_2 = final pressure (0.1 torr).

This gives t = 5744 s or 1.6 hours, which is a very reasonable time considering the evacuated volume. The pumping speed of 1.4×10^6 l/s will not be degraded by pipe conductances, etc., since the pumps will be located in close proximity to the building.

3.2.4.2 Leak Tolerance

Qualitatively, the breakdown threshold for He is an order of magnitude higher than for Xe, and thus it would seem that if the He gas pressure in the chamber was equivalent to that of Xe (0.5 torr), this implies a He leak rate of 7×10^5 torr l/s. At an average pressure of one atmosphere (average between 2 atm and 0.5 torr) this amounts to 921 l/s.

Leakage in the viscous flow regime where pd > 0.55 torr-cm the conductance of a hole is given by:

$$C = \frac{1333\,\pi\,r^4\,p}{8000\,\eta\,l} \quad \text{liters/s}$$

where

r = hole radius,
p = average pressure,
d = hole diameter,
η = gas viscosity, and
l = length of hole.

For this equation to be valid d must be:

$$d > (0.55 \text{ torr-cm}) / (760 \text{ torr})$$

$$d > 7.2 \times 10^{-4} \text{ cm}$$

We can now calculate the size of the hole needed to produce a leak of 921 l/s:

$$r = \left[\frac{8000\,C\,\eta\,l}{1333\,\pi\,p}\right]^{1/4}$$

The viscosity of He gas at 760 torr and 1500 K is 615×10^{-6} g/cm·s and l, the FW thickness, is 1.0 cm. This gives an r = 0.19 cm or a hole of 0.38 cm diameter.

A more realistic way of looking at this problem is to see how many holes of smaller diameter can be tolerated. It is likely that there will be many small leaks rather than several large ones. Figure 3.44 shows the number of pin holes in the FW as a function of hole diameter. It can be seen that there can be 1.4×10^9 holes of 20 μm diameter to obtain this leak rate. On the other end, the number of 500 μm diameter holes is 3670.

There is very little information on the leak tightness of 3D and 4D weaves of C/C composites. We have assumed that the inside surface (Li_2O side) of the chamber channels will be coated with a thin coating of SiC for which there is some leak tightness information. It is postulated that the most likely leaks will be very small tortuous ones longer than the FW thickness. From the above analysis, it seems that this system is amenable to many such leaks.

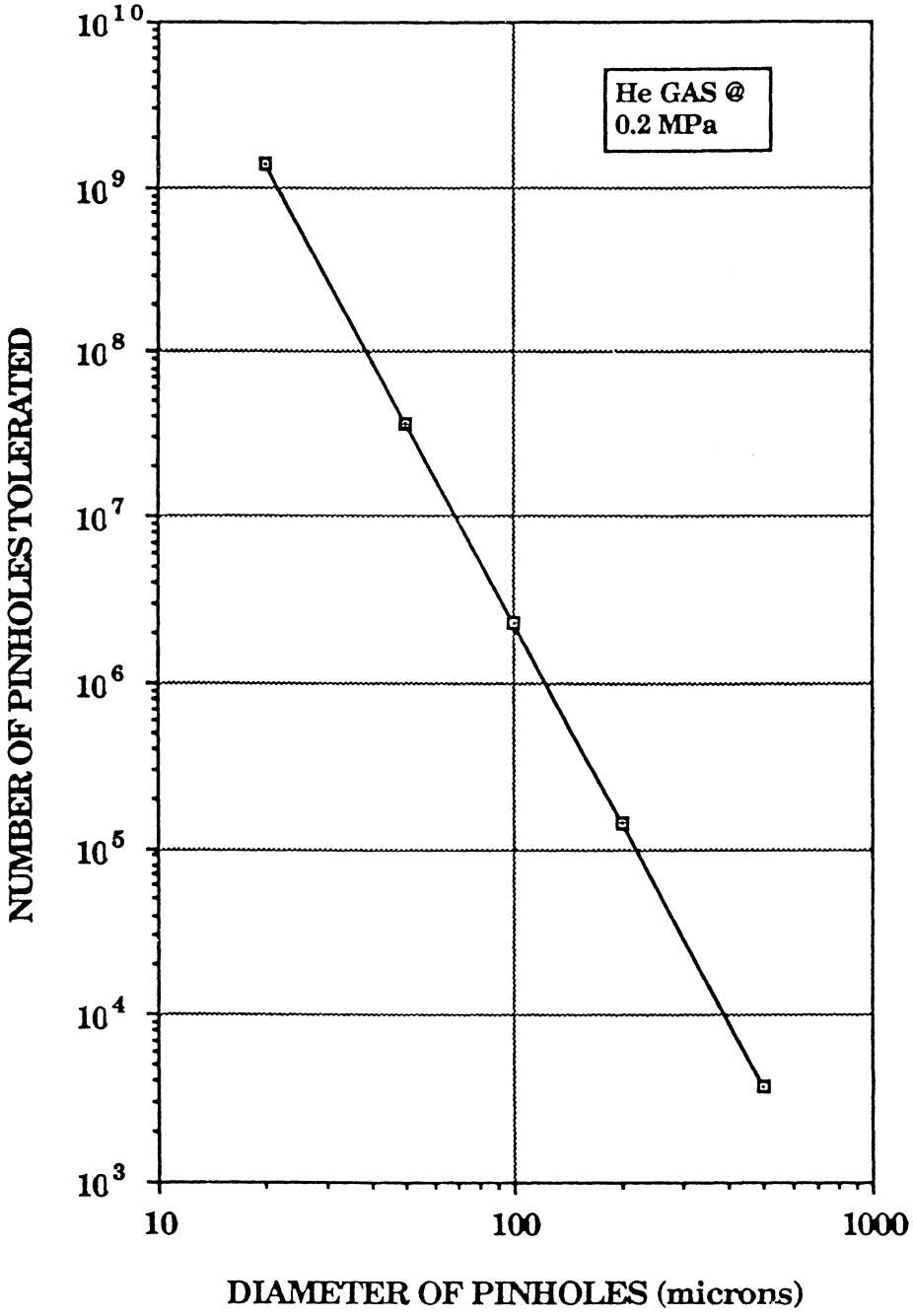

Fig. 3.44. Leak tolerance of SOMBRERO chamber - Number of pinholes tolerated as a function of pinhole diameter.

3.2.4.3 Vacuum System Design

The most appropriate pumps to operate in the 0.5 torr regime are Roots blowers. They comes in large capacity, are very rugged, dependable, and do not use oil for sealing. Instead they depend on well balanced rotors and definite clearances between the moving parts, such that operation at high rotational speeds are possible. Among the attributes of Roots blowers are:

- High Volumetric Efficiency
- High Pumping Speed Over Large Pressure Range
- Sturdy Construction, Small Size, Quiet Running
- Contact Free Rotation Of Interlocked Impellers
- Lubrication Free Pump Chamber
- Reliable Operation with Little Maintenance
- Easy oo Dismantle And Clean
- Low Operating Cost
- Unaffected by Contaminating Gases, Vapors, and Dust.

The recommended pressure rise for Roots blowers is 40 torr. Thus the primary Roots blowers' pressure will raise the effluent pressure from 0.5 torr to 40 torr and the secondary blowers to 80 torr. Dry sealed mechanical pumps will then deliver the effluents to Xe purification and hydrogen isotope recovery and separation system at near atmospheric pressure. Roots blowers with capacities of 10^4 l/s are currently available. It is not out of the question that pumps with capacities of 2 or 3×10^4 l/s will be available in which case, the number of primary blowers will be 46. These will be backed up by 10 secondary blowers. The estimated power consumption is 15 MW. Table 3.11 summarizes the vacuum system parameters.

Table 3.11. Vacuum System Parameters

Chamber Volume (l)	1.37×10^6
Reactor Building Volume (l)	9×10^8
Pressure of Xe in Chamber (Torr)	0.5
Estimated Pumping Speed (l/s)	1.4×10^6
Estimated Time to Evacuate Building (h)	1.6
Capacity of Roots Pumps (l/s)	3×10^4
Number of Primary Pumps	46
Number of Secondary Pumps	10
Power Consumption (MW)	15

3.2.5 Neutronics Analysis

3.2.5.1 Neutronics Model and Assumptions

The main objective of the neutronics analysis is to optimize the blanket design to insure tritium self-sufficiency while maximizing the overall reactor energy multiplication. The solid angle fraction subtended by the 60 beam ports in the SOMBRERO chamber is only 0.25% resulting in negligible loss of breeding. Hence, overall tritium self-sufficiency can be achieved with a modest local (1-D) tritium breeding ratio (TBR). This attractive feature of inertial confinement reactors allows for a simple blanket design in which no special neutron multipliers are needed. The local TBR for SOMBRERO is required to be at least 1.15 to achieve overall tritium self-sufficiency taking into account radioactive decay, loss between production and use, and maintaining the equilibrium tritium inventory in the different reactor components. In order to enhance the safety and environmental features of the design, low activation materials are used. Carbon/carbon composite structure and Li_2O breeder are used in the SOMBRERO blanket. The 1-cm-thick bare chamber structural wall has a minimum distance of 6.5 m from the target and is protected from the target x rays and debris by a 0.5 torr of Xe gas. In this section, the neutron-induced damage in the blanket structure is calculated to determine the achievable lifetime. The lifetime of the final optics is also determined. In addition, an objective of this neutronics analysis is to provide adequate biological shielding to maintain an acceptable operational biological dose rate <2.5 mrem/hr everywhere outside the reactor building.

Neutronics calculations for SOMBRERO have been performed using one-dimensional spherical geometry. The discrete ordinates code ONEDANT[3.30] was utilized along with 30 neutron - 12 gamma group cross section data based on the ENDF/B-V evaluation. A point isotropic source is used at the center of the chamber emitting neutrons and gamma photons. The target spectrum takes into account neutron multiplication, spectrum softening, and gamma generation resulting from the interaction of the fusion neutrons with the dense target material. One-dimensional spherical geometry neutronics calculations have been performed for a generic single shell target configuration at ignition.[3.31] The DT core is compressed to 485 times its solid density to a ρR-value of 2 g/cm^2 resulting in significant neutron target interactions. A uniform 14.1 MeV neutron source was used in the compressed DT fuel zone. For each DT fusion reaction, 1.025 neutrons are emitted from the target with an average energy of 11.64 MeV. In addition, 0.013 gamma photons are emitted with 3.85 MeV average energy. The energy spectra of neutrons and gamma photons emitted from the target are shown in Fig. 3.45. 2.1% of the fusion energy is lost in endoergic reactions in the target, and 69.5% of the target yield is carried by neutrons and gamma photons, which interact with the blanket material resulting in tritium breeding, nuclear heating, and radiation damage. The rest of the target yield is carried by x rays and debris which deposit their

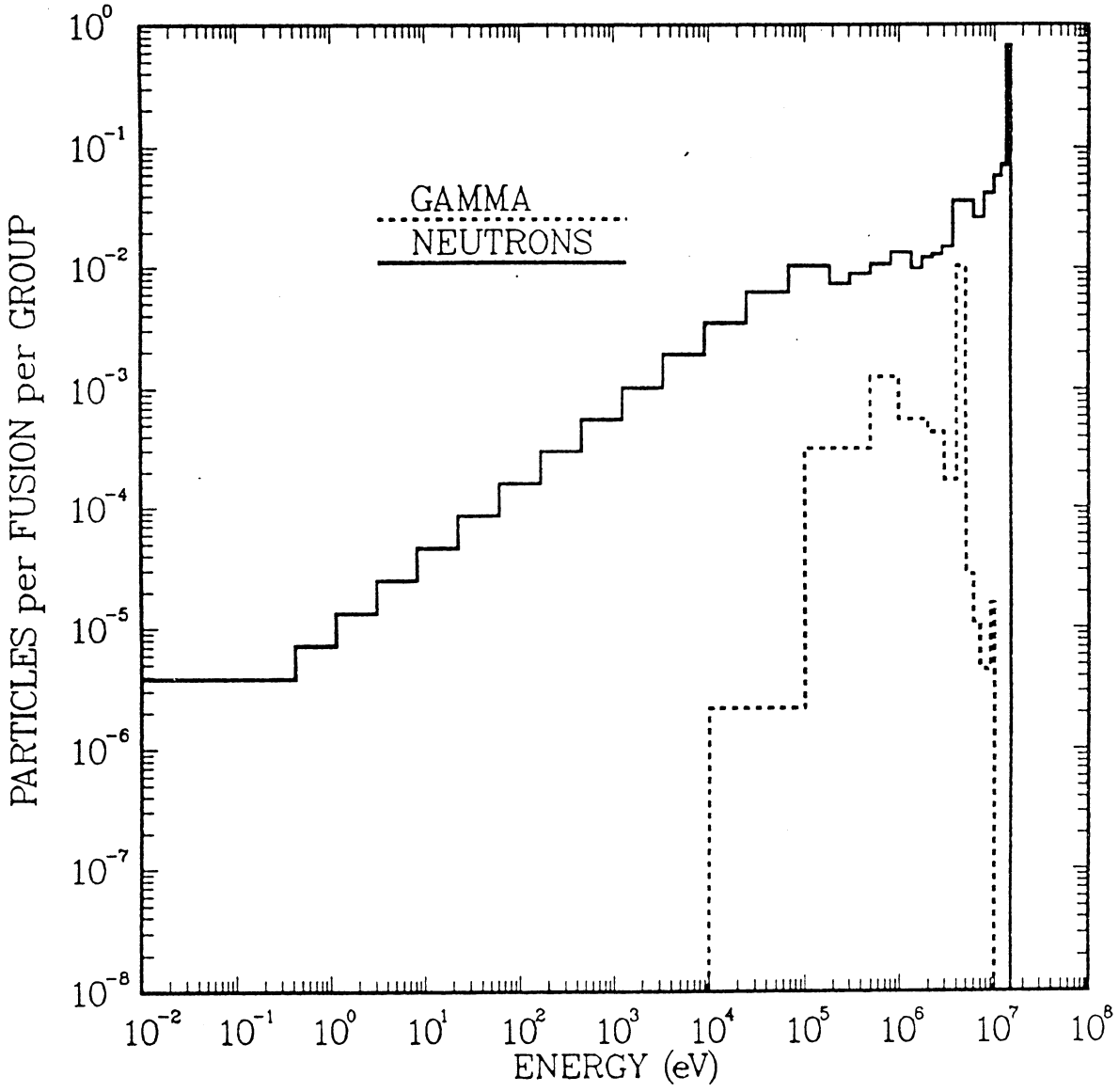

Fig. 3.45. Energy spectra of neutrons and gamma photons emitted from the target.

energy at the front surface of the blanket. The blanket nuclear energy multiplication (M_n) is defined as the ratio of the total blanket nuclear heating resulting from neutron and gamma interactions to the energy carried by the direct neutrons and gamma photons incident on the first wall. This quantity is a measure of the energy multiplication capability of the blanket and is to be compared with the energy multiplication factor commonly used in magnetic confinement designs. To take into account the surface energy deposited by x rays and ion debris and the energy lost in target endoergic reactions, an overall energy multiplication factor (M_o) can be defined for IFE reactors. M_o, which depends on the target design, is the ratio of total thermal power deposited in the target and blanket to the DT fusion power. For the target design used here, M_o is related to M_n via

$$M_o = 0.979\ [0.695\ M_n + 0.305]\ .$$

The results presented here are normalized to a target DT fuel yield of ~400 MJ and a repetition rate of 6.7 Hz.

3.2.5.2 Blanket Parametric Analysis

Several neutronics calculations have been performed to investigate the impact of the different design parameters on the nuclear performance of the blanket. In these calculations, the lithium enrichment, blanket thickness, and structure content have been varied. In addition, the impact of using a metallic reflector was assessed. The nuclear performance parameters considered in this analysis are the tritium breeding ratio (TBR) and the overall energy multiplication (M_o). In the calculations, a 1-cm-thick carbon/carbon first wall is located at 6.5 m from the target. Li_2O solid breeder moving bed is used in the blanket at a packing fraction of 0.6. The density of the Li_2O used to be 90% of the theoretical density. In the preliminary analysis, the carbon/carbon (C/C) composite structural material is considered to occupy 5% of the blanket volume. The option of using a 0.5 m thick metallic reflector consisting of 90% low activation ferritic steel and 10% He coolant was investigated. A concrete biological shield was used behind the reflector in the neutronics model.

The effect of lithium enrichment on TBR and M_o is shown in Fig. 3.46 for a 0.5 m thick blanket without a metallic reflector. The TBR increases slightly as lithium is enriched from 7.4 (natural) to 10% ^6Li. Increasing the enrichment beyond 10% reduces the TBR significantly. The peak TBR value is only 0.4% larger than the value achieved with natural lithium. In addition, enriching the lithium results in a small (<3%) enhancement in M_o. Based on these results, natural lithium is used in the Li_2O breeder. The effects of blanket thickness on TBR and M_o are shown in Figs. 3.47 and 3.48 for both cases with and without a metallic reflector. Using a metallic reflector increases the TBR by only 1.3% and M_o by 3.5% for a 0.7 m thick blanket. Since the

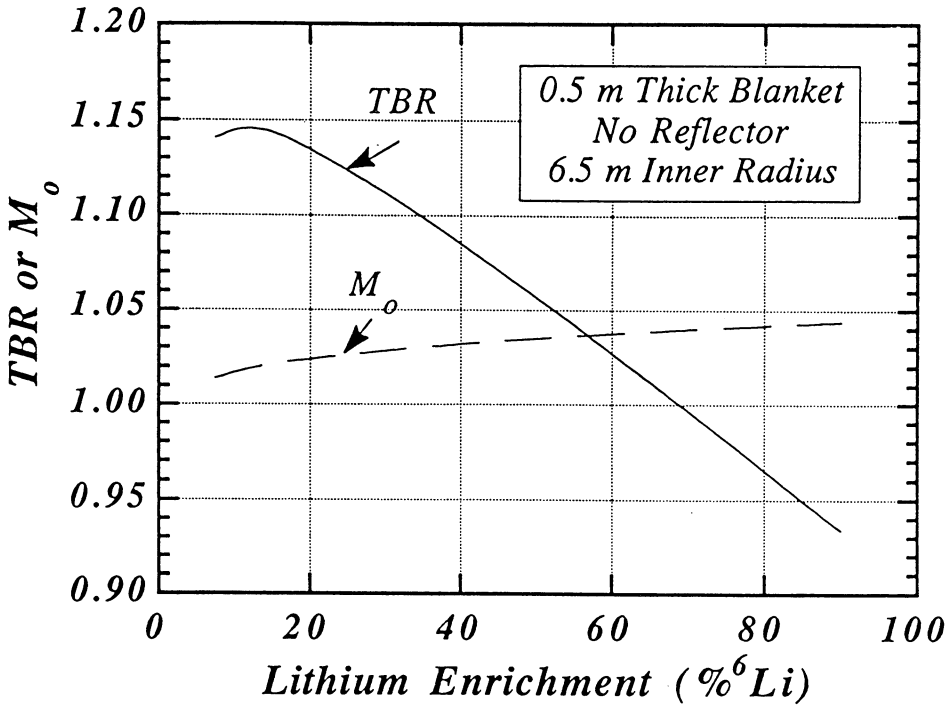

Fig. 3.46. Effect of lithium enrichment on TBR and M_o.

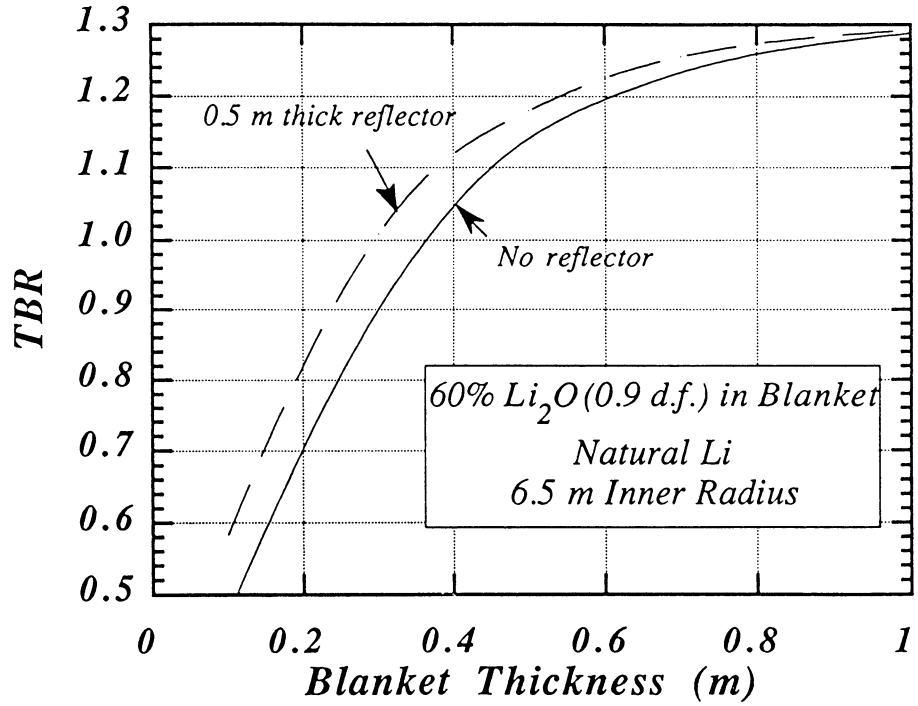

Fig. 3.47. Effect of blanket thickness on TBR.

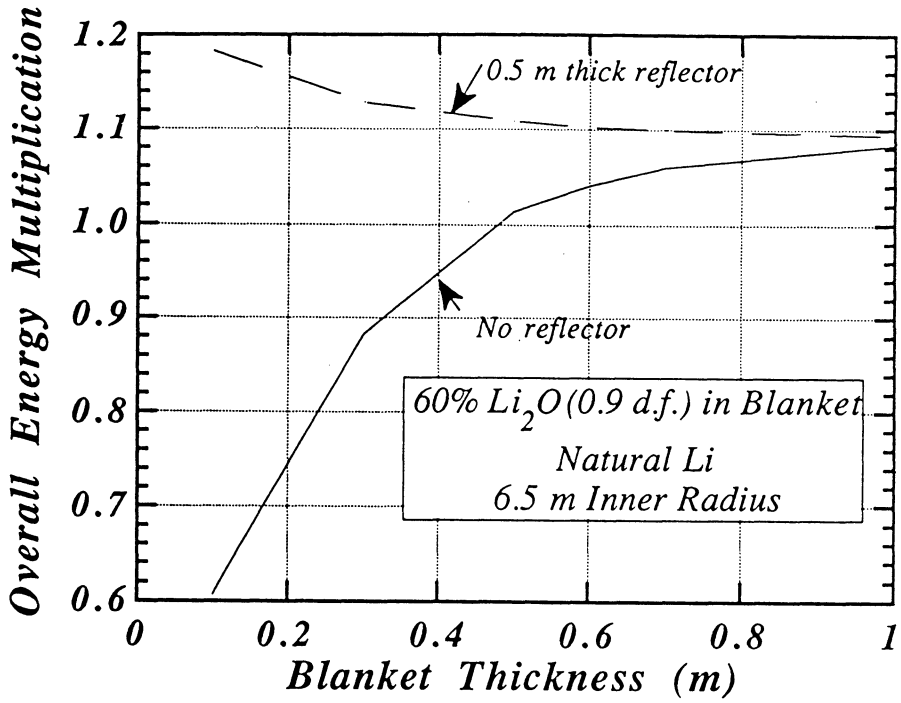

Fig. 3.48. Effect of blanket thickness on M_o.

enhancement of TBR and M_o is not significant, it was decided not to use a metallic reflector to avoid design complexity and steel activation. The TBR and M_o values achieved for a 0.7 m thick blanket without a reflector are 1.24 and 1.062, respectively. It should be noted that the preliminary parametric analysis given above overestimates the TBR and M_o values since the concrete shield is placed right behind the blanket. In the reference building layout, the concrete shield has an inner radius of 10 m. Hence neutron leakage at the back of the blanket will be excessive reducing neutron utilization in the blanket. The number of neutrons leaking from the back of the 0.7 m thick blanket is 0.124 per DT fusion in the target. This results in decreasing the TBR and M_o values to 1.174 and 1.039, respectively.

In order to increase neutron utilization in the blanket, the use of a carbon reflector is considered. Table 3.12 lists the nuclear performance parameters for different design options utilizing a carbon reflector. In option 1, no reflector is used and the carbon structure content is 5% in the blanket. In option 2, a 0.5 m thick carbon reflector with 10% He coolant is used behind the 0.7 m thick blanket. The TBR and M_o values increased to 1.275 and 1.069, respectively. Notice that nuclear heating in the reflector amounts to only 2% of the total nuclear heating and is not included in the calculated energy multiplication. In option 3, 4, and 5, instead of using a separate carbon reflector, a relatively thicker blanket is used with the volumetric content of the carbon structure varying increasing towards the back. The blanket is divided into three zones with

different structure contents. In these options, the total blanket and reflector thickness is reduced compared to the case with a separate shield. The values for neutron leakage at the back of the blanket are 0.017, 0.016, and 0.009 neutrons per fusion in options 3, 4, and 5, respectively, compared to 0.124 without a reflector. Comparing the results for options 3, 4 and 5, it is clear that TBR and M_0 are not sensitive to the thickness and structure content of the back layer of blanket. Therefore, design option 3 is chosen for the reference SOMBRERO blanket design.

Table 3.12. Nuclear Performance for the Different Design Options.

Option	Blanket * Thickness (m)	Zone Thickness (cm)	%C in Blanket	Reflector Thickness (m)	TBR	M_o
1	0.7	69	5	0	1.174	1.039
2	0.7	69	5	0.5	1.275	1.069
3	1.0	19/40/40	3/20/50	0	1.251	1.080
4	1.0	19/40/40	3/20/60	0	1.251	1.080
5	1.1	19/40/50	3/20/50	0	1.259	1.083

* Includes 1-cm-thick C/C first wall

3.2.5.3 Neutronics Parameters for the Reference Design

The radial build of the reference SOMBRERO blanket design is given in Fig. 3.49. A 1-m-thick blanket is used with increasing carbon content towards the back. The 1-D local TBR for the reference blanket is 1.25. The overall TBR value is expected to be close to the 1-D value since the solid angle fraction subtended by the 60 beam penetrations is less than 0.3%. The overall reactor energy multiplication is 1.08. For a DT fusion power of 2677 MW, the total thermal power is 2891 MW with ~800 MW deposited at the surface of the first wall by x rays and debris and 2100 MW deposited volumetrically in the blanket by neutrons and gamma photons. Figure 3.50 shows the radial variation of power density in the blanket. The peak first wall power density is 10.9 W/cm^3. The power density in the blanket varies from 12.6 W/cm^3 at the front to 0.1 W/cm^3 at the back.

Figure 3.51 gives the radial variation of damage rate in the carbon/carbon composite structural material used in the blanket. The peak dpa rate is 15.3 dpa/FPY, which occurs in the first wall at the reactor midplane. The dpa rate drops to 0.05 dpa/FPY at the back of the blanket. The peak helium production rate in the structure is 3770 He appm/FPY at the first wall. The main problem for the c/c composite is the dimensional stability after operating at high temperature in a neutron environment for long periods of time. During high temperature irradiation, the graphite

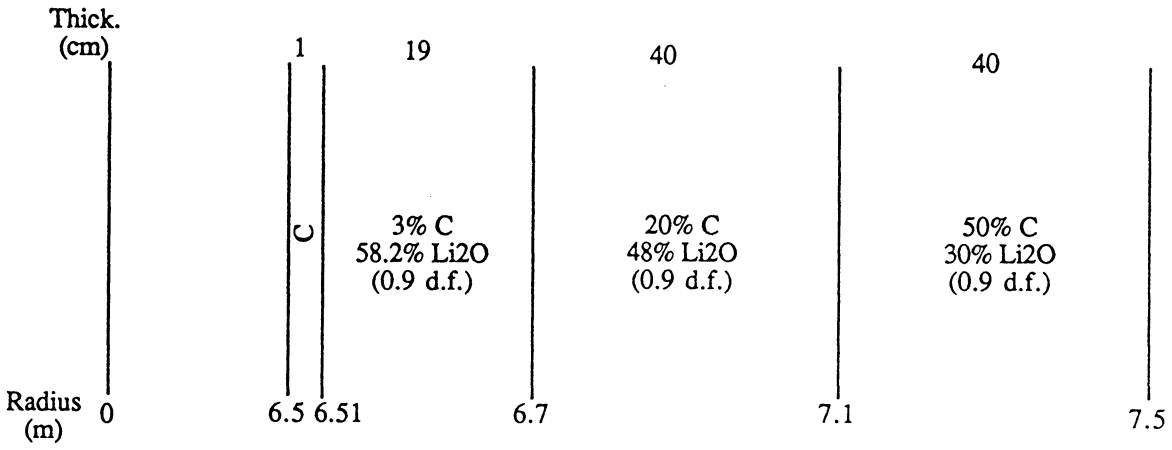

Fig. 3.49. Radial build of reference SOMBRERO blanket design.

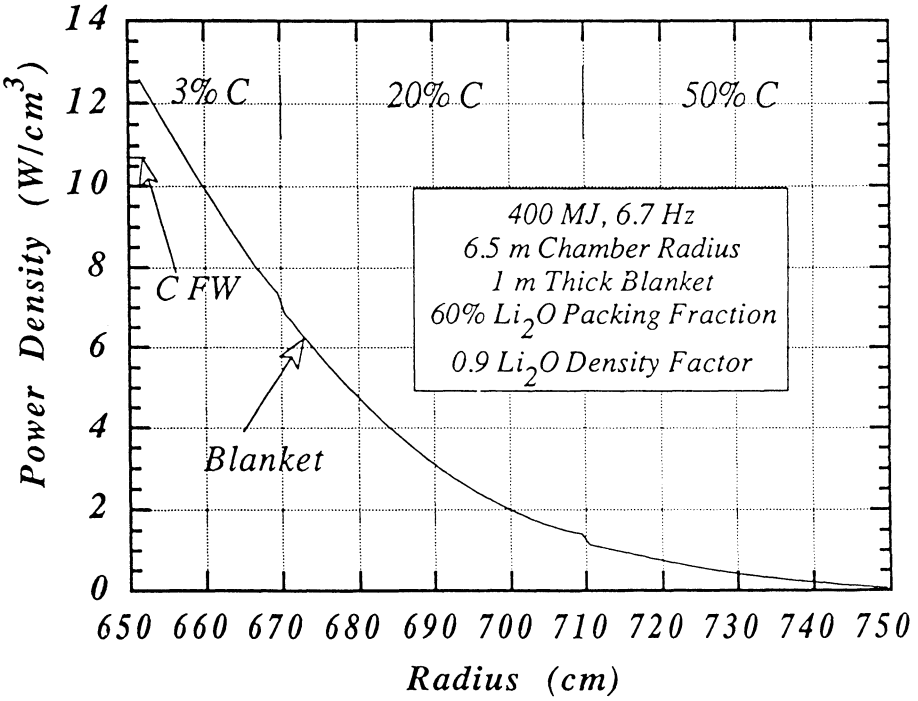

Fig. 3.50. Radial variation of power density in blanket.

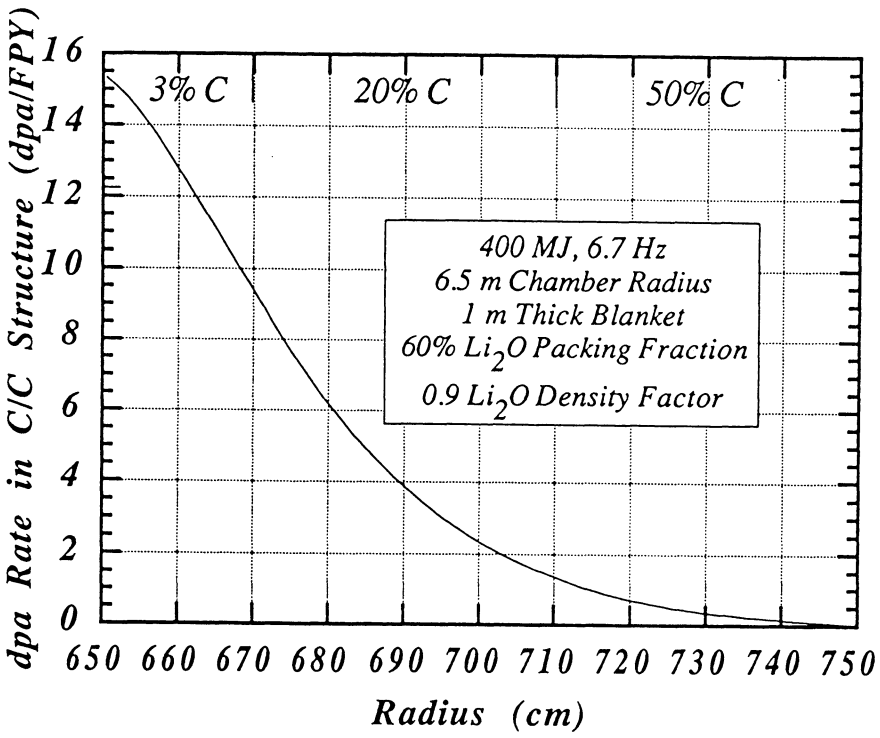

Fig. 3.51. Radial variation of structure damage rate in blanket.

first shrinks and then expands at a very rapid rate. A useful lifetime is usually determined when the dimensional change reverses and crosses the zero swelling line. Birch and Brocklehurst[3.32] reported data on three forms of graphite showing that AXZ-5Q1 graphite will reach the zero swelling point at a fluence of 35 dpa at 1300°C. The graphites tested thus far have not been optimized for the fusion environment. We assume that the dpa limit can be increased to 75 dpa by optimizing the graphite for a fusion neutron environment in a materials development program. With a dpa limit of 75 dpa, the C/C composite first wall is expected to have ~5 FPY lifetime.

3.2.5.4 Biological Shielding

The concrete biological shield thickness required to achieve an operational dose rate of 2.5 mrem/hr depends on the location of shield and material between target and shield. Several 1-D calculations have been performed to determine the required shield thickness. The shield is composed of 70% concrete, 20% steel, and 10% He coolant. It was found that 25 cm of the steel reinforced concrete shield will reduce the dose rate by an order of magnitude.

Figure 3.52 shows the effect of shield thickness on the biological dose rate during operation at the back of the shield. The inner surface of the shield is at a distance of 50 m from the target with no material used in the region between the target and the shield. This is representative of the areas of the reactor building exposed to the direct source neutrons streaming through the

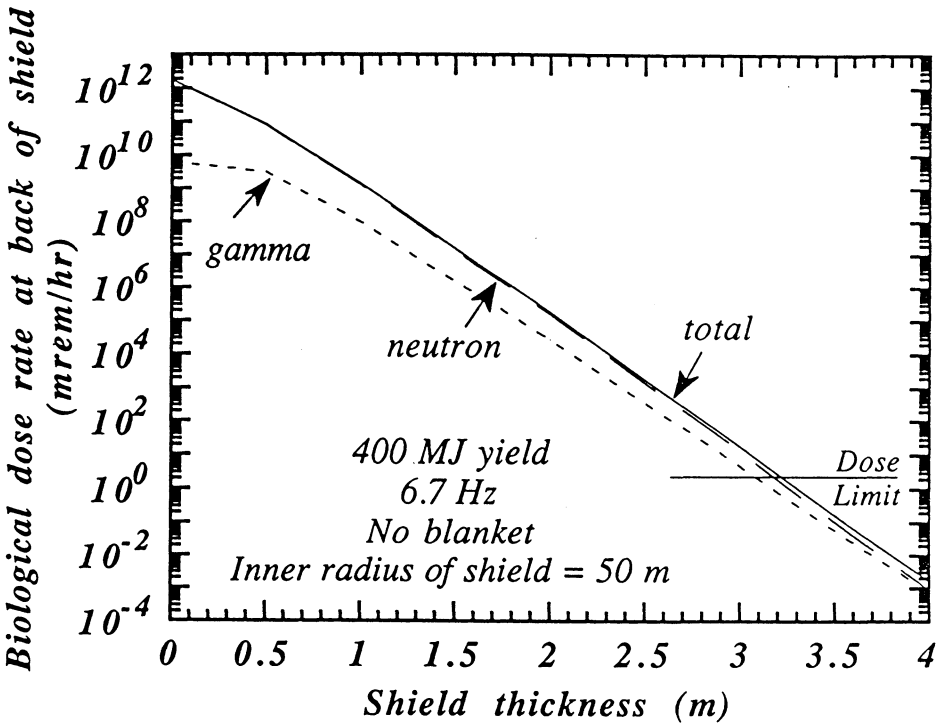

Fig. 3.52. Operational biological dose rate as a function of shield thickness without blanket.

beam ports. The results indicate that a wall thickness of 3.2 m is required in these zones located inside the direct neutron traps attached to the containment building. Figure 3.53 gives the effect of shield thickness on the operational dose rate for a concrete shield located at 10 m from the target with the 1-m-thick blanket included in the model. It is clear from the results that a total shield thickness of 2.7 m is required behind the blanket.

The chamber is surrounded by a cylindrical concrete shield with an inner radius of 10 cm. The IHX and steam generators are located in the space between this inner shield and the outer containment building. The thickness of the inner shield is determined such that hands-on-maintenance can be performed on these components following shutdown. The dose rate resulting from the decay gamma emitted from the activated material should not exceed 2.5 mrem/hr one day after shutdown. Activation analysis for previous reactor designs indicate that activation of the shield and outlying components result in a dose rate of 2.5 mrem/hr one day after shutdown if the neutron flux at the back of the shield is kept at a level of ~10^6 n/cm^{2}s during operation. The results in Fig. 3.54 imply that a 1.7 m thick shield wall surrounding the reactor at a radius of 10 m makes it possible to perform hands-on-maintenance in the space between it and the outer containment building. This is confirmed by the activation analysis discussed in Section 6. The outer building wall, therefore, needs only to be 1 m thick.

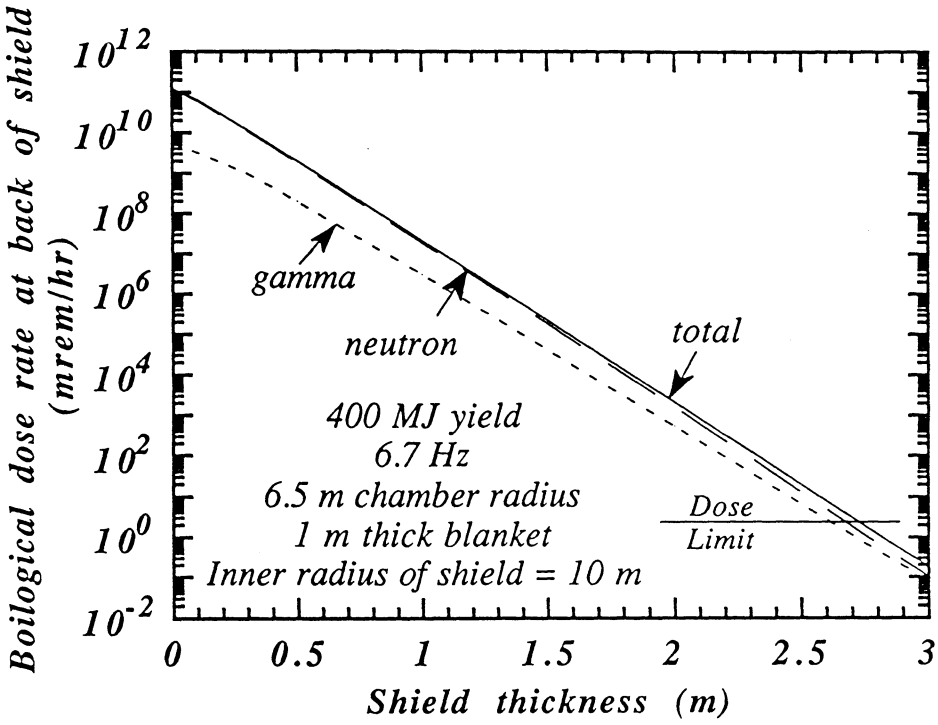

Fig. 3.53. Operational biological dose rate behind the blanket as a function of shield thickness.

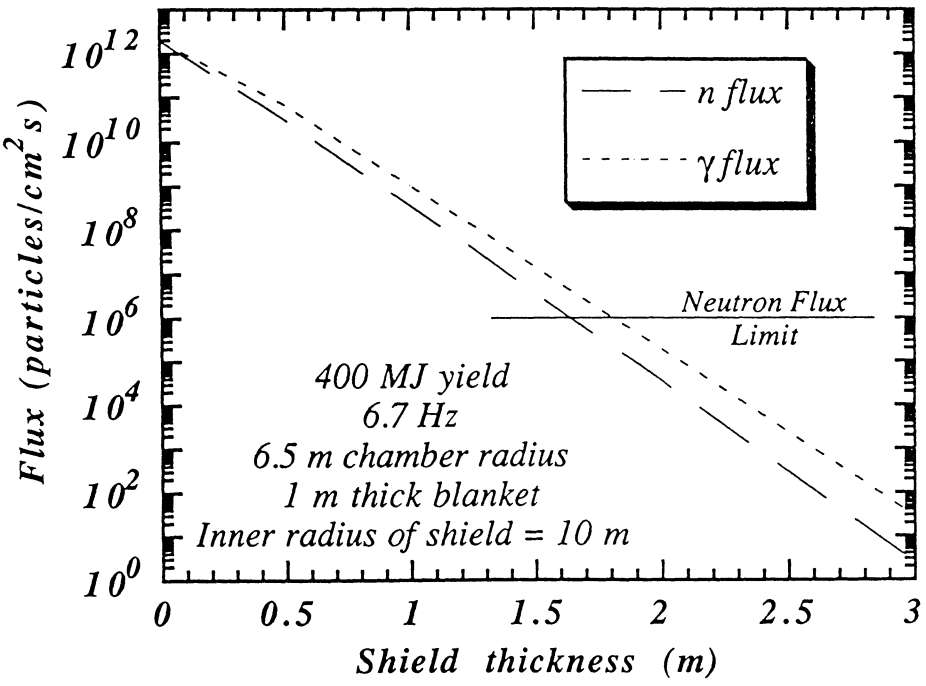

Fig. 3.54. Neutron and gamma flux at the back of the inner biological shield.

3.2.5.5 Lifetime of Final Optics

The lifetime of the final focusing (FF) mirrors depends on the neutron fluence limit for the dielectric coated or metal mirror, the solid angle fraction subtended by the beam ports ($\Delta\Omega/4\pi$), damage recovery with annealing and the location of the mirror relative to the target. The solid angle fraction subtended by the 60 beam ports in SOMBRERO is only 0.25%. The fast neutron flux ($E_n > 0.1$ MeV) level at the grazing incidence metal mirror (GIMM) located in the direct line-of-sight of the source neutrons at 30 m from the target has been determined to be 8.2×10^{12} n/cm^{2}s and is due mostly to the direct source neutrons. Figure 3.55 gives the lifetime for these mirrors as a function of the fast neutron fluence limit and the recovery fraction with annealing. The lifetime without annealing is determined by dividing the fast neutron fluence limit by the fast neutron flux at the mirror. If partial recovery is possible with annealing, the lifetime can be extended until time between anneals becomes very small. A minimum time of one month between anneals is assumed. It can be seen that a GIMM at 30 m from the target, assuming an 80% annealing recovery, can have a lifetime of 17 FPY if the limit is 10^{21} n/cm^2. If the limit is 10^{22} n/cm^2, it can have a lifetime of 40 FPY with no annealing. It is clear that the lifetime of the GIMM is very sensitive to the neutron fluence limit and damage recovery by annealing. Experimental data on radiation damage to metallic mirrors are essential to allow for a more accurate prediction of the GIMM lifetime.

Although the dielectric coated mirrors are placed out of the direct line-of-sight of the source neutrons, secondary neutrons resulting from the interaction of the streaming source neutrons with the GIMM and outer reactor building can cause significant radiation damage to the coating. To reduce the secondary neutron flux, the source neutrons are directed into high aspect ratio traps as shown in Fig. 3.1. Neutronic evaluations show that holes with aspect ratios ~2 will effectively trap most of the neutrons, allowing a negligible amount (<5%) of low energy neutrons to backscatter. As a result, the fast neutron flux ($E > 0.1$ MeV) at the dialectic coated mirrors located at 50 m from the target was determined to be 8.6×10^8 n/cm^{2}s. Figure 3.56 gives the lifetime of the FF mirrors as a function of fluence limit and distance from the target. At a 10^{18} n/cm^2 fast neutron fluence limit, the SOMBRERO FF mirrors will be lifetime components with a lifetime of 37 FPY if they are located at 50 m from the target. Again, experimental data on the impact of radiation damage on the reflectivity of the dielectric coating of the FF mirrors are required.

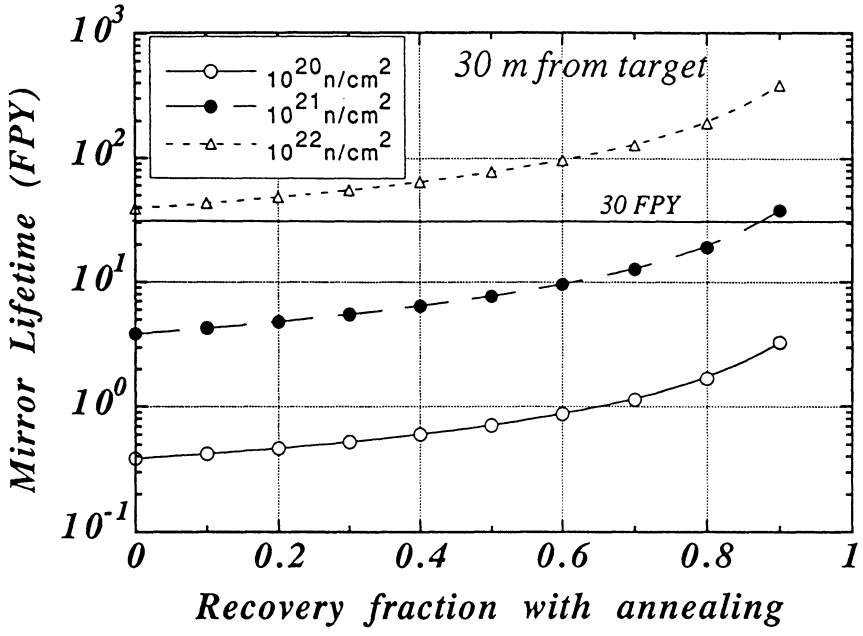

Fig. 3.55. Lifetime of metallic grazing incidence mirrors.

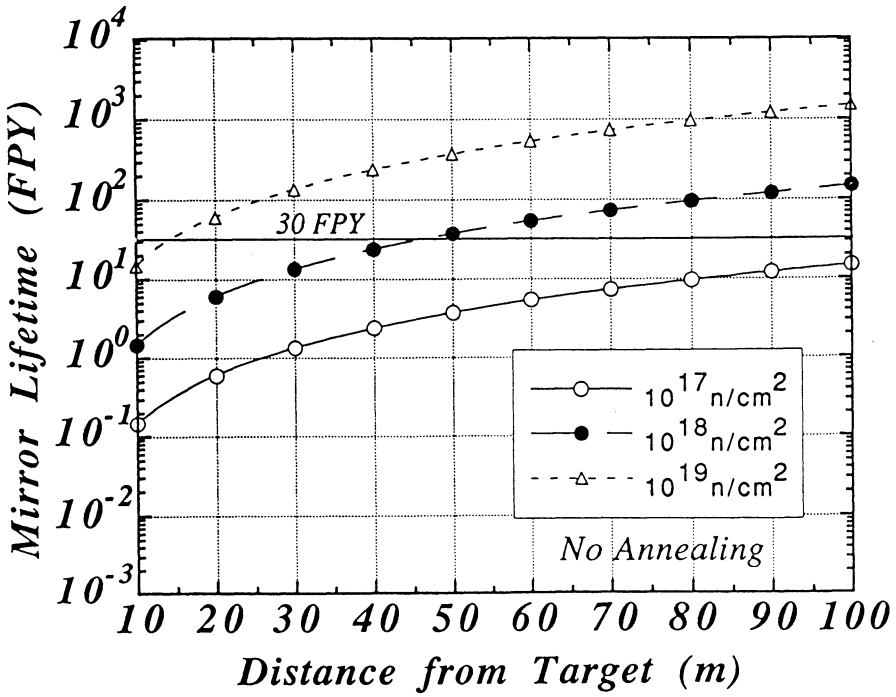

Fig. 3.56. Lifetime of dielectric coated FF mirrors.

3.2.6 Tritium Considerations

3.2.6.1 Chemical State of the Tritium

To produce ~2700 MW of fusion power in the SOMBRERO chamber, tritium is burned at a rate of 410 g(T)/d. Tritium is produced in the Li_2O breeder at the burn rate times the tritium breeding ratio (1.25) to yield 513 g(T)/d. This tritium is soluble in the oxide and is especially difficult to desorb from the surface of the oxide particles. For this reason, most experimentalists utilize a hydrogen overpressure in a circulatory He gas stream to aid in the desorption of T_2 from the in-situ breeder in the blanket.[3.33] Although the breeder particles in SOMBRERO circulate in a closed loop to the heat exchanger, the simplest T recovery scheme still appears to be based upon the evolution of T from the breeder to the gas phase with subsequent recovery of the T from the gas.

The use of H_2 overpressure does not appear practical in the SOMBRERO design because of the formation of HT, which would be carried by the He to the IHX and result in a high permeation rate of T into the lead intermediate heat transfer fluid and eventually into the steam. Because lead has a low solubility for T_2, the only technique to reduce the T_2 concentration in the intermediate loop would be by vacuum pumping, which is very expensive at the low pressures required.[3.34] Another reason to avoid the use of excess H_2 is that the oxygen activity can be decreased to 10^{-25} atm at which point decomposition of Li_2O begins[3.35] forming gaseous species Li and LiH(T), both of which would react with the carbon structure. For these reasons, the oxygen activity was kept $>10^{-10}$ atm so that the T exists as the species HTO, which would permit only very limited T permeation at the IHX. These objectives were accomplished by the addition of H_2O vapor to the He in an amount calculated by the relationship,

$$H_2 + \frac{1}{2} O_2 = H_2O \qquad K_{eq} = 3.2 \times 10^{11}\ \text{atm}^{-1/2} \ @\ 900\ \text{K}.$$

In order to obtain an O_2 activity of 10^{-10} atm, approximately 64 Pa of H_2O were added so that the ratio H_2O/H_2 was 3×10^6. The vapor pressure of the H_2O is much less than the vapor pressure of 3150 Pa required to form a second-phase[3.33] of LiOH(T) in the Li_2O. Such a second-phase would be detrimental because it melts at 417°C and would subsequently agglomerate the oxide particles.

In order to determine the solubility of T in the Li_2O, it is necessary to estimate the HTO partial pressure in the He and the rate of the HTO desorption from the surface of the particles. The determination of the steady-state concentration of HTO in the He is difficult in this design because the He is used at several different velocities for entrainment of the particles; consequently, four sets of He entrances and exits are provided, and the T content in the He of each set may be different.

Initially, we consider the He/HTO concentration which exists within the chamber. The inventory of Li_2O within the chamber is ~668 Mg, and the Li_2O flow rate is 5.55 Mg/s, which gives an average residence time of 120s. The volumetric flow rate is ~5 m^3/s. The He flows counter-current to the breeder at a slow velocity, ~2.5 m^3/s, and a pressure of 2 atm. At steady-state the T desorbs as HTO from the particles at the breeding rate; consequently, the partial pressure of HTO is 5.93 Pa.

Based upon the HTO partial pressure, the solubility of (OH) in the Li_2O can be calculated by use of the relationship,[3.33]

$$S_{OH}\ \text{appm} = 10^{-A}\,(9.864 \times 10^{-6}\,P_{H_2O})^{B} + 173\,(\exp - 2950/T)\,P_{H_2})^{1/2} \qquad (1)$$

where A and B are functions of temperature. The second term, P_{H_2} is very small compared to the first term because of the addition of H_2O. The first term was calculated, therefore, and corrected for the ratio of P_{HTO}/P_{H_2O} and the fact that HTO has only 1 T per molecule. The result indicated that the solubility of T in the Li_2O is 0.10 wppm, in good agreement with an initial estimate of ~0.08 wppm; therefore, for the total 2000 Mg of Li_2O, the T inventory is 160-200 g.

Alternatively, the tritium inventory was estimated based upon the desorption rate of HTO from the surface of the particles, based upon the relationship of the mean residence time,[3.36]

$$\tau = \frac{a^2}{15\,D} + \frac{a}{3}\left[\frac{a \cdot A_s \cdot \rho_{th} \cdot k}{3}\right]^{-1}$$

where

a	=	radius of the grains (~10 μm),
A_s	=	specific surface area (~5×10^{-2} m^2/g),
ρ_{th}	=	theoretical density of Li_2O (~2 g/cm^3),
k	=	desorption coefficient, and,
D	=	diffusion coefficient.

The first term in the above equation represents the diffusive holdup within the particles and is very small because of the small grain size. The measured desorption coefficient, k, has been observed[3.37] to be similar to that for H_2 desorption (i.e., ~1.1×10^{-5} cm/s); hence, the τ value calculated is 94 s. If the breeder were stationary in the chamber, it would have an inventory of ~57 g of (T) before it released T at the breeding rate. This result indicates that the tritium release does not reach steady-state until the breeder material has traveled 75% of the path through the chamber; consequently, some additional HTO will be released to the gas phase as the breeder particles circulate external to the chamber. Additionally, this result suggests that because the entire breeder circuit contains three times as much Li_2O as in the chamber, the total inventory is ~170 g of

T, in good agreement with the solubility data. Other factors to consider in the use of H_2O to control the oxidation state of the oxide breeder are (1) the sublimation of LiOH, (2) the vapor pressure of Li, and (3) potential corrosion of the carbon structure, as noted in the following discussion.

1) The vapor pressure of LiOH will be ~1.6×10^{-2} Pa (1.6×10^{-7} atm)[3.35] at 900 K. The sublimation of this material through the four He exit ports was calculated by use of the relationship,

$$\text{Sublimation Rate} = \frac{\text{velocity of vapor}}{4} \times \frac{\text{moles (LiOH)}}{m^3}$$

This calculation indicated that the sublimation rate would be

$$\frac{5 \times 10^{-4} \text{ moles (LiOH)}}{m^2 \cdot s}$$

Consequently, for 4 He exit ports of ~2.5 m^2/each, the total sublimation would be ~100 kg/day or only ~5% of the total Li_2O in the system.

2) The vapor pressure of metallic Li at 900 K is < 10^{-12} atm (Ref. 3.35) and would cause very minor corrosion of the carbon.

3) The corrosion of neutron irradiation pyrotitic graphite by H_2O vapor has been determined by Hirooka and Imai[3.38] at a series of temperature. For instance, at 880°C the corrosion rate is:

$$R = \frac{4.5 \times 10^{-10} \text{ g}}{cm^2 \cdot s \cdot atm^{1/2}}$$

Consequently, at the H_2O vapor pressure of 64 Pa, the graphite corrosion rate would be only 1.5 μm/yr.

In summary, the addition of a small excess vapor pressure of H_2O is advantageous for the following reasons:

1) It retains the T as the species HTO, which lowers the permeation rate at the IHX.
2) The corrosion rate of the graphite structure is not adversely affected.
3) The vaporization of LiOH(T) is not excessive.

3.2.6.2 Tritium Recovery

Tritium must be continuously recovered from two streams which exit from the chamber, namely (a) the breeder particle stream, and (b) the unburned target fuel which exits through the laser beam holes. Each stream must be processed separately, as described in the following scheme.

The Breeder Stream. Previously, in Section 3.2.6.1, it was noted that the steady-state rate of tritium desorption as HTO from the breeder particles would be the same as the tritium breeding rate, $\sim 6 \times 10^{-3}$ g(T)/s or $\sim 2 \times 10^{-3}$ moles (HTO)/s. Much of this HTO will exit with the He flowing at a rate of 2.5 m^3/s through the chamber; however, additional HTO will be released as the particles transit the entire system. During this transit four entrance/exist streams of He will be used to entrain the particles. If these streams have the same volumetric He flow rates, then, the HTO will be diluted by 10 m^3/s of He at a 2 atm pressure to yield a concentration of 2×10^{-4} moles (HTO)/m^3 with a partial pressure of HTO at 1.5 Pa. In order to recover the tritium at the breeding rate, 10 m^3/s of He must be processed to remove this HTO, and the H_2O at a pressure of 64 Pa. This removal step will utilize adsorption on a molecular sieve drying-bed with a dew-point comparable to -60°C or 1 Pa of H_2O vapor pressure. The HTO vapor pressure at the exit from the dryer will be therefore only 2.3×10^{-2} Pa.

In order to recover the tritium in the water desorbed from the desiccant, a water distillation column could be used to concentrate the HTO, followed by a catalyzed vapor-phase treatment with excess H_2 to yield HT, H_2 and H_2O. The H_2O would be removed by condensation and the gaseous species HT and H_2 would be sent to a cryogenic distillation system which is part of the Fuel Reprocessing System to prepare pure T_2. Alternatively, a newly developed high-temperature processing system[3.39] could be employed to catalytically treat the tritiated water with excess H_2 without using the water distillation system. Such a system avoids the undesirable feature of preparing concentrated tritiated water but increases the volume of gases for the cryogenic distillation system. In either case, pure T_2 would be prepared and sent to the target factory.

Processing the Unburned Target Fuel. Following each target burn event, the unburned fuel, approximately 70% of the injected fuel, together with the waste from the target shell are vaporized and propelled toward the chamber walls, where most of these vapors together with the Xe fill-gas are expelled through the beam ports. After these gases cool, Xe external to the chamber would rush into the partial evacuated chamber. The vaporized condensable gases would begin to condense and perhaps interfere with the subsequent laser beams. For this reason, clean Xe gas is injected into the chamber at a rate sufficient to refill the chamber once per second to a pressure of 0.5 torr. This sweep gas will contain 20.5×10^{-3} g(T)/m^3(Xe)STP plus deuterium and some target shell material, such as a CH-polymer.

The exhaust gases from the chamber will fill the open-spaces in the containment building to a pressure of 0.5 torr. The containment building has a volume of ~1.1×10^6 m^3, but several spaces are excluded for equipment; hence, the space open for the chamber exhaust might be ~30% of the total, e.g., 3.4×10^5 m^3. When filled with Xe, the Xe inventory would be 223 m^3(Xe)STP (1.3 tonnes). Using the previously determined T concentration per m^3(Xe) and the Xe inventory, we note that the total T inventory would be only 4.6 g(T) for the atmosphere in the containment building.

The atmosphere in the containment building would be processed continuously to remove the T, Xe, and other gases exhausted from the chamber. This process would require the removal of 0.54 m^3/s of Xe(STP), comparable to 4×10^5 torr-liters/s. At a pressure of 0.5 torr the required pumping speed is 8×10^5 l/s which could be readily accomplished with several Roots Blowers. This side-stream is purified using the following steps:

1) Filter the gases to remove large particles and cold-trap at 0°C to remove H_2O and oil vapors.
2) Catalytically oxidize to form CO_2, H_2O, DTO, etc.
3) Adsorb water species on a desiccant and CO_2 on an absorbant.
4) After removal from the desiccant, the H_2O species are catalytically treated with excess H_2 to yield the hydrogen species HT, DT, HD, etc. which are sent to the cryogenic distillation columns for the preparation of pure T_2 and returned to the target factory.
5) The Xe would be further purified, if needed, by distillation at -107°C which could also separate any He which might be leaked from the chamber blanket.

3.2.6.3 Permeation of Tritium Into the Power Cycle

A routine release of tritium from the breeder to the environment does occur via permeation of T_2 from the He carrier gas through the tubes of the intermediate heat exchanger (IHX) into the Pb intermediate heat transfer fluid. Lead was selected for the IHX because it would not react exothermally via chemical reactions with either the Li_2O particles or the steam, during accidents, while large exothermal reactions occur when Li_2O reacts with H_2O. Unfortunately, Pb has a very low solubility for T_2; hence, any T_2 which permeates into the lead is retained as gas bubbles, which eventually attain the same T_2 vapor pressure as the primary loop. Therefore, T_2 will permeate into the steam generator at the same rate as through the IHX. Gaseous T_2 could be recovered from the IHX loop by the use of ultra-low pressure vacuum pumps, but would be very costly. For this reason, this system has been designed to limit the permeation of T_2 at the IHX by the addition of H_2O to the primary loop to form HTO which will not permeate.

For ferritic steel tubes in the IHX, the permeation rate of T_2 is,

$$\phi_{T_2} = \frac{2 \times 10^5 \text{ Ci·mm}}{B \text{ m}^2\text{·d·(Pa)}^{1/2}} \left[\exp\left(\frac{11{,}100 \text{ cal/mole}}{RT}\right)\right] \frac{A (P_{T_2})^{1/2}}{t_w}$$

where

A = tube area (5.54×10^3 m^2),

t_w = tube wall thickness (1 mm),

R = 1.98 cal/mole·K,

T = temperature (918 K), and

B = oxide barrier factor

The barrier factor is due to the oxide on the steam side of the steam generator, which reduces the tritium penetration of ferritic steel[3.40] by a factor of ~100. The helium has a P_{T_2} of 2.1×10^{-6} Pa as it exists the top of the chamber. If this gas were transported to the IHX, the tritium would diffuse; however, this stream is subjected to 3 new streams of He with very low T_2 concentration so that the P_{T_2} could easily be diluted by 90% to 2.1×10^{-7} Pa when the He reaches the IHX. Based upon these assumptions, the tritium loss to the steam cycle would be only 12 Ci/d.

3.2.6.4 Pathways of Tritium Release

Some tritium does reach the off-site environment during normal and off-normal operations. In order to assess the potential for these releases, the inventories and rates of processing of tritium in each of the processing systems were determined and the vulnerability of equipment to failure with release of tritium was assessed. The routine releases from the several processing systems were based upon the quantity of tritium processed per day and followed recent experience at TSTA.[3.41] TSTA indicated that only 1.5 Ci of T were released through the stack during the processing of 100 g of T in 38 hr, which is ~1 Ci/d/100 g(T) or a decontamination factor of 10^6. The accidental releases were estimated from the T inventory in the apparatus and the passive safety system in-place which would mitigate the T release. The major systems considered for this study were 1) The Target Factory and Delivery System, 2) the Reactor System, 3) the Fuel Reprocessing System, and 4) the Reactor Building, as summarized in Table 3.13

The Target Factory. This facility must process ~1400 g of tritium per day. For well-enclosed glove boxes and other secondary enclosures, the predicted routine release of T would be 14 Ci/d though through the stack. As described in Section 4.0, only a small inventory of tritium-loaded targets will be continuously prepared; therefore, the quantity of tritium in use along the production line is only 300 g. However, 200 g(T) is enclosed in two liquid cryogenic containers which are usually surrounded by evacuated chambers which have sufficient volumes to contain the total T_2 inventory at a low pressure; consequently, these are fail-safe systems unlikely to release tritium.

Table 3.13. SOMBRERO Tritium Locations, Inventories, Flow Rates, and Potential Release Rates

Location	Inventory g(T)	Flow Rate g(T)/d	Tritium Releases Routine Ci/d	Accident g(T)
Reactor Building				
Atmosphere	4.6	900	23	4.6
Surfaces	<0.1	-		-
Fuel Injection	1.0	1400		1
Reactor System				
Breeder	162	~500	11	80(50%)
Graphite	10	-		-
Helium	5	~500		5
Steam Generator			15	
Fuel Reprocessing				
Desiccant Beds	61	1500		-
Distillation System	13	1500	30	-
Other System	1			-
Target Factory	300	1400	14	100

The Reactor System. The reactor systems consists of the chamber with the breeder blanket, the breeder circuit, and the heat transfer system. The Li_2O breeder particles produce ~500 g(T)/day; however, at steady-state all of this tritium is released to the circulating He. The tritium inventory in the breeder is ~0.081 wppm; consequently, for the total breeder, ~2000 tonnes, the inventory is 162 g(T).

The graphite chamber structure will also absorb some tritium. Only a small quantity HTO should be absorbed by the heat temperature graphite containing the breeder circuit, as shown by the calculated small amount of corrosion by the H_2O vapors. The first wall of graphite facing the target ,however, is subjected to bombardment by D^+ and T^+ ions following each target explosion. Because of the Xe gas protection, these energetic ions do not impinge directly upon the first wall; however, they have been observed to dissolve in graphite particularly along grain boundaries and saturate[3.42] at a concentration of ~5 ppm atom H/atom C. Based upon the mass of the first wall, 165 tonnes of C, the total inventory would be 10 g(T).

The He circuit contains HTO at a partial pressure of 6 Pa and a average temperature of 918°C, giving a total inventory of 5 g(T). This circuit will also process a flow of ~500 g(T)/day. Under routine operation, breeder particles and the accompanying He circuit would process a total of ~1100 g(T)/d and expect to release ~11 Ci/d. At the same time the tritium permeation through the steam generator would be 15 Ci/d. Under accidental conditions, all the helium would be released, containing 5 g(T), and perhaps half of the breeder particles, containing 80 g(T).

Fuel Reprocessing. The fuel reprocessing system generally has high tritium inventories in two pieces of equipment; namely, 1) the dryer beds used to adsorb HTO from both the He and Xe circuits, and 2) the cryogenic distillation system for the separation of the hydrogenic isotopes. For one-hour operation of the desiccant beds, their inventory would be 61 g(T). During continuous operation of the distillation system, it would have an inventory of 13 g(T) based upon an advanced distillation system design.[3.43] Each system processes ~1500 g(T)/d so that the total routine release from these systems could be ~30 Ci/d. Under accidental conditions, all the tritium in the distillation system would be vented to an evacuated tank so that no tritium release would occur. During reheat of a desiccant bed, some tritium could escape; however, the enclosure containing this equipment would also be vented to an evacuated tank so that no tritium release would occur.

Reactor Building. The containment building atmosphere of Xe has a continuous inventory of ~4.6 g(T), but has a daily flow rate of ~900 g(T)/d. The inventory of tritium-loaded targets in the target injector located in the containment building is kept small, ~1 g(T); however, the system handles ~1400 g(T)/d. These two systems would be expected to release routinely ~23 Ci/d of tritium and ~5.6 g(T) during an accidental breach of the containment system.

The wall surface, nearly 1.3×10^5 m^2, of the containment building which contains the Xe and tritium represents many potential sites for tritium adsorption. For this reason these walls should be covered with thin sheets of stainless steel which has a low adsorption for molecular T_2 or DT. This adsorption has been measured experimentally to follow the relationship,[3.44]

$$y = 2.54\ [x]^{1.03}$$

where

x = tritium concentration in the atmosphere (mCi/m^3), and
y = dis/min ($\times 10^{-3}$)/100 cm^2 (of surface).

Based upon the tritium concentration of 135 mCi/m^3 (Xe) @ 0.5 torr, the total adsorption on all of the steel surfaces is very small, 2.5×10^{-4} g(T); however, this adsorption could exceed 1 kg if 10% of the tritium existed as HTO.

3.3 SOMBRERO POWER CONVERSION AND PLANT FACILITIES

3.3.1 Heat Transport System

Primary Coolant Loop. The heat transport system proposed for the SOMBRERO reactor concept is shown in Fig. 3.57. The primary coolant selected is lithium oxide granules fluidized with gaseous helium. It operates between 550°C and 700°C. The primary loop consists of four coolant circuits including one heat exchanger in each circuit. The number of circuits was based on the size of the heat exchangers. A state-of-the-art heat exchanger design was assumed.

Intermediate Coolant Loop. The need for an intermediate loop has been discussed for the OSIRIS case. A similar rationale applies to the case of SOMBRERO. The intermediate loop consists of two circuits including one steam generator in each circuit. This selection was based on the projected steam generator capacity. Each steam generator capacity needed for the SOMBRERO plant is 1450 MWt. Although this capacity level has not been demonstrated to date, no show stoppers are anticipated in the development of steam generators of this power level.

Intermediate Heat Exchanger. There are four intermediate heat exchangers (IHX), and each is sized for 25% of the thermal capacity of the plant. Thus, each IHX has a rated capacity of 725 MWt. The key parameters of each IHX are shown in Table 3.14.

Table 3.14. IHX Design Parameters

Number of IHX	4
Duty (MWt)	725
Core Height (along Li_2O flow) (m)	5.68
Core Depth (along lead flow) (m)	3.0
Core Width (m)	4.1
Tube Outside Diameter (cm)	2.54
Tube Inside Diameter (cm)	2.22
Heat Transfer Area (m^2)	
Outside	18,300
Inside	16,000
Lead Pressure Drop (MPa)	0.27

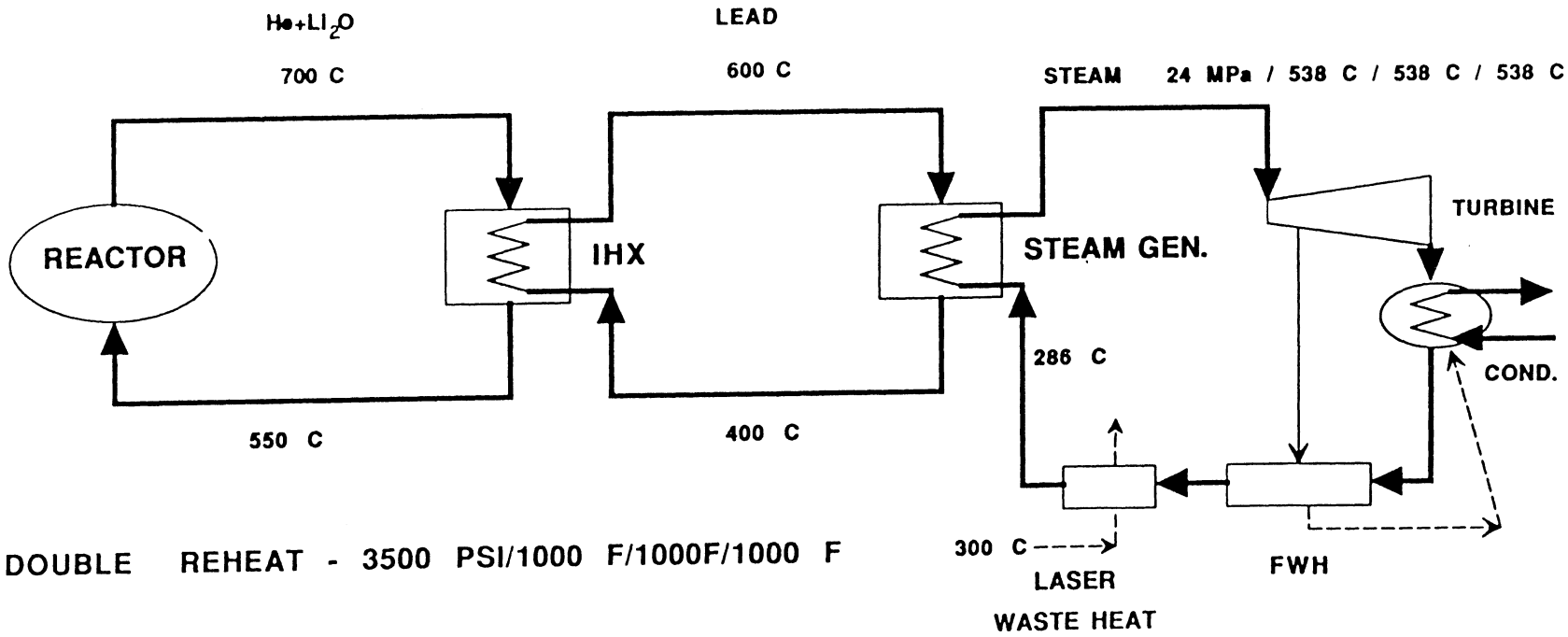

Fig. 3.57. SOMBRERO power conversion cycle diagram.

3.3.2 Power Conversion System

Power Cycle. To achieve a high efficiency power conversion, a high-pressure, high-temperature steam cycle was adopted for the SOMBRERO reactor concept. The steam pressure and temperature conditions chosen are consistent with the intermediate coolant temperature. These conditions also represent the state-of-the-art steam conditions used for fossil-fired steam power plants. A supercritical pressure double reheat steam cycle is used with the following steam conditions:

24.2 MPa / 538°C / 538°C / 538°C
[3,500 psig / 1,000°F / 1,000°F / 1,000°F]

The above pressure and temperature conditions refer to the steam conditions at the turbine inlet. The three temperature values stand for initial superheat, first reheat, and second reheat, respectively. These conditions are similar to those of the Osiris plant and provide a net cycle efficiency of 45 percent. The SOMBRERO plant has an additional source of heat for the power cycle. The waste heat from the laser system amplifiers is rejected at a reasonably high temperature such that it can be used to supplement the heat required to preheat the feedwater before it enters the steam generator. 270 MWt waste heat is rejected from the amplifiers at 300°C. The result of this additional heat is to effectively improve the steam cycle efficiency from 45% to 47%. The heat transport and power cycle schematic for SOMBRERO is shown in Fig. 3.57.

Steam Generator. There are two steam generators, and each is sized for 50% of the thermal capacity of the plant. Thus, each steam generator has a rated capacity of 1450 MWt. As in the case of Osiris, to accommodate the double reheat feature of the power cycle, each steam generator is made up of three stages, and each stage is provided with a separate vessel. These stages are the superheater, first reheater, and second reheater. These steam generator vessels are supplied with liquid lead from the intermediate heat exchangers (IHXs). There are two IHXs. These two IHXs are supplied with the fluidized lithium oxide coolant from the four primary coolant circuits. The key parameters of each steam generator are given in Table 3.15.

Turbine-Generator. The SOMBRERO reactor plant is provided with a turbine-generator capable of generating the required gross electrical power (1360 MWe). The turbine-generator is supplied with steam from the two steam generators. The turbine-generator consists of one high-pressure section, one intermediate-pressure section, and two low-pressure sections arranged in a cross-compound configuration. Turbine-generator has a size limitation, however. The largest turbine which has been built for advanced steam conditions was a 325 MWe machine. Currently, all of the techniques needed to build much larger capacity turbines do not exist in the

Table 3.15. Steam Generator Design Parameters

Parameter	Superheater	1st Reheater	2nd Reheater
Thermal Duty (MWt)	1064	241	122
Shell Inside Diameter (m)	3.7	2.1	2.1
Tube Bundle Length (m)	19.5	18.0	19.2
Number of Tubes	11862	4634	4983
Tube Size (cm)	1.27	1.27	1.27
Tube O.D. (cm)	2.13	2.13	2.13
Tube Wall Thickness (cm)	0.374	0.277	0.277

United States; they exist to a large extent in Europe. Thus for units 800 MWe or larger, a cross-compound configuration may very well only be practical at a much higher cost.

3.3.3 Plant Facilities

The facilities for the SOMBRERO plant are shown in Figs. 3.58 through 3.63. The Plot Plan, shown in Fig. 3.58, shows the major structures of the plant. These structures include:

- Reactor Building
- Laser Buildings
- Hot Cell (Maintenance) Building
- Auxiliary Building
- Target Fabrication Building
- Steam Generator Building
- Turbine-Generator Building

Figure 3.59 shows an isometric view of the optics configuration within the reactor building. The final focusing mirrors as well as the grazing incidence mirrors are arranged in a near-uniform illumination form. The grazing incidence mirrors are all located 30 m from the center of the reactor chamber, and the final focusing mirrors are all 50 m from the center of the chamber. The plan and cross-sectional views of the Fusion Island, primarily consisting of the reactor building, hot cell building, and steam generator building, are shown in Figs. 3.60 and 3.61.

Reactor Building. The reactor building is the most important building for which a concept has been developed for the SOMBRERO plant. The building provides housing for the

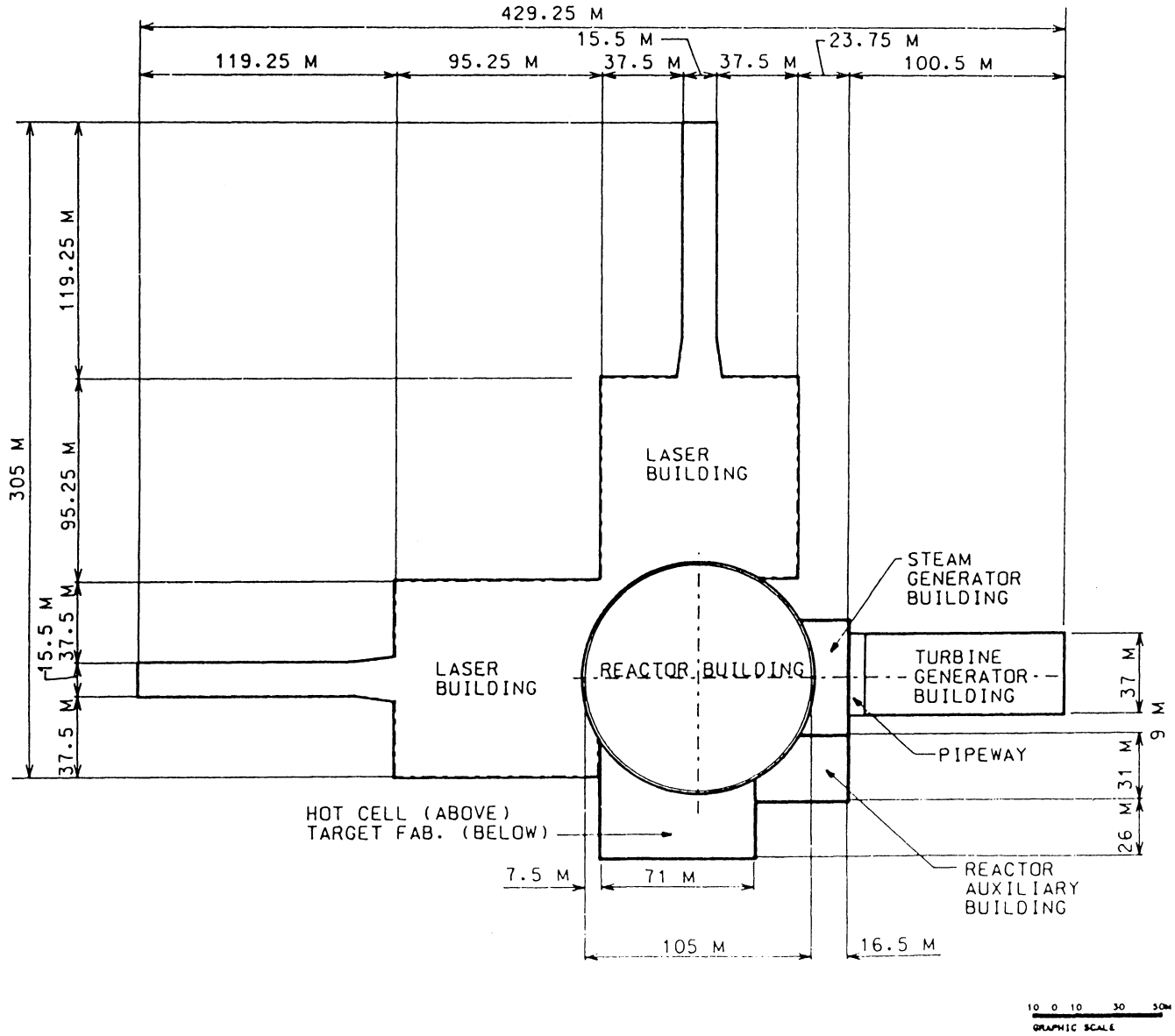

Fig. 3.58 Plot plan for SOMBRERO power plant.

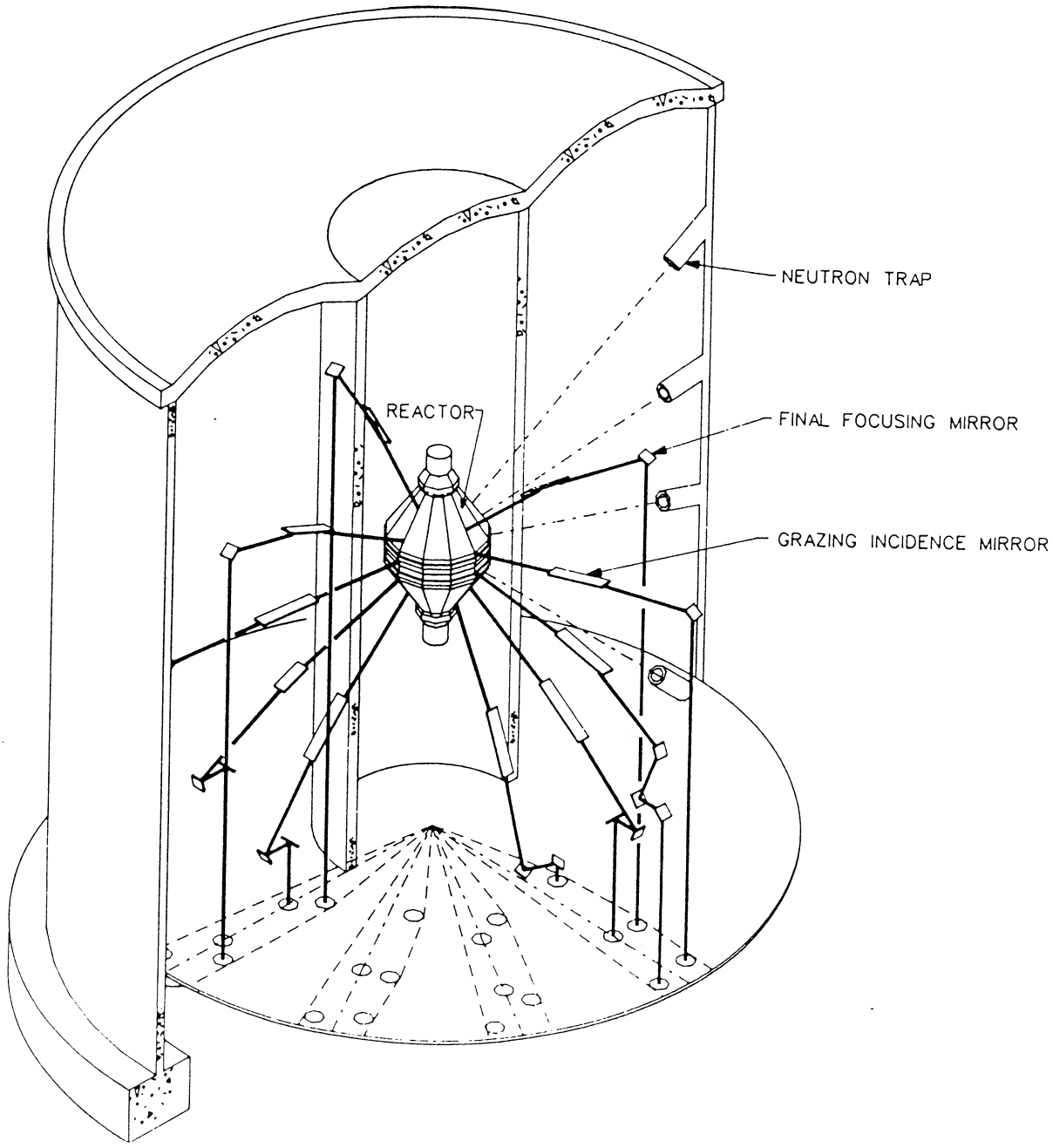

Fig. 3.59. Isometric view of the optics configuration in the SOMBRERO reactor building.

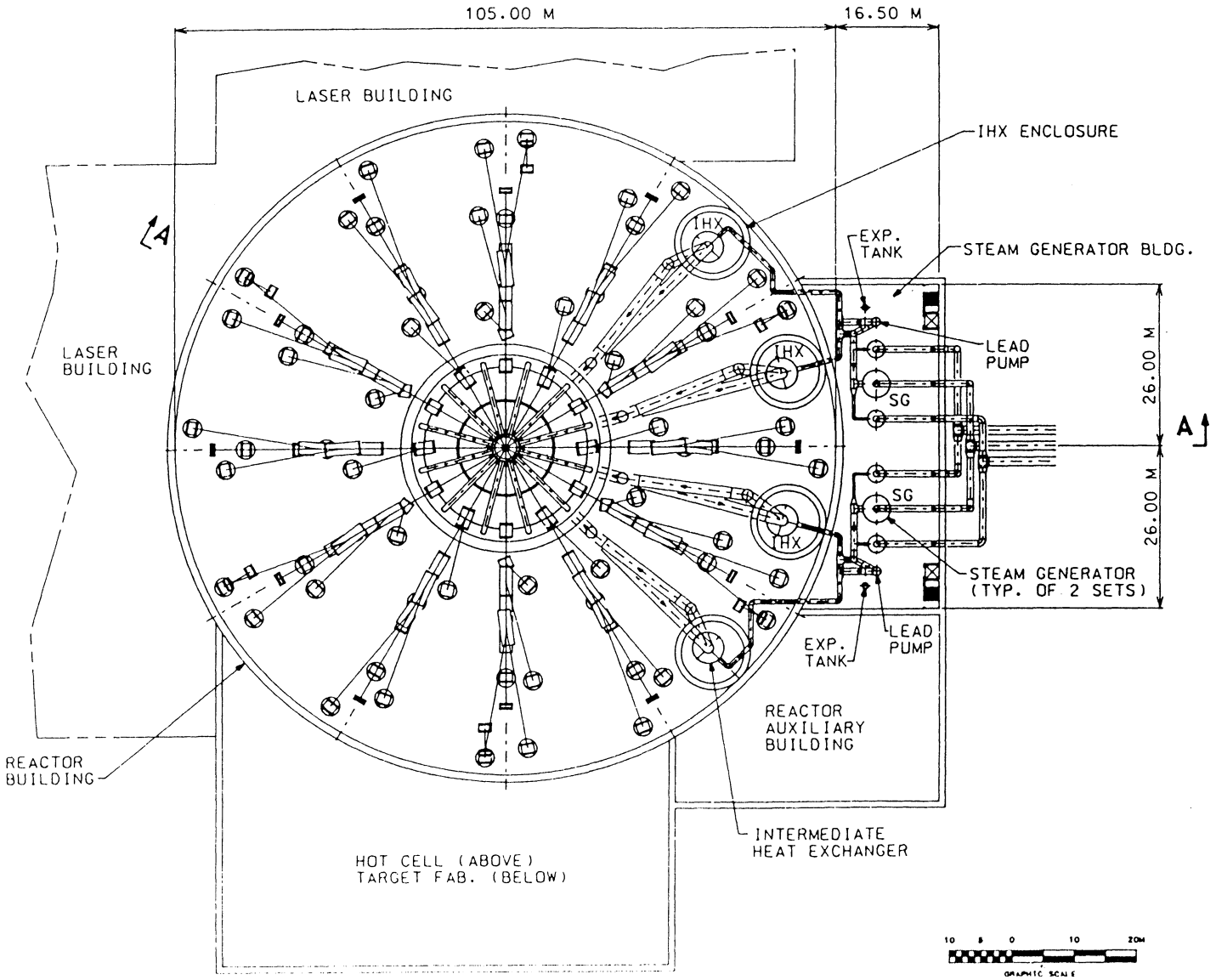

Fig. 3.60 Plot plan for SOMBRERO reactor building.

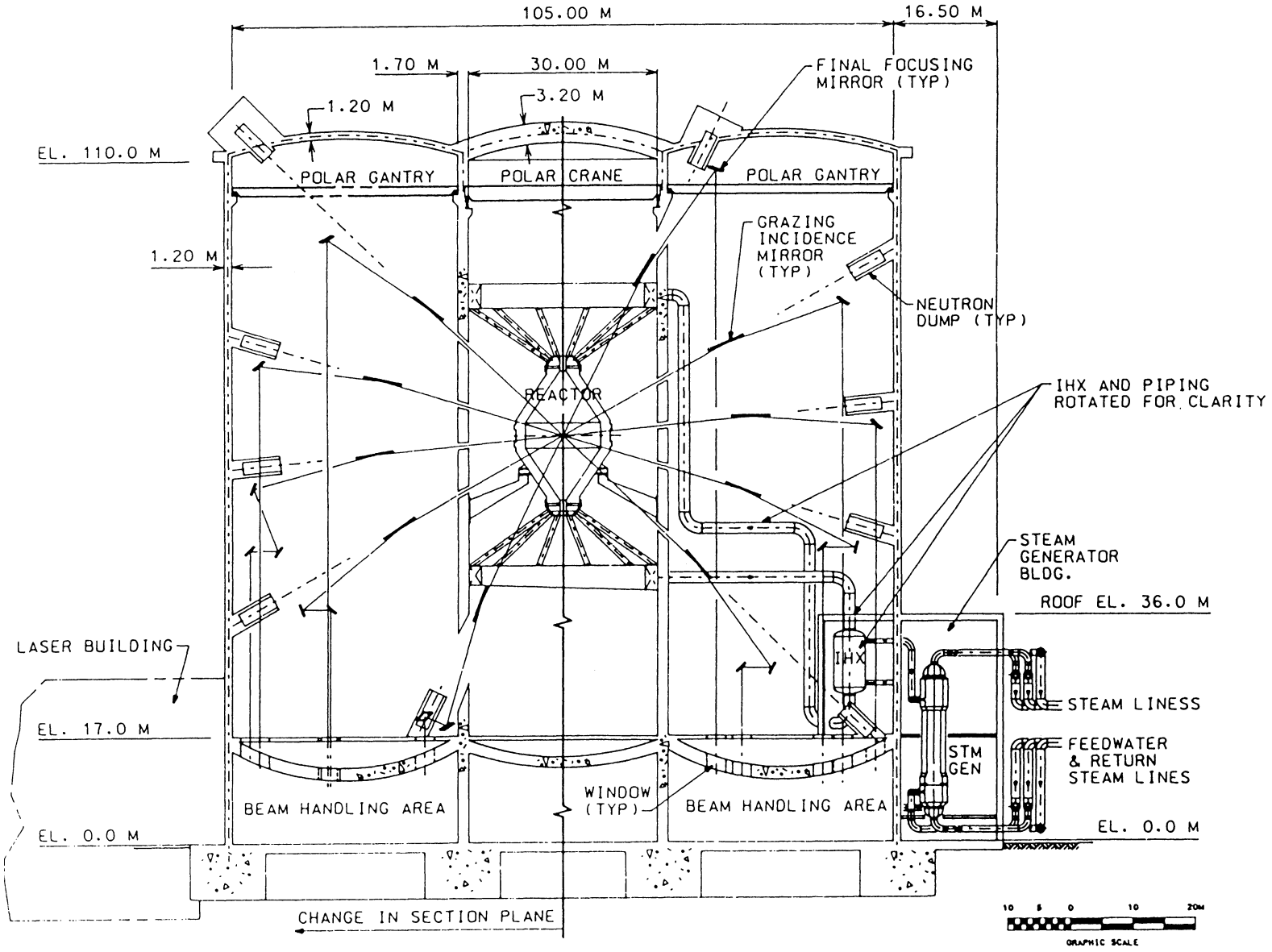

Fig. 3.61 Elevation view of SOMBRERO (Section A-A of Fig. 3.60).

reactor and the final optics, shielding of the public from fusion neutrons, and confinement barrier to the accidental release of tritium. In addition, the building also accommodates remote maintenance of the reactors. The size of this building is primarily dictated by the requirements for housing the final optics of the laser driver. It accommodates 60 beam lines that offer a near-uniform illumination. All the beam lines penetrate the reactor building through a basement level called "Beam Handling Area." The building vacuum boundary is located at the building floor where the beam lines penetrate the floor through "windows" (see Fig. 3.61). The other vacuum boundaries are the reactor building walls located at a radius of 52.5 m and the building ceiling.

Final Optics. The layout of the final optics adopted for this design is determined by the requirement for reasonable lifetimes of the final turning and focusing optics. It was determined that a dielectric mirror in the line of sight of the target would not have a reasonable life (i.e., one year) for a reactor operating at the design power unless it is placed at an impractically long distance from the target. Therefore, it was decided to introduce an aluminum mirror operating at grazing incidence as the first optic with the dielectric focusing mirror located out of the line of sight. There are almost no data on radiation damage of either metal or dielectric optics in high neutron fluences. The choice was thus made based on reasonable model assumptions.[3.45] This has led to the location of the grazing incidence mirrors at 30 m from the target and the first dielectric mirrors 20 m beyond them. The grazing angle on the aluminum mirror is limited to less than six degrees by the absorption of the incident laser beams. The angle of incidence on the dielectric mirror was also chosen to less than 45° to minimize the fabrication cost of these optics. It is clear that the damage threshold of these optics under neutron illumination is one of the major uncertainties in this design. If the optics were to have higher fluence tolerances than assumed then the optics could be placed closer to the target and the whole structure reduced in size. This might reduce the cost of the SOMBRERO reactor building significantly. As a result of the 45° limitation, up to two mirrors, in addition to the final focusing mirror, are needed to direct some of the beam lines to the floor of the reactor building. These additional mirrors are needed only for some of the beams which penetrate the reactor chamber below the reactor mid-plane.

To minimize the neutron activation of the optics, a neutron dump is provided to trap the primary neutrons escaping the reactor chamber through each opening for the beam lines. This subjects the equipment within the reactor building only to the secondary neutrons. The grazing incidence mirrors are of course subject to the primary neutrons. In addition to the neutron dumps, the reactor building is also provided with a shield floor below the lowest reflecting mirror to reduce the impact of neutrons on the windows as well as on the equipment in the beam handling area.

The IHXs are located within the reactor building. However, they are housed in their respective cylindrical chambers at atmospheric pressure. This arrangement accommodates the 0.1 MPa differential pressure (between the IHX chambers and the rest of the reactor building) and

at the same time allows limited access to the IHX chambers during normal power operation. The steam generators are located in a separate building outside the reactor building.

Several unique features are incorporated in the reactor building structural concept. Since the building is required to maintain a vacuum (approx. 10 Pa), its internal pressure is assumed to be 0 MPa (for structural design purposes), and it is subject to an external pressure of about 0.1 MPa. Thus a cylindrical shaped building is chosen for an efficient structural design. The following requirements and design features characterize the reactor building (Fig. 3.61):

- Codes and Standards - ACI-349 (American Concrete Institute) applicable to Seismic Category I Structures:

Operating Basis Earthquake (OBE)	0.15 g
Safe Shutdown Earthquake (SSE)	0.30 g

- Building Pressure - Pressure within the building is dictated by the operations and maintenance requirements.

Normal Operation	0.0 Pa (approx.)
Maintenance	0.1 MPa

These pressure conditions apply to the spaces above and below the building floor. In addition, the conditions can occur in either space independent of the other.

- Building Size - The size of the building is determined by the requirements for the final optics layout.

Overall Height	110.0 m
Height of the Beam Handling Area	17.0 m
Internal Diameter of the Inner Shield Wall	30.0 m
Internal Diameter of the Outer Wall	105.0 m

- Wall, Floor, and Roof Thicknesses - These thicknesses are controlled by the shielding requirements (not by the structural requirements).

Inner ShieldWall	1.7 m
Outer Wall	1.2 m
Building Floor (below inner shield chamber)	1.7 m
Building Floor (below annular space)	1.2 m
Shield Floor	0.6 m
Roof Over the Inner Shield Chamber	3.2 m
Roof Over the Annular Space	1.2 m

- Floor and Roof Configuration - To resist the external pressure efficiently, the floors and roofs are designed as curved surfaces:

Floor and roof of the inner cylindrical space	Spherical
Floor and roof of the annular space	Toroidal

- Buckling - A factor of safety of 7.3 was applied to the outer cylindrical wall to resist the external 0.1 MPa pressure against buckling.

- Seismic Design - The building has been designed as Seismic Category I Structure. The operating basis earthquake (OBE) events control the design over the safe shutdown earthquake (SSE) events due to the load factor and damping differences.

	OBE	SSE
Acceleration (g's)	0.15	0.30
Load Factor	1.9	1.0
Damping (%)	4	7

Optics Support Concept. A concept for the support of the grazing incidence and final focusing mirrors has been developed. As shown in Figs. 3.62 and 3.63, each mirror is separately supported. However, for structural rigidity, some of the supports are also tied together. Each support is a combination of reinforced concrete members. The supports are also configured such that the remote maintenance equipment can access the mirrors without interference for replacement or refurbishment. Although not shown in the figure, each support is configured to accommodate alignment of the supported mirror. A continuous alignment may be required for each mirror to accommodate thermal movement of the supports as well as of the building.

The following requirements and design features characterize the optics support concept:

- Major criteria
  - Extremely high rigidity
  - Avoid interferences with laser beams, cranes, and equipment
  - Avoid neutron streaming
  - Minimize activation by minimizing metals
  - Facilitate maintenance

- Structural concept for mirrors that are not close to the building structure (i.e., wall, floor, or ceiling):
  - For grazing incidence mirrors, a ladder-type structure is envisaged. Each mirror is

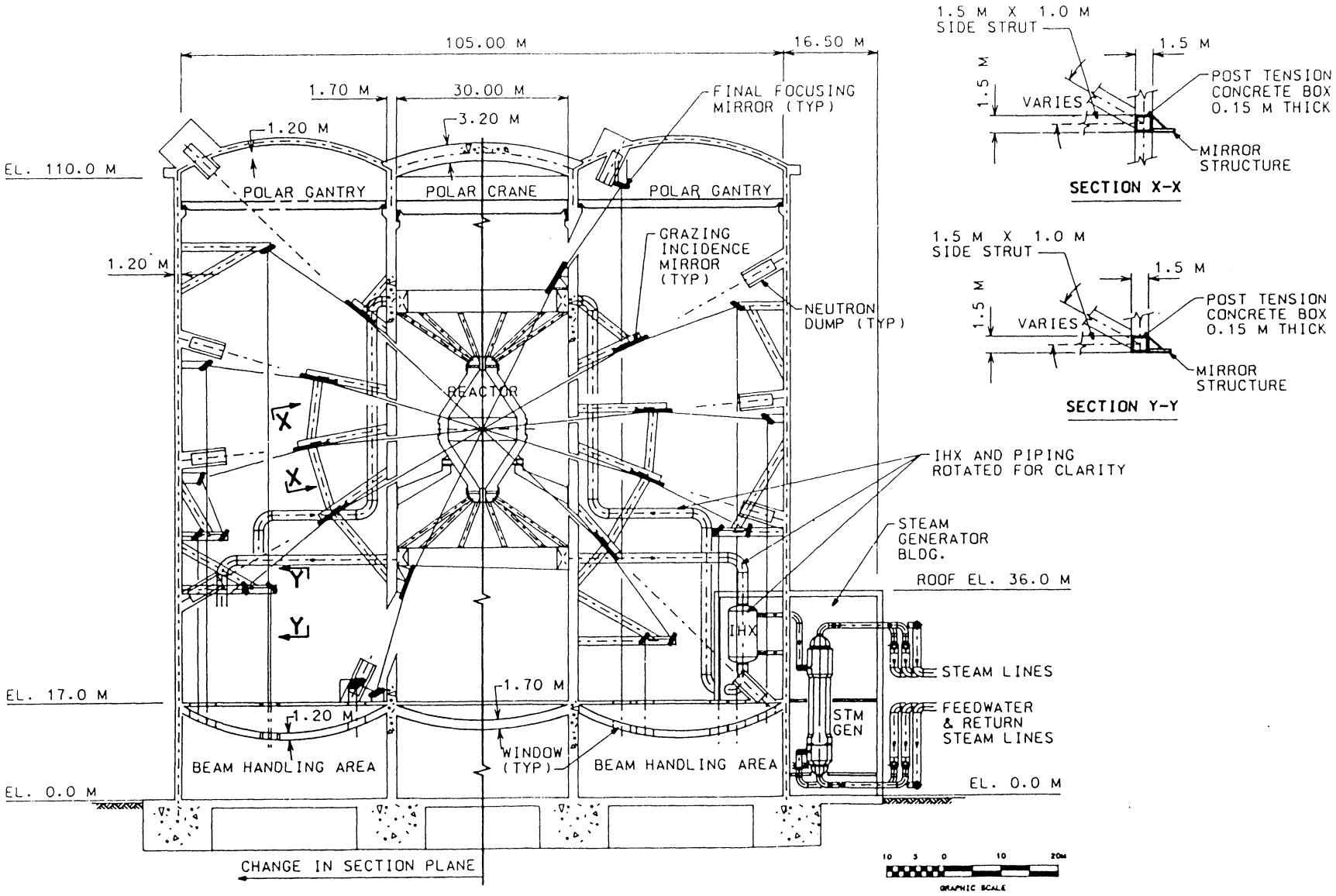

Fig. 3.62 Reactor building optics support concept.

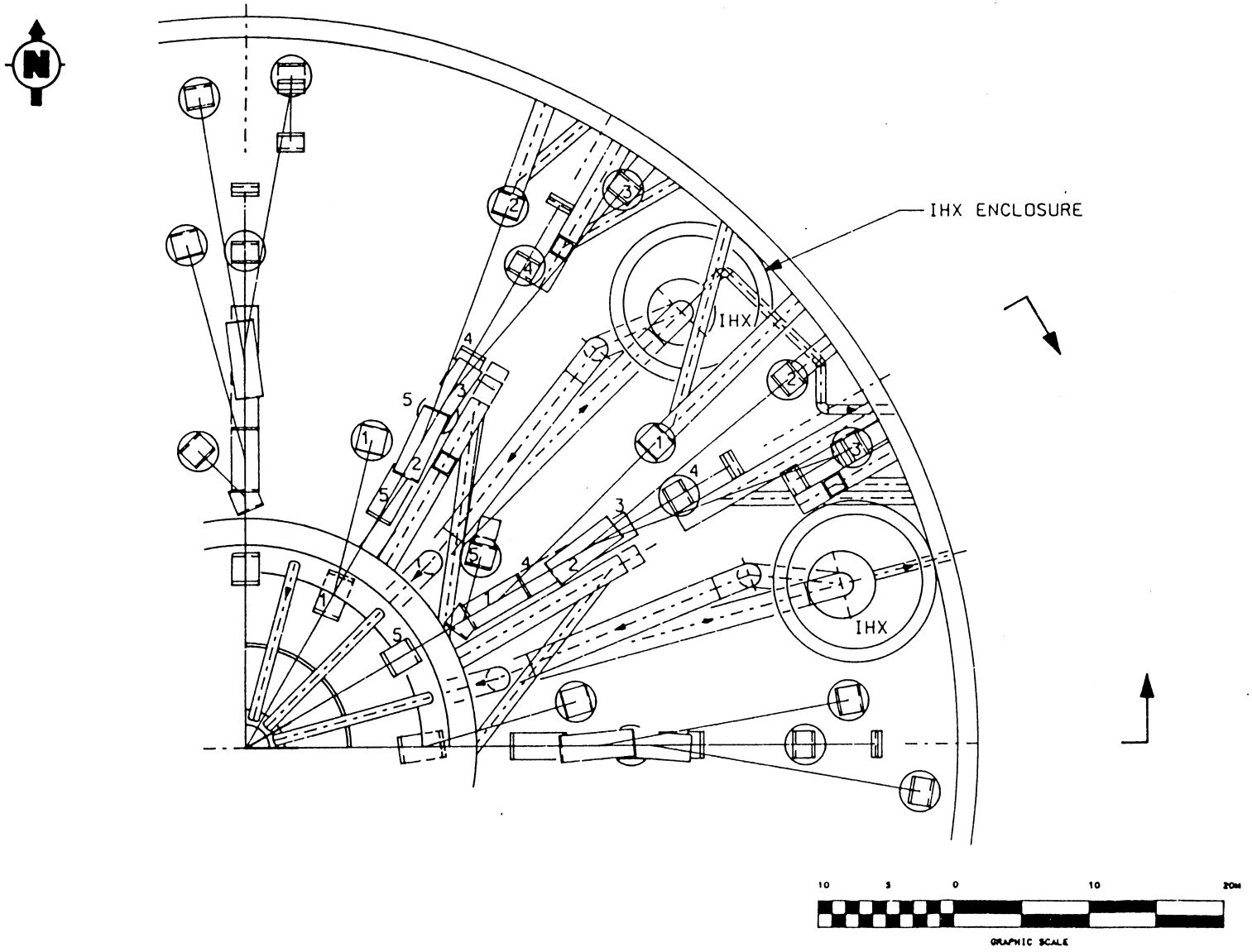

Fig. 3.63. Optics support concept.

supported by a "rail" and a radial "ring", both in a vertical pane, and a strut that lies in a plane that contains the ring and is perpendicular to the plane that contains the rails and the rings.

- For each final focusing mirror, a tripod structure consisting of three struts is provided.
- All struts, rails, and rings are precast concrete box modules. These modules are assembled to the required lengths by pulling steel tendons through tendon sheaths embedded longitudinally in precast modules. The tendons are tensioned by jacking creating a strong, economical structural element.

- Structural concept for mirrors that are close to the building structure (i.e., wall, floor, or ceiling):
  - For each of these mirrors, a strut made of precast concrete box module is used. The strut is supported from the nearest structure and the configuration of each strut is tailored to the location of the respective mirror.

- All mirrors are located on one side of the concrete box module as shown in the Sections X-X and Y-Y on the Fig. 3.62. This facilitates maintenance, prevents interference between the support structure and the laser beam, and keeps the support structure away from the neutron path.

Tritium Confinement Barrier. The reactor building provides a leak-tight barrier to tritium leakage into the environment. The leakage from the building can be reduced to limit the tritium leak rate to an acceptable level. The leakage from the building is generally controlled by properly sealing the penetrations, access doors, and equipment hatches. In addition to this, all the interior surfaces of the building walls, floors, and ceiling are coated with epoxy paint to minimize tritium permeation into the concrete. Similarly, all equipment surfaces are also painted with suitable coatings to minimize tritium permeation.

Vacuum Pumping System. As indicated earlier, the walls, floor, and the ceiling of the reactor building constitute the vacuum boundary (i.e., the entire reactor building is evacuated to a pressure of 10 Pascal (0.08 torr)). Since this is not a very high vacuum and falls under the "medium" vacuum category, roughing vacuum pumps, such as roots blower, are adequate for initial pumpdown as well as for maintaining the vacuum during normal operation. Six vacuum pumps are provided to initially pumpdown the building from atmospheric pressure to 10 Pa in 24 hours. Each pump is nominally rated at 2 m^3/sec pumping capacity. The building gaseous effluent from the vacuum pumping system exhaust is sent to the atmosphere cleanup system for further processing.

Atmosphere Cleanup System. To maintain an equilibrium tritium concentration as well as to cleanup the tritium following an accidental leakage within the reactor building, an atmosphere cleanup system is provided. The system also maintains the tritium concentration within the building well below the maximum permissible level during maintenance operations. After processing by the system, the recovered tritium is pumped back into the tritium processing system provided to recover tritium from the blanket and coolant systems.

Laser Building. There are two laser buildings. The plan and cross-section views of the buildings are shown in Figs. 3.64 and 3.65, respectively. The buildings house the KrF driver system components including:

- Temporal and spatial pulse shaping components
- Intermediate amplifying and multiplexing stages
- Demultiplexing arrays
- Penultimate amplifiers
- Final amplifiers

The first two items of the above list are housed in a laser support building located between the two laser buildings. This support building is common to both the laser buildings and also houses common electrical equipment associated with the first two items.

To maintain the quality of the beams, three alternative building environments were considered:

- Helium-filled building
- Evacuated building
- Evacuated beam tubes

A helium-filled building arrangement would require tightly sealed enclosures to minimize helium leakage. In addition, helium temperature must be maintained within a very tight tolerance. These aspects would make the building very expensive and would impose difficult maintenance requirements. Thus, this alternative was not chosen. The second alternative, a completely evacuated building, was also not chosen because it will require a tightly-sealed building to minimize leakage. This would make the building expensive. In the third alternative, a conventional steel-framed structure is provided. Here all the beamline components are housed in evacuated beam tubes. This allows the buildings to be always accessible and provide easier maintenance. Thus this alternative is selected as this also provides the least expensive building.

Other Facilities. A brief description of the other major facilities is given here. Only outlines of these facilities are shown in the Plot Plan (Fig. 3.58) to indicate that facilities are needed to support the operation of the plant. No design has been developed for them at this stage.

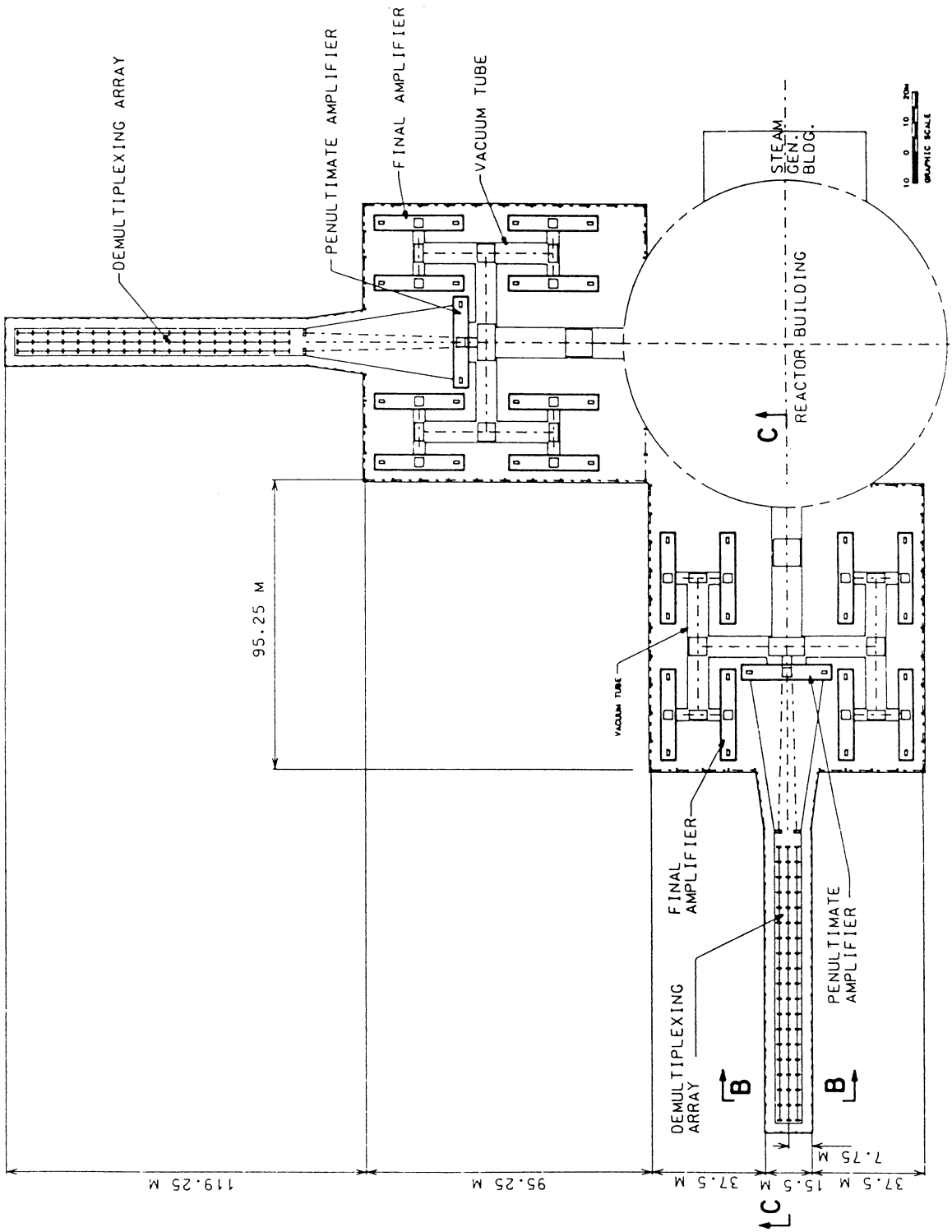

Fig. 3.64. Top view of KrF laser building.

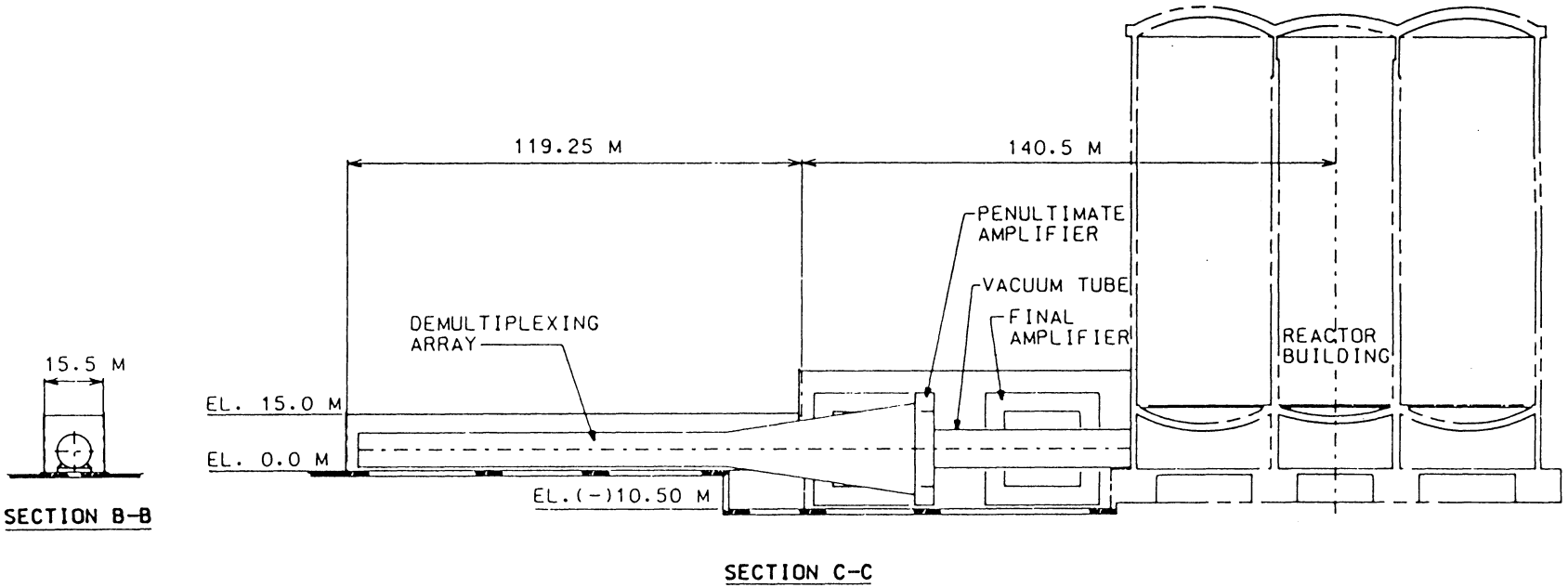

Fig. 3.65. Cross-sectional view of KrF laser building.

Maintenance Building. The maintenance building houses the equipment for assembly and disassembly of the SOMBRERO components and provides space for both irradiated and refurbished modules. The building is designed as a earthquake and tornado hardened structure.

Auxiliary Building. This building houses the reactor and heat transport system auxiliary equipment. These include auxiliary cooling system, plant electrical systems, heat tracing system, coolant handling system, heating, ventilation, and air conditioning (HVAC) system, vacuum system as appropriate, etc. The building is designed as an earthquake- and tornado-hardened structure.

Target Fabrication Building. This building houses all the systems and components necessary for storage, fabrication, and delivery of the fuel pellets. The building is located below the maintenance building. The building is designed as an earthquake- and tornado-hardened structure.

Steam Generator Building. A concept has been developed for this building as shown Figs. 3.60 and 3.61. The tall structure of this building is dictated by the height of the steam generator. The building is designed as an earthquake- and tornado-hardened structure.

Turbine-Generator Building. The building is sized to house the 1360 MWe cross-compound turbine-generator and its auxiliaries, steam system components, feedwater heating and condensing system components, etc. The building is envisaged as a conventional building similar to that of fossil-fired plants.

3.4 KrF DRIVER

3.4.1 KrF Driver System Requirements

The KrF driver system is required to deliver 3.4 MJ, divided equally among 60 beam directions, uniformly distributed over 4π steradians, at repetition rate of 6.7 Hz. The energy spatial distribution must be identical for each of the 60 directions and match a given profile; the target diameter is $d(mm) = 5.6\ (E(MJ)/4)^{1/3} = 5.3$ mm.[3.46] Power uniformity among the 60 beams should be $\leq 5\%$ rms. Random beam mispointing of ~10% rms of the target radius can be tolerated. The temporal distribution of energy in the pulse will be defined for an operating system, but is not defined for this study. Nominal peak power is defined as $P(TW) = 240\ E(MJ)^{2/3} = 5.4 \times 10^{14}$ watts; an approximate pulse duration is thus E/P = 6.3 ns.

We have assumed the NRL, NIKE system approach for direct drive targets of "echelon-free ISI" in which a desired intensity profile is imaged onto the target through the laser chain, using partially coherent light. Broadband KrF emission with $\Delta\nu/\nu \sim 0.1\%$ is used to provide coherence times < 1 ps and thus allow rapid spatial averaging on the target. It is an approach which utilizes imaging of a front end aperture through the whole amplifier chain, including angular multiplexing, to the target. It thus allows for the target beam spatial profile to change during the pulse and thereby take advantage of the higher direct drive target gains that occur for a system that can zoom the target illumination spot as the target diameter decreases during irradiation. We have not taken credit for zooming in the base case parameters cited earlier (i.e., G = 118 at E = 3.4 MJ).

3.4.2 Background

There are several goals in the design of a KrF driver system for IFE: 1) high operating efficiency, 2) low capital cost, 3) technical credibility, 4) high availability/reliability, and 5) low operating costs. In this study we were to assume technology that could be mature in the year 2040, and a plant that would be the tenth of its kind. We have assumed physics issues as they are understood today, such as laser efficiency based on our best models for kinetics and extraction as anchored by available data; we have not, for example, assumed the finding of some "new" laser gas mixture by the year 2040 that would increase the laser efficiency by another 10%.

In creating a design, we have focused on how to optimize overall laser system operating efficiency because of the continuous operation of the plant. In a single pulse test facility, capital cost is the more dominant consideration, and efficiency is mainly considered in the context of its effect on capital cost.

3.4.2.1 Direct vs. Indirect Drive

The gain curves provided for this study by DOE clearly favored direct drive. We saw no difficulty with making a laser system for this choice and no advantage for the laser system for choosing indirect drive. As far as the laser driver system is concerned, we believe we could meet the requirements for an indirect drive target with a very similar system at similar cost. The ability of KrF driver systems to meet the brightness requirements for indirect as well as direct drive targets was described in a paper in Osaka in 1991.[3.47] In the Osaka paper it was concluded that for an indirect drive spot diameter of 1.5 mm, 3 MJ on target with 50 m to the final focusing optics, that a beam quality of 5.2 times the diffraction limit was adequate. It was then shown that with reasonable assumptions for phase errors introduced through the system that 0.32 waves rms of phase error accumulate, which is consistent with the beam quality requirement. Since direct drive targets have larger gain, and there is little practical difference in geometry of beam delivery to the target, it seems sensible to select the direct drive option. Should this story change at a future date and indirect drive be the favored target choice, an appropriate KrF driver system design could generated

3.4.2.2 E-Beam Pumping

KrF laser kinetics and extraction physics have been studied in some detail since the first KrF lasing was achieved in 1975. Despite promising theoretical predictions for discharge and e-beam + discharge pumping, these approaches have not come close to the intrinsic efficiencies achieved by pure e-beam pumping(intrinsic efficiency is (laser output energy)/(energy deposited in the laser gas mixture); $\eta_I \sim 14.5\%$ for our present design parameters). Low efficiency of the e-beam itself has been an area of concern for e-beam pumped systems; however, we have recently published a description of a technology for e-beams that will allow them to operate at high average power, for long durations, and at high efficiencies - constrained only by the albedo of the laser gas mixture and the foil.[3.48] E-beam efficiencies of $\eta_{eb} > 80\%$ are possible in the system we describe herein with 1 atm of 50% Ar + 50% Kr (+small amount of F_2) mixtures and titanium foils; η_{eb} approaching 90% should be possible with beryllium/aluminum foils. In these designs the e-beam is not allowed to intercept the foil support structure (i.e., the so called "hibachi" structure). The ability to achieve such "non-intercepting" operation has been experimentally demonstrated at Textron. This technology, coupled with the high voltage, cable based pulse forming lines (Section 3.4.4.1), a double foil system for removal of steady state waste heat (Section 3.4.4.2), and the demonstrated high intrinsic efficiencies (14.5%) at high pump rate (400 kW/cm^3) and high specific energy (30 J/l-atm for our design projections) for e-beam pumping make this approach our clear choice.

3.4.2.3 Angular Multiplexing

Pulse shortening from the many hundreds of nanoseconds, at which large e-beam pumped amplifiers may be efficiently made, to the ~ 6 ns required for target irradiation may be reliably and efficiently achieved, at reasonable system cost, by the use of angular multiplexing. This pulse compression approach has been developed for the Aurora (Los Alamos) and Nike (Naval Research Lab.) systems, as well as others at Rutherford in England, at the University of Alberta in Canada, and the Electrotechnical Laboratory in Japan. In some of these systems, angular multiplexing was used in concert with Raman beam combining. We have not utilized Raman technology because we believe we can achieve adequate beam quality from our amplifiers without the added cost and complication of Raman conversion.

3.4.2.4 Generic Driver System Description

The KrF driver system consists of 1) a front-end which produces a pulse of the desired bandwidth and temporal and spatial intensity characteristics, 2) several stages of intermediate amplification and progressive temporal/angular multiplexing, 3) final amplification by large e-beam pumped 2-pass amplifiers, and 4) demultiplexing and beam delivery to the reactor building. This is illustrated in Fig. 3.66. (Note that here and throughout this chapter, we describe the design of a 3.6 MJ driver, which is slightly larger than the eventually selected reference design point of 3.4 MJ.) In the reactor building, the beams are brought through a mirror system that provides neutron protection to the laser stages and brings equal amounts of KrF illumination to the target from 60 uniformly spaced directions by way of grazing incidence metal mirrors, which are the only optical element subjected to direct neutron flux. The Ultimate Amplifiers (UA's) in our system operate with a two-pass gain of 16, so the Penultimate Amplifiers (PA's) only supply ~ 6% as much energy. From this, it is clear that the efficiency and the capital cost of the laser driver system is dominated by the UA's. Because of this our design discussion at the conceptual stage focuses on consideration of these amplifiers, how their efficiency may be optimized, and how they may most effectively be assembled into an architecture that satisfies the target requirements. Our approach for efficiency optimization is described in Section 3.4.3.

3.4.2.5 Laser Reject Heat Utilization

With a KrF laser intrinsic efficiency of ~15%, it is clear that a large fraction of the input energy ends up as waste heat. In 1987 Pendergrass[3.49] showed that the effective laser efficiency could be greatly enhanced by thermodynamically making use of the waste heat. For example, a driver system with 10% wall plug efficiency, for which 70% of the waste heat could be recovered at 250°C or higher and converted with 75% of Carnot efficiency into electricity (75% · 45% = 34%) would result in an effective laser efficiency of 12.7% - an improvement of 27%. The waste

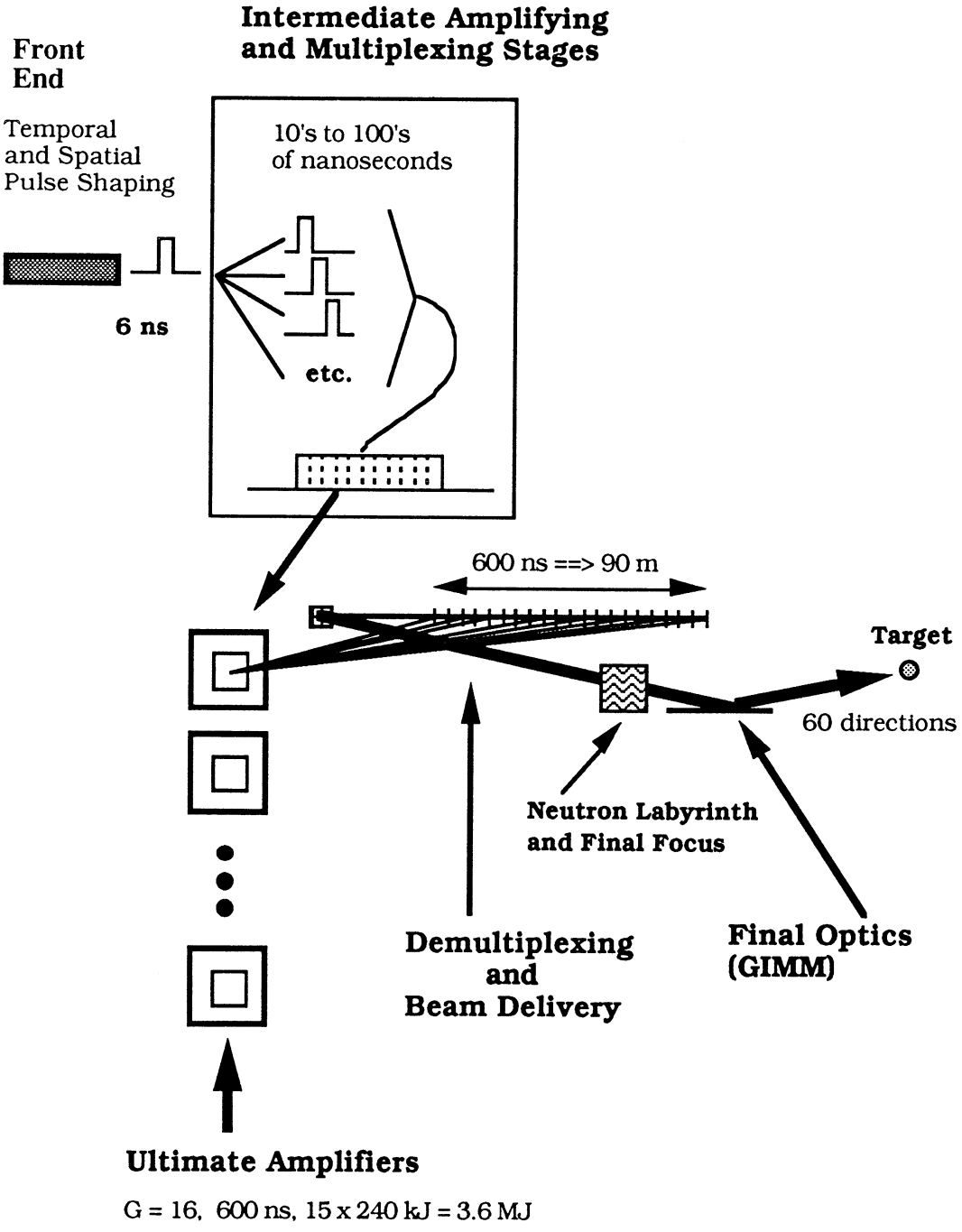

Fig. 3.66. Generic diagram of KrF laser driver system.

heat recovery assumptions are reasonable, because most of the waste heat ends up in the laser gas mixture, which is being circulated in a flow loop with heat exchangers that are already required to remove the waste heat for purposes of recycling the gas. The ΔT due to ~300 J/liter of energy deposition is ~320°C after pressure equilibration and is diminished, on average, by a factor of 1.3 due to the "flush factor" of 1.3 of the flow system design. This design has some unpumped gas passing through the laser cavity following each slug of e-beam pumped gas that is flushed out after each laser pulse. Thus we may assume 50°C gas temperature going into the laser cavity, ΔT = 320° diluted to ΔT ~ 250°, giving an average temperature of T = 300°C going to the heat exchanger.

3.4.3 Amplifier Efficiency Optimization

High overall efficiency of the final or ultimate amplifiers (UA's) as used in the system is key for determining the overall driver system efficiency. To determine the best values for the design parameters, we first write the overall amplifier efficiency as the product of its identifiable components, which are illustrated in Fig. 3.67.

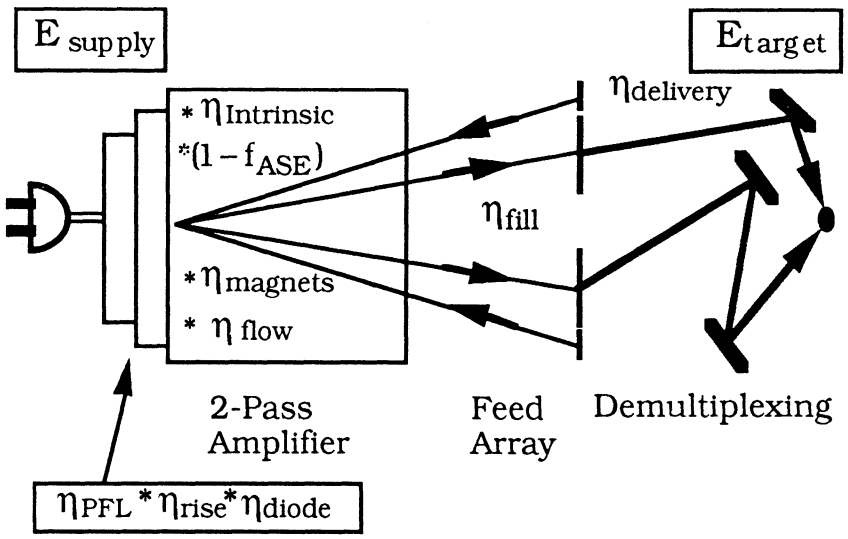

Fig. 3.67. Schematic of KrF amplifier showing the efficiency components contributing to the overall amplifier efficiency.

Thus we write:

$$\eta_{LaserSystem} = \eta_{PFL} \cdot \eta_{RiseTime} \cdot \eta_{Diode} \cdot \eta_{Intrinsic} \cdot \eta_{ASE} \cdot \eta_{Magnets} \cdot \eta_{Flow} \cdot \eta_{Fill} \cdot \eta_{Delivery}$$

where the terms refer respectively to:

$\eta_{LaserSystem}$ Efficiency of converting electricity, taken from the gross plant output, into photon energy impinging on the target. Known as "wall plug efficiency" in other contexts. We are assuming the flow of power to the ultimate amplifiers and on to the targets dominate this term; it will be reduced a small amount by the different efficiencies of the preceding amplifier stages. We note that the immediately preceding stage, the penultimate amplifier stage, uses identical cavities to the ultimate stage, and thus will run at approximately the same efficiency.

η_{PFL} Efficiency of charging the pulse forming line (cables), ~ 90%.

$\eta_{RiseTime}$ Losses due to expenditure of energy during the rise and fall time of the e-beam current, when non useful pumping of the medium occurs. This term is dependent on L/Z (inductance/impedance) for the e-beam load, and thus becomes unfavorable for large cathode areas and short pump durations. For very large amplifiers it makes sense to segment the e-beams, each with its own return current path, on each side of the amplifier. This also has the benefit of lowering the magnitude of the e-beam self B-field. $\eta_{Rise\ Time} \sim 1/[1+(\tau_{rise}/\tau_{extract})] \sim 94\%$ in our 60 kJ design.

η_{Diode} Efficiency of the diode itself - mainly due to back scatter determined by the foil system and the laser gas mixture. For our 1 atm Ar:Kr ~ 50%:50% mixtures, e-beam voltage of ~610 kV, and beryllium/aluminum foils, the albedo is ~ 91%. For our "non-intercepting" e-beam design, this is the limiting value for η_{Diode}. We have, however, assumed 90% efficiency exclusive of the albedo effects, so an overall $\eta_{Diode} = 82\%$ is used.

$\eta_{Intrinsic}$ $= \eta_{Formation} \cdot \eta_{Extraction}$, the formation efficiency of upper laser states (KrF*) at the given pump rate and laser gas composition and pressure, multiplied by the extraction efficiency for the given length of pumped laser gas, unpumped but absorbing end regions adjacent to the window and mirror, for two-pass extraction, with an input flux (W/cm^2) consistent with operating at a specified two-pass amplifier gain. $\eta_{Intrinsic} \sim 14.5\%$ for our design conditions.

η_{ASE} = $(1-f_{ASE})$, where f_{ASE} is the fractional loss of extractable energy due amplified spontaneous emission; we have used an analytical correlation formula developed at Los Alamos.[3.50] It is dependent on the Sullivan parameter $Su = GR_s wh/L^2$, where G is the amplifier two-pass gain, R_s is the sidewall reflectivity at the laser wavelength, w is the width, h is the height, and L is the length. η_{ASE} ~ 85% at our design conditions.

$\eta_{Magnets}$ This term accounts for the power which must be expended to operate the magnets. It is ~ 99% or higher since we only require ~ 6 kG fields and we use super-conducting magnets.

η_{Flow} This term accounts for the power which must be expended to operate the flow loop.

η_{Fill} The fill factor refers to the degree with which one fills the amplifier volume with two-way photon flux, for efficient extraction, given that we need to angularly encode about 100, time multiplexed, beams per amplifier. This factor depends on the size of the mirrors we need to use, which depends on the average fluence (J/cm^2) we design for on the input/output "feed" array of mirrors and the separation distance from the amplifier to the feed array. Finally, there is a constraint in how close output beam angles may be due to small angle scattering by the output window and the need to keep light from one angularly encoded channel from entering another channel and giving a pre-pulse of energy on the target. We use $\alpha \geq 4$ mrad.[3.51] η_{Fill} ~ 97% for a nominal 60 kJ size amplifier with 5 J/cm^2 optics and $\alpha = 4$ mrad. The separation distance required is ≥ 24 m in this case.

$\eta_{Delivery}$ Small reflection losses (~ 0.5% per surface) on each of the mirrors in route to the target (~ 8 surfaces) give ~96% for this term. Beam delivery is done in vacuum so there are no losses due to absorbing or scattering gasses.

Using our KrF kinetics code and amplifier extraction code, we generated parametric expressions for $\eta_{Intrinsic}$ as a function of gas composition, amplifier gain G, amplifier length L, pump rate P, and extraction time τ_e. We assumed enough F_2 for the amount of total pumping J/liter = $P\tau_e$, given our experience with data and calculations fitting data to this parameter. We also did calculations using a Los Alamos set of rate constants in our code and found no important difference in the calculated results for net amplifier efficiency.

With all of the component efficiencies expressed analytically, we performed parametric variations and created the following graphs of the results. In the following examples we used the

following parameters: Two-pass G = 12, E = 240 kJ at the output window, 1 atm Kr + F_2 at 323 K, 400 kW/cm^3 pumping, 600 ns extraction, and h/w = 2. We then varied the length, which occurs at almost constant volume, because the output energy was specified and the efficiency varies slowly over most of the range of interest. Thus, the output window area goes down as ~ 1/length, but at constant h/w.

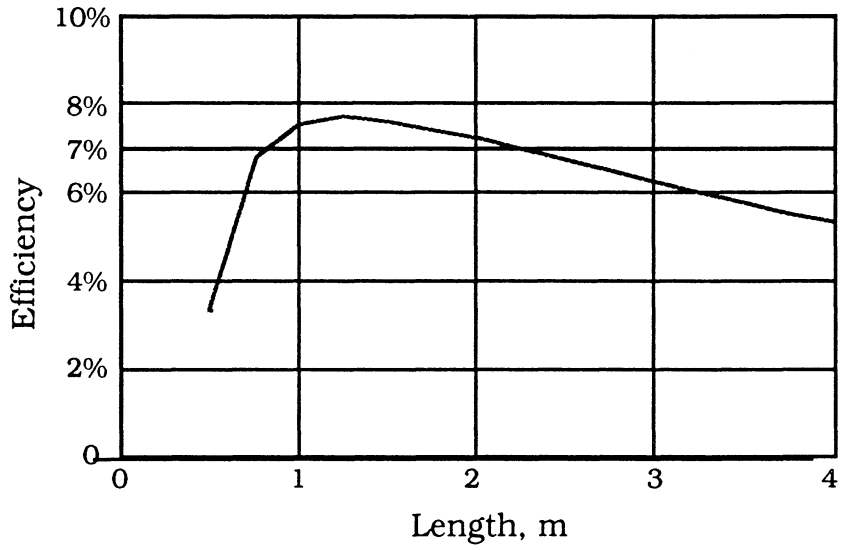

Fig. 3.68. $\eta_{LaserSystem}$ vs pumped gas length; Two-pass G = 12, E = 240 kJ at the output window, 1 atm Kr + F_2 at 323 K, 400 kW/cm^3 pumping, 600 ns extraction, and h/w = 2.

Figure 3.68 shows a peak efficiency of ~ 7.6% at ~ 1.25 m of length. To explain why the efficiency cuvre has a peak, we next examine the four components which are responsible for the shape of the curve in Fig. 3.68.

Figure 3.69 shows η_{ASE} and the intrinsic efficiency as a function of amplifier length. At short lengths the amplifier has large transverse dimensions which give rise to large ASE losses; the parameter Su ~ hw/L^2 is highly sensitive since hw ~ 1/L for our constant amplifier energy. Intrinsic efficiency drops off at long lengths because of the departures of the average total extracting flux, [$\phi_{left} + \phi_{right}$], from optimum extraction flux, $\phi_{opt} = [\sqrt{(g_o/\alpha)}-1]$, imposed on the solution by the assumed gain and other design parameters.

Figure 3.70 shows η_{Fill} and η_{Flow} versus amplifier length. The efficiency term attributable to the flow power requirement becomes low at short amplifier lengths because the flow dimension h ~ 1/$\sqrt{L}$ (at constant h/w), and flow power ~ Mach number squared ~ h^2. The Fill Factor monotonically decreases with L because the aperture is getting smaller at the same time the

length is increasing, both of which increase the fraction of partially extracted regions for a given feed array size and location.

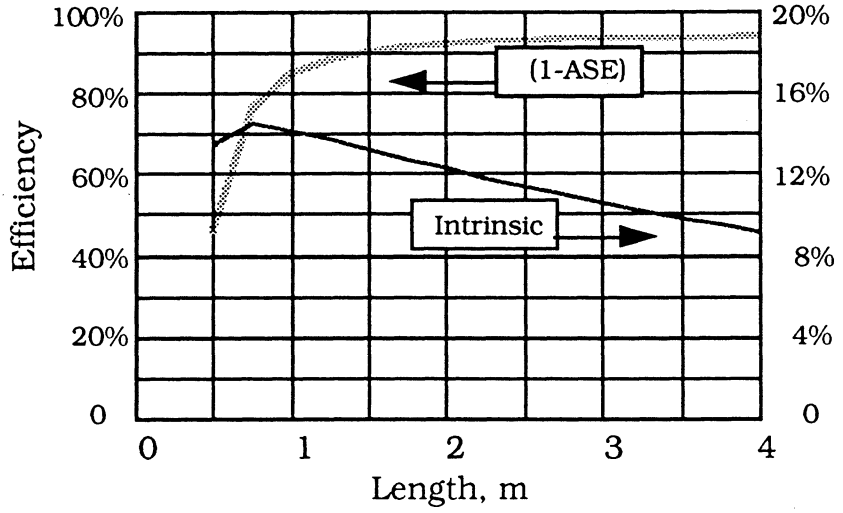

Fig. 3.69. $\eta_{ASE} = (1\text{-}f_{ASE})$ **and intrinsic efficiency vs length for the conditions of Fig. 3.68.**

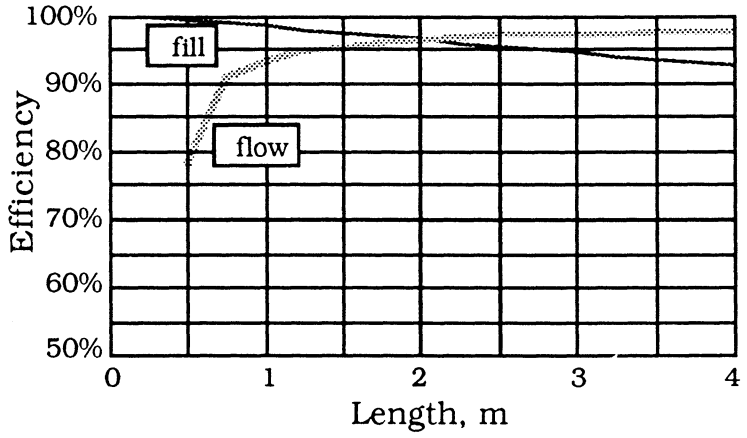

Fig. 3.70. Fill factor and η_{Flow} vs length for the conditions of Fig. 3.68.

Figure 3.71 shows the benefit of our choice of a high pump rate, 400 kW/cm^3, relative to a more traditional choice of 250 kW/cm^3. The higher pump rate gives higher efficiency, and it gives it at a relatively short design length. Even higher pump rates did not further increase the efficiency significantly.

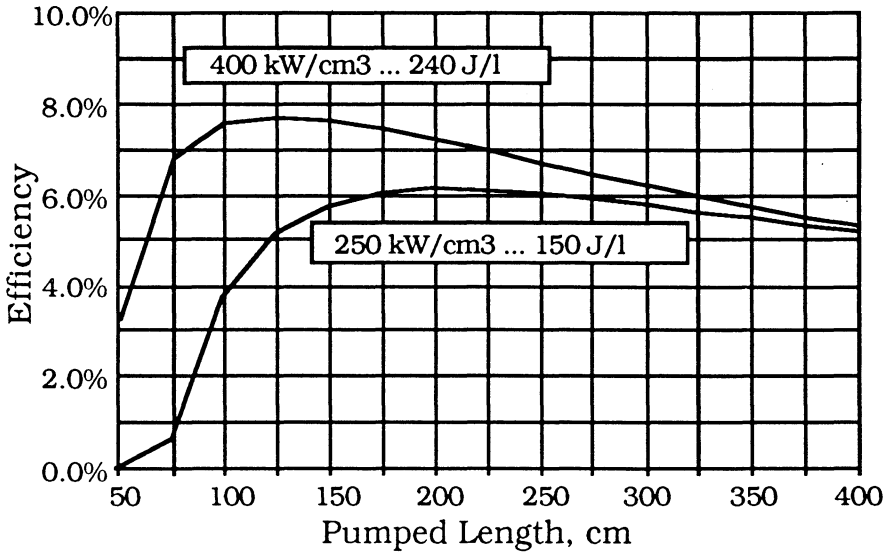

Fig. 3.71. $\eta_{LaserSystem}$ at pump rates of 250 and 400 kW/cm^3 vs length; energy deposited during 600 ns pulse lengths given; 1 atm Kr + F_2, two pass, G=12 amplifier extraction.

Figure 3.72 shows the benefit on efficiency of operating with smaller amplifier size. We also calculated efficiency for even smaller amplifier sizes, with no further improvement of note.

Figure 3.73 shows the beneficial effect of waste heat recovery, as discussed in Section 3.4.2.5 on the de facto laser efficiency when used in a total system which may efficiently make use of the waste heat. In the systems analysis, the efficiency is accounted for in the thermal conversion efficiency of the power cycle.

We have also examined the effect of amplifier two pass gain G in the vicinity of our interest, G = 10 to 20. The net effect is small; the higher gains had better intrinsic efficiency but offsetting ASE losses.

The choice of gas mixture is one of choosing the relative fractions of argon and krypton since F_2 is determined by the Joules/liter desired. Our code calculations show best intrinsic efficiency at ~ 50% argon, but there is little change in going to pure krypton. More krypton means higher e-beam voltage, lower current. Lower voltages are an advantage in reducing standoff

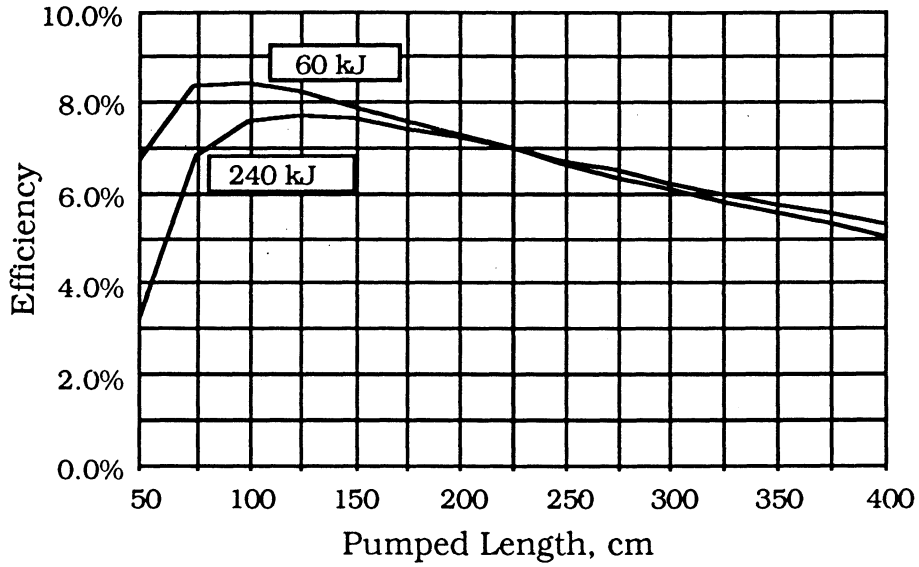

Fig. 3.72. $\eta_{LaserSystem}$ for 60 kJ and 240 kJ amplifiers; 1 atm Kr + F_2, G=12 two pass amplification, 600 ns extraction, 400 kW/cm^3 pumping.

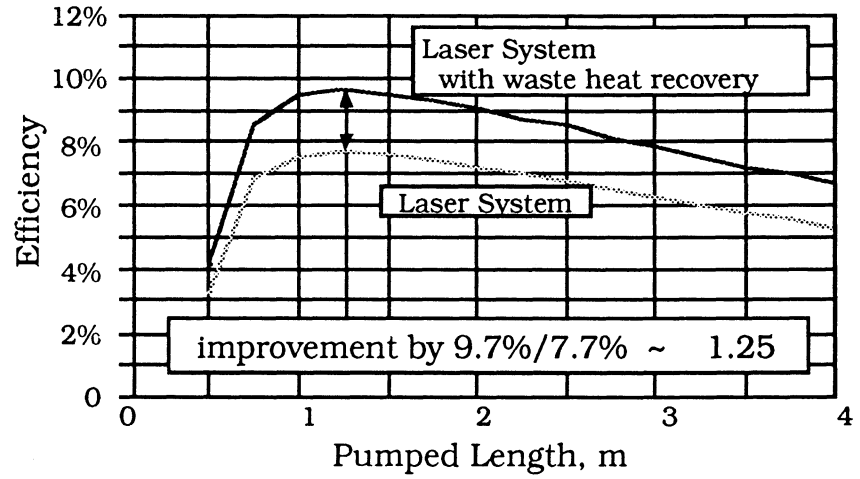

Fig. 3.73. $\eta_{LaserSystem}$ as shown in Fig. 3.68 and as it is with credit given for utilization of waste heat as discussed in Section 3.4.2.5.

distances, and thus inductance, but lower voltage/higher current means lower impedance; since the ratio L/Z determines rise time, these are competing effects. We can design a diode for either case, and the cathode technology we invoke has been demonstrated at the μcoulombs/cm^2 that we require for 50% argon, so we have made that choice to optimize efficiency.

We have chosen 60 kJ as the nominal amplifier size because it has higher efficiency, has no higher capital cost per Joule of electrical input energy to the laser amplifier, and is more

attractive for development in terms of size of components and operating voltage. The 60 kJ size leads to a very reasonable architecture, as we show later. Larger amplifiers would require longer pulse lengths (to keep $\tau_{rise}/\tau_{extract}$ reasonable), with greater number of multiplexing channels, though probably not more mirrors in number since there are more amplifier cavities in the system. Larger amplifiers would require larger e-beam voltages, and larger B-fields. Segmented e-beams is a way of helping this problem, but since each requires its own return current path, there appears no decisive advantage over more, smaller amplifiers. Amplifiers even smaller than 60 kJ would have no appreciable efficiency advantage and would have lower diffraction limited optical performance because of smaller final optic dimension (w) and angular beam spread ~ λ/w, where λ is the KrF wavelength.

Our choices for amplifier specifications are given in Table 3.16. Most of the terms are familiar to the reader by now, but we note "d" is the "dead" space of unpumped laser gas adjacent to amplifier window and mirror. The flush factor is the ratio of $v\tau/h$, where v is the flow velocity in the cavity, τ is the pumping time, and h is the cavity height. K is the ratio of the total amount of flow losses (Δp pressure drop) in the flow loop per cavity divided by the dynamic pressure in the laser cavity ($q = 1/2\rho v^2$). Fluence is the average fluence on the short pulse (6 ns) optics of the feed array, demultiplexing optics, etc. We assumed two sided e-beam pumping. Some of the amplifier operating parameters given in Table 3.17.

Table 3.16. Amplifier Cavity Specifications Chosen for KrF Laser Driver Design

E on target	60 kJ	l (optical)	1 m
Ar in Kr	50%	h (flow)	2 m
Pressure	1 atm	w (e-beam)	1 m
$T_{initial}$	50°C	d, unpumped gas	15 cm
Pumping	400 kW/cm^3	Flush factor	1.3
$\tau_{extract}$	600 ns	K ($\Delta p/q$)	6
Gain	16	Fluence	5 J/cm^2
PRF	7 Hz		

Table 3.17. Amplifier Operating Parameters

e-beam voltage	610 kV	$\tau_{rise}/\tau_{extract}$	6.1%
J_{Diode}	40.6 A/cm^2	$\eta_{Intrinsic}$	14.5%
Z_{Diode}	0.6 ohms	η_{Net}	7.6%
L	23 nH	$B_{Applied}$	6 kGauss

3.4.4 Final Amplifier Technology

3.4.4.1 Pulse Power

For pulses as short as 0.6 msec, it becomes difficult to design a lumped element PFN with sufficiently low inductance as to give fast rise and fall times. There are two well-established PFL variants which are more suitable, based on water and paper-oil dielectrics, respectively. Water lines have been the choice in virtually all previous studies, most of which are oriented toward single pulse test facilities.[3.52-55] The paper-oil system, available in cable form, has been developed in recent years for high energy, high rep rate DoD applications. Its dielectric constant is high enough that it is competitive on a power per unit area basis. In addition it has a much higher resistivity so that a slow wave form or even DC charging is possible. In contrast, the resistivity of de-ionized water is such that unacceptable losses occur for charging times of more than 2 μsec, unless the water has antifreeze added and is cooled.

The paper-oil system has been tested at Avco/Textron at charge voltages of 800 kV and 50 Hz repetition rate, delivering 15 kJ/pulse in 1.6 μsec flat top wave forms. In this experiment the cable was charged using a pulse (step-up) transformer with a charging time of 30 μsec. A cable and cable termination have been fabricated for 1.5 MV, but have not yet been tested.

Because of leakage inductance, which is inevitable in high voltage pulse transformers, it is not possible to design high energy transformers which will transfer charge to a water line in less than ~2 μsec, so a Marx generator is required. A Marx could also be used to charge cables; however, in the present study we have selected a pulse transformer approach with cables because of better reliability from the fewer number of internal switches, with consequent lower maintenance. Thus, the two systems we focused on for final selection were a Marx + Water Lines system versus a Modulator + Pulse Transformer + Cable PFL system. The two systems are illustrated in Figs. 3.74 and 3.75.

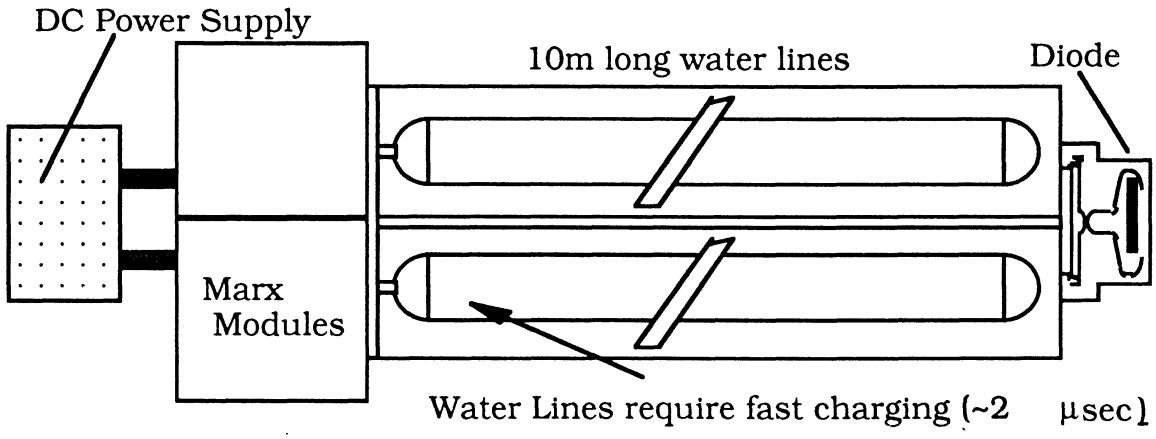

Fig. 3.74. Pulse power system with Marx driven water line PFL.

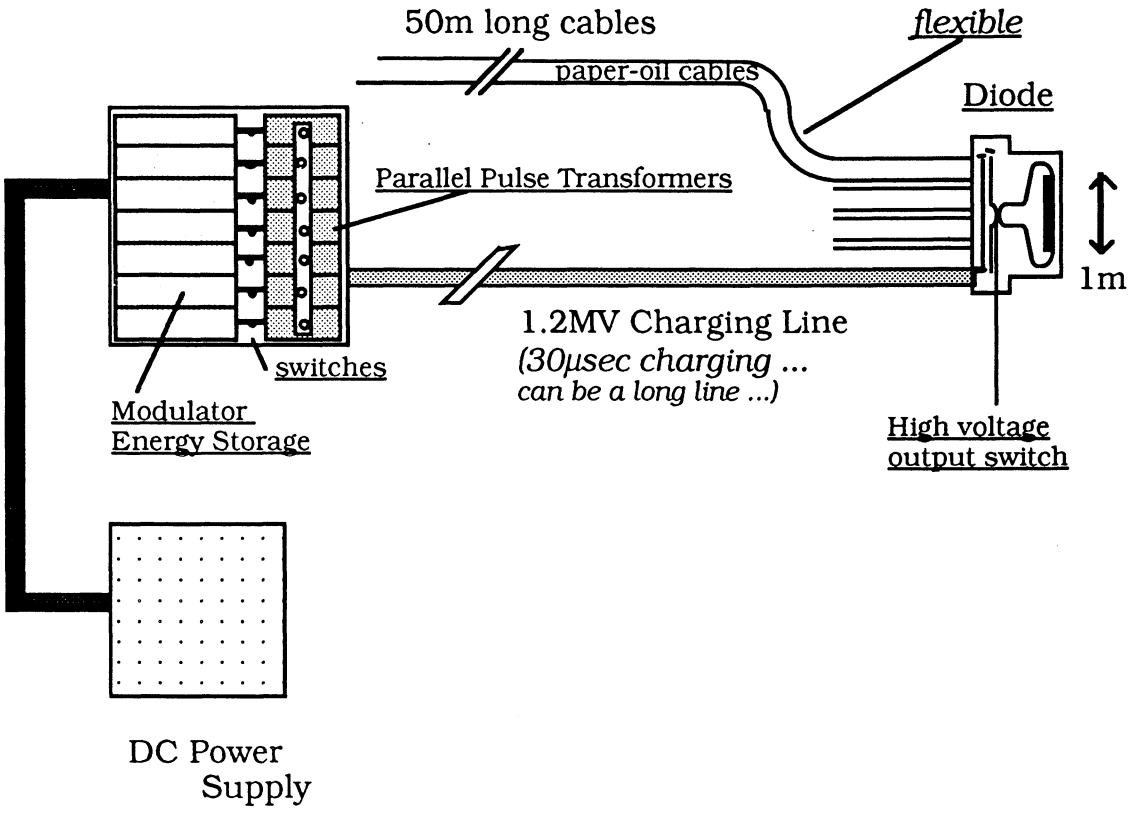

Fig. 3.75. Pulse power system with cable PFL and pulse transformer charging.

A fundamental performance parameter of a PFL is the power per unit cross sectional area that it can supply. We have compared water lines and cables of inner radius "a" and outer radius "b" with dielectric constants of K = 81 and 3.4, respectively. Cooled water has K = 45. We make use of the following equations:[3.57]

Impedance of a coax cable or water line is

$$Z = 60 \frac{1}{\sqrt{K}} \ln\left(\frac{b}{a}\right) \text{ ohms.}$$

Electric field at the surface of the center conductor is

$$E_a = \frac{V}{a \cdot \ln\left(\frac{b}{a}\right)}$$

Capacitance per unit length is

$$C = \frac{2\pi K \varepsilon_o}{\ln\left(\frac{b}{a}\right)}$$

Stored energy per unit length is

$$E = \frac{1}{2} CV^2 = \pi K \varepsilon_o a^2 E_a^2 \ln\left(\frac{b}{a}\right)$$

The line delivers power at voltage V/2 into a matched load impedance Z; thus the line power is

$$W_L = \frac{V^2}{4Z} = \frac{a^2 \sqrt{K} E_a^2}{240} \ln\left(\frac{b}{a}\right)$$

If we assume a number of parallel lines are required, each with an outer diameter of 2R and an area of $4R^2$ in a stacked array, then the power delivered per unit area is

$$W_u = \frac{a^2 \sqrt{K} E_a^2}{960\ R^2} \ln\left(\frac{b}{a}\right)$$

Thus in comparing water and paper-oil, the relative figure of merit is $\sqrt{K} \cdot E_a^2$. We next consider the allowable electric stress.

The allowable electric stress for 50% probability of breakdown in water is given by Martin[3.57] as

$$F\, t^{1/3}\, A^{1/10} = k$$

where F is in MV/cm, t is in μsec, and A is electrode area in cm^2. The parameter k is $k^- = 0.6$ at the negative electrode, and $k^+ = 0.3$ at the positive electrode. In addition to this consideration, one needs to apply a de-rating factor to provide for a lower probability of breakdown. For a 10^{-4} probability, the field stress should be reduced to 60% of F as given above, based on material from Physics International as reported by Parks.[3.58] For even lower probabilities, as we presumably would desire, the behavior of the curve is suggestive of very little additional de-rating being required, although further work is clearly needed. As an example, the storage of 500 kJ (approximately what is needed for one 60 kJ laser cavity) will require an electrode area of $A \approx 6 \times 10^5\ cm^2$; we assume the inner electrode, which carries the greatest stress, is at negative polarity, and the charging time is 2 μsec. In this case we get $E_a = 75$ kV/cm. For a total system with 3.6 MJ laser energy on target, the waterline electrode area is ~80 times larger, which implies an $80^{0.1} = 1.5$ further de-rating to $E_a \approx 50$ kV/cm.

For paper-oil storage, the DC insulator strength is 1 MV/cm in small volumes ($\sim 10^4\ cm^3$). If we de-rate by $(\text{Volume})^{0.1}$, use $7 \times 10^6\ cm^3$ for 500 kJ so the volume de-rating is 50%, and use a factor of 0.7 on the allowable field stress for pulsed operation, then we would obtain $E_a = 350$ kV/cm. There is presumably further de-rating for the volume associated with the total system, but we note that the de-rating for paper oil with increasing volume is probably not as

severe as it is for a homogeneous insulator such as liquid water because of the way the two components break up the incipient path of breakdown channels. Therefore, we will stay with 350 kV/cm for our total laser system.

Returning to our figure of merit of $\sqrt{K \cdot E_a^2}$, for water vs paper oil we have $\sqrt{81 \cdot 50^2} = 22{,}500$ and $\sqrt{3.4 \cdot 350^2} = 226{,}000$; the paper-oil is preferable by a factor of 10 in power per unit area delivery capability. To complete the comparison, we need to recognize the requirement for a field grading structure for the termination, at the diode, of these two different approaches. We estimate the termination of the cables can be done with an outer radius of R = 1.6b, where "b" is the outer electrode radius of the cable. For water lines, careful present day designs have line center separations of 1.2b. These estimates lead to a reduction in the paper-oil advantage by $(1.2/1.6)^2 = 56\%$ to 5.6 more power per unit area for cables than for water.

In absolute terms, we now estimate the power per unit area for paper-oil cables, with terminations, at 1.7×10^7 W/cm^2; waterlines would be lower by a factor of 5.6. This may be compared with a diode requirement of 600 kV · 40 A/cm^2 = 2.4×10^7 W/cm^2. Thus, we need a 40% reduction in area. This can be accomplished with a transition section incorporating the high voltage output rail gap switch, which we will show in the next section. Finally, we note that further improvements in design electric field stress may come with additional work devoted to this goal; cable development to date has been for power transmission applications, for which low stored energy is desired.

Cable pulse forming lines have very low residual resistivity, possibly dominated by resistively graded terminator resistances, so they can be charged on a relatively long time scale of 30 to 50 μsec - limited by leakage inductances. Therefore, one may use a pulse transformer rather than a Marx bank for their charging. This technology has been demonstrated at repetition rates up to 100 Hz, delivering 40 kJ at 1.5 MV.[3.59] Energy scaling of this, at constant voltage, is possible through an increase in the cross sectional area of the transformer core; we expect Energy ≈ Area$^{1.5}$. At 1.5 MV it appears possible to scale to at least 100 kJ per transformer. Thus, one could charge multiple cables with one pulse transformer and switch. The primary of the transformer must be fed by a modulator in which the Coulomb transfer is greater than that in the diode by the transformer turns ratio. Again a rail gap would be justified because of its large electrode area over which to distribute erosion. The switch closure speed is much less critical than in a Marx, so it may be possible to design a diffuse discharge switch with lower erosion rates than a spark channel switch. Current developments in the area of psuedospark switches[3.60] give hope for solutions developing over the next decade. The same amount of erosion would take place in a Marx generator for this job. In a Marx the switches are in series, while in the modulator they are in parallel. In fact, since the switches would be in parallel, we could split the modulator into separate units, each feeding a single transformer via a single switch.

A comparison of PFL parameters for a 1.5 MV pulse power system using Marx-driven water lines and using pulse transformer driven paper-oil cables is given in Table 3.18.

Table 3.18. Comparison of Water Line Design with Paper-Oil Cable

	Water Line	Paper-Oil Cable
Inner Radius, a	40 cm	8.6 cm
Outer Radius, b	66 cm	14.2 cm
Energy Stored / Length	10.1 kJ/m	0.43 kJ/m
Length for 600 ns Pulse	10.0 m	48.8 m
Energy Stored / Line	101 kJ	20.9 kJ
Number of Lines for 400 kJ	4 lines	19 cables

In the laser system architecture, we can take advantage of the flexibility of cables to bend them 90° or more and fit the system components closely together. They have restrictions on bend radius, but it is of order 20:1 for turn radius to cable radius; thus, our 14.2 cm cables radius means ~ 3 m radius turns. The cables may be routed to convenient storage trenches or overhead racks. The slow charge time possible with cables means there can be a long cable connecting the modulators and pulse transformers to the cathode + PFL cables (see Fig. 3.75). The modulators for the whole laser driver system may be co-located in a single area, where as the Marx drivers must be distributed and located contiguous to their water lines, as in Fig. 3.74.

Concluding Remarks on Pulsed Power. The comparison between energy storage in water and paper-oil dielectrics has been examined to a certain point. An informed decision will require more operational experience. For example, large scale water lines storing up to 100 kJ have never been run at repetition rate, whereas a cable system has been run at 50 Hz at 800 kV charge voltage, although at a relatively low energy of 15 kJ per pulse. The cable system has advantages in architecture flexibility and possibly in reliability, in that it can be charged using a pulse transformer. Cable manufacture is a mature technology, but cable terminations will require further development to become compact and cost competitive. The energy transfer efficiency for the water line system is thought to be about 90% from power at 150 kV DC to power off the diode cathode. For the cable system the efficiency should be better, of order 95%.

3.4.4.2 Electron Beam System

Cathode. Most e-beam driven excimer lasers have been single pulse machines and have used cold cathodes of metal blades, carbon felt, velvet, etc. Unfortunately, this technology is inappropriate for long life repped operation. One issue is that a more uniform emitter such as

carbon felt has a lifetime < 10^5 pulses. In addition, as it ages it develops emission non-uniformities which are transported by the applied B-field to the foil where the high current areas produce localized foil heating. A technology appropriate for repetitive pulse operation is the thermionic cathode. It was used on the EMRLD laser (100 Hz XeF laser for DoD) and in designs for longer running machines. It does require significant power (to maintain the ~1200°C cathode temperature in the face of radiative heat loss), and it requires advanced thermal engineering. For the high current density required of our fusion amplifiers (40 A/cm^2), one would need > 20 W/cm^2 of thermal power to be supplied (and removed from where it ultimately is absorbed as radiation). This may be compared to 100 W/cm^2 of average power carried by the e-beam itself (600 kV · 40 A/cm^2 · 0.6 μsec · 7 Hz = 100 W/cm^2). Obviously for higher rep-rate lasers, the thermionic cathode heater power is less significant. The thermal engineering must cope with keeping a hydrocarbon and moisture free vacuum system at < 10^{-6} torr while at ~1200°C. Clearly, ceramic bushings would be required.

In response to these issues, we have introduced a new plasma cathode[3.48] in our KrF laser driver system. A 10 cm x 30 cm version of this cathode has been demonstrated in Textron's laboratory. Key features such as its ability to achieve very high efficiency and have a construction scalable to larger sizes have been shown. The e-beam diode is illustrated in Fig. 3.76.

This technology requires < 1 W/cm^2 to operate the plasma and has a currently projected lifetime > 10^8 pulses, based on erosion rates of switch components. In addition, it is a non-closing diode; unlike traditional cold cathodes, it does not have a plasma that closes the anode-cathode gap (AK gap) during the 0.6 μsec pulse. This has several beneficial effects:

1) With no change in AK gap, the space charge limited cathode current does not vary. This means we have a constant impedance load, so near perfect impedance matching is possible.

2) With constant impedance, we can design for constant voltage and thus optimum deposition uniformity and pulse-to-pulse consistency for the sequence of 6 ns multiplexed pulses traversing the amplifier.

3) These features also imply the ability to run at higher current densities for longer times (i.e., higher coulombs/cm^2 than with closing diodes, which had constraints in this area).

4) Non-intercepting diode design is possible. With constant B_{self} and $B_{applied}$, the electron trajectories are constant. This, together with our ability to make cathodes emit only in areas that map into open areas of the foil supporting "hibachi," means we can have a diode with transmission efficiency limited only by the albedo of the foil(s) and the laser gas (minimized by low atomic number, Z, materials and gases).

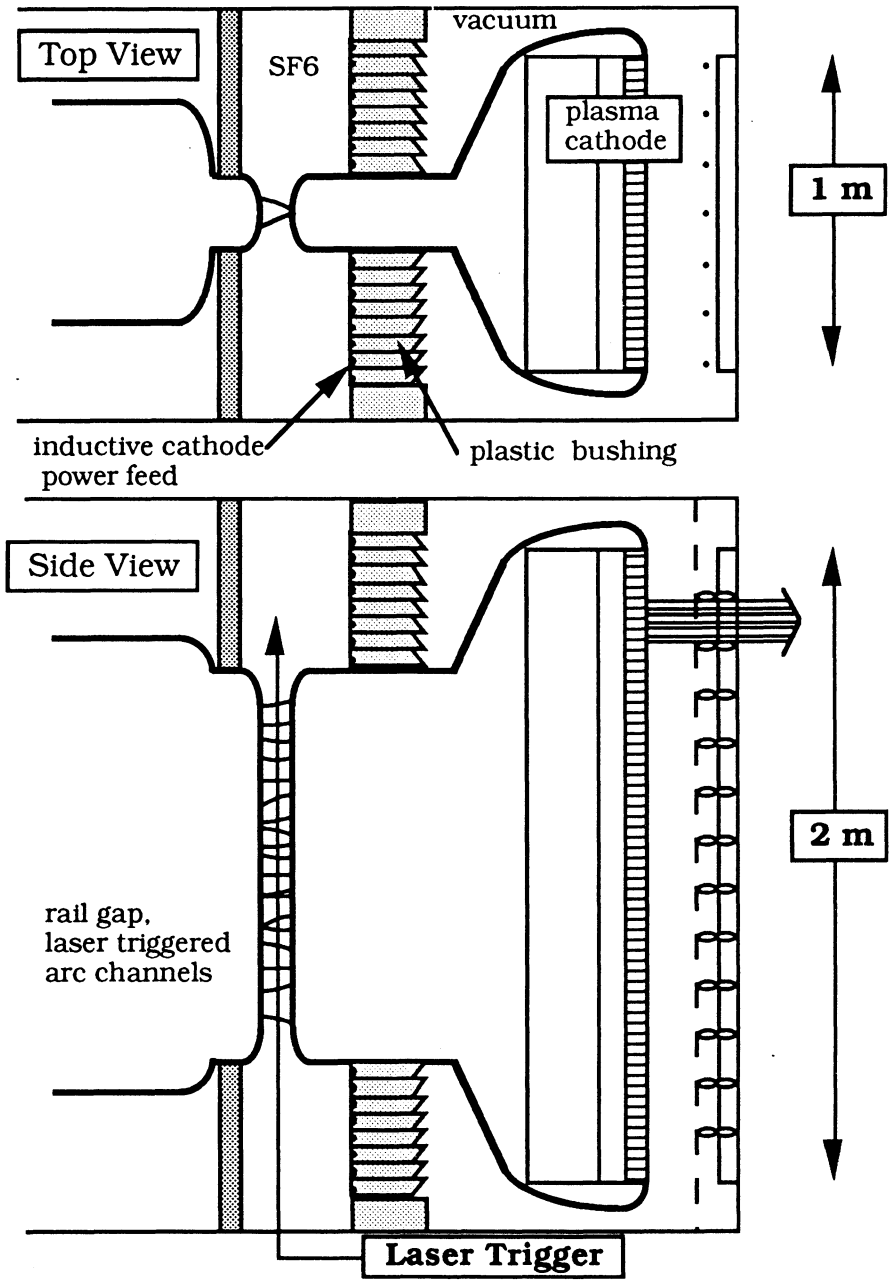

Fig. 3.76. Top and side views of Textron's electron-beam diode for a 60 kJ amplifier.

We require in the present design 40 A/cm^2 · 0.6 μsec = 24 μcoul/cm^2 (plus rise and fall time requirements). In response to a particular DoD program need, our research on this cathode technology has demonstrated 6 A/cm^2 for 5 μsec and 15 A/cm^2 for 1.5 μsec. Operation at 2 Hz has been demonstrated; 10 Hz should be possible with a small cooling circuit and more efficient use of gas in the plasma. We have operated with applied magnetic fields up to 2.3 kG, and our present design should work to over 4 kG. Some modification to the design may be necessary for

the 5 to 6 kG needed in the present case. Thus, we are fairly confident of meeting the present design requirements with a reasonable amount of further R&D and demonstration.

The plasma cathode has a power requirement of its own for the low voltage discharges in its structure. This requirement is modest because it operates with about the same current per unit area of cathode face area, but at a voltage of ~ 1.5 kV. Since the e-beam in the present design operates with 600 kV, the plasma cathode power requirement is only 1.5 kV/600 kV = 0.25% of the e-beam power. The average current requirement is

$$J \cdot 1.5\tau\nu A = 40\ A/cm^2 \cdot 1.5 \cdot 0.6\ \mu sec \cdot 7\ Hz \cdot 2\ m^2 = 5\ A$$

in the present case (the cathode operation is ~1.5 times longer in duration than the e-Beam). This current is easily carried by a thin wire wound in a bifilar spiral up the bushing structure. The inductance of such a spiral is high enough to give good isolation during the 0.6 μsec pulse. It can also be used to inductively grade the bushing.

The plasma cathode also requires a small puff of low pressure gas into its structure for each pulse; here we examine the gas consumption and pumping speed requirements. Our research versions of the cathode have operated with an input of about 15 gas molecules per electron emitted; we believe there is scope for a large reduction in this ratio to less than one molecule of gas per electron. This will be accomplished by designing for smaller manifold volume in the gas distribution system (i.e. gas release closer to the required discharge volumes). In addition, we would use sorption pumping at LN_2 temperature in the cathode back space where the pressure is 10^{-2} torr (as opposed to $5x10^{-5}$ torr in the AK gap). With these improvements the required pumping speed, $S = J\tau\nu A / qP_{base}$, would then become

$$S = 40\ A/cm^2 \cdot 0.6\ \mu sec \cdot 7\ Hz \cdot 2\ m^2 / (1.6x10^{-19}\ coul \cdot 5x10^{-5}\ torr) = 17{,}000\ liter/s$$

This pumping speed represents less than 10% "open wall" pumping speed for one side of the diode.

Relative to simpler cold cathodes, there is more depth required for the structure of the plasma cathode assembly. Based on our present designs, this depth is $(17 + J\ \tau\ 10^6 / 2)$ cm. The first term is composed of 4 cm for the discharge region, 8 cm for the gas distribution region, and 5 cm for switches and controls. Future designs will require less gas distribution depth, as we discussed above, but will require depth for the sorption pump. The term with $J\tau$ represents energy storage requirements; this depth may reduce by up to two fold for more advanced future energy storage. In summary, the depth requirement is a design consideration, but is not an issue.

As we have mentioned, the non-closing plasma cathode will allow a patterned emission that releases electrons only in areas that map, by the net B-field transport, into open areas of the foil support ribs ("hibachi" structure). We have demonstrated in the laboratory 92% transmission through a fine featured foil support structure; near 100% should be possible for a structure with 2 to 5 cm openings, such as we could use in our KrF amplifiers. Given this, the albedo of the foil-gas combination becomes controlling for the overall e-beam efficiency. In the next section we discuss the foil and foil cooling design.

Foil. If we design our foil support structure with 1 inch openings and a support angle of 25°, as shown in Fig. 3.77, and assume titanium foil material (Ti 15-3-3-3), for which we have the best data base for e-beam pumped lasers, with a working peak cyclic stress of 60 ksi at up to 600°F for 10^7 to 10^9 cycles,[3.61] then for 1 atm plus 2 atm over pressure, we conclude a thickness of 2.4 mil (0.0024 inch) is required. We have also checked the elongation and find it to be 0.3%, which is less than the 1% allowed. While this is a possible solution, we prefer to believe that good beryllium and beryllium-aluminum foils could be made in the requisite sizes by the time the technology was needed. The advantage is the lower stopping power (~ Z = 4 for Be, and Z = 22 for Ti); hence, more efficient e-beam transport and lower heating would be achieved. Recently, large width beryllium foils have been manufactured, and some preliminary testing at Textron has shown that they can be used for large span, high pressure, vacuum/gas windows. Pure beryllium is brittle, but beryllium/aluminum alloys with 25% to 40% aluminum have been made and are much less brittle. The strength of the 25% alloy is as good as the pure beryllium, 85 ksi as rolled. We assume the fatigue strength of the 25% alloy is 80% of its tensile strength (the same ratio as for pure beryllium). Thus, we assume 60 ksi for 10^9 cycle fatigue at up to 600°F; these numbers are comparable to those for Ti 15-3-3-3.

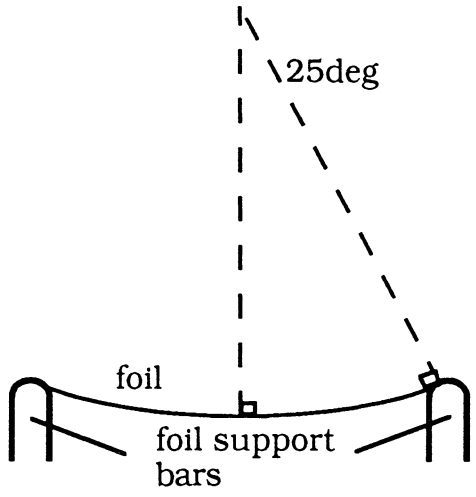

Fig. 3.77. Foil support bars with foil at design support angle of 25°.

Foil heating occurs with each pulse of the e-beam, so a steady state removal of heat is required. For support bar spacings that are relatively large, as is advantageous for non-intercepting design, it is difficult to conduct the heat to a foil support bar, which could have water cooling passage. A better solution, which we have assumed in our design, is to use a double foil system with gaseous helium flowing between the foils for convective heat removal, as shown in Fig. 3.78. We have used a 1-D Monte-Carlo (TIGER) code to calculate the e-beam energy deposition in a dual foil system consisting of 1 mil (= 0.001 inch = 2.5×10^{-3} cm) of Be and 1 mil of Be sandwiched with 1 mil of Al.. We include an estimate of the additional energy deposited by electrons reflected by the laser gas; it is a 25 to 35% effect. The average heat load into the Be/Al foil is then $\delta V J \tau v = 35$ kV · 40 A/cm^2 · 0.6 μsec · 7 Hz = 5.9 W/cm^2. The second foil of Be alloy will have a heating rate of ~2.3 W/cm^2. The stopping power of 0.5 atm of helium between the two foils is negligible, and thus so is the e-beam heat input . Overall we need to remove ~5.9 + 2.3 + 0.5 (from anode wire radiation) or ~9 W/cm^2. For the present design, we estimate 300 g/sec of helium for the 2-m-high × 1-m-wide e-beams on the ultimate amplifiers. The temperature rise in the helium will be ~120 °C. The titanium option would require ~2.6 times greater heat removal.

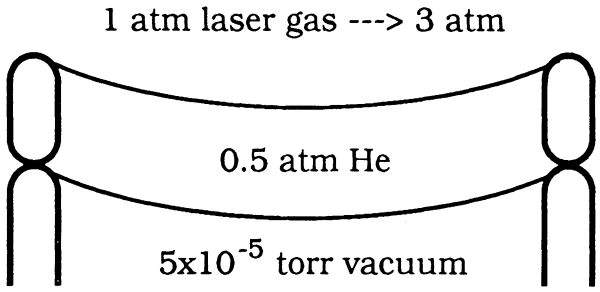

Fig. 3.78. Double foil system with gaseous helium for convective foil cooling.

Diode Inductance and Rise Time. We have modeled the diode structure for purposes of determining its inductance, which divided by the impedance determines the rise time $\tau \approx L/Z$ In our present 60 kJ design, the rise time is about 30 nH / 0.6 Ω = 50 ns = 8% of 600 ns. Larger lasers quickly loose efficiency in this area because inductance grows and impedance decreases with laser size. This of course was quantified at the time we did the amplifier efficiency optimization described in Section 3.4.3.

Anode. The anode in the e-beam diode is composed of a plane of parallel wires or filaments. It is desirable to minimize the interception of electrons by the anode and to have it cool

by passive radiation, if possible. We write the equation for the heat input per unit length as $2aJV\tau\nu$, where a is the filament radius, J the current density, V the e-beam voltage, τ the pulse time, and ν the rep-rate. This is balanced by the radiative loss per unit length of $2\pi a\varepsilon\sigma T^4$, where ε is the emissivety of the wire at temperature T, and σ is the Stefan-Boltzmann constant. Equating these terms gives

$$T = \left[\frac{JV\tau\nu}{\pi\varepsilon\sigma}\right]^{1/4}$$

For $J = 40\ A/cm^2$, $V = 600\ kV$, $\tau = 0.6\ \mu sec$, $\nu = 7\ Hz$, $\varepsilon = 0.5$, and $\sigma = 5.7 \times 10^{-12}\ W/cm^2 \cdot K^4$, we get T = 1830 K or 1560 °C. The anode material could be carbon or tungsten filaments under small tension, since carbon sublimes at 3700 °C and tungsten melts at 3387°C. The lack of diode closure arcs should allow the anode a long lifetime.

Assuming the anode wires represent a 1% interception, as in 0.25 mm filaments spaced every 2.5 cm (the A-K spacing is ~5 cm), then the heat load per unit of cathode or foil area is $0.01 \cdot JV\tau\nu = 1\ W/cm^2$. Half will go to the cathode (adding to the $0.7\ W/cm^2$ cathode plasma/discharge dissipation) to be carried away by the continually pumped out gas, and half will go to the foil system - a contribution already included in the helium cooling load.

Lifetime Issues. We list the following lifetime issues:

1) Erosion of laser triggered spark-gap electrodes,
2) Aging of the foil by e-beam irradiation,
3) Chemical attack on the foil by the 0.6% fluorine containing laser mixture,
4) Erosion of cathode discharge electrodes,
5) Life of discharge commutator in the plasma cathode,
6) Life of cathode discharge capacitors,
7) Bushing deterioration due to x-rays.

We have examined each of these issues. In general, those components suffering erosion are of most concern when considering 1.6×10^8 pulses per year (75% duty at 6.7 Hz). The laser triggered rail gap we estimate would need service once a month if it were of simple fixed construction. On the other hand, if the emitting area is a rotatable rod or cylinder, new surface could be rotated into place via a 30° rotation each month, giving a year of operation before replacement of a part is necessary. The cathode discharge electrodes are estimated to have a 10-year lifetime. Other areas of concern in the cathode have service intervals of a year or longer. Similar concerns occur in the commutator for the cathode discharge current since it carries about the same number of coulombs as the e-beam itself. We propose the use of psuedospark switches

in this area,[3.60] and, again, the principle of designing switches that allows the introduction of new surface material is a design concept that we propose could be developed for this application.

3.4.4.3 Flow

The flow loop must provide homogeneous gas with very small density perturbations ($\delta\rho/\rho$ of order 10^{-5}) in the laser cavity for each new pulse. It is a closed cycle system, which means that steady state waste heat removal is required, along with acoustic suppression of the over pressure from the e-beam deposition. Figure 3.79 gives representative dimensions for a 60 kJ laser cavity operating at 10 Hz with 1 atm of Ar:Kr = 1:1 at 300 K, with 290 J/liter energy deposition. The over pressure is calculated to be 1.9 atm. With a 2 m cavity in the flow direction, a flush factor of 1.5, and a 10 Hz rep-rate, the flow speed is 30 m/s and Mach number in the cavity, based on initial gas conditions is 0.12. The Reynold's number is 3.2×10^6.

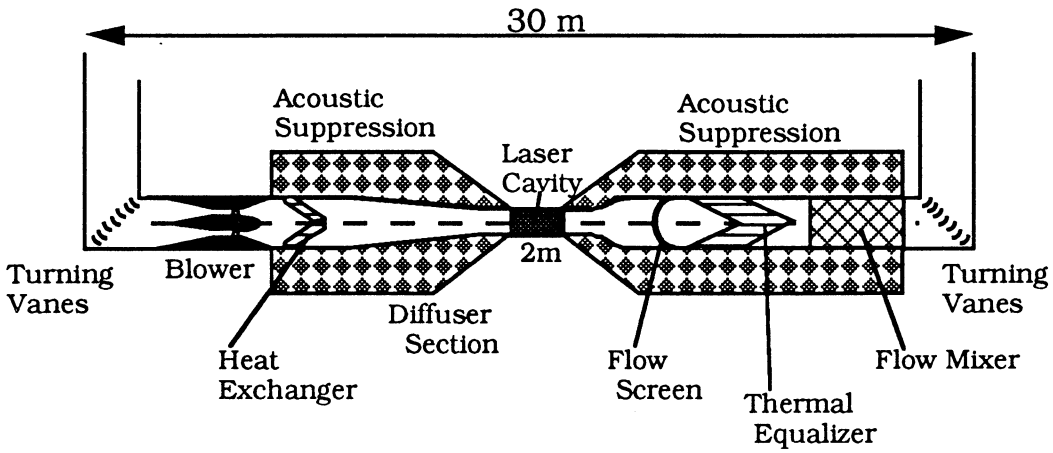

Fig. 3.79. Flow system for 60 kJ amplifier cavity; flow is from right to left in the figure.

The design shown was sized based on design approaches developed in the EMRLD program (a DoD high average power, e-beam pumped, XeF excimer laser) and scaling studies done for laser fusion.[3.62] The diffuser operates with a total angle of 8°, expanding the flow area by a factor of three. This area ratio allows the other flow components, such as the heat exchanger, flow mixer, and thermal equalizer, to operate at lower dynamic head by a factor of $3^2 = 9$. The pressure drop across the flow hardware (turning vanes, mixer, heat exchanger, and so forth) determines the blower size. This design will require that it supply Δp of about six dynamic heads ($1/2\rho v^2$) of pressure drop, based on ρ and v in the laser cavity. Thus,

$$\Delta p \sim 6 \cdot 1/2 \cdot 2.3 \times 10^{-3}\ g/cm^3 \cdot (2000\ cm/sec)^2 \Rightarrow 0.4\ psia.$$

Clearly, the size of a laser is determined by the flow loop, which is related to the need to suppress acoustic energy between pulses. This is related to total energy deposition, which is proportional to laser energy required for the target. Given that Fig. 3.79 represents what is required for each 60 kJ cavity, and that we need 60 such cavities for 3.6 MJ on target, we could eliminate the 90° turning vanes, shown in the figure, and link 60 such segments into a single circular loop of circumference 60 · 30 m = 1800 m, or a diameter of 600 m. Perhaps two loops of 300 m diameter or four loops of 150 m diameter would make more sense. These large flow loops could be centered on the SOMBRERO reactor building. These chains of amplifiers would not have to be circular, but could be oval, hexagonal (etc.), serpentine, rectangular, or square. A large number of amplifier cavities in a single flow loop, puts them all at risk if there is trouble with flow loop components of one of them. For this reason, we have settled on the arrangement shown in Fig. 3.80. Fifteen of these flow loops, each with four cavities, will supply the nominal requirements of 3.6 MJ on target. We also include a spare loop with four cavities for speed and ease of supplying the required laser beams while servicing an amplifier.

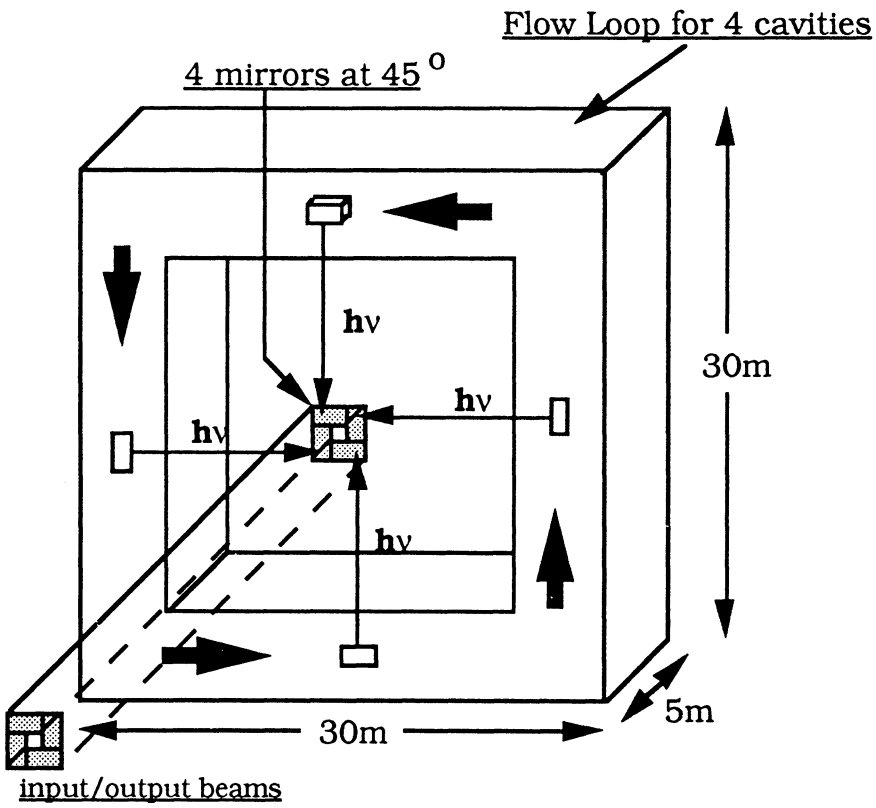

Fig. 3.80. Flow loop with four 60 kJ amplifier cavities.

The cavities in Fig. 3.80 operate as two pass amplifiers. We show in the figure a grouping of four mirrors, at the center of the flow loop, one for each cavity, each at 45° angle to the line of sight to its cavity window and mirror, each of dimensions 1.4 x 2 m (1x2 m projected area at 45°), matching the beam dimensions at the cavity mirror. The individual beams (each 6 ns long) are largest at the cavity mirrors and decrease as they go to the feed arrays. The bundels of beams from/to the feed array require approximately constant cross sectional area. Since we are carrying the beam paths in vacuum from the large amplifiers, there is advantage in packing them together as we turn 90° to transmit from/to the feed arrays.

3.4.4.4 Optics

Short pulse (~ 6 ns) optics are assumed to operate with loadings of 5 J/cm^2. This is the same fluence as was assumed for the more near term LMF single pulse KrF laser fusion experimental facility.[3.63] It is difficult to know what is truly credible for 1.6×10^8 pulses per year. We note that good progress has been made in damage limit improvement in recent times, and this application is for tenth of a kind in the year 2040. Recently, damage values as high as 28 J/cm^2 were reported for laser annealed, multi-layer coated optics operating at 248 nm with 15 ns pulses.[3.64] We de-rate from this in our system design to account for shorter pulse lengths, non-uniformities in the fluence, including those from diffractive effects, long term repetitive operation, and to account for non-uniformities in coating manufacture and performance.

The steady state heat load for repped operation is ~ 5 J/cm^2 · 7 Hz · 0.1% absorption = 0.035 W/cm^2. This is a modest load that may be removed by cooling passages in the substrate.

Propagation. Long path beam propagation of 248 nm in the atmosphere is an issue for several reasons. They include Rayleigh, aerosol, and Raman scattering, the absorption by atmospheric gases (especially by ozone), and phase front distortion by density fluctuations and gradients caused by thermal eddys and thermal gradients. These issues are discussed by Rosocha et al. for the Aurora system.[3.65] We add to that discussion by noting that for an IFE driver the total path lengths are larger, of order 1 km and more, thus exacerbating the problems. In addition, the broad band width of KrF fluorescence means that there is already radiation at the N_2 S(8) Raman wavelength (76 cm^{-1} shift) to seed the Raman transition. The Raman gain is ~1 cm^{2}MW^{-1}km^{-1}. The short pulse beamlets get up to 5 J/cm^2/6 ns ≈ 1 GW/cm^2, so gains of several decades occur in 10's of meters and one has self seeding. It seems likely that multiple uncontrolled Raman shifts would occur. Thus it is clear that an optically inert gas or a vacuum should be used for the long beam paths.

The advantage of a gas medium at 1 atm, as opposed to vacuum, is that the ducting does not have to hold off an atmosphere of pressure. On the other hand one does need a scheme for

introducing the gas, while displacing the air without mixing, in a system of interconnected paths, elbows and T's. In addition, the walls must be multiply insulated because the fluctuations need to be of order $\delta\rho/\rho = 3 \times 10^{-5}$ or less (i.e. $\delta T < 0.01^{o}K$) if the path lengths are of kilometer scale. This is true even if the gas is helium (the best possible optical choice) and the density non-uniformities transverse to the beams are disordered.

Vacuum is our choice because the architecture we have developed consolidates beam lines and makes cylindrical vacuum ducts practical and of reasonable cost. With vacuum we eliminate any uncertainties related to the propagation medium.

3.4.4.5 Magnetic Field Coils

A pair of coils is required to produce an applied magnetic field, parallel to the e-beam direction, of magnitude ~3 times the self field from the e-beam current flow in the diode. The self field for our nominal design is ~1.75 kG, so our applied field should be ~ 6 kG. The rectangular coil dimensions are roughly 2 m x 3 m spaced by 1.5 m. They require ~10^6 amp-turns to produce the desired field at the center of the pair.

We assumed NbTi superconductor at 6.2 K, which allows 2^{o} margin for pool boiling of helium. The current density was taken at about 200 kA/cm^2 for each of the two coils, which includes a 2x safety margin for the superconducting operation. The copper stabilizer is designed for 3200 A/cm^2, which is very conservative.

3.4.4.6 Controls

We made an estimate of the controls required for each e-beam, pulse power system, flow loop and mirror system. We assumed the need for a large number of sensors per unit to ensure the ability to keep continuous intelligence about developing maintenance needs. For example, for each e-beam we have a total of 23 sensors, for each e-beam pulse power system - 40 sensors, for each flow loop - 12 sensors. We included control rooms and displays.

3.4.5 System Architecture

3.4.5.1 Ultimate and Penultimate Amplifier Layout

Given the module shown in Fig. 3.80, and the symmetric irradiation requirements of 60 directions uniformly spread over 4π steradians, one can draw an architecture with a group of four flow loops, each having four 60 kJ cavities, on each of four sides, call them north, south, east, and west. This gives one flow loop with four cavities as a spare for system redundancy. The west side lasers are shown with a 100 m diameter SOMBRERO reactor building in Fig. 3.81. By symmetry one can visualize the other three sides.

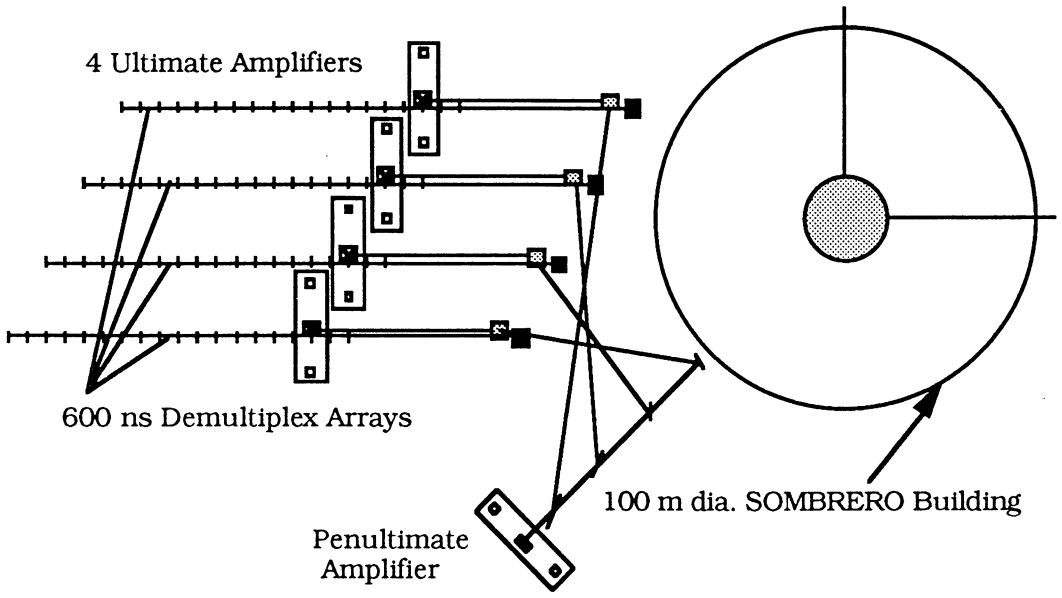

Fig. 3.81. One fourth of a laser driver system in an architecture spreading the lasers uniformly around the SOMBRERO building; four flow loops, each with four 60 kJ amplifier cavities, and their associated 600 ns demultiplexing arrays, are shown as well as a the preceding stage Penultimate amplifier.

This architecture has two difficulties. There is need for room on the east and the south sides for various balance of plant equipment to be located. In addition, one desires to compact the laser system to minimize building costs. Our desire to carry the beam lines in vacuum, or in high thermal uniformity helium, calls for a design that brings beam lines together as much as possible. Figure 3.82 shows an architecture that responds to these constraints.

In Fig. 3.82 the total system is split into two equal parts located on the north and west sides. On the north side we label the input/output array for the thirty-two 60 kJ amplifier cavities housed in 8 flow loops. On the west side we show a representative optical path of a single 6 ns beam leaving its 2x4 cm feed mirror, going north to a 45° turning flat, going east to a next 45° turning flat, then going north to the turning flat in the center of the flow loop, discussed for Fig. 3.80, and then going into the appropriate one of the four 60 kJ cavities of this flow loop. One of these 6 ns pulses gets amplified to energy ~60 kJ/100 = 600 J since we have multiplexed the 600 ns amplifiers to one hundred 6 ns beamlets. Thus, after a double pass transit of the amplifier, the beamlet follows an angularly offset path back to the input/array where it is picked up on an 8x16 cm mirror which recollimates it and sends it west to the demultiplex array. The demultiplex array provides a designed time delay, and then sends the beam on to the beam handling area under the SOMBRERO building.

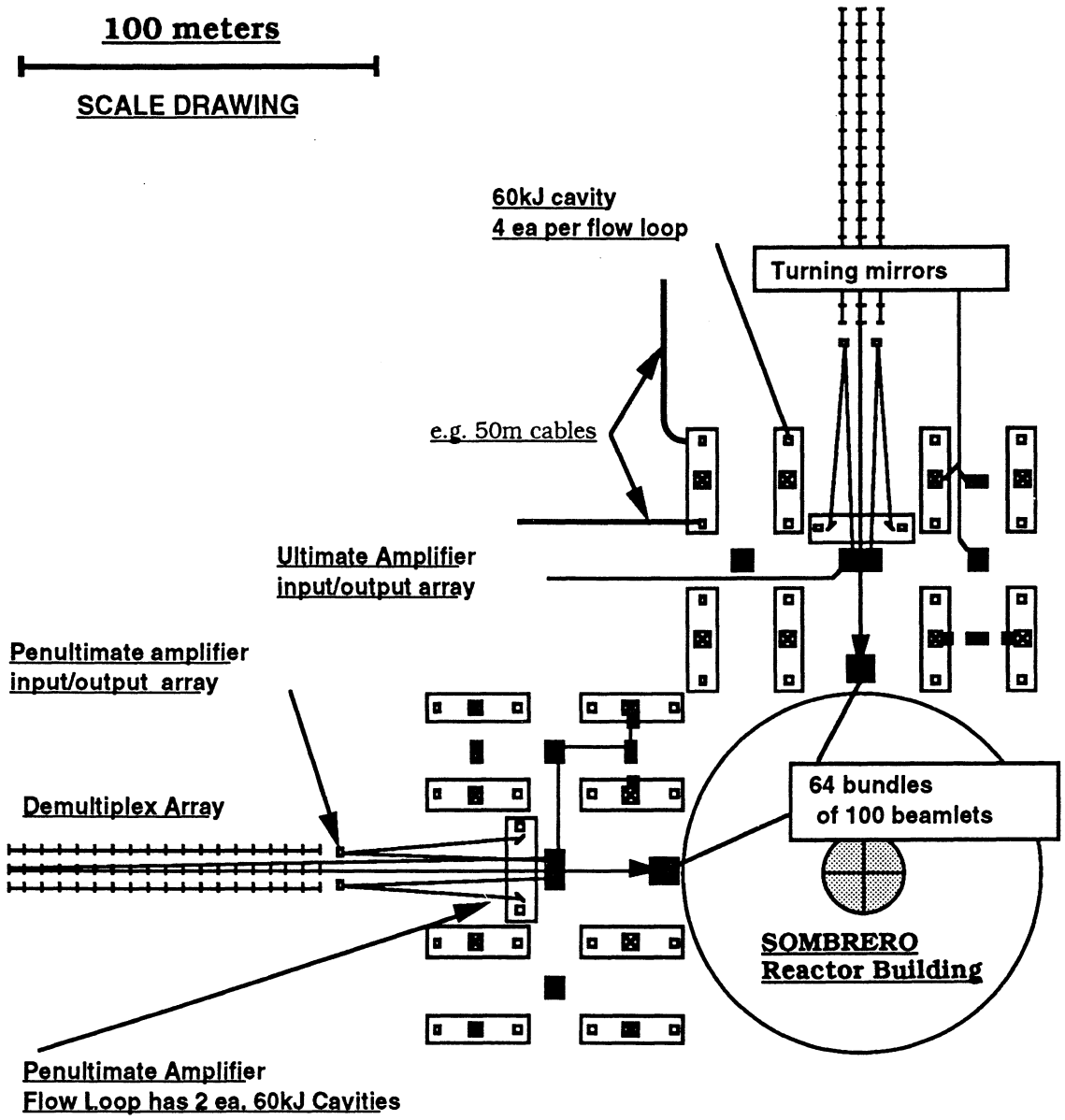

Fig. 3.82. Architecture for Ultimate and Penultimate amplifiers.

There are two penultimate amplifier flow loops, each with two 60 kJ cavities, located on the west and north sides, respectively. The counting is clear since the ratio of 64 ultimate amplifier cavities divided by their Gain = 16 implies 4 penultimate cavities of the same energy output. There are some optical losses between stages obviously, but we are not considering this at this stage of conceptual design. The penultimate amplifiers can be in flow loops identical to those of the ultimate amplifiers, but with two sides vacant of amplifier cavities. However, we would have cavities in three sides to give redundancy at this stage of the amplifier chain. The extra cavity would have flow continuously going through it and its blower operating, but would not be e-beam pumped unless needed, at which time mirrors would redirect beams to the standby cavity.

The total number of 6 ns beamlets is $64 \cdot 100 = 6400$. 6,000 of these are active at any time and are distributed into 60 directions onto the target. The directions are sorted in the beam handling area under the SOMBRERO building. If the beams go the most direct route possible, there are different path lengths to the target for each of the 60 directions. Appropriate time delays may be introduced via optical "trombones" in this area and/or by use of the demultiplex array trombones. Use of the extra four laser cavities when needed will require them being able to supply any of the 60 directions, which will call for special trombones and mirror insertion possibilities in the design.

Figure 3.82 shows to scale, schematically, pulse power cables of the requisite ~50 m length, with 3 m radius turns, which can be used to bring them to a suitable rack or trench. The modulators and pulse transformers may be located in a building on the NW corner, between the two systems.

As mentioned in Section 3.4.3 on amplifier optimization, we will use interleaved input/output arrays. For our amplifier h/w = 2 window aspect ratio, we use mirrors with aspect ratio two. The geometry of the interleaved arrays is illustrated in Fig. 3.83. Starting in the upper left, we see a 2×4 cm mirror that feeds energy (600 J / 16 = 38 J in 6 ns), by way of 3-fold

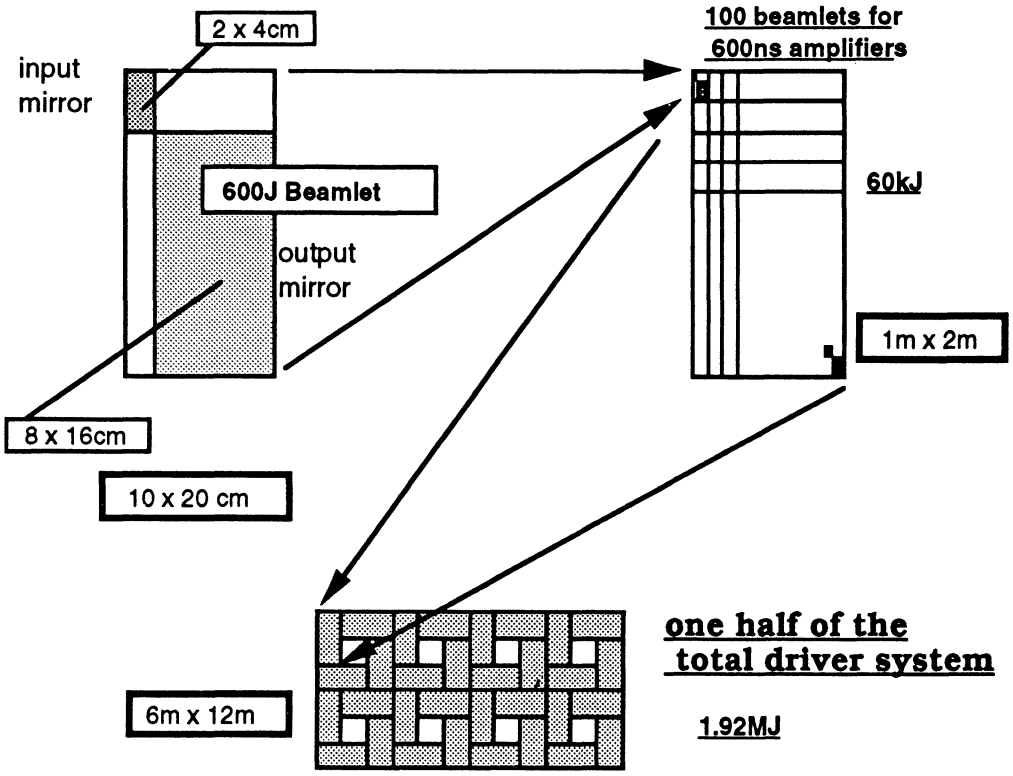

Fig. 3.83. Interleaved mirror arrays for input / output to the 60 kJ Ultimate Amplifiers.

mirrors, into one of the 60 kJ cavities where in a 2-pass transit it is amplified to 600 J and is picked up, after 3-fold mirror reflections, by an 8 × 16 cm output mirror. The pickup mirror is not the one adjacent to the input mirror but is equal distance diagonally across the center of the array of 100 input mirrors interleaved with 100 output mirrors. One of these arrays is shown schematically in the upper right of Fig. 3.83. Finally, 32 of these arrays of 100 input/output mirrors are grouped as shown in the bottom of Fig. 3.83.

3.4.5.2 Intermediate Stages

There are a number of architectures that may precede the Penultimate and the Ultimate amplifier stages. We list in Table 3.19 a possible set of prior stage specifications for illustration.

Table 3.19. System Amplifier Sequence

Stage	Total Energy	# Amp's + Spares	Cavity Energy	Amp Gain	Extraction Time	Total # of Beamlets
Ultimate	3,600 kJ	60 + 4	60 kJ	16	600 ns	6,000
Penultimate	240 kJ	4 + 2	60 kJ	16	600 ns	400
AntePenU...	20 kJ	1 + 1	20 kJ	20	600 ns	100
PreAntePenU..	1.4 kJ	1 + 1	1.4 kJ	25	150 ns	25

3.4.5.3 Front End

The front end for the system has several requirements. We desire broad band KrF emission ($\Delta\nu/\nu \sim 0.1\%$). This is consistent with the natural fluorescence bandwidth of KrF so that the approach such as NRL[3.66] has developed, for running KrF itself as a broadband, spatially incoherent initial source is suitable. In addition, we note that the de facto target gain is considerably enhanced if the individual beams which illuminate the target reduce their diameter at the target, as the target implodes, by a factor of two in diameter during the ~ 6 ns of the most intense part of the illumination (the remainder of the implosion occurs after this). This is referred to as the "zooming" front-end option. For the overall system design that is appropriate for non-echelon ISI direct drive target illumination, this approach leads to easily understood front end requirements. The entire laser system images the front-end aperture onto the target, with amplification at the spatial Fourier transform of the front-end aperture. If one needs a two times smaller spot on the target, then a two times smaller aperture at the front-end source is required. Unfortunately one will need the same amount of power (watts, not watts/cm^2) through the variable size aperture in order to extract the same amount of energy from each of the amplifier stages. It

seems possible one could design an electro-optical controlled aperture whose diameter vs time, d = d(t), can be controlled in a programmed way during the ~6 ns illumination. It would then need to be coupled to a source whose W/cm^2 was ~ 1/d(t)^2. Alternatively, and easily conceivable with present day technology, is an approach in which d = d(t) is approximated by stepwise changes in diameter. It would be a matter for target physics calculations to project target gain under the assumption of optimized 2, 3, 4, etc. step changes in spot size; it may be that as few as two or three sizes achieves most of the benefit. For step changes in spot diameter at constant power, we propose a system using a "switchyard," based on pockel cells, in which different front end sources are successively made the origin of the whole KrF driver system. What may seem large and expensive for the amount of energy generated at this point (~0.1 to 1 J) is insignificant in the context of the total system.

Figure 3.84 illustrates a concept using pockel cells and polarized light to provide four different aperture sizes during the pulse. The four "lasers" are operated as broad band sources with uniform emission over their aperture

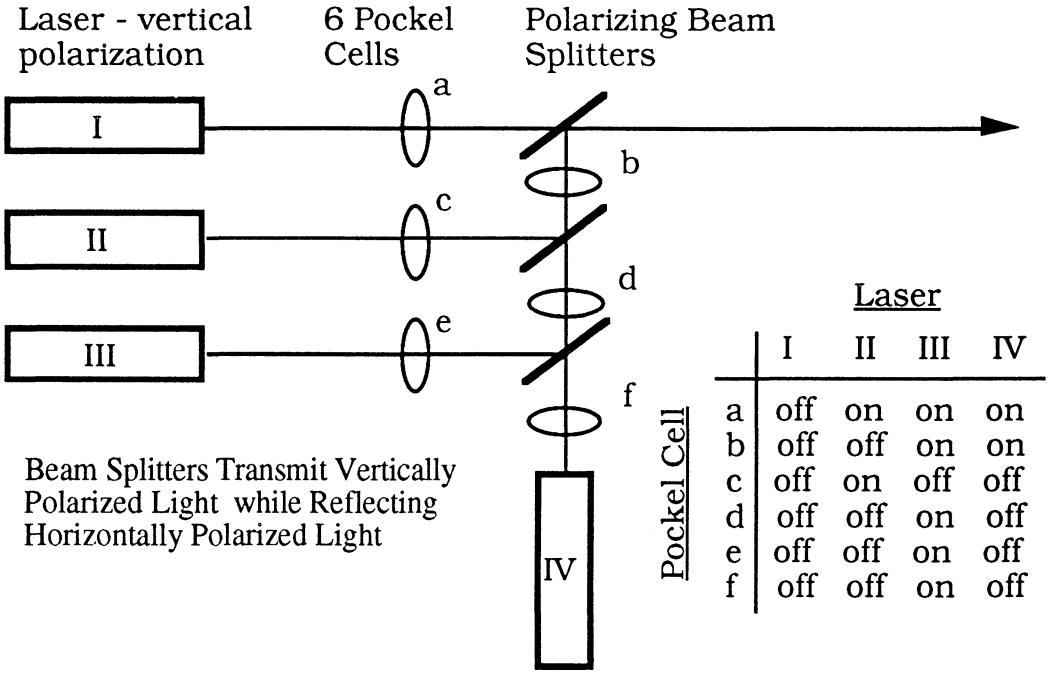

Fig. 3.84. Pockel cell based "switch yard" to provide four different aperture sizes to image on the target during the ~ 6 ns irradiation.

3.4.6 Grazing Incidence Metal Mirrors

Grazing incidence metal mirrors (GIMM) were first analyzed as a solution to the problem of neutron damage to final optics in 1991.[3.45] This section of the report will summarize important requirements and critical issues for final focusing systems using GIMM. The reader is referred to the original paper for a more detailed analysis.

3.4.6.1 Requirements for Protecting Sensitive Optics

Any beam-line element which is not shielded from the target must be protected from target debris, x-rays, and neutrons. Fortunately, the high-energy x-rays which come from the target can be stopped by the xenon gas that fills the chamber and reactor building. The target debris will either be stopped by the gas (our base assumption) or by a high-speed shutter in the beam line. Shielding optics from neutrons is a much more difficult problem. Neutrons leaving the target move at relativistic speeds and can not be intercepted by a high-speed shutter, and any element which will stop a 14 MeV neutron will not be transparent to a short wavelength laser.

Neutron radiation can destroy dielectric mirrors in three ways:

- degrading the optical transmission of the dielectric materials,
- chemical decomposition of the dielectric materials, and
- destroying the interfaces between dielectric layers.

Transmission degradation data is sparse, and the damage may be removable through continuous annealing. Measurements for MgF_2 and ZnS show an order of magnitude decrease in transmission after 10^{16} neutrons/cm^2 (or about an hour of operation for an unshielded dielectric 50 m from a 1000 MWe reactor). Chemical decomposition is a critical issue for all dielectrics. All ionics will undergo significant radiolysis after energy depositions of about 1 eV/atom. Energy deposition of a few eV/atom will also cause significant amorphization in SiO_2. Chemical mixing at the interfaces of dielectric layers may be the most difficult damage issue to avoid. Any collisional cascade at an interface will cause mixing of the two dielectrics and create a thin, possibly amorphous, region with unknown optical properties. Collisional mixing at the interfaces will occur over a thickness of roughly 3 nm/(DPA)$^{1/2}$ (1 DPA, or displacement per atom, corresponds to roughly 10^{20} 14 MeV neutrons/cm^2 for most dielectrics), and enhanced diffusion will cause mixing over a thickness 10 times the collisional mixing distances. If the existence of a third phase does not destroy the optical properties of a multilayer mirror, a change of layer thickness of $\lambda/16$, or about 20 nm, will destroy the constructive interference used by a $\lambda/4$ mirror. Under the most optimistic assumptions, it seems highly unlikely that an unshielded dielectric mirror will last more than a fraction of a full power year.

3.4.6.2 Design of an Optical Protection System using GIMM

Grazing incidence mirrors can protect more sensitive optics by removing them from the line-of- sight for target neutrons. Figure 3.85 shows a schematic of the final elements of a laser driver. Two layers of shielding represent the chamber and surrounding concrete wall. These will remove almost all of the neutrons which are not coming directly down the beam line. In the SOMBRERO design, the entire reactor building is filled with low-pressure xenon so further protection from x-rays is not needed. The grazing incidence mirror deflects the beam by a few degrees, but will deflect only a small fraction of lower energy neutrons towards the dielectric mirror. Because most of the high-energy neutrons coming directly from the target will pass through the grazing-incidence mirror, a neutron dump or "get-lost hole" placed behind the GIMM can greatly reduce the scattered neutron flux in the rest of the reactor building. In our design, the GIMM is located 30 m from the target, and the final turning mirror is 50 m from the target (i.e., about 20 m behind the GIMM). An analysis of neutron damage to optical elements is given in Section 3.2.5.

3.4.6.3 Damage Limits for GIMM

The reflectivity of a conducting metal is a function of the wavelength and polarization of the incident light and the angle at which the light strikes the surface of the metal. If we orient the GIMM so that the incident light has the polarization (transverse electric) which gives the highest reflectivity, the reflectivity of an undamaged aluminum alloy (Al 7475) mirror with an angle of incidence for the light of 85° will be 99.3%. Neutron damage can lower this reflectivity by increasing the resistivity of the metal by introducing defects, transmutations, and surface roughening on an atomic scale (giving an increase in absorptance from the anomalous skin effect), and by introducing microscopic surface roughening which increases the absorptance of the mirror. Based on limited information, we assume that neutron damage will lower the 85° angle of incidence reflectivity to 98.9%. At this reflectivity, thermal stress limits the maximum beam energy intensity to 1.88 J/cm^2 for a 10 ns pulse. This damage limit sets the minimum required mirror area for a uniform beam. Heat removal requirements will be on the order of 1% of this number, or 0.02 J/cm^2 per shot.

If damage to the mirror surface can be prevented, the lifetime of the GIMM will be limited by mirror deformation from swelling and creep which lead to defocusing of the beam. Because the defocusing limits for swelling and creep depend on relative fluxes, the limits depend on the longest dimension of the mirror. Longer GIMM lifetimes can thus be obtained by using elongated beams.

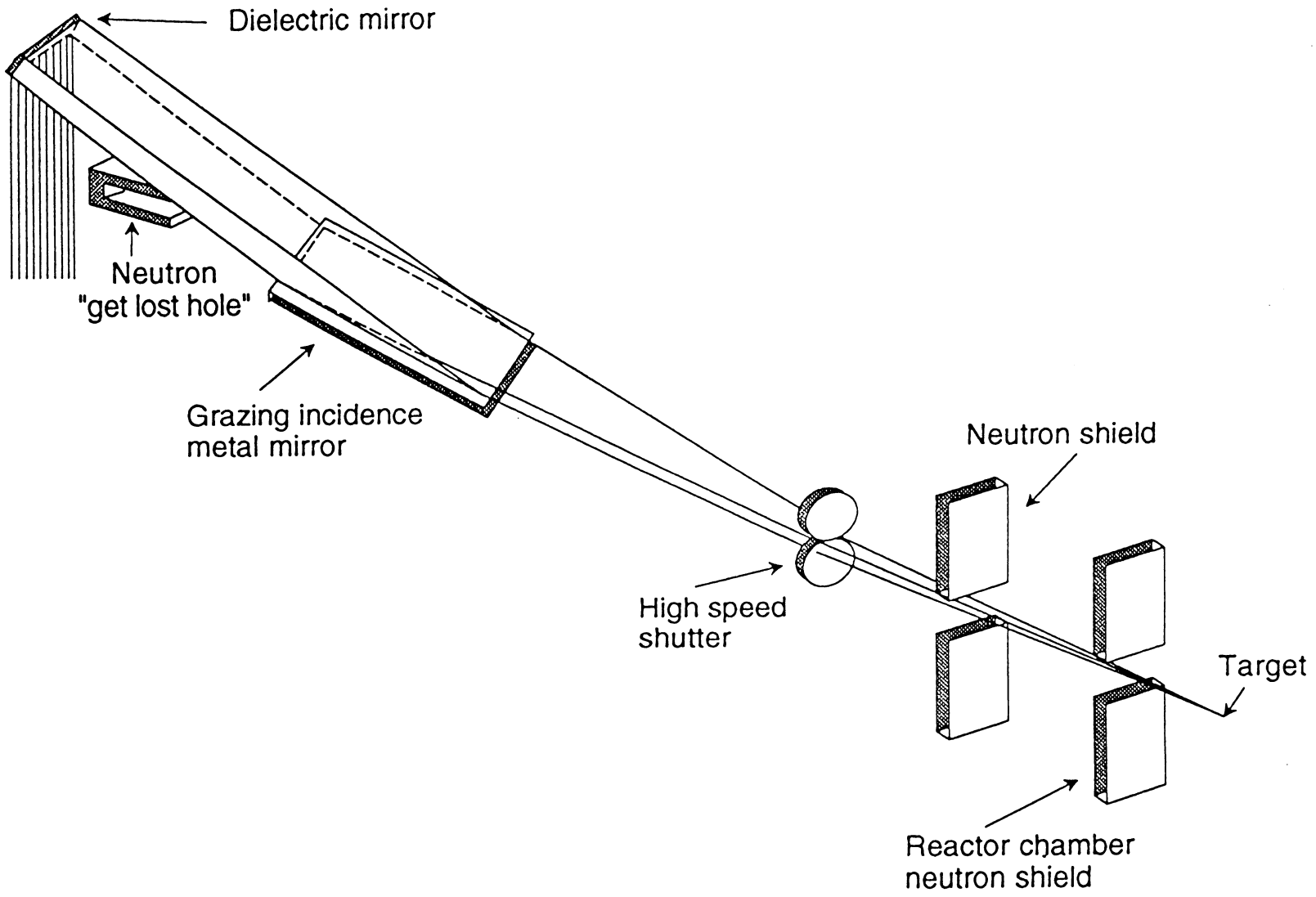

Fig. 3.85 Schematic of focusing scheme using grazing incident metal mirrors.

3.4.6.4 Required Mirror Sizes for Different Grazing Angles

There are two limits on the mirror size. The mirror must be large enough so that the absorbed energy is below the damage limit for the mirror (discussed above), and the mirror must have dimensions that are equal to the beam cross-section for the angle of incidence chosen. If the grazing angle, θ_g, is defined as 90° minus the angle of incidence, the second constraint will give the mirror area as the normal-incidence beam cross section divided by $\sin\theta_g$. As long as the mirror area calculated from the beam cross-section is large enough to give incident beam energies below the damage limit, the design is workable, but the smaller mirror area can be achieved by adjusting the angle of incidence or the aspect ratio (width / height) of the beam so that the GIMM is operating at both limits.

At small grazing angles, the reflectivity decreases linearly with increasing grazing angle. The damage limit is determined by the absorbed energy, so for small grazing angles, the limit on the beam energy intensity (I_{beam}) at the GIMM can be approximated by scaling the damaged reflectivity with the undamaged reflectivity

$$I_{beam} = 1.88\ \text{J/cm}^2 \cdot \frac{5^o}{\theta_g}$$

This is not exactly correct, since the undamaged absorptance has a small term independent of θ_g, but it will be a good approximation for angles near 5°. The minimum GIMM area based on the intensity limit, A_I, will then be given by

$$A_I = \frac{E}{1.88\ \text{J/cm}^2} \cdot \frac{\theta_g}{5^o}$$

Figure 3.86 shows both the required mirror area based on the above constraint and the mirror area based on the beam geometry (beam cross section divided by $\sin\theta_g$). The minimum mirror area is about 4.1 m^2 and occurs at a grazing angle of about 6°. For this figure, we have assumed the beam cross section area at 50 m is (60 kJ) / (5 $J/cm^{2)}$ = 1.2 m^2; therefore, at the GIMM (30 m from the target) the normal cross-section is 0.43 m^2. For a beam aspect ratio of 1, a 6° grazing angle will give mirror dimensions of 6.3 m by 0.66 m. Changing the aspect ratio to 2.3 to 1 gives a mirror size of 4.1 m by 1.0 m. Because non-uniform swelling limits are worse for longer mirrors, and because polishing and support are easier for shorter mirrors, we adopt the 4.1 m by 1 m mirror with a 6° grazing angle as our base design.

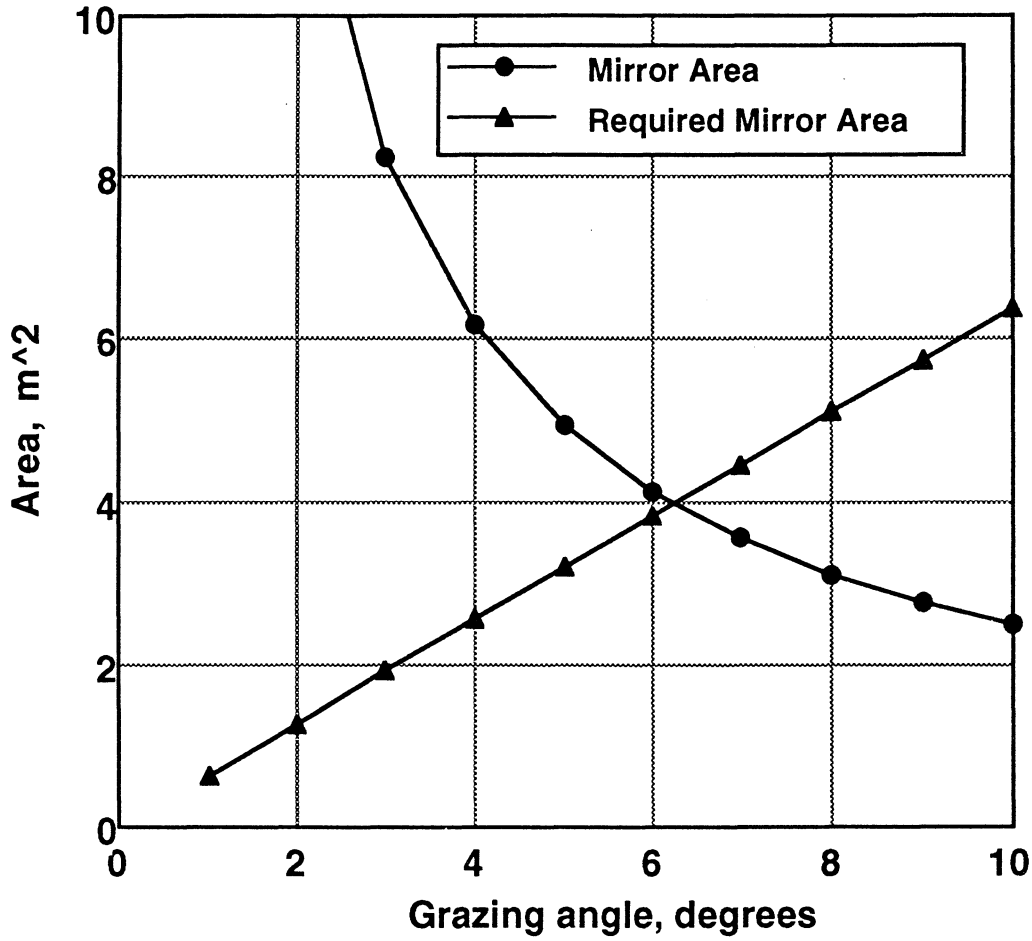

Fig. 3.86. Mirror area based on beam geometry and mirror area required to keep the energy intensity below the damage limit based on thermal stress.

3.4.6.5 Critical Issues for GIMM Use and Survival

Grazing incidence metal mirrors have the potential to solve a critical problem for laser drivers. The most important issues that need to be addressed to assure their integrity include:

- Experimental verification of laser damage thresholds for unirradiated and irradiated mirrors.

- Protection of the GIMM surface from damage or contamination.
  A particle or surface defect on the mirror surface will be exposed to the full, normal incidence, beam intensity and could cause explosive "pitting" of the mirror surface. Accumulation of material from the reaction chamber on the mirror surface must be prevented. It may be necessary to have a cleaning system that removes surface

contaminants between shots. A lower energy beam used between shots could be used to vaporize contaminants without explosive "pitting".

- Beam uniformity studies.
  Transverse heat flow and stress release during a 10 ns pulse can only average out nonuniformities over distances of a micron or less. Peaks in beam intensity which are wider than a micron could lead to local failure unless the beam is enlarged enough to lower the peak power below the damage threshold. Therefore, if the peak-to-average power ratio is large, the final requirement on mirror sizes may be larger than previously calculated .

- Beam pointing requirements and mirror support.
  Moving one end of a 5 m long mirror by only half of a millimeter will move the beam center 1 cm from the target. If the allowed deviation from a perfect plane is limited to $\lambda/4$, the limits on local distortions is less than 100 nm.

3.4.7 Technology Development Requirements

In Table 3.20, we list major R & D requirements on the path to developing a full scale IFE laser driver system. We also note that in most areas of importance there are alternate technical paths available. Lifetime testing all critical components is clearly required.

Table 3.20. Technology Development Requirements

Main Amplifier Technology
• High current density, 600 ns plasma cathode w/ sorption pumping
• Cable terminations of compact, low cost design
• Cable for required impedance and voltage w/ optimum insulation for energy storage
• Dual foil with helium cooling
• Race track bushing in size required
• Laser triggered rail gap output switch
• e-beam demonstration, 1 m × 2 m, 7 Hz, 20 min
• Flow loop demonstration
• 60 kJ module demonstration as an oscillator, 7 Hz, 20 min.
• 60 kJ, rep-rated, angular multiplexed, laser system, 7 Hz, required pulse shape, delivered to diagnostics at a representative target location ...
• 4 x 60 kJ prototype (square perimeter flow loop); 1 month, 7 Hz operation
Other System Issues
• Front -End: demonstrate zooming, spatial, temporal and spectral requirements
• Laser Physics: demo. high η at high J/liter
• Optical coating damage limits for sizes required, with spatial and temporal pulse shapes per system design requirements
• Final Focus mirror coatings: neutron damage
• Grazing incidence mirrors: neutron damage and optical J/cm^2 and absorption
• Be/Al alloy foils for e-beams

3.8 REFERENCES FOR CHAPTER 3

3.1 Y. Gohar et al., "U.S. Solid Breeder Design for ITER," *Fusion Technol.*, **19**, 1538 (1991).

3.2 F. Najmabadi et al., "The ARIES-I Tokamak Reactor Study," *Fusion Technol.*, **19**, 783 (1991).

3.3 D.K. Sze et al., "Gravity Circulated Blanket Design for a Tokamak Fusion Reactor," Proc. 2nd Topical Meeting on the Technology of Controlled Nuclear Fusion, Richland, WA (1976).

3.4 R.W. Conn et al., "SOLASE - A Conceptual Laser Fusion Reactor Design," UWFDM-220, Fusion Research Program, Nuclear Engineering Dept., Univ. of Wisconsin, Madison (Dec. 1977).

3.5 H.T. Buscher, R.G. Tomlinson, and E.K. Damon, "Frequency Dependence of Optically Induced Gas Breakdown," *Phys. Rev. Lett.*, **15**, 847 (1965).

3.6 R.E. Palmer, J.P. Anthes and M.A. Palmer, "The Effect of Background Gas on the Propagation of a High-Intensity Laser Beam to a Target," 1980 IEEE/OSA CLEOS Meeting, San Diego, CA, (February 26-28, 1980).

3.7 J.A. Stamper, B.H. Ripin, R.E. Peterkin, Jr., and R. F. Stellingwerf, "Aneurisms in Laser-Driven Blast Waves," *Phys. Fluids*, **31**, 3353 (1988).

3.8 R.R. Peterson, J.J. MacFarlane, and G.A. Moses, "CONRAD - A Combined Hydrodynamic-Condensation/Vaporization Computer Code," University of Wisconsin Fusion Technology Institute Report UWFDM-670 (July 1988).

3.9 J.J. MacFarlane, "IONMIX - A Code for Computing the Equation of State and Radiative Properties of LTE and Non-LTE Plasmas," University of Wisconsin Fusion Technology Institute Report UWFDM-750 (December 1987).

3.10 "T-4 Handbook of Material Properties Data, Vol. 1c: Equations of State," Los Alamos National Laboratory Report LA-10160-MS (November, 1984).

3.11 "Structural Properties of Multidimensional Composites," Southern Research Institute, Presented at the Workshop on CMC's for Structural Applications in Fusion Reactors, Santa Barbara, CA (21-22 May 1990).

3.12 R.H. Jones, C. H. Haneger, Jr. And G. W. Hollenberg," Composite Materials for Fusion Applications," PNL, Richland, Wash., 5th International Conference on Fusion Reactor Materials, Clearwater, Florida (Nov. 17-21, 1991).

3.13 R.F. Mattas, "Properties of Bulk Graphical N3M Nuclear Graphite," Argonne National Laboratory.

3.14 K. Noda et al., "Summary Report for the ITER Specialists Meeting on Blanket Materials Data Base," Garching, FRG (7-9 Feb. 1990).

3.15 D.J. Suiter, "Lithium Based Oxide Ceramics for Tritium Breeding Applications," McDonnell Douglas, MDC E2677 (1983).

3.16 *Materials Handbook for Fusion Energy Systems,* Handford Engineering and Development Laboratory, DOE/TIC-10122 (1980).

3.17 T. Takahachi and T. Kikuchi, "Porosity Dependence on Thermal Diffusivity and Thermal Conductivity of Li_2O from 200°C - 900°C," *J. Nucl. Mat.*, **91** (1980).

3.18 J. S. Botterill, *Fluid-Bed Heat Transfer*, Academic Press (1975).

3.19 H.S. Mickley and D. F. Fairbanks, *A.I.Ch.E.J.*, **1**, 374 (1955).

3.20 B.V. Berg, A. P. Baskakov, *Khim. Prom.*, **43**, 439 (1961).

3.21 A.P. Baskakov, *Inzh. Fiz. Zh. Akad. Nauk. Belorussk.*, **6**, 20 (1963).

3.22 A.P. Baskakov, *Int. Chem. Engin.*, **4**, 320 (1964).

3.23 N.I. Gelperin, V. G. Einstein, A. V. Zakovski, *Khim. Prom.*, **6**, 418 (1966).

3.24 N.I. Gelperin and V. G. Einstein, *Fluidization* (Edited by Davidson and Harrison), Academic Press, London, 471 (1971).

3.25 W.N. Sullivan and R. H. Sabersky, "Heat Transfer to Flowing Granular Media," *Int. J. Heat Mass Trns.*, **18 (1)**, 97-107 (1975).

3.26 R. Nietert, " Heat Transfer Characterization of Flowing and Stationary Particle Bed Type Fusion Reactor Blankets," Ph.D. Thesis, Nuclear Engineering Dept. University of Wisconsin, Madison (1982).

3.27 R.G. Deissler and J.S. Boegli, "An Investigation of Effective Thermal Conductivities of Powders in Various Gases," *Trans. ASME*, **80 (7)**, 1417-1425 (1958).

3.28 R.D. McCarty, "Thermophysical Properties of Helium-4 from 2-1500 K with Pressure to 1000 Atmospheres," National Bureau of Standards, Boulder, CO (1972).

3.29 W.V. Green, D.L. Smith, and B.T. Kelly, "Summary of the RIGI-KALTBAD Workshop on Graphite," *J. of Nucl. Mater.*, **122&123**, 14-16 (1984).

3.30 R.D. O'Dell et al., "User's Manual for ONEDANT: A Code Package for One-Dimensional, Diffusion-Accelerated, Neutral Particle Transport," Los Alamos National Laboratory Report, LA-9184-M (1982).

3.31 B. Badger et al., "LIBRA - A Light Ion Beam Fusion Conceptual Reactor Design," University of Wisconsin Fusion Technology Institute Report UWFDM-800 (1989).

3.32 M. Birch and J.E. Brocklehurst, "A Review of the Behavior of Graphite Under the Conditions Appropriate for Protection of the First Wall of a Fusion Reactor," Springfield Nuclear Power Development Lab., ND-R-1434(S) (Dec. 1987).

3.33 M.C. Billone, C.C. Lin, H. Attaya, and Y. Gohar, "Tritium Retention and Release Analysis for US-ITER Blanket," *Fusion Technol.*, **19**, 976 (1991).

3.34 K.E. Plute, E.M. Larsen, and L.J. Wittenberg, "Tritium Recovery from Liquid Lithium-Lead by Vacuum Degassing," *Nuclear Tech./Fusion*, **4**, 407 (1983).

3.35 C.E. Johnson and A.K. Fischer,"Blanket Materials for Fusion Reactors: Comparisons of Thermochemical Performance," *J. Nuclear Materials*, **130**, 445 (1985).

3.36 M.C. Billone and C.C. Lin, "Input for Tritium Retention/Release Analysis anbd Steady-State Results," presented at the ITER Nuclear Group Mtg. (May 9, 1990).

3.37 S. Tanaka, A. Kawamoto, D. Yamaki, K. Yamaguchi, and M. Yamawaki, "In situ Tritium Release Experiments from Solid Breeding Materials (TTTEx) - Surface Reactors of Li_2O and $LiAlO_2$ for Sweep Gases of He + H_2 and He + H_2O," *J. Nuclear Materials*, **179-181**, 867 (1991).

3.38 Y. Hirooka and H. Imai, "Reaction of Neutron Irradiated Pyrolytic Graphite with Water Vapor," *JAERI-Memo*, 57-218 (1982).

3.39 A. Busigin, S.K. Sood, and K.M. Kalyanan, "A New High Temperature Isotopic Exchange Fuel Processing Loop Design for ITER," *Fusion Technol.*, **20**, 179 (1991).

3.40 J.T. Bell, J. D. Redman, and H.F. Bittner, "Tritium Permeability of Structural Materials and Surface Effects on Permeation Rates," Proc. ANS Topical Meeting on Tritium Technology, Dayton, OH, April 29-May 1, 1980, pp. 48-53 (CONF-800427).

3.41 J.L. Anderson et al., "Experience of TSTA Milestone Runs with 100 Gram-level of Tritium," *Fusion Technol.*, **14**, 438 (1988).

3.42 R.A. Causey, M. I. Baskes, and K.L. Wilson, "The Retention of Deuterium and Tritium in POCO AXF-5Q Graphite," *J. Vac. sci. tech.*, **A4**, 1189 (1986).

3.43 K.B. Woodall, S.K. Sood, and A. Busigin, "Conceptual Design of a Laboratory Scale Impurity Detritiation and Hydrogen Isotope Separation System," *Fusion Technol.*, (1991), in press.

3.44 C.J. Sienkiewicz, "Tritium Surface Contamination," *Fusion Technol.*, **8**, 2444 (1985).

3.45 R.L. Bieri and M. W. Guinan, "Grazing Incidence Metal Mirrors as the Final Elements in a Laser Driver for Inertial Confinement Fusion." *Fusion Technol.*, **19** (May 1991).

3.46 R.C. Davidson et al. "Inertial Confinement Fusion Reactor Design Studies Recommended Guidelines" prepared for Department of Energy Office of Fusion Energy (Sept. 1990).

3.47 R.R. Berggren, R.L. Gibson, R.H. Lehmberg, and C.W. vonRosenberg, Jr., "Large KrF Lasers as High-Brightness, High-Energy Sources," also D.B. Harris, et al. "Strengths and Weaknesses of KrF Lasers for ICF Applications Learned from the AURORA Laser," IAEA Technical Committee Meeting on Drivers for Inertial Confinement Fusion, Osaka, Japan, (April 15-19, 1991).

3.48 M. McGeoch "A High Current Density Non-Closing Plasma Cathode," *J. Appl. Phys*, **71** (3), 1163 (1 Feb. 1992); also U.S. Patent No. 5,003,226.

3.49 J.H. Pendergrass, *Fusion Technol.*, **11**, 732 (1987).

3.50 J.A. Sullivan, "A Simplified Model for Designing Large KrF Amplifiers," Los Alamos, NM 87545

3.51 This value is consistent with presentation of Y. Owandano "High Power KrF Laser System, ASHURA," Paper WA-1, KrF Laser Technology Workshop, Santa Fe, April 19-21, 1989; also R.H. Lehmberg "Optical Beam Smoothing in the NIKE Laser," presentation to Fusion Policy Advisory Committee, Berkeley, May 10, 1990 - Q > 3 mrad is suggested; the LMF design assumed 5 mrad.

3.52 D.B. Harris, J.A. Sullivan, J.H. Pendergrass, N.A. Kurnit, E.A. Rose, and J. McLeod "KrF Laser-Driven Laboratory Microfusion Facility," Los Alamos National Laboratory LA-UR-91-2915 (Dec. 17, 1991).

3.53 J.A. Sullivan and C.W. von Rosenberg, Jr. "High energy krypton fluoride lasers for laser-induced fusion," *Lasers and Particle Beams,* **4**, 91 (1986).

3.54 J.H. Parks "Angular multiplex laser fusion drivers," Proceedings of SPIE **270** , 81 (1981); also J.H. Parks "Conceptual Design of an Angularly-Multiplexed Rare Gas Halide Laser Fusion Driver," Avco final report for DoE contract DE-AC08-79DP40113 (Nov. 1980).

3.55 "Conceptual Design of a 1.5MJ, 2Hz KrF Fusion Laser System," Lawrence Livermore Lab Report, UCRL-53077 (1980).

3.56 R. Limpaecher, R. Litte, and S. Ghoshroy, "High Voltage Cable PFL Test Results," 17th Power Modulator Symposium, Seattle, WA (June 23-25, 1986).

3.57 J.C. Martin, AWRE report SSWA/JCM/704/49 (1970).

3.58 J.H. Parks "Conceptual Design of an Angularly-Multiplexed Rare Gas Halide Laser Fusion Driver," Avco final report for DoE contract DE-AC08-79DP40113 (Nov. 1980).

3.59 R. Limpaecher and S. Ghoshroy, unpublished data (1987).

3.60 M.A. Gundersen and G. Schaefer, "Physics and Applications of Psuedosparks," Plenum Press, New York (1990).

3.61 M.W. McGeoch, A.J. DeFuria and C.T. Pike "Pulsed Electric Discharge Laser Technology - Electron Beam Window Foil Material," report for Contract DAAH01-82-D-A013, (1984).

3.62 C.W. von Rosenberg, Jr., "Repetatively Pulsed KrF Amplifiers for Laser Fusion," Final Report of Task 3 of Contract No. 9-XT9-E9580-1 (Nov. 1990).

3.63 D.B. Harris, J.A. Sullivan, J.H. Pendergrass, N.A. Kurnit, E.A. Rose, and J. McLeod, "KrF Laser-Driven Laboratory Microfusion Facility," Los Alamos National Laboratory LA-UR-91-2915 (Dec. 17, 1991).

3.64 T. Izawa et al., Syowa Optical Co., Ltd., Japan, "Laser Damage Thresholds of Optical Coatings for High Power Lasers," presented at IAEA Technical Committee Meeting on Drivers for Inertial Confinement Fusion, Osaka, April, 1991.; see also Los Alamos Report LA-UR-91-2915, KrF Laser Driven Laboratory MicroFusion Facility - Conceptual Design Report, David B. Harris, et al. (Dec., 1991).

3.65 L.A. Rosocha, J. McLeod and J.A. Hanlon, "Beam Propagation Considerations in the Aurora Laser System," *Fusion Technol.* **11**, 624 (1987).

3.66 A.V. Deniz, M.S. Pronko, S.P. Obenschain, R.H. Lehmberg "Production of Flat KrF Focal Profiles for Laser Fusion Experiments," CLEO'91 (1991).

Chapter 4

Target Systems

CONTENTS

4.1 TARGET PRODUCTION 4-1
4.1.1 Objectives and Requirements 4-1
4.1.2 Overview of the Reference Design 4-3
4.1.3 Capsule Production 4-4
4.1.4 DT Fuel Filling 4-9
4.1.5 Developing a Uniform DT Layer 4-12
4.1.6 Capsule Handling and Transport 4-19
4.1.7 Quality Assurance 4-20
4.1.8 Target Protection by Sabots 4-20
4.1.9 Target Storage 4-21
4.1.10 Tritium Inventory 4-22
4.1.11 Production Facility Building 4-22
4.1.12 Summary 4-22
4.2 TARGET INJECTION, TRACKING, AND POINTING 4-24
4.2.1 Objectives and Requirements 4-24
4.2.2 Overview 4-24
4.2.3 Injection System Design 4-29
4.2.4 Target Tracking 4-31
4.2.5 Beam Pointing 4-34
4.2.6 Integrated Target Injection, Tracking, and Pointing Systems 4-35
4.2.7 Injection, Tracking, and Pointing Errors 4-37
4.2.8 Summary 4-38
4.3 TARGET HEATING DURING INJECTION 4-39
4.3.1 Target Conditions 4-39
4.3.2 PELLET Computer Code 4-41
4.3.3 Target Heating Results 4-46
4.4 REFERENCES FOR CHAPTER 4 4-52

4.0 TARGET SYSTEMS

4.1 TARGET PRODUCTION

4.1.1 Objectives and Requirements

In this portion of the study, we identify a viable set of elements of an IFE reactor target production facility and develop a plan for the combination of the elements into an operable factory design. The objects were to

- Identify primary production steps and options for each step
- Identify features with significant impact on cost, reliability, and safety
- Attempt to minimize cost and enhance reliability and safety in facility design

The baseline design of the production facility contains a deuterium-tritium (DT) handling and storage facility, a fuel container (capsule) production facility, a system for filling the capsules with DT fuel, a measurement system for quality assurance (QA) purposes, and a target storage and delivery section. The characteristics, such as size, production rates, etc., have been estimated and interfaces included where necessary and appropriate. A helium liquefaction and cryogenic plant and production control systems have been included as necessary parts of the complete production facility. Figure 4.1 is a block diagram of the IFE reactor target production facility showing the major production steps. Other peripheral facilities such as receiving, chemical preparation room, materials storage, etc., are not shown and should not add significantly to the cost of the facility other than a per-square-foot building cost, which should be, at most, 5-10% of the overall facility foot-print.

The facility has several important features worth pointing out. The production equipment and overall building area are quite compact. This is largely the result of using production techniques that minimize the production time per target and thus the inventory of targets being handled at any one time. The compact design also helps minimize target production costs. While cost reduction or minimization has not been an overriding part of this study, determination of a plausible cost estimate for the target production facility is addressed later in Chapter 8. Operational safety and the minimization of total tritium inventory have been considered to be critical aspects of the facility design. The tritium inventory is minimized by 1) using rapid production techniques and 2) reducing the inventory of filled targets in storage. The inventory of filled targets can be small because the system is very reliable. As indicated in Fig. 4.1, the proposed production facility is 100% redundant in order to give high reliability. Under normal conditions, each production line operates at half of its possible production rate. If a component on one line fails or requires repair, the other line is brought to full production capacity. To further enhance the safety characteristics of

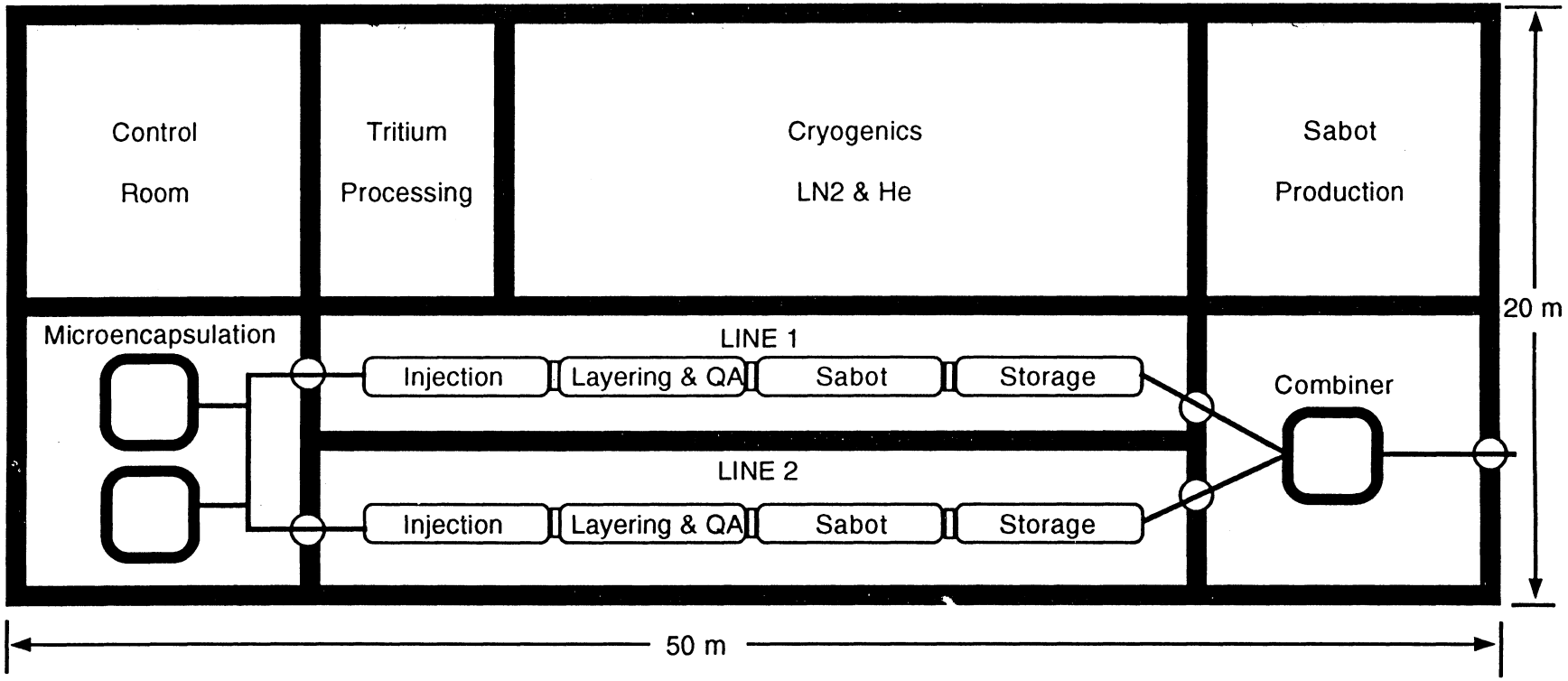

Fig. 4.1. Layout of baseline target production facility.

the production facility, the production stages and components are compartmentalized to reduce the consequences of a tritium leak in any one part of the system.

In order to produce targets economically, the production facility must be operated as a completely automated factory, not as a research facility. We assume that all processes to be employed in producing the capsules, filling the capsules with fuel, adding sabots as target carriers, and handling and manipulating targets will have been developed, tried, tested, integrated and demonstrated in a pilot plant, and perfected before use in an IFE power plant. One of the major implications of this assumption is that complete characterization of the individual targets is not required. Only an occasional measurement will be made to ensure the several fabrication processes are operating as they should. While it may be sufficient to monitor the target yield per pulse as a check on target production processes, other factors could reduce the yield (e.g., a degradation of driver output or alignment accuracy). Thus, it will be necessary to statistically monitor target quality in each of the production steps to assure of the continued correct operation of the factory.

The major production steps are

1) Capsule Production
2) Fuel Fill
3) Fuel Layering
4) Capsule Insertion into Sabots
5) Storage of Complete Targets

Several sub-steps are associated with these major production categories. For example, capsule material must be acquired and loaded into the capsule production apparatus, DT must be stored, transported to the fill system, set to the correct temperature, and flowed into the capsules in a metered and controlled manner.

4.1.2 Overview of the Reference Design

The design is based on the production of direct drive targets as used in the SOMBRERO reactor. Production steps for indirect drive targets would be the same, except for the final step of loading the capsule into a hohlraum. Depending on its characteristics, the hohlraum could possibly serve as the sabot for the indirect drive target, thus eliminating the sabot loading step. From the various options for each of the production steps, we have chosen a reference design approach listed in Table 4.1. These choices and the sizing of production facility components were based on the target parameters given in Table 4.2. Note the fuel mass is calculated assuming a yield of 400 MJ (i.e., the SOMBRERO yield) and a burn fraction of ~ 30%, which is a typically cited value for future reactor-class targets. The choices were made after considerations of several options for each of the elements of the target production facility. The options and the reasons for

Table 4.1. Baseline Target Production Techniques

Production Step	Chosen Technique
Capsule Production	Drop Generator / Microencapsulation
Fuel Fill	Injection Fill Techniques
DT Layer Formation	Freeze - Laser Pulse Vaporization - Refreeze

Table 4.2. Reference Case Target Design

Target Type	CH shell with solid DT fuel layer
Nominal Yield	400 MJ
Nominal Dimensions	5 - 6 mm outer diameter
	0.03 - 0.05 mm thick shell
Production Rate	~ 6.7 Hz (~ 400/min or ~ 580,000/day)
Fuel Mass per Target	~ 4 mg DT (~ 2.4 mg T)
Tritium Throughput	~ 1.4 kg/day

the choices are discussed in the next several sections. The advantages and disadvantages of each option are compared.

4.1.3 Capsule Production

4.1.3.1 Capsule Production Options

Several techniques can be used to produce the hollow, spherical, thin wall capsules necessary for the IFE targets. Table 4.3 lists a number of the techniques and briefly notes some of the advantages and disadvantages of each of the primary techniques. It should be noted here at the outset that no claim is made that the list of techniques presented here is exhaustive, nor is it claimed that there will not be other techniques developed which may be better, cheaper, or easier than those which have been considered. This is certainly true for the other production steps as well as for capsule production.

Drop tower generation refers to the technique whereby uniform drops of a liquid precursor solution of the capsule material are formed by means of a drop generator at the top of a heated vertical column. As the drops fall freely through the hot column, the solvent in the drops evaporates and leaves a shell of the solute material. If the shell is to be a hollow polymer shell, the

Table 4.3. Capsule Production Options

Technique	Advantages (+) and Disadvantages (-)
Drop Tower Generation	+ Consistent constant shell mass and dimensions + High production rate (up to 1000's per second) - Shell uniformity may decrease as size increases
Microencapsulation	+ Low vacuole density in shell walls + Uniform shell wall thickness - Process inherently produces a wide range of diameters and wall thicknesses
Drop Generator / Microencapsulation	+ Combines the advantages of both techniques (i.e., uniform shell mass, diameter, and wall thicknesses)
Hollow DT Shells from Drop Generator	+ Shells formed directly from liquid DT drops: + Uniform mass + Ablative layers formed by condensation of CH_4 gas + Shells formed as needed (i.e., no storage required) + On-demand delivery

solvent is probably an organic liquid that can be evaporated at a relatively low temperature leaving a shell of the polymer material. Shells of polystyrene have been formed by this technique using mixtures of ethyl chloride, methyl chloride, and methylethyl ketone as solvents and high molecular weight polystyrene as the solute.[4-1] The column temperatures have been less than 200 ^{o}C and column heights as small as two meters. If the shells were to be formed of some type of inorganic glass, then the column temperatures would range from 1000^{o}C to 1600^{o}C, depending on the glass shell composition being used.

With the drop generator and heated column technique, the rate of production of shells can be as high as several thousand per second. Techniques have been employed to reduce the production rate to several hundred per second by removing, for example, all but every 100th or 200th drop.[4-2] This leaves large spaces between successive drops preventing collisions between drops as they fall through the hot column. It also reduces the rate at which solvent must be removed from the column.

A concern about the drop technique is that the shells might become less uniform as the size of the shell is increased. This, however, has not been proved and indeed, has been shown not to be the case with production of shells up to several millimeters diameter. Further work may show that the drop generator / hot column technique is the most satisfactory means of producing fuel capsules in large quantities.

Capsules have also been produced by a technique known as microencapsulation.[4-3] This is a proven technology with high reliability and no major development issues. In the micro-encapsulation technique, as shown schematically in Fig. 4.2, mixtures of water, solvent, and solutions of polystyrene in a solvent are physically shaken to form minute droplets of immiscible components in a complex emulsion. The polymer shells form around the droplets and the liquid inside the shells is subsequently diffused out in alcohol to leave hardened, hollow shells of polystyrene. Careful control of the solvents, mixtures, and polymer molecular weight allow the production of uniform shells without vacuoles in the walls of the shells. However, the shaking process inherently produces a wide range of particle sizes and, hence, a wide range of shell diameters and wall thicknesses.

A method to make DT shells directly has been demonstrated[4.4] and is shown in the diagram in Fig. 4.3. The DT shells can be formed by initiating bubble growth in a liquid droplet of DT which is maintained at a temperature above the triple point. If a bubble is nucleated ultrasonically, the bubble will grow and result in a hollow liquid shell of DT. By passing the liquid shell through an orifice into a region at lower pressure, the evaporation of a very small amount of the DT will cause the shell to freeze and thus produce a solid hollow shell of DT. If the frozen shell of DT is introduced into a region containing a small partial pressure of a gas such as methane (CH_4) some methane can be condensed onto the DT shell to produce an ablative shell of CH around the DT. The composite CH-DT shells can be produced at high rates or one at a time at the chamber rep-rate (i.e., on demand). Thus, no storage of targets would be necessary and the tritium inventory would be reduced to a minimal amount. There are large advantages to this totally cryogenic technique for target production. However, even though the technique has been experimentally demonstrated using normal hydrogen and other gases, it is not considered to be a proven target production technique and is not being chosen as the base case option.

4.1.3.2 Selected Approach for Capsule Production

The option selected for capsule production in the base case is the combination of drop generators to produce uniform liquid drops of water layered with a solution of an appropriate polymer. This has been called the controlled microencapsulation technique. It combines the advantages of the drop generator technique, which produces droplets with a fractional standard deviation in diameter of better than 10^{-5}, and the microencapsulation technique which delivers

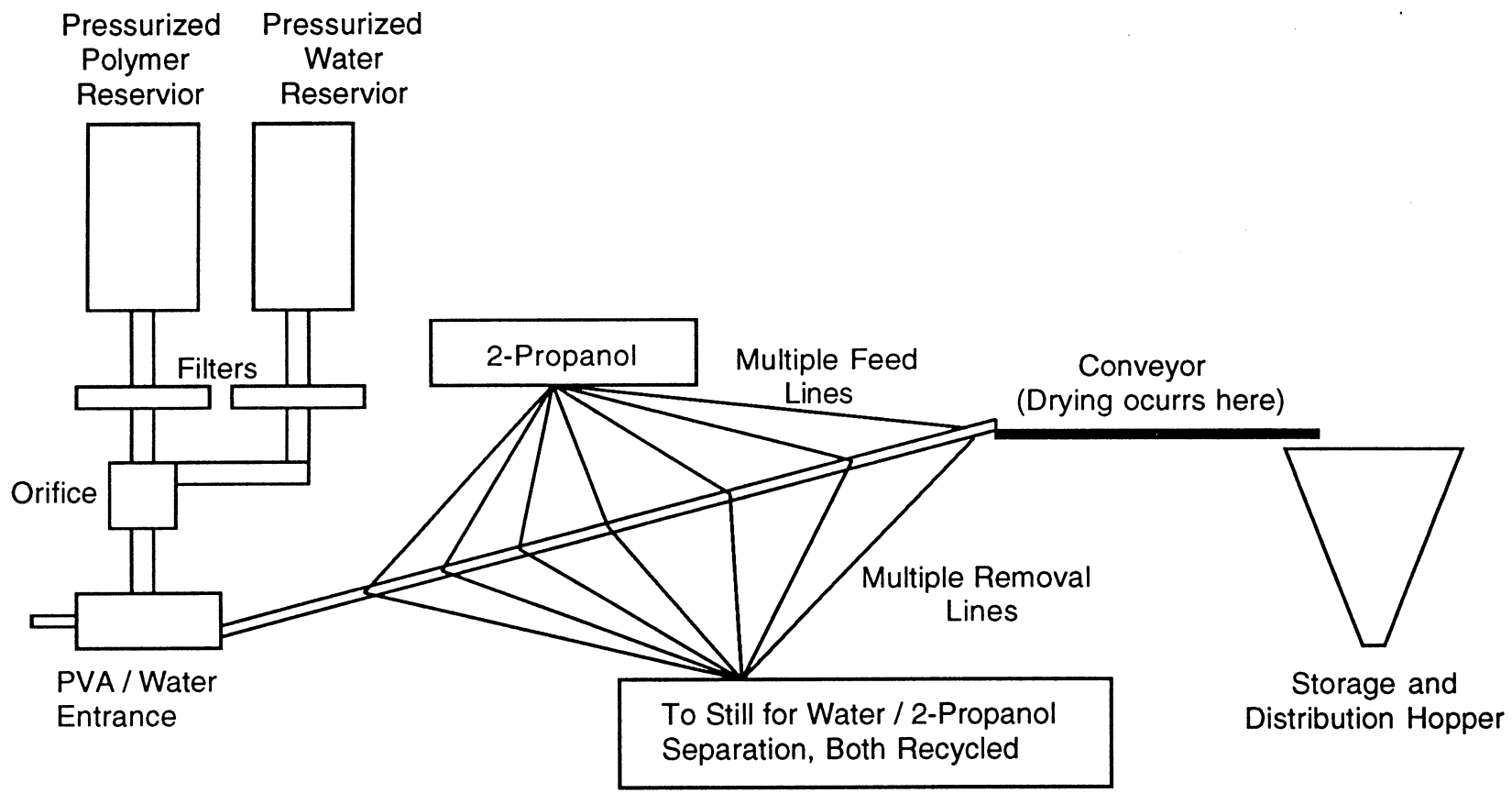

Fig. 4.2. Schematic representation of microencapsulation equipment.

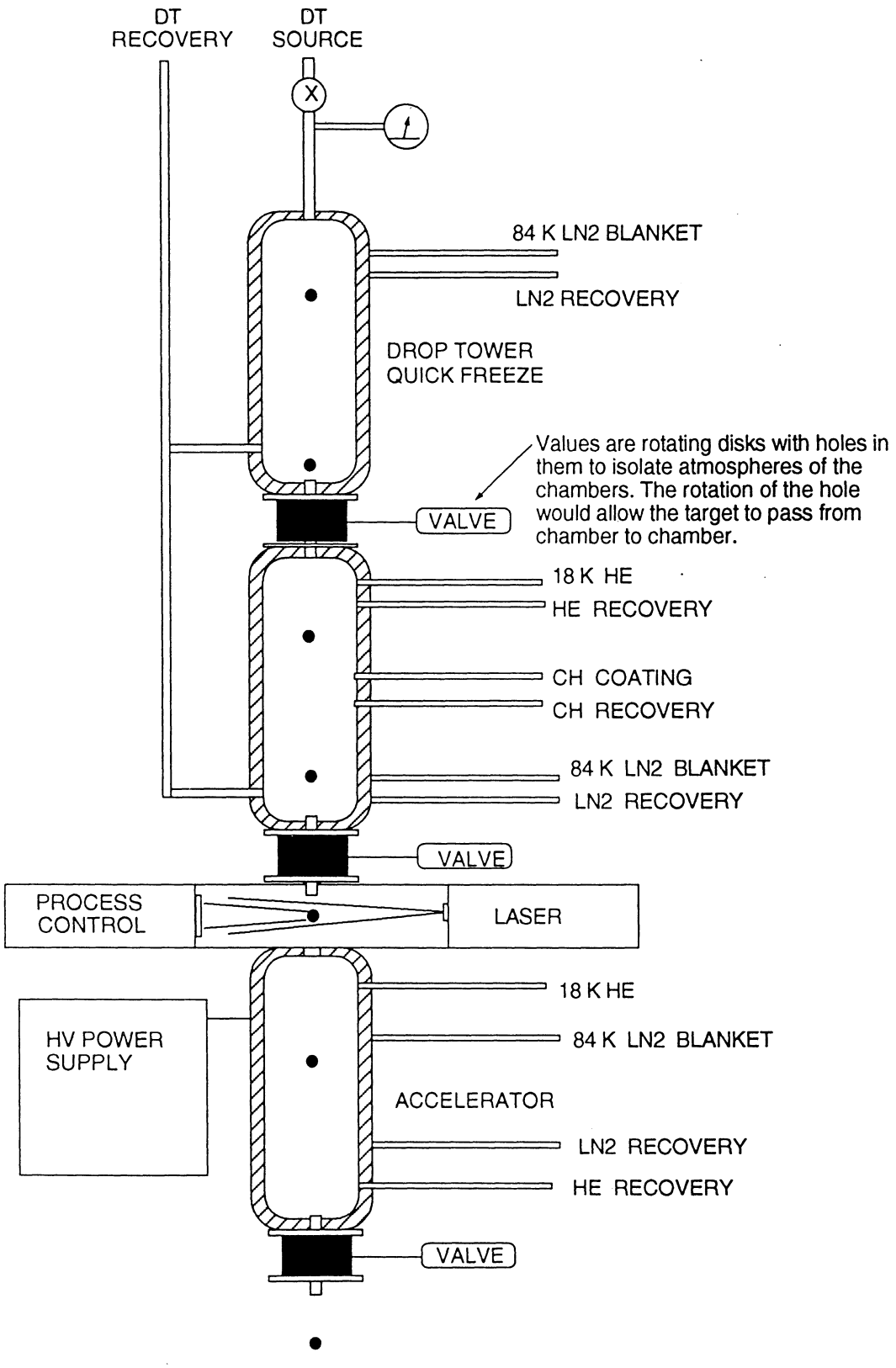

Fig. 4.3. Schematic of system for producing frozen DT targets.

shells which are round and have uniform wall thicknesses. A drop generator is used to produce uniform drops of polystyrene or other suitable polymer. The drops are injected directly into a liquid where they are treated to form shells as in the microencapsulation technique. Thus, shells will have uniform mass, diameter, wall thickness, and shape like those produced by the shake-type microencapsulation technique.

The multilayer drop is either generated directly in water where the solvent in the polymer solution diffuses out to leave a shell which can be subsequently recovered, or the multilayer drops are formed in air and injected into an appropriate liquid such as water in which the drops can be processed to produce the desired capsules. An important advantage of the combination technique is the control which can be exercised over the various aspects of the process. It is not necessary to depend on selection of the shells from a randomly-produced melange of shells with varying diameter and wall thickness. The shells as produced are the correct diameter and wall thickness and have the quality necessary to serve as the fuel capsules for IFE reactor targets. Using this method, the capsules can be produced in large numbers and stored in preparation for the fuel fill step in the target production process.

4.1.4 DT Fuel Filling

4.1.4.1 DT Fuel Fill Options

Several techniques were considered for the fuel fill step in target production. Because of the use of radioactive tritium, two major considerations were tritium inventory and safety for operating personnel. Table 4.4 presents the options which were considered and the advantages and disadvantages of each.

Because of the importance and difficulty of filling the capsules with the DT fuel, it is clear that much more research and development are required before a final fuel fill technique can be established. However, during this study, it became apparent that the presently used standard method of fuel filling, diffusion of DT gas through the capsule wall, is quite unattractive for reactor targets. It is, therefore, important that a development program be initiated to generate better methods for fuel filling.

Figure 4.4 is a schematic diagram of a typical permeation fuel fill system. Filling the capsules by permeating the DT through the capsule walls from a gaseous environment requires very long times (estimated at approximately 60 hours) and also requires a large tritium inventory. The process requires high pressure DT handling systems and fast cool-down after the fuel fill operation to minimize fuel loss through outward permeation.

The technique of making hollow frozen spherical shells of DT directly with condensation coating of CH layers is very attractive (Fig. 4.3). However, even though the technique has been demonstrated experimentally,[4.5] the study guidelines specified that the DT filled, polymer capsules

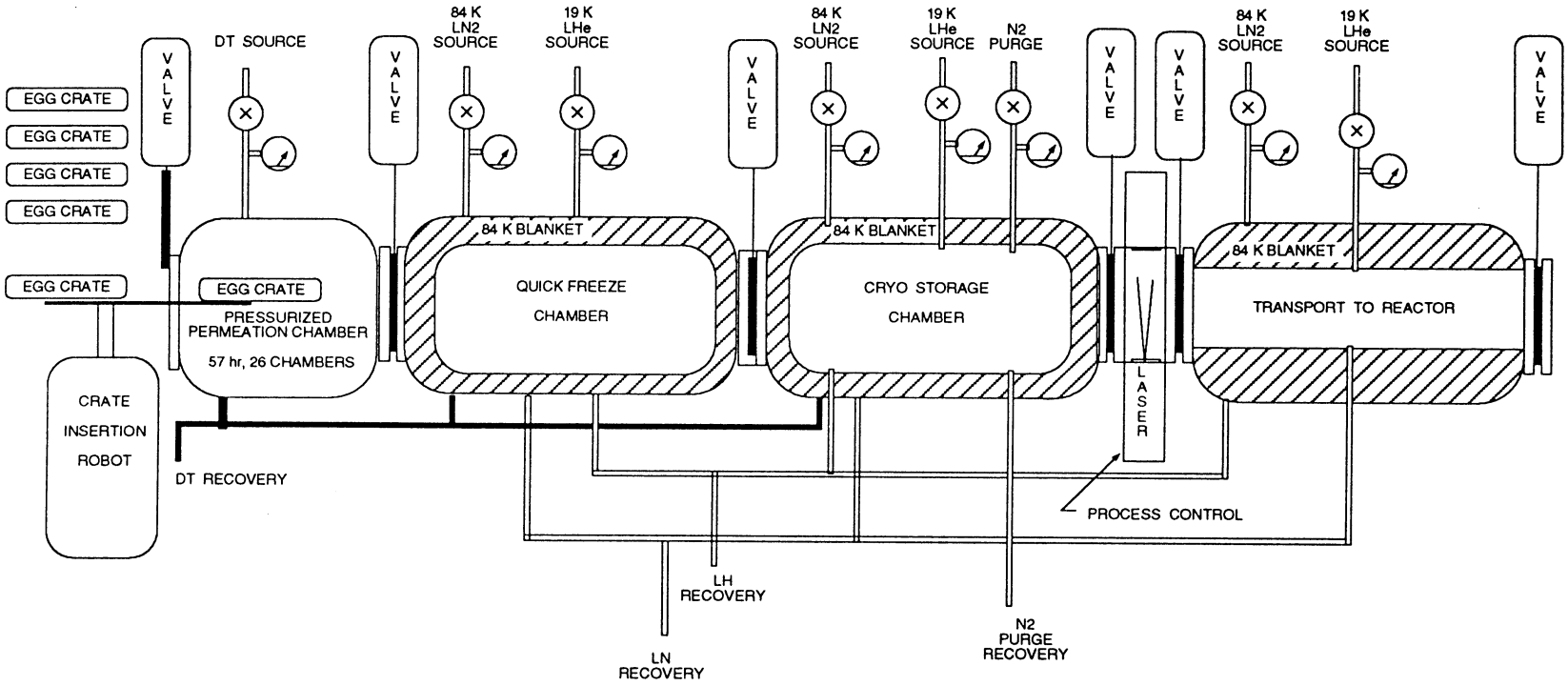

Fig. 4.4. Target prodution line for permeation fill approach.

Table 4.4. DT Fuel Filling Options

Technique	Advantages (+) and Disadvantages (-)
Permeation Fill	+ Proven technique
	- Excess DT handling required
	- Long fill times
	- High pressures required in the DT handling system
	- Fast post-fill cool-down required to reduce permeation
Frozen DT Shells	+ No "handling" of targets (make-one, burn-one)
	+ No storage required
Injection Fill of Liquid Fuel	+ Precise delivery of DT
	+ Rapid fill (times ~1 shell / min / injector)
	+ High fill pressures not required
	- Development of technique is required

be used as the based case for the target factory design. At some future time, generating frozen shells of fuel may be the least expensive, require the lowest tritium inventory, provide high quality targets directly with no storage requirements (make one, burn one capability) and require only a low cost building and maintenance facility. However, at present , the decision was made to use the injection fill option for putting fuel into the IFE target capsules.

4.1.4.2 Selected Approach for Fuel Filling

A new and undeveloped method, called injection fill, has been selected for the DT fuel filling process because the presently available method of diffusion fill was judged to be unattractive. The basic approach to the injection fill technique is as follows:

1) A very small hollow fiber or needle is inserted through the wall of a capsule,
2) Liquid DT flows through the needle into the capsule,
3) The needle is removed from the capsule wall, and
4) The wall smoothed to a quality sufficiently high for use as an IFE target.

A hollow optical fiber could be used as the transport tube for the liquid DT fuel. The wall of the fiber forms an optical waveguide for a laser pulse that softens the wall of the capsule allowing the tip of the hollow fiber to easily penetrate the capsule. The outside surface of the fiber can be coated with a material which does not "wet" the capsule wall material. Thus, when the fiber is inserted through the wall, the wall material does not become attached to the fiber, and the wall is

not severely damaged. When the fiber is removed, none of the wall material is removed by the fiber. As the end of the fiber leaves the wall, a pulse of laser light can be used via the fiber wall to heat the material around the hole. This will allow the material around the hole to flow back into the hole to repair any irregularities left by the fiber.

A large number of capsules can be filled simultaneously by using a manifold of the hollow fibers which are inserted into an equal number of capsules carried by a tray with an array of holes or cups similar to an "egg crate." The entire injection process will be carried out at cryogenic temperatures as shown in Figs. 4.5 and 4.6, or at room temperatures as shown in Fig. 4.7. Filling the capsules at cryogenic temperatures will ensure that there will be no disruption of the capsules because of excessive internal pressure of the fuel. If the capsules are filled at room temperature, a high external pressure would be necessary to prevent disruption of the capsule from internal pressure until the capsules were cooled enough to reduce the internal pressure to manageable values.

The primary issues involved with the fill process are that 1) the technology is unproven and undeveloped, 2) mechanical movement at cryogenic temperatures is difficult (however, high speed pumps do operate at cryogenic temperatures to pump liquid oxygen, hydrogen, etc.), and 3) achieving necessary capsule surface quality after injection through its wall may be difficult.

4.1.5 Developing a Uniform DT Layer

Following the fill process, the DT fuel in the capsule must be formed into a solid layer inside the capsule. The layer must be very uniform and must be maintained until the target is irradiated in the reactor chamber or the layer must be re-formed before the target is injected into the chamber. In this section, the various methods of forming the solid DT layers are discussed and the reasons for choosing a particular technique are presented.

4.1.5.1 Layering Options

Some of the most stringent requirements imposed on IFE targets are on their geometry (i.e., the limits of surface roughness, wall thickness variations, concentricity of inner and outer surfaces, and volumetric uniformity of the capsule materials). The limits are particularly stringent when applied to the fuel layer inside the capsule. The fuel layer is required to be the correct thickness (i.e., correct quantity of fuel), and uniformity. If the capsule is filled with fuel in either liquid or gaseous form, in a subsequent step the fuel must be frozen into a uniform layer on the inner surface of the capsule.

Several techniques have been developed to cause the original freezing process to produce a uniform layer or to remelt and/or vaporize the fuel and implement a refreeze process leading to a very uniform layer. Table 4.5 presents the techniques considered viable for producing uniform

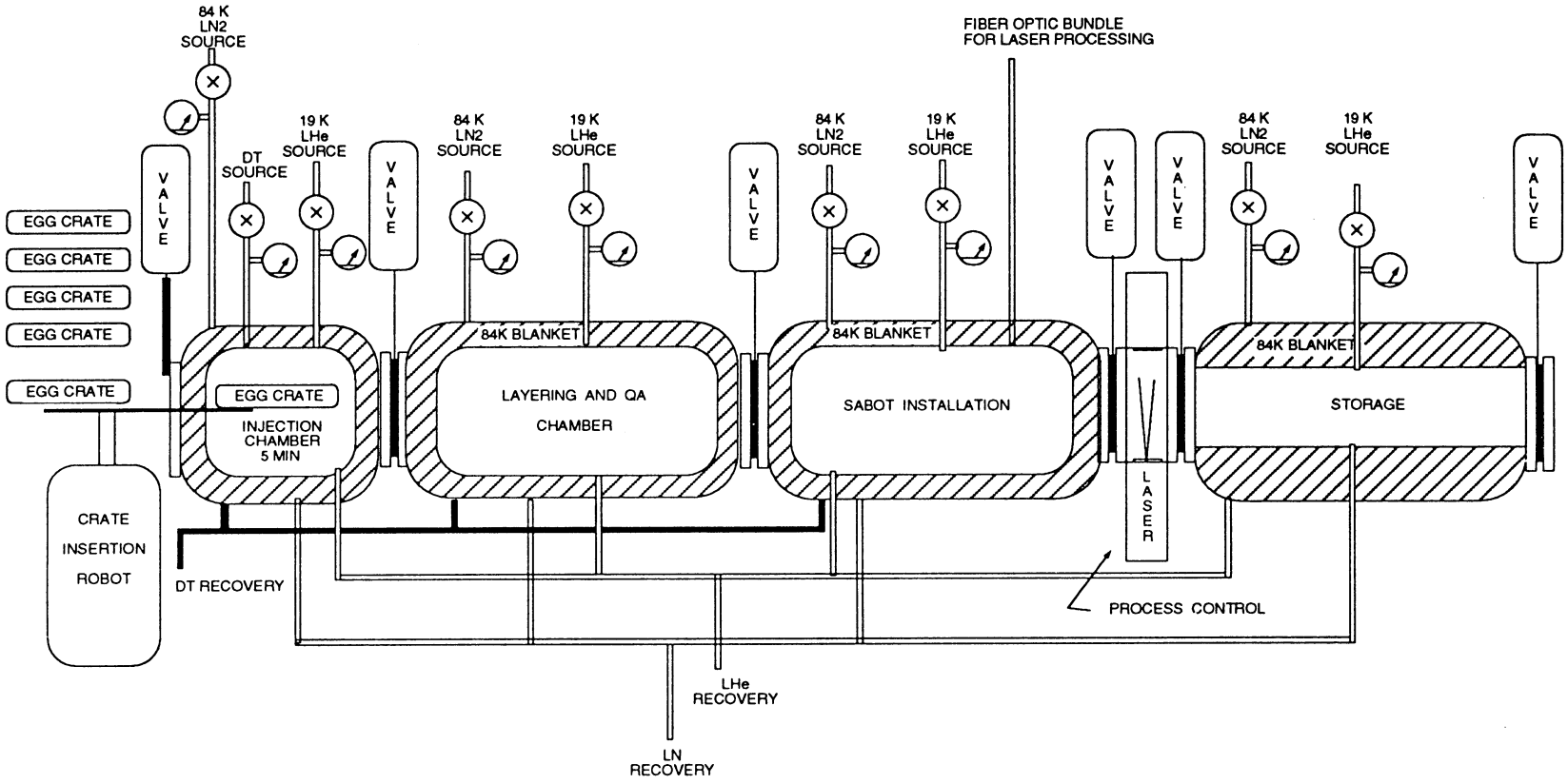

Fig. 4.5. Target produciton line using cryogenic injection fill.

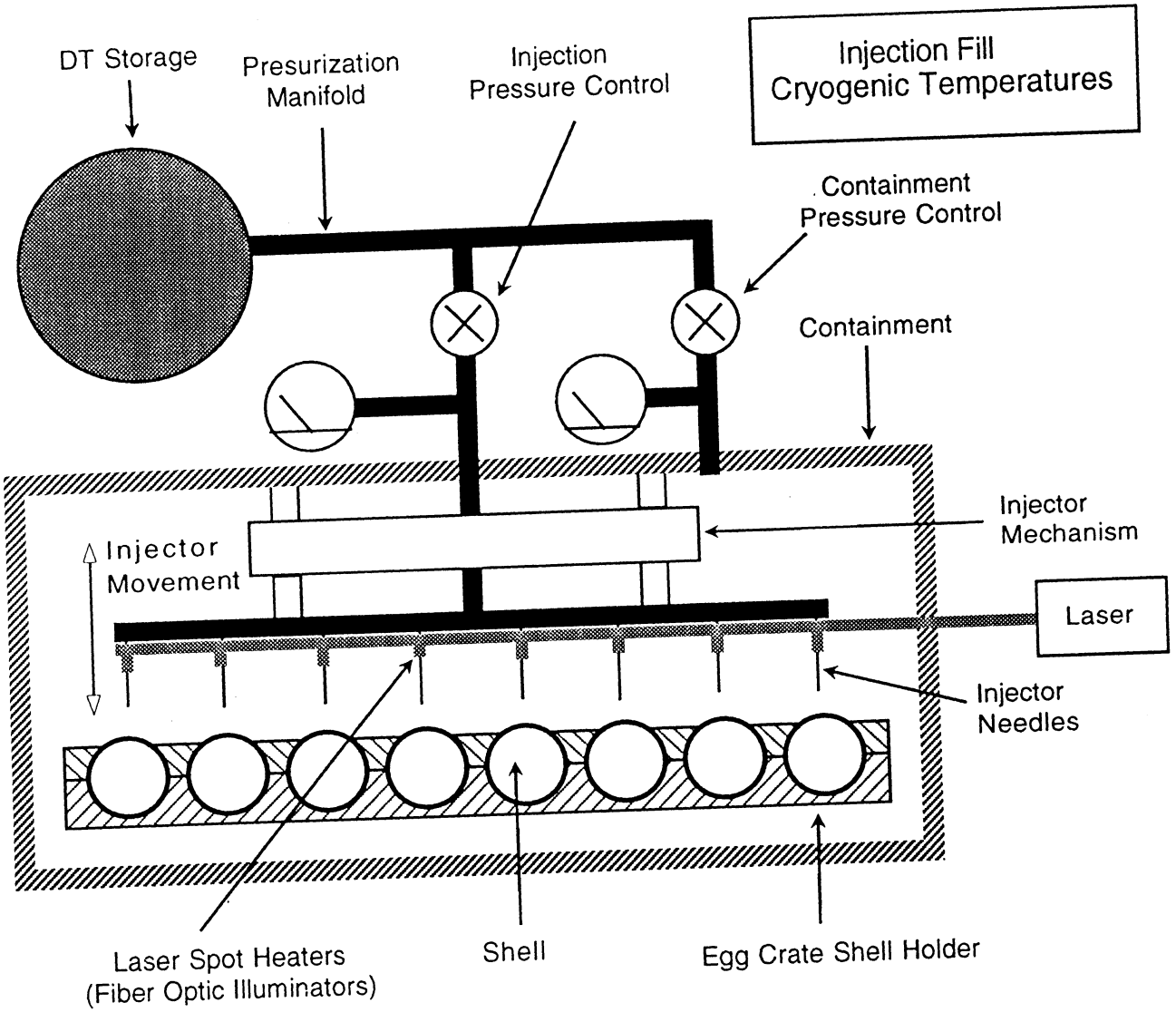

Fig. 4.6. Schematic of injection fill equipment operating at cryogenic temperatures.

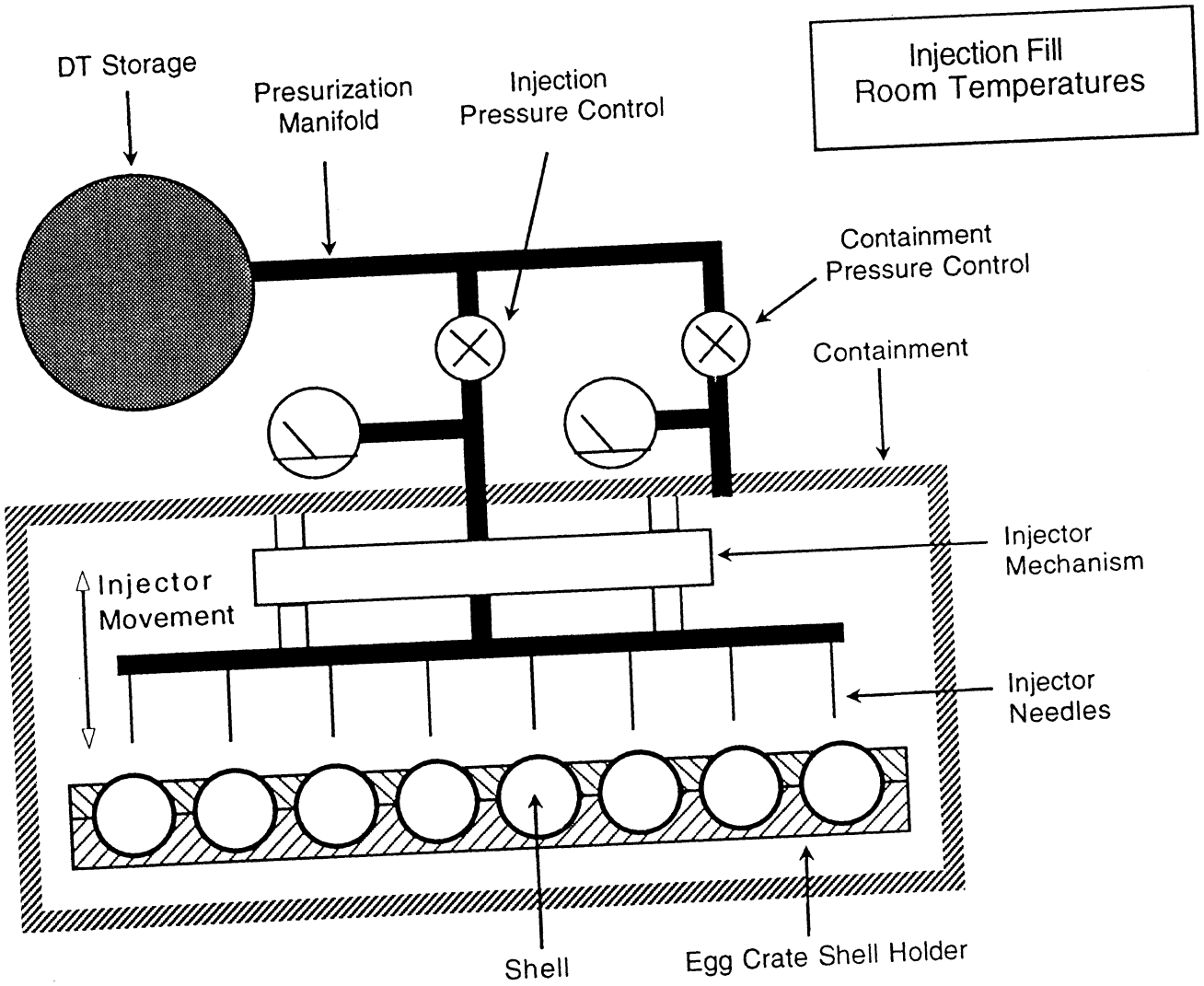

Fig. 4.7. Schematic of injection fill equipment operating at room temperature. Higher pressure fill lines are required, but laser spot heating is not.

Table 4.5. Methods for Producing a Uniform Fuel Layer in the Capsule

Technique	Advantages (+) and Disadvantages (-)
Pulse Laser / rf Heating / Refreezing	+ Target temperature regulated (intensity-graded laser) to produce uniform layer + Can be the last step prior to delivery to transport system + Simultaneous interferometric monitoring possible
Cold Gas Jets	+ Short time constant (seconds or less) - Insertion removal problems - Control problems with large numbers of capsules
Beta Layering	+ Forms a uniform DT layer automatically by self-distribution of fuel in the layer - Requires holding the capsule for a long time (4 hours)

layers in reactor-scale capsules together with some of the advantages and disadvantages of each. The major techniques are 1) laser or rf heating and refreezing,[4.6] 2) temperature controlled gas jets impinging on the capsule to cause melting/refreezing and uniform layering,[4.7] and 3) using the heat from the beta decay of tritium to cause slow migration of fuel from thick to thin portions, a process known as beta layering.[4.8]

Figure 4.8 illustrates the beta-layering technique in schematic form. The fuel filled capsule is held at a low enough temperature that the DT fuel is in a solid layer although it may be very irregular. If the capsule is held at the low temperature for a long period of time (4 hours) the energy deposited in the DT by the beta electrons from the decaying tritium causes some of the DT to be evaporated from the thicker portions and redeposited in the thinner regions of the solid DT. Because there is more tritium in the thicker parts of the layer, more energy will be deposited in the thick parts per unit time than is deposited in the thin parts. Thus, DT preferentially moves from the thick regions to the thin regions and gradually produces a uniform layer. The inner surface of the DT layer seeks the shape of a spherical isotherm. Definitive studies to determine whether or not the beta-layering technique will produce thick layers of sufficiently good quality are now in process at Los Alamos National Laboratory. Although the fuel layers seem to be adequately uniform, the poor surface quality (~ 1 μm) is still an issue. In addition, the long time required for the process to cause transport of the DT into a uniform layer reduces the attractiveness of the technique as a uniform layer generating method for reactor target production. Perhaps beta-layering could be supplemented with another method giving greater control.

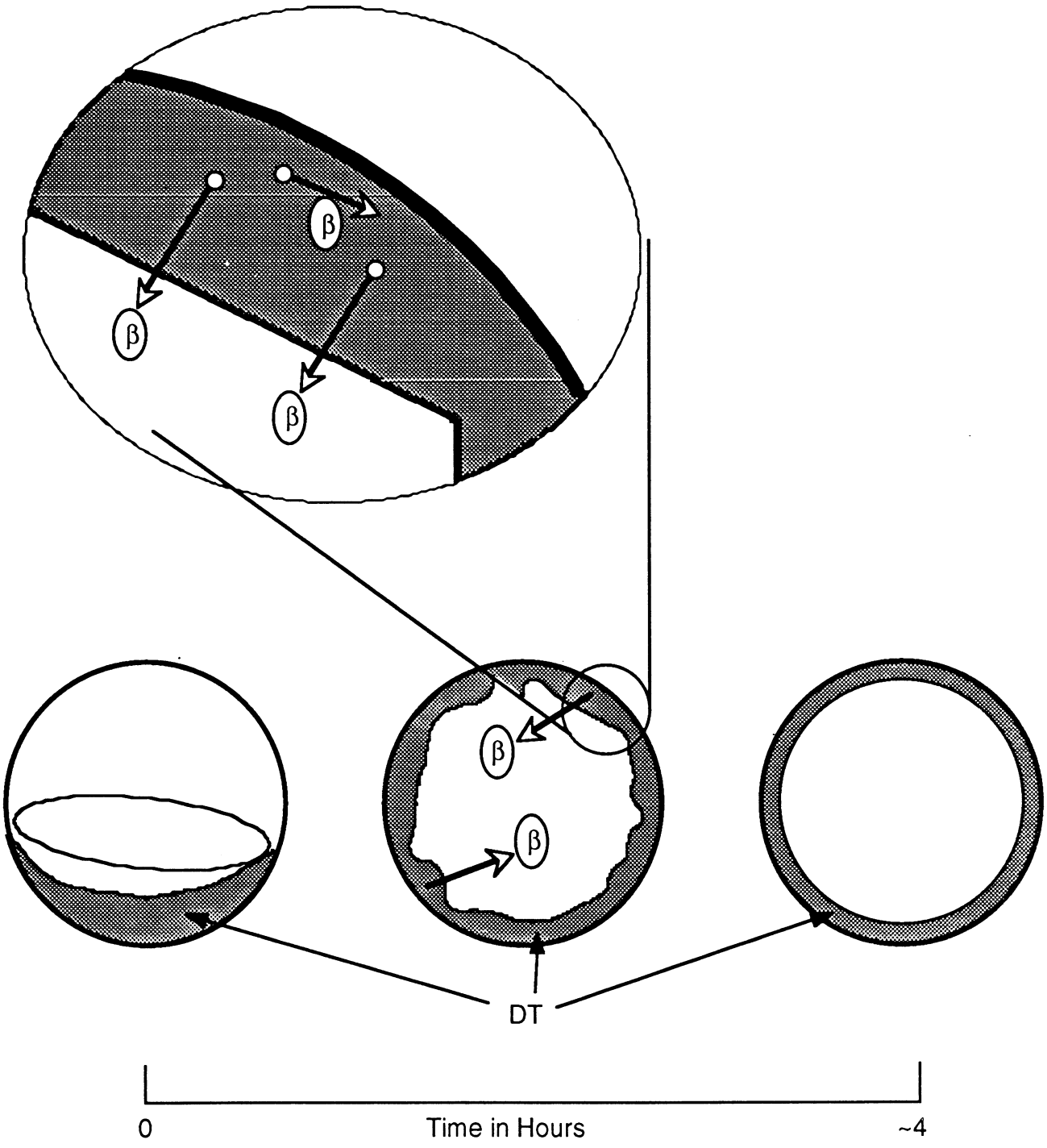

Fig. 4.8 Schematic of beta-layering process for establishing a uniform fuel layer.

The use of temperature-controlled cold gaseous helium jets for freezing and producing uniform layers of fuel in fusion targets has been analyzed and experimentally demonstrated.[4.7] Figure 4.9 shows schematically how a cold gas system operates. Gas jets impinging on the capsule from top and bottom provided the cooling to freeze the fuel into a solid layer in the capsule. By adjusting the relative temperatures of the jets, the fuel can be caused to migrate properly to form a uniform layer in the shell. The capsule could be levitated on the lower jet to avoid contact with any surfaces which could perturb the process and lead to nonuniform layers. However, the perceived transport, suspension, and control problems make it unlikely that the gas jet process could be used by itself to generate uniform layers in production targets.

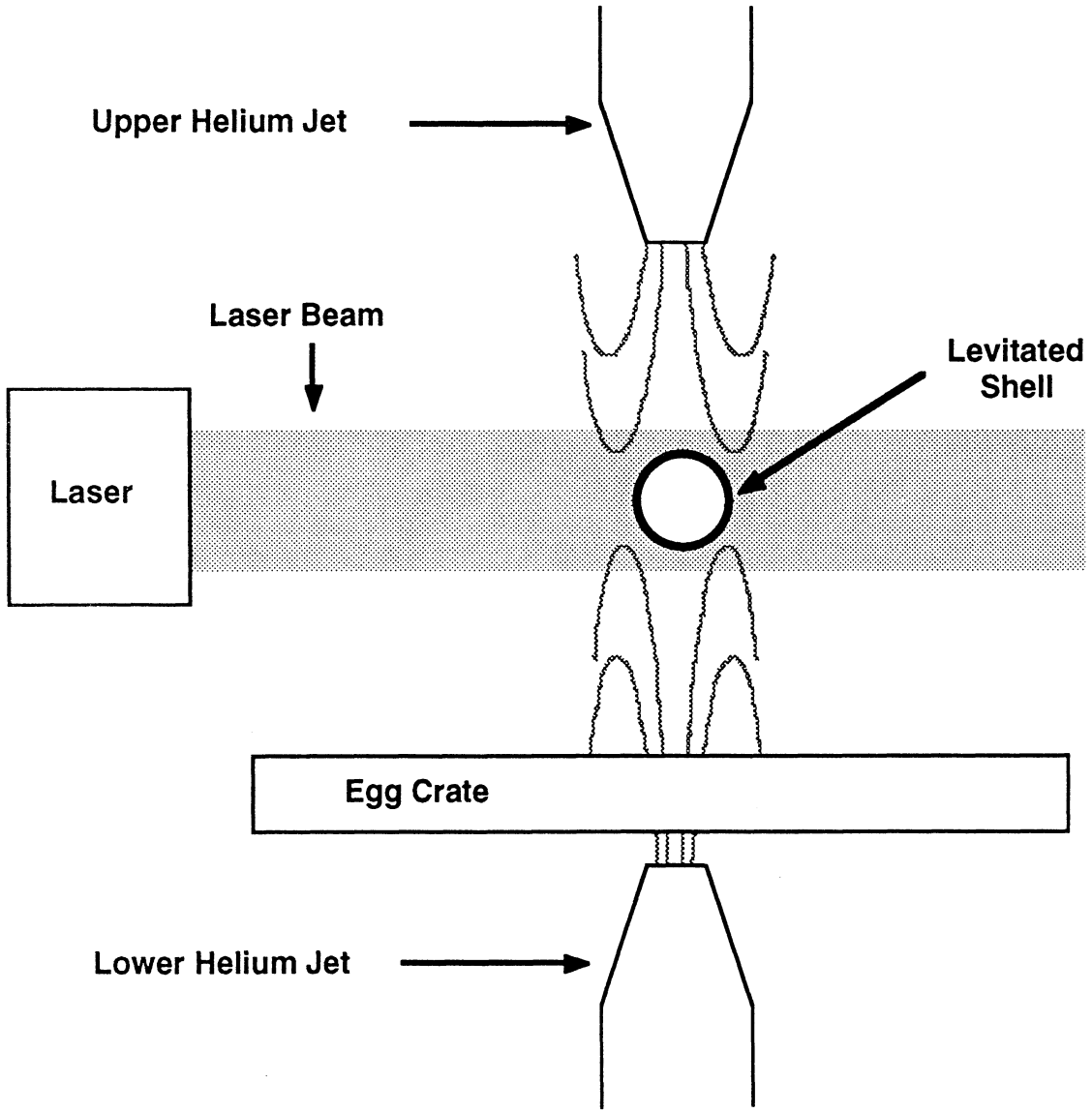

Fig. 4.9. Use of cold gas jet and pulsed laser to form a uniform fuel layer.

4.1.5.2 Selected Layering Option

For our reference design, we combine the use of gas jets to levitate the capsule with a pulsed laser for rapid heating and refreezing. This technique has been demonstrated experimentally at small scale with thin fuel layers.[4.9] We proposed that this could be the last step just prior to insertion into the sabot and transport to the chamber. We also note that simultaneous interferometric monitoring would be possible during the layer step.

4.1.6 Capsule Handling and Transport

Some of the capsule handling and transport considerations are summarized in Table 4.6. After they are formed, the capsules will be handled and transported in egg-crate type trays holding approximately 2000 capsules in each tray. The trays will nominally be about 35 cm by 35 cm and will be designed for handling by conveyers, robots, and other automated equipment. The construction of the egg-crate trays is shown schematically in Fig. 4.10. The construction of the trays will permit handling by conveyers, robots, and other automated equipment needed to move the filled trays through the various stages of the target fabrication process. The trays will also permit automated stacking for storage and retrieval of the finished targets. To deliver targets one-at-a-time to the reactor, the trays must be unloaded and each target inserted into a sabot. The sabot is used to protect the target during transport from the production facility to the target injector and during acceleration by the injector. The halves of the sabot will be ejected prior to entering the reactor chamber, and the target will continue to the irradiation point in a completely uncovered state.

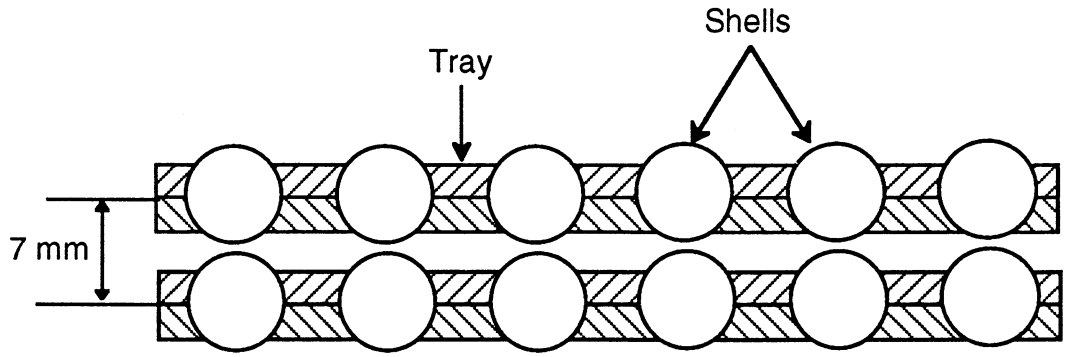

Fig. 4.10. Cross section of transport trays showing shell placement and tray spacing during storage.

Table 4.6. Capsule Handling and Transport Issues

- Mechanisms operating at cryogenic temperatures:
  - Gate valves between chambers
  - Conveyer belts between chambers
  - Robot arm inserting trays into fuel fill chamber
  - Device to unload trays from storage into reactor transport
- Material limitations at cryogenic temperatures and in the presence of tritium (damage from beta radiation)
- Low mass (small size) of moving parts to minimize thermal shock to systems

4.1.7 Quality Assurance

Because the target fabrication processes must be completely industrialized by the time an IFE reactor power generation plant is built, there is no need to do a detailed characterization of each target. It will only be necessary to statistically monitor the various processes to ensure that the processes are not degrading with time. As is shown in Fig. 4.11, a laser interferometer will be used to generate real-time interferograms or holograms, which will be "read" by a high speed camera (e.g., a CCD array camera) and compared by a computer with a hard-wired, built-in pattern to determine if a given target matches the reference pattern within some predetermined limits. If differences exceed the chosen limits of size, wall and/or layer thickness, uniformity of wall, sphericity, or other parameters, alarms can alert operating personnel to potential problems. Because the target production rate is relatively low, there is sufficient time (~150 ms per target) to make all process determinations by computer. With exception of total mechanical failure of a part or system, the systems and processes should only be expected to change over long periods of time. Thus, human intervention can reset parameters to prevent slow problem build-up to catastrophic failure situations.

4.1.8 Target Protection by Sabots

During the process of acceleration and transport to the outer wall of the reactor chamber, the targets should be protected by either a thick coating of frozen gas or by a solid sabot. If the choice is to protect by a thick cryogenic layer, it must be permitted to ablate during the travel to the irradiation point in the chamber. This would protect the actual target from the high temperature ambient atmosphere in the chamber and also afford protection during the transport and acceleration phases before the target reaches the wall of the reactor chamber.

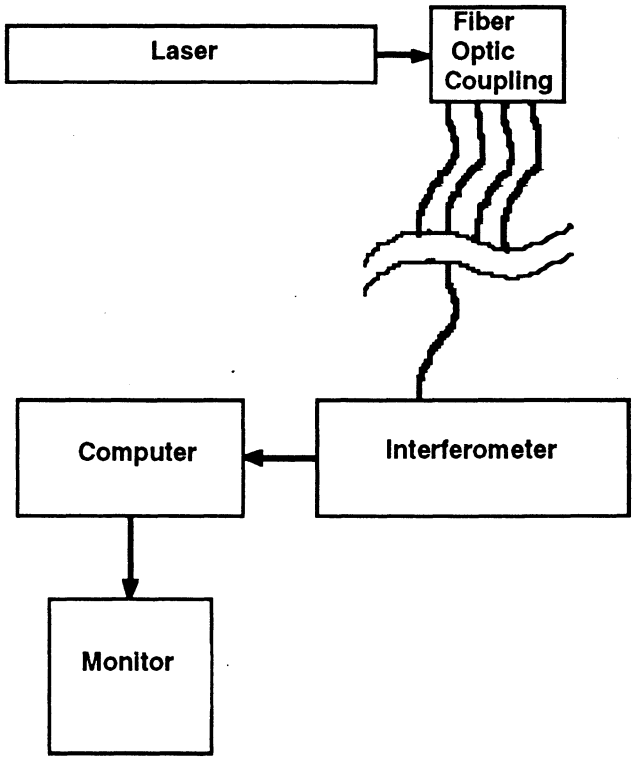

Fig. 4.11. Schematic of interferometric technical for monitoring capsule quality.

If the choice were to use a sabot around each target for protection during acceleration and transport phases, the sabots should be ejected from the target prior to entry into the chamber. The sabots would be re-usable and would not add to the gas loads and contaminants dumped into the chamber at each shot. It is also advantageous to remove the sabot prior to entry into the chamber in order to keep the sabot material out of the high radiation environment.

4.1.9 Target Storage

With two production lines, each operating at half capacity, it should not be necessary to store more than 6000 finished targets in each line for a total of 12,000 targets (~30 g of tritium). This would provide for 1/2 hour of reactor operation in the event of a failure of one production line. The probability is high that the remaining line could be brought to full-up capacity in the half-hour provided by the stored targets. Alternatively, if the production facility were to have two operating lines and a third line on ready stand-by, the idle line could be brought into operation very quickly, providing sufficient redundancy for almost any foreseeable problem. In this case, the stored target inventory could probably be reduced to half or even a third (i.e., perhaps 4000 target with a tritium inventory of ~ 10 g). Because the target production processes will have been tested and perfected, reliability should be very high by the time an operating target facility is constructed.

4.1.10 Tritium Inventory

The tritium inventory of the entire target production facility can be determined within the bounds of the assumptions made for target storage, target transport during fabrication, fill process tritium requirements, and tritium in pipes leading to the fill stations. There will be a minimum of two independent parallel process lines each operating at half the maximum production rate. The targets will move into the fill chamber in a 2000-capsule tray and a 2000-needle injection unit will fill the entire batch at one time. The fill time is less than 1 minute, but 10 minutes will be scheduled to allow for opening of valves, moving trays in and out, and for the insertion and removal of injectors. After filling, each tray of capsules will contain about 5 g of tritium. The tritium fill reservoir is assumed to contain 20 times the capacity of a single tray or about 100 grams of tritium. High pressures will not be required in the injection fill system because the fill is done at cryogenic temperatures at which the DT pressure will be very low.

Table 4.7 provides a tabulation of the tritium inventory for the IFE fusion reactor target production facility. The total tritium inventory for the target production facility is estimated to be about 300 g. Note that this does not include the tritium inventory associated with the recovery and processing of tritium generated in the breeding blanket since that is accounted for with the reactor and its enclosure.

4.1.11 Production Facility Building

Throughout this entire design study the issue of cost of building and footprint has been an underlying consideration. We propose that the capsule production, fill system, transport, storage, sabot production and loading, and other target handling functions will all be accomplished in clean (10-100 class), enclosed "boxes." Thus, it will not be necessary to build the target production facility building to clean room specifications. It will be sufficient to have the entire facility at 10,000 to 100,000 class cleanliness.

The entire apparatus in which targets are filled, transported, manipulated, and stored will be constructed for total containment of the tritium so the building itself need not be more costly than ordinary construction. This, in addition to the absence of formal clean rooms in the building, should help minimize the cost of the facility.

4.1.12 Summary

The follow points summarize the features of the target production facility design:

- Our design approach will lead to high reliability due to 100% redundancy of process lines.
- The tritium inventory is minimized by using fill and layering techniques that can be completed in seconds instead of hours.

- A small capsule storage inventory is judged to be acceptable because of the redundancy and high reliability.
- The required building is compact, which should lead to acceptably low cost.
- Much of the technology is unproven and requires development.
- The payoff in pursuing these innovative target production approaches is very high in terms of reducing the tritium inventory and the size and cost of production equipment and buildings.

Table 4.7. Total Tritium Inventory

Process Step	Tritium Inventory (grams)
Injection Step	
2 tritium reservoirs @ 100 grams each	200
2 trays of capsules @ 5 grams each	10
Layering and Q/A Steps	
2 trays of capsules @ 5 grams each	10
Sabot Loading	
2 trays of capsules @ 5 grams each	10
Storage of Complete Targets	
12,000 @ 2.4 mg each	29
Transport Chain to Chamber	
50 meters @ 1 m/sec = 50 seconds	
50 seconds of targets @ 6.7 Hz = 335 targets	
335 targets @ 2.4 mg/target = approx.	1
Piping and Purge Lines	
500 m of 1-cm diameter piping at 3 atm.	40
Total Tritium Inventory	**300**

4.2 TARGET INJECTION, TRACKING, AND POINTING

4.2.1 Objectives and Requirements

The objective of this study was to develop conceptual designs of target injection, target tracking, and beam pointing systems for both laser and heavy-ion beam driven IFE reactors. Performance requirements for these systems are quantified and examined for a proposed base conceptual design. Wherever possible, the requirements for the base design are compared with demonstrated state-of-the-art component performance. Development needs for detailed modeling and proof-of-principle experiments are outlined and discussed.

4.2.2 Overview

In order for the driver to ignite the target and produce the gain necessary for an IFE reactor, the final driver beams must all be centered on the target and hit the target simultaneously. Three separate systems must work together to accomplish this.

1) Target delivery to the correct location in the chamber must be as consistent and accurate as possible.
2) A tracking system must be able to detect small variations in the placement of individual targets in time to correct the beam pointing.
3) An active beam alignment system must be able to quickly and accurately point the beams to each target's final location.

The match between the center of the beams and the center of the target must be to within 10% of the capsule radius for a direct-drive laser target (roughly 0.3 mm) or to within 20% of the focus spot radius for heavy-ion indirect targets (roughly 0.5 mm). The accuracy with which one can track the target will be limited by the amount of time required to process the tracking information and steer the beams.

Figure 4.12 is a schematic of the components of a target injection and tracking system that uses a gas gun for target acceleration. The distances and times necessary to characterize the injection and tracking system are also shown in Fig. 4.12. The target is accelerated at a constant acceleration, a, over an acceleration length, L_a. After leaving the acceleration section, the target travels a constant velocity, $\sqrt{2\,a\,L_a}$, to the center of the chamber. A removable sabot is used to protect the target during acceleration. The target is given an angular velocity during acceleration, so the sabot will be separated into two pieces by centrifugal force after acceleration. The distance from the exit of the acceleration section to the center of the chamber is divided into three segments: the sabot removal length, L_{sr}; the tracking length, L_t; and the radius to the outer edge of the chamber, R_c. We also define the following time periods:

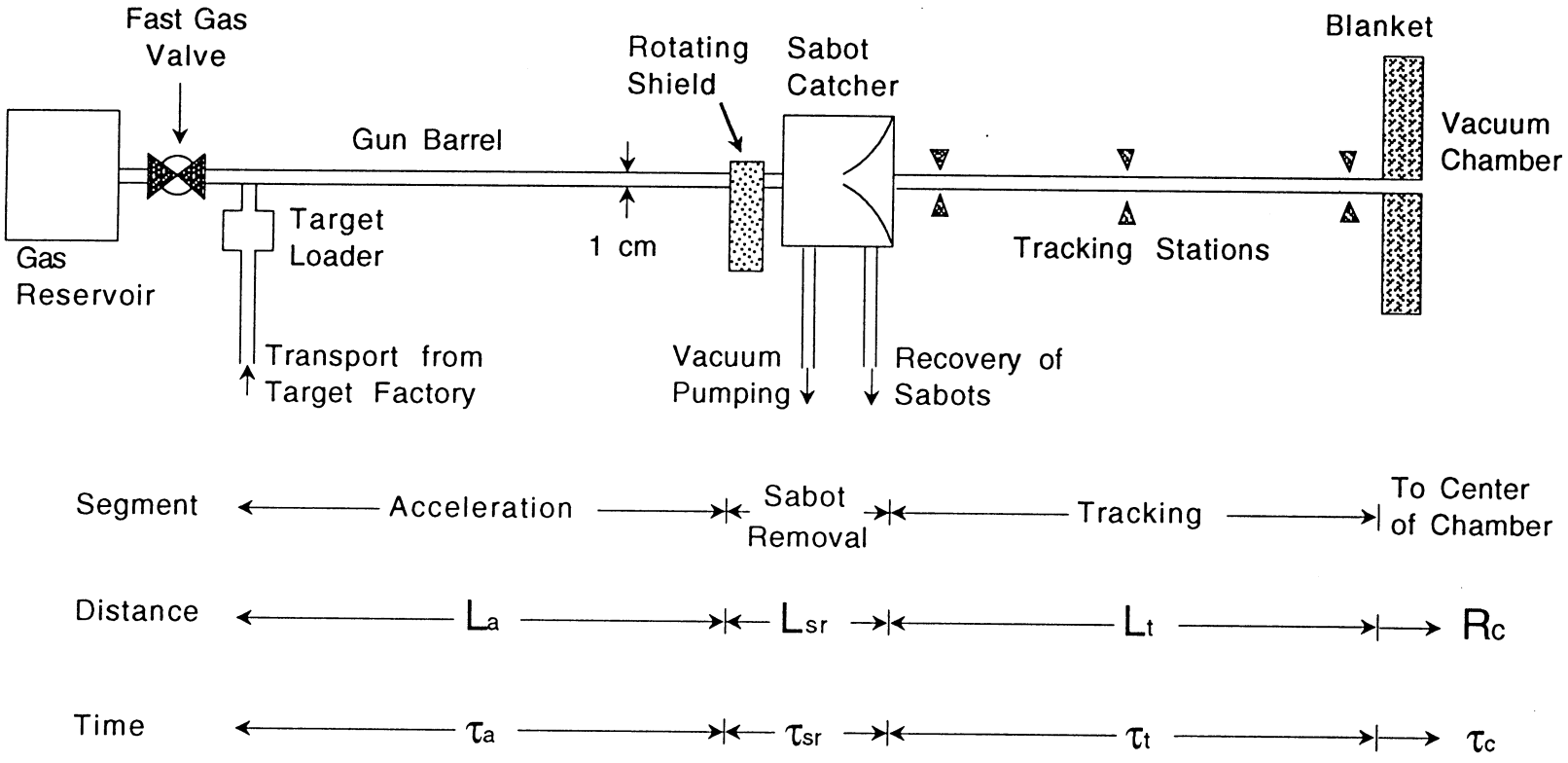

Fig. 4.12. Schematic of target injection and tracking system.

τ_a = time of acceleration, s

τ_{sr} = time for sabot removal, s

τ_t = time for tracking before entering chamber, s

τ_c = time in chamber, s

τ_p = interpulse time = 1/rep-rate, s

If several tracking points are used over a total tracking length, with the last tracking point at the outer chamber wall, then there are two times of interest: the time between the first tracking data and target ignition, which is given by $\tau_{p1} = \tau_t + \tau_c$; and the time between the last tracking point and ignition, $\tau_{p2} = \tau_c$. The first time interval, τ_{p1}, is the time allowed for preliminary (relatively large) pointing corrections, and the second time interval, τ_{p2}, is the time allowed for final (relatively small) pointing corrections. The total (processing and pointing) response time must be smaller than τ_{p1} for large corrections, and smaller than τ_{p2} for small corrections.

The conceptual design of the target injection system was based on the following design constraints:

1) Only one target is allowed in the accelerator at a time: $\tau_a \leq 0.8\ \tau_p$ (allowing $0.2\ \tau_p$ for loading), or

$$L_a \leq \frac{a\,(0.8\ \tau_p)^2}{2}$$

2) The target can be in the chamber for only 1/3 of the interpulse time: $\tau_c \leq \tau_p/3$, or

$$L_a \geq \frac{1}{2a} \cdot \left(\frac{3R_c}{\tau_p}\right)^2$$

3) Pointing commands are received and processed for only one target at a time: $\tau_t + \tau_c \leq \tau_p$, or

$$L_a \geq \frac{1}{2a} \cdot \left(\frac{L_t + R_c}{\tau_p}\right)^2$$

These design constraints are shown in Fig. 4.13 on a map of the acceleration length versus acceleration. The SOMBRERO design parameters of R_c = 7.5 m and τ_p = 0.15 s (rep-rate = 6.7 Hz) were used to generate Fig. 4.13. A sabot removal length of 2.5 m and tracking length of 7.5 m were also assumed. To minimize the forces on the target during injection, the minimum permissible acceleration should be used. The operating point, with L_a = 9.0 m and a = 130 g's, is indicated in Fig. 4.14, and the design parameters for our baseline system are given in Table 4.7. The system is shown schematically in Fig. 4.14.

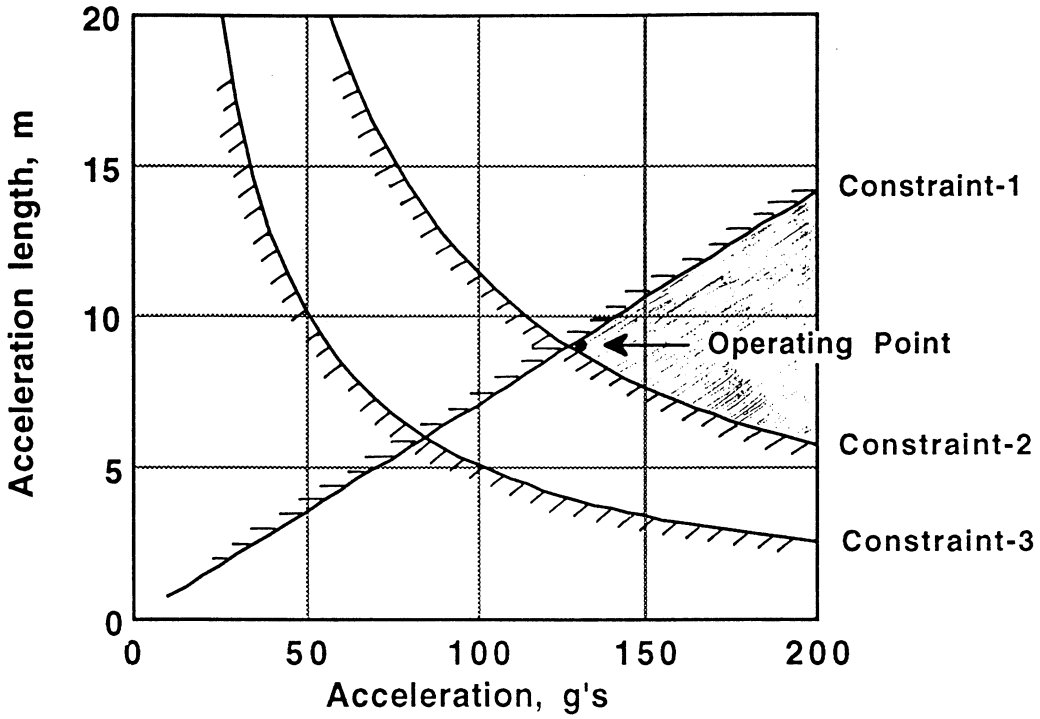

Fig. 4.13. Acceleration length versus acceleration. The three constraints limit the design space as indicated.

Table 4.7. Baseline Target Injection Parameters

Acceleration (a)	130 g
Accelerator Length (L_a)	9 m
Final Injection Velocity (v_f)	151 m/s
Time in Accelerator (τ_a)	119 ms
Sabot Removal Length (L_{sr})	2.5 m
Time for Sabot Removal (τ_{sr})	17 ms
Rotational Velocity for Sabot Removal	570 RPM
Time for Tracking (τ_t)	50 ms
Time in Chamber (τ_c)	50 ms
Total Time from Target Firing to Ignition (τ_{tot})	235 ms
Time Allowed for Coarse Corrections (τ_{p1})	100 ms
Time Allowed for Fine Corrections (τ_{p2})	50 ms

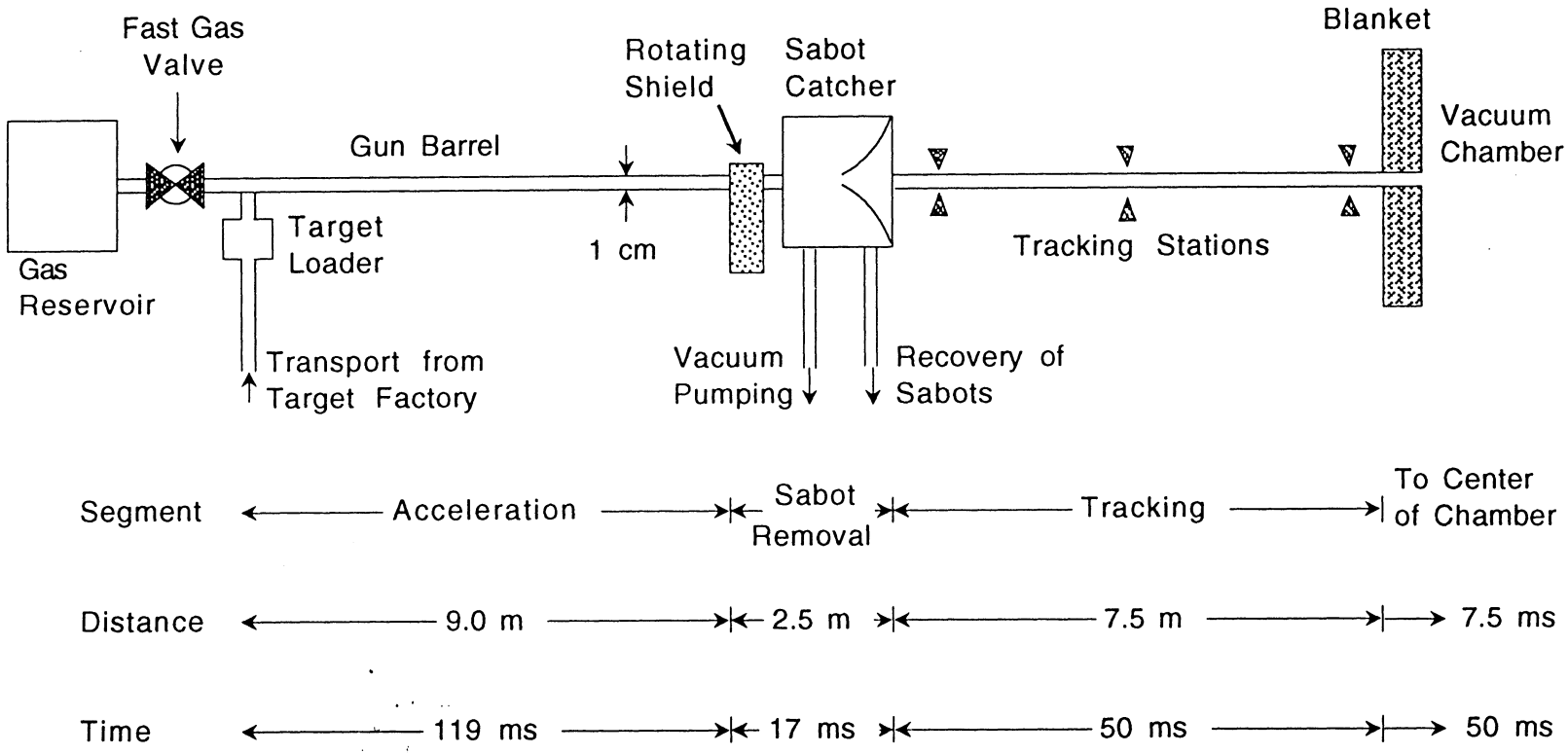

Fig. 4.14. Schematic of the reference design for the target injection and tracking system.

This injector meets the goal of only tracking or accelerating one target at a time, but one target will be tracked while the next target is accelerated. The required rotational velocity is set by the sabot velocity, the length allowed for sabot removal (2.5 m), and displacement (~ 0.5 cm) needed to separate the sabot from the target. If lower rotational velocities are desired, longer regions must be allowed for the sabot catcher, or the separation of the halves of the sabot could be assisted by a plastic spring integral to the sabot design. If targets can not tolerate acceleration on the order of 100 g, accelerators and tracking systems that can accommodate two or more targets with separation less than the acceleration and/or tracking length must be designed or two systems could operate in an alternating fashion.

4.2.3 Injection System Design

4.2.3.1 Injector System Selection

Several acceleration options exist for a target injector.[4-10] The concepts receiving the most interest are light gas guns, centrifuge launchers, and rail guns. The light gas gun is chosen as our base injector, but the advantages and drawbacks of each of these concepts are briefly discussed.

Light Gas Guns. A light gas gun uses a high pressure hydrogen, deuterium, or helium gas to accelerate the frozen pellets of fuel through a tube or barrel. The velocity of the pellet is limited by the driving gas parameters and the projectile size and mass. Rifling of the barrel can be used to provide the required spin rate for sabot removal. A gas gun will require that the sabot form a tight seal with the barrel of the injector. Light gas guns have been demonstrated at a number of locations. In the mid 1980's, ORNL successfully demonstrated high velocity operation of a light gas gun at greater than 2 Hz.[4.11] Barrel wear and pellet heating are issues which must be addressed in the injector design.

The light gas gun is chosen as our base injector because of its relative technical maturity, low risk, and its ability to give accurate target placement at required repetition rates. Preliminary calculations indicate that the gas gun can be modeled as a constant pressure accelerator with a mass flow rate of 2 mg/s for a helium gun. The final pellet velocity should be repeatable to within 3%, and the shot-to-shot variation in pointing should be on the order of $\pm$ 1 mrad. These variations are small enough to be consistent with our tracking and pointing system designs.

Centrifuge Injector. A centrifuge injector for adding fuel to tokamaks has been developed by ORNL.[4.12] In this injector, radial u-shaped channels in a rotor cut off a section of extruded frozen hydrogen near the rotor spin axis and then accelerate the pellet toward the outer radius of the rotor. The pellet exits the tube with a velocity which may exceed the velocity of the rotor tip by a factor of almost two. One such centrifuge consists of a Kevlar-epoxy hoop with a built-ion pellet chute. With a 1-m-diameter hoop rotating at 20,000 RPM, pellets of 1.3 mm

diameter have been accelerated to speeds of roughly 800 m/s with injection rates of 20 Hz. This technique would require significant development before it could be used with sabots and targets, and the shot-to-shot pointing variations for such an injector could be prohibitively large.

Electromagnetic Railgun Accelerator. Railguns are receiving increased attention as candidates for injectors. The railgun accelerates a projectile along parallel tracks by connecting a capacitor bank (or other voltage source) to each of the rails, with a conducting projectile or sabot completing the circuit. The current loop carries a current, I, and creates a magnetic field, B, with an accompanying force of I×B on the projectile. The energy stored in the circuit is given in terms of the inductance, L, by $E = 1/2\ LI^2$, and the force for a constant discharge current is given by dE/dx, or $F = 1/2\ I^2\ dL/dx$. A railgun using a conducting sabot with an open front could decelerate the sabot at the end of the injector to recover the sabot while allowing the target to continue into the reactor.

Because of the need for high injection velocities and a cryogenic target, it is difficult to design an electrical connection between the sabot and the rails. A sliding contact or a plasma discharge could be used to complete the circuit, but both would produce heating of the sabot. A proposed injection system for HIBALL[4.13] avoids this problem by using a solenoid in the injection barrel with a ferromagnetic recoverable sabot. This system gives electromagnetic acceleration without requiring contact between the sabot and the barrel. Cryogenic railguns operating at high repetition rate with repeatable velocity and pointing will require further research and experiments to be credible.

Other Acceleration Concepts. Electrostatic accelerators and laser rocket accelerators have also been proposed for injectors, but these systems have not been sufficiently developed for a feasibility analysis to be possible.

4.2.3.2 Critical Issues for the Base Injector

Acceleration Limit on Targets. Careful design is required for the pellet support within a sabot or an indirect target. The amount of acceleration that can be tolerated by the pellet was estimated by LLNL[4.14] to be ~ 170 g. More detailed information on the design of direct and indirect drive targets is needed to examine this limit.

Heating and Wear of Sabots. The sabot must be designed to protect the pellet from heating from either the propellant gas or the friction from the barrel. Reusing sabots would simplify the demands on the target factory, but will require that the sabots survive several launches and recoveries. Because of the need for consistent target placement, even small damage to the sabot surface could prevent them from being reused.

Barrel Wear. Because of the need for a tight seal between the sabot and the barrel, any damage to the barrel surface will affect the injector's performance. Requirements for barrel

cleaning, maintenance, and replacement will need to be investigated.

Loading, Recovery, and Refilling of Sabots. Unless multiple barrels are used (as in a gatling gun), the time allowed for reloading the injector is small (~ 0.03 s). If the sabots are to be reused, they need to be recovered, inspected, cooled, and reloaded in an automated processes. A more likely scenario is that recovered sabot material would be used in the production of new sabots with the required tolerances.

4.2.4 Target Tracking

4.2.4.1 Tracking Requirements

A tracking and pointing system is required to aim the driver at the pellet and to assure that the target will ignite. The match between the center of the beams and the center of the target must be to within 10% of the pellet radius for a direct-drive laser target (roughly 0.3 mm) or to within 20% of the pellet radius for heavy-ion indirect targets (roughly 0.5 mm). If tracking and final pointing elements are 10 m from the target, this limits the tracking, alignment, and pointing errors to the order of 10 microradians or less. If the final pointing element for a laser driver is on the order of 100 m from the target, it will need an accuracy on the order of a microradian. The required pointing accuracy has been demonstrated in various Directed Energy Weapons programs sponsored by the Strategic Defense Initiative Organization (SDIO).[4.15] Tracking systems with these accuracies were built and flown aboard the Airborne Laser Laboratory.[4.16] An alignment transfer system, ARTS, was built and tested as part of the Alpha/LODE program.

A critical problem is the alignment of the tracker's measurement system with the device's line of sight. An alignment laser in the optical train can help sight a laser driver, but some kind of bore sighting is required for the injector and the heavy-ion driver. The total alignment accuracy should be less than a third of the total tracking error budget, or less than a microradian. The ability to periodically measure the pellet position at intercept would help the alignment system. This could be done simply by imaging the target x-ray output through a pinhole to determine the location of the last target. If tracking at intercept is not possible for ignited targets, periodic adjustment could be made with a low powered marker (e.g. laser) aligned with the device and aligned to hit a dummy target.

"Beam bug" techniques developed at LLNL and the beam position monitor developed at LANL could provide a solution to the HIB sensing problem if the accuracy of the sensing can be on the order of 0.1%. An alignment system must still be developed. Pointing of the HIB will be accomplished using a pair of crossed steering dipoles at the end of the final focusing. These steering coils could be incorporated in the windings of the final focusing quadrupole and should achieve a steering bandwidth on the order of a MHz, well beyond pointing requirements.

The target can either be tracked prior to entering the chamber, or it can be tracked inside the chamber. Figure 4.15 shows a representative system for tracking the target outside the chamber. This system is described in more detail in the following section. An alternative design, shown in Fig. 4.16, uses laser tracking to track the target within the chamber.[4-17] Although the second system would give more accurate tracking of the final target trajectory, we chose the first system as our base design because it is protected from the harsh reactor environment, and it allows more time for beam pointing corrections after the final tracking measurements.

4.2.4.2 Description of Tracking System

Our base tracker consists of a laser Doppler velocimeter followed by a series of crossed light axis position and time detectors as shown in Fig. 4.15. The assumed pointing accuracy for the gas gun (10 microradians) and the expected shot-to-shot velocity variation (± 3 %) combine to set limits on tracker field of view. The tracker design must be sized to accommodate these variations in gun performance.

A possible one-dimensional tracker for use in an x-y position detector could consist of a Ga-As laser diode beam which is expanded to approximate 5 cm in diameter and then be refocused on a silicon diode array of 40×100 elements for Y direction and 20×100 for the X direction to accommodate the initial pointing inaccuracy. Each array will be scanned at 10 MHz to assure that the pellet is repeatedly sampled as it passes through the beam. This approach allows at least ten totally independent measurements of the target position at each station (two pair of cross-axis laser and detector rings), providing noise reduction and accuracy improvement in each axis. Noise performance should not be a limiting factor since the laser diode can be selected to permit high signal levels. Further, by using knowledge of the approximate time of arrival of the pellet, gating techniques can be applied to reduce the background signal. Should crosstalk between the laser diode pairs become a problem, the laser diodes can be doped to operate at slightly different wavelengths and appropriate filters can be used on the sensors.

Processing of the data will utilize matched filter techniques to generate a best estimate of target location for each scan. This data will then be processed using a tracker, such as the Fitts-gradient tracker developed as part of the Airborne Laser Laboratory program, to an accuracy of better than 1/20 of a detector element. Resultant accuracy of each station's target position data will be approximately 10^{-5} m.

State-of-the-art laser diodes allow operation at about 100 MHz, and trackers have been built and tested with tracking accuracies of 1/100 of a detector element. While difficult to meet, the target tracking requirements for IFE are well within the state of the art.

Velocity will be estimated at each station. Because of the limited distances between measurements, the accuracy of the velocity measurement can be greatly improved by using at least

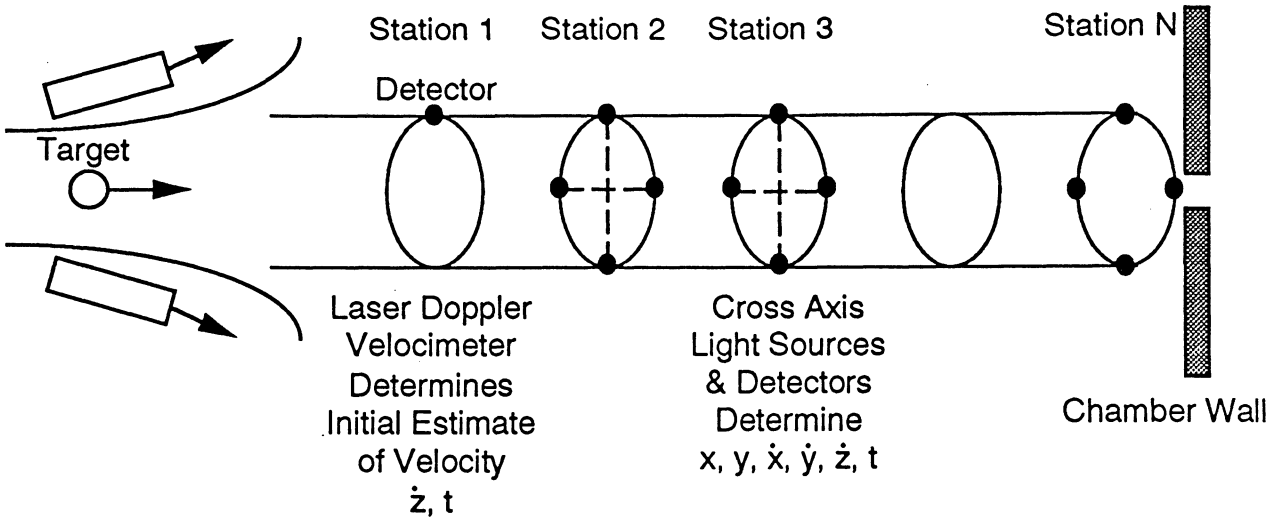

Fig. 4.15. Tracking system using multiple tracking stations.

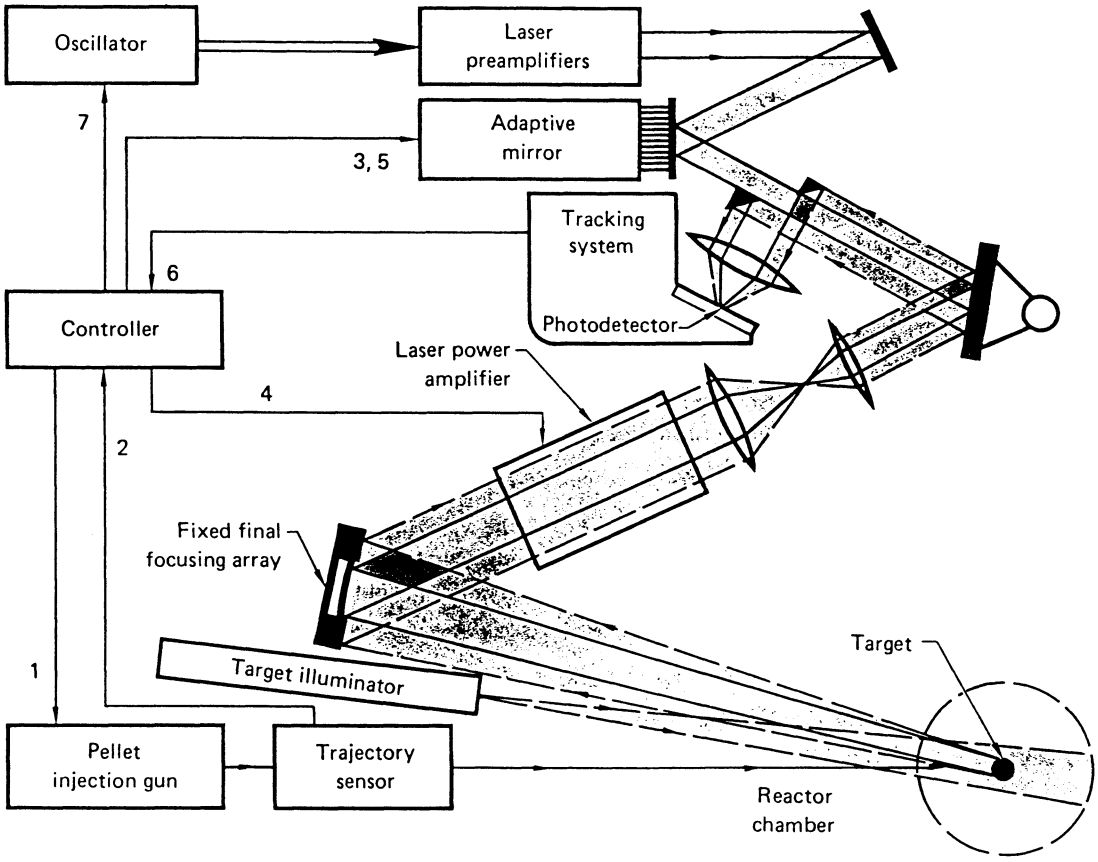

Fig. 4.16. Alternative tracking system that uses a laser to track the target within the chamber.

four sets of stations. These stations will give independent velocity measurements separated by 10 ms, and Kalman filter prediction algorithms will be developed to estimate the target trajectory to the intercept point. If greater accuracy is needed, additional stations can give accurate estimates of higher order derivatives of the trajectory to be used in the estimator / predictor. The first estimate of intercept location and time will be available 100 ms before intercept, requiring that the beam pointing element have a bandwidth of > 100 Hz. This will allow at least ten time constants for the system to accurately settle and match the intercept location. This estimated settling time can be reduced by application of modern control techniques such as dead beat digital control algorithms.

4.2.5 Beam Pointing

4.2.5.1 Laser Beam Pointing

If the pointing system has most of the 100 ms available for settling, the requirements on fast steering mirrors are minimized. Fast steering mirrors with settling times well below 100 ms have been built as part of SDIO programs.[4.18] One example is the cooled fast steering mirror system with a 600 Hz bandwidth used by United Technology Optical Systems for the FEL program, but these highly accurate cooled mirror systems are expensive and complex. The uncooled 10 cm size, 100 Hz bandwidth mirrors needed by this design are less complicated and have lower demands; they should not be a driving cost item in the laser system.

4.2.5.2 Heavy-Ion Beam Pointing

Pointing the HIB requires measuring the location an direction of the beam and referencing it to the tracking system. The first problem is to measure the beam location. While it is unlikely that a beam measurement on a single shot could be used to focus that same shot, beam sensing can be used for shot-to-shot corrections of a driver. Beam bug techniques developed at LLNL and the beam position monitor developed at LANL for the SDIO Neutral Particle Beam (NPB) program could be used to provide the basis for a beam-sensing design.

Pointing of the heavy-ion beams will be done by a pair of crossed dipole steering magnets. These steering magnets could consist of coils inside the final focusing quadrupole magnets. Preliminary calculations give steering bandwidths on the order of 100 kHz which far exceeds the required response time for an IFE pointing system. Critical issues which must be investigated are the linearity, repeatability, and accuracy of the steering magnets. In the NPB program, third order magnetic optics models are used to obtain adequate system performance at larger steering angles.

4.2.6 Integrated Target Injection, Tracking, and Pointing Systems

The architecture of the tracking equipment is an important consideration. A method to reference the tracker and the driver must be incorporated in the pointing system. One architecture which may be applicable to the IFE is shown in Fig. 4.17. Although this architecture is configured with the Wire and Fluorescent Fiber Optical Grid (WAFFOG) in mind as the beam sensor, it is not limited to the WAFFOG beam sensor. The technique can be reconfigured for other beam sensing techniques. Some of the key architectural factors are shown in Table 4.8.

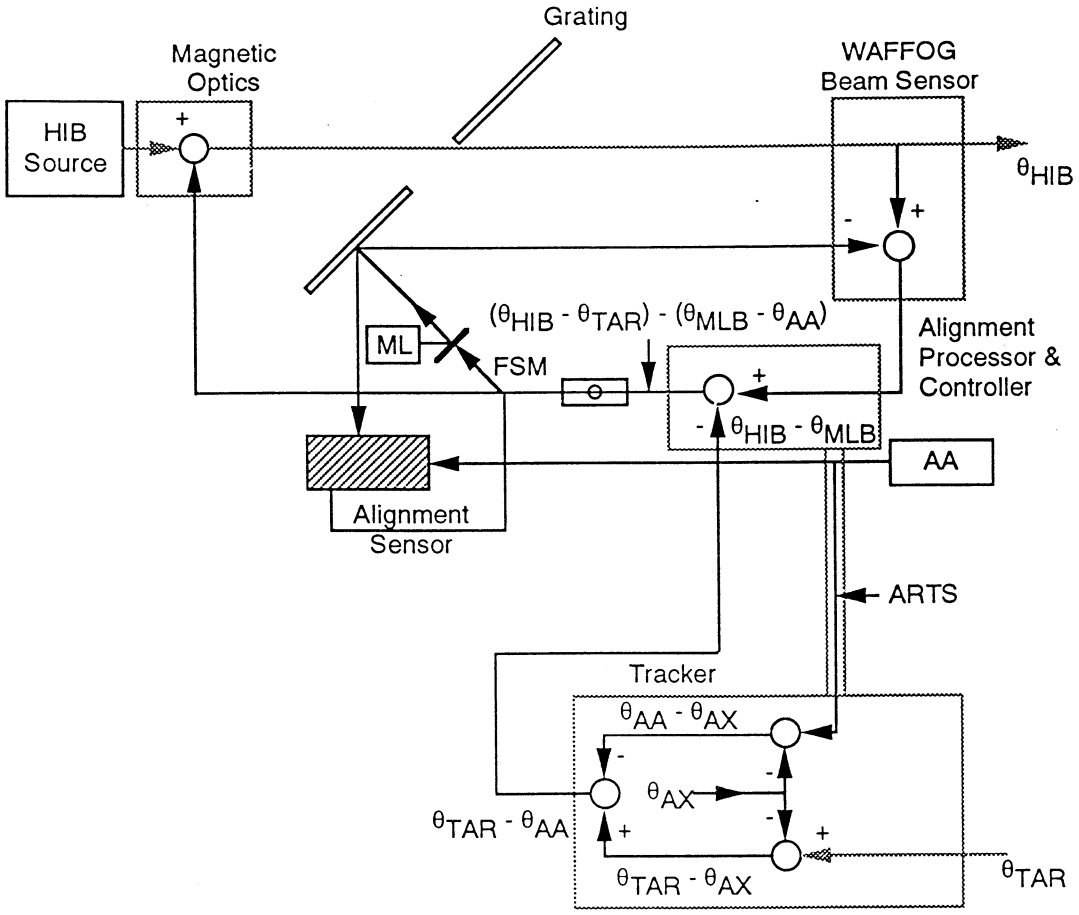

ARTS - Alignment Reference Transport System

FSM - Fast Steer Mirror

HIB - Heavy Ion Beam

MLB - Measurement Laser Beam

WAFFOG - Wire And Fluorescent Fiber Optical Grid

Fig. 4.17. A method to reference the tracker and beam for a HIB driver.

Table 4.8. Key Architectural Factors

Component	Issues/Concerns
Beam Sensor	Alignment Bandwidth Accuracy
	Large Angular Range
	Temporal Resolution / Processing Time
Magnetic Optics	Control Bandwidth
	Intrapulse Control
	Steering Range
	Structural Dynamic Input
	Induced Aberrations

In this architecture, the basic reference can be considered to be alignment beam generated by the box labeled AA. This Reference Alignment Beam (RAB) is injected into the Alignment Sensor and into the Tracker via an Alignment Reference Transfer System (ARTS). The ARTS injects the RAB into the tracker by displacing it while keeping parallel to the original direction. The tracker also detects radiation (either thermal emissions, reflected ambient light, or from an illuminator) from the target. Since both the RAB position and the target position are measured with respect to the optical axis of the tracker block in Fig. 4.17, these measurements relative to the optical axis are processed to yield the target position relative to the alignment beam. Before considering how we use this relative measurement, we consider the relationship of the RAB to the Measurement Laser Beam (MLB).

The MLB is directed onto a fast steering mirror, which directs the MLB onto a diffraction grating. This grating directs diffracted beams into the particle beam path and onto the Alignment Sensor. These diffracted orders beam a definite angular relationship to each other so that by controlling one, the other is also controlled. The order that is diffracted into the Alignment Sensor is the order that is measured and directly controlled.

The order that is diffracted into the Alignment Sensor is measured with respect to the RAB. This difference signal is the error signal which drives the servo loop which includes the fast steering mirror. By driving this error to zero, the MLB is aligned to the RAB. Actually, this diffracted order of the MLB is driven to specific direction with respect to the RAB. For now let us select 90 degrees as the relative angle. Let us also select 90 degrees as the relative angle between this diffracted order and the diffracted order that is injected into the particle beam path. Thus, the beam injected into the particle beam path and the RAB are now parallel. Hereafter, we will call the diffracted order injected into the particle beam path the MLB.

The MLB is now injected into the Beam Sensor which measures the position of the particle beam relative to the MLB. This relative measurement then goes to a processor which subtracts the signal from the track processor. This difference signal, whose terms are grouped for clarity, is:

$$\Delta\theta = (\theta_{HIB} - \theta_{TAR}) - (\theta_{MLB} - \theta_{AA})$$

Remembering that the MLB has been aligned to the RAB, the difference signal is ideally given by

$$\Delta\theta = (\theta_{HIB} - \theta_{TAR})$$

This signal drives the beam steering loop which nulls this error signal. Thus, without needing to accurately reference the beam sensor itself to the tracker reference, the HIB is directed to the target.

4.2.7 Injection, Tracking, and Pointing Errors

To quantify the sensing and control requirements, one can separate the HIB line errors (deviations of the beam from the desired direction) into divergence and pointing components. That is, the variance of the driver line errors is given by

$$\sigma^2_{HIB} = \sigma^2_{DIVERGENCE} + \sigma^2_{POINT}$$

where

$$\sigma^2_{DIVERGENCE} = \sigma^2_E + \sigma^2_J + \sigma^2_C + \sigma^2_S + \sigma^2_M$$

and

$$\sigma^2_{POINT} = \sigma^2_{BS} + \sigma^2_T + \sigma^2_B + \sigma^2_{AA} + \sigma^2_{PA}$$

Both components contribute to the overall beam divergence as averages over the entire ensemble of engagements.

The principal contributors to the divergence and pointing errors are given in Tables 4.9 and 4.10, respectively. The contributions to the pointing error (as defined here) consist of the error inherent in the output beam sensing system and the tracking and pointing system errors. The beam jitter due to tracker errors is also a function of the control loop servo characteristics. In general, this beam jitter component can be written as follows:

$$\sigma^2_J = G(F_{bw}) \cdot \sigma^2_{tr}$$

where G(F) is a function of the servo characteristics, F_{bw} is the control bandwidth, and σ^2_{tr} is the variance of the single-look tracker error.

Table 4.9. Principal Contributions to Beam Divergence

Component			Influenced By
σ_E	=	Transverse Emittance	Output Beam Radius
σ_J	=	Mechanical Jitter	Platform Stability
σ_C	=	Chromatic Aberration	Output Lens Radius, Drift Length
σ_S	=	Spherical Aberration	Output Lens Radius, Drift Length
σ_M	=	Steering Magnet Jitter	Beam Steering Dynamic Range

Table 4.10. Principal Contributions to Pointing Errors

Component			Influenced By
σ_{BS}	=	Beam Steering	Beam Sensing Technique
σ_T	=	Track Loop Jitter	Track Sensor, Algorithm, Servo Loop
σ_B	=	Boresight Error	Transfer of Beam Sensor Info to ATP/FC
σ_{AA}	=	Auto-Alignment Errors	Alignment Sensors and Servo Loops
σ_{PA}	=	Point Ahead Errors	Tracker, Estimation Algorithms

4.2.8 Summary

Target systems for target injection, target tracking, and beam pointing all require significant development work. Fortunately, many of the required elements have been demonstrated by directed energy weapon research programs. We have presented a conceptual design for an integrated injection, tracking, and pointing system using existing technology which should be able to meet all the requirements of an IFE reactor after a significant design development effort.

4.3 TARGET HEATING DURING INJECTION

The targets contain cryogenic fuel, which must not liquify or vaporize prior to implosion. The targets also have very precise dimensions in their non-fuel shells, which must be maintained prior to irradiation by the driver beams. The required vapor pressure inside the central void of the target is not known, but that pressure is a strong function of the fuel temperature. The purpose of this section is to assess the effects of heating due to radiation from the target chamber walls and due to convective heat transfer from the target chamber gas.

4.3.1 Target Conditions

Target designs and heat loads determine the temperatures in the target prior to irradiation by the driver beams. The target designs considered here are representative of future reactor scale targets. Other designs (e.g., different materials or shell thicknesses) may lead to different conclusions. Because there is some uncertainty in the heating rates on the target surfaces, we performed calculations over a range of heat loads.

4.3.1.1 Target Designs

There are two target designs considered in this study: one for direct drive with laser beams (i.e., SOMBRERO) and one for the heavy ion beam driver (i.e., Osiris). Both designs include a low conductivity plastic shell around the cryogenic deuterium-tritium (DT). This shell slows the diffusion of heat from the outside surface of the targets to the cryogenic fuel.

The SOMBRERO target was taken from work performed at the University of Rochester.[4.19] The DT fuel is frozen onto the inside surface of the hollow spherical plastic shell. This frozen DT layer must remain highly uniform until it implodes. The cavity that remains in the center of the DT shell is filled with a very low density DT vapor. The temperature of the fuel must remain low enough that the DT does not melt and distort or that the too much DT evaporates and fills the inner cavity. The fuel temperature must certainly remain below the triple point of DT, which is 21 K. With no better information available, we assume 21 K is the temperature limit for the fuel.

We have used the heavy ion target design of Bangerter and others,[4.20] even though this is probably not correct for an indirect-drive target. One difference between the target design used here and that used in other sections of this report is the choice of material for the outer shell. For the target heating calculations we used a lead outer shell. Later in the study, it was determined that tantalum would be a better material for use with Osiris since it is soluble in Flibe. The thermal diffusivities of the two materials at room temperature are very close (0.218 s for tantalum and 0.235 s for lead), so heat transfer will be similar. We assumed that the same

constraints hold for the maximum temperature reached in the DT fuel in the Osiris as in the SOMBRERO target.

4.3.1.2 Heat Loads

We have considered two types of heat loads on the surfaces of both target types; convective heat transfer from the chamber gas to the target and radiative heat transfer from the target chamber walls.

As the target moves through the target chamber gas, heat is absorbed by the surface of the target at a rate that is a function of the target velocity, V, the mass density of the cavity gas, ρ, the target diameter, D, the viscosity of the chamber gas, μ, the thermal conductivity of the gas, k_f, and the temperature difference between the gas and the surface of the target, ΔT. The surface conductance for a spherical target with a subsonic velocity is

$$\bar{h}_c = \frac{0.37\, R_e^{0.6}\, k_f}{D}$$

where R_e is the Reynolds number of the cavity gas,

$$R_e = \frac{V\, D\, \rho}{\mu}$$

The surface heating rate in power per unit area is

$$\ddot{q} = \bar{h}_c\, \Delta T$$

The radiation heat load is assumed to be the black body radiation power produced by a body at the wall temperature T_w,

$$\ddot{q}_r = \sigma_s\, T_w^4$$

where σ_s is the Stefan-Boltzmann constant.

The gas conditions are very different in the two reactor designs. The target velocity for both reactor concepts are in the range of 100 to 200 m/s. The approximate heat loads for the two target are given in Table 4.11. The viscosity and thermal conductivity of the xenon gas are extrapolated from lower temperature data. The viscosity and thermal conductivity for Flibe vapor are calculated directly from the kinetic theory of gases and are not based on experimental measurements. The gas densities are only approximate. For SOMBRERO, the density may be a factor of two lower. In any case, the heat fluxes to both targets are dominated by radiation. The

SOMBRERO conditions are worse by an order of magnitude because of the higher temperature of the first wall.

Table 4.11. Target Heat Loads

	SOMBRERO	Osiris
Wall Temperature (K)	1758	923
Gas Temperature (K)	1758	923
Gas Density (cm^{-3})	3.55×10^{16}	3.55×10^{12}
Gas Species	Xenon	Flibe
Gas Mass Density ($\mu g/cm^3$)	7.79	8.38×10^{-5}
Target Speed (m/s)	200	150
Target Diameter (cm)	0.6	0.6
Gas Viscosity (μPoise)	900	0.022
Reynolds Number	107	29.2
Gas Conductivity (W/cm-K)	2.45×10^{-4}	0.13×10^{-7}
Surface Conductance (W/cm^2-K)	2.42×10^{-3}	5.85×10^{-8}
Conductive Heat Load (W/cm^2)	4.2	6×10^{-5}
Radiative Heat Load (W/cm^2)	54.2	4.12
Total Heat Load (W/cm^2)	58.4	4.12

4.3.2 PELLET Computer Code

The PELLET computer code was developed at the University of Wisconsin to simulate the heating of ICF targets by the target chamber environment. PELLET uses information on the target geometry and the surface heat load to calculate the temperature at every position in the target as a function of time. In this section we will describe the numerical method used and the thermal properties used in these calculations.

4.3.2.1 Numerical Method

PELLET is a one-dimensional finite-difference computer code. A one dimensional mesh is defined in slab geometry. Therefore, this code is accurate only for targets where the material is thin compared to its radius, which is true for all reasonable targets. Heat transfer inside the central cavity void is not considered. Heat is deposited at the outer surface only and diffuses into the target as predicted by the standard temperature diffusion equation,

$$\frac{\partial T}{\partial t} = \frac{1}{C_p}\left[\nabla \cdot \chi \Delta T + Q\right]$$

Here, C_p is the specific heat of the target material, and χ is the conductivity. Both are functions of temperature. Q is an energy source which is a function of position and time. T is the material temperature.

We have used an implicit differencing scheme[4.21] to solve the temperature diffusion equation. We have used the Crank-Nicholson method,[4.22] which is always numerically stable, to advance the time step. To achieve reasonable accuracy, we use time steps, Δt, that obey the condition,

$$\Delta t \leq \frac{(\Delta x)^2}{2\sigma}$$

Here, $\sigma = \chi/C_p$ is the thermal diffusivity, and Δx is the width of a spatial zone. This is required because χ and C_p are strong functions of temperature in the cryogenic regime. A zero heat flux boundary condition is applied at the inside edge of the innermost zone and a time-dependent heat flux equal to Q(t) is imposed at the outer edge of the outermost zone.

4.3.2.2 Thermal Properties

Temperature dependent thermal properties are used in these target heating calculations. We have used reported values for thermal properties.[4.23,4.24] For example, the thermal conductivity and specific heat for polystyrene from the first reference are shown in Figs. 4.18 and 4.19, respectively. One can clearly see the strong temperature dependence in these properties. The plastic parts of the targets present the greatest barrier to heat diffusion. We have chosen the properties of polystyrene as representative for the plastic in actual targets. Thermal conductivities for solid hydrogen are shown in Fig. 4.20. Several curves are shown, reflecting different concentrations of molecular spin state J = 1 in the diatomic hydrogen molecules. The J = 1 state hydrogen molecules are very effective in reducing heat flow because they have a larger phonon cross-section. Souers has recommended using the H_2 curve with a J = 1 concentration of 0.70 for DT.[4.23] The specific heat of DT is shown in Fig. 4.21. Temperature dependent thermal properties of lead (not shown here) were also used in the calculations.

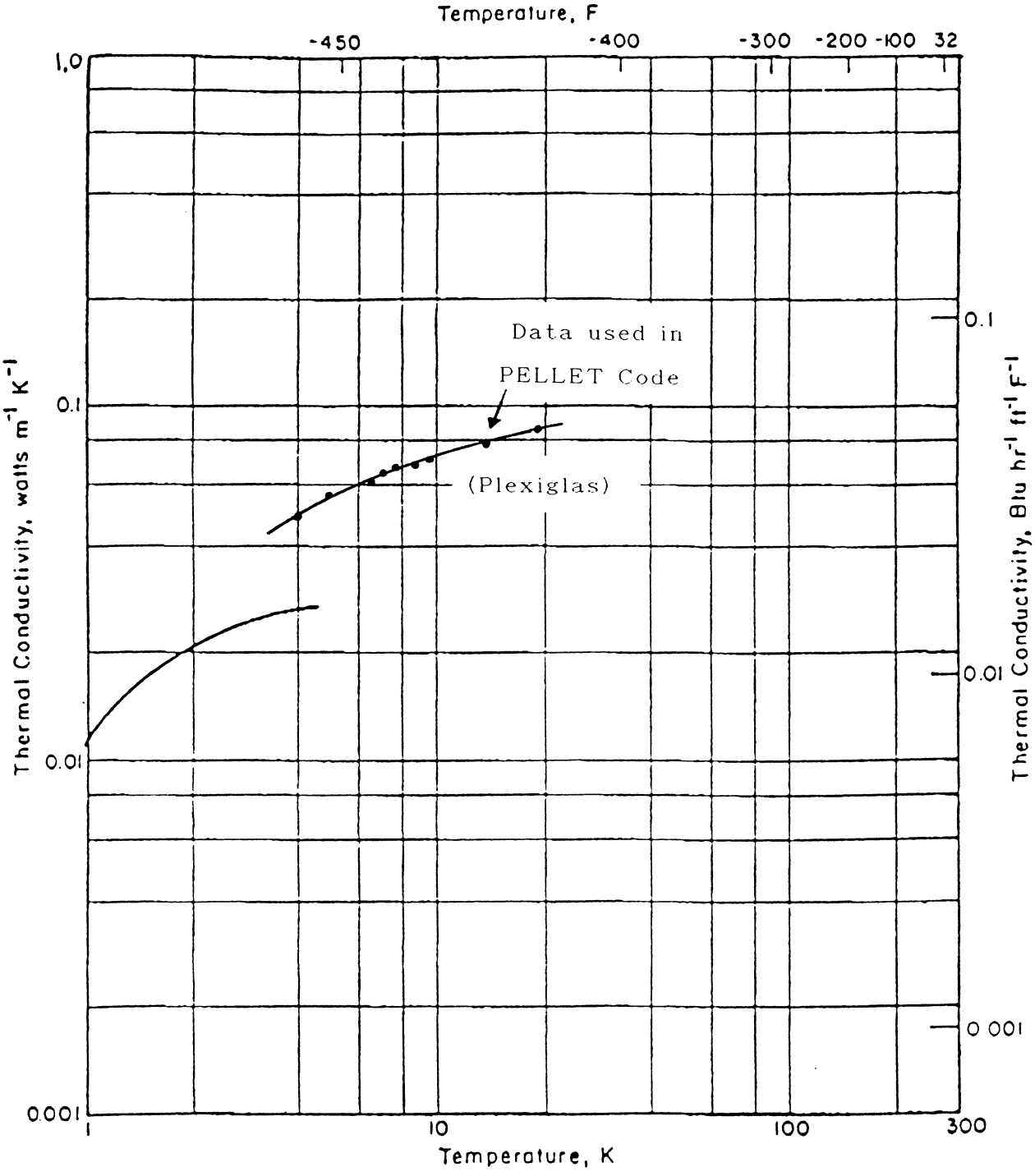

Fig. 4.18. Thermal conductivity of polystyrene.[4.23]

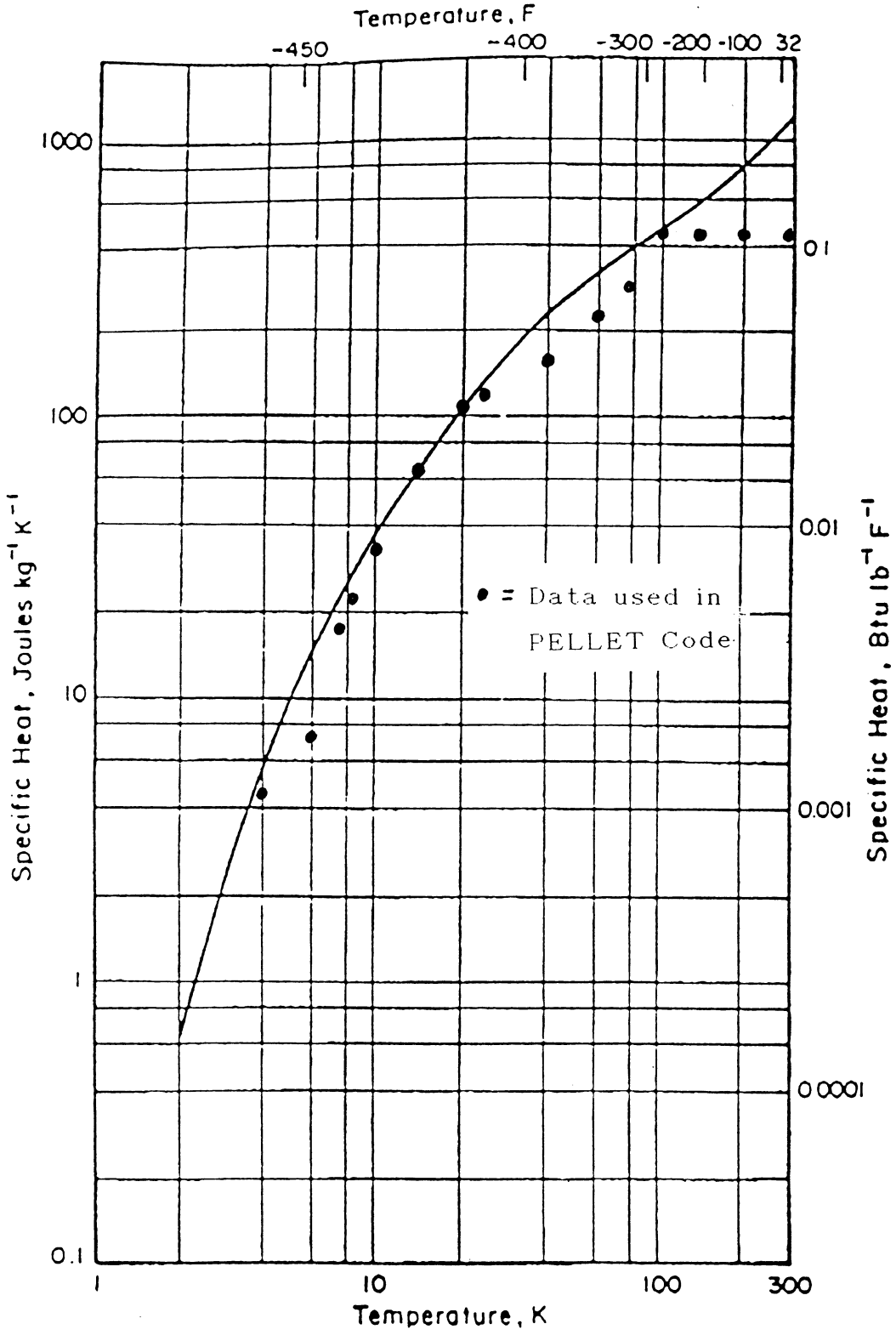

Fig. 4.19. Specific heat of polystyrene.[4.23]

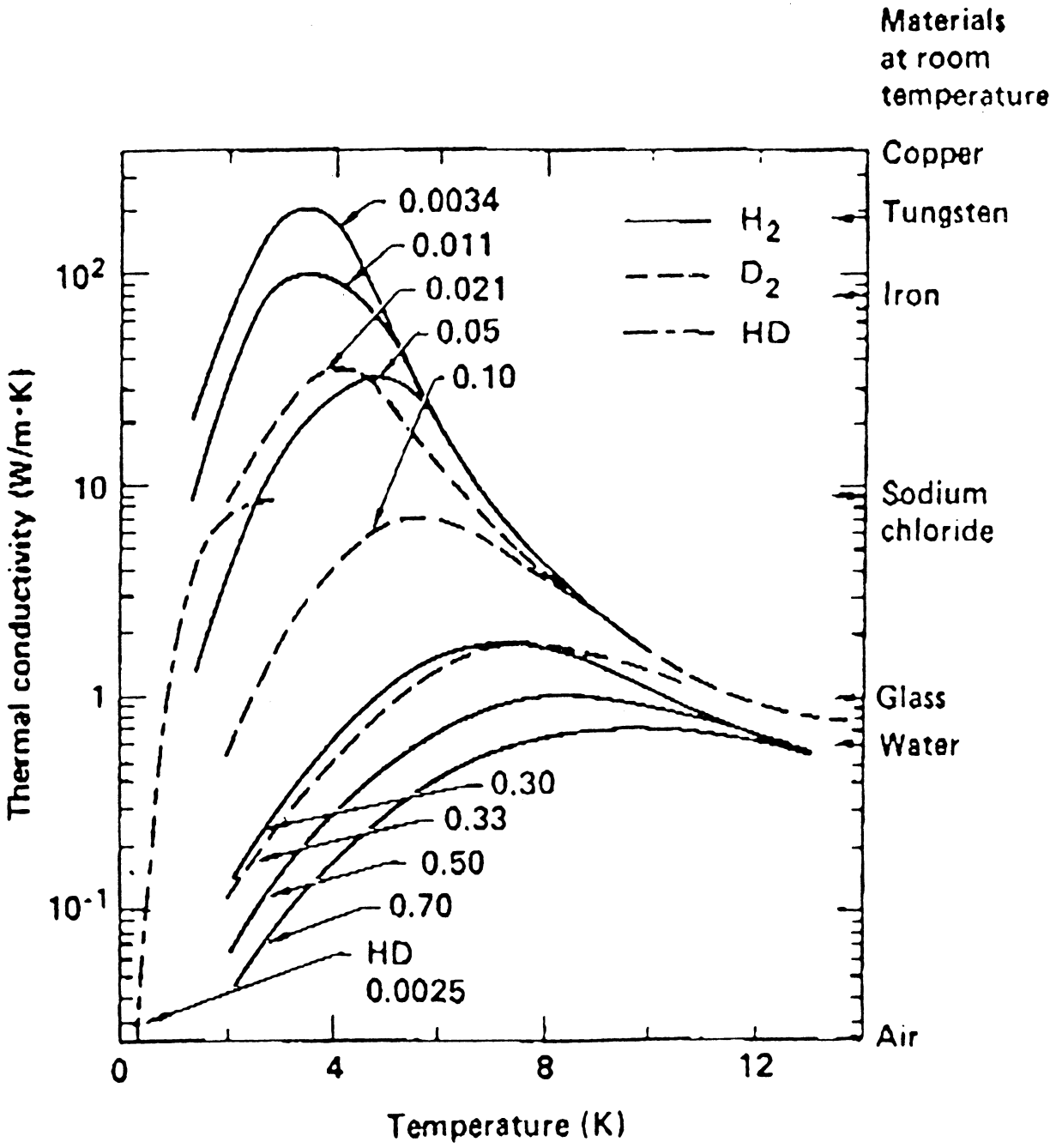

Fig. 4.20. Thermal conductivity of solid H_2, HD, and D_2 as a function of temperature for different J = 1 concentrations.[4.24]

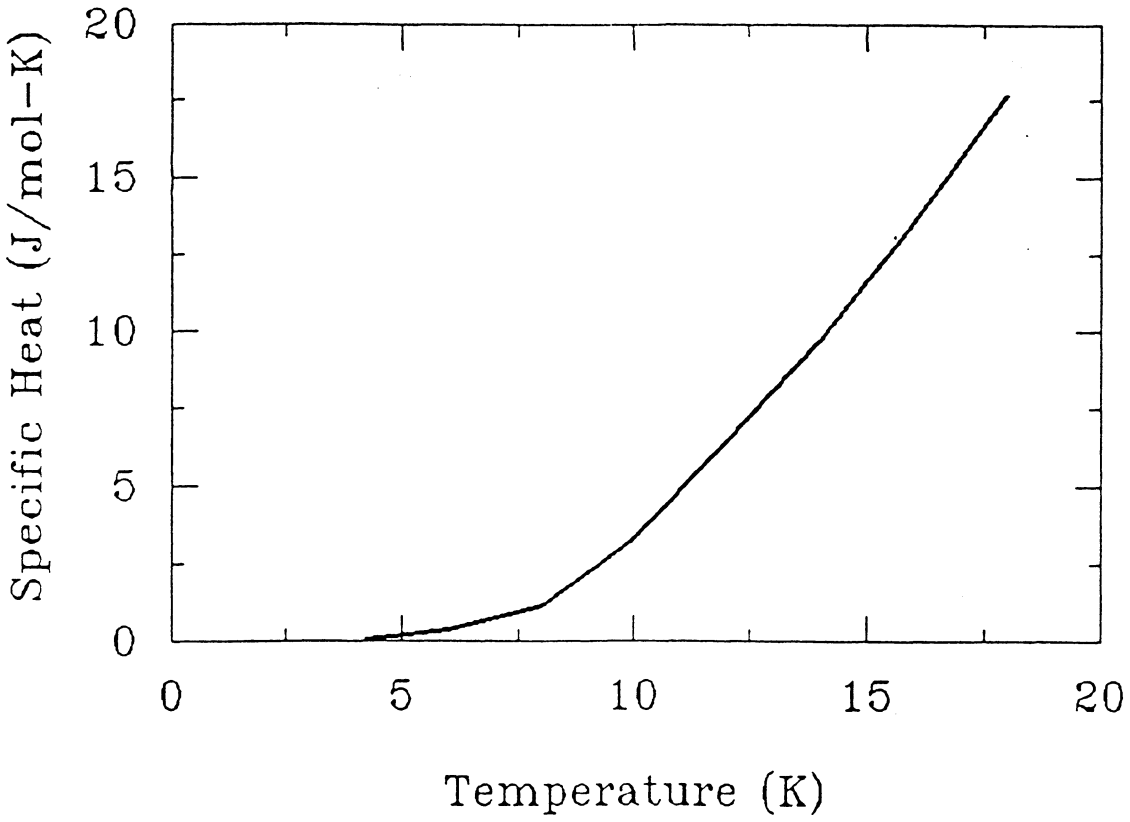

Fig. 4.21. Specific heat of DT.[4.24]

4.3.3 Target Heating Results

We have used the PELLET code to calculate the temperatures in the targets parametrically for a number of different heat loads. Estimates of the heat loads for both reactor designs are discussed in an earlier section. In all cases, we assumed that the whole target was initially at 4 K and have, therefore, assumed that β decay heating of the fuel during storage has been accommodated by appropriate cooling.

4.3.3.1 Heavy Ion Target

The results of PELLET calculations for the Osiris target design are shown in Figs. 4.22 through 4.24. Figure 4.22 shows temperature profiles in the target material at various times for the case of a heat load of 2 W/cm^2. While this is lower than the 4 W/cm^2 calculated in

Table 4.11, one sees that the steepest temperature drop occurs in the plastic shell, indicating that the plastic is the most important impediment to heating of the fuel. The lead and the DT have flat temperature profiles because they both have high thermal diffusivity. If the target must travel ~ 5 m through the chamber and is injected at a velocity of 150 m/s, ~ 33 ms will be required for the target to reach the ignition point. From Fig 4.22, one sees that for this heat load, the fuel would only reach about 7 K by this time. Figures 4.23 and 4.24 show the temperature versus time at the outer and inner edges of the fuel, respectively, for a variety of heat loads. These show that even at a heat load of 500 W/cm^2, the fuel temperatures would be well below the triple point at 33 ms.

4.3.3.2 Laser Target

The results of PELLET calculations for the SOMBRERO target design are shown in Figs. 4.25 through 4.27. Temperature profiles in the SOMBRERO target at various times are shown in Fig. 4.25 for a constant heat flux of 50 W/cm^2 (slightly less than the estimated 58 W/cm^2). Note the substantial temperature drop across the plastic shell. Once again, the thermal diffusivity of the plastic provides thermal protection for the fuel. The temperatures at the outer and inner edges of the DT fuel are plotted as a function of time in Figs. 4.26 and 4.27, respectively, for a variety of heat loads. If the targets must travel 6.5 m through the chamber before it is imploded and if the targets travel at 200 m/s, the target surface is heated for 33 ms. From these two figures, one can see that for a heat load of 58 W/cm^2 the temperature at the outer and inner edges of the fuel at 33 ms is 13 K and 10 K, respectively. This is still well below the DT triple point. The 200 m/s target velocity was assumed before the final target injector design point of 151 m/s was chosen (see Section 4.2). If the targets are only accelerated to 151 m/s, the heat load, which is dominated by radiation, will not be reduced much, but the time that the target experiences the heat load would increase to 43 ms. Extrapolating the curves to this time, we estimate the outer and inner fuel temperatures to be ~ 17 K and 11 K, respectively. This is still below the triple-point, but there is only a 4 K margin for error.

While the fuel remains below the triple point, the outer surface temperature of the polystyrene capsule is ~ 700 K (see Fig. 4.25). Since this is well above the melting point of polystyrene, it will be necessary to protect the capsule during transit through the chamber. One possibility is to keep the capsule in the sabot for most of the transit time. Another option is to freeze a thin layer of inert gas (e.g., Xenon) on the outer surface of the capsule. The frozen gas would act as a sacrificial heat sink and evaporate as the capsule transits the chamber. This could reduce the time that the bare capsule is exposed to the hot chamber to a few ms. Clearly, this is an area that requires further investigation.

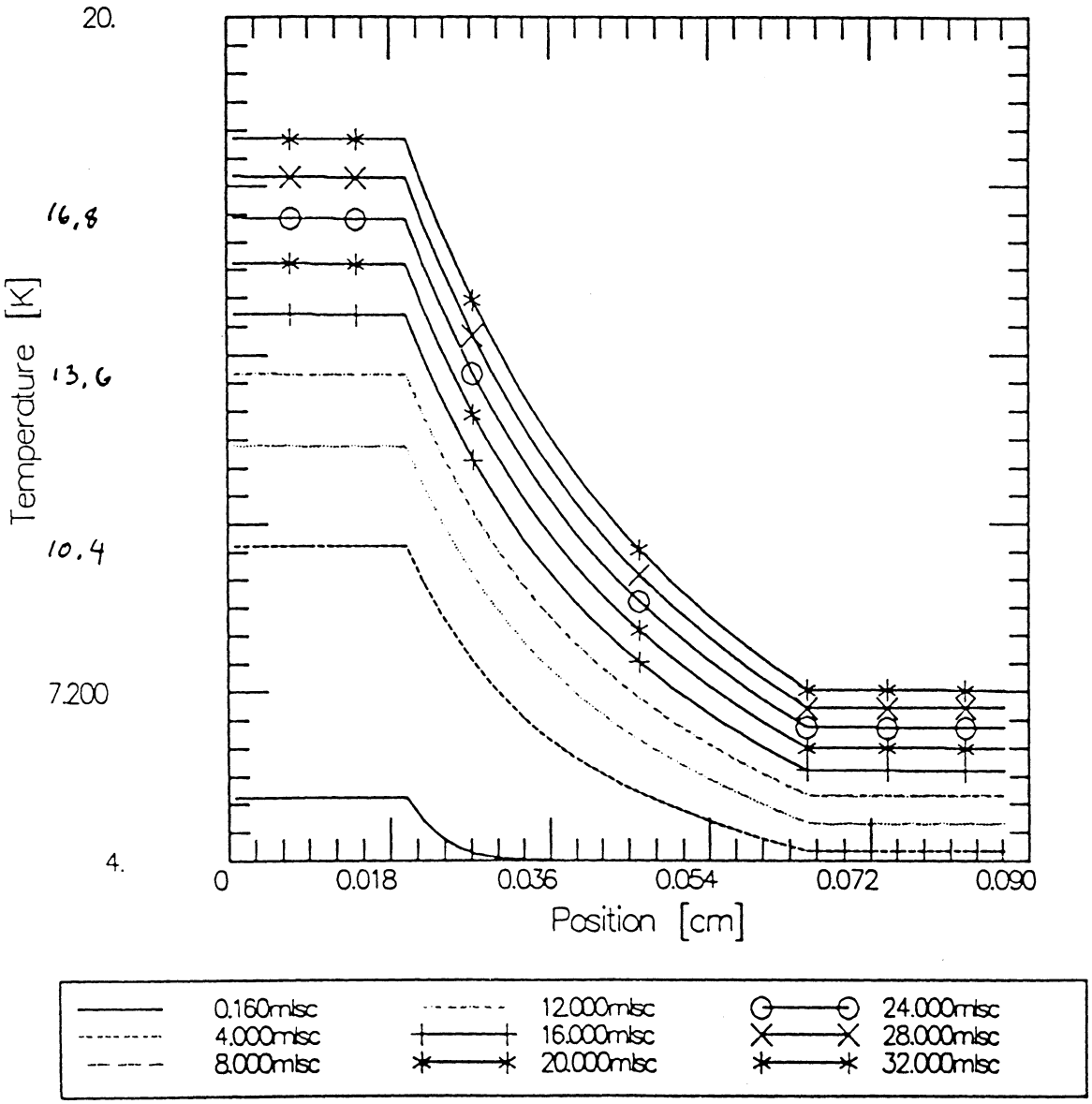

Fig. 4.22. Target material temperatures versus distance from outer edge of target at several times for the Osiris target. The surface heat flux is 2 W/cm^2.

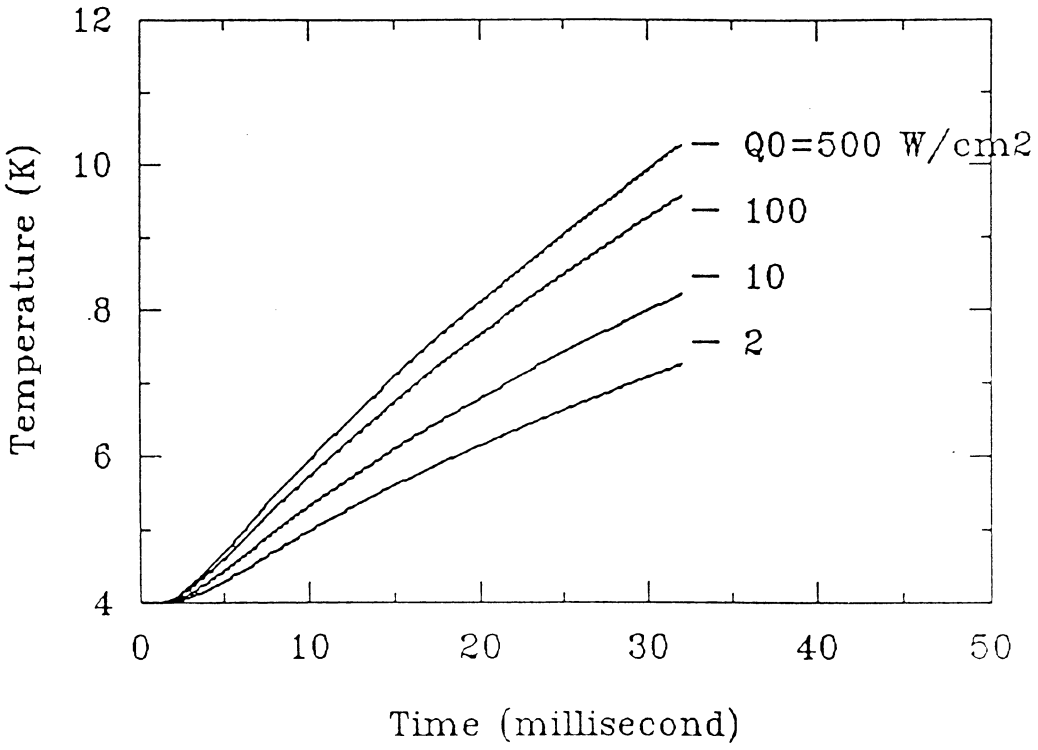

Fig. 4.23. **Temperature at the outside edge of the fuel in the Osiris target versus time for several surface heat fluxes.**

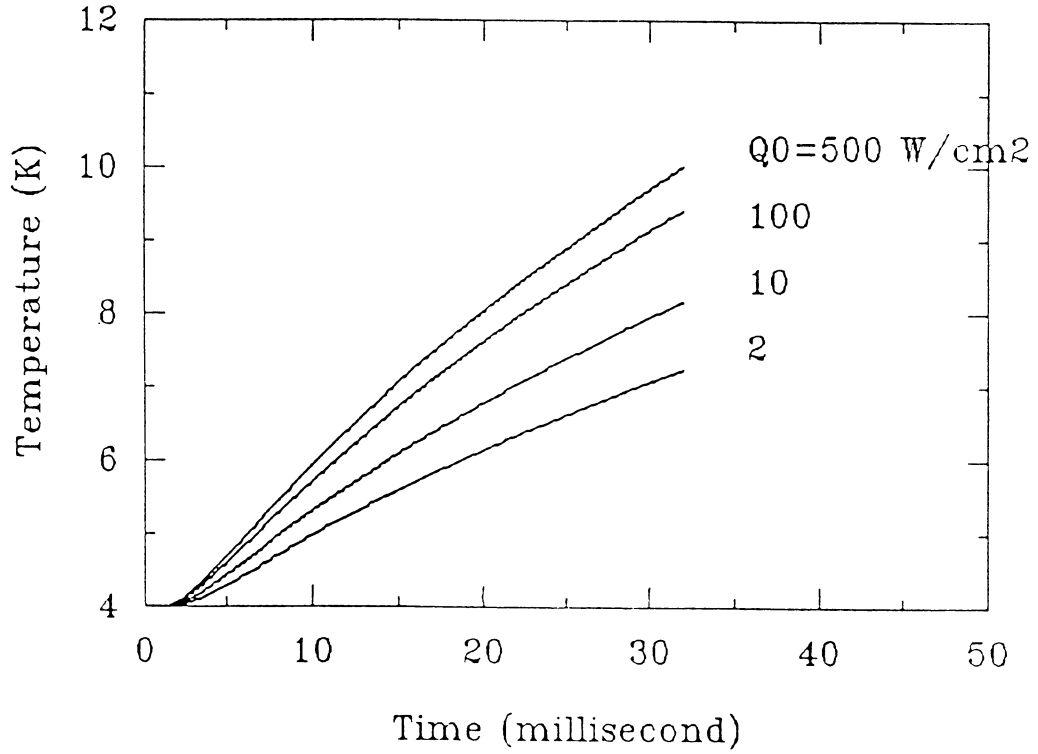

Fig. 4.24. **Temperature at the inside edge of the fuel in the Osiris target versus time for several surface heat fluxes.**

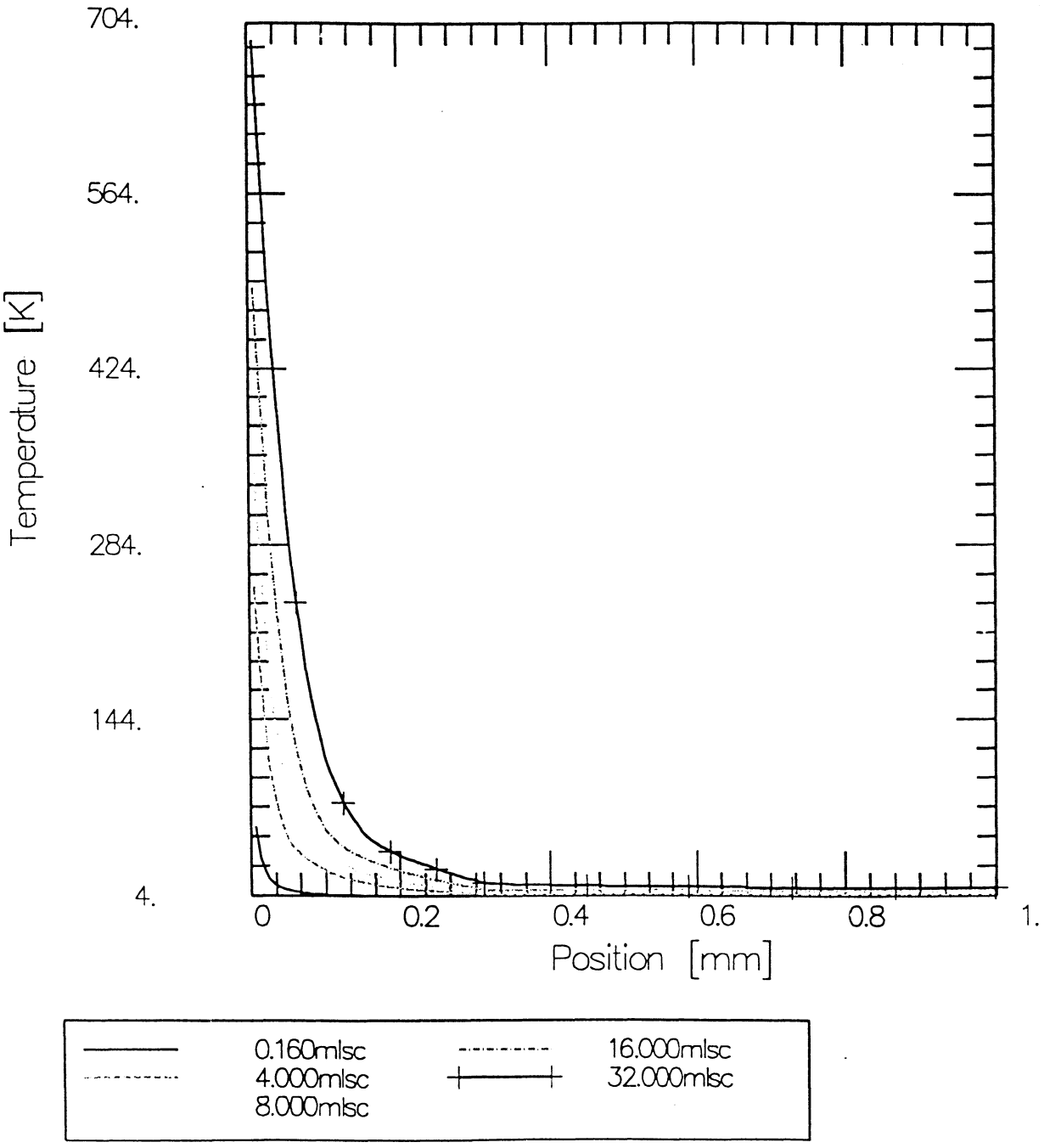

Fig. 4.25. Target material temperatures versus distance from outer edge of target at several times for the SOMBRERO target. The surface heat flux is 50 W/cm^2.

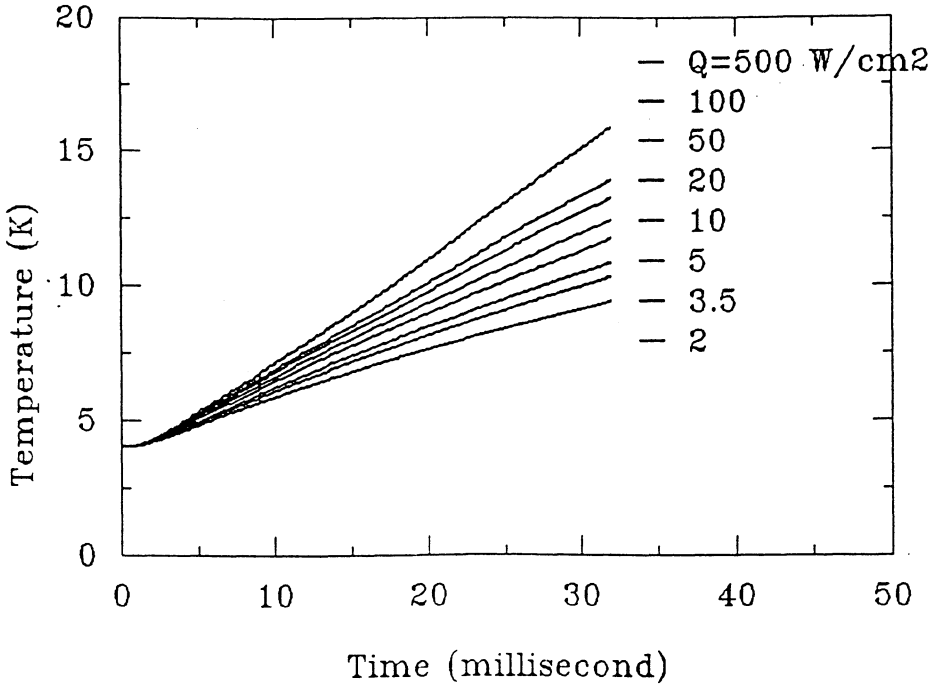

Fig. 4.26. Temperature at the outside edge of the fuel in the SOMBRERO target versus time for several surface heat fluxes.

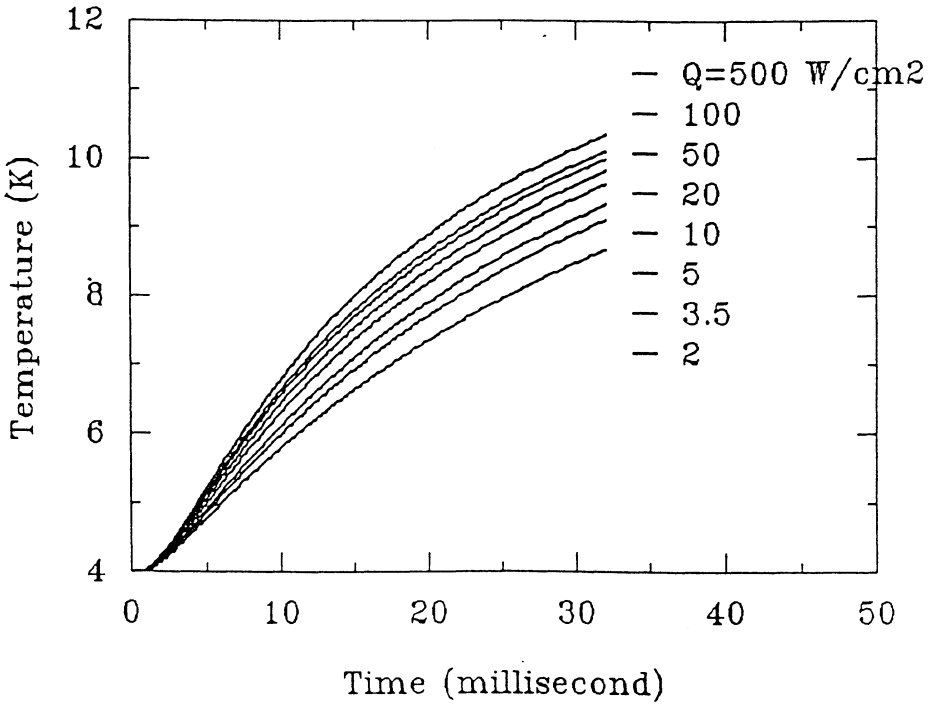

Fig. 4.27. Temperature at the inside edge of the fuel in the SOMBRERO target versus time for several surface heat fluxes.

4.4 REFERENCES FOR CHAPTER 4

4.1 C.D. Hendricks, "Production of Thin Wall Small Diameter Polystyrene Shells," American Association for Aerosol Research, Annual Meeting, Seattle, WA, Paper 15A (Sept. 14-17, 1987).

4.2 C.D. Hendricks, "Hollow Glass Sphere Production," Lawrence Livermore National Laboratory Laser Program Annual Report, UCRL-50021-76, 4 (1976).

4.3 U. Kubo et al., ILE Osaka University, ILE-APZ-79, 177 (1979).

4.4 C.D. Hendricks, C.A. Foster, "Hollow Hydrogen Shells for Laser Fusion Targets," American Physics Society Series II, **19,** 927 (Oct. 1974).

4.5 C.D. Hendricks, C.A. Foster, "Hollow Hydrogen Shells for Laser Fusion Targets," *Applied Physics Letters*, **26**, 580 (May 15, 1975).

4.6 J.F. Miller, "A New Method for Producing Cryogenic Laser Fusion Targets," *Advancements in Cryogenic Engineering*, **23** (1978).

4.7 C.D. Hendricks, et al., "A New Technique for Fabricating Cryogenic Laser Fusion Targets Using Cold-gas Jets," *Applied Physics Letters*, **34,** 282 (Feb. 15, 1979).

4.8 J.D. Simpson, J.K. Hoffer, and L.R. Foreman, "Beta-Layering of Solid Deuterium-Tritium in a Spherical Polycarbonate Shell," *Fusion Technology*, **21**, 330 (1992).

4.9 H. Rieger et al., "Cryogenic Laser Target Fabrication System Directly Operable Inside a Target Chamber," Lawrence Livermore National Laboratory, UCRL-83079 (1979).

4.10 S.L. Milora, "Review of Pellet Fueling," *Journal of Fusion Energy*, **1**, 15 (1981).

4.11 S.L. Milora and C.A. Foster, *Rev. Sci. Instrum.*, **50**, 482 (1979).

4.12 C.A. Foster and S.L. Milora,"ORNL Pellet Acceleration Program," *Proc. Fusion Fueling Workshop*, Princeton N.J., DOE CONF-771129, 117 (1978).

4.13 R. Kreutz, "Pellet Delivery for the Conceptual Inertial Fusion Reactor HIBALL," *Fusion Technol.*, **8**, 2708 (Nov. 1985).

4.14 J. Woodworth, Lawrence Livermore National Laboratory, Personal Communication (Jan. 1991).

4.15 P. Kevin, et al., "Relay Mirror Experiment / Wideband Angular Vibration Experiment," Phillips Laboratory, PL-TR-91-1088, **1**, (1992).

4.16 "Airborne Laser Laboratory," Kirkland AFB, AFWL-TR-8C, Vol. I-IV (1988).

4.17 M.J. Monlser, "Laser Fusion: An Assessment of Pellet Injection, Tracking and Beam Pointing," *Proc. 3rd Topical Meetinfg on the Technology of Controlled Nuclear Fusion*, Santa Fe, New Mexico, (May 1978).

4.18 M.R. Lee and J. Sesak, "Control System Requirement Extracted from the Stanlab Hardware Specification, EM-238," Lockheed Missiles and Space co., F185873 (1988).

4.19 "The University of Rochester Laboratory for Laser Energetics, Annual Report, 1 October 1984 - 30 September 1985," DOE/DP/4020-05, 126 (Jan. 1986).

4.20 R.O. Bangerter, J. W.-K. Mark, and G. Magelssen, "Simple Target Models for Ion Beam Fusion Studies," LLNL Report, UCID-20578 (1985).

4.21 R.D. Richtmeyer and K.W. Morton, "Difference Methods for Initial-Value Problems," Interscience Publishers, New York, (1967).

4.22 J. Crank and P. Nicholson, "A Practical Method for Numerical Integration of Solutions of Partial Differential Equations of Heat-Conduction Type," *Proc. Cambridge Philos. Soc.*, **43**, 50 (1947).

4.23 "Handbook on Materials for Superconducting Machinery," Metals and Ceramics Information Center, Battelle Columbus Laboratories Report (1977).

4.24 P.C. Souers, "Hydrogen Properties for Fusion Energy," Univ. of California Press, Berkeley, CA (1986).

Chapter 5

Environmental and Safety Assessment

CONTENTS

5.1 INTRODUCTION 5-1
5.2 SAFETY DESIGN GOALS 5-1
5.3 OFF-SITE DOSE DEFINITIONS 5-2
5.4 CALCULATIONAL PROCEDURE 5-3
5.5 SOMBRERO SAFETY ANALYSIS 5-4
5.5.1 Activation Analysis 5-5
5.5.2 Maintenance 5-10
5.5.3 Radwaste Classification 5-12
5.5.4 Routine Atmospheric Effluents 5-13
5.5.5 Accident Analysis 5-15
5.6 OSIRIS SAFETY ANALYSIS 5-19
5.6.1 Activation Analysis 5-19
5.6.2 Maintenance 5-23
5.6.3 Radwaste Classification 5-24
5.6.4 Routine Atmospheric Effluents 5-25
5.6.5 Accident Analysis 5-26
5.7 TARGET FACTORY ANALYSIS 5-32
5.8 FUEL REPROCESSING FACILITIES 5-33
5.9 NUCLEAR GRADE COMPONENTS 5-33
5.10 COMPARISON OF SOMBRERO AND OSIRIS 5-35
5.11 REFERENCES FOR CHAPTER 5 5-36

5.0 ENVIRONMENTAL AND SAFETY ASSESSMENT

5.1 INTRODUCTION

A strong emphasis has been given to the environment and safety issues in both the SOMBRERO and Osiris reactor designs. Carbon/carbon composite has been used as the chamber material to avoid a high level of induced radioactivity in both reactor structures. Similarly, the use of Li_2O in SOMBRERO and Flibe in Osiris as coolant and breeder materials eliminates the hazard posed by the energy-producing chemical reactions usually associated with the use of lithium and, hence, reduces the risk of mobilizing the radioactive inventory present in both reactors. The methodology used in this analysis does not depend on the probability of accident-initiating scenarios; we have adopted the principle of considering the worst possible accident scenario. To evaluate the possible radiological hazard to the public, we used a two-step approach in calculating the possible off-site dose. The first step in our approach is the identification of the sources and locations of the radioactive materials inside the reactor building. However, since the existence of radioactivity does not in itself represent a safety hazard, the second step in our approach was to consider a set of pessimistic, but rather credible, accident scenarios for mobilizing and releasing the radioactive material.

A detailed activation analysis was performed in order to calculate all possible radioactive inventories for each of the two reactor designs. Results of the radioactivity calculations are used to evaluate the following:

1. The biological dose rate at different locations inside the reactor building following shutdown to assess the feasibility of hands-on maintenance
2. The radwaste classification for each region of the reactor
3. The maximum public dose from routine operational effluents
4. The off-site doses from accidental release of the radioactive inventories present in the reactor building, target factory, and fuel reprocessing facility.

5.2 SAFETY DESIGN GOALS

The main safety goals pursued for both the SOMBRERO and Osiris reactor designs are:

1. Limiting the need for remote maintenance and allowing for hands-on maintenance by reducing the biological dose rate following shutdown below 2.5 mrem/hr by increasing the biological shield where it is possible.

2. Disposing the reactor structure and coolant as either Class A or Class C low-level wastes as regulated by the Nuclear Regulatory Commission's (NRC) 10CFR61 guide lines.
3. Limiting the public dose to the maximally exposed individual (MEI) from routine operational effluents to less than 5 mrem/yr.
4. Limiting the whole-body (WB) early dose during a conservative accident scenario to 25 rem, which was recommended for this study by the study guidelines. The low off-site dose will allow for the avoidance of early fatalities in case of an accidental release of radioactivity.
5. Eliminating the need for the use of N-Stamp nuclear grade components.

5.3 OFF-SITE DOSE DEFINITIONS

Off-site dose is used to predict the degree of radiological hazard to the public posed by any routine or accidental release of radioactivity from the reactor. However, the health effects to the various human organs are dependent on both the length and method of exposure. While dose from external exposure (cloudshine and groundshine) is only limited to the length of the exposure, decay of the radionuclides inside the irradiated body (from inhalation and ingestion) leads to a continuous internal exposure. In this chapter we used the following of dose definitions:

Prompt Dose at 1 km: This is the dose delivered to a particular organ at 1 km from the release. It includes the dose from cloudshine during plume passage, the dose from 7 days of groundshine, and the dose commitment over an organ-dependent, critical acute time period from inhalation during plume passage.

WB: Whole body, t_{acute} = 2 days
BM: Bone marrow, t_{acute} = 7 days
Lung: Lung, tacute = 1 year
LLI: Lower large intestine, t_{acute} = 7 days

WB Early Dose: The whole body early dose is the dose from initial exposure: cloudshine during plume passage, 7 days of groundshine, plus the 50-year dose commitment from radioactivity inhaled during plume passage.

WB Chronic Dose at 1 and 10 km: These are the whole body doses at 1 and 10 km from the release due to both initial and chronic (50-year) exposures.

Inh + grd: Chronic exposure considers the 50-year groundshine exposure plus the 50-year dose commitment from inhaled resuspended radioactivity.

Ing: Chronic exposure considers the ingestion pathway only.

Total: Chronic exposure considers all three pathways: groundshine, resuspension, and ingestion.

Cancers: This is the total number of cancers in a 50-mile radius from initial and chronic exposure.

Sum Organs: The number of cancers where the body is treated as a sum of individual organs and calculations are based on organ-specific dose factors and dose responses.

WB: The number of cancers where the body is treated as a single organ and the whole body dose conversion factors and dose response are used.

Population Dose WB (Man-Rem): This is the total whole body man-rem due to both initial exposure plus an 80-year chronic exposure to the whole body.

5.4 CALCULATIONAL PROCEDURE

Neutron transport calculations have been performed using the one-dimensional discrete ordinates neutron transport code ONEDANT.[5.1] The analysis uses a P_3 approximation for the scattering cross sections and S_8 angular quadrature set. The problem has been modeled in spherical geometry with a point source at the center of the chamber. The source emits neutrons and gamma photons with energy spectra determined from target neutronics calculations for a generic single shell target. The neutron flux obtained from the neutron transport calculations has been used in the activation calculations. The calculations have been performed using the computer code DKR-ICF[5.2] with the ACTL[5.3] activation cross section library. The DKR-ICF code allows for accurate modeling of the pulsing schedule. The pulse sequence used in the activation calculations is shown in Fig. 5.1. In order to achieve 75% availability, the reactor has been assumed to shutdown for a period of 5 days following every 25 days of operation for routine maintenance and for the last 40 days of each calendar year for an annual extended maintenance. The radioactivity generated in the reactor chamber and shield has been calculated for the 40-year reactor life-time.

The decay gamma source produced by the DKR-ICF code is used with the adjoint neutron flux to calculate the biological dose rate after shutdown using the DOSE[5.2] code. The dose rate calculations have been performed at different locations inside the reactor building. The activation results have also been utilized in the radwaste classification and the off-site dose calculations

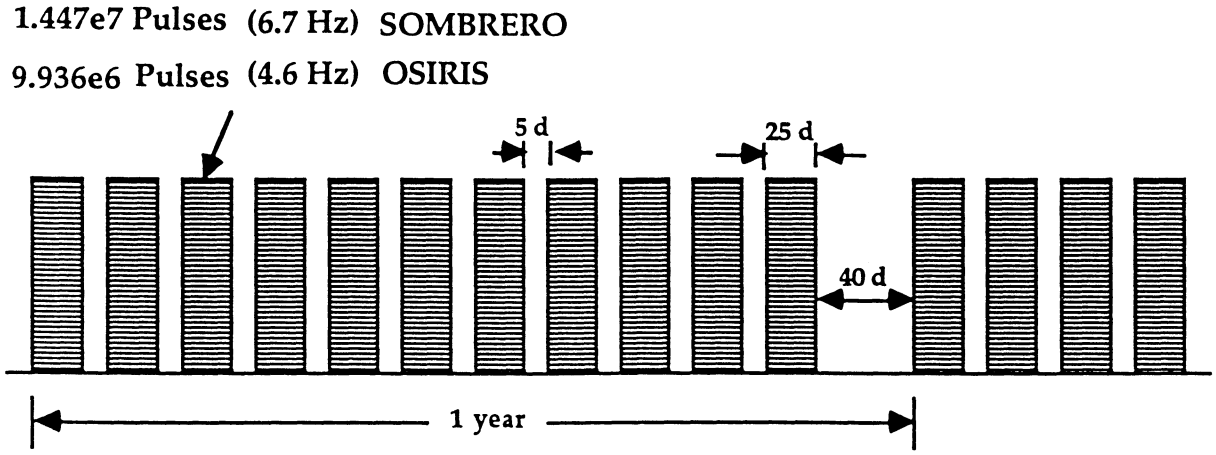

Fig. 5.1. Pulse sequence used in activation calculations.

performed by the FUSCRAC3 code.[5.4] The off-site doses are produced by the accidental release of the radioactive inventory from the reactor building assuming the worst case weather conditions. Finally, the EPA code AIRDOS-PC[5.5] has been used to estimate the off-site dose due to the routine release of tritium.

5.5 SOMBRERO SAFETY ANALYSIS

Activation and safety analysis has been performed for the chamber, shield, and Li_2O coolant of SOMBRERO. The reactor chamber is made of a low activation carbon/carbon composite and the blanket consists of a moving bed of solid Li_2O granules (90% density factor) flowing through the chamber by gravity. The particles are transported in a fluidized state by helium gas at 0.2 MPa. There are 60 laser beams in near symmetric distribution. The laser energy is 3.4 MJ, the gain is 118, and the rep-rate is 6.7 Hz. The reactor first wall is 1 cm thick and is made of 100% graphite. To maximize the tritium breeding ratio (TBR) and overall energy multiplication M_o, the blanket is divided to three different regions. The first region is 19 cm thick and consists of 52.4% Li_2O and 3% C. Each of the second and third regions is 40 cm thick. However, the second region consists of 43.2% Li_2O and 20% C while the third region is made of 27% Li_2O and 50% C. The increase in the graphite fraction in the blanket with distance from the target obviates the need for a separate reflector behind the blanket. The chamber is surrounded by a 170-cm thick shield to allow for hands-on maintenance at selected locations behind it. The steel-reinforced concrete shield is made of 70% concrete, 20% mild steel and 10% helium coolant. The radial build used in the calculations is shown in Fig. 5.2.

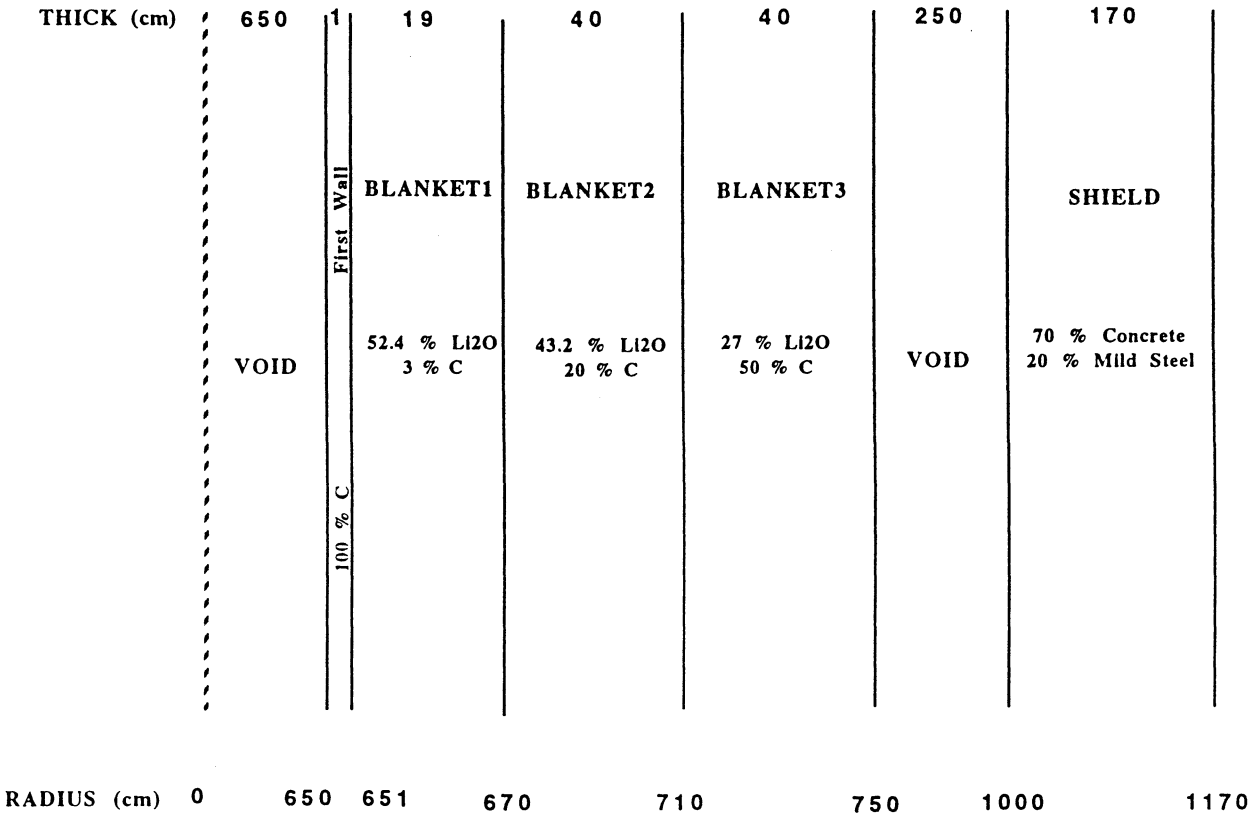

Fig. 5.2. Radial build used in activation calculations.

5.5.1 Activation Analysis

The radioactivity generated in the reactor carbon/carbon composite chamber and steel-reinforced shield was calculated for the 40-year reactor life-time with 75% availability. The elemental composition of the chamber and shield materials are shown in Table 5.1. A separate calculation was performed for the coolant. The composition of the Li_2O coolant used in this analysis is given in Table 5.2. The residence time of the Li_2O coolant in the chamber is 100 seconds. The total inventory of Li_2O takes 300 seconds to go through the reactor chamber. Therefore, the coolant activity has been calculated to allow for the fact that the Li_2O granules spend only 33% of the time exposed to neutrons in the reactor chamber. The total activity generated in the different regions of SOMBRERO as a function of time following shutdown is shown in Fig. 5.3. The total activity in the chamber at shutdown is 0.054 MCi and drops to 0.016 MCi in one day and 0.0015 MCi in one year. Most of the steel-reinforced concrete shield activity is due to

Table 5.1. Elemental Composition of the Carbon/Carbon Composite, Concrete, and Mild Steel Used in the Calculations.

Nuclide	Graphite	Concrete	Steel
	(wppm unless wt% indicated)		
H	----	0.56 wt%	----
B	2	1.04 wt%	----
C	99.999 wt%	----	200
N	----	----	70
O	----	33.8 wt%	----
F	----	0.23 wt%	----
Na	10	1.21 wt%	----
Mg	1	0.23 wt%	----
Al	4	0.64 wt%	----
Si	21	3.31 wt%	0.31 wt%
P	----	----	160
S	1	9.15 wt%	400
K	----	100	4
Ca	22	6.26 wt%	----
Ti	1	----	----
V	1	----	----
Mn	----	200	0.52 wt%
Fe	3	2.19 wt%	98.747 wt%
Ni	----	1.32	60
Cu	----	0.22	0.16 wt%
Zn	----	0.66 wt%	----
Ba	----	40.13 wt%	2
Nb	----	200	1
Mo	----	800	3
Pb	7	----	----

Table 5.2. Elemental Composition of Li_2O

Nuclide	wppm unless wt% indicated
^{6}Li	39.61991 wt%
^{7}Li	4.86447 wt%
Be	1
B	1
C	100
N	2
O	55.46493 wt%
F	0.1
Na	60
Mg	10
Al	50
Si	50
P	1
S	0.1
Cl	10
K	20
Ca	100
Ti	10
V	1
Cr	1
Mn	1
Fe	50
Co	0.2
Ni	10
Cu	10
Zn	10
As	0.1
Br	0.1
Zr	1
Mo	0.1
Cd	0.1
Sn	1
Sb	1
Ba	5
Pb	0.1

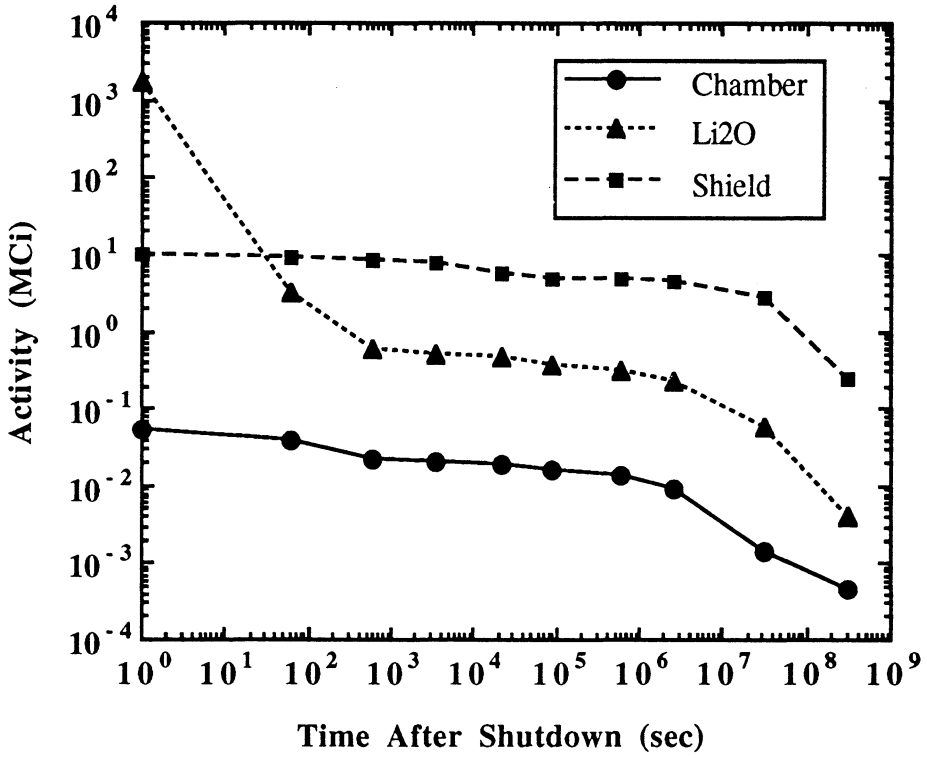

Fig. 5.3. Activity after shutdown in different regions of SOMBRERO.

its steel component. At shutdown, the total activity amounts to 10.12 MCi and drops to 4.95 MCi within a day and 2.68 MCi within a year. ^{6}He ($T_{1/2}$ = 807 ms) produced from $^{6}Li(n,p)$ and $^{7}Li(n,d)$; and ^{16}N ($T_{1/2}$ = 7.13 s) produced from $^{16}O(n,p)$ are the major contributors to the high coolant activity at shutdown. The activity of Li_2O drops from 1700 MCi to 0.38 MCi during the first day following shutdown. Table 5.3 shows the dominant contributors to the activity generated in SOMBRERO during different time periods following shutdown. Table 5.4 compares the activity, decay heat, and biological hazard potential (BHP) in the chamber and shield of SOMBRERO. The biological hazard potential has been calculated using the maximum permissible concentration limits in air for the different isotopes according to the Nuclear Regulatory Commission (NRC) regulations specified in 10CFR20.[5.6]

The temporal variation of the decay heat and BHP after shutdown is similar to that of the activity. In general, the decay heat and biological hazard potential are dominated for the most part by the same nuclides shown in Table 5.3. One value useful for predicting the thermal response of the shield to a loss of coolant accident is the integrated decay heat. Fig. 5.4 shows the integrated decay heat generated during the first two months following shutdown in the different regions of SOMBRERO. The integrated decay heat generated in the reactor shield during the first two months following shutdown is 23 GJ, which will only increase the shield temperature by less than 3 °C.

Table 5.3. Dominant Contributors to Radioactivity in SOMBRERO

Time After Shutdown	Chamber	Shield	Li_2O
< 1 day	^{28}Al, ^{37}Ar, ^{24}Na	^{56}Mn, ^{54}Mn, ^{55}Fe	^{6}He, ^{16}N, ^{37}Ar
1 day - 1 yr	^{3}H, ^{37}Ar, ^{55}Fe	^{55}Fe, ^{54}Mn, ^{37}Ar	^{55}Fe, ^{35}S, ^{37}Ar
1 yr - 10 yr	^{3}H, ^{55}Fe, ^{10}Be	^{55}Fe, H^3, ^{54}Mn	^{55}Fe, ^{14}C, ^{39}Ar
> 10 yr	^{10}Be, ^{14}C, ^{39}Ar	^{39}Ar, ^{63}Ni, ^{14}C	^{14}C, ^{39}Ar, ^{63}Ni

Table 5.4. Radioactivity After Shutdown in the Different Regions of SOMBRERO

Time After	Activity (MCi)		Decay Heat (MW)		BHP (km^3 air)	
Shutdown	Chamber	Shield	Chamber	Shield	Chamber	Shield
0	5.36e-2	10.12	7.69e-4	1.10e-1	4.12e+3	1.31e+6
1 hour	2.02e-2	7.98	1.77e-4	5.55e-2	2.84e+3	1.23e+6
1 day	1.63e-2	4.95	8.64e-5	1.09e-2	1.61e+3	1.06e+6
1 week	1.31e-2	4.69	3.60e-5	8.24e-3	1.21e+3	1.02e+6
1 month	8.87e-3	4.29	2.28e-5	7.05e-3	1.17e+3	9.61e+5
1 year	1.48e-3	2.68	8.89e-7	2.89e-3	1.00e+3	4.72e+5
10 years	4.67e-4	0.24	1.57e-7	9.56e-5	8.78e+2	2.18e+4
100 years	1.46e-4	1.70e-3	1.10e-7	1.49e-6	8.69e+2	1.12e+4

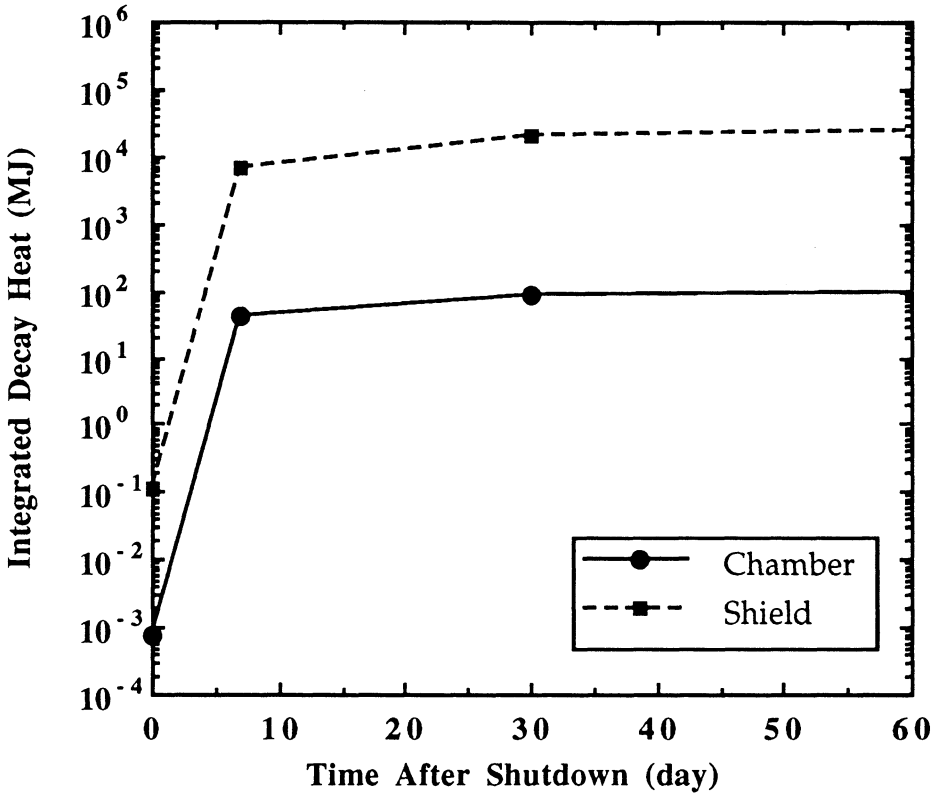

Fig. 5.4. Integrated decay heat generated in SOMBRERO.

5.5.2 Maintenance

Biological dose rate calculations have been performed at selected locations behind the concrete shield and in the space between the chamber and shield. Fig. 5.5 shows the calculated dose rate behind the shield as a function of time following shutdown. ^{56}Mn ($T_{1/2}$ = 2.6 hr) and ^{54}Mn ($T_{1/2}$ = 313 day) dominate the biological dose rate during the first day. The dose is dominated by ^{54}Mn and ^{55}Fe ($T_{1/2}$ = 2.7 yr) within the first few years. As shown in the figure, the dose rate drops to 1.6 mrem/hr after one day following shutdown. A limit of 2.5 mrem/hr for hands-on maintenance is used in this analysis assuming that the maintenance personnel work for 40 hours a week and 50 weeks a year. Hence, hands-on maintenance will definitely be allowed on the intermediate heat exchangers (IHX) behind the concrete shield within a day following shutdown. The dose rate between the chamber and shield is quite high. As shown in Fig. 5.6, the dose rate at shutdown is 25 rem/hr and drops to 1.1 rem/hr one year after shutdown. Therefore, only remote maintenance is feasible in the space between the chamber and shield of SOMBRERO.

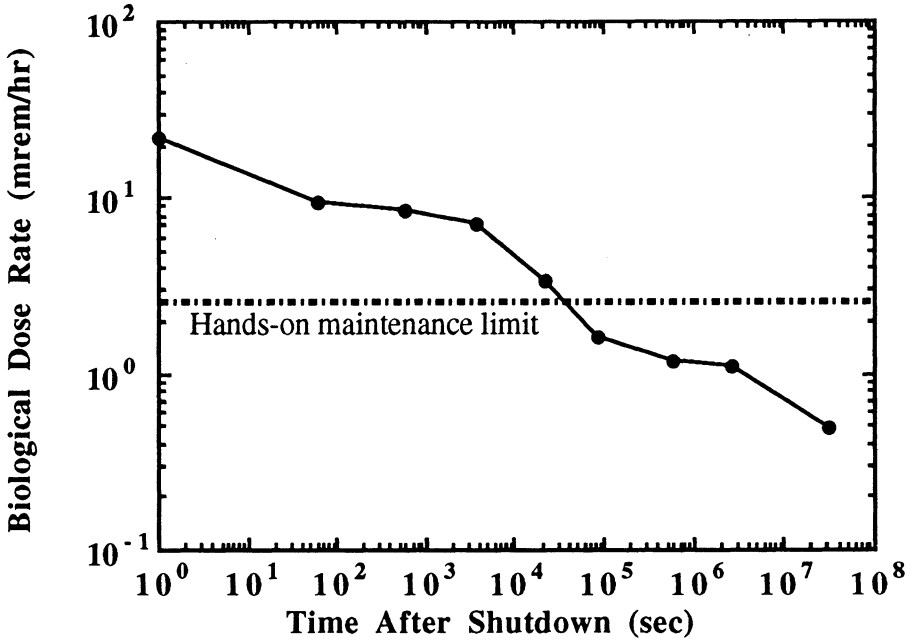

Fig. 5.5. Biological dose rate in the IHX enclosures.

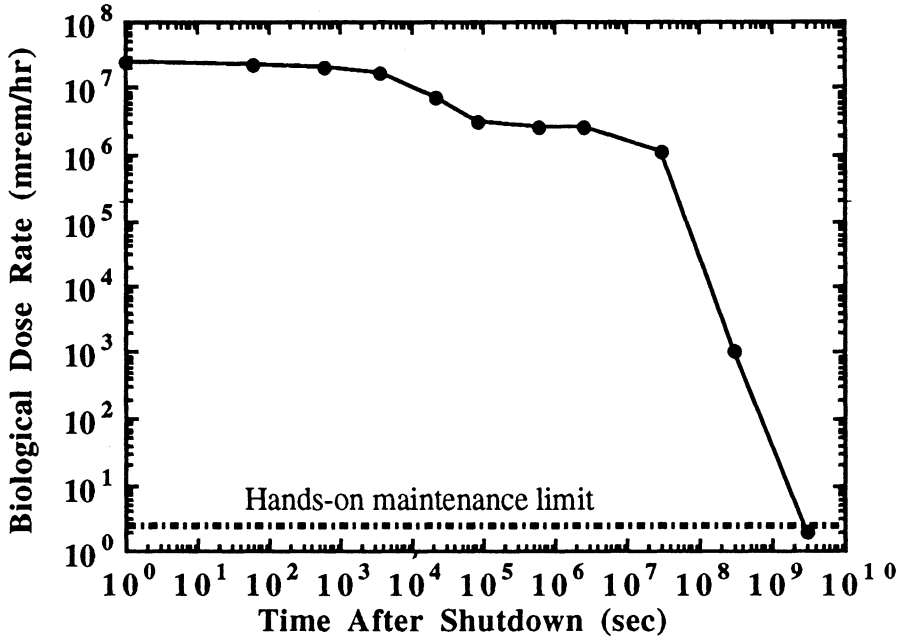

Fig. 5.6. Biological dose rate in the space between the chamber and shield.

5.5.3 Radwaste Classification

The waste disposal ratings for SOMBRERO have been evaluated according to both the NRC 10CFR61[5.7] and Fetter[5.8] waste disposal concentration limits (WDL). The 10CFR61 regulations assume that the waste disposal site will be under administrative control for 100 years. The dose at the site to an inadvertent intruder after the 100 years is limited to less than 500 mrem/year. The waste disposal rating (WDR) is defined as the sum of the ratio of the concentration of a particular isotope to the maximum allowed concentration of that isotope taken over all isotopes and for particular class. If the calculated WDR ≤ 1 when Class A limits are used, the radwaste should qualify for Class A segregated waste. The major hazard of this class of waste is to individuals who are responsible for handling it. Such waste is not considered to be a hazard following the loss of institutional control of the disposal site. If the WDR is > 1 when Class A WDL are used but ≤ 1 when Class C limits are used, the waste is termed Class C intruder waste. It must be packaged and buried such that it will not pose a hazard to an inadvertent intruder after the 100-year institutional period is over. Class C waste is assumed to be stable for 500 years. Using Class C limits, a WDR > 1 implies that the radwaste does not qualify for shallow land burial. Fetter developed a modified version of the NRC's intruder model to calculate waste disposal limits for a wider range of long-lived radionuclides, which are of more interest for fusion researchers than the few that currently exist in the current 10CFR61 regulations. Fetter's model included more accurate transfer coefficients and dose conversion factors. However, while the NRC model limits the whole body dose to 500 mrem or the dose to any single organ (one of seven body organs) to 1.5 rem, Fetter limits are based on the maximum dose to the whole body only.

The specific activities calculated for the different radionuclides have been used to evaluate the radwaste classification of the SOMBRERO's chamber, shield, and Li_2O solid breeder. Table 5.5 shows the waste disposal ratings (WDR) for each of the reactor regions in the compacted form. Compacted values correspond to crushing the solid waste before disposal. On the other hand, non compacted values are based on averaging over the total volume of a particular region implying that internal voids will be filled with concrete before disposal. Both the chamber and shield would easily qualify as Class A low level waste. ^{14}C ($T_{1/2}$ = 5730 yr) generated from $^{14}C(n,\gamma)$ reaction is the major contributor to the WDR of the graphite chamber if Class A limits were used. ^{3}H ($T_{1/2}$ = 12.3 yr) produced from the boron impurities in the graphite via the $^{10}B(n,2\alpha)$ reaction is a distant second. If Class C waste disposal limits were used, ^{14}C and ^{26}Al ($T_{1/2} = 7.3 \times 10^5$ yr) produced from $^{27}Al(n,2n)$ reaction are the major dominant nuclides if the 10CFR61 and Fetter limits were used, respectively. About 70% of the Class A waste disposal rating of the shield is contributed by tritium due to the high boron content of the concrete. ^{63}Ni ($T_{1/2}$ = 100 yr) produced from ^{63}Cu and ^{94}Nb ($T_{1/2}$ = 20,000 yr) produced from ^{93}Nb and ^{94}Mo

Table 5.5. Waste Disposal Ratings of the Different Regions of SOMBRERO

WDR	Chamber	Shield	Li_2O
Class A (10CFR61 limits)	0.043 (0.038 ^{14}C, 5.5e-3 ^{3}H)	0.058 (0.041 ^{3}H, 0.01 ^{63}Ni)	4.07 (4.07 ^{14}C)
Class C (10CFR61 limits)	3.76e-3 (3.76e-3 ^{14}C)	7.57e-4 (4.5e-4 ^{94}Nb, 2.6e-4 ^{14}C)	0.4 (0.4 ^{14}C)
Class C (Fetter)	7.05e-4 (5.6e-4 ^{26}Al, 8.8e-5 ^{10}Be)	8.17e-4 (4.5e-4 ^{94}Nb, 3.2e-4 ^{26}Al)	0.077 (0.053 ^{14}C)

are the other major contributors. Both ^{63}Ni and ^{94}Nb are generated in the steel component of the shield.

As shown in Table 5.5, the Li_2O granules would not qualify for Class A LLW even after extracting all the tritium out of the granules due to the high ^{14}C activity. Unlike the graphite chamber, this ^{14}C is generated by $^{17}O(n,\alpha)$ reaction. Using Class C waste disposal limits, the Li_2O would qualify for shallow land burial. It is important to keep in mind that this calculation is based on the Li_2O remaining for the whole 30 full power years (FPY). However, Li_2O may qualify for Class A LLW if it is replaced at least four times during the reactor life.

5.5.4 Routine Atmospheric Effluents

The radiological dose to the population in the vicinity of the reactor site due to the routine release of tritium has been estimated by using the EPA AIRDOS-PC code. The code calculates the effective dose equivalent (EDE) as mandated by 40 CFR 61.93 and 61.94 to the maximally exposed individual (MEI) and at several distances from the point of release. Dose values are computed from ingestion, inhalation, air immersion, and ground surface pathways. The routine releases from the several processing systems were based upon the quantity of tritium processed per day and followed recent experience at TSTA, which indicated that a barrier factor of 10^6 is an acceptable one. As discussed in Sec. 3.2.6.4, we considered the routine release of tritium from the reactor system, reactor building, fuel reprocessing facility, and the target factory.

The three sources of tritium release from the reactor system are the Li_2O breeder, the helium circuits, and the steam generator. Under routine daily operation, each of the breeder and helium circuits processes 550 grams of tritium and is expected to release 5.5 Ci/day. In addition, the tritium permeation through the steam generator is 15 Ci/day, giving a total daily routine release

of tritium from the reactor system of 26 Ci. A separate examination of the reactor building showed that each day both the building atmosphere of Xe and the target injector system handle 900 and 1400 grams of tritium, respectively. Hence, these two systems are also expected to release the sum of 23 Ci/day. The fuel reprocessing system has high tritium inventories in both the desiccant beds and the cryogenic distillation system. Each of the two systems handles 1500 grams of tritium per day and result in a routine release of 15 Ci/day. Finally, a 14 Ci/day of tritium are released from the target factory as it processes about 580,000 targets.

Assuming the release parameters listed in Table 5.6 and using meteorological conditions at different cities, we calculated the dose expected at typical locations near Boston, Chicago, Albuquerque, and Los Angeles.

Table 5.6. Routine Atmospheric Release Parameters

Site Information:	
Locations:	Albuquerque Boston Chicago Los Angeles
Temperature:	15 °C
Rainfall:	75 cm/yr
Emission Information:	
Year-Round Averaging	
Stack Height:	125 m
Stack Diameter:	30 cm
Momentum:	1 m/s
Tritium Pathways:	
Reactor System:	26 Ci/day
Reactor Building:	23 Ci/day
Fuel Reprocessing:	30 Ci/day
Target Factory:	14 Ci/day
Total (adjusted for 75% availability):	25,460 Ci/yr

A summary of the results is shown in Table 5.7. The worst dose was in the Albuquerque area, but was only 0.93 mrem/yr. More than 85% of the doses at all sites are incurred via the ingestion pathway. The estimated doses at all sites are far below the current EPA effluent limit of 10 mrem/yr and less than the 5 mrem/yr limit adopted by ITER. It is important to keep in mind that the estimated doses depend strongly on the stack height. For example, using a 30-meter stack height results in an EDE of 18 mrem/yr at the site boundary (1 km) if the Los Angeles meteorological conditions were used. Actually, the rule of thumb for determining the necessary stack height is to use 2.5 times the height of the nearest tall building in order to avoid downwash of

Table 5.7. Dose to the Maximally Exposed Individual (MEI)

Site	Dose (mrem/yr)	Distance (m)
Albuquerque	0.93	1000
Boston	0.23	3000
Chicago	0.36	1000
Los Angeles	0.69	3000

the plume into the wake of the building.[5.9] A shorter stack must be justified with appropriate analysis. If one were to apply the rule of thumb to SOMBRERO, the stack would be on the order of 300 m. The EDE values calculated at all sites would be one to two orders of magnitude lower than those presented in Table 5.7.

5.5.5 Accident Analysis

An accidental release of the radioactivity from the reactor building is another potential source of off-site doses. In this section we calculated the potential off-site doses using the ESECOM[5.10] methodology due to the release of some of the radioactive inventory of the chamber, shield and Li_2O granules. In addition, we calculated the doses produced by the release of all the tritium contained in the reactor building during an accident. To account for the worst possible accident, a containment failure is postulated in order to produce significant off-site doses even though the probability of such a failure is very low.

5.5.5.1 Chamber and Shield

During a loss of coolant accident (LOCA) or loss of flow accident (LOFA), the amount of evaporated graphite would not exceed 50 kg, which is equivalent to about 0.44% of the 1 cm first wall. This amount of evaporated graphite will increase the carbon partial pressure in the reactor building by one torr. The higher carbon vapor pressure would prevent the laser beam from propagating to the target and hence shutdown the reactor. Using the worst release characteristics as defined by the ESECOM methodology (Table 5.8), we calculated the off-site doses produced by the release of 0.44% of the graphite first wall (FW). The whole body (WB) early dose at the site boundary (1 km) only amounts to 1.31 mrem. The dose is dominated by radionuclides produced from the graphite impurities. As shown in Table 5.9, ^{24}Na, ^{48}Sc, and ^{54}Mn are the major contributors to the off-site dose.

Table 5.8. Activation Products Release Characteristics

Pasquill Stability Class	F
Wind Speed	1 m/s
Inversion Layer Height	250 m
Deposition Velocity	0.01 m/s
Duration of Release	0.05 hr
Population Density	50 person/km^2
Ground Level Release	
Site Boundary	1 km and 10 km
Initial Plume Dimensions	
Sigma-Y	100 m
Sigma-Z	50 m
Percentage of Land	
Crop Farming	15 %
Milk/Meat Products	15 %
Groundshine Shielding	
Prompt Dose	0.70
Chronic Dose	0.33

Table 5.9. SOMBRERO's WB Early Dose Dominant Nuclides

Chamber	Li_2O	Shield
^{24}Na ($T_{1/2}$ = 14.96 h)	^{24}Na ($T_{1/2}$ = 14.96 h)	^{54}Mn ($T_{1/2}$ = 312 d)
^{48}Sc ($T_{1/2}$ = 43.7 h)	^{60}Co ($T_{1/2}$ = 5.27 yr)	^{56}Mn ($T_{1/2}$ = 2.6 h)
^{54}Mn ($T_{1/2}$ = 312 d)	^{58}Co ($T_{1/2}$ = 70.88 d)	^{64}Cu ($T_{1/2}$ = 12.7 h)
^{46}Sc ($T_{1/2}$ = 83.81 d)	^{65}Zn ($T_{1/2}$ = 243.8 d)	^{59}Fe ($T_{1/2}$ = 44.5 d)

The decay heat generated in the steel-reinforced concrete shield is very low. The decay heat generated within the first two months following a LOCA would only increase the shield temperature by < 3 °C. Since the shield average operating temperature is less than 500 °C, the full mobilization of the shield radioactive products is impossible. The highest temperature the shield

would reach determines the release fraction of its radioactive products. Since most of the radioactive inventory is contributed by the mild steel (20% of the shield), off-site dose calculations have been performed using steel experimental volatility rates.[5.11] Adjusted PCA volatility rates at 600 °C in dry air were used in this analysis. To estimate conservative release fractions, we assumed a 10-hour LOCA in which the 1-hour release rates have been used for the full 10 hours to account for any possible loss of iron oxide protection. At 600 °C, the whole body early dose at the site boundary is 24.7 mrem. Most of the dose is produced by the manganese isotopes, ^{54}Mn and ^{56}Mn. Even at 1000 °C, the shield would only produce a WB early dose of 167 mrem.

5.5.5.2 The Li_2O Solid Breeder

SOMBRERO's blanket consists of a moving bed of solid Li_2O particles flowing through the chamber by gravity. Tritium is continually extracted from the Li_2O granules by helium gas. The total inventory of Li_2O in the reactor is 2000 tonnes. Since the Li_2O particles are from 300-500 μm in diameter, we do not anticipate that more than 1% of the total Li_2O inventory would be released outside the reactor building in case of a failure of the containment and chamber. The Whole body early dose at the site boundary would be 551 mrem. ^{24}Na produced from the sodium impurities in the Li_2O is the major contributor to the early dose. ^{60}Co and ^{58}Co are the second and third contributors to the dose, respectively.

5.5.5.3 Tritium

The fourth and final source of potential off-site doses considered in this analysis is produced by the accidental release of the tritium contained inside the reactor building at any moment. We identified the tritium inventories in the Li_2O granules present in the reactor system as our major source of concern. The tritium solubility in the Li_2O at an average temperature of 650 °C is 0.081 wppm. For a total Li_2O inventory of 2000 tonnes, the steady state inventory is 162 g. The other two sources of tritium in the reactor system are the graphite structure and the helium circuit. The graphite reactor structure will absorb some tritium. Based upon the first wall, 165 tonnes of C, the total inventory would be 10 grams of tritium. On the other hand, the He circuit contains HTO at a partial pressure of 6 Pa and an average temperature of 918 °C, giving a total inventory of 5 grams of tritium. In addition, the reactor building atmosphere of Xe has a continuous tritium inventory of about 4.6 g. Finally, the target feed channel leading to the injector within the reactor building is about 50 m long which allows it to handle about 1400 grams of tritium per day. However, since the number of targets present inside the channel is limited to one minute fueling time, the total tritium inventory in this system is kept at about 1 g. Assuming a 100% release, the whole body early dose produced by the release of all of the 182.6 g of tritium is 1.64 rem.

Table 5.10 shows the potential off-site doses produced by simultaneous occurrence of the four previous scenarios. The total whole body early dose at the site boundary mounts only to 2.22 rem, which is far below the 25 rem value recommended for this study by the oversight committee as a threshold for avoidance of early fatalities. The WB early dose is also below the 5 rem level where evacuation plans are required.

Table 5.10. SOMBRERO's Potential Off-Site Doses

	Chamber (0.44%FW)	Shield (600°C)	Li_2O (1 %)	Tritium (100 %)	Total
Prompt Dose at 1 km (Rem)					
WB	1.24e-3	2.41e-2	4.84e-1	2.12e-1	7.21e-1
BM	1.29e-3	2.81e-2	5.22e-1	7.77e-1	1.33
Lung	2.06e-3	5.44e-2	9.95e-1	1.69	2.74
LLI	1.09e-3	2.55e-2	4.11e-1	2.70e-1	7.08e-1
WB Early Dose (Rem)					
At 1 km	1.31e-3	2.47e-2	5.51e-1	1.64	2.22
At 10 km	8.31e-5	1.53e-3	3.62e-2	3.81e-1	4.19e-1
WB Chronic Dose at 1 km (Rem)					
Inh + Grd	3.72e-3	1.34e-1	7.22	2.26	9.62
Ingestion	7.97e-3	1.69e-1	22.5	84.71	107.4
Total	1.17e-2	3.03e-1	29.72	86.97	117
WB Chronic Dose at 10 km (Rem)					
Inh + Grd	2.47e-4	9.04e-3	4.99e-1	5.24e-1	1.03
Ingestion	5.52e-4	1.17e-2	1.56	19.61	21.19
Total	7.99e-4	2.07e-2	2.06	20.13	22.22
Cancers					
Sum Organs	3.62e-3	1.77e-2	2.71	25	27.73
WB	1.23e-3	1.59e-2	3.59	50.73	54.34
Population Dose (Man-Rem)					
WB	7.78	101	2.27e+4	3.21e+5	3.44e+5

5.6 OSIRIS SAFETY ANALYSIS

A separate activation and safety analysis was performed for the chamber, shield, and Flibe coolant of Osiris. The reactor target yield is 432 MJ and the rep-rate is 4.6 Hz, resulting in 1987 MW of fusion power. Osiris has a wetted-wall chamber that uses Flibe coolant and has a carbon fabric structure. A thin layer of the Flibe leaks through the carbon fabric and is renewed on each shot. The reactor uses a blanket constructed of a porous carbon fabric filled with the molten salt Flibe (67% LiF and 33% BeF_2). The reactor pool-type configuration helps contain the radioactive Flibe in a concrete pool with a double-layer steel liner. The Osiris chamber is surrounded by a 3-meter thick shield for protection from direct neutrons and gammas during operation. The steel-reinforced concrete shield is made of 70% concrete, 20% mild steel, and 10% helium coolant.

5.6.1 Activation Analysis

The radioactivity generated in the reactor chamber and shield was calculated for the 40 year reactor life-time. A second calculation was performed to determine the amount of radioactivity induced in the tantalum high-Z target material. The Ta debris which is soluble in Flibe is continuously removed from the Flibe, recycled, refabricated, and reinjected in the chamber. Since Ta has been assumed to go through this cycle once a week, Ta has been only exposed to only 1560 (number of weeks in 30 years) shots during the reactor life-time. Even though Ta is continuously extracted from Flibe, a steady state concentration of 10 wppm of radioactive Ta in the Flibe has been assumed at all times during operation. A third calculation has been performed for the coolant. The residence time of the Flibe coolant in the chamber is 60 seconds. However, the 660 tonnes of Flibe take 90 seconds to go through the reactor chamber. Therefore, the coolant activity has been calculated to allow for the fact that Flibe spends only 67% of the time exposed to neutrons in the reactor chamber. In addition to the tantalum impurities, we used a Flibe composition which contains eleven other impurity elements (Table 5.11). The radial build used in this analysis is shown in Fig. 5.7.

5.6.1.1 Chamber and Shield

A small amount of activity is induced in the Osiris chamber during the reactor life-time. The total activity generated in the carbon fabric structure at shutdown is only 12,326 Ci. It drops to 3,512 and 364 Ci, respectively, at one day and one year after shutdown. During the first day after shutdown, the activity is dominated by radionuclides such as ^{28}Al ($T_{1/2}$ = 2.25 m), ^{37}Ar ($T_{1/2}$ = 35 d), and ^{24}Na ($T_{1/2}$ = 14.96 hr), which are induced from the impurity elements, aluminum (4 wppm), calcium (22 wppm) and sodium (10 wppm), respectively. The intermediate and long-term activities are dominated by ^{10}Be ($T_{1/2} = 1.6 \times 10^6$ yr) and ^{14}C, produced from the

Table 5.11. Elemental Composition of Flibe

Nuclide	wppm unless wt% indicated
Li	14.038 wt%
Be	8.975 wt%
C	91
O	987
F	76.848 wt%
Mg	5.5
Al	77
Si	27
Ti	19
Cr	9
Mn	11
Fe	139
Ni	13
Cu	7

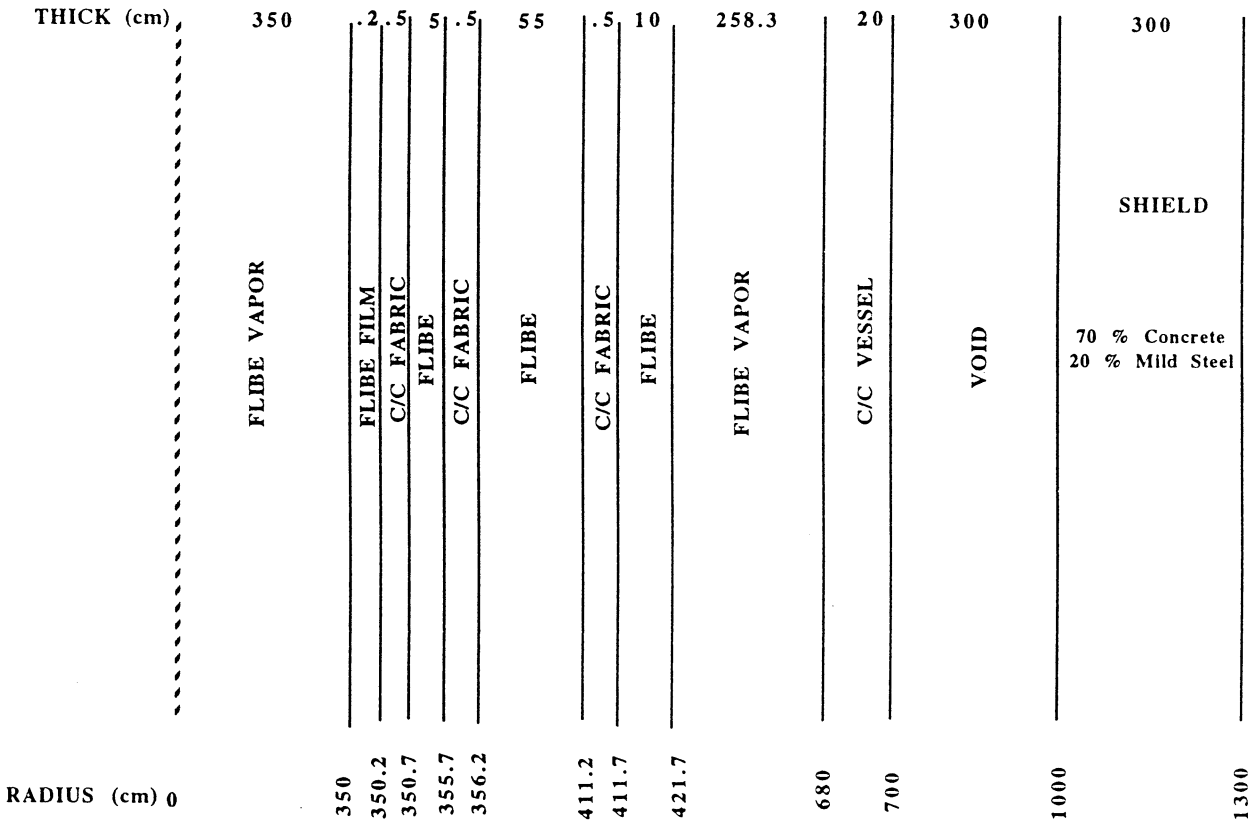

Fig. 5.7. Radial build used in activation calculations for Osiris.

main constituent element, carbon. Fig. 5.8 shows the activity generated in the different regions of Osiris as a function of time following shutdown. The activity generated in the steel-reinforced concrete shield is dominated by contribution from its steel component (20% of the shield). At shutdown, the total activity is 2.33 MCi and drops to 1.2 MCi within a day and 0.69 MCi after one year. The products of iron, ^{54}Mn, ^{56}Mn, and ^{55}Fe are the major sources of activity present in the shield during the first year following shutdown. The long-term activity (> 10 yr) is dominated by ^{39}Ar ($T_{1/2}$ = 269 yr), ^{63}Ni, and ^{14}C which are all induced from impurities in both the steel and concrete used in this analysis.

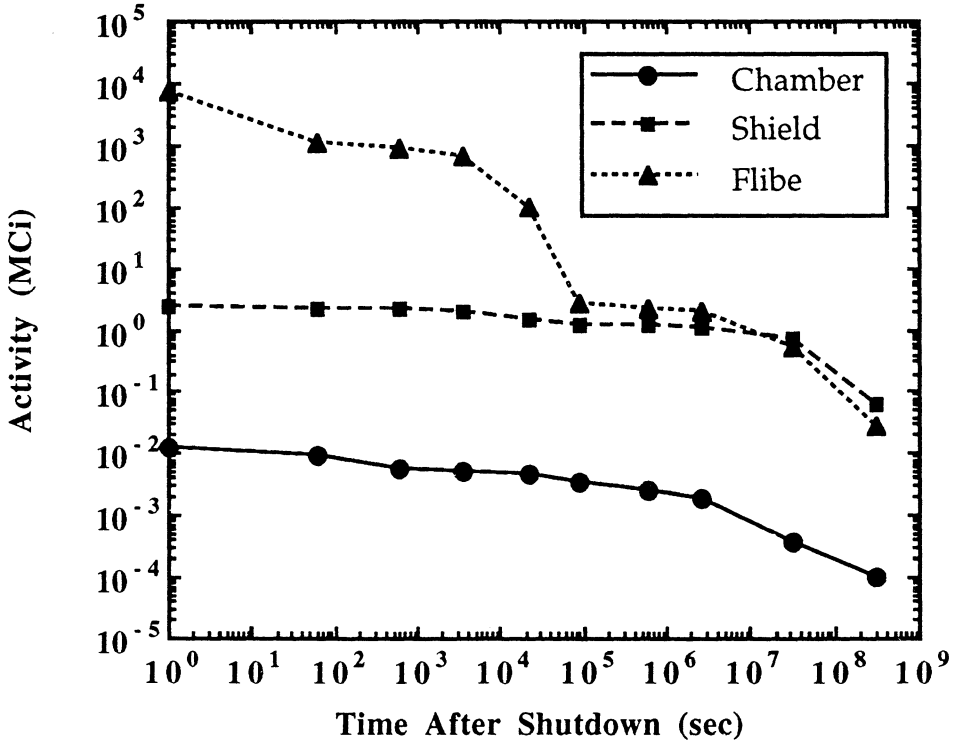

Fig. 5.8. Activity after shutdown in different regions of Osiris.

Table 5.12 compares the activity, decay heat, and biological hazard potential (BHP) in the chamber and shield of Osiris. The biological hazard potential has been calculated using the maximum permissible concentration limits in air for the different isotopes according to the NRC regulations specified in 10CFR20. For the most part, the decay heat and biological hazard potential are dominated by the same nuclides that dominate activity. The integrated decay heat generated in the chamber structure is insignificant and poses no safety concern in a case of loss of coolant accident (LOCA). In the same time, the shield has an integrated decay heat of only

Table 5.12. Radioactivity After Shutdown in the Different Regions of Osiris

Time After	Activity (MCi)		Decay Heat (MW)		BHP (km^3 air)	
shutdown	Chamber	Shield	Chamber	Shield	Chamber	Shield
0	1.23e-2	2.33	1.92e-4	2.29e-2	1040	2.63e+5
1 hour	4.88e-3	1.91	5.97e-5	1.30e-2	758.1	2.45e+5
1 day	3.51e-3	1.19	2.53e-5	2.32e-3	413	2.04e+5
1 week	2.58e-3	1.13	6.80e-6	1.65e-3	270	1.96e+5
1 month	1.78e-3	1.05	4.31e-6	1.41e-3	260.1	1.83e+5
1 year	3.64e-4	0.69	2.01e-7	5.99e-4	204.8	9.03e+4
10 years	1.06e-4	6.44e-2	3.62e-8	2.59e-5	172.8	4.64e+3
100 years	3.81e-5	3.23e-4	2.46e-8	3.00e-7	170.5	2.07e+3

1.5 GJ, one month after shutdown. This amount of decay heat cannot increase the shield temperature by more than 1 to 2 degrees.

5.6.1.2 High-Z Target Material

Tantalum is used in the Osiris target because of its high solubility in Flibe. The Ta has been assumed to have a 4-mm inner radius and 90 μm thickness. Ta debris has been assumed to be continuously removed from the Flibe, returned to the target factory to be reused in the fabrication of new targets, and finally reinjected into the reactor. Hence, the time cycle assumed for this process is one week. The radioactivity calculations have been performed using a total of 2.782×10^6 targets (847 kg of Ta), which represents the number of targets used in Osiris every week. As shown in Table 5.13, the activity at shutdown is dominated by ^{180m}Ta ($T_{1/2}$ = 8.15 hr) produced from (n,2n)* reaction with ^{181}Ta. The intermediate-term activity is dominated by ^{179}Ta ($T_{1/2}$ = 1.8 yr) and ^{182}Ta ($T_{1/2}$ = 114.43 d). The only remaining source of activity, 100 years after shutdown is ^{180}Ta ($T_{1/2} = 1.2 \times 10^{15}$ yr).

5.6.1.3 Coolant

Flibe is used in Osiris as the coolant and tritium breeder. The Flibe composition analyzed contains a total of eleven impurities in addition to 10 wppm of Ta. The 10 wppm of Ta represents the steady state concentration that exists in the Flibe at all times and is determined by assuming a 50% extraction efficiency on 10% of the Flibe flow. Therefore, unlike the rest of the Ta

Table 5.13. Total Tantalum-Induced Activity at Osiris Shutdown

Nuclide	Activity (Ci)
^{177}Lu	1.65e+4
^{181}Hf	5.46e+4
^{179}Ta	1.50e+5
^{180}Ta	4.14e-8
^{180m}Ta	3.43e+8
^{182}Ta	7.63e+5
^{182m}Ta	5.64e+6
^{183}Ta	7.17

inventory, which is only exposed to the neutron flux only during one shot every week, we conservatively assume that this amount of Ta (6.7 kg) is also continuously exposed to the neutron flux throughout the 30 full power years.

After 30 years of irradiation (1 shot/week), the Ta composition changes to 2.5% ^{180}Ta and 97.5% ^{181}Ta replacing the original composition of 0.012% ^{180}Ta and 99.998% ^{181}Ta. Using this Ta composition with Flibe yields a shutdown activity of 7000 MCi. By far the major source of activity at shutdown is ^{18}F ($T_{1/2}$ = 1.83 hr). As shown in Fig. 5.8, the Flibe activity drops to only 2.55 MCi during the first day following shutdown. ^{179}Ta and ^{182}Ta produced from the Ta impurities dominate the activity during the first five years following shutdown. The tritium steady state inventory in the Flibe is kept at a low level of 1 g or 10,000 Ci.

5.6.2 Maintenance

Biological dose rate calculations have been performed at selected locations behind the concrete shield and in the space between the chamber and shield. Fig. 5.9 shows the calculated dose rate between the chamber and shield as a function of time following shutdown. At shutdown the dose rate is 7.95 rem/hr and only drops to 191 mrem/hr after one year. The biological dose rate is dominated by ^{56}Mn and ^{54}Mn during the first day and by ^{54}Mn and ^{55}Fe within the first few years. A limit of 2.5 mrem/hr for hands-on maintenance is used in this study assuming that maintenance personnel work for 40 hours a week and 50 weeks a year. Therefore, only remote maintenance would be feasible in the space between the chamber and shield. The dose rate behind

the shield, however, is quite low. The dose rate at shutdown is only 0.11 μrem/hr allowing for hands-on maintenance on the IHX behind the concrete shield.

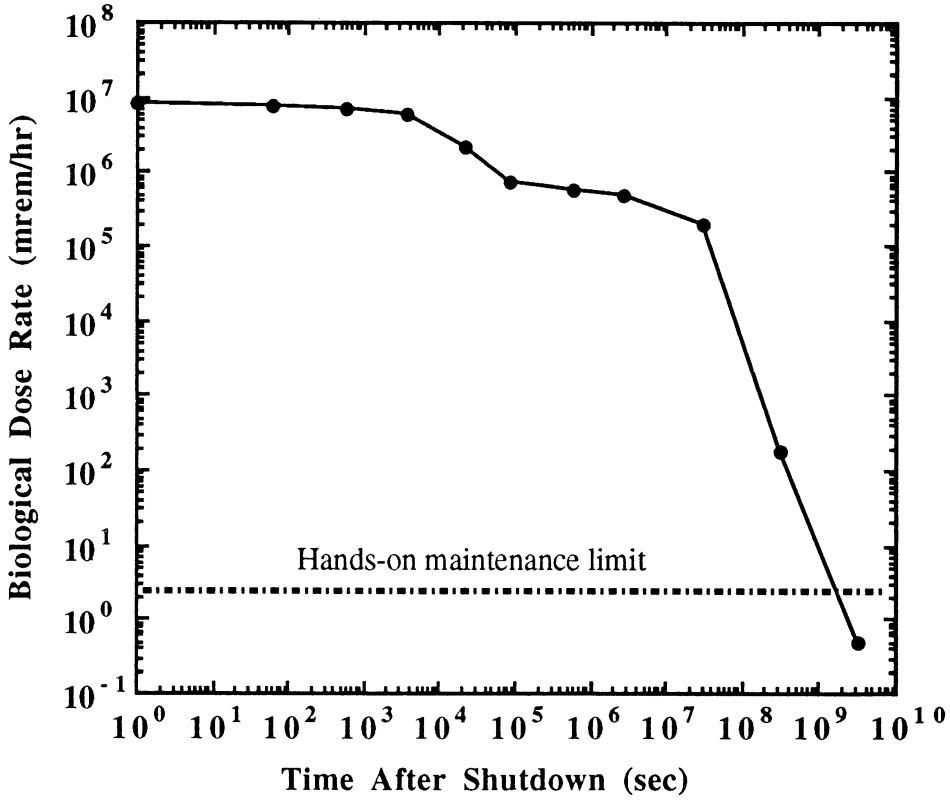

Fig. 5.9. Biological dose rate in the space between Osiris chamber and shield.

5.6.3 Radwaste Classification

The radwaste classifications of the Osiris chamber, shield, and coolant were evaluated according to both the NRC 10CFR61 and the Fetter waste disposal concentration limits (WDL). The specific activities calculated by the DKR-ICF code were used to calculate the different waste disposal ratings (WDR). Table 5.14 shows the waste disposal ratings (WDR) for each of the reactor regions. Both the chamber and shield would qualify as Class A low level waste. The ^{14}C generated from $^{13}C(n,\gamma)$ reaction is the major contributor to the WDR of the chamber if Class A limits are used and ^{3}H produced from the boron impurities in the carbon fabric via the $^{10}B(n,2\alpha)$ reaction is the other contributor. If Class C waste disposal limits are used, ^{14}C and ^{26}Al produced from $^{26}Al(n,2n)$ reaction are the major dominant nuclides if the 10CFR61 and Fetter limits are used, respectively. Sixty five percent of the Class A waste disposal rating of the shield is contributed by tritium due to the high boron content of the concrete. ^{63}Ni produced from ^{63}Cu and

Table 5.14. Waste Disposal Ratings (WDR) of the Different Regions of Osiris

WDR	Chamber	Shield	Flibe
Class A (10CFR61 limits)	0.023 (0.021 ^{14}C, 1.7e-3 ^{3}H)	6.09e-3 (4.e-3 ^{3}H, 1.1e-3 ^{63}Ni)	0.23 (0.21 ^{63}Ni)
Class C (10CFR61 limits)	2.15e-3 (2.15e-3 ^{14}C)	1.01e-4 (5.3e-5 ^{94}Nb, 4.3e-5 ^{14}C)	2.3e-3 (0.001^{63}Ni, 0.001^{14}C)
Class C (Fetter)	3.00e-4 (2.4e-4 ^{26}Al, 2.9e-5 ^{14}C)	8.78e-5 (5.3e-5 ^{94}Nb, 3.e-5 ^{26}Al)	0.048 (0.047 ^{26}Al)

^{94}Nb produced from ^{93}Nb and ^{94}Mo are the other major contributors. Both ^{63}Ni and ^{94}Nb are generated in the steel component of the shield.

It is important to keep in mind that the waste disposal concentration limits used to calculate the waste disposal ratings of the chamber and shield are those assigned for the disposal of solid waste. As shown in Table 5.14, the Flibe coolant could qualify for shallow land burial as Class A LLW. However, Flibe has to be in solid form before such disposal can take place and the feasibility and practicality of such a process has to be determined. Almost all of the contributors to the Flibe waste disposal rating are induced by the impurities included in the Flibe composition used in this analysis.

5.6.4 Routine Atmospheric Effluents

The EPA AIRDOS-PC code was used to calculate the off-site dose to the maximally exposed individual (MEI) as a result of the routine release of tritium to the environment. Once again the amount of tritium estimated for routine release is based upon the daily flow rate of tritium through each system, based upon the TSTA experience that about 1 Ci/day of tritium is released per 100 grams of tritium processed (i.e., a barrier factor of 10^6 is considered). As discussed in Sec. 2.2.7.2 and Sec. 2.2.7.3, we considered the routine release of tritium from the reactor system, reactor building, fuel reprocessing facility, and the target factory.

In Osiris, the major sources of tritium release from the reactor system are the breeder, the heavy-ion beam lines, and the steam generator. The total amount of Flibe in the reactor, vacuum disengager, IHX, and connecting pipes is 330 m^3, resulting in a tritium flow rate in the breeder of 1045 g/day. Hence, a well-enclosed system would only release 10 Ci/day of tritium to the environment. At the same time, a total of 156 g/day of tritium are expected to effuse into the

heavy-ion beam ports where they get absorbed by cryogenic adsorption traps. Since most of these traps would be recycled every hour, only a 1.5 Ci/day of tritium is projected to be lost into the beam facility assuming a tightly controlled adsorption and degassing of these adsorbers. In addition, the tritium permeation through the steam generator is 40 Ci/day giving a total daily routine release of tritium from the reactor system of 51.5 Ci. An analysis of the reactor building identified the target delivery system as the major source of tritium release. The system handles 1020 grams of tritium per day and, therefore, is projected to release 10 Ci/day. The third source of tritium is the fuel reprocessing system. Osiris' fuel reprocessing system has high tritium inventories in both the vacuum pumps of the vacuum disengager and the cryogenic distillation system. Each of the two systems handles 1024 grams of tritium per day and results in a routine release of 10 Ci/day. The last source of tritium considered in this analysis is the target factory. The factory processes some 400,000 targets a day with a total of 1020 grams of tritium and, hence, would be expected to routinely release about 10 Ci/day.

Assuming the release parameters listed in Table 5.15 and using meteorological conditions at different cities, we calculated the dose expected at typical locations. A summary of the results is shown in Table 5.16. The worst case occurs in the Los Angeles area, but is only 2.43 mrem/yr. More than 85% of the doses at all sites are incurred via the ingestion pathway. Notice that these results are obtained assuming a 75-meter stack height which is 2.5 times the height of the Osiris reactor building. As mentioned before, the rule of thumb for determining the necessary stack height is to use 2.5 times the height of the nearest tall building in order to avoid downwash of the plume into the wake of the building. The estimated dose values strongly depend on the stack height. For example, using a 35 meter stack height results in an EDE of 11 mrem/yr at the Los Angeles site boundary (1 km). However, a shorter stack must be justified with appropriate analysis. The estimated doses at all the sites are within the current EPA effluent limit of 10 mrem/yr and less than the 5 mrem/yr limit adopted by ITER if the 75 m stack height is assumed.

5.6.5 Accident Analysis

In this subsection, we calculated the potential off-site dose produced in Osiris during an accident. In general, the existence of highly radioactive products does not in itself pose a radiological hazard without a credible accident scenario for mobilizing and releasing it to the environment. Even though it is quite unlikely that any of the radioactive products would escape the building under reasonable conditions, we calculated the potential off-site doses using the ESECOM methodology assuming a sequence of sever accidents. In addition, we have calculated the doses produced by the release of all the tritium contained in the reactor building during an accident. To account for the worst possible accident, a reactor containment failure is postulated in order to produce a significant off-site dose even though the probability of such a failure is low.

Table 5.15. Routine Atmospheric Release Parameters

Site Information:	
Locations:	Albuquerque
	Boston
	Chicago
	Los Angeles
Temperature:	15 °C
Rainfall:	75 cm/yr
Emission Information:	
Year-Round Averaging	
Stack Height:	75 m
Stack Diameter:	30 cm
Momentum:	1 m/s
Tritium Pathways:	
Reactor System:	51.5 Ci/day
Reactor Building:	10 Ci/day
Fuel Reprocessing:	20 Ci/day
Target Factory:	10 Ci/day
Total (adjusted for 75% availability):	25,050 Ci/yr

Table 5.16. Dose to the Maximally Exposed Individual (MEI)

Site	Dose (mrem/yr)	Distance (m)
Albuquerque	1.82	300
Boston	0.76	1000
Chicago	1.11	1000
Los Angeles	2.43	1000

5.6.5.1 Chamber and Shield

During a loss of coolant accident (LOCA) or loss of flow accident (LOFA), the chamber first wall surface would still be protected with Flibe as long as there is Flibe in the blanket. However, should the Flibe drain out altogether, then as much as 2 to 3 kg of the carbon first wall would evaporate from a single shot. This is equal to the evaporation of about 0.2% of the first wall which is 0.5 cm thick. At the same time, the high Flibe vapor pressure would stop beam propagation and, hence, shutdown the reactor. Using the worst release characteristics as defined by the ESECOM methodology (Table 5.8), we have calculated the off-site dose produced by the release of 0.2% of the first wall (FW). The whole body (WB) early dose at the site boundary (1 km) only amounts to 0.28 mrem and is dominated by ^{24}Na, ^{48}Sc, and ^{54}Mn, which are produced from the sodium, titanium and iron impurities in the carbon fabric.

The decay heat generated within the first month in the steel-reinforced concrete shield following a LOCA would only increase the shield temperature by < 2 °C. Since the shield average operating temperature is much less than 500 °C, the full mobilization of the shield radioactive products is impossible. The highest temperature the shield would reach determines the release fraction of its radioactive products. Since most of the radioactive inventory is contributed by the mild steel (20% of the shield), off-site dose calculations were performed using steel experimental volatility rates. Adjusted PCA volatility rates at 600 °C in dry air were used in this analysis. To estimate conservative release fractions, we assumed a 10 hour LOCA in which the 1 hour release rates have been used for the full 10 hours, to account for any possible loss of iron oxide protection. At 600 °C, the whole body early dose at the site boundary is only 5.69 mrem which comes from ^{54}Mn and ^{56}Mn mainly produced from the iron in the shield.

5.6.5.2 High-Z Target Material

In this subsection we investigated the safety hazard posed by using tantalum in the target. As mentioned before, activated Ta debris is exposed to one shot a week before being recycled and reinjected into the reactor. Hence, there are 847 kg of Ta in 2.78 x 10^6 targets circulating through the reactor once a week. However, there are only about 300 targets (92 g of Ta) present inside the target injector at any moment (1 minute fuel). In the same time 6.7 kg (as 10 wppm impurity in the Flibe) of this Ta would also be exposed to further irradiation as they circulate around the chamber with the Flibe coolant. The potential whole body early dose caused by 100% release of all the radionuclides produced in the 300 targets and the 6.7 kg of Ta contained in the 660 tonnes of Flibe at the reactor shutdown is shown in Table 5.17. ^{182}Ta produced from ^{181}Ta via (n,γ) reaction is the most dominant isotope. As will be shown in the next subsection, we only anticipate the mobilization of 0.5 kg of the Flibe in case of an accident. In addition, we assumed that the release of 1% of the Ta contained in the target inside the reactor building (3 targets) is conservative

Table 5.17. Tantalum-Induced WB Early Off-Site Dose (Rem)

Nuclide	Ta in Targets (300 targets)	Ta in Flibe (6.7 kg)
^{177}Lu	2.54e-5	3.36e-4
^{81}Hf	1.40e-3	2.93e-2
^{179}Ta	4.17e-4	7.01e-3
^{180m}Ta	1.30e-2	2.49e-2
^{182}Ta	4.72e-2	1.15e+3
^{182m}Ta	2.38e-4	4.71e-4

enough. In such a case the WB early doses induced by the release of the Ta contained in the Flibe vapor and the release of 1% of the Ta contained in the target are 0.91 and 0.6 mrem, respectively.

5.6.5.3 Flibe

Flibe is used as a coolant and breeder in Osiris. The tritium inventory in the Flibe is kept very low by its continuous removal during the reactor operation. We calculated the potential off-site dose produced by the mobilization of the Flibe during an accident where a breach of the reactor building is postulated. Also, the 10 wppm of Ta contained in the Flibe as an impurity is included in this analysis. Following every fusion explosion, x-rays vaporize 2.78 mg/cm^2 or 14.1 μm of Flibe from the chamber wall. For a 3.5 m radius first wall, we calculated that 4.3 kg of vapor Flibe are produced per shot. A simultaneous breach in the reactor building and chamber would allow the cold air to flow into the chamber. The air starts cooling the Flibe vapor and hence reducing its vapor pressure. As Flibe vapor pressure falls, Flibe starts condensing rapidly. Condensed Flibe begins to form aerosol particles, which in turn start falling into the hot pool in the bottom of the chamber. However, a fraction of the aerosol particles can be carried out by the hot air leaving the chamber. In the HYLIFE-II study[5.12], the ratio of the mobilized Flibe is estimated at about 10% of the total Flibe evaporated after each shot. Using a similar assumption, we performed the off-site dose calculation assuming that 0.5 kg of the vapor Flibe is mobilized in the form of aerosol particles. The whole body early dose at the site boundary would be 7.2 mrem. More than 85% of the dose is produced by the ^{18}F isotope. The rest of the dose is caused by ^{182}Ta produced from the target material impurities and ^{24}Na and ^{54}Mn produced from the natural impurities in the Flibe.

The 0.5 kg of Flibe escaping the reactor building contains 165 g of BeF_2. The BeF_2 is a major source of safety hazard because of the beryllium toxicity. Using the same assumptions as in the HYLIFE-II study, a one-hour release of BeF_2 would result in its concentration at the reactor site boundary being about 1.5 $\mu g/m^3$. This value is below the level of concern as the recommended upper limits for continuous and peak exposures are 2 and 25 $\mu g/m^3$, respectively (US Federal Register, 1975; National Institute of Safety and Health, 1972).

5.6.5.4 Tritium

Finally, we considered the potential off-site doses produced by the accidental release of the tritium from both the reactor systems and the reactor building at any moment. The three major sources of tritium in the reactor system are the Flibe breeder, the graphite fabric and the heavy ion beam lines. The tritium concentration in Flibe is 3.4 mg/m^3 and the total Flibe inventory in the reactor, vacuum disengager, and IHX is 330 m^3. Consequently, the steady state tritium inventory in the Flibe salt is only 1 g. The graphite fibers forming the chamber first wall (3000 kg) are subjected to T_2 pressure from the tritium dissolved in the Flibe resulting in a maximum tritium inventory in these fibers of about 4 g. The two sources of tritium accumulating inside the heavy-ion beam ports are due to the continual evaporation of TF from the Flibe and the unburned target fuel produced by chamber blasts. Cryogenic adsorption traps installed along the internal surface of the beam tubes accumulate about 156 grams of tritium per day. However, as mentioned before (Sec. 2.2.7.2) most of the adsorption traps would be recycled every hour so that their total tritium inventory is only 6.5 g. We identified the tritium contained in the targets present in the target delivery system as the major source of potential tritium release from the reactor building during an accident. The target delivery system handles 1020 grams of tritium every day, out of which 1.2 g of tritium (contained in the number of targets needed for the order of one minute of fueling) are vulnerable to any accidental release. An accident releasing 100% of the specified tritium inventory (12.7 g) would produce a whole body early dose of 114 mrem.

Table 5.18 shows the potential off-site doses produced by simultaneous occurrence of the previous accident scenarios. The total whole body dose at the site boundary mounts to only 128 mrem, which is far below the 25 rem value recommended for this study by the oversight committee as a threshold for avoidance of early fatalities. The WB early dose is also far below the 5 rem level where evacuation plans are required.

Table 5.18. Osiris' Potential Off-Site Doses

	Chamber (0.2%FW)	Shield (600°C)	Flibe (0.5 kg)	Tantalum (3 targets)	Tritium (12.7 g)	Total
Prompt Dose at 1 km (Rem)						
WB	2.70e-4	5.57e-3	7.08e-3	5.58e-4	1.49e-2	2.83e-2
BM	2.78e-4	6.50e-3	8.57e-3	6.72e-4	5.41e-2	7.01e-2
Lung	4.15e-4	1.29e-2	1.23e-2	3.66e-3	1.19e-1	1.48e-1
LLI	2.36e-4	6.01e-3	5.38e-3	9.17e-4	1.85e-2	3.11e-2
WB Early Dose (Rem)						
At 1 km	2.81e-4	5.69e-3	7.20e-3	6.03e-4	1.14e-1	1.28e-1
At 10 km	1.79e-5	3.50e-4	2.41e-4	4.10e-5	2.65e-2	2.71e-2
WB Chronic Dose at 1 km (Rem)						
Inh + Grd	7.19e-4	2.55e-2	1.75e-2	4.52e-3	1.57e-1	2.05e-1
Ingestion	1.43e-3	3.45e-2	2.71e-2	1.41e-2	5.90	5.97
Total	2.15e-3	6.00e-2	4.46e-2	1.86e-2	6.06	6.18
WB Chronic Dose at 10 km (Rem)						
Inh + Grd	4.74e-5	1.71e-3	8.56e-4	3.12e-4	3.64e-2	3.93e-2
Ingestion	9.88e-5	2.37e-3	1.87e-3	9.86e-4	1.37	1.38
Total	1.46e-4	4.08e-3	2.73e-3	1.30e-3	1.40	1.42
Cancers						
Sum Organs	6.19e-4	3.79e-3	4.99e-2	2.73e-2	1.74	1.82
WB	2.23e-4	3.53e-3	8.53e-3	4.55e-3	3.54	3.56
Population Dose (Man-Rem)						
WB	1.41	22.33	54.1	28.93	2.24e+4	2.25e+4

5.7 TARGET FACTORY ANALYSIS

The target factory facility processes a total of 400,000 and 580,000 targets per day for Osiris and SOMBRERO, respectively. Hence, the facility is expected to handle a daily flow of tritium of 1020 grams for Osiris and 1400 grams for SOMBRERO. For both reactors, the rate of target production is maintained at the rate of usage to minimize the amount of stored tritium in the fabricated fuel targets. The total tritium inventory along the production line is limited to only 300 g. Even though 200 g of this tritium is stored in two liquid cryogenic containers, surrounded by evacuated chambers making it very unlikely for the tritium to be released in case of an accident, we still assumed that a worst accident scenario should involve the release of the total 300 grams of tritium. Table 5.19 shows the potential off-site doses produced during such an accident. As shown in the table, the maximum WB early dose projected as a result of a severe accident involving the target factory of either reactor designs would be 2.7 rem. Therefore, no evacuation plans are required.

Table 5.19. Off-Site Doses Due to Tritium Release from Target Factory

Prompt Dose at 1 km (Rem)	
WB	0.35
BM	1.28
Lung	2.80
LLI	0.44
WB Early Dose (Rem)	
At 1 km	2.70
At 10 km	0.63
WB Chronic Dose at 1 km (Rem)	
Inh + Grd	3.72
Ingestion	139.24
Total	142.95
WB Chronic Dose at 10 km (Rem)	
Inh + Grd	0.86
Ingestion	32.25
Total	33.11
Cancers	
Sum Organs	41.11
WB	83.40
Population Dose (Man-Rem)	
WB	5.29e+5

5.8 FUEL REPROCESSING FACILITIES

Most of the tritium present in SOMBRERO's fuel reprocessing facility is located in its cryogenic distillation system and the desiccant bed used to absorb the HTO from He. The tritium inventory in the distillation system during continuous operation is 13 g and the inventory of the desiccant beds during two-hours of operation is 61 g. At the onset of an accident, the tritium released from the two systems is vented to an evacuated tank and hence disallowing any tritium release. However, a failure in the venting system and 100% release of the tritium contained in SOMBRERO's fuel reprocessing facility would result in a WB early dose of 676 mrem at the site boundary (1 km).

On the other hand, in the fuel reprocessing facility of Osiris constant tritium inventories exist in the cryogenic distillation system (9.5 g) and the vacuum pumps from the vacuum disengager. The vacuum disengager is used to separate T_2 from Flibe by the use of vacuum pumps capable of maintaining low pressure. If the pumps are on stream for one-hour, their tritium inventory would be 44 g. Once again, assuming a venting system failure and 100% release of the 53.5 grams of tritium during an accident would result in a WB early dose of 482 mrem. Table 5.20 shows the different off-site doses expected during accidents involving the fuel reprocessing facilities of both SOMBRERO and Osiris.

5.9 NUCLEAR GRADE COMPONENTS

N-Stamp nuclear grade components are only required if the estimated off-site dose released is above the 25 rem limit. As shown in the previous analysis, none of the two reactor components would produce an off-site whole body early dose in access of 25 rem during a conservative accident scenario. However, a total release of the Flibe or Li_2O radioactive inventories would produce an off-site dose which exceeds the 25 rem limits. In such a case, some N-Stamp components would be required. A total release is quite impossible due to the lack of energy sources sufficient to mobilize most of the Flibe or Li_2O. Therefore, we conclude that none of the components (from either reactor) would require nuclear grade materials. Also, none of the fuel reprocessing facilities proposed for SOMBRERO and Osiris would produce more than 1 rem at the onset of an accident, allowing them to avoid the N-Stamp requirements. Similarly, due to the low tritium inventory present in the target factory at any moment (300 g), we can also avoid the use of nuclear grade components in the proposed target factory.

Table 5.20. Off-Site Doses Due to Tritium Release from Fuel Reprocessing Facility

	SOMBRERO	Osiris
Prompt Dose at 1 km (Rem)		
WB	0.09	0.06
BM	0.32	0.23
Lung	0.70	0.50
LLI	0.11	0.08
WB Early Dose (Rem)		
At 1 km	0.68	0.48
At 10 km	0.16	0.11
WB Chronic Dose at 1 km (Rem)		
Inh + Grd	0.93	0.66
Ingestion	34.81	24.83
Total	35.73	25.49
WB Chronic Dose at 10 km (Rem)		
Inh + Grd	0.22	0.15
Ingestion	8.07	5.75
Total	8.28	5.90
Cancers		
Sum Organs	10.28	7.33
WB	20.85	14.87
Population Dose (Man-Rem)		
WB	1.32e+5	9.42e+4

5.10 COMPARISON OF SOMBRERO AND OSIRIS

The SOMBRERO and Osiris reactor designs have distinct favorable safety characteristics. Because of the double wall layout used in SOMBRERO, the biological dose rate behind the steel-reinforced concrete shield is low enough to allow hands-on maintenance inside the IHX enclosures within a day after shutdown. The dose rate after shutdown behind the 3 meter biological shield of Osiris is only 0.11 μrem/hr allowing for hands-on maintenance. However, only remote maintenance is allowed in the space between the chamber and shield of both reactors. The chamber and shield of both reactor designs qualify for near surface burial as Class A low level waste. Using the NRC waste disposal limits for solid waste, both the Li_2O solid breeder and Flibe could qualify for shallow land burial as Class C and Class A low level wastes, respectively. However, Flibe has to be in solid form before such disposal can take place and the feasibility/practicality of such a process has to be determined.

Some tritium does reach the off-site environment during normal operation. The reactor system, the reactor building, the fuel reprocessing facility, and the target factory are the major sources of routine release of tritium. Assuming a barrier factor of 10^6, the doses from the atmospheric routine release of tritium from SOMBRERO and Osiris to the maximally exposed individual are 0.93 and 2.43 mrem/yr, respectively. Both values are far below the 10 mrem/yr EPA current effluent limit. The site boundary is assumed to be at 1 km from the point of release. The off-site doses caused by an accidental release of radioactivity from both reactor designs are dominated by the dose resulting from the off-normal release of tritium. During an accident, the maximum vulnerable inventory of tritium in SOMBRERO is 182.5 g. Most of the tritium (162 g) is contributed by the Li_2O granules. On the other hand, due to the small tritium inventory in Flibe salt (1 g), the maximum vulnerable inventory of tritium in Osiris is only 12.7 g. The estimated off-site whole body (WB) early dose released from SOMBRERO due to a highly unlikely sequence of simultaneous accident scenarios involving, the reactor chamber, biological shield, breeder, and tritium is 2.22 rem. This dose is below the 5 rem level where evacuation plans are needed and far below the 25 rem value recommended for this study by the oversight committee as a threshold for avoidance of early fatalities. Assuming similar accident scenarios, the Osiris design would result in a WB early dose of only 128 mrem.

An accident analysis involving the target factory facility showed that a 100% release of the 300 grams of tritium expected to be present inside the facility at any moment would result in a WB early dose at the site boundary of only 2.70 rem, which again is below the limits required for public evacuation. Finally, an accident resulting in the release of the total inventory of tritium existing in the fuel reprocessing facilities of SOMBRERO and Osiris would produce off-site doses of only 676 and 482 mrem, respectively. The very low off-site dose for either reactor designs

eliminates the need for N-Stamp nuclear grade reactor components, which are only required if the dose exceeds the 25 rem limit.

5.11 REFERENCES FOR CHAPTER 5

5.1 R. O'Dell et al., "User's Manual for ONEDANT: A Code Package for One-Dimensional, Diffusion--Accelerated, Neutral Particle Transport," Los Alamos National Laboratory, LA-9184-M, (1982).

5.2 D.L. Henderson and O. Yasar, "DKR-ICF: A Radioactivity and Dose Rate Calculation Code Package," University of Wisconsin, UWFDM-714, Vol. 1 (April 1987).

5.3 M.A. Gardner and R. J. Howerton, "ACTL: Evaluated Neutron Activation Cross Section Library - Evaluation Techniques and Reaction Index," Lawrence Livermore National Lab, UCRL-50400, Vol. 18 (1978).

5.4 L.J. Porter, "Upgrade of a Fusion Accident Analysis Code and Its Application to a Comparative Study of Seven Fusion Reactor Designs," Massachusetts Institute of Technology PFC/RR-89-10 (June 1989).

5.5 User's Guide for AIRDOS-PC, Version 3.0, EPA 520/6-89-035, U. S. Environmental Protection Agency, Office of Radiation Programs, Las Vegas, NV (Dec. 1989).

5.6 Nuclear Regulatory Commission, 10CFR part 20, "Standards for Protection Against Radiation," (1975).

5.7 Nuclear Regulatory Commission, 10CFR part 61, "Licensing Requirements for Land Disposal of Radioactive Waste," Federal Register, FR 47, 57446 (1982).

5.8 S. Fetter, E. Cheng, and F. Mann, "Long Term Radioactive Waste from Fusion Reactors," *Fusion Engineering and Design*, **13**, 239 (1990).

5.9 USNRC Regularity Guide 1.145/Rev.1 (February 1983).

5.10 J.P. Holdren et al., "Report of the Senior Committee on Environmental, Safety, and Economic Aspects of Magnetic Fusion Energy," Lawrence Livermore National Laboratory, UCRL-53766 (1989).

5.11 S.J. Piet et al., "Initial Experimental Investigation of the Elemental Volatility from Steel Alloys for Fusion Safety Applications," Idaho National Engineering Laboratory, EGG-FSP-8459, (April 1989).

5.12 R.W. Moir et al., "HYLIFE-II Progress Report," Lawrence Livermore National Laboratory, UCID-21816 (1990).

Chapter 6

Reliability, Availability, and Maintainability Assessment

CONTENTS

6.1 INTRODUCTION 6-1
6.2 AVAILABILITY ASSESSMENT 6-1
6.2.1 Approach and Methodology 6-1
6.2.2 Plant Availability Goal 6-2
6.2.3 Systems Availability Allocations 6-2
6.3 MAINTAINABILITY OF THE OSIRIS PLANT 6-5
6.4 MAINTAINABILITY OF THE SOMBRERO PLANT 6-9
6.5 REMOTE HANDLING CAPABILITY & UTILIZATION CONSIDERATIONS . 6-10
6.6 REFERENCES FOR CHAPTER 6 6-14

6.0 RELIABILITY, AVAILABILITY, AND MAINTAINABILITY ASSESSMENT

6.1 INTRODUCTION

This section describes the reliability, availability, and maintainability (RAM) assessments performed on the SOMBRERO and Osiris reactor plants. The primary objectives are to assess the RAM aspects of the two designs and to establish availability goals for the major plant systems to aid in planning future development efforts.

6.2 AVAILABILITY ASSESSMENT

6.2.1 Approach and Methodology

The SOMBRERO and Osiris power plant designs are not detailed enough to estimate plant availability with any confidence. The approach, therefore, is to first make a rough estimate of the availability of the plant subsystems and then to use these estimates to establish availability goals for the major plant systems that combine to the give the desired availability goal for the entire plant. The initial estimates are in essence weighting factors for allocating system availability goals.

For RAM assessment purposes, each reactor plant is partitioned into four major systems: driver, reactor, target (fabrication, injection, and tracking), and energy conversion/balance-of-plant. In assessing the availability, each major system is divided further into several functional subsystems, and an achievable availability is estimated for each subsystem. The estimated availability is determined based on existing similar systems or comparable systems taking into account expected component lifetime, equipment random failure rate, power output fractions, manufacturing process capacity factor, and in-process storage capacity. For systems in which RAM data are nonexistent, the estimated availability is projected with the consideration of the complexity and technology risk associated with the system: a projected availability of 0.9 for systems of high complexity, 0.99 for systems of moderate complexity, and 0.999 for systems of low complexity.

Based on the estimated subsystem availability, the overall plant availability goal is apportioned to individual subsystems according to a model described in Ref. 6.1. The availability goal for each subsystem is:

$$A_i = (A_{goal})^{w_i}$$

where

A_{goal} = availability goal for plant,

w_i = $\ln(A_s) / \ln(A_p)$ = weight factor for the i-th subsystem,

A_p = estimated availability for power plant, and

A_S = estimated availability for i-th subsystem.

6.2.2 Plant Availability Goal

The plant availability is defined as the actual annual MWh output divided by the potential annual MWh output of the plant. An overall plant availability goal of 75% is assumed for the IFE reactor plants so as to be comparable to other fusion reactor studies and current large electric power generating systems (e.g., the conventional nuclear power systems, which are operating with an availability of 60 to 80%, and up to 90% for CANDU reactors, which have on-line refueling). To achieve this goal, the required effective operation availability is 81% after allowing for an assumed downtime of four weeks each year to account for preventive maintenance activities.

6.2.3 Systems Availability Allocations

Preliminary estimates indicate that the availability of the SOMBRERO power plant is 0.68, and the availability of the Osiris power plant is 0.70. The high reliability of the KrF driver is due mainly to spare amplifiers (64 provided while 60 normally used). The estimated availability values for the major SOMBRERO and Osiris systems and subsystems are summarized in Tables 6.1 and 6.2, respectively.

Availability allocation is apportioned for plant systems from the top down according to the reliability and maintainability characteristics of the systems in such a way as to achieve the plant availability goal. The availability apportionment indicates the optimum balance of availabilities for all systems in the plant. The allocation process serves as a means of assessing the design and defines availability improvement targets in system design refinement. These improvements include better system design, application of redundancy, changes in maintenance concepts, or combination of these options.

Using an effective operation availability goal of 81% for the IFE reactor system and the estimated system availability values in the above section, the availability goals for various SOMBRERO and Osiris plant systems are established as indicated in Table 6.3. Comparing these goals to the rough estimates given in Tables 6.1 and 6.2 indicates that for both plants, 4-5% improvements are needed for the drivers, reactors, and target systems, and a 2% improvement is required for the BOP availability in order to meet the overall plant availability goal. However, since RAM data for these systems are mostly nonexistent, or at best available from limited experimental results, these results should not be considered conclusive. More definitive assessments will require detailed designs and evaluations of the plant systems, additional data

obtained from extended test periods, and eventually the integration of driver, target, reactor, and BOP systems in an experimental test facility.

Table 6.1. Estimated Availability for SOMBRERO Plant Systems

System	Complexity Rating	Estimated Availability	Based on
Driver Systems		**0.8877**	
Front End Waveform Generation	Low	0.9990	System complexity
Intermediate Amplifying	Moderate	0.9900	System complexity
Final Amplifying	High	0.9985	Estimated MTTR
Optical Compression & Final Focus	High	0.8989	Estimated MTTR
Reactor Systems		**0.8896**	
Reactor Vacuum Vessel	Moderate	0.9620	Estimated MTBF, MTTR
First Wall and Blankets	Moderate	0.9360	Estimated MTBF, MTTR
Fluidized Bed Transport	Low	0.9960	Conventional system
Vacuum	Low	0.9920	Estimated MTBF, MTTR
Target Systems		**0.8991**	
Target Injection	High	0.9000	System complexity
Target Cryogenics	Low	0.9990	System complexity
Tritium Recovery	Low	1.0000	Assumed storage
Target Manufacture	Moderate	1.0000	Assumed capacity
Energy Conversion & BOP Systems		**0.9604**	
Heat Exchange Loop	Moderate	0.9730	Estimated MTBF, MTTR
Turbines	Low	0.9900	Conventional system
Heat Recovery and Rejection	Low	0.9990	Conventional system
Electrical Equipment	Low	0.9990	Conventional system
Instrumentation and Controls	Low	0.9990	Conventional system
Overall Power Plant		**0.6819**	

Table 6.2. Estimated Availability for Osiris Plant Systems

System	Complexity Rating	Estimated Availability	Based on
Driver Systems		**0.8733**	
Ion Injector	Moderate	0.990	System complexity
Induction Linac and PFN	High	0.900	System complexity
Beam Combiner & Final Focusing	Moderate	0.990	System complexity
Vacuum and S.C. Cooling	Moderate	0.990	System complexity
Reactor Systems		**0.9211**	
Reactor Vacuum Vessel	Moderate	0.962	Estimated MTBF, MTTR
First Wall and Blankets	Moderate	0.973	Estimated MTBF, MTTR
Flibe Transport	Low	0.992	Estimated MTBF, MTTR
Vacuum	Low	0.992	Estimated MTBF, MTTR
Target Systems		**0.8991**	
Target Injection	High	0.900	System complexity
Target Cryogenics	Low	0.999	System complexity
Tritium Recovery	Low	1.000	Assumed storage
Target Manufacture	Moderate	1.000	Assumed capacity
Energy Conversion & BOP Systems		**0.9604**	
Heat Exchange Loop	Moderate	0.973	Estimated MTBF, MTTR
Turbine	Low	0.990	Conventional system
Heat Recovery and Rejection	Low	0.999	Conventional system
Electrical Equipment	Low	0.999	Conventional system
Instrumentation and Controls	Low	0.999	Conventional system
Overall Power Plant		**0.6946**	

Table 6.3. Allocated Availability Goals for SOMBRERO and Osiris

	Allocated Availability Goals	
Systems	**SOMBRERO**	**Osiris**
Driver	0.94	0.93
Reactor	0.94	0.95
Target	0.94	0.94
BOP	0.98	0.98

6.3. MAINTAINABILITY OF THE OSIRIS PLANT

In an effort to develop an approach for remote maintenance of the Osiris reactor, an analysis was performed on the sequence and type of activities required in order to remove and replace the Osiris vacuum cover, fabric blanket assemblies, and the maintenance of other reactor support equipment. This analysis resulted in the definition of "theaters" and "classes" of operations. Theaters of operation are defined by geometric constraints which are primarily driven by available access points, and classes of operation are defined by the physical constraints of payload (weights of components to be removed/replaced) and available work envelope (dictated by plausible reach limits of remote handling (RH) equipment and available work space within the internals of the reactors which might impose joint singularity concerns). For the purposes of this study, the theaters of operation are defined as follows:

- Reactor Building / Reactor Top-Hat Area
- Driver Seal Flange Area
- Reactor Internals
- Hot Cell and Maintenance Area.

The theaters of operation were then cross-compiled with the identified activities required for equipment maintenance, removal, and/or replacement. An evaluation of the activities was performed to define the classes of operations that would be conducted. The class of operation is typically characterized by the size and weight range of the components that need to be handled from each of the access points and by the available work envelope in which to conduct the RH system-supported operation. The basic functional specifications for the RH equipment are normally developed from this information. However, due to the conceptual nature of the IFE reactor designs, it would be premature to try to detail discreet specifications for the RH

equipment. In an effort to determine a baseline case for overall RH equipment operational envelopes and equipment and component handling sequences (for maintenance activities), the activities that define the classes of operation for the Osiris reactor design are as follows:

- High and Low Pressure Flibe Inlet Pipe Disconnect
- Driver Seal Flange Unbolting and Retraction
- Vacuum Chamber Cover Unfastening and Interference Removal
- Vacuum Chamber Cover and Attached Internals Removal
- Reinstallation.

The Osiris reactor building size is dictated by the maintenance handling requirements for the vacuum vessel cover and reactor internals. These requirements are due to the complexity of refurbishment operations associated with these components and constraints which dictate that the cover and internals be removed as one piece. The physical size of these components and the complexity of refurbishment operations suggest that it is prudent to "replace in kind" rather than "refurbish in place." With this in mind, it is apparent that the remote handling equipment needs to have common access to both the reactor building and the hot cell/maintenance areas. To accommodate this requirement, a large movable shield wall is provided. This shield wall is located between the reactor building and hot cell. The crane bay containing all of the overhead-operated remote handling equipment is open to both (Figs. 6.1 and 6.2). The remote handling equipment is protected from neutron activation during reactor operation by extending the shield wall in place and locating the equipment at the far end of the hot-cell facility. The hot cell contains both a clean room in which to store the new replacement cover and reactor internals (thus isolating them from the old contaminated internals being removed) and a hot storage area, which is a large temporary containment that houses the old components being removed.

The range of tasks required to be performed by the remote handling equipment is not trivial. It is quite apparent that the majority of the tasks to be performed will require significant coordination and the probable use of hybrid systems (in which there will be the use of relatively simple high payload capacity rigid or semi-rigid manipulators/crane system in conjunction with a highly dexterous, force-reflective manipulator system, and special tooling). In addition, great attention to detail will need to be paid to the logistics of component and equipment handling and maintenance requirements. Each of these things will have the potential for significant impact on the overall design of these facilities.

It is worthy to note that design impact and integration considerations of automated systems, advanced work systems (robotics), and remote handling equipment at the conceptual design stage of a project is something of a novel practice. Retrofit operations are extremely

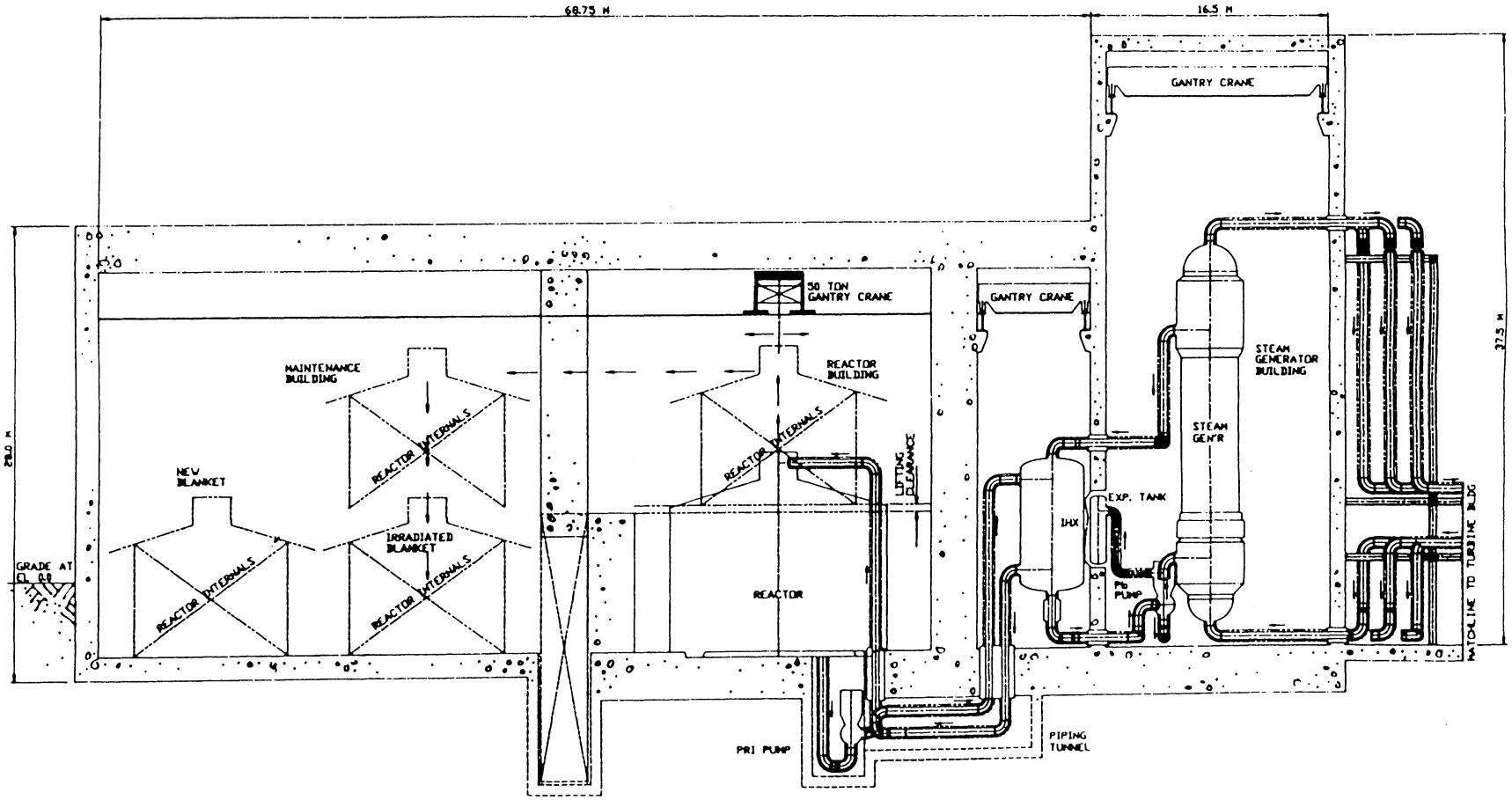

Fig. 6.1. Cross section view of Osiris maintenance procedure.

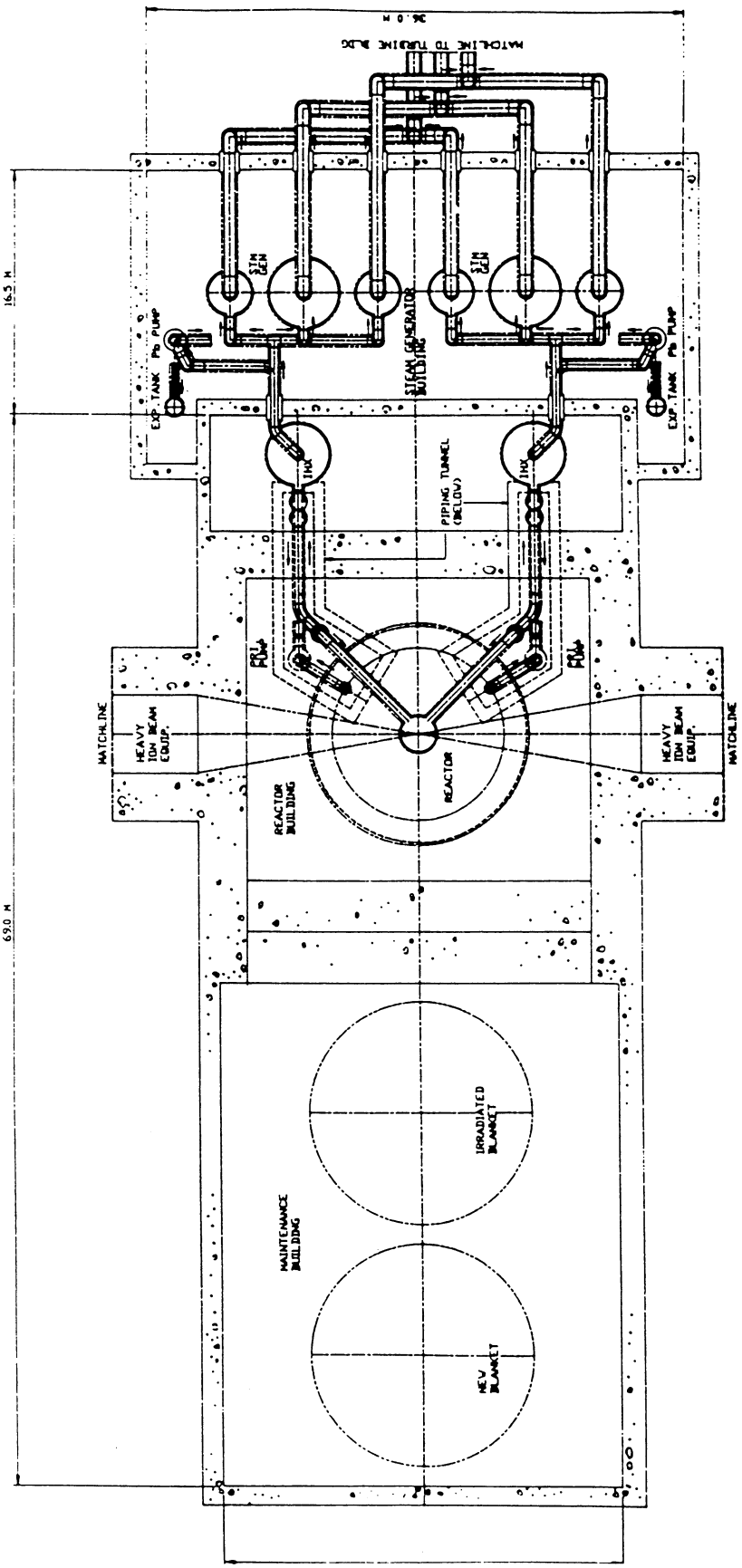

Fig. 6.2. Plan view of Osiris maintenance procedure.

design stage of a project is something of a novel practice. Retrofit operations are extremely expensive and not nearly as successful as accomplishing these tasks by design. A review of current practices in existing nuclear and hazardous materials handling facilities (for retrofit operations in using this type of equipment) and the projected remote maintenance and operation requirements of the current tokamak designs indicates that this practice of advanced work systems integration at the conceptual design stage may be well justified.

6.4 MAINTAINABILITY OF THE SOMBRERO PLANT

A methodology similar to the Osiris was used to develop an approach for remote maintenance of the SOMBRERO reactor. An analysis was performed on the sequence and type of activities required in order to remove and replace the reactor module assemblies and the optics within the reactor building. This analysis resulted in the definition of theaters and classes of operations for the SOMBRERO reactor. For the purposes of this study, the theaters of operation are defined as follows:

- Central Reactor Building Volume
- Outer Annular Reactor Building Volume
- Intermediate Heat Exchanger (IHX) Vault
- Optics within the Reactor Building
- Maintenance Hot Cell and Lay Down Area.

The theaters of operation were then cross-compiled with the identified activities required for equipment maintenance, removal, and/or replacement. An evaluation of the activities was performed to define the classes of operations that would be conducted. In an effort to determine a baseline case for overall remote handling equipment operational envelopes and equipment and component handling sequences (for maintenance activities), the activities that would define the classes of operation for the SOMBRERO reactor design are as follows:

- Upper Plenum / Inlet Pipe Removal
- Module Removal/Replacement
- Mirror and Optics Maintenance
- IHX Maintenance
- Reactor Support Equipment Maintenance
- Beam Handling Equipment Maintenance
- Hot Cell Operations.

Due to the large physical size of reactor building (dictated by the optics requirements), an innovative approach to crane operations and rigging and handling of components is necessary. For this case, both the polar crane and annular crane make use of the National Institute for Standards and Technology (NIST) high payload automated crane concept. This concept employs a modified Stewart platform where the hook and block-and-tackle are normally located. This platform allows for very stable control of heavy offset payloads at long distances from the cable drum and trolley assembly. The most unique design feature of SOMBRERO is the remote handling equipment designed to handle the chamber modules. Each of these modules is approximately 24-m tall and 8-m deep. Due to space restrictions in the center reactor building volume, each of these modules is designed to be removed and replaced one at a time. The removal sequence dictates that the module be lowered to the bottom of the inner cylindrical chamber, installed on a polar carriage assembly (which accommodates radial positioning), and tilted out of the lower access door via a transport carriage, through the annular space and into the hot cell facility (Figs. 6.3 and 6.4). This whole evolution is analogous to current practices in fuel bundle handling systems currently in use.

6.5 REMOTE HANDLING CAPABILITY AND UTILIZATION CONSIDERATIONS

There are several factors which affect remote handling equipment capabilities. These include, but are not limited to, the current trends in remote handling equipment development within the international community, the development efforts for an integrated graphics/CAD based control architecture (supervisory control system), the class of operations to be performed, the geometric limitations imposed by the intended theater of operation, the amount of technology transfer (from other industries and/or applications) to IFE's domain set, and the level of integration of the envisioned remote handling equipment with the baseline design of IFE.

The previously-stated maintenance operations may be considered to be rigorous for the level of remote handling equipment development that could be expected within the next ten years. It should be noted, however, that these operations are typically predicated upon the current level of implementation of remote systems within the nuclear community in this country as well as abroad. Several notable examples of remote-handling system developments that belie the predicted trends assumed above include those prototype systems currently being developed, tested, and demonstrated by various National Laboratories and industrial organizations to address the needs of the DOE/DoD Environmental Restoration and Waste Management Programs. These would include the hybrid multi-manipulator systems, fused sensor packages, and graphics-based control architectures being developed for underground storage tank remediation. Also, from the European offshore service community, several generations of a graphics-based supervisory

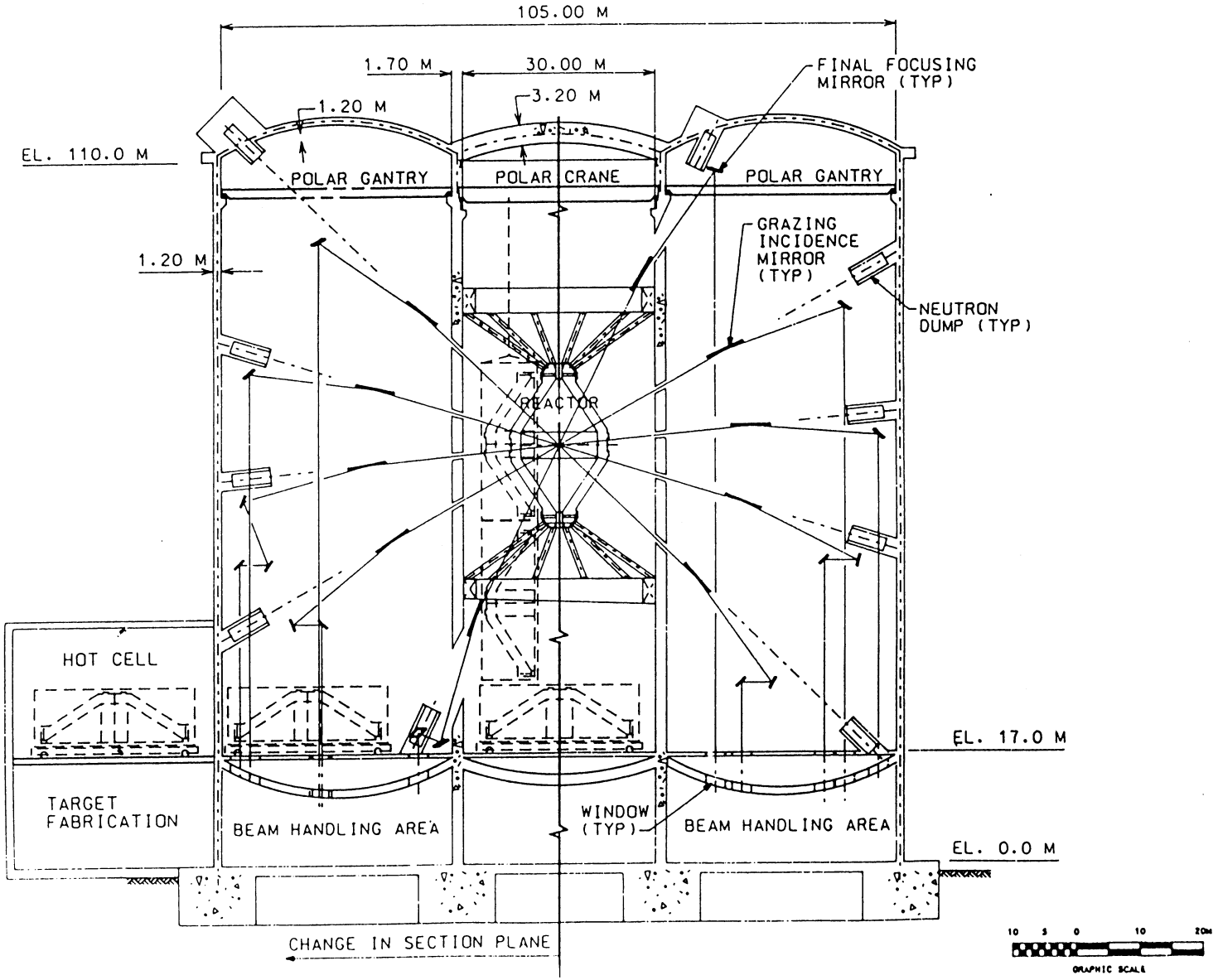

Fig. 6.3. Cross section view of SOMBRERO maintenance procedure.

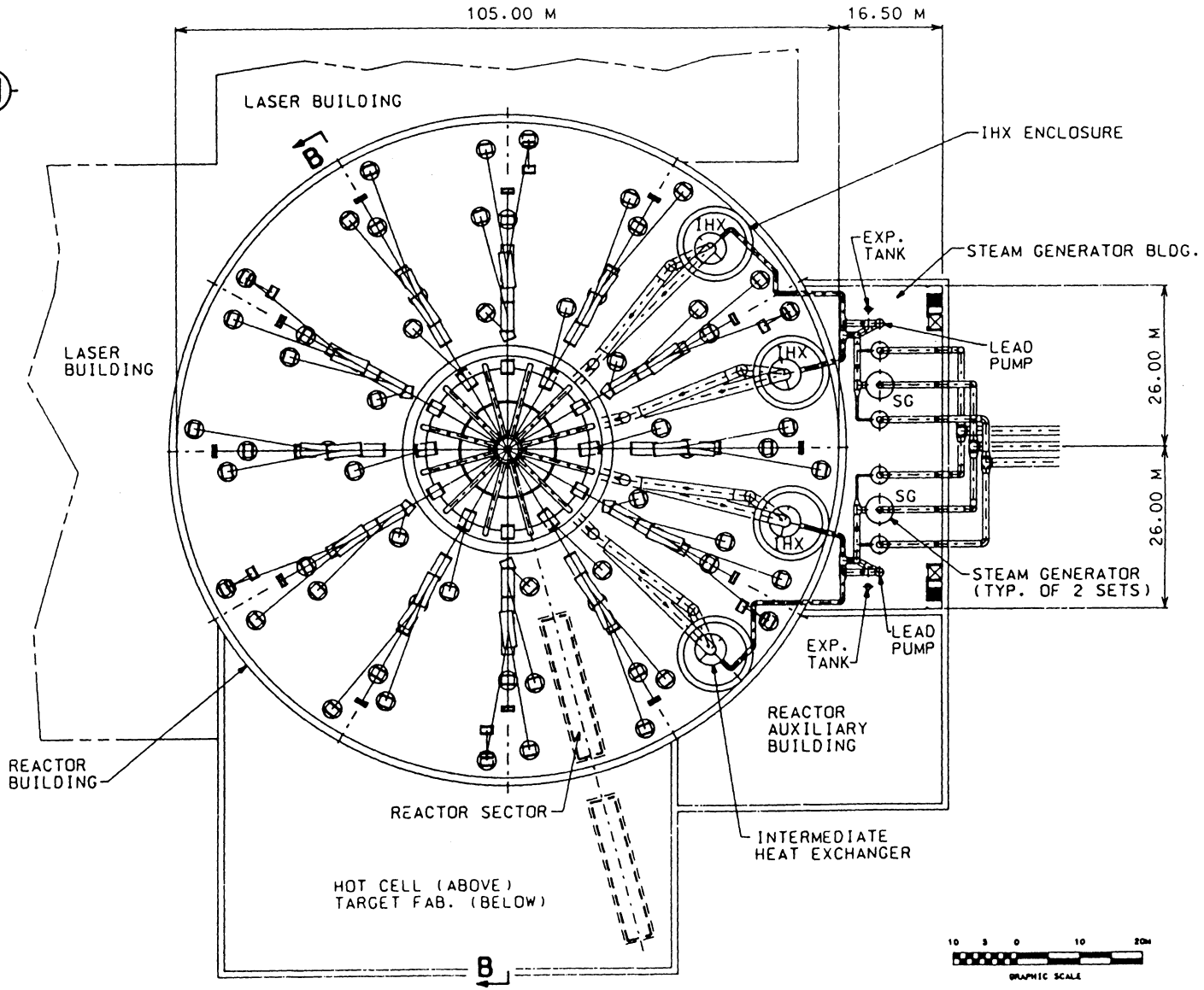

Fig. 6.4. Plan view of SOMBRERO maintenance procedure.

control system has been developed, tested, demonstrated, and implemented. These systems are controlling remotely operated vehicles (ROVs) with manipulator based NDT and work-package end effectors (e.g., cleaning and cutting tools) in a dynamic unstructured 3–D environment associated with sub-sea operations and maintenance activities at extreme depths. (They have been tested at depths of 1000 meters).

There are several assumptions underlying the remote maintenance approach discussed here:

- The plant is assembled with appropriate reference marks, types of bolts, fittings, and accessories so that robotic equipment may be used to its highest potential.
- Task performance is automated to the greatest possible extent, and the remote handling equipment is an integral component of the facility design, construction, and operation.
- A computer data base and documentation including a 3–D model are available in conjunction with physical reference points in IFE allowing automatic and precision indexing of robots.

Each of these assumptions is based upon the complexity of IFE and on the technology-based driver for a graphics-based control system. Given the current state of the art of positioning systems and their integrated use in closed loop control of remote system hardware, it is very likely that a combination of these positioning systems and a graphics-based control architecture would allow for the automated deployment and positioning of the remote handling equipment to the necessary degree of accuracy. Once again, these assumptions are based upon observations of currently available control systems and sensor packages that are being used in other industrial theaters of operation and the continued research and development efforts to further these applications. These types of systems and research trends can be observed in the manufacturing (flexible automation), construction (automated heavy construction equipment with integral force reflective feedback), environmental restoration (remote systems being developed for DOE/DoD cleanup operations), and the military (Bradley tank operating systems) sectors.

Other assumptions are based on considerations that would apply whether one were using automated or tele-presence type remote-handling equipment. These assumptions are as follows:

- The remote handling equipment electronics and support equipment (cameras, etc.) would be able to tolerate the intense radiation fields
- All of the required remote handling equipment is available when needed with no time scheduled for the design, fabrication, and testing of the requisite equipment

- All access locations are fully staffed and have a full complement of equipment and necessary support services required to allow parallel, simultaneous operations where required.

The configuration concepts of several state-of-the-art remote maintenance equipment are presented in Appendix E.

6.6 REFERENCES FOR CHAPTER 6

6.1 D. Orvis et al., "Guidebook for RAM Analysis," General Atomics Company Technical Report, ONWI-334 (April 1981).

Chapter 7

Technology Assessment

CONTENTS

7.1 APPROACH AND METHODOLOGY 7-1
7.2 OSIRIS ISSUES AND DEVELOPMENT NEEDS 7-2
7.2.1 Reactor Chamber 7-2
7.2.2 Shielding 7-5
7.2.3 Reactor Building 7-5
7.2.4 Flibe Pumps and Ducting 7-5
7.2.5 Intermediate Heat Exchanger 7-6
7.2.6 Steam Generators 7-6
7.2.7 Power Conversion System 7-7
7.2.8 Heavy Ion Beam Driver 7-7
7.2.9 Target Fabrication 7-9
7.2.10 Target Injection 7-9
7.3 TECHNOLOGY ASSESSMENT RATINGS FOR OSIRIS 7-9
7.4 SUMMARY OF DEVELOPMENT PRIORITIES FOR OSIRIS 7-19
7.5 SOMBRERO ISSUES AND DEVELOPMENT NEEDS 7-21
7.5.1 Reactor Chamber 7-21
7.5.2 Shielding 7-23
7.5.3 Final Optics 7-24
7.5.4 Lithium Oxide Transport and Ducting 7-24
7.5.5 Intermediate Heat Exchanger 7-25
7.5.6 Steam Generator 7-25
7.5.7 Reactor Building 7-25
7.5.8 Power Conversion 7-26
7.5.9 Driver 7-26
7.5.10 Target Fabrication 7-27
7.5.11 Target Injection 7-28
7.6 TECHNOLOGY ASSESSMENT RATINGS FOR SOMBRERO 7-28
7.7 SUMMARY OF DEVELOPMENT PRIORITIES FOR SOMBRERO 7-37
7.8 GENERIC IFE ISSUES 7-39
7.8.1 Target Design Innovations 7-39
7.8.2 Reactor Modeling 7-40
7.8.3 Low Activation and Neutron-Resistant Materials 7-40
7.8.4 Remote Maintenance 7-43
7.9 TECHNOLOGY ASSESSMENT RATINGS FOR GENERIC ISSUES 7-43
7.10 SUMMARY 7-46
7.11 REFERENCES FOR CHAPTER 7 7-46

7.0 TECHNOLOGY ASSESSMENTS

7.1 APPROACH AND METHODOLOGY

Many assumptions have been made during this study about materials capabilities, component availability and performance, and cost. In this chapter we attempt to put all this in perspective and assess the technical issues, development needs, and level of urgency. A semi-quantitative approach is taken with issues weighted on a scale from zero (low) to 100 (high) in increments of 25. The issues and weighting factors are given in Table 7.1.

Table 7.1. Technical Issues and Weights

Technical Immaturity	10%
Critical Technology	30%
High Development Cost	30%
Long Lead Time	20%
% Cost in Experiments	10%

Note that they are defined in terms of concerns (e.g., technical immaturity rather than maturity) so that a high score always indicates a problem. The weightings are obviously judgmental. Technical immaturity is far less important than critical technology (i.e., no alternative technologies or approaches exist) or development cost. These last two are considered the most important. Long lead time is also an issue. An example of an issue with a long lead time would be materials development. Some account is also made of the greater developmental uncertainty when many experiments are required.

The areas covered for Osiris and SOMBRERO are reactor chamber, shielding, final beam transport, coolant and ducting, IHX, steam generator, power conversion, driver, and target fabrication and injection. Other areas are issues generic to IFE that are of concern regardless of the specifics of the reactor chamber and driver: target design and innovations, systems modelling, low activation materials, and remote maintenance. The issues for each reactor concept are discussed and then generic issues are addressed. Tabulations using the criteria in Table 7.1 are then given.

7.2 OSIRIS ISSUES AND DEVELOPMENT NEEDS

7.2.1 Reactor Chamber

The reactor chamber uses a woven carbon fabric blanket with flowing liquid Flibe as neutron absorber and coolant. Flibe also weeps to the surface of the fabric, providing a sacrificial protective layer. Technical issues are rep-rate, fabric weave control, fabric stitching, blanket replacement, effect of shock waves, carbon/Flibe chemistry and surface physics, and tritium extraction from the Flibe. Each of these is discussed below.

Chamber Repetition Rate. The maximum allowable repetition rate for an Osiris chamber will be determined by the rate at which vaporized Flibe can be recombined and condensed. Simple calculations indicate that the vapor pressure returns to a low enough level to allow beam propagation fast enough to allow a repetition rate of up to 10 Hz. If the condensation time is much longer than currently estimated (i.e., by a factor of 10), this would be a feasibility issue for Osiris. A factor of two is not critical since the cost of electricity is relatively insensitive to repetition rate over this range. Uncertainties can probably be removed with analysis and small-scale experiments, so the lead time and costs to resolve this issue should both be small.

Fabric Weave and Flow Control. The unique feature of the Osiris reactor chamber is the flexible fabric first wall, which is protected by Flibe bleeding through the weave. It is important to control this bleed rate with high precision. The correct weave density and fabric construction must be found to allow sufficient flow to coat the surface of the fabric and replenish vaporized Flibe while preventing excess flow that could lead to dripping. If too much Flibe bleeds through it will not run down along the roof but will fall off in a rain. This raises concerns about droplets in the path of the next beam pulse and the possibility of an increase in the vapor pressure due to the presence of heated droplets.

Carbon fabric can be woven over a wide range, from see-through to as tight as a seat belt; therefore, it is likely that the proper weave can be established. It can also be combined with solid carbon, carbon composites, and carbon felt. However, work is required to determine the flow of Flibe through carbon pores. Because Flibe doesn't wet carbon, hydraulic pressure is needed to drive it through the fabric. The required pressure depends on the Flibe surface tension and the characteristics of the carbon fabric. The Flibe droplets must coalesce into a continuous

film and not just bead up. Because of the non-wetting, this film must be supported through capillary tension by the bulk Flibe on the other side. This will require a fairly fine pore structure in the fabric, which places lower limits on hydraulic pressure.

This is a new and untried concept, and much more work is needed to demonstrate its feasibility. The development costs, however, should be low because simple, low cost experiments can validate the concept.

Fabric Stitching. The first wall/blanket is made up of carbon fabric panels stitched together to form a tent-like structure using an air mattress type of configuration to withstand the Flibe pressure. Because the Flibe first makes a high-speed pass down the first wall to limit temperature rise, the blanket assembly will be at least three carbon panels thick, all of which must be reliably stitched together. The stitches should be redundant, lightly stressed, and not exposed to the target X-rays. This technology is quite well established for such things as circus tents.

Blanket Replacement. Blanket fabrication must be done on-site at a location where the new blanket can be readily transported to the reactor vacuum chamber. Assuming annual replacements at most, an entire year is available for fabrication and checkout. Because there will be activation products in the hot Flibe in the bottom pool, remotely controlled removal and replacement systems will be needed.

Shock Waves. Target X-rays and debris will cause surface shocks on the first wall that will propagate into the blanket. Isochoric heating will also cause sudden pressurization of the solid material that will be relieved by expansion from the surface inward. Since any protective Flibe film that forms is likely to be held in place only by capillary tension with Flibe in the pores of the fabric, these complex shocks might be able to blow the film off the surface, creating falling droplets in the chamber. The pressure resulting from X-ray blowoff may overpower inward motion from isochoric heating and keep the film in place. The complex interaction of reflected shocks and bulk blanket motion could strip off the film, especially if its hold on the fabric is tenuous.

The impact of these shock waves is a significant feasibility issue. Because the processes are so complex and so little is known, the current technical maturity is considered low. The development needs may be high, because resolution requires accurate simulation, which is difficult to achieve without experimental verification. While code work can provide some

insight, it is unlikely that financial commitment to this concept would be made without results from quality experiments.

Fabric/Flibe Chemistry and Surface Physics. There are two aspects to the interaction between the molten Flibe and the carbon fabric: (1) chemistry, particularly HF, F_2, and H_2 reactions, and (2) the wetting of carbon by Flibe and possible coatings that may increase it. The compounds in (1) are gaseous and are released by tritium breeding and, possible, by hard X-rays. Unlike solid carbon, micron-sized carbon fiber cannot tolerate much chemical etching. The lack of wetting may be an advantage here, although escaping fluorine gas compounds may still cause problems.

Coating the carbon with another material could solve both the chemistry and wetting problems. Flibe does wet most metals. A thin (monolayer) coating of tungsten or molybdenum, which match carbon's thermal expansion, would solve the wetting and corrosion problems and may not produce that much activation. Because such thin layers may not require matching thermal expansion, boron, B_4C, beryllium, Be_2C, aluminum, and Al_2O_3 are also interesting possible coatings for carbon fabric. Much could be learned with small, inexpensive experiments.

Tritium Extraction. The Flibe exits the Osiris blanket at the top and cascades down the outside of the blanket, releasing tritium to the vacuum pumping system. Since tritium retention in Flibe is very low, in principle most of it can be extracted this way.

With an intermediate heat exchanger, complete removal of tritium from the Flibe stream is not required. It is desirable, however, in order to minimize vulnerable tritium inventory. More work is needed to determine if the cascade flow will remove enough tritium. If it doesn't, separate spray tanks and boost pumps will be needed to provide a fine mist and large Flibe surface area.[7.1]

The overall current technical credibility of this novel reactor concept must be considered to be fairly low. However, because much can be learned from fairly simple and inexpensive experiments, development needs may only be moderate in cost and time.

7.2.2 Shielding

The neutron flux is reduced several orders of magnitude by the Flibe blanket and pool. The exception is the beam penetrations. Biological shielding, which can be room temperature, is required around all sides of the vacuum chamber and possibly around much of the driver final focusing envelope. Almost any low activation material can be used for biological shielding: water, polyethylene, asphalt, sand, or, as in the current design, concrete. The limited amount of heat generated can be conducted to the surroundings. Access to the shielded regions is required for maintenance of the hardware inside.

Biological shielding technology has been well established in existing fusion experiments and in fission reactors. Development requirements should be low, including requirements for high material purity. The primary issue is cost of shield material (not development cost, which should be low), particularly long sections of the final beam transport section of the driver.

7.2.3 Reactor Building

The size and cost of the reactor building depends on the classification of the reactor. If the reactor components are non-nuclear grade, and the reactor is considered inherently safe, and the vulnerable tritium inventory is sufficiently low, then a tin shed will do. Otherwise, 2-3 m thick concrete walls are required. There is a good possibility that the former may be sufficient, or not much more. The main uncertainty is probably the tritium issue. The current design uses thick concrete walls, which also serve for biological shielding. If the N-stamp is eliminated, this shielding could be moved in closer, making it smaller, and a less expensive reactor building could be used. In any event, the current technical credibility of reactor buildings of this modest size is high and development requirements are low.

7.2.4 Flibe Pumps and Ducting

At least two types of Flibe pumps are required: one low and one high pressure. Flibe is compatible with Hastelloy and some stainless steels, and ordinary centrifugal pumps can be used. Graphite seals are especially attractive here, because the non-wetting by Flibe will reduce leakage, and chemical reactions should be minimal provided generated gases are removed upstream. Ducting is low pressure and modest diameter and is, therefore, less challenging than in conventional steam plants. It should be quite simple to provide a tritium barrier around the

pumps and pipes. The pumps and ducts must be thermally insulated, and heater tape is needed to prevent Flibe solidification.

7.2.5 Intermediate Heat Exchanger

The IHX has molten low-pressure Flibe at up to 630°C on one side and molten low-pressure lead or lead-based eutectic at up to 620°C on the other side. These temperatures are those in contact with the tube walls. The total heat transfer area is about 12,000 m^2, which can be met with two transportable heat exchanger cores roughly 4 x 8 x 3 meters in size. Key issues are lead chemistry, tritium permeation into the lead, effect of cross leakage should a tube fail, avoidance of solidification, and draining.

The Blanket Comparison and Selection Study[7.2] found that $Li_{17}Pb_{83}$ was more corrosive to stainless and ferritic steels than pure lithium, suggesting that it is the lead that is causing the problem. With ferritic steel, the temperature limit for lithium is around 600°C while it is below 500° for lithium-lead. With vanadium alloy, on the other hand, over 750° can be tolerated. Elemental additions to the liquid lead like titanium may serve as corrosion inhibitors. It is believed that the titanium reacts with carbon or nitrogen in the steel to form a protective layer of TiC or TiN. This method has generally been more successful than plasma-sprayed coatings, which can flake off. The Liquid Metals Handbook shows liquid lead to be compatible with Type-347 stainless to 630°C and low-alloy chrome-moly steel to 625°C. Inconel, surprisingly, is worse. The key issue is the purity of the lead. Technical credibility is considered moderate, and the development requirements are low.

7.2.6 Steam Generators

The lead side of the steam generator has the same corrosion issues as the IHX. Otherwise, they are similar to those using liquid sodium, which has a substantial technology base. Because the tubes are highly stressed, a key issue is the effect a tube failure has on the IHX. Some fail-safe means of depressurizing, such as blowout plates, must be considered. Like the IHX, the current technical credibility is considered moderate, and the development requirements are low.

7.2.7 Power Conversion System

Despite numerous attempts to develop advanced power conversion systems, conventional Rankine cycles using steam appear to be the best choice with moderate operating temperatures, such as those used with Flibe. Brayton cycles begin to be attractive at higher temperatures.

The main issue for the steam power conversion system is the heat rejection system. Because of the large land area needed for the driver, siting may be restricted to remote areas where cooling water could be limited. Dry air cooling must be considered, and this raises steam condensing temperature from 43°C to about 60°C. With 540°C steam temperature at turbine inlet, this increase in rejection temperature will reduce efficiency from 45% to about 43%, including air pumping loss. Because dry air cooling reduces costs of the site, the cooling towers, and the low pressure turbines (exit pressures are higher), the overall impact on plant economics could be small. These are design issues, however, and require little development.

7.2.8 Heavy Ion Beam Driver

The driver represents the most difficult engineering challenge of the entire IFE power plant. Nothing of this scale has ever been built with the combination of requirements that are discussed below.

Reliability. If we assume unscheduled downtime for the power plants is to be limited to about 10% of total time, and that the driver cannot cause more than about a third of the outage time, then a reliability figure of at least 97% is required. Considering the number of components in the driver, it is clear that the reliability of each must be very high.

Beam Current. While long, high-energy, linear accelerators have been built (e.g., SLAC) none approach the kiloamp beam currents required here. This is largely a physics issue that will have to be resolved early on and will require large, expensive experiments.

Beam Propagation into Chamber. There was considerable discussion during this study as to the type and amount of vapor that could be in the cavity and still have a focussed beam delivered to the target. The greater the allowable vapor pressure of Flibe, the higher the temperatures can be in the chamber region, resulting in higher conversion efficiencies. Low atomic number vapors appear more benign, at least for beam stripping. There is ongoing research into the self-pinched propagation mode at LLNL and NRL, which would allow higher gas pressures. There has also been some discussion of propagation in plasma channels, though

there are many uncertainties in this propagation mode. Because this issue can drive so many aspects of reactor (and BOP) design, it should be resolved early on with a convincing combination of analysis and experiments.

Rep Rate. Single shot accelerators are easier to design than one that must be reliably rep-rated at several Hz. Steady-state cooling is required, and inductor cores will be repeatedly pulsed. Super-conducting magnets must be shielded from AC losses.

Vacuum Maintenance. The beam line must be maintained at 10^{-6} torr while the plasma chamber must be at 10^{-4} torr. Considerable pumping is required at the final focus magnets as well as throughout the long accelerator. Large vacuum systems of this sort already exist in the high-energy physics community. The main issue that could cause vacuum problems is discussed below.

Material Deposition. Flibe vapor, as well as target shell material, will drift into the beam tubes and plate out. The buildup rate must be determined and its effect. In particular, the effect of plating of any electrically conducting material on beam formation and propagation must be determined. It may be necessary to run the beam tubes hotter than the Flibe melting point in order to continuously drain deposited material. Use of shutters can reduce inflow, but with considerable added complexity.

Neutron and Ion Activation. Bending magnets and neutron dumps can virtually eliminate primary neutron propagation down the beam tubes. Scattered neutrons remain a problem for the final focussing and drift compression regions of the driver. Shielding must be added around the bores of the final focussing magnets. The neutrons travel too rapidly to be stopped by mechanical shutters. In addition to neutron activation, some of the high energy ions in the beam can lose their charge and impact the accelerator tube, leading to activation.

The current technical credibility seems low for controlling scattered neutrons and neutralized beam particles, so potential activation of the entire driver is an important issue. Much can be learned here by analysis; therefore, development needs are considered only moderate.

Final Focus Hardware. The final focussing magnets are shielded from primary and secondary neutrons with shielding around the bore. The amount of bore shielding determines how close the final magnets can be spaced, which impacts beam envelope and building requirements. These magnets are quite complex and could be subjected to severe bending loads. The ongoing work on magnet technology in the MFE program is of value here.

Power Supplies. The power supplies for reliable rep-rated operation will be different from the pulsed energy systems used in today's high energy experiments. Issues include their cost, reliability, conversion efficiency, potential for reject heat recovery, and buss network. High energy, rep-rated power supplies are being developed for other applications, for example, SDI.

7.2.9 Target Fabrication

The target factory will need to be fully automated. The production process must have high reliability, high quality control, and low capital and operating costs. Recycling of target material will be required.

7.2.10 Target Injection

In our conceptual design, targets are accelerated at ~ 130-g to about 150 m/s in a 9-m long gas gun accelerator. Targets must survive (i.e., maintain required quality specifications) the acceleration and transit to the center of the chamber. The target injection and tracking systems must be protected from the damaging effects of the fusion energy pulse with distance and/or shielding. The injector must be highly reliable and position the targets accurately in time and space with the correct orientation. The tracker must supply targeting information to the driver early enough to allow for beam steering and pointing.

Several approaches exist that could potentially meet the injection and tracking requirements, but none has been built and tested. While frozen hydrogen has been accelerated to typical IFE parameters, precision multi-layer fuel capsules have not. Calculations indicate that the outer plastic shell protects the cryogenic fuel from overheating during transit through the hot chamber. The effects of heating on the ablator surface finish requires further analysis and / or experimentation.

7.3 TECHNOLOGY ASSESSMENT RATINGS FOR OSIRIS

Table 7.2, which extends for several pages, shows a graphical summary of the primary criteria discussed in Section 7.1: technical immaturity, critical technology, development cost, lead time, and amount of experimental effort. They are ranked from low (0) to high (100), and a weighted average, the overall urgency factor, is given at the end of each issue. Critical

technology (no other options exist) and development cost weigh highest, followed by long lead time. Less weight is given to technical immaturity and the extent of experimental effort required. The entries are displayed such that the further to the right an entry is, the greater the attention it should have.

In general, issues scoring 50 or greater are of considerable importance while those with 25 or less can be deferred. In the reactor chamber, issues scoring 50 or greater in overall urgency are chamber rep-rate, chemistry and surface physics, blanket replacement/repair, shock waves, and tritium. None of the BOP-related issues score very high. A number of driver issues score 50 or greater: reliability, beam current, beam propagation, rep rate, vacuum maintenance, final focus, and power supplies. Target fabrication and injection also scored 75 in overall urgency.

Table 7.2. Technology Assessment for Osiris

OSIRIS - REACTOR CHAMBER

CHAMBER REP-RATE:

	Low 0	25	50	75	High 100
Technical Immaturity (10%)				●	
Critical Technology (30%)					●
High Development Cost (30%)		●			
Long Lead Time (20%)		●			
% Cost in Experiments (10%)			●		
Overall Urgency Factor			★		

FABRIC WEAVE CONTROL:

	Low 0	25	50	75	High 100
Technical Immaturity (10%)				●	
Critical Technology (30%)		●			
High Development Cost (30%)	●				
Long Lead Time (20%)	●				
% Cost in Experiments (10%)				●	
Overall Urgency Factor		★			

FABRIC STITCHING:

	Low 0	25	50	75	High 100
Technical Immaturity (10%)		●			
Critical Technology (30%)		●			
High Development Cost (30%)	●				
Long Lead Time (20%)	●				
% Cost in Experiments (10%)				●	
Overall Urgency Factor		★			

Table 7.2 (continued)

OSIRIS - REACTOR CHAMBER (continued)

BLANKET REPLACEMENT/REPAIR:

	Low 0	25	50	75	High 100
Technical Immaturity (10%)					●
Critical Technology (30%)			●		
High Development Cost (30%)		●			
Long Lead Time (20%)		●			
% Cost in Experiments (10%)				●	
Overall Urgency Factor			★		

EFFECT OF SHOCK WAVES:

	Low 0	25	50	75	High 100
Technical Immaturity (10%)				●	
Critical Technology (30%)					●
High Development Cost (30%)			●		
Long Lead Time (20%)			●		
% Cost in Experiments (10%)				●	
Overall Urgency Factor				★	

FABRIC/FLIBE CHEMISTRY AND SURFACE PHYSICS:

	Low 0	25	50	75	High 100
Technical Immaturity (10%)			●		
Critical Technology (30%)					●
High Development Cost (30%)		●			
Long Lead Time (20%)	●				
% Cost in Experiments (10%)				●	
Overall Urgency Factor				★	

Table 7.2 (continued)

OSIRIS - REACTOR CHAMBER (continued)

TRITIUM EXTRACTION:

	Low 0	25	50	75	High 100
Technical Immaturity (10%)					●
Critical Technology (30%)		●			
High Development Cost (30%)			●		
Long Lead Time (20%)		●			
% Cost in Experiments (10%)			●		
Overall Urgency Factor			★		

OSIRIS - SHIELDING

	Low 0	25	50	75	High 100
Technical Immaturity (10%)			●		
Critical Technology (30%)		●			
High Development Cost (30%)		●			
Long Lead Time (20%)	●				
% Cost in Experiments (10%)		●			
Overall Urgency Factor		★			

OSIRIS - REACTOR BUILDING

	Low 0	25	50	75	High 100
Technical Immaturity (10%)		●			
Critical Technology (30%)	●				
High Development Cost (30%)	●				
Long Lead Time (20%)	●				
% Cost in Experiments (10%)	●				
Overall Urgency Factor	★				

Table 7.2 (continued)

OSIRIS - FLIBE PUMPS AND DUCTING

	Low 0	25	50	75	High 100
Technical Immaturity (10%)			●		
Critical Technology (30%)		●			
High Development Cost (30%)	●				
Long Lead Time (20%)	●				
% Cost in Experiments (10%)		●			
Overall Urgency Factor		★			

OSIRIS - INTERMEDIATE HEAT EXCHANGER

	Low 0	25	50	75	High 100
Technical Immaturity (10%)		●			
Critical Technology (30%)	●				
High Development Cost (30%)		●			
Long Lead Time (20%)	●				
% Cost in Experiments (10%)		●			
Overall Urgency Factor		★			

OSIRIS - STEAM GENERATOR

	Low 0	25	50	75	High 100
Technical Immaturity (10%)		●			
Critical Technology (30%)	●				
High Development Cost (30%)		●			
Long Lead Time (20%)	●				
% Cost in Experiments (10%)			●		
Overall Urgency Factor		★			

Table 7.2 (continued)

OSIRIS - POWER CONVERSION

	Low 0	25	50	75	High 100
Technical Immaturity (10%)	●				
Critical Technology (30%)	●				
High Development Cost (30%)	●				
Long Lead Time (20%)	●				
% Cost in Experiments (10%)	●				
Overall Urgency Factor	★				

OSIRIS - HIB DRIVER

RELIABILITY:

	Low 0	25	50	75	High 100
Technical Immaturity (10%)					●
Critical Technology (30%)					●
High Development Cost (30%)			●		
Long Lead Time (20%)			●		
% Cost in Experiments (10%)				●	
Overall Urgency Factor				★	

BEAM CURRENT:

	Low 0	25	50	75	High 100
Technical Immaturity (10%)				●	
Critical Technology (30%)					●
High Development Cost (30%)				●	
Long Lead Time (20%)				●	
% Cost in Experiments (10%)					●
Overall Urgency Factor				★	

Table 7.2 (continued)

OSIRIS - DRIVER (continued)

BEAM PROPAGATION INTO CHAMBER:

	Low 0	25	50	75	High 100
Technical Immaturity (10%)				●	
Critical Technology (30%)				●	
High Development Cost (30%)				●	
Long Lead Time (20%)			●		
% Cost in Experiments (10%)			●		
Overall Urgency Factor				★	

DRIVER REP RATE:

	Low 0	25	50	75	High 100
Technical Immaturity (10%)		●			
Critical Technology (30%)				●	
High Development Cost (30%)			●		
Long Lead Time (20%)			●		
% Cost in Experiments (10%)				●	
Overall Urgency Factor			★		

VACUUM MAINTENANCE:

	Low 0	25	50	75	High 100
Technical Immaturity (10%)		●			
Critical Technology (30%)				●	
High Development Cost (30%)		●			
Long Lead Time (20%)		●			
% Cost in Experiments (10%)				●	
Overall Urgency Factor			★		

Table 7.2 (continued)

OSIRIS - DRIVER (continued)

MATERIAL DEPOSITION:

	Low 0	25	50	75	High 100
Technical Immaturity (10%)			●		
Critical Technology (30%)		●			
High Development Cost (30%)		●			
Long Lead Time (20%)		●			
% Cost in Experiments (10%)				●	
Overall Urgency Factor		★			

NEUTRON DAMAGE / HEATING:

	Low 0	25	50	75	High 100
Technical Immaturity (10%)			●		
Critical Technology (30%)			●		
High Development Cost (30%)		●			
Long Lead Time (20%)		●			
% Cost in Experiments (10%)	●				
Overall Urgency Factor		★			

FINAL FOCUS HARDWARE:

	Low 0	25	50	75	High 100
Technical Immaturity (10%)				●	
Critical Technology (30%)				●	
High Development Cost (30%)			●		
Long Lead Time (20%)			●		
% Cost in Experiments (10%)				●	
Overall Urgency Factor				★	

Table 7.2 (continued)

OSIRIS - DRIVER (continued)

DRIVER POWER SUPPLIES:

	Low 0	25	50	75	High 100
Technical Immaturity (10%)			●		
Critical Technology (30%)			●		
High Development Cost (30%)			●		
Long Lead Time (20%)		●			
% Cost in Experiments (10%)			●		
Overall Urgency Factor			★		

OSIRIS - TARGET FABRICATION

	Low 0	25	50	75	High 100
Technical Immaturity (10%)				●	
Critical Technology (30%)					●
High Development Cost (30%)				●	
Long Lead Time (20%)			●		
% Cost in Experiments (10%)				●	
Overall Urgency Factor				★	

OSIRIS - TARGET INJECTION

	Low 0	25	50	75	High 100
Technical Immaturity (10%)				●	
Critical Technology (30%)					●
High Development Cost (30%)			●		
Long Lead Time (20%)		●			
% Cost in Experiments (10%)				●	
Overall Urgency Factor				★	

7.4 SUMMARY OF DEVELOPMENT PRIORITIES FOR OSIRIS

Table 7.3 gives a summary of the above discussion and a tabulation which distills it by listing current technical credibility (i.e., the current state-of-the-art) for each item, as well as development needs for reactor applications. It also shows a ranking of the development priorities for each major subsystem and, where appropriate, for issues within the subsystem. The development needs are not necessarily the inverse of technical credibility, because, in many cases, rather simple experiments can resolve major issues. The level of expense and difficulty has been included, as has the impact of the issue on reactor performance and cost.

Not surprisingly, the driver ranks first in development priority. Part of this is due to the enormous potential expense and part because of the limited development paths: RF or induction and once-through or recirculating. Because the driver is truly the tail wagging the dog, the primary IFE effort must go here, at least for now.

The target factory ranks second, because so little is known about economic fabrication of complex indirect targets. Hopefully, the current work on target fabrication will help. Nevertheless, a concerted effort must be undertaken to scope out a reactor-relevant target factory in some detail.

While one might expect the reactor chamber to top the list, it is preceded by the two above partly because the development needs can probably be met with less expense, and if the Osiris concept simply doesn't work, there are many other reactor concepts to fall back on. This is not true with the driver and target factory.

Target injection and tracking doesn't rank as high as expected in development priority partly because of the relatively modest scale experiments that are required and because of related technology existing in the MFE and SDI programs.

The remaining items lie some distance down the development priority scale although there are certainly numerous design issues that must be addressed.

Table 7.3. Osiris Development Priorities

ITEM	CURRENT TECHNICAL CREDIBILITY	DEVEL. NEEDS	DEVEL. PRIORITY
DRIVER	**LOW**	**HIGH**	**1**
Beam Current	Moderate	Moderate	1
Beam Chamber Propagation	Low	Moderate	2
Economics	Low	High	3
Neutrons	Low	Moderate	4
Final Focus	Moderate	Moderate	5
Reliability	Low	High	6
Rep Rate	Moderate	Moderate	7
Vacuum Maint.	High	Low	8
Mat'l Deposition	Moderate	Moderate	9
Power Supplies	High	Low	10
TARGET FABRICATION	**LOW**	**HIGH**	**2**
REACTOR CHAMBER	**LOW**	**MODERATE**	**3**
Fabric/Flibe	Low	High	1
Rep-rate	Low	Mod	2
Shocks	Low	High	3
Weave Control	Low	Low	4
Stitching	High	Low	5
T Extraction	Moderate	Low	6
Blanket Replacement	High	Low	7
TARGET INJECTION	**MODERATE**	**MODERATE**	**4**
IHX	**MODERATE**	**LOW**	**5**
STEAM GENERATOR	**MODERATE**	**LOW**	**6**
FLIBE PUMPS/DUCTS	**HIGH**	**LOW**	**7**
SHIELDING	**HIGH**	**LOW**	**8**
REACTOR BUILDING	**HIGH**	**LOW**	**9**
POWER CONVERSION	**HIGH**	**LOW**	**10**

7.5 SOMBRERO ISSUES AND DEVELOPMENT NEEDS

This is the companion section to Section 7.2 and gives a technology assessment of the SOMBRERO reactor concept. The areas covered are the reactor chamber, shielding, final optics, Li_2O transport and ducting, IHX, steam generator, reactor building, power conversion, laser driver, and target factory and injection.

7.5.1 Reactor Chamber

The reactor chamber has cylindrical symmetry and is built up of layers of carbon composite plates between which flows Li_2O granules fluidized by 2 atmospheres of helium gas. Low pressure xenon gas in the chamber absorbs target soft X-rays and debris so that wall vaporization is avoided. Technical issues are carbon structure fabrication, leak-tightness including detection and repair, fireball/blast response, Li_2O heat transfer, Li_2O and carbon structure erosion, fluidized flow, and neutron lifetime.

Carbon Structure Fabrication. The chamber structure is made up of concentric layers of carbon-carbon composite with increasing panel thickness as one moves away from the first wall. Carbon composites are fabricated by infiltrating built-up carbon fabric with an appropriate hydrocarbon that carbonizes upon heating. An oven is therefore required, and panel size are therefore limited by oven size. It may be possible to preform panels in an oven with a limited infiltration so that they have some stiffness, and then assemble the reactor and do the remaining infiltration in-situ. The chamber then becomes its own oven. This would be necessary for seamless fabrication. If the chamber is built up of individual panels, the joints must be sealed to prevent helium leakage. An SiC coating is postulated, which would have to be done after assembly.

The current technical credibility of large, vacuum-tight carbon-carbon structures is at most moderate. The level of development needed to establish the necessary feasibility is also moderate and should not be overly expensive because developing the necessary procedures (e.g., using the chamber as an in-situ oven) can be developed on a modest scale.

Leak Tightness and Detection. Assuming the vacuum chamber has fairly high pumping capacity, thousands of pinhole-sized leaks of 2 atmosphere helium can be tolerated. Double sealing of the first wall is almost certainly required. Some ductility of the seal material would help; using brittle SiC as the seal material will be troublesome. If a large leak occurs, means must be available for detection of the leak location and repairing it. The question also remains about how much helium is acceptable in the target chamber. Laser propagation may actually be so tolerant to helium that vacuum pumping is in the high-speed viscous regime.

Remote Maintenance and Assembly. Although low activation materials are used throughout, there will be short-term activity that must be considered when changing out blankets. Trace impurities can generate longer-term activity severely restricting access to the chamber. The technology of remote manipulation, assembly, and repair must be extended to accommodate very large subassemblies. This technology is proceeding in other areas such as remotely-piloted vehicles and aircraft for the military, and telerobots for space applications.

Fireball/Blast Response. While the chamber gas prevents vaporization of the first wall surface, the expanding fireball in that gas will subject the wall to a blast effect. The dynamic stresses and induced vibrations raise concerns about damage (e.g., cracking) to brittle seals. Further analysis and experimental verification will be required to address the effects of pulsed loading on the composite structure and seals.

Li_2O Heat Transfer. The high thermal capacity and substantial mixing of the Li_2O greatly increases the heat transfer capacity of the low pressure helium gas. The gas can flow upward at sufficient velocity so that the granules just lift off of each other and flow down much like a fluid. There is a wide body of heat transfer data for this type of flow, and relatively simple experiments could refine it for these specific conditions. Because carbon temperatures can be much higher than the Li_2O, fairly high heat transfer rates are possible with moderate heat transfer coefficients.

Li_2O and Structure Erosion. Lithium oxide is not very hard and will wear down by transport against a hard surface like silicon carbide. Pure carbon structure, if used instead, will also wear. Granule to granule impact and impact with ducts and heat exchanger tubes also cause breakup of this relatively weak material. Means will have to be provided to extract fractured granules and fabricate new ones. Other lithium bearing ceramics, such as lithium aluminate, may be worth considering if Li_2O ends up being too soft and weak. Coatings on the granule, such

as silicon carbide, can also be considered. The New Production Reactor for Savannah River was designed to use $LiAlO_2$ particles coated with SiC, and this technology may be useful here.

Fluidized Flow. Fluidized flow of the Li_2O granules has been discussed above with respect to heat transfer. Helium carrier gas is used to fluidize the granule flow through the reactor and the IHX and to carry the granules upward to the top of the reactor and the top of the IHX. When properly fluidized, granule beds behave much like liquids and can readily flow though complex ducting.

This technology is well established in the chemical industry for large-scale transport of solid particles. It, therefore, has high technical credibility. Development needs are expected to be low centering mainly on design issues like the erosion discussed above and on helium recovery and pumping power.

Beam Propagation into Chamber. The allowable vapor density in the chamber is much higher for lasers than for ballistic propagation of ion beams. In SOMBRERO, 0.5 torr Xenon stops all the soft X-rays, eliminating first wall vaporization altogether. Yet the chamber radius is still very large. Tradeoffs are needed to determine if a higher gas density, coupled with a smaller radius, will still give adequate beam propagation. Also, because leakage into the chamber of the helium carrier gas is a possibility, could a high helium density be used to protect the wall instead of the xenon? Answers to these questions are likely to require experiments as well as analysis.

7.5.2 Shielding

The carbon chamber and Li_2O granules provide primary shielding, and the reinforced concrete biological shield and building structure provide the rest. Beam dumps behind the final mirrors stop primary neutrons coming from the chamber penetrations. Key issues are the absorption of neutrons scattered back from the beam dumps and activation of the concrete building - primarily from impurities in the concrete. Codes exist now that can perform the required level of analysis. High purity concrete and reinforcement are available. Much of the work being done in the MFE program can be leveraged here.

7.5.3 Final Optics

The final optics consist of final focussing mirrors and glancing incidence metal mirrors (GIMMs). The GIMMs are used to bend the optical path so as to move the focusing mirrors away from the neutron line-of-sight. Critical issues are cost, neutron lifetime, and pointing accuracy and stability. The first two are, of course, related. In SOMBRERO, GIMMs are placed 30 m from the target and the final focus mirrors are 50 m away. The primary neutron dumps also serve as support for the focusing mirrors. This arrangement may allow both mirrors to last the life of the plant, assuming the GIMMs can be periodically annealed. The GIMMs are polished metal and should be able to take 10^4 times more neutron fluence than the coated final focus mirrors.

There are 60 beam ports. Preliminary cost estimates (see Chapter 8) suggest that each glancing incidence/final focus mirror combination may cost $0.2 million per set, giving a total cost of $12 million. If costs are in fact this low, then incentive exists to bring the optics in closer, replacing them more often and reducing the cost of the large reactor building.

Little experimental data exists on neutron damage of optical surfaces and possible recovery by annealing. Little exists on boundary mixing for multilayer mirrors, which could be critical. These data will be difficult to obtain in anything but a full-scale IFE reactor, because it is likely that both energy fluence per pulse as well as cumulative fluence are important.

Pointing accuracy is a very critical issue. For example, a 2% deviation of a 5 mm spot size over 50 m is an angular deviation of only 2 μrad. Mirrors must not only be rigidly mounted with near total vibration and thermal isolation, but active optics must be employed which account for small motions and deviations in target trajectory. Because of the doubling effect of reflected beams, both types of mirrors must be twice as accurate as the beams. Fortunately, much of the technology developed during the SDI program is applicable here.

7.5.4 Lithium Oxide Transport and Ducting

Transport of Li_2O through the reactor has already been discussed. The granules must also be transported though the ducting and IHX. As with the reactor, granule erosion and fracture are key issues, particularly during the high-speed elevating portion of the circuit. Also, ducting must be designed to avoid settling points. Helium recovery and pumping power must be considered as well.

There are a number of ways of coating Li_2O (e.g., with SiC) to reduce erosion. Also, alternate materials such as lithium aluminate could be used. The fluidized bed technology already in place can be exploited to design ducts and helium pumps. Issues are related more to design than to development. Therefore, technical credibility is considered high and development requirements fairly low.

7.5.5 Intermediate Heat Exchanger

The liquid lead side of the IHX is similar to that for Osiris. Provided oxygen content is kept very low, liquid lead is compatible with iron, mild steel, and stainless steel up to about 630°C. The maximum surface temperature on the lead side is 617°C. The granule side is a fluidized flow heat exchanger, which has a well-established technology behind it. Although the IHX is fairly large, because it is low pressure on both sides, tube walls can be thin and total mass is moderate. Costs are expected to be quite acceptable. Suitable barriers exist for the small amount of tritium that diffuses from the Li_2O during transit.

7.5.6 Steam Generator

The steam generator is similar to the one for Osiris. Low pressure liquid lead flows on one side and supercritical steam on the other. Maximum wall temperature is under 600°C. As with the IHX this temperature is acceptable with stainless steel (but not with inconel), provided oxygen is excluded, perhaps with an O_2 scavenger in the loop.

7.5.7 Reactor Building

The 100-m diameter (and high) reactor building provides vacuum barrier, optics support, and supplementary biological shielding as well as protection of the reactor chamber from the outside world. While thick concrete buildings in this size range exist, none are known to have all of these requirements. Critical issues are cost, contamination by tritium and activation by scattered neutrons, decommissioning, and the ability of such a large structure to accurately support the optics with minimal deflection due to ambient temperature swings and induced vibration.

Optics support has been discussed above, and care should be taken to avoid double counting. All of the other issues appear tractable. For example, scattered neutrons can be

absorbed by using borated concrete in the inner biological shield, which has much lower mass. The vacuum can be moderate, on the order of one torr.

As discussed above, there is a strong tradeoff between final optics cost and life and reactor building cost. For example, cutting the building diameter and height in half would bring the focusing optics in to a point where they would have to be replaced perhaps four times in 30 years, rather than being lifetime components. This may well be cost effective since the reactor building cost may drop by a factor of four. On the other hand, this would place more severe demands on the GIMMs.

7.5.8 Power Conversion

The power conversion is nearly the same as that used in Osiris, supercritical steam with about 45% net efficiency. Because the laser driver takes up less land area than a heavy ion beam, siting may not be as constrained and, therefore, less effort may be needed in the area of dry air cooling. If the laser heat loss can be recovered for feedwater heating (as is assumed in our design, the power conversion efficiency is increased to about 47%.

7.5.9 Driver

As with the heavy ion beam driven reactor, the laser driver for SOMBRERO is the most expensive and most challenging component of the reactor plant. Key issues are reliability and component lifetime, beam stability, rep rate, efficiency/energy recovery, noise suppression, chemistry/toxicity, and cost.

Reliability and Component Lifetime. The driver consists of 64 beams total, of which 4 are spares. Full-time operation is then possible when the reliability of all individual beams exceeds 94%, not a very demanding figure provided beams can be switched in and out at will. The plasma cathode patented by Textron shows promise, but further development is needed. Similarly, high voltage pulsed power systems have not yet demonstrated the ability to last the lifetimes required for a power plant. Other components such as blowers, heat exchangers, and noise suppressors are relatively low-tech and should have sufficient reliability.

Beam Stability. The final optics stability is a major issue as was discussed above. The stability of the rest of the beam is also critical. Successive beams must consistently follow the same paths. This is not trivial considering the high level of turbulence, heating and noise in the

laser gas flow system. Gas temperature uniformity is critical. The entire system must be mounted on the equivalent of a large optical bench. Beams leaving the laser must pass through thermally homogeneous helium or vacuum; active optics control are required to maintain beam quality and pointing accuracy. Over two decades of work in these areas can be brought to bear, as well as more recent work during the SDI program. Many of these issue are design, rather than development, related.

Rep-Rate. The rep rate issue permeates through all of the other issues listed here. While small-scale repped KrF lasers have been developed for laboratory use, continuous repped operation day in and day out will introduce new problems, such as pulsed energy systems and heat removal, that need to be addressed.

Efficiency/Energy Recovery. The projected KrF laser efficiency is in the 7-8% range, which should be acceptable for power reactors with high gain targets. A two percentage point gain in powerplant efficiency can be realized by recovering a portion of the waste heat with feedwater heating. Whether or not this is worth the added complexity depends on its impact on capital cost, reliability, and increases in coolant pumping power. Many issues here are design, rather than development, related.

Noise Suppression. With the high flow speeds, acoustic noise is an issue with KrF lasers. Acoustic suppression entails considerable bulk and expense. Noise level in the laser cavity must be low enough not to perturb beam propagation. Considering the high level of development in noise suppression in small repped lasers, and in other areas (e.g., aircraft engines) technical credibility is high and development needs are expected to be low although some effort at cost reduction would be beneficial.

Chemistry/Toxicity. Even small amounts of free fluorine can cause problems, because fluorine is the most reactive of all the elements and is toxic at below 1.0 ppm. It is, therefore, important that the entire flow system be well-sealed. Despite these hazards, safe handling techniques have been developed elsewhere, and it is now possible to transport liquid fluorine by the ton.

7.5.10 Target Fabrication

Direct-drive targets for KrF lasers should be easier to fabricate than the indirect targets for heavy ion beams, because direct-drive targets do not use a hohlraum. Nevertheless, the

technical credibility of fabrication of direct-drive targets at high rep-rate is currently low, and development requirements are quite high.

7.5.11 Target Injection

Target injection requirements and concerns are comparable to those discussed for Osiris.

7.6 TECHNOLOGY ASSESSMENT RATINGS FOR SOMBRERO

Table 7.4 below is the SOMBRERO counterpart of the summary table for Osiris. The issues are generally similar with some differences due to the type of reactor chamber and driver. While Osiris is very leak tolerant, leak-tightness is an issue in SOMBRERO. While shock waves are a concern in the high vacuum Osiris chamber, fireball and blast response, while requiring consideration, does not appear to be a serious issue for SOMBRERO. The final optics of the KrF laser are a more serious concern than the final focus hardware is for the heavy ion beam; however, mass flow up the beam lines, which was a major concern for Osiris, is not a concern for SOMBRERO.

The Overall Urgency Factor is a weighted average of the five issues listed (weights are given in Table 7.1). In general, values of 50% or over deserve serious consideration, especially if lead time is shown to be long.

Table 7.4. Technology Assessment for SOMBRERO

SOMBRERO - REACTOR CHAMBER

CARBON STRUCTURE FABRICATION:

	Low 0	25	50	75	High 100
Technical Immaturity (10%)				●	
Critical Technology (30%)				●	
High Development Cost (30%)		●			
Long Lead Time (20%)			●		
% Cost in Experiments (10%)				●	
Overall Urgency Factor			★		

LEAK TIGHTNESS AND DETECTION:

	Low 0	25	50	75	High 100
Technical Immaturity (10%)					●
Critical Technology (30%)				●	
High Development Cost (30%)	●				
Long Lead Time (20%)		●			
% Cost in Experiments (10%)				●	
Overall Urgency Factor			★		

REMOTE MAINTENANCE AND ASSEMBLY:

	Low 0	25	50	75	High 100
Technical Immaturity (10%)			●		
Critical Technology (30%)				●	
High Development Cost (30%)			●		
Long Lead Time (20%)		●			
% Cost in Experiments (10%)				●	
Overall Urgency Factor			★		

Table 7.4 (continued)

SOMBRERO - REACTOR CHAMBER (continued)

FIREBALL / BLAST RESPONSE:

	Low 0	25	50	75	High 100
Technical Immaturity (10%)			●		
Critical Technology (30%)			●		
High Development Cost (30%)		●			
Long Lead Time (20%)		●			
% Cost in Experiments (10%)		●			
Overall Urgency Factor		★			

Li_2O HEAT TRANSFER:

	Low 0	25	50	75	High 100
Technical Immaturity (10%)	●				
Critical Technology (30%)			●		
High Development Cost (30%)		●			
Long Lead Time (20%)	●				
% Cost in Experiments (10%)			●		
Overall Urgency Factor		★			

Li_2O AND STRUCTURE EROSION:

	Low 0	25	50	75	High 100
Technical Immaturity (10%)				●	
Critical Technology (30%)				●	
High Development Cost (30%)			●		
Long Lead Time (20%)		●			
% Cost in Experiments (10%)				●	
Overall Urgency Factor				★	

Table 7.4 (continued)

SOMBRERO - REACTOR CHAMBER (continued)

FLUIDIZED FLOW:

	Low 0	25	50	75	High 100
Technical Immaturity (10%)		●			
Critical Technology (30%)			●		
High Development Cost (30%)		●			
Long Lead Time (20%)	●				
% Cost in Experiments (10%)			●		
Overall Urgency Factor		★			

BEAM PROPAGATION INTO CHAMBER:

	Low 0	25	50	75	High 100
Technical Immaturity (10%)				●	
Critical Technology (30%)			●		
High Development Cost (30%)		●			
Long Lead Time (20%)			●		
% Cost in Experiments (10%)			●		
Overall Urgency Factor			★		

SOMBRERO - SHIELDING

	Low 0	25	50	75	High 100
Technical Immaturity (10%)			●		
Critical Technology (30%)		●			
High Development Cost (30%)		●			
Long Lead Time (20%)	●				
% Cost in Experiments (10%)		●			
Overall Urgency Factor		★			

Table 7.4 (continued)

SOMBRERO - FINAL OPTICS

	Low 0	25	50	75	High 100
Technical Immaturity (10%)					●
Critical Technology (30%)					●
High Development Cost (30%)			●		
Long Lead Time (20%)			●		
% Cost in Experiments (10%)				●	
Overall Urgency Factor				★	

SOMBRERO - Li_2O TRANSPORT AND DUCTING

	Low 0	25	50	75	High 100
Technical Immaturity (10%)		●			
Critical Technology (30%)		●			
High Development Cost (30%)		●			
Long Lead Time (20%)		●			
% Cost in Experiments (10%)			●		
Overall Urgency Factor		★			

SOMBRERO - INTERMEDIATE HEAT EXCHANGER

	Low 0	25	50	75	High 100
Technical Immaturity (10%)			●		
Critical Technology (30%)	●				
High Development Cost (30%)		●			
Long Lead Time (20%)	●				
% Cost in Experiments (10%)			●		
Overall Urgency Factor		★			

Table 7.4 (continued)

SOMBRERO - STEAM GENERATOR

	Low 0	25	50	75	High 100
Technical Immaturity (10%)		●			
Critical Technology (30%)	●				
High Development Cost (30%)		●			
Long Lead Time (20%)	●				
% Cost in Experiments (10%)			●		
Overall Urgency Factor		★			

SOMBRERO - REACTOR BUILDING

	Low 0	25	50	75	High 100
Technical Immaturity (10%)				●	
Critical Technology (30%)				●	
High Development Cost (30%)			●		
Long Lead Time (20%)	●				
% Cost in Experiments (10%)		●			
Overall Urgency Factor			★		

SOMBRERO - POWER CONVERSION

	Low 0	25	50	75	High 100
Technical Immaturity (10%)	●				
Critical Technology (30%)		●			
High Development Cost (30%)	●				
Long Lead Time (20%)	●				
% Cost in Experiments (10%)	●				
Overall Urgency Factor	★				

Table 7.4 (continued)

SOMBRERO - LASER DRIVER

RELIABILITY AND COMPONENT LIFETIME:

	Low 0	25	50	75	High 100
Technical Immaturity (10%)			●		
Critical Technology (30%)				●	
High Development Cost (30%)					●
Long Lead Time (20%)					●
% Cost in Experiments (10%)				●	
Overall Urgency Factor				★	

BEAM STABILITY:

	Low 0	25	50	75	High 100
Technical Immaturity (10%)		●			
Critical Technology (30%)				●	
High Development Cost (30%)				●	
Long Lead Time (20%)			●		
% Cost in Experiments (10%)				●	
Overall Urgency Factor				★	

REP RATE:

	Low 0	25	50	75	High 100
Technical Immaturity (10%)			●		
Critical Technology (30%)				●	
High Development Cost (30%)			●		
Long Lead Time (20%)			●		
% Cost in Experiments (10%)				●	
Overall Urgency Factor			★		

Table 7.4 (continued)

SOMBRERO - LASER DRIVER (continued)

EFFICIENCY/ENERGY RECOVERY:

	Low 0	25	50	75	High 100
Technical Immaturity (10%)		●			
Critical Technology (30%)	●				
High Development Cost (30%)		●			
Long Lead Time (20%)	●				
% Cost in Experiments (10%)		●			
Overall Urgency Factor		★			

NOISE SUPPRESSION:

	Low 0	25	50	75	High 100
Technical Immaturity (10%)		●			
Critical Technology (30%)		●			
High Development Cost (30%)		●			
Long Lead Time (20%)	●				
% Cost in Experiments (10%)			●		
Overall Urgency Factor		★			

CHEMISTRY/TOXICITY:

	Low 0	25	50	75	High 100
Technical Immaturity (10%)		●			
Critical Technology (30%)		●			
High Development Cost (30%)	●				
Long Lead Time (20%)	●				
% Cost in Experiments (10%)			●		
Overall Urgency Factor		★			

Table 7.4 (continued)

SOMBRERO - LASER DRIVER (continued)

DRIVER - COSTS:

	Low 0	25	50	75	High 100
Technical Immaturity (10%)					●
Critical Technology (30%)				●	
High Development Cost (30%)				●	
Long Lead Time (20%)			●		
% Cost in Experiments (10%)				●	
Overall Urgency Factor				★	

SOMBRERO - TARGET FABRICATION

	Low 0	25	50	75	High 100
Technical Immaturity (10%)				●	
Critical Technology (30%)					●
High Development Cost (30%)			●		
Long Lead Time (20%)			●		
% Cost in Experiments (10%)				●	
Overall Urgency Factor				★	

SOMBRERO - TARGET INJECTION

	Low 0	25	50	75	High 100
Technical Immaturity (10%)			●		
Critical Technology (30%)					●
High Development Cost (30%)		●			
Long Lead Time (20%)		●			
% Cost in Experiments (10%)				●	
Overall Urgency Factor			★		

7.7 SUMMARY OF DEVELOPMENT PRIORITIES FOR SOMBRERO

Table 7.5 gives a summary of the above discussion and lists technical credibility of the current state-of-the-art for each item, as well as development needs for reactor applications. It also shows a ranking of the development priorities for each major subsystem and, where appropriate, for issues within the subsystem. The development needs are not necessarily the inverse of technical credibility, because, in many cases, rather simple experiments can resolve major issues. The level of expense and difficulty has been included, as has the impact on reactor performance and cost.

As with the Osiris reactor, the driver ranks first in development priority. The key issue is costs, which translates into technical issues like material selection, fabrication techniques, and tolerances. Reliability and component lifetime are related to costs, of course, but they have been separated out here as an issue that will require considerable development. The remaining driver issues have moderate to low development needs.

Target fabrication and injection rank 2nd and 4th, respectively, primarily because of the newness of the technology. Being simpler than hohlraum targets, direct drive targets should be easier to fabricate.

The reactor chamber appears to have fewer development problems than the driver/target systems. The key issues here are sustained leak tightness and erosion. The first depends on the allowable helium density in the target chamber, which will certainly be much higher than the allowable xenon density, and on the pumping capacity of the vacuum system.

The final optics concerns rank fifth in development priority to the driver, because the problems here are less severe and because there are fewer of them. Final optics problems center around pointing stability and neutron damage. The last could be a show stopper if lifetimes are much less than our estimates.

The reactor building, although very large, is technically fairly credible. Key issues are cost, vacuum maintenance, dimensional stability, and activation from scattered neutrons.

The remaining issues (i.e., Li_2O transport, IHX, steam generator, shielding, and power conversion) are all quite credible today and require little costly development.

Table 7.5 SOMBRERO Development Priorities

ITEM	CURRENT TECHNICAL CREDIBILITY	DEVEL. NEEDS	DEVEL. PRIORITY
DRIVER	**LOW**	**HIGH**	**1**
Costs	Low	High	1
Reliability	Moderate	High	2
Rep Rate	Moderate	Moderate	3
Efficiency	Moderate	Low	4
Beam Stability	High	Moderate	5
Chemistry	High	Low	6
Noise	High	Low	7
TARGET FABRICATION	**LOW**	**HIGH**	**2**
REACTOR CHAMBER	**MODERATE**	**MODERATE**	**3**
Leak Tightness	Low	Moderate	1
Carbon Fabrication	Moderate	Moderate	2
Li_2O Structure and Erosion	Moderate	Moderate	3
Fluidized Flow	High	Low	4
Blast Response	High	Low	5
Li_2O Heat Transfer	High	Low	6
TARGET INJECTION	**MODERATE**	**MODERATE**	**4**
FINAL OPTICS	**MODERATE**	**MODERATE**	**5**
REACTOR BUILDING	**MODERATE**	**MODERATE**	**6**
Li_2O TRANSPORT	**HIGH**	**LOW**	**7**
IHX	**HIGH**	**LOW**	**8**
STEAM GENERATOR	**HIGH**	**LOW**	**9**
SHIELDING	**HIGH**	**LOW**	**10**
POWER CONVERSION	**HIGH**	**LOW**	**11**

7.8 GENERIC IFE ISSUES

Some of the issues discussed here have been touched on in previous sections and some have not. They are pulled out separately here to emphasize that they are not specific to any reactor/driver combination and must be pursued for the general benefit of IFE.

7.8.1 Target Design Innovations

While this study pointedly avoided getting into target design, it became clear that this issue can significantly impact the design of the plant. In particular, pushing the knee in the gain curve toward lower driver energies and reducing illumination uniformity requirements could greatly reduce plant cost and complexity. If HIB and KrF laser cost estimates remain at the level predicted in this study, $100-200/Joule, then getting reasonable gains with about 2 MJ driver energy would give very reasonable plant costs. Factored into this, of course, is rep-rate. This could increase to fairly high levels. For example, with 2 MJ driver and a target gain of 60, target yield is only 120 MJ, and a 20 Hz repetition rate is required for 2400 MW of fusion power. This impacts target injection, chamber design and clearing, and driver power conditioning. While it is likely that these issues will force an upper bound on rep-rate, one can always look at lower total thermal power levels. This would be a great attraction initially until investors feel confident enough to fund larger power plants.

Illumination requirements had some impact on Osiris, but a great impact on SOMBRERO. Single-sided illumination would eliminate bending magnets in Osiris, and reduce beam growth due to momentum spread, but the cost savings is likely to be small. Some bending will still be needed to dump neutrons. If polar illumination requirements could be reduced for SOMBRERO, then the very expensive reactor building could be substantially reduced. The ideal situation is to have all laser beams on the ground. Then final optics can be placed as far away as desired, and optics support is made much easier. This would require considerable innovation in target design, perhaps involving cylindrical, rather than spherical symmetry.

These are just some of the issues relating to targets. Clearly, future activities should keep the ultimate reactor requirements in mind, with every effort aimed toward lower cost and greater simplicity. Further interaction between target designers and reactor designers could lead to much more attractive power plants.

7.8.2 Reactor Modeling

The results from this study underscore the importance of integrated modelling of IFE reactors. Systems codes, using distillations of more complex analyses, provide invaluable parametric scans that show where optima and sensitivities actually lie. This provides a good counterbalance against intuition, which is often wrong. Reactor design studies, like this one, show the necessary development critical paths and, conversely, where work can be curtailed.

Most important is timeliness. Results must be early enough to influence large, expensive development programs before commitments are made. In the MFE program, early reactor modeling had little influence, because they paralleled the experiments. Now that the models exist and are quite sophisticated, they are having a substantial impact in the planning of large experiments like ITER. We need to have similar models in place soon, so they can influence planning for near term experimental facilities.

When performed in sufficient depth, modelling of reactor and driver systems can give at least a relative costing of the various components. This is valuable in showing where emphasis should be placed in the development program. Clearly, the results are sensitive to the values used as installed unit costs (e.g., $/kg, $/Joule, $/Watt). This is where much care is required to ensure that the best values available are used. Where cost uncertainties are great, sensitivity studies are important. Often, similar components can be found in other areas like the fission, high energy physics, and space, military and SDI programs. Unit costs found here can be used after suitable adjustment for the fusion environment.

7.8.3 Low Activation and Neutron-Resistant Materials

This issue permeates all of fusion. Even in the unlikely case of D-^{3}He fuel working, there are enough neutrons to cause activation concerns. With D-T, both activation and lifetime are issues. There are two ways of dealing with these problems:

Liquid First Wall/Blanket. Enough liquid blanket is placed in front of the first material wall that most of the neutrons don't reach it. This is the approach in HYLIFE,[7.3] HYLIFE-II[7.4] and the LIFE reactor discussed in Appendix D. Almost any material compatible with the liquid can be used with little activation and lifetime usage. This is a very appealing approach in that the need for specially developed materials for fusion is essentially eliminated.

It does, however, place constraints on the reactor design. Coolants need to be low activation, contain lithium, and be capable of high temperature operation without excess vapor pressure in the chamber. Possible candidates are liquid lithium, lithium-lead, and Flibe. Lithium has chemical hazard concerns, and lithium-lead has concerns about polonium production (although one could possible remove it using a side stream). The use of Flibe avoids the safety concerns of liquid lithium and the activation concerns of lithium lead. Fortunately, Flibe has a considerable data base from the molten salt reactor program.[7.5]

Geometries are generally limited to cylindrically symmetric with axis vertical for gravity flow systems and horizontal for rotating systems. This places constraints on illumination, which is especially difficult with vertical flow because the streams must be parted to get the beams through. The rotating LIFE and Cascade (which uses granules instead of liquid) reactors have natural beam access through the ports.

Low-Z Ceramics. Materials containing low atomic number materials like carbon, silicon, hydrogen, lithium, beryllium, boron, aluminum, oxygen, and fluorine (but not nitrogen) have little long-life activation from fast neutrons. Unfortunately, for high temperature use the only engineering materials containing these elements are brittle ceramics. The materials of greatest interest to fusion[7.6] are carbon and graphite, silicon carbide (SiC), alumina (Al_2O_3), boron carbide (B_4C), beryllium carbide (Be_2C), and beryllia (BeO). Composites of these, such as carbon-carbon, SiC-SiC, and carbon-SiC are also being investigated. The brittleness of ceramics is mitigated by using ceramic-ceramic composites that have high fracture toughness.

Osiris uses low activation graphite in a way that eliminates the brittleness problems, as a fabric. Flibe is allowed to bleed through to provide a wetted wall. There are, however, issues concerning Flibe wetting and chemistry, as discussed above.

SOMBRERO uses large composite or graphite panels with SiC as a sealant. The sealing requirements are modest because (1) the gas to be sealed is helium, of which a fairly large quantity can probably be tolerated in the chamber, and (2) the gas pressure is no more than two atmospheres. Nevertheless, the sealing issue is critical to the success of the concept.

Ceramic composites have the promise of providing fracture toughness and a modicum of ductility. Carbon-carbon, SiC-SiC, and carbon-SiC are all being investigated using chemical vapor infiltration. One interesting feature is the ability to prepare a preform consisting of laid-up fabric and a small amount of matrix infiltration. This preform has a stiffness similar to

styrofoam and can be machine-finished with conventional tooling. It can then be further infiltrated to near full density and possess essentially the final desired dimensions. This could possibly be done in SOMBRERO with final infiltration done in-situ. The chamber would serve as its own oven.

These composites can be densified to up to 90% of theoretical density. The infiltration process requires residual porosity and permeability; therefore, they are not leak tight. Solid surface coatings are required, preferably in multiple, loosely bound layers for redundancy. For high pressure use, they are best used as an outer structural layer for solid ceramic pressure tubes and ducts.

General Atomics (GA) is looking at a carbon fiber/SiC matrix composite called "VCS" (Vapor-Carbon-Silicon) that uses annealed vapor grown carbon fibers in a CVD SiC matrix. The fibers have an axial thermal conductivity approaching diamond. They are also more resistant to fast fission neutrons than SiC. In a 50% matrix with isotropic fibers, thermal conductivity would be about that of copper. The composite could take heat fluxes of around 40 MW/m^2-cm thickness at up to 1100°C. It could take substantial neutron doses and not be inclined to absorb tritium. GA has made preforms that are readily machinable. General Motors is pursuing development of the fibers for automotive use.[7.7]

The ability of the first wall/blanket material to withstand fast neutrons impacts the minimum first wall radius and the frequency of change-outs. The neutron lifetime is defined as that operating interval beyond which the material can no longer perform its function. Much then depends on what this function is. The lifetime can be longer if loads and stresses are light, if allowance can be made for dimensional changes due to neutron irradiation, and if the material can be periodically cycled down to room temperature during shutdowns. Much of the thinking that went into the Osiris and SOMBRERO design concepts included these principles.

There are metallic, weldable materials that need to be pursued even though their activity is higher, because they are easier to fabricate into large, leak-tight assemblies. Among them are ferritic steels, vanadium alloys, and possibly other austenitic stainless steels besides 316. Innovations such as dispersion-strengthening of stainless steels should be explored. Most likely, near-term reactors will be made of welded metal. Because of the long lead times required to have a new material approved for use in construction, material research must begin well before reactor construction designs.

7.8.4 Remote Maintenance

Use of low activation materials is more valuable in reducing long-term waste storage than in providing manned access to the reactor chamber immediately after shutdown. Yet, in a power reactor, such access is required if availability is to remain high. While mentioned in the Osiris and SOMBRERO assessments, it is called out as a generic issue here, because it tends to be ignored, or it is assumed that the technology will be available when the time comes.

Remote maintenance can borrow heavily from the fission program, the remotely-piloted vehicle and aircraft programs, from NASA's telerobot program, and from the industrial robotic manufacturing and AI programs. However, there are issues specific to each design concept that require specially-tailored remote maintenance approaches. Removing the drained fabric blanket from Osiris, for example, requires different remote maintenance scenarios than leak detection and repair in SOMBRERO. While many of these issues are design, rather than developmental in nature, we should at least be able to see the way toward viable remote maintenance systems.

7.9 TECHNOLOGY ASSESSMENT RATINGS FOR GENERIC ISSUES

Table 7.6 shows a semi-quantitative technical assessment for the four generic issues discussed above. The table follows the format of the Osiris and SOMBRERO assessment.

All of these are critical in that they impact all elements of IFE powerplant development. Innovations in targets, or discoveries from reactor modelling, for example, could move the program in totally unexpected directions. For this reason, lead times are considered long so that results can impact the program before long-term commitments or premature down-selections are made.

It is important to look at the individual entries in Table 7.3 (and the other tables, for that matter), and not just the overall urgency factor. For example, while the last is fairly low for reactor modelling, criticality is high and lead time is long. Development cost, however, is very low compared to other items. This suggests an on-going, low-level effort in reactor modelling so that results can influence the IFE development program.

Low-activity, neutron-resistant materials must be vigorously pursued without delay at a fairly high level, unless a commitment is made to reactor designs that have thick "healable" flowing liquid or granule blankets like HYLIFE, Cascade, or LIFE. A main attraction for fusion

is the ability to design reactors with low radioactivity and little radioactive waste. If this is ignored, fusion will be much more difficult to sell to the voting public.

Remote maintenance, while critical, can borrow from other programs. Effort is required, however, to tailor it to the IFE program.

Table 7.6. Technology Assessment for Generic IFE Issues

TARGET DESIGN INNOVATIONS

	Low 0	25	50	75	High 100
Technical Immaturity (10%)				●	
Critical Technology (30%)				●	
High Development Cost (30%)		●			
Long Lead Time (20%)				●	
% Cost in Experiments (10%)			●		
Overall Urgency Factor			★		

REACTOR MODELING

	Low 0	25	50	75	High 100
Technical Immaturity (10%)		●			
Critical Technology (30%)				●	
High Development Cost (30%)	●				
Long Lead Time (20%)				●	
% Cost in Experiments (10%)	●				
Overall Urgency Factor		★			

Table 7.6 (continued)

LOW ACTIVITY, N-RESISTANT MATERIALS

	Low 0	25	50	75	High 100
Technical Immaturity (10%)				●	
Critical Technology (30%)				●	
High Development Cost (30%)			●		
Long Lead Time (20%)				●	
% Cost in Experiments (10%)				●	
Overall Urgency Factor				★	

REMOTE MAINTENANCE

	Low 0	25	50	75	High 100
Technical Immaturity (10%)			●		
Critical Technology (30%)				●	
High Development Cost (30%)		●			
Long Lead Time (20%)		●			
% Cost in Experiments (10%)			●		
Overall Urgency Factor			★		

7.10 SUMMARY

We have performed technology assessments two ways:

1. Qualitative task prioritization
2. Semi-quantitative assessment of development issues and urgency

While target and driver development dominate, there are several other tasks that should be pursued in parallel, but generally at a lower level. These tasks can impact driver and target development. In particular, reactor modelling and parametric studies, fusion materials, reactor chamber concepts, and beam delivery all synergistically impact the overall program. They should be supported on a continuous, but moderate, level.

A detailed development plan devised by a task force consisting of contractors, DOE, and the laboratories would provide a valuable road map to commercialization and ensure that nothing gets left out.

7.11 REFERENCES FOR CHAPTER 7

7.1 R.N. Lyon, ed., "Liquid Metal Handbook," USAEC/NAVY Report NAVEXOS P-733 (Rev) (June 1952).

7.2 D.L. Smith et al., "Blanket Comparison and Selection Study - Final Report," Argonne National Laboratory, ANL/FPP-84-1 (Sept. 1984).

7.3 J.A. Blink et al., "The High-Yield Lithium-Injection Fusion Energy (HYLIFE) Reactor," Lawrence Livermore National Laboratory Report, UCID-53559 (1985).

7.4 R.R. Moir et al., "HYLIFE-II Progress Report, Lawrence Livermore National Laboratory, UCID-21816 (Dec. 1991).

7.5 M. Rosenthal et al., "Development Status of Molten Salt Breeder Reactors," Oak Ridge National Laboratory, ORNL-4812 (Aug. 1972).

7.6 C.C. Baker et al, "Fusion Reactor Design Studies," General Atomics, GA-A13430 (April 1975).

7.7 J. Heremans and C.P. Beetz, Jr., "Thermal Conductivity and Thermopower of Vapor Grown Graphite Fibers," *Physical Review B*, **32**, No. 4, 1981 (1985).

Chapter 8

Economic Assessment

CONTENTS

8.1 INTRODUCTION 8-1
8.2 COST OF ELECTRICITY 8-2
8.3 CALCULATING PLANT OPERATING PARAMETERS 8-4
8.3.1 Thermal Power 8-4
8.3.2 Target Gain and Yield 8-5
8.3.3 Driver Efficiency 8-7
8.3.3 Pulse Repetition Rate 8-9
8.3.4 Gross Electric Power, Driver Power, and Auxiliary Power 8-10
8.4 COST MODELING FOR OSIRIS 8-12
8.4.1 Introduction 8-12
8.4.2 Direct Capital Cost for the Reference Design 8-12
8.4.3 Cost Scaling Relationships 8-17
8.4.4 Results of Parametric Studies 8-21
8.5 COST MODELING FOR SOMBRERO 8-25
8.5.1 Introduction 8-25
8.5.2 Direct Capital Cost for the Reference Design 8-25
8.5.3 Cost Scaling Relationships 8-30
8.5.4 Results of Parametric Studies 8-38
8.6 COMPARISON OF OSIRIS AND SOMBRERO 8-42
8.7 SUMMARY 8-44
8.8 REFERENCES FOR CHAPTER 8 8-45

8.0 ECONOMIC ASSESSMENT

8.1 INTRODUCTION

At the beginning of the IFE Reactor Design Studies, we performed preliminary parameter studies to help us select a set of reference design parameters, which were used to develop the detailed point designs discussed in the previous sections of this report. These preliminary parametric studies used costs and cost scaling relationships from earlier IFE reactor and driver designs documented in the SAFIRE code.[8.1] These cost scaling relationships were coupled with the new target gain curves supplied with the study guidelines.[8.2] This procedure provided us with our best guess of parameters to use for the point designs.

After completing the conceptual designs of Osiris, SOMBRERO, and the two drivers, cost estimates were made for the point designs, and new cost scaling relationships were developed and incorporated into systems economic codes for Osiris and SOMBRERO power plant. (The codes were written using MathCAD™). These codes were then used to do parametric studies of the two designs to determine the cost of electricity (COE) as a function of design and operating parameters. Not surprisingly, the optimum operating points (minimum COE) for Osiris and SOMBRERO do not coincide with the reference point parameters selected at the beginning of the study.

In this chapter, we report the costs for the reference point design, describe the cost scaling algorithms used in the modeling, and present results of the parametric studies using the new economic models. The costs are given in 1991 dollars and represent costs for a fully commercial system. Studies such as ARIES have applied learning curve factors to calculate the 10th-of-a-kind plant cost. We have not applied any learning curve credits to our costs for several reasons.

1) The results can be misleading if learning curve effects are improperly applied. For example, learning curves should not be applied to the cost of concrete or to construction labor since it is unlikely that the same crew will be building all ten plants. Multi-unit plants might benefit, but that scenario is not part of our baseline configuration.

2) Many of the large cost items are already costed assuming large quantity purchases where the costs are dominated by the cost of materials and not manufacturing costs. For example, the metglas for the induction cores is costed on a $/kg basis assuming orders greater than 1000 tonne. We have not further reduced this cost assumption for the 10th-of-a-kind plant. Likewise, the costs of conventional plant equipment (i.e., buildings, turbines, electric plant equipment, etc.) are already based on commercialized systems.

3) Since the cost estimates are uncertain to begin with, applying imprecise learning curve effects will only lead to greater uncertainly.

The costs presented here are most useful for 1) relative comparisons to other fusion designs costed on the same basis and 2) for determining an attractive operating point in the plant design space. More detailed design work and costing are needed before any meaningful comparisons can be made to future fission or coal power plants. The accuracy of the costs on an absolute basis is clearly questionable. It is interesting to note that a construction firm such as Bechtel will spend on the order of 1% of the project cost in developing detailed cost estimates for the project (i.e., $10 M for a $1 B plant). Even with that level of effort and even for a conventional, Nth-of-a-kind coal plant, a project contingency of 20% is included to account for items that can not be precisely estimated or events that can not be anticipated during construction.

8.2 COST OF ELECTRICITY

The figure of merit used in our economic assessment is the constant dollar cost of electricity (¢/kWh) which is given by

$$COE = \frac{FCR \cdot TCC + OM + F}{0.0876 \cdot \alpha \cdot Pn} + D$$

where

FCR	=	constant dollar fixed charge rate, yr^{-1}
TCC	=	total capital cost, $M
OM	=	annual O&M cost, $M/yr
F	=	annual fuel cost, $M/yr
α	=	availability factor
Pn	=	net electric power, MWe
D	=	allowance for decommissioning, ¢/kWh

The economic parameters used in these studies are summarized in Table 8.1. The values presented here were agreed on with the Technical Oversight Committee for the Reactor Design Studies and the McDonnell Douglas design team,

The total capital cost (TCC) is the sum of the direct capital cost, indirect capital costs, and time related costs. It is calculated from the following equation using the factors given in Table 8.1.

$$TCC = (1 + f91 + f92 + f93) \cdot (1 + f94) \cdot (1 + f96) \cdot (1 + f97 + f98) \cdot TDC$$

Table 8.1. Economic Parameters Used in This Study

Plant Operating Lifetime, yrs		30			
Plant Construction Lead Time, yrs		6			
Contingency Factor, Project and Progress		See below			
Spare Parts Multiplier		1.0 (no spares)			
Constant Year Dollars		1991			
Nominal Year Dollars		1997			
Inflation Rate, %/yr		5.0			
Escalation Rate, %/yr		5.0			
		Average		Tax-Adjusted	
Effective Cost of Money, Nominal Dollars		0.1135		0.0957	
Effective Cost of Money, Constant Dollars		0.0605		0.0435	
Fixed Charge Rate, Nominal Dollars		0.1638			
Fixed Charge Rate, Constant Dollars		0.0966			
Indirect Cost Factors		LSA 1	LSA 2	LSA 3	LSA 4
f91 Construction Services and Equip.	(× TDC)	0.113	0.120	0.128	0.151
f92 Home Office Engr. and Services	(× TDC)	0.052	0.052	0.052	0.052
f93 Field Office Engr. and Services	(× TDC)	0.052	0.060	0.064	0.087
f94 Owners Cost	(× TDC+91+92+93)	0.150	0.150	0.150	0.150
f95 Process Contingency	(× TDC+91+92+93+94)	0.000	0.000	0.000	0.000
f96 Project Contingency	(× TDC+91+92+93+94)	0.1465	0.173	0.184	0.195
		Constant $		Nominal $	
f97 IDC Factor		0.1652		0.3178	
f98 EDC Factor		0		0.2436	

where TDC = total direct capital cost. Note that f91, f93, and f96 depend on the level of safety assurance (LSA). For LSA = 2, the total capital cost is

$$TCC = 1.936 \cdot TDC$$

This overall multiplier varies from 1.870 for LSA = 1 to 2.066 for LSA = 4.

The TDC for the major subsystems are expressed as functions of the plant operating parameters. These cost scaling relationships are given in Section 8.4 for Osiris and Section 8.5 for SOMBRERO.

8.3 CALCULATING PLANT OPERATING PARAMETERS

The costs of the major subsystems of the power plants are scaled as a function of various system design parameters such as the driver energy, pulse repetition rate, thermal power, and gross electric power. These key design parameters can all be related to the driver energy, which then serves as the independent variable in our analysis.

8.3.1 Thermal Power

The total thermal power (MWt) of the plant is given by

$$Pt = \frac{Pn}{\eta t \cdot \left(1 - fa - \frac{1}{\eta d \cdot G \cdot M \cdot \eta t}\right)}$$

where

- Pn = net electric power, MWe,
- ηt = thermal conversion efficiency,
- fa = auxiliary power fraction (for pumping and other in-plant power requirements),
- M = total energy multiplication factor (ratio of total energy deposited in target and blanket to fusion yield per pulse),
- G = target gain, and
- ηd = driver efficiency.

The thermal power is a function of driver energy because the target gain and driver efficiencies are function of E. The net electric power, thermal conversion efficiency, auxiliary power fraction, and energy multiplication factor are fixed parameters for both designs. The base case values for these fixed parameters are given in Table 8.2. The guidelines for the study specified that the base case net electric power of the plant should be 1000 MWe.

Table 8.2. Base Case Fixed Parameters for Calculating Thermal Power

	Osiris	SOMBRERO
Pn (MWe)	1000	1000
ηt (%)	45	47
fa (%)	4	4
M	1.26	1.08

8.3.2 Target Gain and Yield

For the HIB driver, the target gain is a function of the driver energy, the beam spot size on target, and the ion range. In our modeling of the driver, the ion energy (GeV) varies with driver energy, and the focusing half angle is selected to give the smallest spot size and, thus, highest gain for a given E. The resulting base case gain curve is shown in Fig. 8.1 for our reference driver design with 12 beams, A = 131 and q = +1. In the parametric analysis, we examined the effects of more optimistic and more conservative target gain relationships. For the optimistic case, the base case gain is increased by a factor of 2, and for the conservative case, the base case gain is decreased by 30%. These curves are also shown in Fig. 8.1.

The target gain curves for direct drive laser targets are shown in Figure 8.2. The optimistic and conservative curves were provided as an supplement[8.3] to the original study guidelines.[8.2] The base case gain is the average of the optimistic and conservative gain.

The target yield (MJ) is the product of the driver energy and target gain, Y = E·G. The target yield as a function of driver energy is shown in Fig. 8.3 for the base case laser and HIB gain curves.

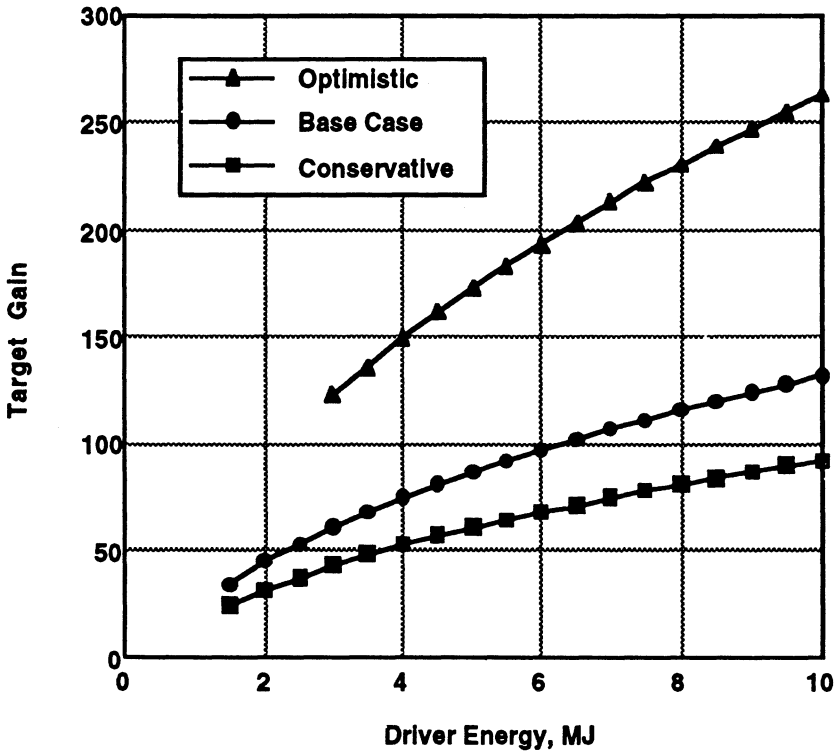

Fig. 8.1. Target gain curves for the base case HIB driver (12 beams, A = 131, q = +1) using indirect drive targets. The optimistic curve is only valid for E > 3.2 MJ, at which point the yield is ~ 400 MJ.

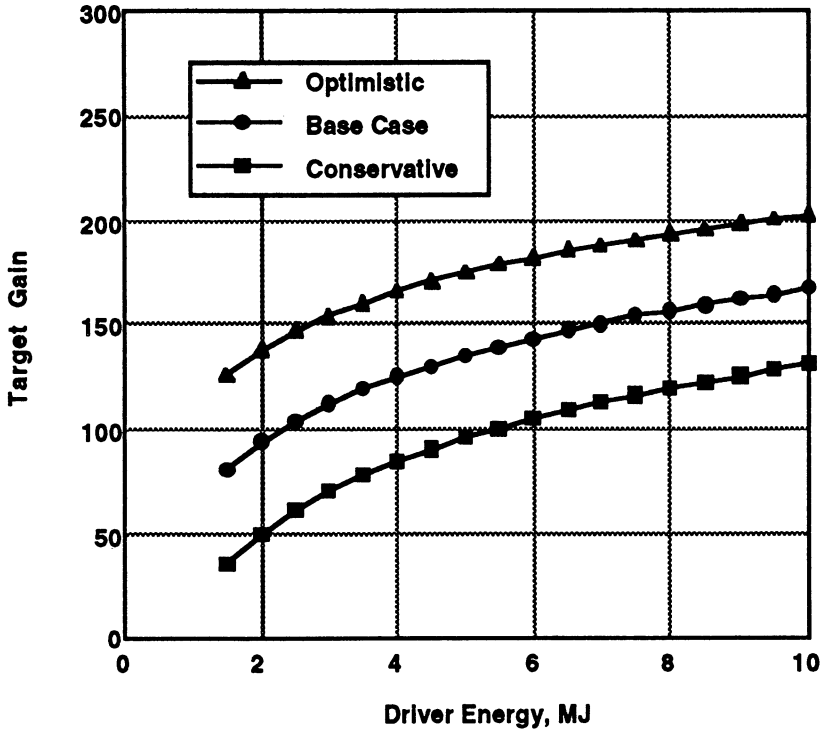

Fig. 8.2. Target gain curves for the KrF Driver. The base case curve is the average of the optimistic and conservative curves.

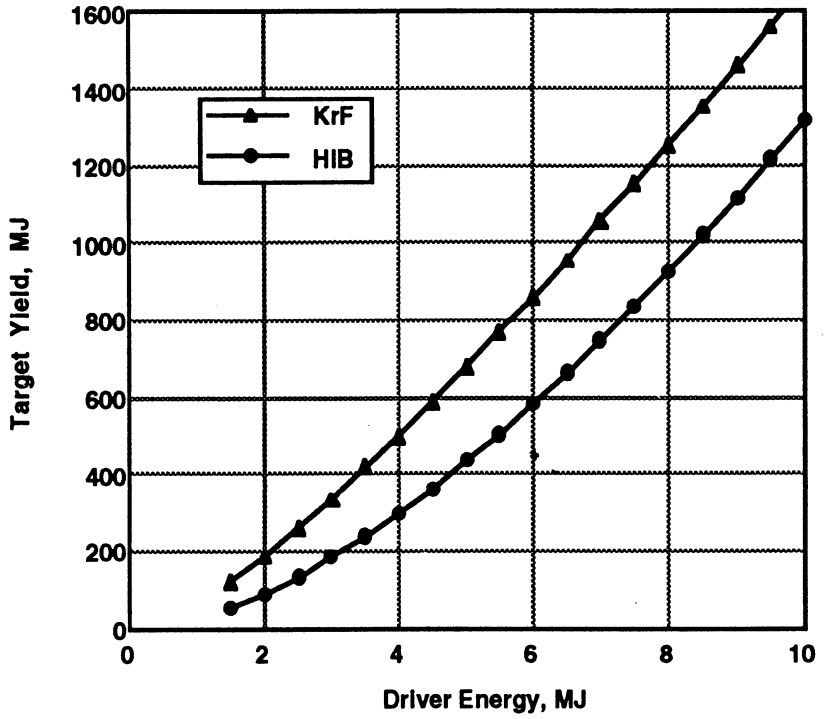

Fig. 8.3. Target yield as a function of driver energy for the two drivers. For a given driver energy, the yield is higher for the KrF laser.

8.3.3 Driver Efficiency

The final parameter required to calculate the thermal power is the driver efficiency, ηd. The HIB driver efficiency is a function of the driver energy (E) and the pulse repetition rate (RR), as described in Section 2.4. As shown below, the rep-rate is calculated from the thermal power. Therefore, we must iterate to find self consistent values for Pt, ηd, and RR. For a given energy, the thermal power is first determined using an estimate for the driver efficiency. The rep-rate is calculated from the thermal power and then used to find a new value for efficiency. This procedure converges rather rapidly. The HIB driver efficiency as a function of energy for the 1000 MWe plant is shown in Fig. 8.4.

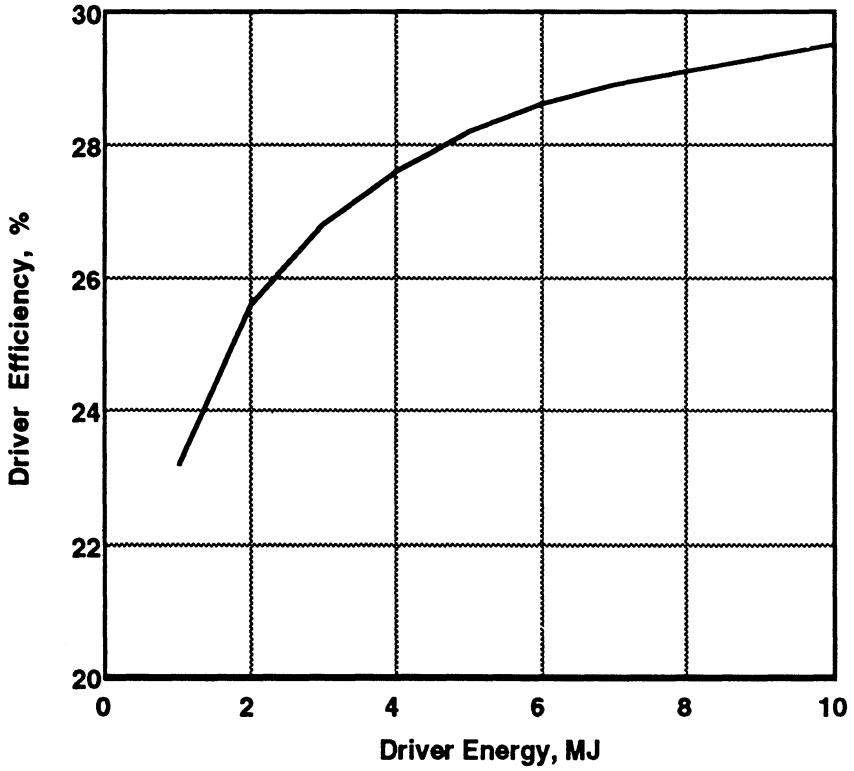

Fig. 8.4. HIB driver efficiency as a function of energy for a 1000 MWe plant.

The KrF driver efficiency is a function of the driver energy and pulse rep-rate. The dependence on rep-rate is very weak (e.g., at E = 3.6 MJ, ηd only decreases from 7.6% at 1 Hz to 7.5% at 10 Hz) and is therefore ignored in these system studies. The dependence on energy is the most important factor. The KrF driver efficiency as a function of driver energy is shown in Fig. 8.5. In the laser model, the amplifier dimensions increase with increasing driver energy while the number of amplifiers remains constant. As discussed in Section 3.4, increasing the length of the amplifier reduces the efficiency as seen in Fig. 8.5. We consider this scaling to be valid from ~1.8 to 5.4 MJ (i.e., ± 50% from the 3.6 MJ design point). (Note that the laser design was done at 3.6 MJ and then scaled to the final base case energy of 3.4 MJ.)

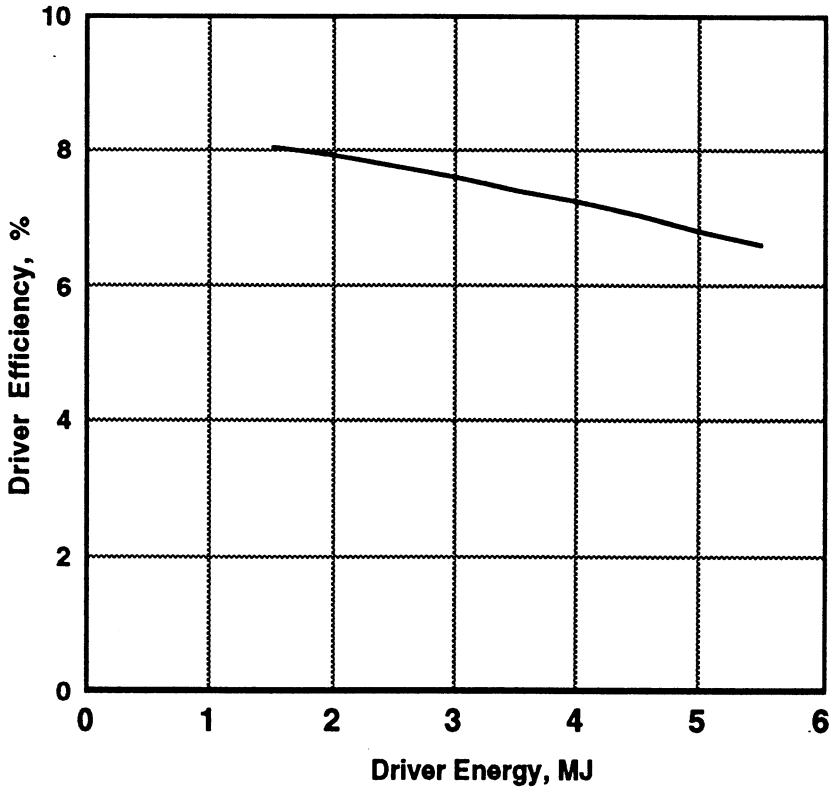

Fig. 8.5. KrF driver efficiency as a function of energy.

8.3.3 Pulse Repetition Rate

The rep-rate (Hz) required for a 1000 MWe plant is given by

$$RR = \frac{Pt}{E \cdot G \cdot M}$$

The rep-rate as a function of driver energy (using the base case gain curves) is shown in Fig. 8.6 for the laser and HIB drivers. The HIB driver operates at a higher rep-rate for a given energy since the target gain is lower.

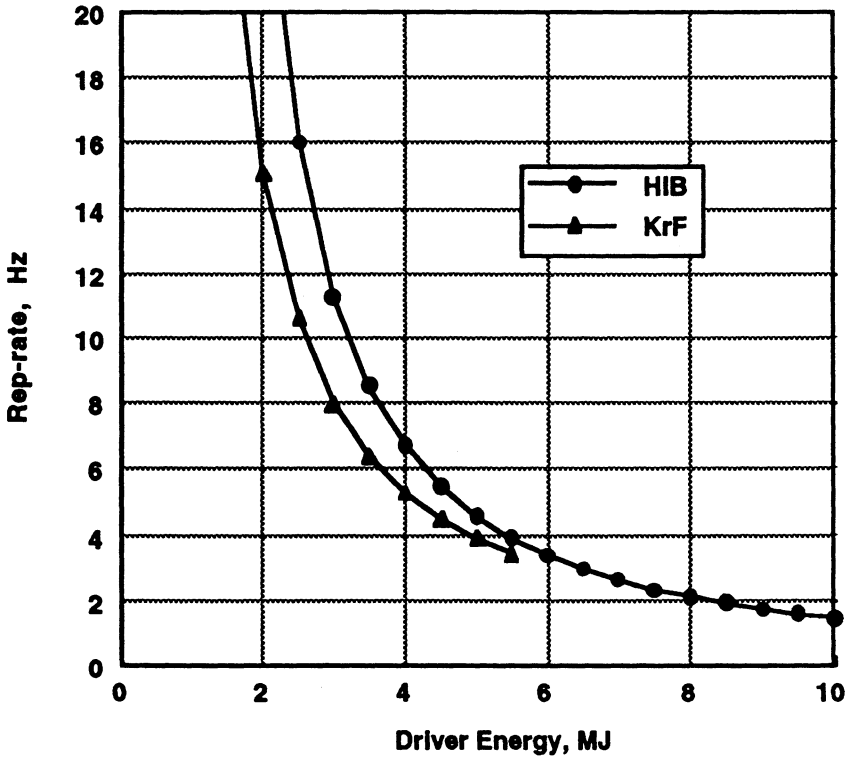

Fig. 8.6. Pulse repetition rate required for a 1000 MWe (net) power plant.

8.3.4 Gross Electric Power, Driver Power, and Auxiliary Power

The gross electric power (MWe) is

$$Pg = \eta t \cdot Pt$$

The power needed to operate the driver (MWe) is given by

$$Pd = \frac{E \cdot RR}{\eta d}$$

The auxiliary power (MWe) is

$$Pa = fa \cdot Pg$$

Figures 8.7 and 8.8 show the gross electric power and driver power as a function of driver energy for the HIB and KrF drivers. The key operating parameters for the Osiris and SOMBRERO base case designs are given in Table 8.3.

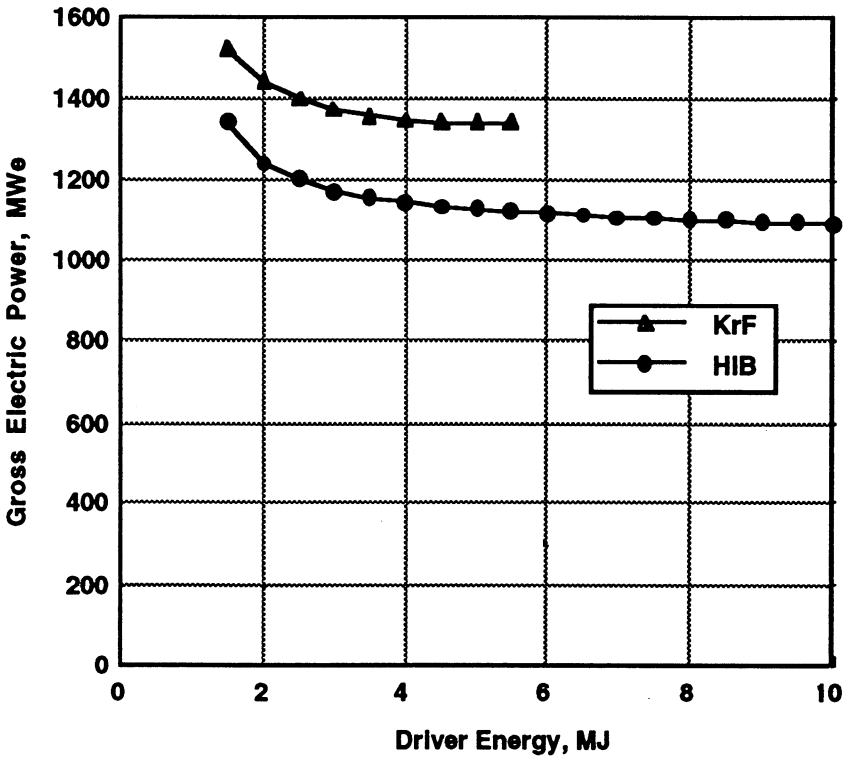

Fig. 8.7. Gross electric power as a function of driver energy. Pg is higher for the laser driven plant due to the larger driver power consumption.

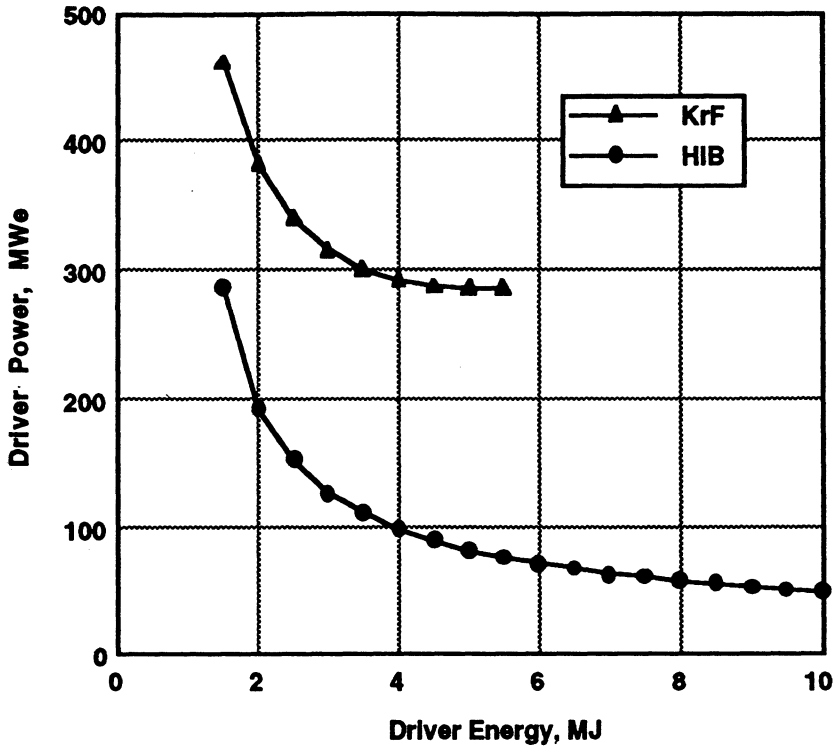

Fig. 8.8. Recirculating power required to run the driver.

Table 8.3. Base Case Operating Parameters

	Osiris	SOMBRERO
Driver energy (MJ)	5.0	3.4
Gain	86.5	118
Yield (MJ)	432	400
Rep-rate (Hz)	4.6	6.7
Driver Efficiency (%)	28.2	7.5
Thermal Power (MWt)	2504	2891
Gross Electric (MWe)	1127	1359
Driver Power (MWe)	82	304
Auxiliary Power (MWe)	45	55
Net Electric Power (MWe)	1000	1000

8.4 COST MODELING FOR OSIRIS

8.4.1 Introduction

Direct capital costs and cost scaling relationships have been developed for the HIB driver, the reactor, balance of plant systems, and the target systems. Through the use of the above expressions, all of these costs can be related to the driver energy.

8.4.2 Direct Capital Cost for the Reference Design

Table 8.4 gives the base case direct capital cost for the Osiris power plant. All costs are presented in 1991 dollars. Note that this base case design is not the minimum COE design. Lower capital cost can be achieved by lowering the driver energy. The basis for these costs and cost scaling relationships is discussed in the next section. Figure 8.9 shows the breakdown of the total direct capital cost for the reference design. The total direct cost is ~$1.6 B with the Reactor Plant Equipment and Driver Equipment making up the largest portions. Figure 8.10 shows the components that contribute to the Reactor Plant Equipment. This account is dominated by the Heat Transfer Equipment, but the breeder and remote maintenance equipment are also large cost items. Figure 8.11 shows the major components of the HI driver cost. Here we see that the inductors, pulsed power, and superconducting quads are the major cost items.

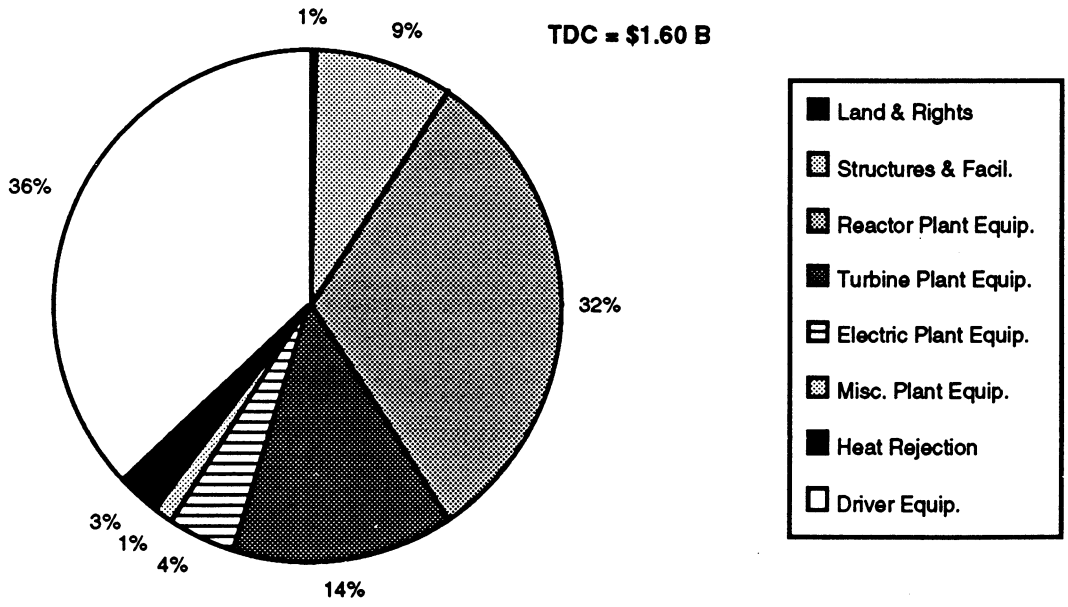

Fig. 8.9. Breakdown of total direct capital cost (TDC) for the Osiris power plant (Base Case, 1000 MWe).

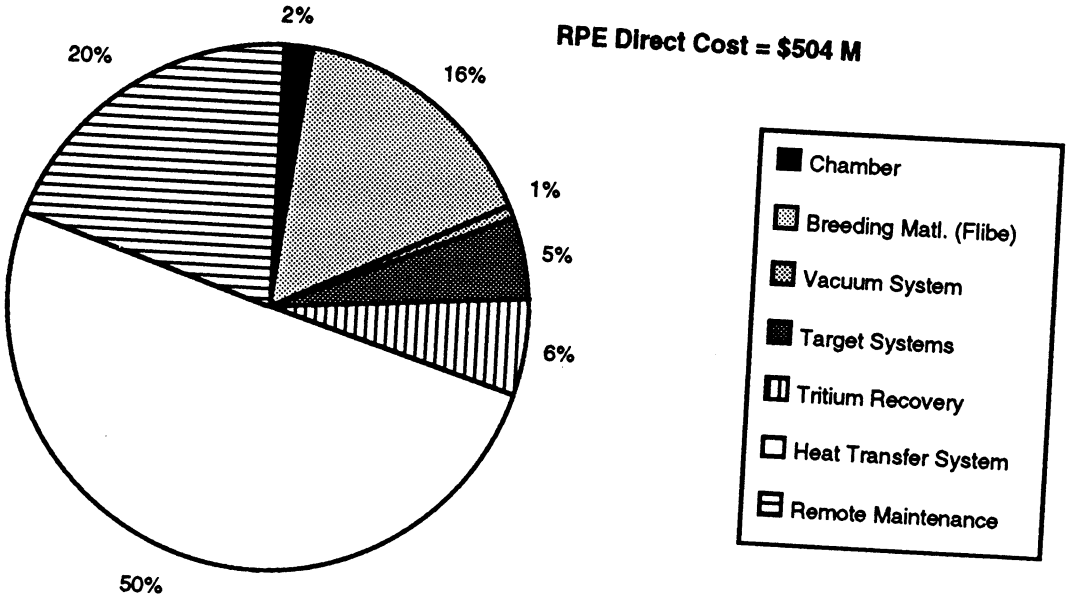

Fig. 8.10. Breakdown of Account 22 - Reactor Plant Equipment Direct Cost (Osiris Base Case, 1000 MWe).

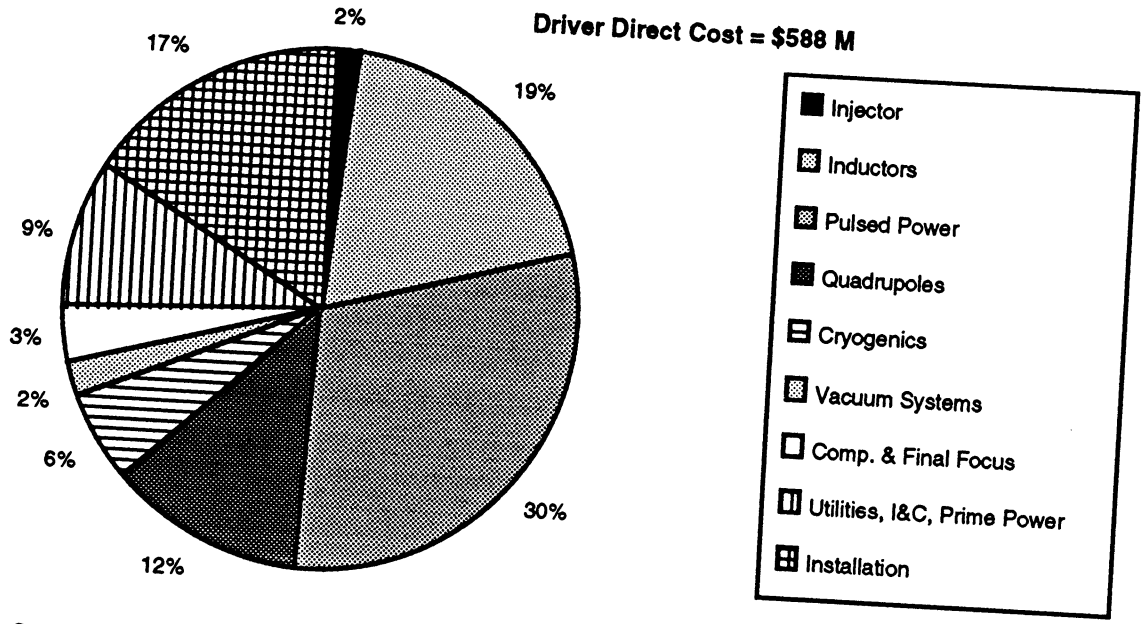

Fig. 8.11. Breakdown of Account 27 - Driver Equipment Direct Cost (Osiris Base Case, 1000 MWe).

Table 8.4. Direct Capital Cost for the Osiris Base Case Design

Account	Title		$M (1991 Dollars)	
20	**Land and Land Rights**			**11.6**
21	**Structures and Site Facilities**			**137.6**
21.1	Site Improvements and Facilities		13.8	
21.2	Reactor Building		32.9	
21.3	Turbine and Control Buildings		29.4	
21.4	Cooling System Structures		5.2	
21.5	Driver Buildings		29.2	
21.6	Miscellaneous Buildings		27.2	
	Reactor Aux. Building	4.0		
	Steam Generator Building	9.8		
	Target Fabrication Building	7.0		
	Control Room Building (w/ 21.3)			
	Admin. and Service Building	5.6		
	Hot Cell Building (w/ 21.2)			
	Misc. Structures and Bldg. Work	0.8		
22	**Reactor Plant Equipment**			**504.3**
22.1	First Wall and Vacuum Vessel		10.1	
	First Wall	0.8		
	Vacuum Vessel	9.3		
22.2	Breeding Material (Flibe)		79.8	
22.3	Vacuum System		5.0	
22.4	Target Systems		24.9	
	Production Equipment	19.9		
	Injection and Tracking	5.0		
22.5	Tritium Recovery		31.1	
22.6	Shielding (w/ 21.2)			
22.7	Heat Transport System		253.3	
	Primary Coolant Piping	27.3		
	Primary Pumps and Motors	22.5		
	Intermediate Heat Exchangers	99.9		
	Intermediate Coolant Piping	14.8		
	Intermediate Pumps and Motors	25.6		
	Intermediate Coolant Clean-up	4.2		
	Steam Generator Set	59.1		
	Remote Maintenance Equipment		100.0	

Table 8.4. Direct Capital Cost for the Osiris Base Case Design (continued)

23	**Turbine Plant Equipment**		**225.8**
23.1	Turbine-Generators	115.5	
23.2	Main Steam System (w/23.6)		
23.4	Condensing Systems	19.0	
23.5	Feed Heating System	23.1	
23.6	Other Turbine Plant Equipment	67.9	
23.7	Instrumentation and Control	0.3	
24	**Electric Plant Equipment**		**66.2**
24.1	Switch gear	12.8	
24.2	Station Service Equipment	9.3	
24.3	Switchboards	1.9	
24.4	Protective Equipment	5.0	
24.5	Electrical Structures	20.5	
24.6	Power and Control Wiring	16.7	
24.7	Electrical Lighting (w/ 21.)		
25	**Miscellaneous Plant Equipment**		**18.5**
25.1	Transportation and Lifting Equipment	6.0	
25.2	Air and Water Service Systems	8.3	
25.3	Communications Equipment	2.6	
25.4	Furnishings and Fixtures	1.6	
26	**Heat Rejection Systems**		**44.7**
27	**Heavy Ion Driver (5 MJ, 4.6 Hz)**		**587.5**
	Injector	10.0	
	Inductors	112.4	
	Metglas	71.7	
	Structure	31.2	
	Insulation	9.6	
	Pulsed Power	177.3	
	Quadrupoles	70.8	
	Cryogenics	33.0	
	Vacuum Systems	13.6	
	Compression and Final Focus	20.0	
	Special Utilities	8.7	
	Instrumentation and Control	21.9	
	Prime Power	21.9	
	Installation	97.9	
	Total Direct Cost		**1596.3**

Table 8.5 gives the total capital cost, unit capital cost, and COE for the base case design. As previously noted, the total capital cost is nearly two times the direct capital cost. The constant dollar cost of electricity is 5.61 ¢/kWh.

Table 8.5. Total Capital Cost, Unit Costs, and Cost of Electricity for Osiris Base Case Design

Total Direct Cost (M$)		**1596**
Indirect Capital Costs (M$)		
Construction Services and Equipment	192	
Home Office Engineering and Services	83	
Field Office Engineering and Services	96	
Owners Cost	295	
Project Contingency	391	
Total		**1057**
Time Related Costs (M$)		
Interest During Construction	438	
Escalation During Construction	0	
Total		**438**
Total Capital Cost (M$)		**3091**
Unit Capital Cost ($/kWe-gross)		**2743**
Unit Capital Cost ($/kWe-net)		**3091**
Constant Dollar Cost of Electricity (¢/kWh)		
Return on Capital	4.54	
Operation and Maintenance	1.00	
Fuel	0.02	
Decommissioning	0.05	
Total		**5.61**

8.4.3 Cost Scaling Relationships

The cost scaling relationships for the Osiris power plant are summarized in Table 8.6.

8.4.3.1 Balance of Plant

A rough capital cost estimate for the balance-of-plant systems and components was prepared by Bechtel. These include all structures and site facilities, steam generators and steam supply systems, turbine plant equipment, electric plant equipment (except equipment integral with the HIB), remote maintenance equipment, and miscellaneous plant equipment. The cost estimate was developed utilizing the Energy Economic Data Base[8.4] estimates for fossil-fired plants and adjusting for plant size and scoping differences. Using non-nuclear construction costs is consistent with the safety features of Osiris as discussed in Section 5. Estimates were prepared for the conceptual-designed components and structures based on past experiences where applicable and based on judgment where no previous experience existed. A specific allowance of $100 million is made for remote operated maintenance equipment. The estimates for BOP include direct labor and materials costs only. Field indirect costs for construction facilities, equipment and services, and engineering and construction management are accounted for with the indirect cost multipliers discussed above.

The scaling of the various accounts is based on the scaling given in the Nuclear Energy Cost Data Base.[8.5] Note that the driver buildings (tunnel and pulsed power building) and the target factory building are included in the Account 21 – Structures and Site Facilities.

8.4.3.2 Reactor Plant Equipment

Reactor plant equipment costs were derived from a variety of sources. The chamber and vessel costs were estimated by GA. Most of the other reactor plant equipment costs were taken from the SAFIRE Code.[8.1] The costs for primary loop piping, the IHX, and the tritium recovery system, however, were scaled from Hoffman's work[8.6] on the molten-salt cooled HYLIFE-II reactor.[8.7] The costs of the steam generator set, vacuum systems, and remote maintenance equipment were provided by Bechtel.

The first wall scales with the fusion power since we assume that the wall radius will be made large enough to last one year. The cost of the wall goes as Rw^2, which is proportional to Pt for a fixed annual fluence. The same scaling holds for the vessel wall since its location is determined by the first wall radius. The Osiris chamber design is insensitive to the yield per pulse. A higher yield simply results in more liquid Flibe being vaporized on each shot, which has to be recondensed between shots in the spray region at the bottom of the chamber. Since the fraction of energy in x rays and debris does not vary significantly with yield, the required spray flow rate is simply proportional to the chamber power.

Table 8.6. Cost Scaling Relationships for Osiris Power Plant

Account		Cost Scaling (M$ unless noted)
20	Land and Land Rights	11.6
21	Structures & Site Improvements	
21.1	Site Improvements & Facilities	13.6 $(Pg/1100)^{0.5}$
21.2	Reactor Building	32.1 (Pg/1100)
21.3	Turbine and Controls Buildings	29.0 $(Pg/1100)^{0.5}$
21.4	Cooling System Structure	5.1 $(Pg/1100)^{0.5}$
21.5	Driver Building	29.2 (L/4.8)
21.6	Miscellaneous Buildings	26.9 $(Pg/1100)^{0.5}$
22	Reactor Plant Equipment	
22.1	First Wall and Vacuum Vessel	10.1 (Pt/2500)
22.2	Breeding Material (Flibe)	79.8 (Pt/2500)
22.3	Vacuum System	5.0
22.4	Target Systems	
	Production Equipment	24.0 $(RR/6)^{0.7}$
	Injection and Tracking	5.0
22.5	Tritium Recovery	41.0 (Pt/3300)
22.6	Shielding (w/ 21.2)	
22.7	Heat Transport System	
	Primary Coolant Piping	27.0 $(Pt/2450)^{0.5}$
	Primary Pumps and Motors	22.1 $(Pt/2450)^{0.74}$
	Intermediate Heat Exchanger	97.8 (Pt/2450)
	Intermediate Coolant Piping	14.6 $(Pt/2450)^{0.5}$
	Intermediate Pumps and Motors	25.2 $(Pt/2450)^{0.74}$
	Intermediate Coolant Clean-up	4.0 $(Pt/2450)^{1.5}$
	Steam Generator Set	58.0 $(Pt/2450)^{0.89}$
22.8	Remote Maintenance Equipment	100.0
23	Turbine Plant Equipment	221.5 $(Pg/1100)^{0.8}$
24	Electrical Plant Equipment	65.6 $(Pg/1100)^{0.4}$
25	Miscellaneous Plant Equipment	18.4 $(Pg/1100)^{0.3}$
26	Heat Rejection Equipment	44.0 (Pt - Pg)/1350

Table 8.6. Cost Scaling Relationships for Osiris Power Plant (continued)

27	Driver Equipment	
	Injector	$10 M
	Inductors	
	Metglas	$5/kg
	Structure	$12.4 k / large core $ 3.1 k / small core
	Insulation	$1.25 k / core
	Pulsed Power	$10/J
	Quadrupoles	$35.8 k / quad array ($3 k / quad)
	Cryogenics	
	Fixed	$19 M
	Variable	$7.2 k / quad array ($600 / quad)
	Vacuum Systems	
	Roughing	$21 k / pump
	Number of pumps	116 (L/10.4)
	Cryopumps	$14 k / pump
	Number of pumps	1920 (L/10.4)
	Compression and Final Focus	$20 M
	Other Driver Costs Special Utilities (2%) Instrumentation and Control (5%) Prime Power (5%)	12% of above
	Installation	20% of above including Other Driver Costs

The costs for the target factory are based on rough estimates of the equipment required for our baseline production approach. This approach uses microencapsulation to produce an empty CH shell, a cryogenic DT injection process, and rapid laser heating to produce a uniform DT layer. For the HIB targets, the fuel capsule is then loaded into a Ta hohlraum before being transported to the reactor building. The cost of the injection system ($5 M) is simply an allowance that we consider to be conservative for the gas gun injector and laser diode tracking system.

8.4.3.3 Driver

The driver cost modeling is largely based on cost information developed by Lawrence Berkeley Laboratory and present in Ref. 8.8. The metglas cost of $5/kg is a cost for large lot orders (>1000 tonne) quoted to LBL by Allied. Our driver design has a metglas requirement of 20,000 tonne. The cost of the quads was estimated from the amount of material (superconducting windings, copper stabilizer, steel structure), which is calculated for the quad model described in Section 2.4. The pulsed power cost of $10/J (electric energy into the pulse forming network) is somewhat lower than LBL's estimate for future commercial systems, but reasonable based on an analysis of pulsed power costs as a function of the output pulsewidth.[8.9] We have not done the design of the pulsed power system, but since pulsed power turns out to be one of the largest cost items, it warrants more detailed analysis in future studies.

8.4.3.4 Operating and Decommissioning Costs

Annual operations and maintenance costs are based on guidance given in the study guidelines.[8.2] For an LSA = 2, the annual O&M cost is $66.4 M and scales with the square root of the gross electric power. We add an annual cost of $2 M for replacing the fabric first wall and blanket.

$$OM = 66.4 \cdot \left(\frac{Pg}{1200}\right)^{0.5} + 2.0$$

Annual fuel costs include the cost of deuterium and materials to manufacture targets. They scale directly with the fusion power, which is proportional to the thermal power.

$$F = 1 \cdot \left(\frac{Pt}{2500}\right)$$

As specified in the guidelines, we have included an allowance of 0.05 ¢/kWh for decommissioning.

8.4.4 Results of Parametric Studies

In this section we examine the capital cost and cost of electricity as a function of driver energy. We also examine the effects of using more conservative and more optimistic gain curves and the effects of operating at different net electric power levels. In most cases, the driver energy is quoted to the nearest 0.5 MJ.

8.4.4.1 Direct Capital Cost vs. Driver Energy

Figure 8.12 shows the direct capital cost of the reactor (Accounts 20-26) and driver, as a function of the driver energy for a fixed net electric power of 1000 MWe. As the driver energy increases,

- target gain and yield increase,
- pulse rep-rate decreases,
- driver power decreases, and
- thermal power decreases.

As a result, the reactor costs decrease with increasing driver energy while the driver cost increases. The minimum direct capital cost is \$1.46 B at a driver energy of ~2 MJ. The TDC of the reference plant design with a 5 MJ driver is ~10% higher at \$1.60 B.

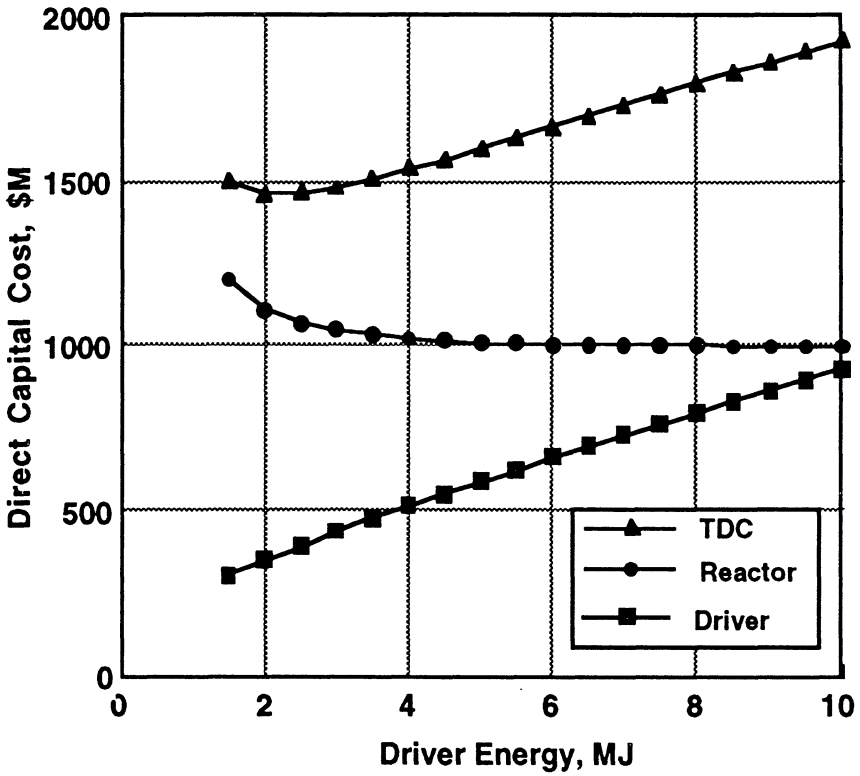

Fig. 8.12. Total direct cost (TDC) vs. driver energy for the Osiris power plant.

8.4.4.2 COE as a Function of Driver Energy

The COE as a function of driver energy is shown in Fig. 8.13. The shape of this curve is essentially the same as the direct capital cost curve. The minimum COE is 5.27 ¢/kWh, and it occurs at a driver energy of 2.5 MJ. The rep-rate at E = 2.5 MJ is 16 Hz, which is probably too high for operation of the Osiris chamber. Increasing the driver energy to 3.5 MJ reduces the rep-rate to a manageable 8.6 Hz. The COE at this point is 5.37 ¢/kWh, only 2% higher than the minimum COE. The COE of the reference point design at E = 5 MJ is 5.61 ¢/kWh, less than 5% higher than the minimum COE and 3% higher than the 3.5 MJ case.

Our original choice of a 5 MJ driver results in a COE that is about 5% higher than the minimum COE and about 3% higher than the practical minimum when we consider the rep-rate limits on the chamber. If we were to select a new point design at this time, we would lower the driver energy to 3.5 or 4 MJ to get a small reduction in COE without significantly increasing the pulse rep-rate. Table 8.7 compare the original point design with the results at 3.5 MJ.

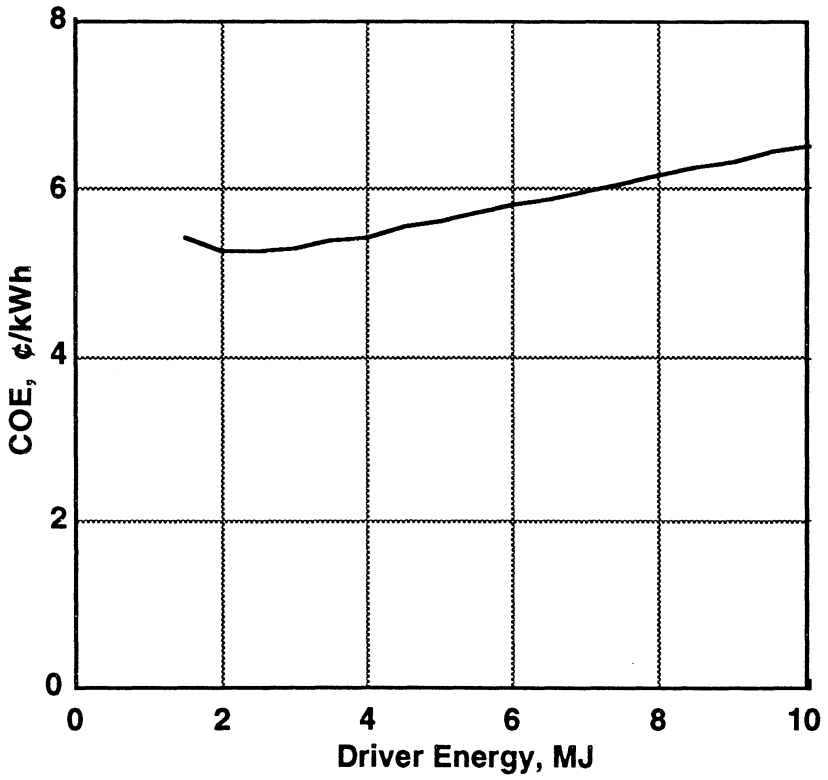

Fig. 8.13. COE for 1000 MWe Osiris power plant.

Table 8.7. Key Parameters for Two Osiris Designs

	Original Point Design	Lower COE Design
Driver Energy (MJ)	5.0	3.5
Gain	86.5	68
Rep-rate (Hz)	4.6	8.6
Gross Electric Power (MWe)	1127	1157
Driver Power (MWe)	82	110
Driver Direct Cost ($M)	587	475
Total Direct Cost ($M)	1596	1506
COE (¢/kWh)	5.61	5.37

8.4.4.3 COE with Different Target Gain Assumptions

Figure 8.14 shows the effect of increasing and decreasing the target gain. For the optimistic case, the base case gain is increased by a factor of 2. For the conservative case, the base case gain is multiplied by 0.7. Decreasing the base case gain curve by 30% shifts the point of minimum COE to E = 3.0 MJ. The rep-rate at this point (17 Hz), however, is too high. At E = 4.5 MJ the rep-rate is down to 8.2 Hz, and the COE is 5.64 ¢/kWh, or about 5% higher than the 5.37 ¢/kWh obtained with the base case gain curve. According to the revised target information supplied by the Oversight Committee,[8.3] the optimistic gain curve is only valid for yields greater than 400 MJ. Therefore, points below ~3.2 MJ on the optimistic curve are not valid. The COE at E = 3.2 MJ is 5.15 ¢/kWh, which is about 4% less than with the base case gain curve. The pulse rep-rate at E = 3.2 MJ is 4.7 Hz.

We see from Fig. 8.14 that the COE is not very sensitive to the target gain assumptions, at least over the range considered. The driver recirculating power fraction is less than 25% even with the conservative gain curve all the way down to 2 MJ. For the HIB driven system, higher driver energies (i.e., greater than 2 MJ) are needed to get higher yield per pulse so that the rep-rate can be low enough to reestablish the Osiris chamber conditions between pulses.

8.4.4.4 COE for Different Net Electric Powers

Finally, we examine the effect on the COE if the net power is increased or decreased by 50%. Figure 8.15 shows the effects of these changes. The penalty for operating at 500 MWe is significant. At 2.5 MJ, the rep-rate is 8.0 Hz, and the COE is 7.69 ¢/kWh, or 43% higher than with the base case gain curve. While the penalty for going to 500 MWe is significant, the resulting COE is in the range of results previously reported for 1000 MWe plants.[8.7,8.10] At 1500 MWe, we would operate at E = 4.5 MJ to give a rep-rate of 8.3 Hz. The COE at this point is 4.48 ¢/kWh, or 17% lower than the 5.37 ¢/kWh obtained at 1000 MWe. Both of these curves were generated using the base case gain curve.

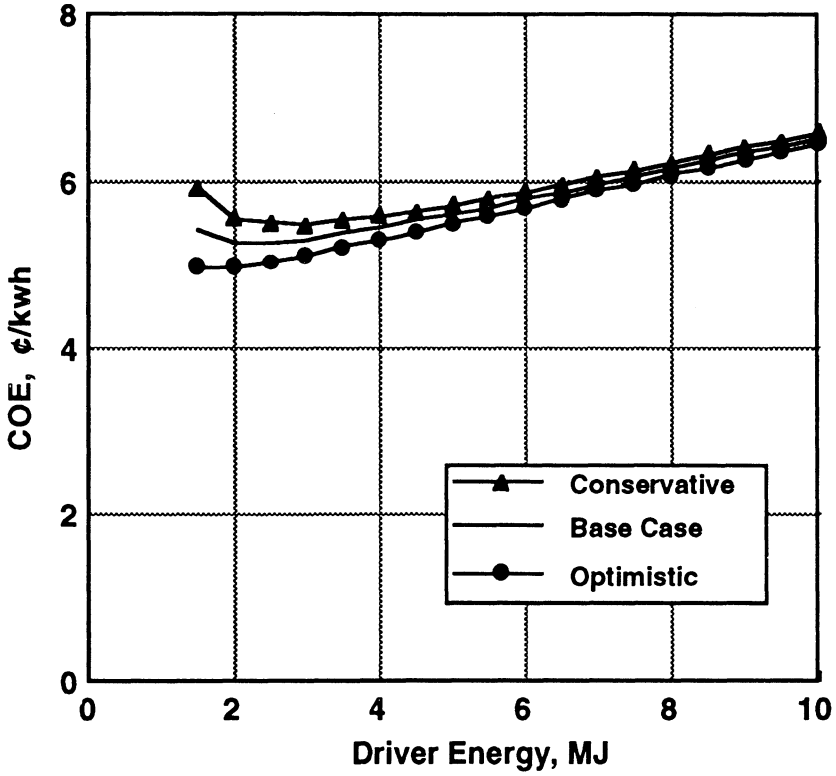

Fig. 8.14. COE for 1000 MWe Osiris power plant with different target gain assumptions. The different gain curves are shown in Fig. 8.1.

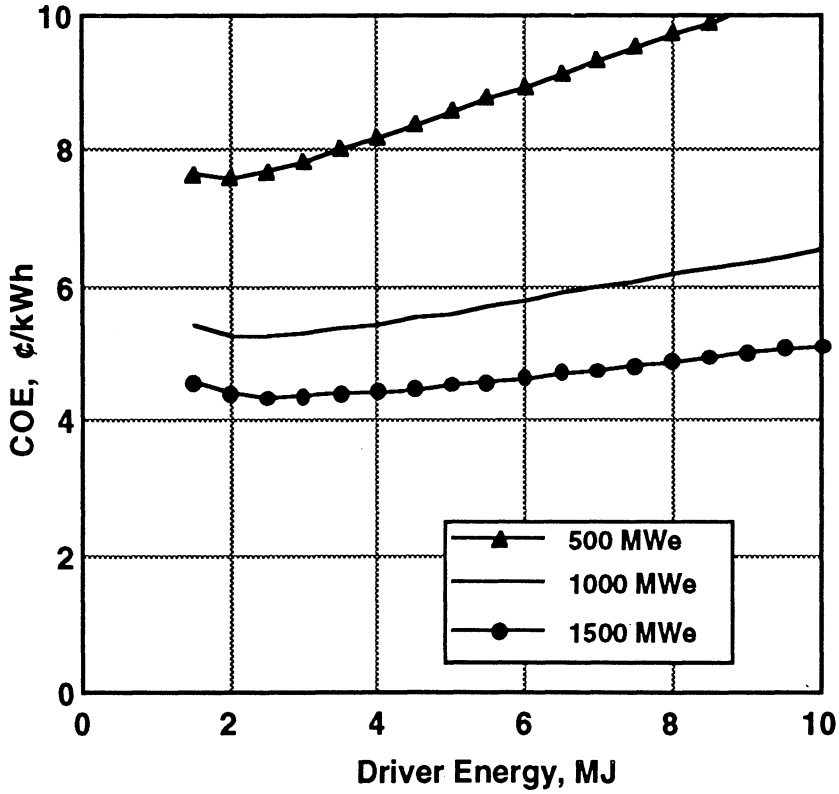

Fig. 8.15. COE for 500, 1000, and 1500 MWe Osiris power plants.

8.5 COST MODELING FOR SOMBRERO

8.5.1 Introduction

Direct capital costs and cost scaling relationships have been developed for the KrF laser, the SOMBRERO reactor, balance of plant systems, and the target systems. The costs are given in 1991 dollars and represent costs for a fully commercial system. As with Osiris, we have not applied any explicit learning curve savings in the cost estimates.

8.5.2 Direct Capital Cost for the Reference Design

Table 8.8 gives the base case direct capital cost for the SOMBRERO power plant. As with Osiris, this base case design is not the minimum COE design. Lower capital cost can be achieved by lowering the driver energy. The basis for these costs and cost scaling relationships is discussed in the next section. Figure 8.16 shows the breakdown of the total direct capital cost for the reference design. The total direct cost is ~$1.9 B with the Reactor Plant Equipment and Driver Equipment making up the largest portions. Figure 8.17 shows the components that contribute to the Reactor Plant Equipment. This account is dominated by the Heat Transfer Equipment, but the breeder and remote maintenance are also be large cost items. Figure 8.18 shows the major components of the KrF laser cost. Here we see that pulsed power and the flow systems are the major cost items.

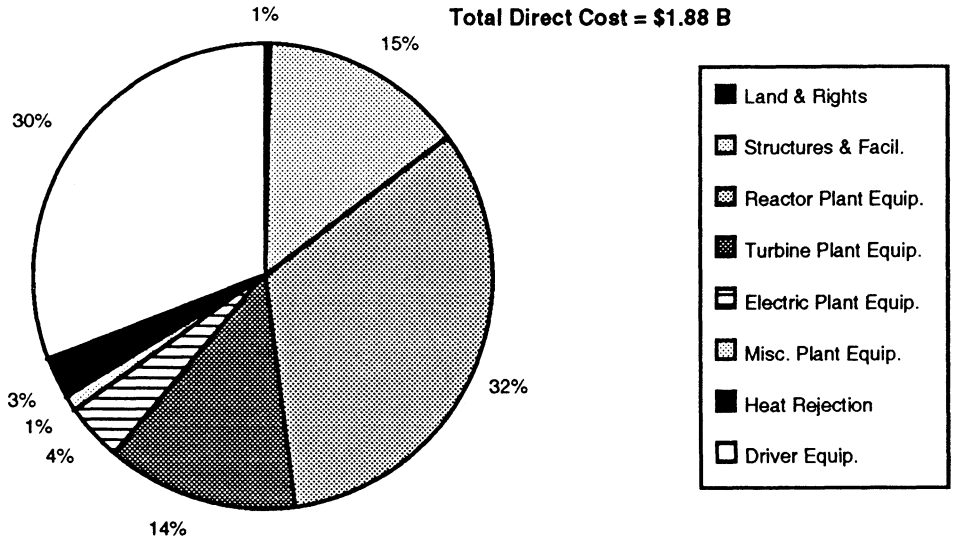

Fig. 8.16. Breakdown of total direct cost for the SOMBRERO power plant (Base Case, 1000 MWe).

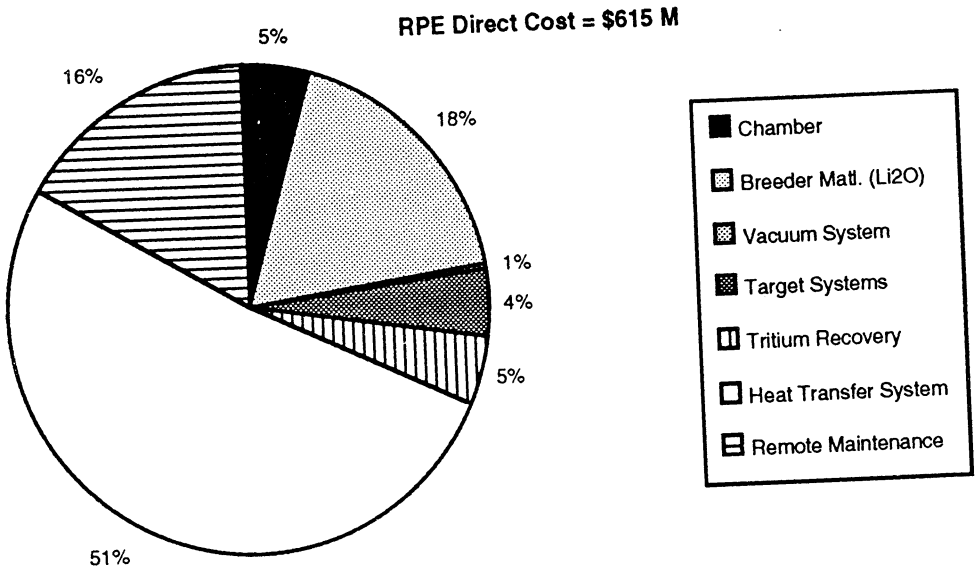

Fig. 8.17. Breakdown of Account 22 - Reactor Plant Equipment Direct Cost (SOMBRERO Base Case, 1000 MWe).

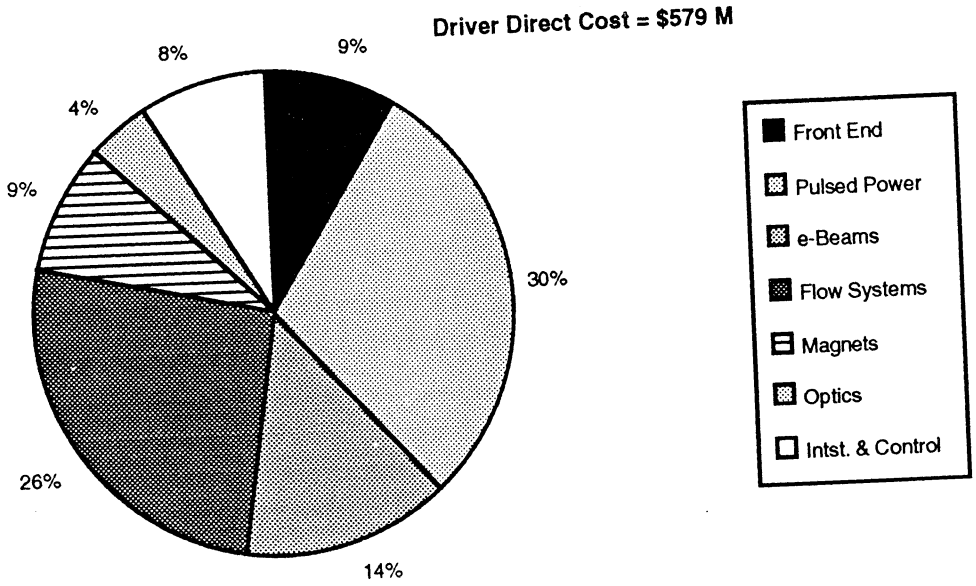

Fig. 8.18. Breakdown of Account 27 - Driver Equipment Direct Cost (SOMBRERO Base Case, 3.4 MJ).

Table 8.8. Direct Capital Cost for the SOMBRERO Base Case Design

Account	Title		$M (1991 Dollars)	
20.	**Land and Land Rights**			**10.5**
21.	**Structures and Site Facilities**			**276.1**
21.1	Site Improvements and Facilities		14.9	
21.2	Reactor Building		143.8	
21.3	Turbine Building		31.8	
21.4	Cooling System Structures		6.1	
21.5	Laser and Power Supply Buildings		31.3	
21.6	Miscellaneous Buildings		48.2	
	Reactor Aux. Building	4.6		
	Steam Generator Building	10.5		
	Target Fabrication Building	6.9		
	Control Room Building (w/ 21.3)			
	Admin. and Service Building	6.1		
	Hot Cell Building	19.2		
	Misc. Structure and Bldg. Work	0.9		
21.7	Ventilation Stack		0.0	
22.	**Reactor Plant Equipment**			**615.5**
22.1	First Wall and Vacuum Vessel		30.2	
	First Wall	9.0		
	Vacuum Vessel	21.2		
22.2	Breeding Material (Li2O)		108.4	
22.3	Vacuum System		5.0	
22.4	Target Systems (6.7 Hz)		26.6	
	Production Equipment	21.6		
	Injection and Tracking	5.0		
22.5	Tritium Recovery		28.0	
22.6	Shielding (w/ 21.2)			
22.7	Heat Transport System		317.3	
	Primary Coolant Piping	29.2		
	Primary Coolant Circulators	6.5		
	Intermediate Heat Exchangers	167.1		
	Intermediate Coolant Piping	15.9		
	Intermediate Pumps and Motors	28.4		
	Intermediate Coolant Clean-up	5.2		
	Steam Generator Set	65.0		
	Remote Maintenance Equipment		100.0	

Table 8.8. Direct Capital Cost for the SOMBRERO Base Case Design (continued)

23.	**Turbine Plant Equipment**			**256.3**
23.1	Turbine-Generators		131.2	
23.2	Main Steam System (w/23.6)			
23.4	Condensing Systems		21.5	
23.5	Feed Heating System		26.2	
23.6	Other Turbine Plant Equipment		77.1	
23.7	Intrumentation and Control		0.3	
24.	**Electric Plant Equipment**			**70.0**
24.1	Switchgear		13.6	
24.2	Station Service Equipment		9.8	
24.3	Switchboards		2.1	
24.4	Protective Equipment		5.3	
24.5	Electrical Structures		21.6	
24.6	Power and Control Wiring		17.6	
24.7	Electrical Lighting (w/ 21.)			
25.	**Miscellaneous Plant Equipment**			**19.9**
25.1	Transportation and Lifting Equipment		7.0	
25.2	Air and Water Service Systems		8.6	
25.3	Communications Equipment		2.7	
25.4	Furnishings and Fixtures		1.6	
26	**Heat Rejection Systems**			**52.0**
27	**KrF Laser (3.4 MJ, 60 beams)**			**579.1**
	Front End		52.6	
	Pulsed Power		170.5	
	DC Power	27.4		
	Modulator	24.6		
	Pulse Transformer	41.0		
	Cables	28.7		
	Switch	48.8		
	e-Beams		81.7	
	Bushing	6.5		
	Diode Box & Pumps	14.7		
	Cathode Surround	47.1		
	Foil Support	3.2		
	Foil Cooling	7.6		
	Foils	2.7		
	Flow Systems		151.3	
	Magnets		50.1	
	Optics		23.8	
	Mirrors	12.5		
	Transmissive	3.7		
	Gracing Incidence	7.7		
	Controls		49.0	
	Total Direct Cost			**1879.4**

Table 8.9 gives the total capital cost, unit capital costs and COE for the base case design. As previously noted, the total capital cost is nearly two times the direct capital cost. The constant dollar cost of electricity is 6.67 ¢/kWh.

Table 8.9. Total Capital Cost, Unit Cost, and Cost of Electricity for the SOMBRERO Base Case Design

Total Direct Cost ($M)		**1879**
Indirect Capital Costs ($M)		
Construction Services and Equipment	225	
Home Office Engineering and Services	98	
Field Office Engineering and Services	113	
Owners Cost	347	
Project Contingency	461	
Total		**1244**
Time Related Costs ($M)		
Interest During Construction	516	
Escalation During Construction	0	
Total		**516**
Total Capital Cost ($M)		**3639**
Unit Capital Cost ($/kWe-gross)		**2678**
Unit Capital Cost ($/kWe-net)		**3639**
Constant Dollar Cost of Electricity (¢/kWh)		
Return on Capital	5.35	
Operation and Maintenance	1.25	
Fuel	0.02	
Decommissioning	0.05	
Total		**6.67**

8.5.3 Cost Scaling Relationships

The cost scaling relationships for the SOMBRERO power plant are given in Table 8.10.

8.5.3.1 Balance of Plant

The balance of plant costs were done by Bechtel using the same assumptions and resources as for Osiris.[8.4] Bechtel used non-nuclear (i.e., coal-fired power plant) data base for their cost estimates. This is consistent with the safety feature of SOMBRERO as discussed in Section 5. The scaling of the various accounts is based on the scaling given in the Nuclear Energy Cost Data Base. Note that the laser buildings and the target factory building are included in the Account 21, Structures and Site Facilities.

8.5.3.2 Reactor Plant Equipment

Reactor plant equipment costs were derived from a variety of sources. The chamber cost, cost of piping, and helium recirculator in the primary coolant loop were estimated by GA. Intermediate loop pumps, piping, and clean-up systems were scaled in the same way as for Osiris. The core mass of SOMBRERO's four IHXs is about 50% greater than the total core mass in the two Osiris IHXs; therefore, the cost/kWt is increased by a factor of 1.5. The tritium recovery system cost is scaled from the Cascade reactor study.[8.5]

The first wall radius (Rw) of SOMBRERO was set large enough to avoid vaporization by x-rays and debris. By scaling Rw with the square root of the yield per pulse, the J/cm^2 is kept constant. The first wall radius is also constrained by heat transfer considerations through the first wall (i.e., a limit on W/cm^2 that can be handled). We assume that the reference case design with a radius of 6.5 m for a fusion power of 2680 MW is near the heat transfer limit. The mass of graphite structure in the SOMBRERO first wall and blanket is then found as a function of Rw as shown in Table 8.10. The total mass of Li_2O breeder is three times the mass of breeder in the breeding blanket.

The target production equipment is the same as for Osiris except the fuel capsules do not have to be loaded into hohlraums. The cost of target production for Osiris is 20% higher to account for the manufacture and loading into Ta hohlraums. The cost of the injection and tracking systems is the same as for Osiris.

Table 8.10. Cost Scaling Relationships for SOMBRERO Power Plant

Component		Cost Scaling ($M unless noted)
20	Land and Land Rights	10.5
21	Structures and Site Improvements	
21.1	Site Improvements and Facilities	17.0 $(Pg/1360)^{0.5}$
21.2	Reactor Building	143.8 (Pg/1360)
21.3	Turbine & Controls Building	31.8 $(Pg/1360)^{0.5}$
21.4	Cooling System Structure	6.1 $(Pg/1360)^{0.5}$
21.5	Driver Building	32.2 $(E/3.6)^{0.5}$
21.6	Miscellaneous Buildings	48.2 $(Pg/1360)^{0.5}$
22	Reactor Plant Equipment	
22.1	First Wall & Vessel	27.3 $(3Rw^2 + 3Rw + 1)/147$
22.2	Breeding Material (Li_2O)	
	Chamber	30.0 $(3Rw^2 + 3Rw + 1)/147$
	Flow loops	60.0 (Pt/2900)
22.3	Vacuum System	5.0
22.4	Target Systems	
	Delivery, Tracking, Alignment	5.0
	Target Factory Equipment	20.0 $(RR/6)^{0.7}$
22.5	Tritium Recovery	28.0 (Pt/2900)
22.6	Shielding (Included in 21.2)	
22.7	Heat Transport System	
	IHX	166.6 (Pt/2900)
	Primary Coolant Piping	29.2 $(Pt/2900)^{0.5}$
	Primary Coolant Circulators	6.5 $(Pt/2900)^{0.74}$
	Secondary Coolant Piping	15.9 $(Pt/2900)^{0.5}$
	Secondary Pumps and Motors	28.4 $(Pt/2900)^{0.74}$
	Secondary Loop Clean-up	5.2 $(Pt/2900)^{1.5}$
	Steam Generator Set	65.0 $(Pt/2900)^{0.89}$
22.8	Remote Maintenance Equip.	100.0
23	Turbine Plant Equipment	256.3 $(Pg/1360)^{0.8}$
24	Electrical Plant Equipment	70.0 $(Pg/1360)^{0.4}$
25	Miscellaneous Plant Equipment	19.9 $(Pg/1360)^{0.3}$
26	Heat Rejection Equipment	52.0 (Pt - Pg)/1540

Table 8.10. Cost Scaling Relationships for SOMBRERO Power Plant (continued)

27	Driver Equipment (KrF Laser)	**($K unless noted)**
	Pulsed Power (per e-Beam)	
	DC Power Supply	245 (Es/365) (RR/6.7)
	Modulator	219 (Es/365)
	Pulsed Transformer	365 (Es/365)
	Cables	256 (Es/365)
	Switch	$300 + 113\ (Acat/2)^{1.5}$
	e-Beams (per e-beam)	
	Bushing	56 (Acat/2)
	Diode B & Pumps	$16\ (Acat/2) + 113\ (Acat/2)^{1.5}$
	Cathode Surround	$200 + 200\ (Acat/2)$
	Foil Support	28 (Acat/2)
	Foil Coiling	$69\ (Es/365)\ (RR/6.7)\ (Acat/2)^{0.5}$
	Foils	23 (Acat/2)
	Flow System (per amp)	$2640\ (Eamp/60)^{0.8}$
	Magnets (per amp)	3600 (Bself/7.5) (Acoil/8)
	Optics	
	Mirrors	
	Cost, k$/m^2	$11.0 + 7.2\ [(E/3.6)\ (5/F)]^{0.5}$
	Area, m^2	734 (E/3.6) (5/F) (Nm/8)
	Transmissive Optics	
	Cost, k$/m^2	$10.2 + 33.2\ [(E/3.6)\ (5/F)]^{0.5}$
	Area, m^2	91.7 (E/3.6) (5/F) (Nt/1)
	Grazing Incidence Mirrors	
	Cost, k$/m^2	$11.0 + 19.1\ (E/3.6)^{0.5}$
	Area, m^2	276 (E/3.6) (Nb/60)
	Controls	49,000
	Front End	10% of all the above

Note: There are 2 e-beams per amplifier
Es = Energy stored per e-beam, kJ
RR = Rep-rate, Hz
Acat = Cathode area, m^2
Eamp = Energy per final amplifier, kJ
Bself = Self magnetic field, kG
Acoil = Magnetic field-coil area (per coil), m^2
E = Total driver energy, MJ
F = Optical fluence, J/cm^2
Nm = Number of mirrors per beam
Nt = Number of transmissive optics per beam
Nb = Number of beam lines

8.5.3.3 KrF Laser

The cost estimates and scaling algorithms for the KrF laser are given in Table 8.10. The reference point from which the costs are scaled is a laser that delivers 3.6 MJ on target. This is slightly higher than the 3.4 MJ we used as our reference point design for the SOMBRERO power plant. To scale the design to the lower energy, the volume of the final amplifiers would be reduced in proportion to the laser energy (i.e., by 5.6%). The cost scaling relationships were developed by Textron and are given in thousands of dollars. The following categories are used for costing:

1) Pulse Power
2) e-Beams
3) Flow Loop
4) Magnets
5) Optics
6) Instrumentation & Controls
7) Front End.

Pulse Power

As indicated in Table 8.10, pulse power is subdivided by the following categories which correspond to the sequential flow of energy through the system: D.C. supply, modulator, pulse transformer, cables, and switch. In these equations, Es is the energy stored per e-beam (kJ), RR is the rep-rate (Hz), and Acat is the cathode area (m^2). There are two e-beams per amplifier, and the energy stored per e-beam (kJ) is calculated from

$$Es = \frac{E_{Amp}}{\eta_{LS}} \cdot \frac{\eta_{wps}}{2 \text{ e-beams/Amp}}$$

where

E_{Amp} = energy on target per amplifier, kJ,
η_{LS} = laser system efficiency, and
η_{wps} = wall plug to stored energy efficiency.

For the 3.6 MJ design that was used as the reference point for costing,

E_{Amp} = 60 kJ,
η_{LS} = 7.4%, and
η_{wps} = 90%,

which gives a stored energy of 365 kJ per e-beam.

The cathode area per e-beam (m^2) is

$$Acat = L \cdot H$$

where

L = cavity pumped length in optical direction, m, and

H = cavity height in the flow direction, m.

The 3.6 MJ design has L = 1.0 and H = 2.0, which give Acat = 2 m^2. These dimensions scale as the cube root of the amplifier energy.

$$L = 1.0 \cdot \left[\frac{E_{Amp}}{60}\right]^{\frac{1}{3}}$$

$$H = 2.0 \cdot \left[\frac{E_{Amp}}{60}\right]^{\frac{1}{3}}$$

The width of the cavity, W, is 1.0 m for the reference design and also scales as the cube root of E_{Amp}. Therefore, the volume of the cavity is proportional to the laser energy as previously stated.

For 60 cavities at 60 kJ per cavity (3.6 MJ total), the pulse power cost is \$1.48 M per e-beam or about \$4 per stored joule (\$3.6 per joule input to pulse power system).

e-Beam

The e-beam system is subdivided by the following categories, which correspond to the sequential flow of energy from the pulse power, via the e-beam system, to the laser gas: bushing, diode box and pumps, cathode and surround, foil support "hibachi", foil cooling, and foils. The total direct cost per e-beam for the 3.6 MJ design is \$0.7 M.

For the e-beam voltage (kV) we use:

$$V_{eB} = \left[\frac{P_{atm} \cdot W}{8.8 \cdot 10^{-4} \cdot (1+\psi_{Ar})}\right]^{\frac{4}{7}}$$

where

P_{atm} = laser gas mixture pressure, atmospheres

ψ_{Ar} = fraction of argon in Ar + Kr of the mixture.

Flow Loop

Flow cost was calculated for relevant point designs using a Textron code for high average power excimer lasers from which a scaling algorithm was generated. As indicated in Table 8.10, the cost per laser amplifier cavity scales as the amplifier energy raised to the 0.8 power.

Magnets

The magnet cost given in Table 8.10 is the cost per amplifier for two cryogenic coils and associated power supply. The cost is proportional to the self field and area of the coil. The self field (kGauss) is calculated from

$$B_{self} = \frac{2\pi}{100} \cdot \frac{J_c \cdot H \cdot L}{(H + L)}$$

where J_c is the cathode current density (A/cm^2) and is given by

$$J_c = \frac{100 \cdot Es \cdot \eta_{wps}}{L \cdot H \cdot V_{eB} \cdot \tau_p}$$

with L and H in meters, V_{eB} in kV, and the pulse time (τ_p) in μsec. The coil dimensions are twice the cathode dimensions, therefore, the coil area (A_{Coil}) equals 2H·2L. We assumed NbTi superconductor at 6.2 K, superconductor costs of $100/kg, and copper stabilizer at $20/kg.

Optics

The cost of optics (excluding grazing incidence mirrors) is

$$C_o = \left[U_M \cdot N_M + U_T \cdot N_T\right] \cdot A_o$$

where

U_M = unit cost of mirrors, k$/m^2,
N_M = number of mirror stages from ultimate amplifiers to target,
U_T = unit cost of transmissive optics, k$/m^2,
N_T = number of transmissive optics in route, and
A_o = total optics area, m^2.

For the reference design, N_M is 8, and N_T is 2. The total area of optics per stage (m^2) is

$$A_o = \frac{E}{F} \cdot \frac{4}{\pi} \cdot 10^2$$

where

E = energy on target, MJ, and

F = design average fluence per pulse, J/cm^2.

For the reference design, F = 5 J/cm^2. The $4/\pi$ factor allows a cushion in the cost by assuming that one may need to pay for an enclosing round optic for square shapes. Rectangular shapes (H/W = 2) may be paired in cutting from a round blank.

For optics cost we mainly examined the LMF cost algorithms and the BDM study done for Los Alamos.[8.10] In Figure 8.19 we show a summary graph of the BDM results for 95 cm round plane mirrors, when done in a 900 unit order. The mirrors are coated for 248 nm, figured to $\lambda/10$ with 20 Angstrom RMS roughness.

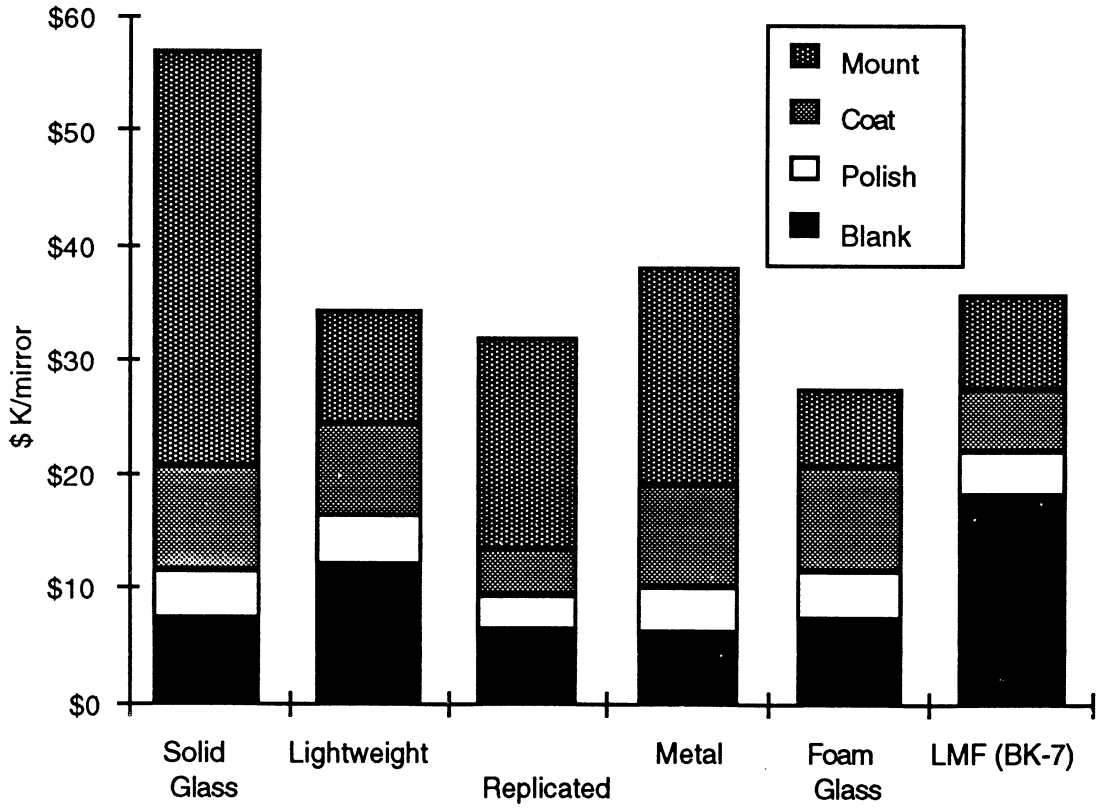

Fig. 8.19. Optics cost comparison for 900 coated 248 nm mirrors, $\lambda/10$ figure, and 20 A finish (information from Ref. 8.10).

The unit costs equations given in Table 8.10 were derived from

$$U_M = 11.0 + 0.47 \cdot \sqrt{\frac{\pi}{4}} \cdot d$$

$$U_T = 10.2 + 2.16 \cdot \sqrt{\frac{\pi}{4}} \cdot d$$

where d is the mirror or transmissive optic diagonal dimension in cm, and U_M and U_T are in \$k/m^2. The diagonal dimension is given by

$$d = \sqrt{\left[\frac{H}{W} + \frac{W}{H}\right] \cdot \frac{E \cdot 10^6}{F \cdot N_A \cdot N_B}}$$

where N_A is the number of amplifier cavities (e.g., 60 at 60 kJ each), and N_B is the number of beamlets per amplifier (600 ns / 6 ns = 100). In our design, we fixed H/W = 2, N_A = 60, and N_B = 100. This gives d = 17.3 cm for E = 3.6 MJ and F = 5 J/cm^2.

The cost scaling for the grazing incidence metal mirrors (GIMMs) is the same as for the mirrors with an appropriate adjustment for the diagonal dimension. It is assumed that the GIMM is made up of 100 individual segments instead of a single large optic. Thus the characteristic dimensions of about 10 by 46 cm are not unreasonably large. Each GIMM has an optical area of 4.6 m^2, giving a total area of 783 m^2 for the 60 beam directions.

Instrumentation and Controls

With reference to the description in Section 4.6, the cost for the KrF driver system instrumentation and controls is estimated at ~\$49 M, or \$13.60 per joule on target.

8.5.3.4 Operating and Decommissioning Costs

Annual operations and maintenance costs are the same as for Osiris except the annual blanket replacement cost is higher. We allow twice (to account for labor) the original cost every five years, or about \$11M/yr.

$$OM = 66.4 \cdot \left(\frac{Pg}{1200}\right)^{0.5} + 11.0$$

The annual fuel cost scales the same as for Osiris

$$F = 1 \cdot \left(\frac{Pt}{2500}\right)$$

As specified in the guidelines, we have included an allowance of 0.05 ¢/kWh for decommissioning.

8.5.4 Results of Parametric Studies

8.5.4.1 Direct Capital Cost vs. Driver Energy

Figure 8.20 shows the direct capital cost of the reactor (Accounts 20-26) and driver, as a function of the driver energy for a fixed net electric power of 1000 MWe. As indicated, the reactor cost decreases with increasing driver energy, while the driver cost increases. The minimum direct capital cost is $1.79 B at a driver energy of ~2 MJ. The TDC of the reference plant design with a 3.4 MJ driver is 5% higher at $1.88 B.

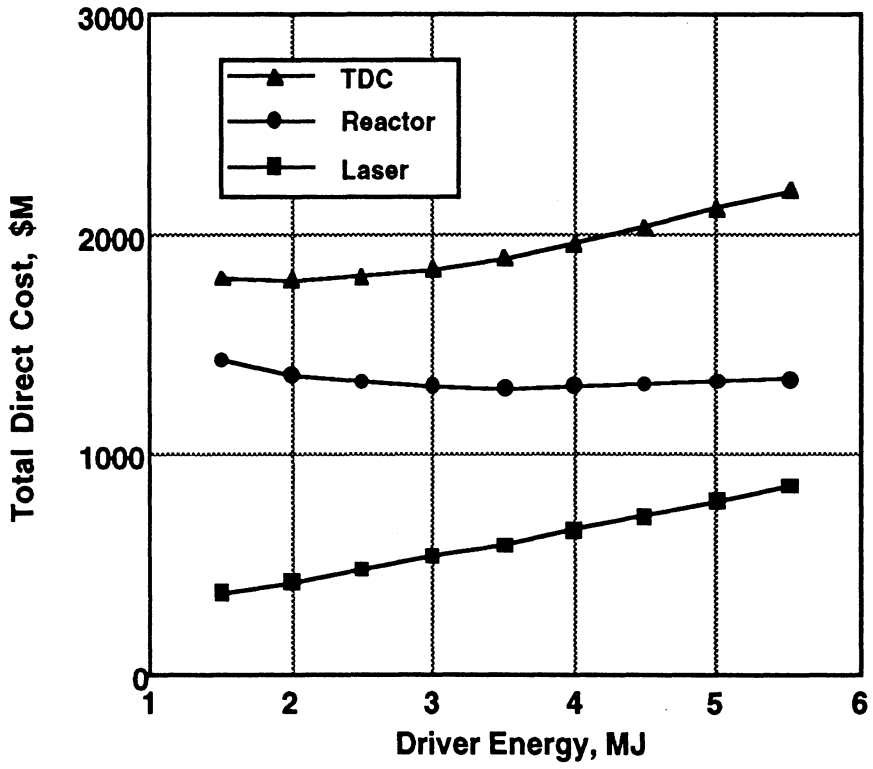

Fig. 8.20. Total direct capital cost vs. driver energy for the SOMBRERO power plant.

8.5.4.2 COE as a Function of Driver Energy

The COE as a function driver energy is shown in Fig. 8.21. The minimum COE is 6.45 ¢/kWh, and it occurs at a driver energy of 2.0 MJ. The rep-rate at E = 2 MJ is 15 Hz. We believe that the SOMBRERO chamber conditions could be reestablished at this frequency, although operating at this rep-rate puts additional stress on the target injection and tracking system.

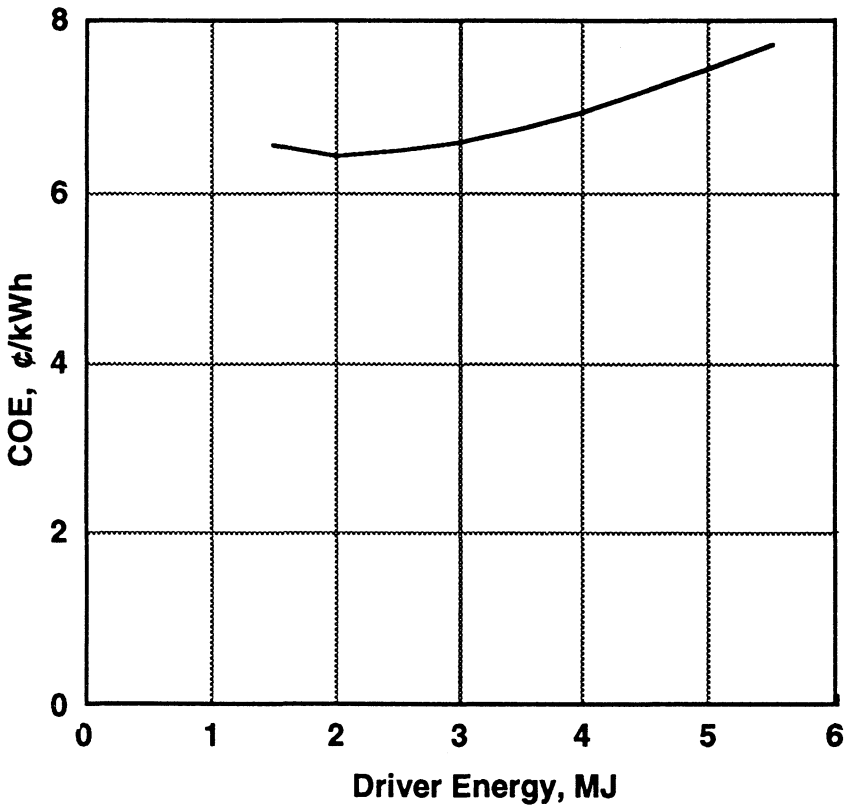

Fig. 8.21. COE for 1000 MWe SOMBRERO power plant.

The COE of the reference point design at E = 3.4 MJ is 6.67 ¢/kWh, about 3% higher than the minimum COE. Table 8.11 compares the original point design with the results at 2.0 MJ. It is interesting to note that lower COE design has a higher recirculating power fraction than the original design. The product of driver efficiency and target gain (ηG) is often used as a measure of attractiveness for IFE systems. This can be a misleading figure of merit, as we see in this example, where the lower COE design has an ηG of 7.4 compared to 8.9 for the reference point design. This occurs because the target gain curves used in this study do not fall off dramatically at low driver energy, while the cost of the laser scales strongly with energy in this range of energies. Therefore, the benefit of higher gain does not offset the cost of a larger driver.

Table 8.11. Comparison of Two SOMBRERO Design Points

	Original Point Design	Lower COE Design
Driver Energy (MJ)	3.5	2.0
Gain	118	93.9
Rep-rate (Hz)	6.7	15.1
Gross Electric (MWe)	1360	1440
Driver Power (MWe)	304	382
Driver Direct Cost ($M)	579	420
Total Direct Cost ($M)	1879	1785
COE (¢/kWh)	6.67	6.45

8.5.4.3 COE with Different Target Gain Assumptions

Figure 8.22 shows the effect of using more conservative and more optimistic target gain curves, which were supplied by DOE with the study guidelines.[8.2] The base case gain curve is the average of the optimistic and conservative curves. Using the conservative gain curve increases the COE by 15% (to 7.44 ¢/kWh) and shifts the point of minimum COE to E = 3.5 MJ. Using the optimistic gain curve lowers the COE by 7% (to 5.98 ¢/kWh) and shifts the optimum driver energy to 2 MJ.

The direct drive laser gain can be improved if the spot size of the beams at the target is zoomed to a smaller size as the pellet implodes. We examined the effect of using the gain curves with zooming. As with the curves without zooming, we have three curves with zooming: conservative (G_{cz}), base (G_{bz}), and optimistic (G_{oz}). At a fixed energy, G_{bz} is about 20 - 30% higher than G_b, the base case target gain without zooming (e.g., G_{bz} = 142 compared to G_b = 118 at E = 3.4 MJ). The minimum COE with G_{bz} is 6.00 ¢/kWh (E = 1.5 MJ, RR = 15.6 Hz, G = 113) or 7% lower than the 6.45 ¢/kWh achieved with the base case curve without zooming and about the same as the 5.98 ¢/kWh obtained with the optimistic curve without zooming. Using the highest curve of all, the optimistic curve with zooming G_{oz}, gives a COE of 5.65 ¢/kWh, or 6% lower than the optimistic curve without zooming. From these results, it does not appear that there is great incentive for zooming the laser spot size as the target implodes.

8.5.4.4 COE for Different Net Electric Powers

We also examined the effect on the COE if the net power is increased or decreased by 50%. Figure 8.23 shows the effects of these changes. (Both of these curves were generated using the base case gain curve.) At 500 MWe, the minimum COE is 8.88 ¢/kWh (E = 1.5 MJ, and RR = 12.4 Hz). This is about 38% higher the 1000 MWe case. At 1500 MWe, the minimum COE is 5.49 ¢/kWh (E = 2.5 MJ, RR = 15.9 Hz), which is 15% less than the 1000 MWe case.

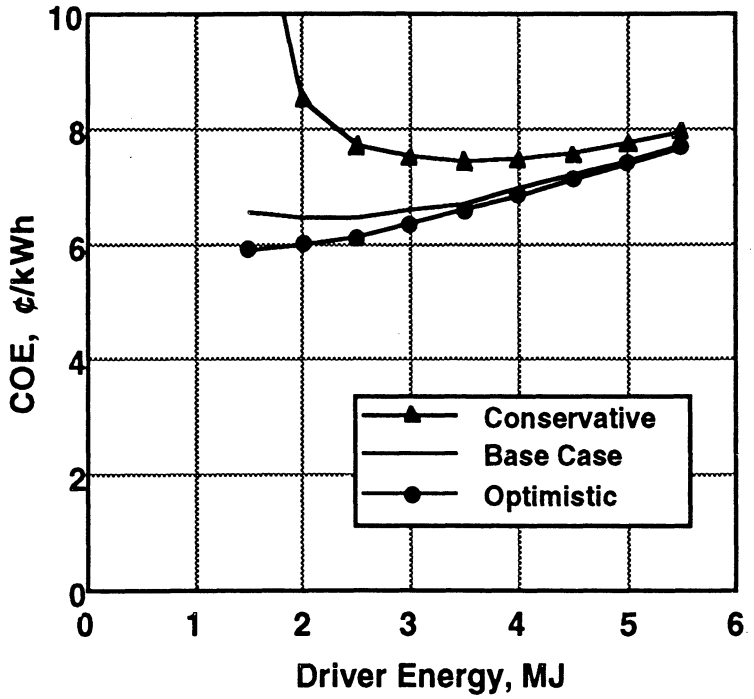

Fig. 8.22. COE for 1000 MWe SOMBRERO power plant with different target gain assumptions. The different gain curves are shown in Fig. 8.2.

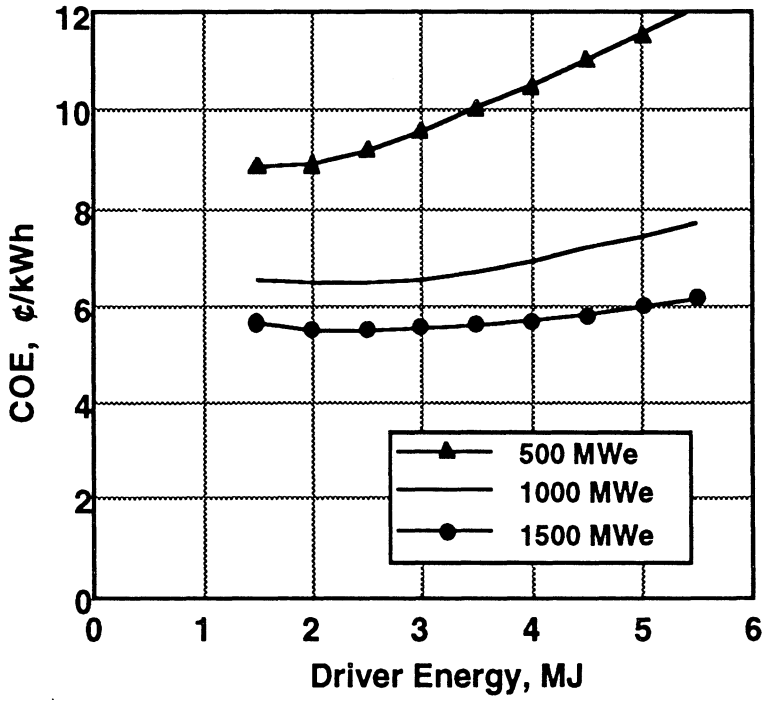

Fig. 8.23. COE for 500, 1000, and 1500 MWe SOMBRERO power plants.

8.6 COMPARISON OF OSIRIS AND SOMBRERO

The following tables compare some key operating parameters for Osiris and SOMBRERO designs that give minimum COE for various assumptions. The rep-rate for the Osiris design has been limited to <10 Hz, and the rep-rate for the SOMBRERO design has been limited to <20 Hz.

The original base case designs are compared in Table 8.12. The recirculating power for SOMBRERO is higher due to a lower efficiency driver (7.5% vs. 28.2%) and a lower energy multiplication factor (1.08 vs. 1.26). These disadvantages are partially offset by a higher gain (118 vs. 86.5) and a higher plant conversion efficiency (47% vs. 45%). As a result, SOMBRERO requires 35% more fusion power and 21% more gross electric power to produce the same 1000 MWe net power. This is reflected in the bottom line COE, which is 19% higher for SOMBRERO.

Table 8.12. Comparison of Reference Point Designs

	Osiris	SOMBRERO
Net Electric Power (MWe)	1000	1000
Gain Curve	Base	Base
Driver Energy (MJ)	5.0	3.4
Gain	86.5	118
Rep-rate (Hz)	4.6	6.7
Fusion Power (MW)	1987	2677
Gross Electric (MWe)	1127	1360
Driver Power (MWe)	82	304
Driver Direct Cost ($M)	587	579
TDC ($M)	1596	1879
COE (¢/kWh)	5.61	6.67

In both cases, the COE can be lowered by reducing the driver energy. The lower COE designs are compared in Table 8.13. The same trends as discussed for Table 8.12 are true for this comparison. In this case, the COE for SOMBRERO is 20% higher than Osiris.

Table 8.14 compares the designs when different target gain curves are used. SOMBRERO is much more sensitive to a reduction in target performance. Comparing the first two columns shows that with conservative target gain assumptions, the COE for SOMBRERO is 32% higher. SOMBRERO also benefits more from better target performance. If the optimistic gain curves are realized, the COE from SOMBRERO is only 14% higher than Osiris.

Table 8.13. Comparison of Lower COE Designs

	Osiris	SOMBRERO
Net Electric Power (MWe)	1000	1000
Gain Curve	Base	Base
Driver Energy (MJ)	3.5	2.0
Gain	68	93.9
Rep-rate (Hz)	8.6	15.1
Gross Electric (MWe)	1157	1440
Driver Power (MWe)	110	382
Driver Direct Cost ($M)	475	420
TDC ($M)	1506	1785
COE (¢/kWh)	5.37	6.45

Table 8.14. Comparison of Results with Conservative and Optimistic Gain Curves

	Osiris	SOMBRERO	Osiris	SOMBRERO
Net Electric Power (MWe)	1000	1000	1000	1000
Gain Curve	Conservative	Conservative	Optimistic	Optimistic
Driver Energy (MJ)	4.5	3.5	3.2	1.5
Gain	56.4	78.1	128	127
Rep-rate (Hz)	8.2	11.6	4.7	13.6
Gross Electric (MWe)	1179	1612	1100	1305
Driver Power (MWe)	132	547	56	253
Driver Direct Cost ($M)	551	622	451	345
TDC ($M)	1598	2103	1438	1612
COE (¢/kWh)	5.64	7.44	5.15	5.89

Results for 500 and 1500 MWe plants are compared in Table 8.15. At 500 MWe SOMBRERO's COE is 15% higher than the COE for Osiris. At 1500 MWe, the difference is 23%.

Table 8.15. Comparison of Results at 500 and 1500 MWe

	Osiris	SOMBRERO	Osiris	SOMBRERO
Net Electric Power (MWe)	500	500	1500	1500
Gain Curve	Base	Base	Base	Base
Driver Energy (MJ)	2.5	1.5	4.5	2.5
Gain	52.8	80.9	80.6	104
Rep-rate (Hz)	8.0	12.4	8.3	15.9
Gross Electric (MWe)	601	761	1701	2096
Driver Power (MWe)	76.5	231	133	512
Driver Direct Cost ($M)	394	342	551	496
TDC ($M)	1080	1224	1891	2295
COE (¢/kWh)	7.69	8.88	4.48	5.49

8.7 SUMMARY

We have developed economic models of the Osiris and SOMBRERO power plants and examined the COE as a function of the driver energy for several different sets of assumptions. For the base case assumptions, the minimum COE is 5.37 ¢/kWh for Osiris and 6.45 ¢/kWh for SOMBRERO. The difference is largely attributable to the larger fusion power and gross electric power required by SOMBRERO to generate the same 1000 MWe output. In addition, the cost of the SOMBRERO reactor building is significantly larger than the Osiris reactor building due to locating the final optics 50 m from the target. The difference in the cost of reactor buildings is ~$110 M, which is about half of the total difference in the direct capital costs of the two plants.

In the context of the level of accuracy of our cost estimates, the 20% difference in the COE is not important enough to eliminate the KrF-driven design from further development. In fact, we note that the COEs for these designs are both quite competitive with cost estimates made for ARIES-I and ARIES-II magnetic fusion energy designs, which reported constant (1988$) dollar COEs of 8.11 ¢/kWh and 6.69 ¢/kWh, respectively.[8.12] While we have not done a careful comparison of the IFE designs with the MFE designs, it is interesting to note that the cost of the drivers (at ~$600 M) is on the same order as the $500 M sum of costs for the magnets ($339 M), current heating ($108 M), and energy storage ($51 M) for ARIES-I (ARIES costs in 1988$). The COEs for Osiris and SOMBRERO are higher than the projected COEs for the 1200 MWe Improved PWR (4.3 ¢/kWh) and 1200 MWe Advanced PWR (4.5 ¢/kWh), but they are competitive with the projected COE from future coal plants (5.8 ¢/kWh) and best experience present day PWRs (5.4 ¢/kWh).[8.13]

The sensitivity of the results to different levels of target performance and net electric output was examined. With optimistic target gain assumptions, the minimum COE is about 4-9% lower (Osiris result given first), and with conservative target gain assumptions, the COE is about 5-15% higher than the base case. Increasing the net power to 1500 MWe reduces the COE by 17-15%, and reducing the net electric power to 500 MWe increases the COE by 43-38%. The cost comparisons are most useful for identifying the most attractive operating space.

8.8 REFERENCES FOR CHAPTER 8

8.1 T.J. McCarville, W. R. Meier, C. F. Carson, and B. B. Glasgow, " SAFIRE - A Systems Analysis Code for ICF Reactor Economics," LLNL Report UCRL-15872 Vol. 1 (Jan. 1987).

8.2 R.C. Davidson et al., "Inertial Confinement Fusion Reactor Design Studies Recommended Guidelines," (Sept. 1990).

8.3 "Revised Target Information for ICF Reactor Studies," Memo prepared by Target Working Group of IFE Reactor Studies Oversight Committee (Feb. 1991).

8.4 "Energy Economic Data Base (EEDB) Program-1X, Phase 9," United Engineers & Constructors/Oak Ridge National Laboratory, Report No. DOE/NE-0091 (July 1988).

8.5 "Nuclear Energy Cost Data Base - A Reference Data Base for Nuclear and Coal-fired Powerplant Power Generation Cost Analysis," U. S. DOE Report DOE/NE-0095 (Sept. 1988).

8.6 M.A. Hoffman, "HYLIFE-II Heat Transport System and Balance of Plant Design, Performance, and Cost Study," UC Davis Final Report No. 2 (Sept. 1991).

8.7 R.W. Moir, "HYLIFE-II Inertial Fusion Energy Plant Design," *Fusion Technol.*, **19**, 617 (May 1991).

8.8 C. Fong, "Update on the Cost of a Linac Driver" Lawrence Berkeley Lab Report (Jan. 1991).

8.9 M.J. Monsler, "A Search for a Minimum Cost Heavy Ion Beam for an Inertial Fusion Test Facility," Sartori Technologies Final Report (Feb., 1987).

8.10. J.H. Pitts et al., "The Cascade Inertial Confinement Fusion Reactor Concept," Lawrence Livermore National Laboratory, UCRL-LR-104546 (Dec. 1990).

8.11 "Cost Reduction Study for the LANL KrF Laser-Driven LMF Design," BDM Report BDM/ABQ-89-0747-TR (Oct. 1989).

8.12 R.L. Miller, R. A. Krakowski, and ARIES Team, "Options and Optimizations for Tokamak Reactors: ARIES," *Fusion Technol.*, **19**, 802 (May 1991).

8.13 J.G. Delene, "Updated Comparison of Economics of Fusion Reactors with Advanced Fission Reactors," *Fusion Technol.*, **19**, 807 (May 1991).

Chapter 9

Comparison of Osiris and SOMBRERO

CONTENTS

9.1 INTRODUCTION 9-1
9.2 CHAMBER AND VACUUM SYSTEMS 9-1
9.2.1 First Wall Protection 9-1
9.2.2 Blanket Designs 9-2
9.2.3 Nuclear Performance 9-3
9.2.4 Vacuum System Designs 9-4
9.3 POWER CONVERSION SYSTEMS 9-5
9.4 BUILDING VOLUME COMPARISON 9-6
9.5 DRIVER SYSTEMS 9-7
9.5.1 Heavy-Ion Driver 9-7
9.5.2 KrF Laser 9-8
9.6 TARGET SYSTEMS 9-8
9.7 OPERATION AND MAINTENANCE COMPARISON 9-9
9.8 ENVIRONMENTAL AND SAFETY COMPARISON 9-10
9.8.1 Tritium Parameters Comparison 9-10
9.8.2 Environmental and Safety Analysis 9-10
9.9 ECONOMIC COMPARISON 9-11
9.10 REFERENCES FOR CHAPTER 9 9-12

9.0 COMPARISON OF OSIRIS AND SOMBRERO DESIGNS

9.1 INTRODUCTION

In this chapter, we give quantitative comparisons of some of the key design features and operating parameters of Osiris and SOMBRERO. We also highlight key advantages and issues of two approaches. No attempt was made to rate and rank the two concepts using a numerical scoring system as in studies such as BCSS[9.1] and ESECOM.[9.2] Both designs have major uncertainties and require significant technology development. At this time, there is no clear choice for the best concept. More meaningful comparisons and judgments of attractiveness can be made after some of the critical issues are addressed and the technologies are developed further.

The design comparisons in this chapter follow the outline of this report; chamber designs, power conversion and plant facilities, driver designs, target systems, environmental and safety, and economics are compared. Each comparison consists of a tabular summary of the key features, parameters, and/or results for each design, followed by a descriptive comparison of the features and some of the key issues for the two designs.

More detailed comparisons can be found on technology development requirements (Chapter 7), environment and safety (Chapter 5), and economics (Chapters 8). In addition, Appendix F gives the results of a survey of our scientists and engineers in which they were asked to assign qualitative "confidence level ratings" for various aspects of the two designs.

9.2 CHAMBER AND VACUUM SYSTEMS

9.2.1 First Wall Protection

Table 9.1 contrasts the key design features of the Osiris and SOMBRERO chamber designs. Osiris and Sombrero use different methods to protect the first wall material. The Osiris design uses a sacrificial layer of molten Flibe which must be replaced between shots. The SOMBRERO first wall is protected from target x-rays and ion debris by 0.5 torr of Xe, which spreads out the energy deposition time and prevents vaporization of the C/C composite. The two design choices were driven by the great difference in the required gas pressures assumed for final beam transport the two drivers. The background gas limits for laser drivers are determined by electrical discharge breakdown of the gas and are much higher than the particle transport limits for heavy-ion beams. Although various high-pressure transport modes (pinch-modes, plasma channel transport, etc.) have been proposed for heavy-ion beams, the most conservative calculations (ballistic transport) require very low background gas pressures to avoid excessive beam loss.

Table 9.1. Chamber Designs for Osiris and SOMBRERO

	Osiris	SOMBRERO
Yield (MJ)	432	400
Rep-Rate (Hz)	4.6	6.7
Fusion Power (MW)	1987	2677
Total Thermal Power (MWt)	2504	2891
First Wall Material	Liquid Flibe, Woven Graphite Fabric	4-D Weave, C/C Composite
X-ray and Debris Protection	Weeping Flibe	3.25 torr-m of Xe
Impulse on FW, Pa-s	90	2.1
FW / Blanket Replacement	Suspended fabric removed with roof	Chamber sections lowered, rotated, and removed
Breeding Material	Molten Flibe	Li_2O Granules
Blanket Thickness (m)	0.7	1.0
Chamber Outer Wall Material	C/C Composite	C/C Composite
Outer Wall Radius (m)	6.5	7.5

Because of the complex chemical kinetics of the Flibe cloud vaporized from the Osiris first wall, radiation transport and hydrodynamics calculations for Osiris are much more complicated than those for SOMBRERO. This leads to greater uncertainty in the fireball and vaporization calculations for Osiris, but in both cases the uncertainties are more likely to affect design parameters (e.g., achievable rep-rate, minimum wall radius) than concept credibility.

Both chamber designs assume carbon-based structural materials, which require further development.

9.2.2 Blanket Designs

Blankets used in fusion reactors must provide heat transport and tritium breeding; in addition, they should minimize potential hazards resulting from activation and chemical hazards. The blankets used in Osiris and SOMBRERO use different approaches to meet these design goals. Osiris uses flowing molten Flibe channels for breeding and heat transport, as well as for replenishing the sacrificial protection layer for the first wall. SOMBRERO, in contrast, uses a fluidized flow of solid Li_2O particles in a helium purge gas to get the advantages of both a solid breeder and a moving blanket.

The fluid dynamics and heat transport rates for the Flibe cooling channels used in Osiris are well established. However, issues connected with the weeping rate of Flibe through carbon fabric and the vaporization behavior of the sacrificial Flibe surface require more experimental and developmental work.

In the SOMBRERO design, blanket concerns are separated from issues associated with chamber dynamics, but assumptions on heat transfer rates and fluidized flow need to be verified by further experimental work.

9.2.3 Nuclear Performance

Nuclear parameters for the two chambers are compared in Table 9.2. Both Osiris and SOMBRERO have a very robust breeding ratio. However, because there is a large quantity of Be in the Flibe, the energy multiplication is higher than in Li_2O. First wall damage, He production, and estimated chamber life are all functions of the chamber radius. Since the first wall radius in Osiris is 3.5 m as compared to 6.5 m in SOMBRERO, the damage rate in Osiris is higher, and the first wall lifetime is lower. There is considerable uncertainty in the estimated first wall lifetime for both systems, because of the scarcity of damage data for the materials in question.

Table 9.2. Comparison of Nuclear Parameters for Osiris and SOMBRERO

	Osiris	SOMBRERO
Tritium Breeding Ratio	1.24	1.25
Overall Energy Multiplication	1.26	1.08
Maximum First Wall Damage (dpa/FPY)	42	15.3
Maximum He Production (appm/FPY)	10,600	3,770
Estimated Chamber Life (FPY)	1.8	5
Estimated Life of Final Optics (FPY)		
Steering Dipoles	40	
Grazing Incidence Mirror		1.7 - 40
Estimated Life of Next-to-Final Optics (FPY)		
Final Quadrupoles	40	
Final Focusing Mirrors		45
Maximum First Wall Surface Heating (MW/m^2)	3.9	1.5
Maximum First Wall Nuclear Heating (W/cm^3)	30.9	10.9
Maximum Breeder Nuclear Heating (W/cm^3)	66.5	12.9

The final and next-to-final optics in Osiris are well shielded and can survive the lifetime of the reactor (30 to 40 full-power-years (FPY)). In SOMBRERO, the grazing incidence mirror is subjected to direct line of sight neutrons, and its life will depend on the degree of recovery by annealing. However, the final focusing mirror is out of the line-of-sight of primary neutrons. Furthermore, the primary neutrons are directed into neutron traps; thus, the final focusing mirror has a full reactor lifetime even if limiting fluence to the dielectric coating is only 10^{18} n/cm^2.

9.2.4 Vacuum System Designs

Key vacuum system characteristics are compared in Table 9.3. While the vacuum systems for the two reactors are vastly different, both are current state-of-the-art. SOMBRERO requires a high pumping capacity at relatively high pressure (0.5 torr) pumping system while Osiris needs a lower capacity system at a much lower pressure (10^{-5} torr). In addition to the low pressure pumps needed for Osiris, some combination of isolation shutters and high speed pumps will be needed to isolate the lower pressure (10^{-8}) beam lines from the chamber. The development needs for such a system are high. SOMBRERO will have 50 pumping stations each with a capacity of 3×10^4 l/s. Roots pump with capacity of 10^4 l/s are available today, so a factor of three extrapolation is reasonable. The development needs for this will be modest. Although the pumping system for SOMBRERO requires less development than that for Osiris, the leak tightness of the carbon panels and seams in SOMBRERO will need to be established.

Table 9.3. Comparison of Vacuum System Characteristics

	Osiris	SOMBRERO
Atmosphere in Chamber	F, Li, Be, He	Xe, He
Steady State Pressure (torr)	10^{-5}	0.5
Evacuated Volume (m^3)	$1.2 \times 10^{3*}$	8.9×10^5
Driver Pressure Requirement (torr)	10^{-8}	NA
Pumping Speed (l/s)		1.4×10^6
Type of Chamber Pumps	Turbomolecular	Roots pumps
Type of Beam-line Pumps	Cryopumps	NA
Driver Beam-line Isolation	Needed	Not needed

*Exclusive of beam lines

9.3 POWER CONVERSION SYSTEMS

Table 9.4 contrasts the power conversion system parameters for Osiris and SOMBRERO. Both reactors use a lead intermediate loop to reduce tritium flow to the steam in the secondary loop and a double reheat steam cycle to maximize the power conversion efficiency. The differences result from the choice of primary coolant and the differences in gross power.

Table 9.4. Power Conversion Systems for Osiris and SOMBRERO

	Osiris	SOMBRERO
Power Balance		
Power Conversion Eff. (%)	45	47
Total Thermal Power (MWt)	2504	2891
Gross Electric Power (MWe)	1127	1359
Primary Loop		
Coolant	Flibe	He w/ Li_2O granules
Temperature Range (°C)	500 - 650	550 - 700
Tritium Inventory (g)	1.0	162
Tritium Removal	Vacuum Pumping	Adsorption of HTO vapor
Intermediate Loop		
Coolant	Lead	Lead
Temperature Range (°C)	400 - 600	400 - 600
Number of IHXs	4	4
IHX Rating (MWt)	625	725
Secondary Loop		
Coolant	Water / Steam	Water / Steam
Temperature Range (°C)	286 - 538	286 - 538
Cycle	Double Reheat	Double Reheat
Peak Steam Pressure (MPa)	24	24
Number of Steam Generators	2	2
S.G. Rating (MWt)	1250	1450
Number Turbine Generators	1	1
T.G. Rating (MWe)	1130	1360
T_2 Permeation to Steam Cycle (Ci/day)	1.0	15

The solubility of T_2 in Li_20 is roughly 50 times higher than in Flibe. That coupled with the factor of 2.1 larger breeder inventory in SOMBRERO accounts for the large difference in tritium inventories in the two designs. This also accounts for the factor of 15 difference in the steady state T_2 permeation into the steam cycle.

The SOMBRERO reactor requires a larger gross power than Osiris because heavy-ion drivers require less power than KrF lasers for a given fusion power. (The ratio of fusion thermal power to required driver power is given by the product of the driver efficiency, the target gain, and the blanket energy multiplication factor.) In order to improve the net efficiency of the SOMBRERO power conversion cycle, waste heat from the laser driver is used in a feedwater heater for the secondary loop.

9.4 BUILDING VOLUME COMPARISON

The volumes of the power plant buildings are compared in Table 9.5. As can be seen, SOMBRERO has a much larger reactor building than Osiris. This is, of course, typical of a direct drive system, which requires a large number of beams using symmetric illumination and the distance required to protect the dielectric optics. The accelerator tunnel and the tunnel service building together have a volume of 3.4×10^5 m^3 whereas the KrF laser building volume is 7×10^5 m^3. The major difference is that the Osiris accelerator is spread over several kilometers. Osiris also has a separate IHX building, while in SOMBRERO the IHX enclosure is inside the reactor building. The steam generator, turbine generator, and auxiliary buildings are comparable in size for both systems.

Table 9.5. Comparison of Building Volumes

	Osiris	SOMBRERO
Reactor Building Volume (m^3)	1.2×10^4	9×10^5
Accelerator Tunnel Volume (m^3)	2.2×10^5	
Laser Building Volume (m^3)		7×10^5
Tunnel Service Building Volume (m^3)	1.2×10^5	N/A
Maintenance Building Volume (m^3)	2.1×10^4	3.1×10^4
IHX Building Volume (m^3)	4.8×10^3	In reactor building
Steam Generator Building Volume (m^3)	2.9×10^4	3.1×10^4
Turbine Generator Building Volume (m^3)	1.3×10^5	1.3×10^5
Auxiliary Building Volume (m^3)	1.8×10^4	1.9×10^4

9.5 DRIVER SYSTEMS

Needed driver performance parameters for the two designs are shown in Table 9.6. Both drivers are far larger than present-day experiments and require a great deal of development work. The KrF laser builds on the Nike and Aurora experiments. The Aurora laser has delivered 10 kJ on target, while the needed energy for SOMBRERO is 3.4 MJ. The principle of multiple beam transport has been demonstrated in Lawrence Berkeley Laboratory's multiple-beam experiment (MBE-4). This experiment has a final voltage of 1 MV, while the needed acceleration voltage for Osiris is 3.8 GV. Predicted driver efficiencies for both driver are based on extrapolations of experimental data and are probably achievable with engineering development. However, accurate estimates for driver reliability for either system are not possible, because the relevant experience base does not exist.

Table 9.6. Driver Parameters for Osiris and SOMBRERO

	Osiris	SOMBRERO
Driver Energy (MJ)	5.0	3.4
Driver Efficiency (%)	28.2	7.5
Repetition Rate (Hz)	4.6	6.7
Power Consumption (MWe)	82	304
Illumination Geometry	Indirect (12 beams, 2 sided)	Direct (60 beams, uniform)

9.5.1 Heavy-Ion Driver

High rep-rated, high energy, accelerators have been operating for decades, but there are no accelerators that approach the required beam currents and powers needed for Osiris. The needed injector currents in the HIB driver are high. Modeling by the Child-Langmuir law has considerable uncertainties. It may be possible to build injectors with current densities much higher than those given by the Child-Langmuir law, but they will require significant development.

Low energy transport of heavy-ion beams is limited by how closely together the focusing quadrupoles can be placed. The achievable linear packing density for magnetic quadrupoles is limited by the field cancellation of adjacent quadrupoles and by the limits on achievable field quality for short magnets. It may be desirable to use electrostatic quadrupoles, which can have much higher linear packing densities at low driver energies.

The critical issue for final HIB transport, pulse compression, and final focusing is the lack of experimental data. Sophisticated modeling of final transport and final focusing has been performed, but there is no experimental verification in the high-current regimes of interest.

Final beam pointing requirements are not demanding (a 2 T dipole field 1 m long can steer the beam ± 10 cm at the chamber center), but the control systems needed for beam alignment, steering corrections, and final pointing will require development.

9.5.2 KrF Laser

Required front-end development work for SOMBRERO's driver can build on experience of the Nike system at NRL as well as recent work done at Los Alamos National Laboratory. What is needed is a repetitively pulsed front end with well controlled beam spatial and temporal profiles, but front-end efficiency can be low. A generic means of achieving stepwise approximation to continuous zooming has been devised for this study; it is likely that a continuous zooming approach can be achieved.

The critical concerns of stress levels, ASE, flow, acoustics, and optics are the same for the intermediate amplifier and the final amplifier, although the demands are much greater for the final amplifier. Intermediate amplification and multiplexing use technology developed in Aurora, Nike, and elsewhere, but the need for high-repetition rate will introduce additional concerns. Flow and acoustic parameters for the final amplifier are critical and will require design verification.

The requirements for demultiplexing and beam delivery do not require sophisticated optics development, but the component mounts, beam control between stages, and optimized architecture with regard to re-imaging between stages will require engineering development work.

Although the required spot sizes are far from diffraction limits, there are still significant issues for the final focusing of laser beams. To prevent destructive interference of the beams, care has to be taken to preserve beam spatial and temporal fidelity in the sequence of amplifying stages.

Beam pointing or steering in lasers is typically achieved by minor adjustments in mirrors located somewhere in the chain in the beam delivery system. Although research on high-speed active mirrors exists, significant development work is needed.

9.6 TARGET SYSTEMS

Although it has been demonstrated that very small targets can be fabricated to tolerances required for IFE, there has been no mass production of targets. Mass production of high tolerance targets, high production rate schemes for tritium filling of targets, and beta or laser layering of thick targets are all unproven and require significant development for both reactor concepts. The integrity of cryogenic DT capsules under acceleration of > 100 g is untested and uncertain.

There are some differences in the concerns for direct and indirect targets. Indirect targets, such as those used in Osiris, are more complicated than the direct targets used in SOMBRERO and may place more severe constraints on the allowable acceleration during target injection. Unlike direct targets, indirect targets must be injected with a preferred orientation. There may or may not be differences in the severity of the requirements for target centering and shot timing for the two types of targets. Indirect drive targets have a higher thermal inertial and less concern for surface quality than direct drive targets, but calculations indicate that both targets can avoid overheating during their flight through the chamber.

9.7 OPERATION AND MAINTENANCE COMPARISON

Characteristics related to plant operation and maintenance are given in Table 9.7. The lifetime of the reactor chambers based on our best estimate from radiation damage are 1.8 FPY and 5.0 FPY for Osiris and SOMBRERO, respectively. However , the Osiris first wall is subjected to much greater pulsed loadings as can be seen from the impulse and peak pressures levels. We expect the flexible fabric wall to be able to withstand the higher impulse, but the effect on the first wall lifetime is uncertain. Removing the chamber in Osiris as a single component of ~43 tonnes simplifies the replacement operation. Parenthetically, most of the mass is in the vacuum chamber cover; the internal chamber structures (fabric blanket and supports) amount to only ~30% of the lifted mass. The SOMBRERO chamber is made up of 12 modules, each weighing 39 tonnes. The chamber is designed for individual modules to be taken out and replaced separately.

Table 9.7. Comparison of Operation and Maintenance Related Characteristics

	Osiris	SOMBRERO
Maximum Impulse on First Wall (Pa-s)	90	2.1
Peak Pressure on First Wall (MPa)	36,900	0.012
Frequency of Chamber Replacement (FPY)	1.8	5.0
Number of Components in Chamber	1	12
Maximum Component Mass (tonnes)	43	39

9.8 ENVIRONMENTAL AND SAFETY COMPARISON

9.8.1 Tritium Parameters Comparison

Key parameters related to the use of tritium in the two reactors are given in Table 9.8. The solubility of T_2 in Li_2O is ~50 times higher than in Flibe. That coupled with the factor of 2.1 larger inventory in SOMBRERO accounts for the tritium inventory difference between the two systems. This also accounts for the factor of 15 difference in the steady state T_2 permeation into the steam cycle. But even at 15 Ci/d, this permeation rate is very low. The total amount of T_2 in the reactor buildings (including the inventory in the breeders) is 12.4 g in Osiris and 182.6 in SOMBRERO, respectively. This difference is also due to the large inventory in the SOMBRERO reactor breeding material.

Table 9.8. Comparison of Tritium Parameters

	Osiris	SOMBRERO
Total Breeder Inventory (tonnes)	940	2000
Tritium Inventory in Breeder (g)	1	162
T_2 Permeation into Steam Cycle (Ci/d)	1	15
Total T_2 Inventory in Reactor Building (g)	12.4	182.6
Tritium Inventory in Target Factory (g)	~ 300	~ 300

9.8.2 Environmental and Safety Analysis

Important environmental and safety parameters are compared in Table 9.9. Both Osiris and SOMBRERO have excellent safety features. They have the same radwaste classifications. For the Flibe material to have a radwaste classification of A, it must be converted to a stable solid form. The confidence level for achieving that is moderately low. Routine T_2 releases are similar for both reactors. An accidental release of all the tritium in the reactor building (a highly unlikely event) produces a whole body early off-site dose at the reactor boundary (1.0 km) of 0.129 rem for Osiris and 2.22 rem for SOMBRERO. Similarly, an accidental release of all the T_2 in the target factory will produce a whole body early off-site dose at the site boundary of 2.34 rem. These values are below the 5 rem level where evacuation plans are needed and far below the 25 rem value recommended for this study by the oversight committee as a threshold for the avoidance of early fatalities.

Table 9.9. Comparison of Environmental and Safety Parameters

	Osiris	SOMBRERO
Maintenance of Chamber Components	Remote	Remote
Maintenance of Power Cycle Components	Hands-on	Hands-on
Chamber Radwaste Classification	A	A
Shield Radwaste Classification	A	A
Breeder Radwaste Classification	A	C
Routine T_2 Release (Ci/d)	91.5	93
Maximum Dose to Exposed Individual from Routine Release (mrem/y)	2.43	0.93
Total T_2 Accidental Release (g)	12.4	182.6
T_2 Accidental Release from Target Factory (g)	260	260
Accidental Whole Body Early Off-Site Dose at 1 km (rem)	0.129	2.22

9.9 ECONOMIC COMPARISON

Key economic parameters are compared in Table 9.10. The economics of Osiris are more favorable than of SOMBRERO. There are several reasons for this, but the main ones are the relative sizes of the chamber, the reactor buildings, and the efficiencies of the drivers. A dry wall chamber is the only viable FW protection scheme for laser drivers, which must guard against condensation of any kind on the mirrors. Inherently, this makes them large and costly. The structures and site facilities are a factor of two higher for SOMBRERO due in large part to the symmetric illumination requirement. The reactor plant equipment is 22% higher for SOMBRERO than for Osiris. The reactor chamber, breeding material, and heat transfer equipment are all higher priced. The equipment related to power generation, such as the turbine plant equipment, electric plant equipment, miscellaneous plant equipment, and heat rejection are all higher for SOMBRERO because it has to produce 232 MWe more than Osiris to make up the difference in the driver efficiency (7.5% KrF laser vs. 28.2% accelerator). The driver costs are almost even, but the KrF laser has a higher cost on a $/J basis. It is interesting to note that the gross-electric unit cost is slightly lower for SOMBRERO than Osiris; however, when the driver power is subtracted, the net-electric unit cost is 15% lower for Osiris. The bottom line is that the cost of electricity for Osiris is ~16% lower than for SOMBRERO.

Table 9.10. Comparison of Economic Parameters

	Osiris (M$)	SOMBRERO (M$)
Land and Land Rights	11.6	10.5
Structures and Site Facilities	137.6	276.5
Reactor Plant Equipment	504.2	615.5
Turbine Plant Equipment	225.8	256.3
Electric Plant Equipment	66.2	70.0
Miscellaneous Plant Equipment	18.5	19.9
Heat Rejection Systems	44.8	52.0
Driver	587.5	579.1
Total Direct Costs	1596	1879
Indirect Costs	1057	1244
Time Related Costs	438	516
Total Capital Costs	3091	3639
Unit Capital Costs ($/kWe - gross)	2743	2678
Unit Capital Costs ($/kWe - net)	3091	3639
Constant Dollar Cost of Electricity (¢/kWh)		
Return on Capital	4.54	5.35
Operation and Maintenance	1.00	1.25
Fuel	0.02	0.02
Decommissioning	0.05	0.05
Total	5.61	6.67

9.10 REFERENCES FOR CHAPTER 9

9.1 D.L. Smith et al., "Blanket Comparison and Selection Study - Final Report," Argonne National Laboratory, ANL / FPP-84-1 (Sept. 1984).

9.2 J.P. Holdren et al., "Report of the Senior Committee on Environmental, Safety, and Economic Aspects of Magnetic Fusion Energy," Lawrence Livermore National Laboratory, UCRL-53766 (Sept. 1989).

Chapter 10

Conclusions and Recommendations

CONTENTS

10.1 INTRODUCTION 10-1
10.2 OSIRIS POWER PLANT 10-1
10.3 SOMBRERO POWER PLANT 10-4
10.4 TARGET SYSTEMS 10-7
10.5 ENVIRONMENTAL AND SAFETY ASSESSMENT 10-8
10.6 RELIABILITY, AVAILABILITY, AND MAINTAINABILITY 10-9
10.7 ECONOMIC ASSESSMENT 10-9

10 CONCLUSIONS AND RECOMMENDATIONS

10.1 INTRODUCTION

The primary objective of the IFE Reactor Design Studies was to provide the Department of Energy with an evaluation of the potential of inertial fusion for electric power production. Based on the results of these studies, we conclude that IFE has the potential of producing technically credible designs with environmental, safety, and economics characteristics that are every bit as attractive as magnetic fusion. Realizing this potential will require additional research and development on target physics, chamber design, target production and injection systems, and drivers.

10.2 OSIRIS POWER PLANT

Osiris Chamber

The Osiris chamber features a very compact, low-activation chamber that uses ceramic material in a flexible, leak-tolerant configuration. The blanket consists of a porous carbon fabric filled with Flibe for cooling and tritium breeding. The Flibe coats the fabric surface, and vaporized Flibe is condensed in a pool at the bottom. The materials and technology needed to construct this blanket exist today. The Osiris vacuum vessel is protected from neutron damage and is a lifetime component. The fabric first wall is replaced periodically (about every two years), but the procedure for doing so is very simple – the entire blanket assembly is drained of Flibe and lifted out the top of the vacuum vessel.

We recommend additional research and development on several aspects of the Osiris design to address unresolved issues, as described below.

First Wall Design. While the materials exist to construct the fabric first wall, research is needed to determine the correct fabric weave to control the flow of Flibe through the fabric first wall. Since Flibe does not wet carbon, it may be difficult to maintain a uniform coating on the first wall. Effects of fabric design parameters and the possibility of using thin wettable metallic coating should be examined. The lifetime of the first wall will be determined by neutron damage and chemical corrosion by free fluorine; the lifetime limits are uncertain and require more research.

Chamber Dynamics. Osiris uses a spray of Flibe at the cold-leg temperature to condense the material vaporized on each shot. Two-dimensional modeling of vapor flow and benchmark experiments are needed. Calculations indicate that recombination of the Flibe after dissociation by the fusion energy pulse will not limit the rep-rate. This should be verified experimentally.

Tritium Recovery and Control. A more detailed analysis of the amount of tritium that can be recovered directly from the Osiris chamber is needed. If all the tritium can not be released by the cascading flow behind the blanket, vacuum disengagers as used in HYLIFE-II will be needed. Vacuum pumping along the beam lines near the chamber are need to prevent the flow of tritium and other radioactive materials into the accelerator. Modeling and small-scale experiments are needed to demonstrate the viability of maintaining the required vacuum conditions.

Vacuum Chamber Structure. The Osiris vacuum chamber is made of carbon/carbon (C/C) structures. The technology to produce large composite structures needs further development.

HIB Driver

The design of the induction linac driver emphasized cost reduction. Costs were reduced by operating at the maximum transportable current in order to minimize length. The 5 MJ driver uses a propagation mode in the accelerator with constant beam radius, quadrupole strength, and quad length – all of which encourage cost-reducing mass production. Twelve beams of Xe^{+1} are accelerated through common cores to a final voltage of 4.8 GeV. Compact Nb_3Sn superconducting quads are used in a standard FODO propagation mode. Complexities from beam combination, separation, or recirculation are avoided. The beams are almost completely neutralized with co-injected electrons just prior to entering the chamber. This gives a relatively small spot size (2.3 mm) and a target gain of ~87. The high-current, low voltage configuration of the accelerator leads to a relatively low cost ($120/J direct cost) design. The high driver efficiency (28%) gives a low recirculating power fraction of only 7%.

We recommend continued development of heavy-ion driver system technology in several areas. Near-term, small-scale research should continue in the following areas:

Injector Development. Because such a large fraction of driver elements are located early in the driver, significant cost savings are possible with improved injector performance. Increasing the injector current and/or voltage would reduce the length and required elements for the low-energy section of the driver by greatly increasing the acceleration gradient allowed by the velocity-tilt limit. Because the normalized emittance for the entire driver and the emittance contribution to the achievable spot size at the target are set by the injector, it is imperative that low-emittance, high-current injectors be demonstrated.

Quadrupole Array Development. Uncertainties in driver cost and transportable current at low energies could be greatly reduced by a prototype design program for superconducting quadrupole arrays. Transportable current at low driver energies is determined by the limits on how short a high-quality quadrupole can be and by how close quadrupoles can be placed without destructive interference of the end fields. Careful design and measurement of short quadrupoles would better establish these limits. In addition, design and demonstration of a single compact

quadrupole array would greatly increase the credibility of size and cost estimates for the entire driver.

Larger experimental programs, such as ILSE, are needed to verify beam scaling and could establish the feasibility of aggressive design options. Recommended experiments are:

Current Transport Limits. MBE-4 has demonstrated the ability to accelerate multiple beams, but a longer driver such as ILSE would also demonstrate high-current transport, scaling of transportable current with voltage, and velocity-tilt limits on acceleration gradients.

Beam Combination and Separation Experiments. Transport and combination or splitting magnets could be added to the end of an ILSE-like accelerator to examine the achievable beam quality after beam combination or separation. As we have shown, neither of these options is necessary for heavy-ion drivers to be credible, but both options could lead to cost reductions once their feasibility is proven.

Beam Bending Experiments. There is great uncertainty concerning the feasibility or performance of a recirculator. One set of uncertainties concerns loss of beam quality in the bending magnets, another concerns resonant instabilities, and a third set concerns maintaining vacuum quality. Scalable experiments on an ILSE-scale device with either a recirculating accelerator section or a loop of quadrupoles and dipoles following the accelerator could give a great deal of information on the feasibility of recirculating drivers. As with beam combination and separation, recirculation is not necessary for heavy-ion drivers, but it could lead to cost reductions.

Drift Compression and Focusing Experiments. A proven accelerator will still need proven final focusing and transport to be of use as an IFE driver. Modeling and scaling of the behavior of high-energy, high-current beams under drift compression and final focusing will greatly benefit from scaled experiments with lower-energy beams.

Power Conversion and Balance of Plant (BOP)

The power conversion system for Osiris is a conventional super-critical steam cycle giving 45% efficiency. A low-pressure liquid lead intermediate heat exchanger provides pressure isolation and prevents the possibility of direct contact between the primary coolant, which contains tritium and other activated material, and the steam system. It appears that the BOP design for Osiris is technically viable, and there do not appear to be any issues that can not be adequately resolved.

The use of an intermediate heat transport loop was adopted for this study as a conservative measure. However, to reduce plant cost and complexity associated with a intermediate coolant and additional equipment, the use of a duplex-tube steam generator approach should be evaluated in more detail. If found appropriate, the technology for this kind of steam generator should be developed in conjunction with the Advanced Liquid Metal Reactors program.

10.3 SOMBRERO POWER PLANT

SOMBRERO Chamber

SOMBRERO chamber is an attractive, high temperature chamber design. It avoids the problem of first wall vaporization by protecting the wall with a low density inert gas (xenon). The first wall and chamber are constructed of a low-activation C/C composite. Granules of Li_2O flow though the chamber and are circulated as the primary coolant. The design retains the advantages of solid breeders while eliminating the problems associated with static blankets. The feasibility of the flowing blanket and fluidized recirculation are within the capabilities of existing industrial practice. The chamber is constructed of 12 independent first wall and blanket modules that must be replaced approximately every five years.

Additional research and development are recommended for SOMBRERO. Some of the key areas are listed below.

First Wall and Chamber Design. Experimental verification of the effectiveness of the first wall protection scheme is recommended. The development of the capability to manufacture larger C/C composite structures is essential to the design concept. Radiation damage tests with composite materials to determine material lifetime the effects on thermal conductivity are needed. A materials development program for this class of materials is needed for both IFE and MFE.

Laser Propagation. If the xenon gas density is too high, breakdown can occur which would reduce the amount of energy delivered to the target. Experiments to quantify the limits on the density of the gas are needed at the correct wavelength and intensity. The implications on target performance if breakdown occurs near the target also need additional study.

Flowing Blanket. Several aspects of the flowing breeding blanket would benefit from further study. Additional experiments on the heat transfer capabilities of the flowing bed examining a wider range to the operating variables and materials should be carried out. The issues of granule break-up and erosion of the blanket and heat transfer components need study.

Tritium Control. Since tritium is present in the xenon gas that fills the reactor building, it is essential that the building walls do not absorb tritium. Verification of the ability of coatings to prevent absorption is needed.

Power Conversion and BOP

The power conversion system for SOMBRERO is the same as for Osiris, except the intermediate heat exchanger has Li_2O granules instead of Flibe on the primary loop side. The system utilizes waste heat from the laser amplifiers to increase the gross conversion efficiency from 45 to 47%. The balance-of-plant design for SOMBRERO appears to be technically viable. Conceptual solutions have been identified for the major issues. The interface between the laser and

the chamber (i.e., the optical train needed to deliver the beams) places significant demands on the design and construction of the reactor building.

As with the Osiris design, a closer look at the feasibility of a duplex wall steam generator (instead of using an intermediate heat exchanger) is advised.

The layout of the final optics adopted for this design is determined by the requirement for reasonable lifetimes of the mirrors. Grazing incidence metal mirrors (GIMMs) have been chosen as the final optics with the dielectric focusing mirrors located out of the line of sight. There are almost no data on radiation damage of either metal or dielectric optics in high energy neutron fluences. It is clear that the damage threshold of these optics under neutron illumination is one of the major uncertainties in this design. If the optics were to have higher fluence tolerances than assumed, then the optics could be placed closer to the target and the whole structure reduced in size. This could reduce the cost of the SOMBRERO reactor building significantly. Thus obtaining radiation damage data is critical.

The CaF windows located on the floor of the reactor building separate the reactor building environment from the beam handling area while letting the laser beams pass through with minimum absorption. While these windows are not in the direct line of sight for neutron irradiation, they will receive some scattered neutron fluence. Neutron damage data is also needed for these optics.

KrF Driver

The KrF driver system we have designed has an overall efficiency of 7.5% and the use of waste heat from the amplifiers increases the power conversion efficiency by ~2%. (This is equivalent to an effective laser efficiency of > 9%.) We have achieved this high KrF system efficiency by

1) careful overall optimization of the final amplifier design parameters,
2) use of high pump rate kinetics to achieve high intrinsic efficiency,
3) use of low inductance e-beam system design to allow low rise/fall time losses,
4) use of a recently patented and demonstrated plasma cathode in the e-beam that is capable of efficiencies limited only by the gas/foil albedo, and
5) operation at high Joules/liter, which allows efficient waste heat utilization.

Our design uses 60 kJ amplifier cavities that are pumped for 600 ns from two sides with 600 kV, 40 A/cm^2 e-beams that are 1×2 meter in dimension. The cavities operate in a 2-pass extraction mode. This is a relatively small size that has high efficiency due to low amplified stimulated emission, excellent fill factor, and low flow power. The small size promises to keep development cost at a minimum for full-size demonstration of key components.

We feel our design represents the best of the possible approaches, given current data on the KrF system. We have not extrapolated physics, but we have made reasonable and defensible

projections for technology development, based on scaling demonstrated technology. Our approach also has the advantage of representing sensible evolution of the technologies developed in Aurora (e-beam pumped 2-pass amplifiers with angular multiplexing for pulse compression), Nike (non-echelon integrated spatial incoherence for smooth beam profiles on high gain direct drive targets), and EMRLD (DoD technology for repped e-beam pumped excimers of excellent beam quality).

We recommend continued development of the KrF driver system technology in the following areas:

Repped e-Beam. The plasma cathode technology should be scaled from 10×30 cm to 1×2 m, and the design optimized for 5 to 10 Hz operation. Operation of a 1×2 m, 600 kV, 40 A/cm^2, 600 ns e-beam with cable-based pulse power should be the final milestone of this effort.

60 kJ Amplifier Module. Demonstrate 10 Hz operation with angular multiplex extraction over at least part of the 600 ns gain duration. Perform an extensive characterization of the operating parameters and develop an understanding of issues for the next generation design, particularly to extend foil lifetime.

Zooming Front End. Develop and test a front end design capable of changing aperture diameter by about two in periods of order 6 ns, with simultaneous control of the power output as required for optimum target implosion.

KrF Kinetics. Demonstrate the high intrinsic efficiency predicted by our codes for 400 kW/cm^3 pump rate for 600 ns, and thus also demonstrate the 30 J/liter design.

Neutron Effects on Optics. With a 14.1 MeV neutron test facility, develop and test designs for the grazing incidence metal mirrors and the dielectric-coated final focusing mirrors.

Cooled Optics. Develop and test designs in the 10×20 cm size operating at 5 J/cm^2 and 10 Hz in the UV.

Lifetime Testing of Critical Components. Besides the neutron effects and the optics fluence and average power testing, there are a number of other components, such as the e-beam cathodes, pulse power switches, and so forth that should be tested.

Overall System Design. The present program was a minimal size effort to accomplish the goals; there is much that should be worked out to the next level of detail to improve the confidence level and guide the subsequent developments.

10.4 TARGET SYSTEMS

Target Production

The target production facility design was motivated by the objectives of high reliability, high safety, and low capital cost. The facility uses controlled microencapsulation for shell production, fuel filling by cryogenic injection, and layer formation by pulsed laser heating and temperature-controlled gas jets. The building area required for target fabrication is quite compact. The production process is expected to have high reliability because there is 100% redundancy in the production lines. The total tritium inventory is low (~300 g) as a result of using rapid fill and layering techniques.

The proposed technologies are speculative and require significant technology development.

Shell Production. Controlled microencapsulation has been demonstrated for small-sized capsules. The process must be scaled up to demonstrate that high quality can be maintained for larger targets characteristic of the high yield targets used for power plants.

Fuel Filling. The proposed cryogenic fill technique has a great advantage in that the fill time is very short (~minutes), and thus the tritium inventory associated with the fill step is small. The technology has not been demonstrated and significant uncertainties exist. Small-scale experiments should be carried out to begin addressing the issues associated with this process.

Fuel Layering. The use of pulsed lasers and cold gas jets has been demonstrated for small targets. Development is needed to see if this technique can be scaled up to be used with larger targets and thicker fuel layers.

Target Injection, Tracking and Beam Pointing

Existing gas gun technology can meet the acceleration and positioning requirements of the IFE applications. The proposed design uses a sabot to protect the target from damage during the acceleration processes. Laser Doppler interferometer and laser tracking station are used to monitor the target trajectory and can provide pointing information in enough time to actively point the beams for each shot. The tracking and pointing requirements can be met with existing technologies. The most critical issues have to do with operating the injector with cryogenic targets.

Small-scale tests should be carried out to demonstrate the integration of the technologies required for target injection, tracking, and beam pointing. The test could be conducted in a phased approach by first developing the gas gun injector, adding tracking systems, and finally demonstrating beam pointing and interception of a target with a low energy ion or laser beams. Operation with cryogenic targets, but not necessarily DT, will be required.

Target Survivability

The target is protected from physical contact with the accelerator by a sabot. Once the target leaves the accelerator, the sabot flies off. As the target travels through the chamber, it is subjected to aerodynamic and radiative heat loads. For indirect drive targets, the hohlraum provides a thermal barrier to protect the fuel capsule. Direct drive targets will have to remain in the sabot for a longer time or incorporate additional thermal protection (e.g., a sacrificial layer of frozen gas on the outer surface of the capsule), especially when used in high temperature chambers such as SOMBRERO. More work is needed to demonstrate the integrity of the DT fuel layer and capsule during acceleration and transit through the chamber.

Experiments are needed to develop appropriate sabot designs that can protect the capsule during acceleration. The integrity of cryogenic hydrogen layers should also be examined to determine acceleration limits for targets. Experiments with schemes to protect the targets from heat loads during injection are also needed.

10.5 ENVIRONMENTAL AND SAFETY ASSESSMENT

Both Osiris and SOMBRERO have attractive environmental and safety characteristics. Both achieve a level of safety assurance of one, and the chamber, breeder, and shielding materials will qualify for disposal as Class A or C low level waste. These results are due to the use of only low-activation materials for the first walls, breeding blankets, and chamber structures. As previously mentioned, minimizing the tritium inventory in the target factory is also an important aspect in achieving the high safety rating.

To realize potential environmental and safety advantages of these designs, the low-activation structural materials used for the SOMBRERO first wall, blanket, and chamber structure and for the Osiris vacuum chamber will require significant technology development. The carbon fabric used for the Osiris first wall and blanket is currently available, but as discussed above, development the proper weave density for flow control is need.

10.6 RELIABILITY, AVAILABILITY, AND MAINTAINABILITY

At a conceptual level of evaluation, the remote maintenance of the Osiris and SOMBRERO reactors appears feasible. However, a detailed evaluation of the remote replacement or refurbishment of the reactor components should be performed to identify the development needs for any special remote maintenance equipment. In addition, "design for remote maintainability" should be factored into the program from the beginning of conceptual designs rather than retrofitting at later stages.

At this stage of the IFE reactor development, a definitive assessment of the reliability, availability, and maintainability (RAM) can not be performed until an in-depth evaluation of the key systems and components is made. In addition, in-depth evaluations are needed on the integrated design and performance of the driver, target, reactor, and the balance-of-plant.

An overall plant availability goal of 75% is assumed here for the IFE reactor plants so as to be comparable to other large electric power generating systems. To be able to meet this target goal, it appears that both concepts require significant improvements in the availability of the constituent systems and components. A detailed RAM assessment is needed to identify the extent of the improvement and to aid in planning future development efforts.

10.7 ECONOMIC ASSESSMENTS

The estimated cost of electricity (COE) for the Osiris power plant is about 16% lower than the COE for the SOMBRERO power plant. The economics for both plants are attractive compared to previous inertial and magnetic fusion reactor designs. The use of low-activation materials and low volatile tritium inventory eliminates the need for N-stamp materials and reduces the estimated construction costs.

The attractive economics are the result of properly integrating the proposed technologies (lower cost heavy ion driver, more efficient KrF laser, good target gain performance, etc.). Continued systems analysis is useful to help identify those areas with high leverage for affecting system performance and bottom line costs. A continuing effort in power plant systems analysis that incorporates the latest information on reactor, driver, and target technologies and performance is recommended. Further work is also recommended to normalize the cost estimates with other IFE and MFE studies so that they can be compared on a more consistent basis. For high leverage systems and subsystems, more detailed designs and cost estimates are warranted.

Appendices

CONTENTS

A STUDY GUIDELINES

B REACTOR CONCEPT SELECTION PROCESS

C THE ONION IFE REACTOR CONCEPT

D THE LIFE IFE REACTOR CONCEPT

E REMOTE MAINTENANCE EQUIPMENT CONFIGURATION CONCEPTS

F ADDITIONAL COMPARISONS OF OSIRIS AND SOMBRERO

Appendix A

Study Guidelines

CONTENTS

A.1 ICF REACTOR DESIGN STUDIES RECOMMENDED GUIDELINES
A.2 REVISED TARGET INFORMATION FOR ICF REACTOR STUDIES

INERTIAL CONFINEMENT FUSION
REACTOR DESIGN STUDIES
RECOMMENDED GUIDELINES

September, 1990

Prepared for

DEPARTMENT OF ENERGY
OFFICE OF FUSION ENERGY

Prepared by

Ronald C. Davidson, Chairman
Massachusetts Institute of Technology

Charles C. Baker
Oak Ridge National Laboratory

Roger O. Bangerter
Lawrence Berkeley Laboratory/
Lawrence Livermore National Laboratory

E.C. Brolin
Princeton Plasma Physics Laboratory

Daniel R. Cohn
Massachusetts Institute of Technology

Donald L. Cook
Sandia National Laboratories

Donald J. Dudziak
North Carolina State University

David B. Harris
Los Alamos National Laboratory

Robert A. Krakowski
Los Alamos National Laboratory

Thomas E. Shannon
Oak Ridge National Laboratory

Weston M. Stacey, Jr.
Georgia Institute of Technology

Charles P. Verdon
University of Rochester

PREFACE

This report, prepared at the request of the Department of Energy Office of Fusion Energy, is intended to provide a summary of guidelines for monitoring technical progress in the inertial confinement fusion power plant design studies recently commissioned by DOE. The information presented here has been prepared by two working groups. One working group, chaired by Robert Krakowski (LANL), has prepared guidelines for comparison of inertial fusion and magnetic fusion reactor designs (Sec. III). The second working group, chaired by Roger Bangerter (LBL/LLNL), has developed unclassified guidelines for the target gain information to be used in the studies. In this report, target information is presented for direct-drive KrF (Sec. IV) and indirect-drive ions (Sec. V). Guidelines for indirect-drive KrF targets and direct-drive ion targets are still being developed by the Target Working Group and will be provided as Addenda to this report as soon as they are available.

Ronald C. Davidson
Chairman
September 14, 1990

TABLE OF CONTENTS

		Page
I.	GOALS OF ICF REACTOR DESIGN STUDIES	1
II.	MAJOR REACTOR SYSTEMS AND GUIDELINES	2
	A. Target Gain	3
	B. Target Factory	4
	C. Drivers	5
	D. Reaction Chamber	5
	E. Balance of Plant	7
	F. Optimization and Interfaces	7
III.	COMMON BASES FOR COMPARISON OF ICF AND MFE REACTOR DESIGNS	8
IV.	TARGET REQUIREMENTS FOR DIRECT-DRIVE KRF	16
	A. Direct-Drive High-Gain Performance	17
	B. Illumination Uniformity Requirements	19
V.	TARGET REQUIREMENTS FOR INDIRECT-DRIVE IONS	25
	A. Target Performance	25
	B. Pulse-Shape Precision, Power Balance and Beam Alignment	28
FIGURE CAPTIONS		30
REFERENCES		31
APPENDIX A: COST ACCOUNTING SYSTEM USED BY ARIES PROJECT		

I. GOALS OF ICF REACTOR DESIGN STUDIES

Since inertial confinement fusion (ICF) was first considered as an energy source in the early seventies, there have been more than forty ICF reactor studies.[1] These studies included a variety of drivers and generally gave predicted cost of electricity (COE) comparable to those of magnetic fusion energy (MFE). The quality, level of detail, and goals of these studies varied widely. Some studies produced relatively complete point designs of power plants,[2] others concentrated primarily on reactor cavity design,[3] and still others were broad parametric searches for attractive operating points.[4] All of these studies are now less current, and most, if not all, are less detailed than the ongoing MFE ARIES study.[5] Therefore, to bring ICF power plant designs more nearly onto a par with MFE reactor design new studies are needed.

The Office of Fusion Energy is preparing to fund two new ICF power plant design studies. These studies should have four goals:

- Advancement of the state-of-the-art in ICF power plant design.
- Comparison of ICF and MFE plant designs.
- Development of a sound basis for future programmatic decisions.
- An assessment of ICF for power production including technical feasibility, economics, safety, and environmental considerations.

In regard to the first goal, it is important to emphasize that the funding for the contracts will exceed the funding of most previous ICF studies. Therefore, the contractors should be expected to address quantitatively a number of issues that have

previously been addressed less quantitatively. The second goal must also be emphasized. A comparison between ICF and MFE can only be meaningful if the studies of the two approaches are done at a comparable level, using similar general rates, assumptions, and guidelines (Sec. III).

It is expected that some aspects of the new designs will be based upon extrapolations of physics and technology beyond the present state-of-the-art. In order to assist DOE to evaluate the magnitude and probability of success of these extrapolations in physics and technology, the contractors should provide, for each major reactor system, an assessment of the development program that is needed to advance the physics and technology from its present status to the status that is required for the performance of that system as specified in the design. This assessment should include a quantification of the magnitude of the extrapolations involved relative to prior advances, the identification of major feasibility issues, and an evaluation of the role of the ICF Defense Program in resolving these issues.

II. MAJOR REACTOR SYSTEMS AND GUIDELINES

The major reactor systems include a target factory, a driver, a reaction chamber, and the balance of plant (BOP). The properties of, and requirements on, all systems except BOP are strongly influenced or determined by target physics and design. Most target designs are classified. The charter to do classified target physics and design resides at Los Alamos National Laboratory, Lawrence Livermore National Laboratory, Sandia National Laboratories, and KMS Fusion. Therefore, as part of the

studies, the Office of Fusion Energy and the Inertial Fusion Division have established a Target Working Group to develop target information. The Target Working Group consists of individuals from the Department's ICF laboratories.*

A. Target Gain

The target information is compiled in unclassified sections of this report (Secs. IV and V) to be used in the studies. The target gain is given as a function of the relevant beam parameters such as total beam energy, focal point radius, wavelength or ion range, alignment tolerance, number of beams, etc. Three cases are provided: a base case using information from current target designs, a more speculative case with higher gain, and a conservative case. Contractors should evaluate the consequences of all cases, but primary emphasis should be given to the base case. The fraction of target output energy in neutrons, x-rays and debris is given in Ref. 6.

It is important for credibility to have all aspects of the studies documented. Therefore, the Target Working Group will produce classified reports documenting the calculations, experiments, and assumptions used to obtain target gain and output of neutrons, x-rays, and debris.

Given target gain and output, the contractors will have enough information to design and evaluate drivers, reaction chambers, and BOP. Thus, to study and design most of the major

---

*R.O. Bangerter (LBL/LLNL), D.L. Cook (SNL), D.B. Harris (LANL), and C.P. Verdon (LLE).

systems, the contractors will have no need of classified information.

B. Target Factory

Targets are currently handcrafted for a few shots per day. For economical power production, the cost of targets must drop several orders of magnitude and the production rate must be increased to about 10^5-10^6 targets per day. Therefore, mass-production techniques must be introduced. These extrapolations in cost and production rate are sufficiently large that, despite some excellent previous studies, large uncertainties remain. It is important to reduce the uncertainties since target production costs appear to contribute significantly to total COE. Therefore, the studies must continue to address this issue.

The most recent and complete DOE-supported study of target costs was performed for the Heavy-Ion Fusion Systems Assessment.[7] Since the completion of this study, there has been some evolution in target design and also substantial progress in handcrafted target fabrication techniques. Furthermore, some of the newer target fabrication techniques appear suitable for mass production. Therefore, new studies are needed. The studies must include conceptual techniques for fabricating the targets and must be performed by a group that includes at least some individuals with industrial experience and demonstrated expertise in the mass production of small, high precision components. These individuals must be familiar with advanced manufacturing R&D. Target inventory and shelf life, and tritium inventory, handling, and control must be addressed. Target factory development needs must be detailed.

The Target Working Group has provided unclassified gain curves (Fig. 4.1). The contractors can use these gain curves for their studies. The Target Working Group will use the methods developed by the contractors to estimate the cost of classified targets. It appears likely that words similar to the following could be included in the reports: "Using the methods described above, we estimate the cost of classified targets to be x times the cost of unclassified targets."

C. Drivers

The contractors have chosen to use KrF lasers and heavy-ion accelerators as drivers. The DOE laboratories have already developed design concepts for these drivers. The contractors should consider the information from the laboratories on each driver. To obtain a balanced view, the contractors should also solicit and evaluate criticism of the various driver candidates. The contractors could adopt or modify existing driver designs or develop their own designs. It is important that the final report, for each driver, address quantitatively technical feasibility, cost, efficiency, lifetime, reliability, beam precision, focusing, pulse shaping, and target performance. Development issues and key required development tests should be specified.

D. Reaction Chamber

There is a spectrum of ICF chamber designs ranging from bare-wall concepts that use distance to achieve wall survivability against neutrons, radiation, charged particles, and target debris to concepts that place a neutronically thick layer (usually

liquid or granules) between the target and the first structural wall. Contractors may choose either extreme or something between. As with regard to drivers, the contractors may choose to adopt or modify existing designs or to innovate. The following topics are representative of those that should be addressed quantitatively: illumination geometry, optics protection, mechanical and thermal stress, fatigue, radiation damage, life-time, tritium breeding, tritium handling, cooling, activation, radioactive inventories, safety, materials, cost, maintenance, decommissioning, and waste disposal, etc. There should also be some discussion of material requirements, resources and avail-ability. Development steps for reactor chambers should be described.

Standard safety evaluations for prompt and delayed dose in severe accidents must be performed. Specifically, it is recommended that the distance to the site boundary be calculated for each of the concepts evaluated such that the whole body dose from all sources does not exceed 25 Rem using the ICRP Report No. 26 weighting factors.

To calculate the maximum dose to an off-side individual for comparison with the above criteria, the following approach should be used:

- The source term for the calculation should be determined using a deterministic analysis to obtain the "maximum credible accident," i.e., the credible accident with the potential for the largest off-site dose. Guidance for performing the deterministic analysis should be obtained from Reference 8.

- Dispersion factors (X/Q) should be determined from USNRC Regulatory Guide 1.145 for stable, light wind conditions (Stability Class F, 1 meter/sec wind-speed).
- Dose conversion factors should be obtained from References 9 and 10. The dose conversion factor given in Reference 10 for tritiated water should be multiplied by 1.5 to account for skin absorption, as per ICRP guidance.

E. Balance of Plant

This category includes all structures and systems not specifically identified above. The design and analysis of this part of the plant should be done at the same level as, and be consistent with, the ARIES study[5] (See Sec. III).

F. Optimization and Interfaces

There are a number of topics that must include joint consideration of the plant parts considered above. The most fundamental of these is overall plant optimization. In this regard, the contractors could use optimization codes such as ICCOMO[11] and SAFIRE[12] to obtain optimal COE and its sensitivity to parametric variations of yield, rep rate, driver characteristics, etc. It is recommended that 1000 MWe be chosen as the net output for the base case, but it should also be determined how the COE depends on net output in a range at least as large as 500-2000 MWe.

Other design topics that must be quantitatively addressed are: target injection and tracking and beam steering systems, optics protection (neutrons, x-rays, debris), optics damage thresholds, the connections among tracking and steering accuracy, target survivability, focal radius, optical mounts, and vibration and distortion of optics. Possible sources of vibration and

distortion include the mechanical effects of the microexplosions on the target chamber and surrounding structure as well as vibration and distortion caused by the passage of the beam, neutron energy deposition, radiation induced swelling, etc. The connection between residual chamber pressure and beam propagation must be addressed. In particular, beam propagation in the chamber appears to be an important issue for ions. Questions of propagation efficiency, beam overlap, instabilities, charge and current neutralization, and the geometry of any needed return current channels must be addressed. Finally, the isolation and maintenance of the major subsystems such as driver, target factory, chamber, and balance of plant must also be addressed.

Target injection, tracking, and survivability may be difficult issues. Because of the differences between direct and indirect drive, it is possible that careful studies using only unclassified information might conclude that ICF is not feasible; however, the perceived difficulties may not apply to classified targets. The opposite situation might also occur. It is therefore recommended that the Target Working Group in concurrence with DOE be given the responsibility to ensure that the conclusion of the studies is consistent with classified information.

III. COMMON BASES FOR COMPARISON OF ICF AND MFE REACTOR DESIGNS

An important result of the ICF reactor study will be a quantitative comparison with contemporary counterpart studies in MFE (e.g., ARIES[5]). It is crucial, therefore, that ground rules and guidelines be clearly established and defined at the onset of the ICF reactor study. Qualitatively, a set of minimal conditions

must be met before meaningful comparisons can be made. Most of these minimal conditions can be met by good planning and goal-setting at the onset of the ICF study, as well as by using existing resources within the ICF and MFE communities, rather than consuming a significant part of the study effort per se. These conditions include:

- Same level of net-electric power (at least for MFE/ICF comparison cases); parametric cost-sensitivity studies around this reference power level would be desirable.
- Similar level of detail in describing physics, engineering, and (plant) operational assumptions. If this does not prove feasible because of less-developed reactor study base for ICF, as a minimum, a clear definition of the physics basis, engineering constraints, accuracy and credibility of technology projections, and plant operational assumptions should be made.
- Same level of conceptual engineering design detail for each of the key reactor subsystems within the conceptual design, when possible.
- Same level of coupling between fusion-power-core (FPC) design (done in greater detail) and balance-of-plant (BOP) design (done in less detail).
- Same costing procedure methodology (e.g., NECDB) and same unit-cost database (both in magnitude and scaling).[13] Feedback between the two studies with regard to the unit-cost base is likely to benefit both studies.
- Same (range of) global plant characterstics [e.g., nth-of-a-kind, net-electric power, BOP recirculating power requirements

* COMPARABLE

(assumptions), plant availability, decommissioning, construction lead time, safety and environmental cost credits, etc.].

- Same* general philosophy vis-a-vis costing, role of parametric systems and tradeoff studies, direction and depth of point conceptual design (i.e., establish and monitor optimum design points using parametric system analysis and cost tradeoff studies).
- Same* level of resolution of safety and environmental issues (including resource estimates, waste disposal requirements, level of inherent/passive safety, etc.); use of a common methodology (e.g., ESECOM[14]) would be desirable.
- Same* ground rules for time and cost estimates of needed R&D to achieve a given point design, as well as assessing the credibility of achieving that end-result within the projected time and cost targets.

Described below are the design procedures, methodologies, and philosophies being used by the ongoing ARIES tokamak reactor study. This material is presented here to provide a base with which to compare similar procedures, methodologies and philosophies to be adopted by the ICF reactor study. The degree to which these can be matched will determine the effectiveness of any eventual ICF/MFE comparisons. It is expected that the feedback between the two studies will be bi-directional.

Figure 3.1 describes schematically a process that has evolved over the years for MFE and is now being applied to the ARIES project. The cost of electricity (COE, mill/kWeh), and to a lesser extent the total cost (TC,M$) and unit direct cost (UDC,$/We), are used as "object functions" in a design-based

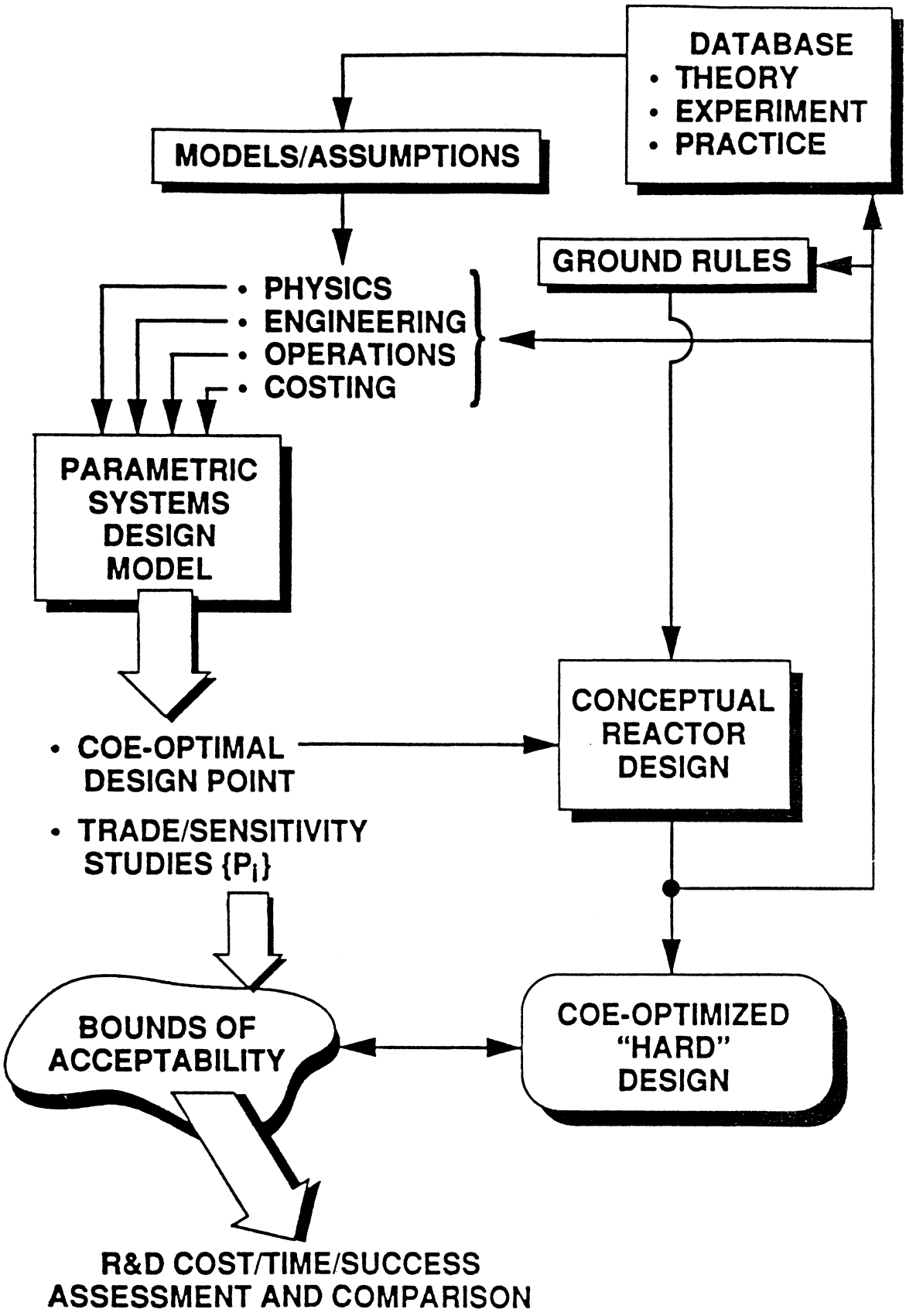
DATABASE
• THEORY
• EXPERIMENT
• PRACTICE
MODELS/ASSUMPTIONS
GROUND RULES
• PHYSICS
• ENGINEERING
• OPERATIONS
• COSTING
PARAMETRIC SYSTEMS DESIGN MODEL
CONCEPTUAL REACTOR DESIGN
• COE-OPTIMAL DESIGN POINT
• TRADE/SENSITIVITY STUDIES {P_I}
BOUNDS OF ACCEPTABILITY
COE-OPTIMIZED "HARD" DESIGN
R&D COST/TIME/SUCCESS ASSESSMENT AND COMPARISON

Figure 3.1

physics/engineering/costing parametrics systems model. This comprehensive model produces a COE-optimal (minimum or otherwise constrained by the design) "strawman" design that in turn provides guidance to the conceptual reactor design activity. As shown in the figure, information from the design process is fed back to the cost-based systems design model. The main role of the systems design model is to perform a range of "credibility checks" using trade-off and sensitivity studies throughout the conceptual design process and the technical assessment that follows. This sensitivity of cost to key physics and engineering assumptions, rather than bottom-line COE, are the important outputs from this design and analysis activity. The final designs are accessed in terms of the range and flexibility of an operating space in which that final (best) design resides, asexpressed in terms of the required R&D cost, time, and success probability (credibility). In short, the bottom-line result should provide a quantified measure of credibility in achieving the optimized end-product projected by the study; it is the engineering and physics needs and means by which an attractive COE is achieved, rather than the value of the COE per se, that is important in assessing the needed R&D. Since most "successful" designs will project a "competitive" COE, and since this COE is subject to the physics and engineering uncertainties underlying all parts of the COE estimate, comparisons and/or ranking concepts on the basis of COE alone is unwise. Instead, the credibility of achieving the physics and engineering needed to report a competitive COE should form the basis for comparing concepts.

Given an "in-principle" acceptance of the above-described design process, or an equivalent methodology, a set of concrete points of comparison should be established, agreed, and implemented in the ICF reactor studies contract. Summarized below is a preliminary (working) list of such ground rules, guidelines, procedures, and normative parameters.

- 10th-of-a-kind commercial plant, but estimate 1st-of-a-kind cost factor.
- P_E = 1000-MWe(net) net-electric output, but examine cost, physics, and engineering sensitivity of lower and higher plant capacity.
- DT fuel cycle.
- Use NECDB[13] methodology and assumptions (typical values given below are for ARIES project,[15,16] in 1988 dollars).

- plant life, yr	30
- plant lead time, yr	6
- contingency factor	0.15 (standard construction) 0.25 (nuclear construction)
- neutron radiation life, L(MW yr/m^2)	20 (nominal, material-dependent)
- spare parts multipliers	1.0 (i.e., no spares for all systems)
- effective cost of money, nominal/constant-dollar (1/yr)*	0.0957/0.0435
- inflation rate (1/yr)	~~0.06~~ 0.05
- effective tax rate	0.3664
- tax depreciation life, yr(plant/replaceables)	15/5

*nominal = then current; constant-dollar = inflation-adjusted cost.

- fixed charge rate, FCR(nominal/constant-dollar)	0.1638/0.0966
- interest during construction, IDC(nominal/constant-dollars)	0.2630/0.1652
- escalation during construction, EDC(nominal/constant-dollar)	0.2335/0.0
- COE components	
- capital	computed
- operating and maintenance[13] (M$/yr, P_E in MWe)	$69.2(P_E/1200)^{0.5}$
- first-walk/blanket replacement	computed
- decommissioning allowance (mill/kWeh)	0-1 (dependent on level of safety assurance)
- deuterium fuel (mill/kWeh)	~0.05
- indirect costs	
- construction equipment and services	12.8% or 15.1% direct cost for LSA rating of 3 or 4
- home office engineering and services	5.2% direct cost
- field office engineering and services	6.4% or 8.7% direct cost for LSA rating of 3 or 4
- owner's cost	15% direct cost, plus the above three

- Use standard unit costs (and scalings) for comparable materials, assembles, and systems that include materials, installation, RDACs, and contingency costs, with all items expressed on an appropriate and common basis.
  - high heat-flux areas, $\$/m^2$
  - first vacuum walls, $\$/m^2$

- structural, breeder, multiplier materials, $/kg
- main heat transport, $/Wt
- reactor building, $/$m^3$
- steam generator, $/Wt
- intermediate heat exchanger, $/Wt
- turbine plant equipment, $/We(gross)
- electric plant equipment, $/We(gross)
- etc.

- Use a common cost accounting system, appropriately adjusted to include accounts specific to ICF or MFE. The attached table gives the cost accounting breakdown used by the ARIES project.
- Use a common cost summary sheet, a sample of which from ARIES is given on the attached table.
- Express key parameters and figures of merit on a common basis [e.g., blanket energy multiplication relative to DT neutron energy; mass power density, kWe/tonne; neutron wall loading, MW/m^2; direct versus base versus total plant cost; "wall-plug" versus direct heating efficiency; engineering versus plasma Q-values; etc.). Other or related points of technical comparison that should emphasized are:
  - Powers: net-electric, gross-electric, thermal, and recirculating power.
  - Fuel Performance: burnup fraction, tritium inventory, breeding.
  - Driver Parameters: energy, power, forces, efficiency.
  - Blanket Performance: neutron and heat fluxes, radiation life, availability, reliability, repairability, safety.

- Safety and Environment: threshold dose release fractions (TDRFs) to give a critical (200 rem) or chronic (25 rem) dose at the site boundary, total radioactive inventories (MCI, BHP), contact doses, waste disposal indices (tonne/MWe, m^3, etc.).

In summary, examples of both guidelines and means of comparison have been suggested for consideration by the ICF reactor-study groups. These guidelines are based on approaches generally followed by past MFE reactor studies, and most recently by the ongoing ARIES studies. Furthermore, it is expected that the assumptions used in the ongoing ARIES tokamak reactor study will not be met with full agreement by the ICF reactor study groups, and adjustments will have to be made. While the exact methodology given herein may not be advisable, desirable, or possible to follow for the ICF study, some methodology, nevertheless, should be proposed, approved and followed. Further insight on how to compare these highly conceptual ideas undoubtedly will be generated by dialogues with the ICF reactor-studies contractors. Careful front-end planning in this area is essential to a meaningful technical comparison of the study results with similar projections for MFE.

IV. TARGET REQUIREMENTS FOR DIRECT-DRIVE KrF

This section provides a brief summary of current high-gain direct-drive KrF capsule designs and illumination uniformity requirements. These designs represent relatively mature designs in that they have undergone a number of iterations with respect to issues associated with hydrodynamic stability, effects of

long-wavelength drive nonuniformities, and laser energy coupling. In these designs we have attempted to use our current "best" understanding of the physics associated with these issues. As more experimental and theoretical work is carried out, some aspects of the current design will change. However, we believe that these changes will not significantly affect the information provided in this summary.

A. Direct-Drive High-Gain Performance

The gain curve(s) (thermonuclear energy out/incident laser energy in) for directly driven KrF capsules are shown in Fig. 4.1. The gain curve is shown as a band to represent our current "level of risk" understanding associated with hydrodynamic stability issues. The upper (optimistic) curve represents designs which have been optimized to implode on a nearly Fermi degenerate isentrope. Using our current understanding of issues related to Rayleigh-Taylor hydrodynamic instability and its effect on capsule performance, these designs would have more restrictive requirements on capsule and drive uniformity than the designs represented by the lower (conservative) gain curve shown in Fig. 4.1. The capsule designs represented by the lower curve have been optimized to reduce the effects of Rayleigh-Taylor unstable growth on capsule performance.

Our present studies of the Rayleigh-Taylor growth rates for directly driven capsules show that the growth rates $\gamma(t)$ can be given (approximately) by the form:

$$\gamma(t) = \sqrt{\frac{A(t)kg(t)}{1 + kL(t)}} - \delta k V_a(t)$$

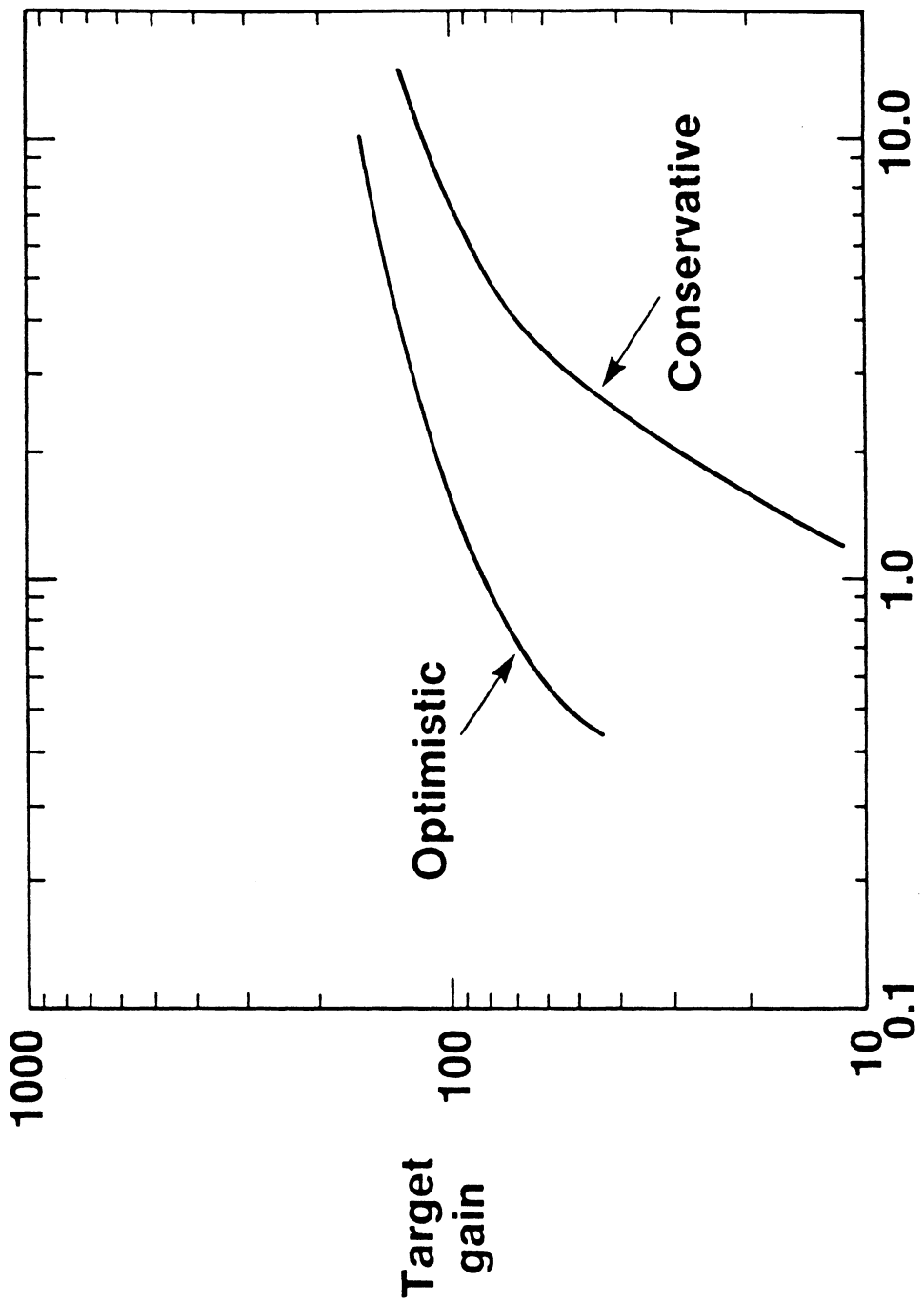
1000
100
10
Target gain
0.1
1.0
10.0
Driver energy (MJ)
Optimistic
Conservative
1793

Figure 4.1

where A(t) is the Atwood number, g(t) is the acceleration, k is the unstable wave number, L(t) is the front surface density scale length, $V_a(t)$ is the ablation velocity, and δ is a constant which ranges between 2-3 depending on the definition of A, L, and V_a. There are two stabilizing terms in this expression (L and V_a). The lower curve on the gain curve(s) represent designs for which the stabilizing effects of L and V_a have been optimized while maintaining relatively high gain performance.

The values of L and V_a can be increased over those found in the capsule designs representing the upper curve by changing the isentrope of the implosion. This could be done by seeding the ablator with high-atomic-number impurities or by using pulse shaping. Currently we have restricted our considerations to pulse-shape modifications so that the capsule designs could be more easily scaled with respect to incident laser energy. For the purpose of this study, the base case capsule gain should be taken to be the arithmetic mean of the optimistic and conservative curves in Fig. 4.1.

An estimate of the required outside surface finish can be obtained using the present understanding of Rayleigh-Taylor unstable growth rates and an initial model spectrum representative of machined surfaces (as $\ell^{-5/4}$).

B. Illumination Uniformity Requirements

The irradiation pattern on the capsule can be represented as the product of two factors: (1) a single-beam factor that depends on the focusing geometry, the f-number of the lens, the capsule conditions, and the individual beam profiles, and (2) a geometric factor that is determined by the number and orientation of the individual beams about the capsule, and the energy or

power imbalance between the beams. (The balance of time-integrated individual beam energies does not preclude the occurrences of instantaneous differences in intensity between beams at different times in the pulse.)

B.1 Number of Beams and Focal Spot Radius

Figure 4.2 shows the predicted rms irradiation nonuniformity on the capsule for 24-, 32-, 60-, and 96-beam irradiation configurations. The individual beam radial-beam profiles in all cases is assumed to be $\sin^2 x/x^2$ characteristic of the intensity envelope produced by distributed phase plates. All of the beam configurations provide adequate uniformity at a focal ratio (beam radius at the 5% intensity point divided by the capsule radius) of ~1 (tangential focus). However, as the capsule implodes, this ratio increases due to the inward motion of the critical surface. By the time the laser pulse has finally turned off, the focal ratio typically doubles. From Fig. 4.2 it is clear that a minimum of 32 beams is required to obtain a high level of uniformity over the duration of the laser pulse. However, when issues associated with other contributions to illumination nonuniformity are included it is found that a 32-beam system requires much more control over power balance and beam mispointing than a system with more beams. Therefore, in terms of stating a requirement on the number of beams and their focal spot radii, a minimum of 60 beams is required and the initial focal spot radius should equal the radius of the capsule. As to the beam placement, assuming that the 60 beams are symmetrically disposed about the capsule is a good first approximation. If a detailed location of the optimal placement of the 60 beams is required, this information can be provided.

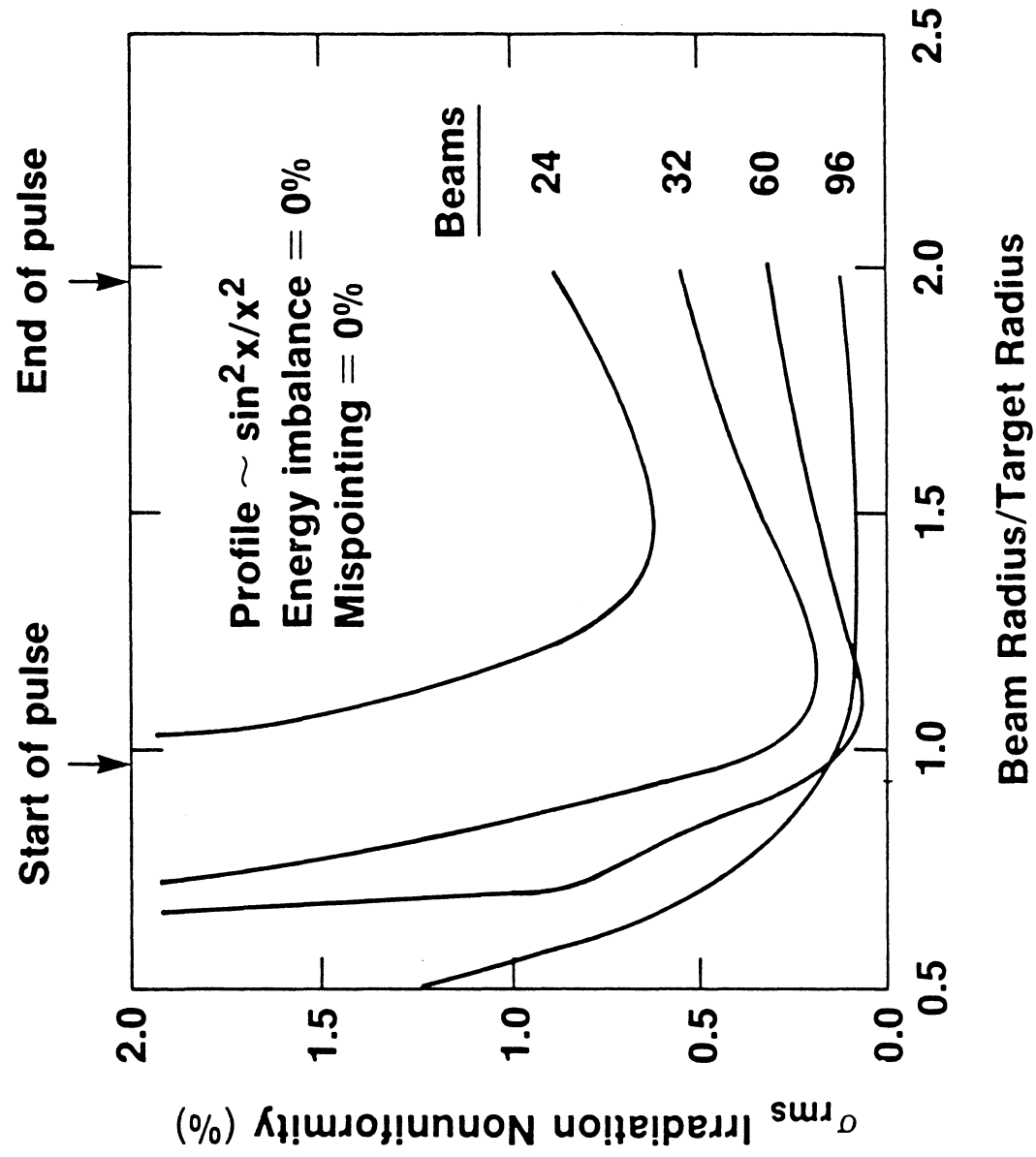

TC2519

Figure 4.2

B.2 Power Balance and Beam Alignment

The effects of beam (power) imbalance and beam alignment on capsule performance results in temporally varying illumination nonuniformities with spectral magnitudes that vary with time. Analysis has shown that these illumination nonuniformities produce mainly low-order modes ($\ell < 6$). Two-dimensional simulations of designs representing the upper gain curve have shown that the $\ell \leq 6$ modes must have amplitudes less that 1-2% (rms). Using this requirement, an estimate of the power imbalance and beam alignment (mispointing) can be obtained. Figure 4.3 shows that a 60-beam system requires power balance which must be better than ~5% rms for 1% rms illumination nonuniformity for $1 \leq \ell \leq 6$. The amount of beam mispointing that can be tolerated is shown in Fig. 4.4. The rms nonuniformity is plotted as a function of the maximum beam mispointing, measured in terms of the target radius. The mispointing is chosen to be random in magnitude (up to the maximum indicated), and random in direction; the error bar indicates the spread in values that is obtained for different sets of pointing errors at a given maximum. For a 60-beam system, a random mispointing of 0.1 of the capsule radius will result in ~1.2% rms illumination nonuniformity. The calculations in Fig. 4.4 assume perfect power balance. The combined results of power imbalance and beam mispointing add in quadrature.

B.3 Capsule Positioning

Uniformity calculations indicate that the capsule mispositioning with respect to the center of the chamber must be less than 0.1 of the capsule radius in order to maintain the nonuniformity below 1% rms. These calculations did not take into

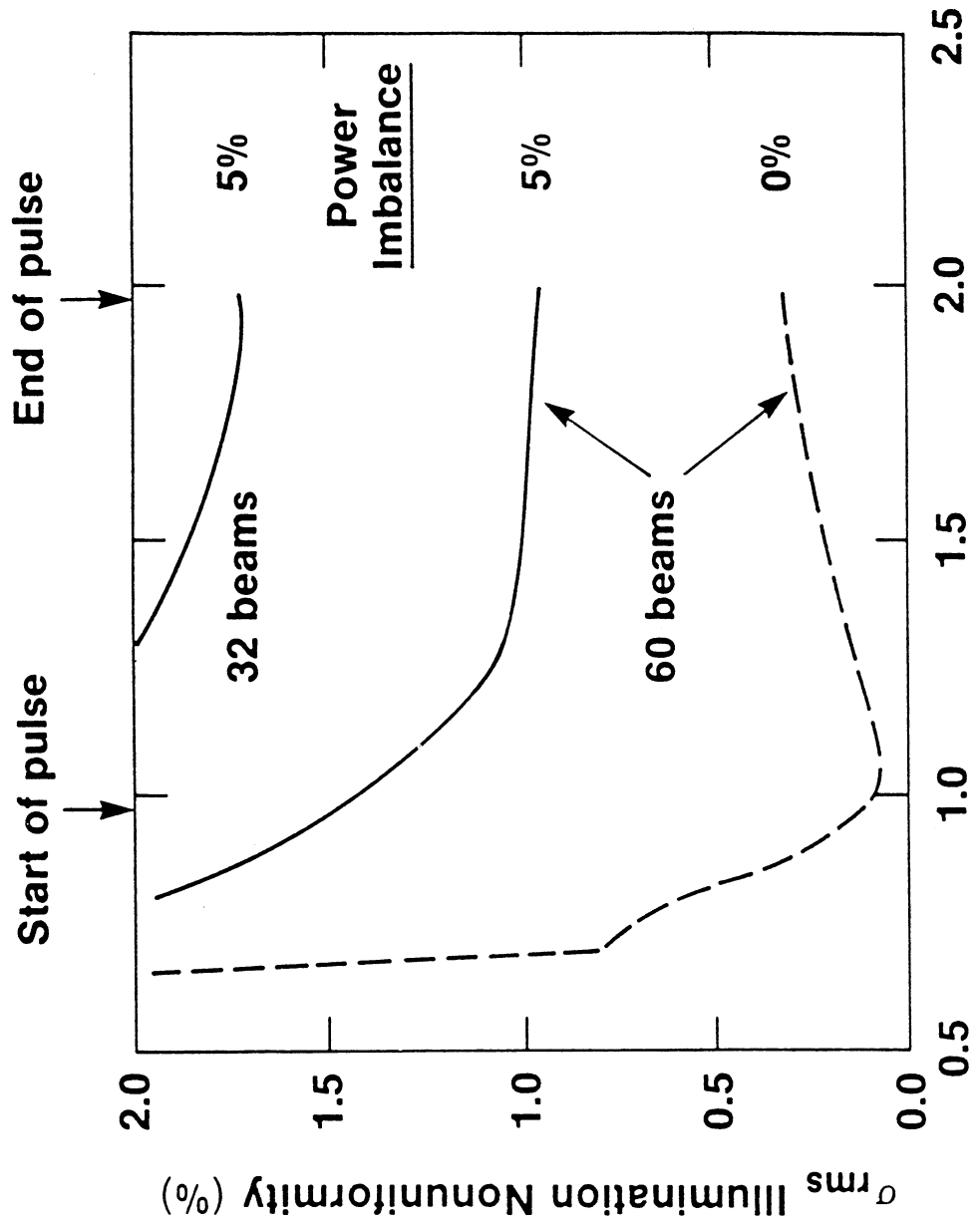

TC2520

Figure 4.3

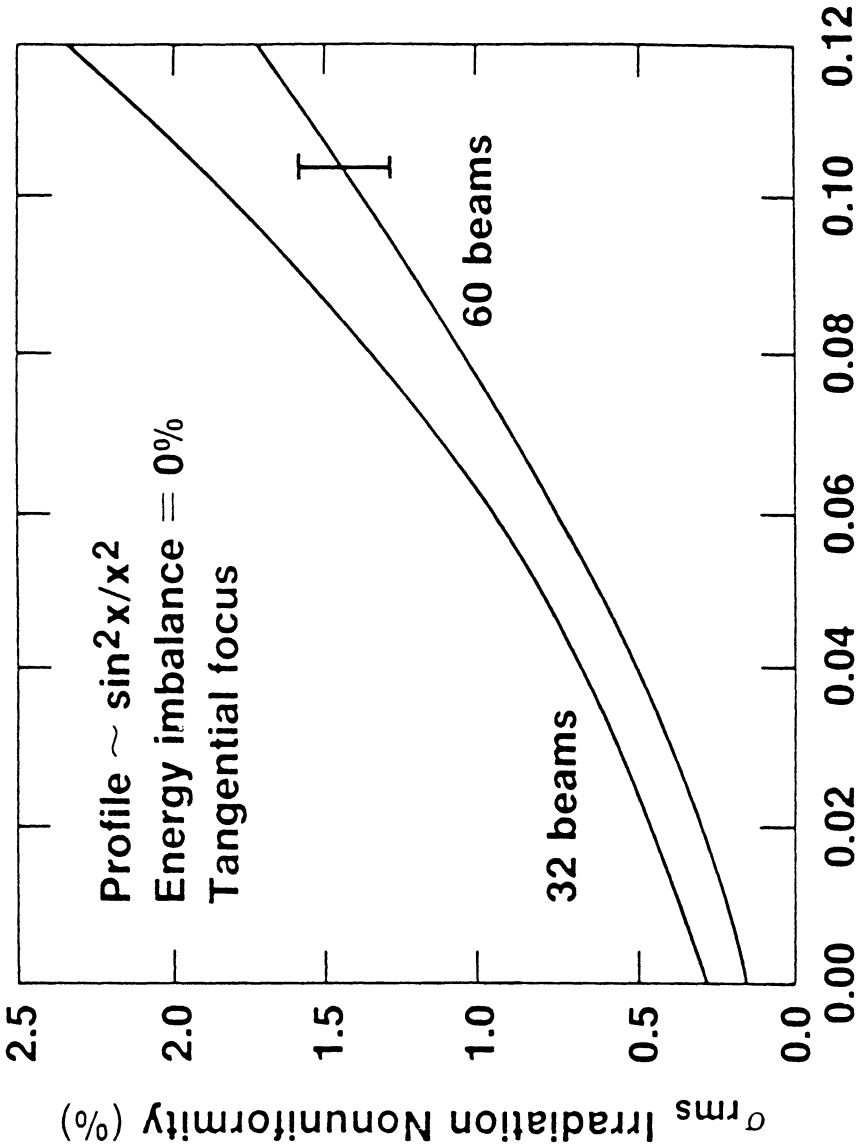

TC2521

Figure 4.4

account the time dependent effects on the capsule drive of the energy which misses the capsule due to its miscentering. This would depend on the particular capsule design and the pulse shape under consideration.

B.4 Individual Beam Uniformity

The required level of individual beam uniformity is still an area of active research. It is difficult to give a precise answer as to the requirements because capsule performance is affected by both the magnitude of the nonuniformity as well as the modal content of the resulting beam overlap pattern. Some form of beam smoothing technique will be required, and smoothing (or averaging) times will have to be as short as possible (tens of picoseconds). Therefore, since this study is limited to a KrF laser system, some form of ISI beam smoothing will have to be employed. As an estimate of the level of illumination uniformity required, initial calculations indicate that the asymptotic level of illumination nonuniformity will have to be $< 1\%$ rms and that the averaging times must be less than 10-20 ps.

V. TARGET REQUIREMENTS FOR INDIRECT-DRIVE IONS

A. Target Performance

Figure 5.1 gives target gain as a function of driver energy, ion range, and focal spot size for targets driven by two diametrically opposed beams or beam clusters. The peak power requirements for these targets are given in Fig. 5.2.

The curves in Figs. 5.1 and 5.2 should be considered the "base case." Concepts exist that should give gains about a factor of two higher. Thus the gain can be multiplied by a

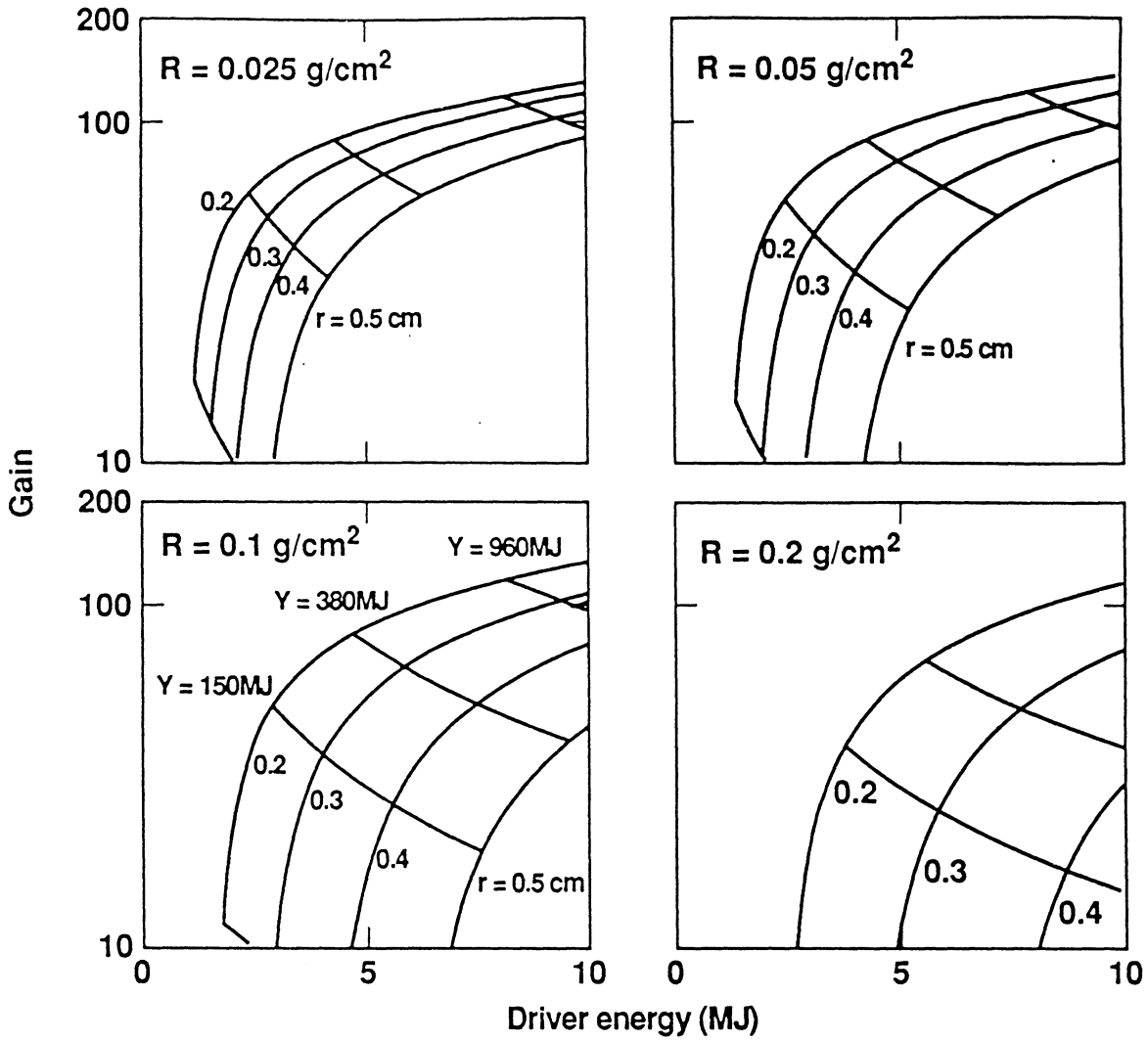
200
100
10
Gain
R = 0.025 g/cm²
0.2
0.3
0.4
r = 0.5 cm
R = 0.05 g/cm²
0.2
0.3
0.4
r = 0.5 cm
R = 0.1 g/cm²
Y = 960MJ
Y = 380MJ
Y = 150MJ
0.2
0.3
0.4
r = 0.5 cm
R = 0.2 g/cm²
0.2
0.3
0.4
0
5
10
0
5
10
Driver energy (MJ)

Figure 5.1

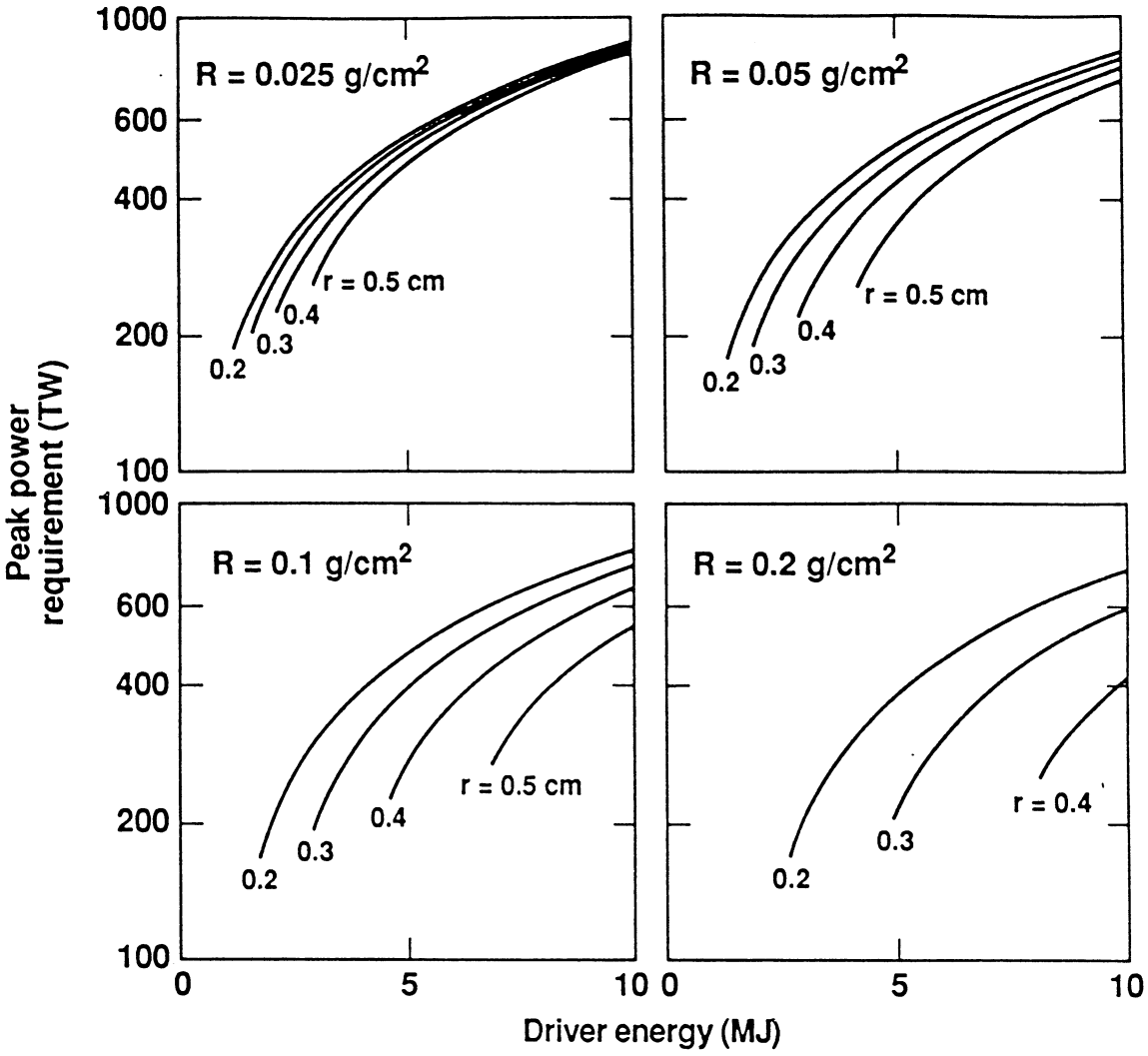
1000
600
400
200
100
R = 0.025 g/cm2
r = 0.5 cm
0.4
0.3
0.2
R = 0.05 g/cm2
r = 0.5 cm
0.4
0.3
0.2
R = 0.1 g/cm2
r = 0.5 cm
0.4
0.3
0.2
R = 0.2 g/cm2
r = 0.4
0.3
0.2
Peak power requirement (TW)
0
5
10
Driver energy (MJ)

Figure 5.2

factor of two to give a more speculative case; the power curves remain unchanged. For a lower limit, the gain should be multiplied by 0.7; the power curves again remain unchanged.

Ion range as a function of ion mass and kinetic energy is given in Fig. 5.3.

B. Pulse-Shape Precision, Power Balance and Beam Alignment

As noted in Sec. V.A, there is considerable flexibility in pulse shape; however, once a pulse shape is chosen, the power at any time during the pulse must be within 3% of its nominal value. This requirement must be met for both beam clusters.

The centroid of each beam or beam cluster must be aligned within 20% of the focal spot radius. If beam clusters are used and if the beam errors are statistically independent, each beam can clearly have looser tolerances than the tolerance on the entire cluster.

Misalignment and imperfections in the beams and lenses may lead to some fuziness in the beam radius. If the conditions on power balance and centroid alignment are satisfied, the effect of beam fuzziness can be estimated by using only that fraction of the beam energy that falls in the focal spot radius when using Figs. 5.1 and 5.2. Thus, within limits, there is a trade-off between target gain and beam alignment.

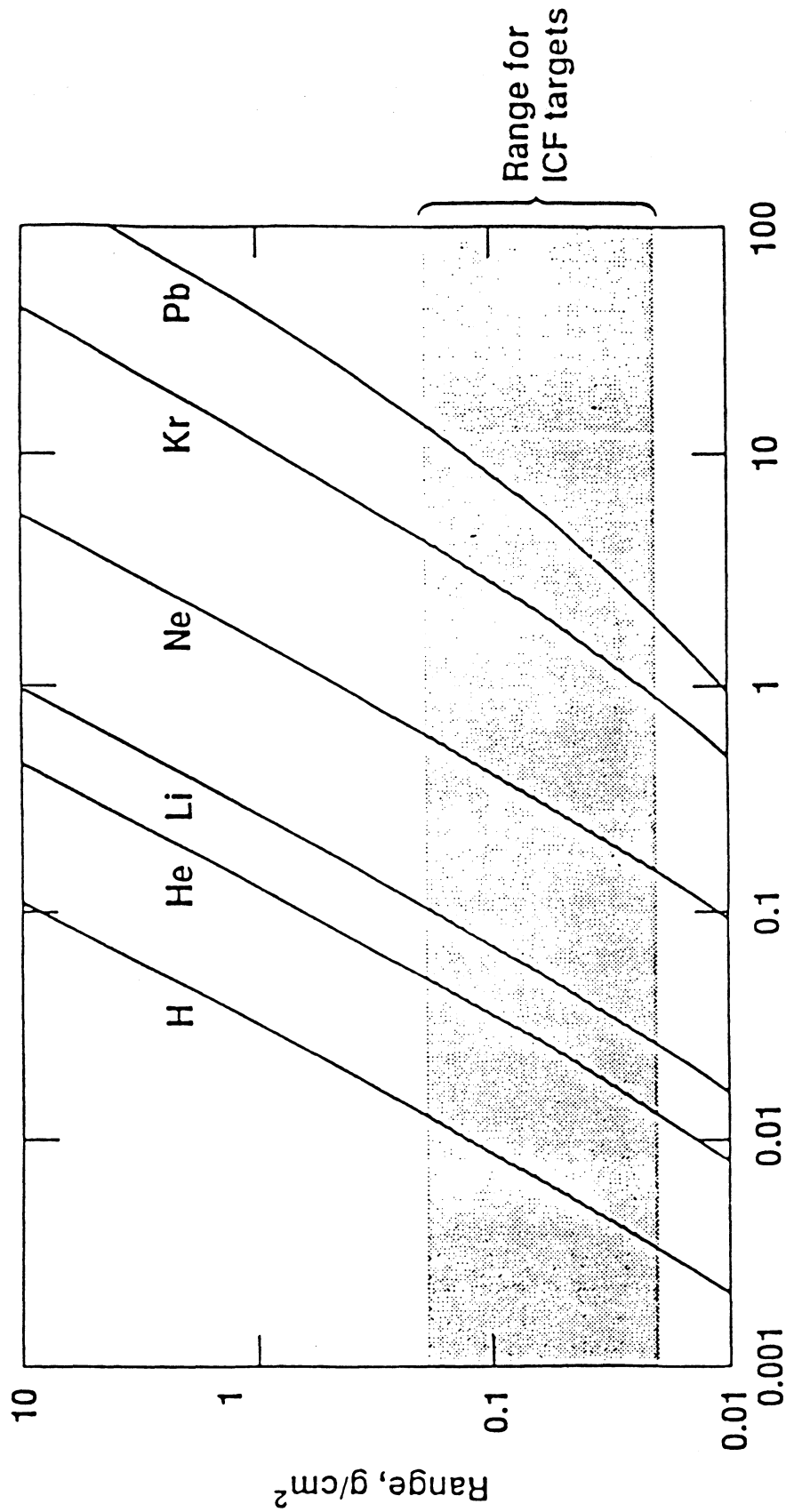
Range for
ICF targets
H
He
Li
Ne
Kr
Pb
Range, g/cm²
Energy (GeV)
10
1
0.1
0.01
0.001
0.01
0.1
1
10
100

Figure 5.3

FIGURE CAPTIONS

Figure 3.1 Study logic used by ARIES project.

Figure 4.1 Target gain versus incident KrF laser energy for directly driven single-shell capsule designs. The lower gain curve represents capsules which have been optimized with respect to reducing the effects of hydrodynamic unstable growth on capsule performance. The upper curve represents designs which would be considered optimistic with respect to capsule surface finish and illumination uniformity requirements.

Figure 4.2 Irradiation nonuniformity (σ rms) as a function of focus ratio for 24-, 32-, 60-, and 96-beam geometries, assuming a smooth $\sin^2 x/x^2$ radial beam profile.

Figure 4.3 Irradiation nonuniformity (σ rms) as a function of focus ratio for 32 and 60 beams, assuming a 5% rms power imbalance and smooth $\sin^2 x/x^2$ radial beam profiles. The dashed line is the reference σ rms for 0% rms power imbalance for the 60-beam system.

Figure 4.4 Effect of beam pointing error on irradiation nonuniformity for 32- and 60-beam system. A smooth $\sin^2 x/x^2$ radial beam profile is assumed.

Figure 5.1 Target gain as a function of driver energy, focal spot radius and ion range.

Figure 5.2 Peak beam power requirement as a function of driver energy, focal spot radius and ion range.

Figure 5.3 Ion range as a function of ion kinetic energy for a variety of ions.

REFERENCES

1. W.J. Hogan, G.L. Kulcinski, Fusion Technology 8, 17 (1985).
2. The HIBALL studies are good examples. "HIBALL: A Conceptual Heavy Ion Beam Driven Fusion Reactor Study," UWFDM-450, University of Wisconsin Fusion Technology Institute (1981); see also KfK-3202, Kernforschungszentrum Karlsruhe (1981) and "HIBALL II: An Improved Heavy Ion Beam Driven Fusion Reactor Study," UWFDM-625, University of Wisconsin Fusion Technology Institute (1984); see also KfK-3840, Kernforschungszentrum Karlsruhe (1984) and FPA-84-4, Fusion Power Associates (1984).
3. The HYLIFE study is a good example. James A. Blink, William J. Hogan, Jack Hovingh, Wayne R. Meier, and John H. Pitts, Lawrence Livermore National Laboratory Report UCRL-53559, (1985).
4. The Heavy-Ion Fusion Systems Assessment (HIFSA) is a good example. Fusion Technology, 13, No. 2, (1988).
5. F. Najmabadi, "The ARIES-I Tokamak Reactor," 9th Topical Meeting on Technology of Fusion Energy (Oakbrook, Illinois, October 7-11, 1990).
6. R.O. Bangerter, J.W.-K. Mark and G. Magelssen, "Simple Target Models for Ion Beam Fusion Systems Studies," LLNL Report UCID-20578 (1985).
7. John H. Pendergrass, David B. Harris, and Donald J. Dudziak, Fusion Technology 13, 375 (1988).
8. DOE/TIC-11603, Rev. 1, "Nonreactor Nuclear Facilities: Standards and Criteria Guide," and LA-10294-MS, "A Guide to Radiological Accident Considerations for Siting and Design of DOE Nonreactor Nuclear Facilities."

9. DOE/EH-0070, "External Dose-Rate Conversion Factors for Calculation of Dose to the Public," 7/88.

10. DOE/EH-0071, "Internal Dose Conversion Factors for Calculation of Dose to the Public," 7/88.

11. David S. Zucherman, Daniel E. Driemeyer, Lester M. Waganer, and Donald J. Dudziak, Fusion Technology 13, 217 (1988).

12. T.J. McCarville, W.R. Meier, C.F. Carson, B.B. Glasgow, Lawrence Livermore National Laboratory Report UCRL-15872, Jan. 12, 1987.

13. "Nuclear Energy Cost Data Base: A Reference Data Base for Nuclear and Coal-Fired Powerplant Power Generation Cost Analysis," US Department of Energy report DOE/NE-0095 (September, 1988).

14. J.P. Holdren et al., "Report of the Senior Committee on Environmental, Safety and Economic Aspects of Magnetic Fusion Energy," LLNL Report URL-53766 (September 25, 1989).

15. J.G. Delene, "Updated Comparisons of Economics of Fusion Reactors with Advanced Fission Reactors," 9th Topical Meeting on Technology of Fusion Energy (Oakbrook, Illinois, October 7-11, 1990).

16. R.L. Miller, "Options and Optimizations for Tokamak Reactors: ARIES," 9th Topical Meeting on Technology of Fusion Energy (Oakbrook, Illinois, October 7-11, 1990).

REVISED TARGET INFORMATION FOR ICF REACTOR STUDIES

This document is a supplement to Sections IV and V of Inertial Confinement Fusion Reactor Studies Recommended Guidelines, September 1990. In some cases the material given here replaces material given in the Guidelines and in some cases it provides additional information.

I. Summary of Target Gain and Driver Requirements for Short Wavelength Laser Driven Indirect Drive Targets

Target gain, using indirectly driven capsules for inertial fusion energy production, will be a function of a large number of variables, including laser geometry, focusability, pointing accuracy, wavelength and possibly beam smoothness and bandwidth, as well as target performance determined by such effects as hydrodynamic instabilities and plasma physics effects in hohlraums. Most of these effects are coupled and a system optimization must be carried out to determine the best set of operating conditions. Since most of the target physics is classified, many of the choices which go into any particular set of gain curves must remain classified. Figure 1 shows two gain curves which we believe span the range of target gains likely to be achievable using standard capsule and hohlraum designs. The lower curve is based on detailed target design studies carried out for the Department of energy Defense Programs LMF (Laboratory Microfusion Facility). This gain curve is consistent with an extrapolation to the megajoule scale of all current data. This curve represents our best estimate of the gain which would be achieved in a first of a kind experimental high gain facility. The higher gain of the upper curve results from an increased coupling efficiency which we believe can be achieved after optimization of both the laser-plasma interaction effects and the target geometry. Advanced target designs could have gains of about a factor of two higher than the upper curve. These designs have increased physics uncertainties and have been less thoroughly analyzed than our baseline designs; however, for these studies the enhanced performance curve should be used as the base case. The LMF baseline

curve is the conservative case. The enhanced performance curve should be multiplied by 2 to give the more optimistic case called for in the Guidelines; however, the optimistic case should not be used for laser energies less than 2.5 MJ. Figure 2 shows the peak power requirements for the two gain curves in Figure 1. The power curve for enhanced hohlraum performance may be used for the optimistic case. About 70% of the total energy is delivered during the peak power part of the pulse. The rest is delivered in a pulse shape which is 4-5 times the duration of the peak power pulse.

In order for the laser energy to be efficiently utilized, it is necessary that the laser beam be capable of achieving a spot size which is near diffraction limited. It is also important that the pointing errors be limited to a few microradians. A convenient way of stating these requirements is to specify a focal spot within which the laser energy can be delivered. Both gain curves in Figure 1 assume that all of the useful energy of each beam can be delivered into a 1.5 mm diameter spot. This spot size includes both the size of the focal spot and any pointing errors. At best, all energy outside this spot will not be useful in driving an implosion. In a worst case scenario, this energy could adversely affect an implosion if it exceeds a few percent of the total energy. In addition, both curves assume a laser geometry similar to that being planned for Nova Upgrade. The Nova Upgrade laser plan calls for 288 independently pointed beams. This large number of beams is distributed in three or four rings of beams on each side of the target at angles distributed between about 30 and 60 degrees from the target axis. The large number of beams allows great flexibility for achieving irradiation uniformity at the capsule. It also relaxes the instantaneous power and energy balance requirements and allows an RMS variation of 10% or more. It should ultimately be possible to reduce the number of beams to a total ranging between 20 and 50. With a smaller number of beams, the power balance must be better than about 5% and the gain may be lower. For these studies we recommend a minimum of 50 beams.

II. Direct Drive Laser Targets

The gain curves for directly driven targets have been modified. Figures 3 and 4 give the curves that should now be used. The curves in Figure 3 assume that the laser focal spot radius is constant in time. Because detailed target designs are not yet available for this study, assume the well known hydrodynamic scaling laws to get focal spot radius, i.e. assume the radius scales as $E_L^{1/3}$ where E_L is laser energy. Use a radius of 2.8 mm at 4 MJ to get the coefficient. Similarly assume that peak power scales as $E_L^{2/3}$. Use a peak power of 500 TW at 4 MJ to get the coefficient. For all other details the original Guidelines remain valid. The curves in Figure 4 assume that the focal spot radius is "zoomed" so that the focal spot radius remains equal to the critical surface throughout the implosion. If the contractors wish to consider zooming, additional details will be provided. In Figures 3 and 4 the lower curve is the conservative case, the upper curve is the optimistic case and the base case is the arithmetic mean.

Researchers at the Naval Research Laboratory (NRL) have proposed a potential direct-drive gain curve (Fig. 5), obtained from scaling published indirect-drive gain results, which would require zooming and the use of capsules containing high Z dopants in the ablator to reduce the number of e-foldings the capsule would experience during the acceleration phase. In addition, in order to achieve high hydrodynamic efficiency and reduce the required laser intensity, NRL designs are assuming larger initial aspect ratio capsules when compared to the Laboratory for Laser Energetics (LLE) designs (Figures 3 and 4). NRL estimates indicate that if the average number of e-foldings experienced by the capsule during the acceleration phase could be reduced to <5, the capsules would survive the acceleration phase without rupturing the over dense imploding shell. As of this date there are no NRL point designs to show that the reductions in growth and the high gain shown in Figure 5 can be achieved simultaneously.

Energetically a simple Meyer-ter-Vehn type of model shows that it is possible to achieve gain levels similar to that shown in Figure 5. In

general, the difference between the LLE gain curves and the NRL proposed gain curve is in the level of optimism associated with the physics of Rayleigh-Taylor unstable hydrodynamics and deleterious plasma physics effects. Based on our present theoretical understanding, the LLE gain curves represent a more conservative view associated with capsule performance than the proposed NRL gain curve with respect to hydrodynamic stability issues.

Considering the present lack of experimental data to verify the theoretical understanding associated with direct-drive Rayleigh-Taylor unstable hydrodynamics and plasma physics issues relevant to high gain capsules, it is difficult to assign a level of risk associated with each laboratory's gain curves. It is certainly the goal of each laboratory's effort to obtain as high a gain as possible at a given incident laser energy while maintaining some finite probability that the implosion would work. Theoretical and experimental research will continue to be applied to resolving the issues associated with the uncertainty in capsule performance due to unstable hydrodynamics and potential plasma physics issues over the coming years.

Due to the present lack of any point designs associated with the proposed NRL gain curve, it is proposed that the contractors use the LLE provided gain curves in their initial analysis. If the LLE gains result in economically feasible power plant designs achieving higher gains, as implied by the NRL proposed curve, based on new capsule design work will only make the problem easier. If the gains from the LLE results prove to be too low, it is then proposed that the contractors use the results from the NRL proposed gain curve to do their analysis. If the NRL gain curve is used, appropriate caveats associated with the fact that no point designs currently exist, which numerically show that such gains can be achieved while maintaining good hydrodynamic stability, should be included.

III. Heavy Ion Target Gain

The curves in the original guidelines remain unchanged; however, the optimistic case (2 times the base case) should not be used at driver energies below the "knee" in the base-case curves. The knee occurs at a target yield of about 200 MJ in the curves of Figure 5.1 in the Guidelines. Therefore, the curves in Figure 5.1 may be multiplied by 2 only if the yield exceeds 200 MJ (400 MJ after multiplication).

Directly driven gain curves are becoming available. The calculations give gains in excess of 100 at about 1 MJ; however, directly driven ion targets have illumination requirements similar to directly driven laser targets. If the contractors wish to use direct drive for ions, we may be able to have detailed information in about a year.

The Target Working Group has considered the case of single-sided illumination for ions. Current calculations indicate that the gain is comparable to the gain for two-sided illumination. Therefore, the contractors may use the curves in the guidelines for single-sided illumination; however, single-sided illumination is still sufficiently speculative that the contractors should continue to carry a two-sided option, even if they wish to evaluate the single-sided option.

IV. Target Costing and Output

No new target designs are currently available for these studies. Therefore, for target cost estimates, the contractors should use the target shown in The University of Rochester Laboratory for Laser Energetics, Annual Report, 1 October 1984-30 September 1985, DOE/DP/4020-05, January 1986, p. 126. CH_2 is not a particularly good structural material. The contractors should use CH instead.

For target output information, HIFSA used R.O. Bangerter, J. W-K., Mark, and G. Magelssen, "Simple Target Models for Ion Beam Fusion Systems Analysis," UCID-20578, Lawrence Livermore National

Laboratory (1985). The contractors should also refer to Charles D. Orth, "Improved Understanding of First-Wall Vaporization-Condensation in Inertial Confinement Fusion Reactors," UCRL-93899, Rev. 1, Lawrence Livermore National Laboratory (1986) and to the Sirius reports. If these three unclassified sources do not contain enough information, the contractors may have to calculate their own spectra.

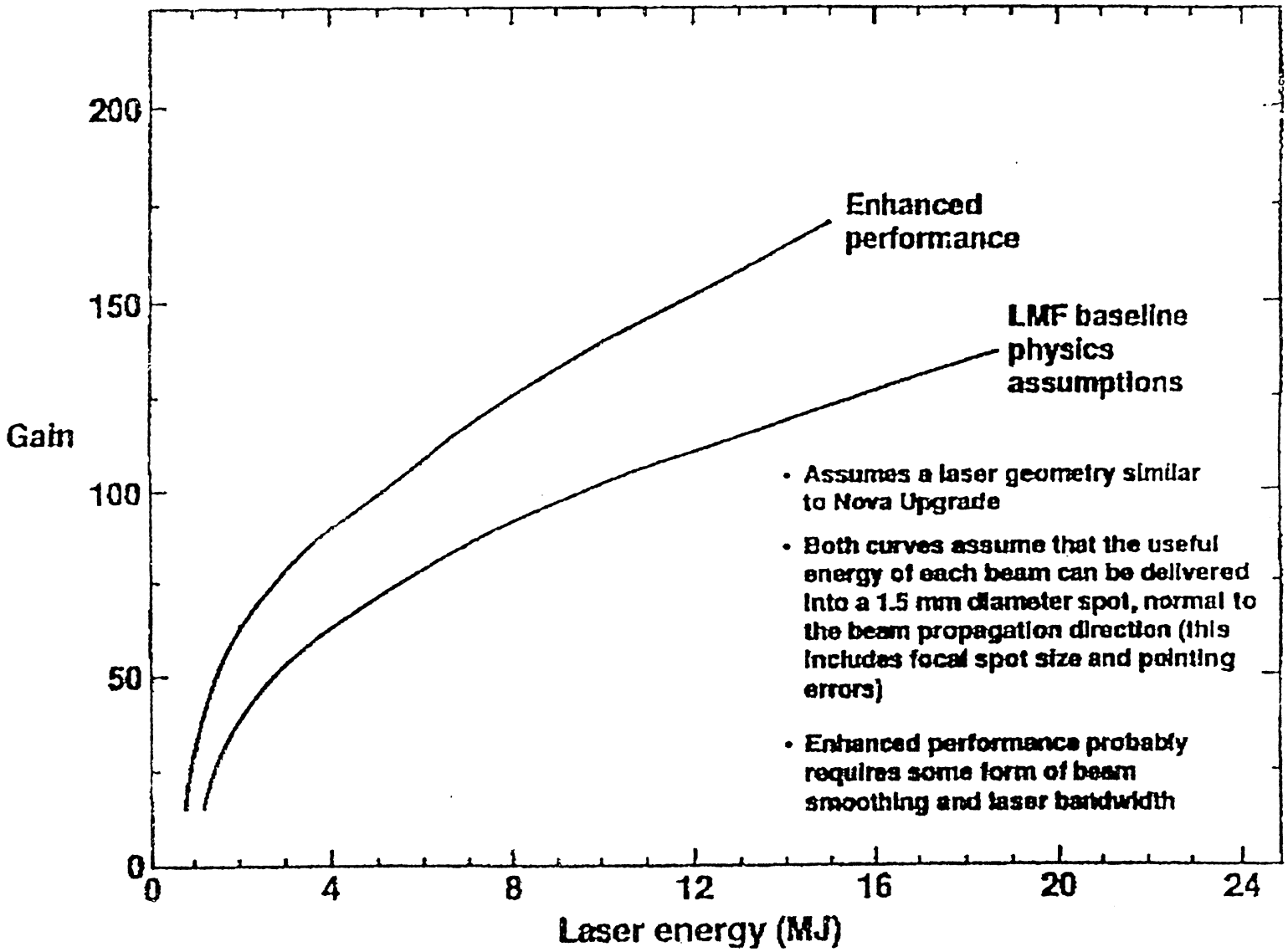

Figure 1. Gain as a function of laser energy for indirectly driven targets.

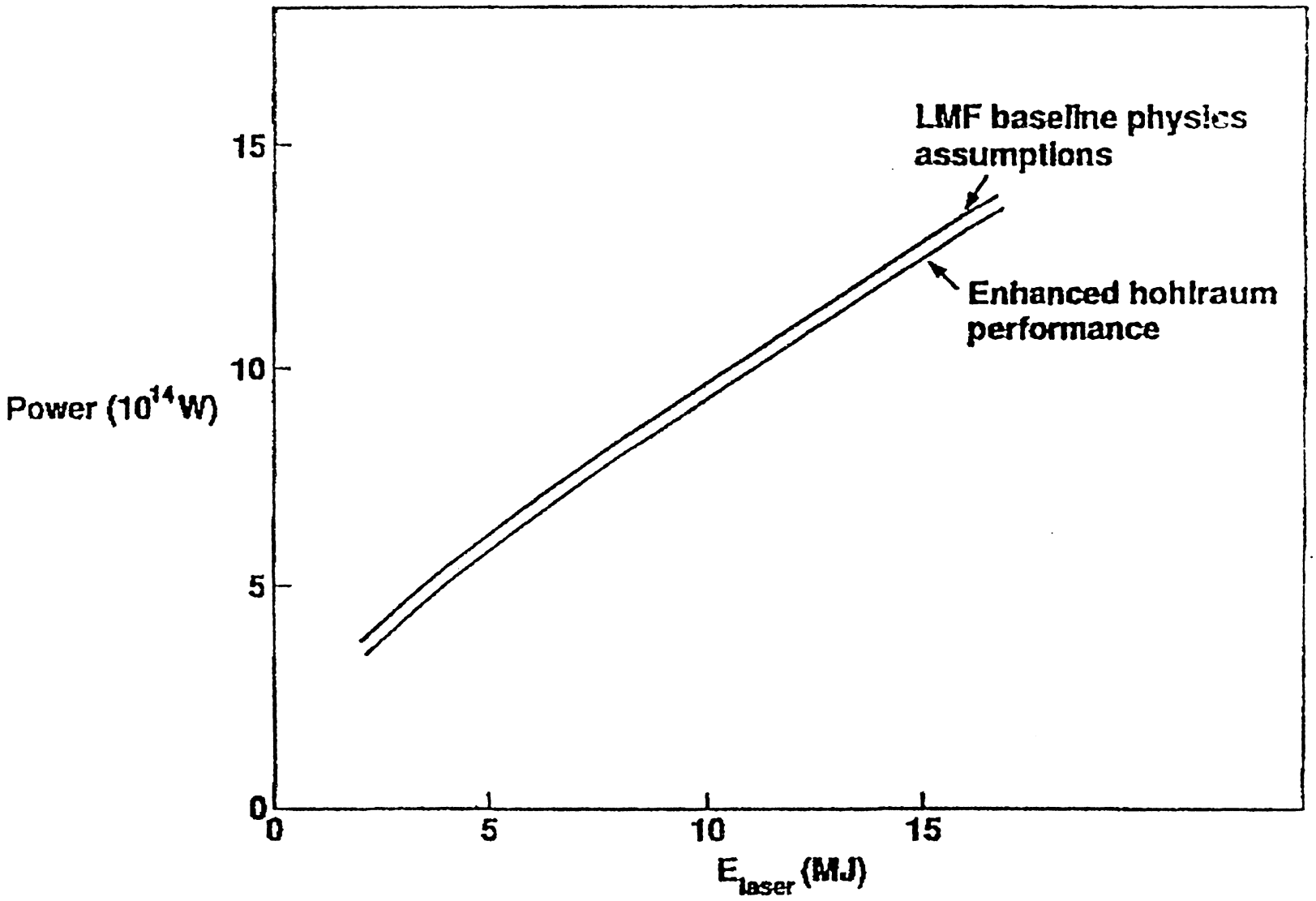

Figure 2. Power as a function of laser energy for indirectly driven targets.

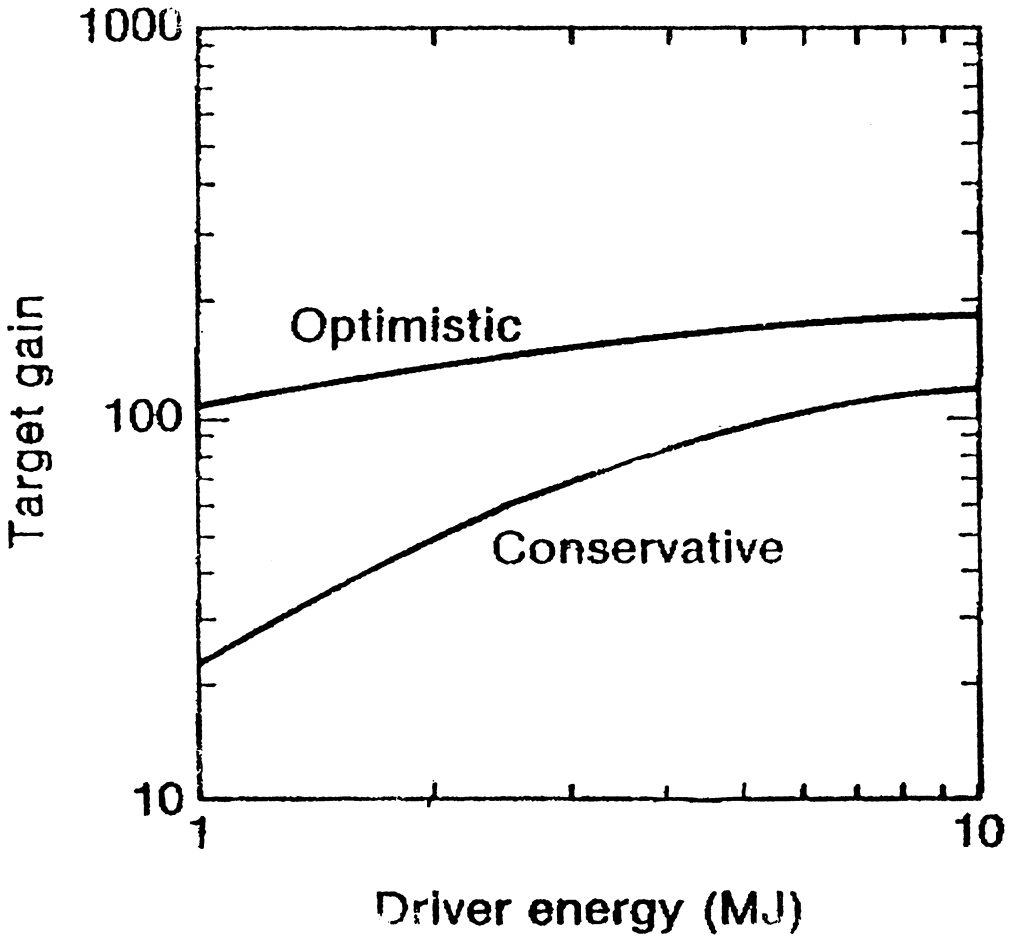

Figure 3. Gain as a function of energy for directly driven laser targets.

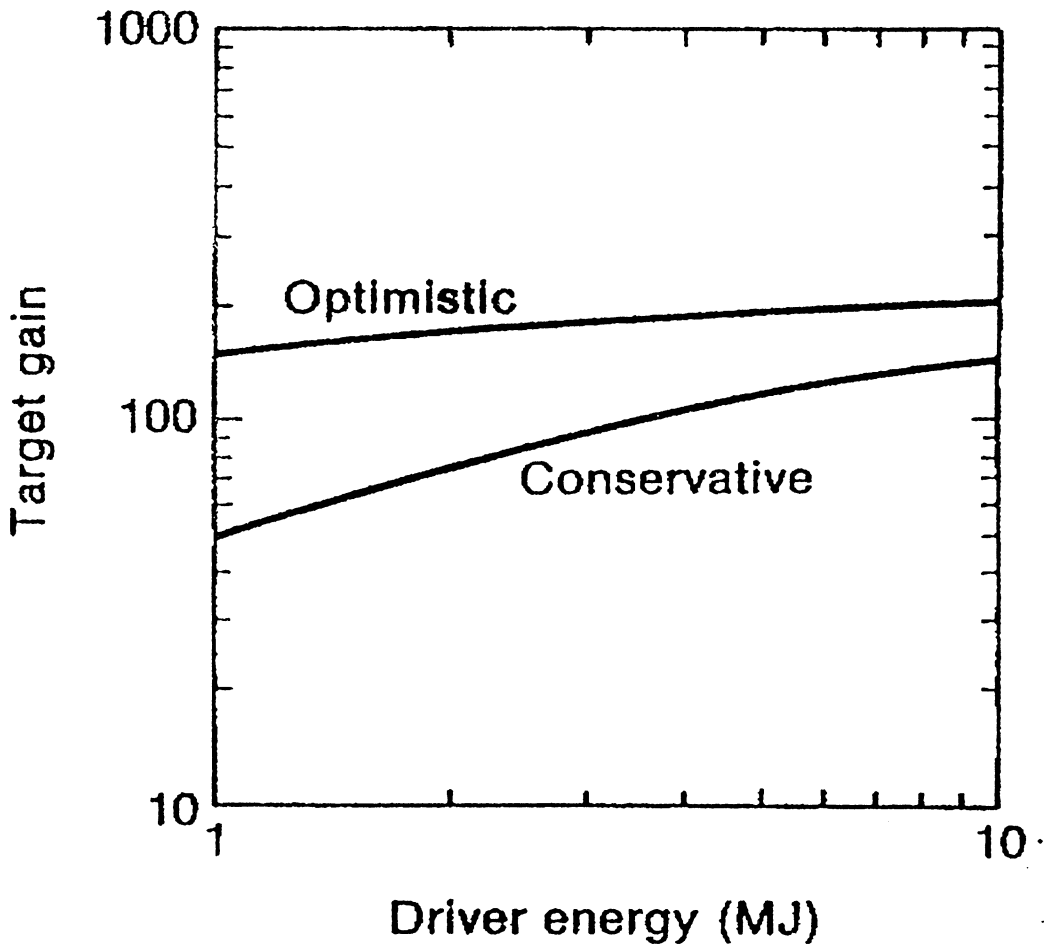

Figure 4. Gain as a function of energy for directly driven laser targets. These curves assume zooming.

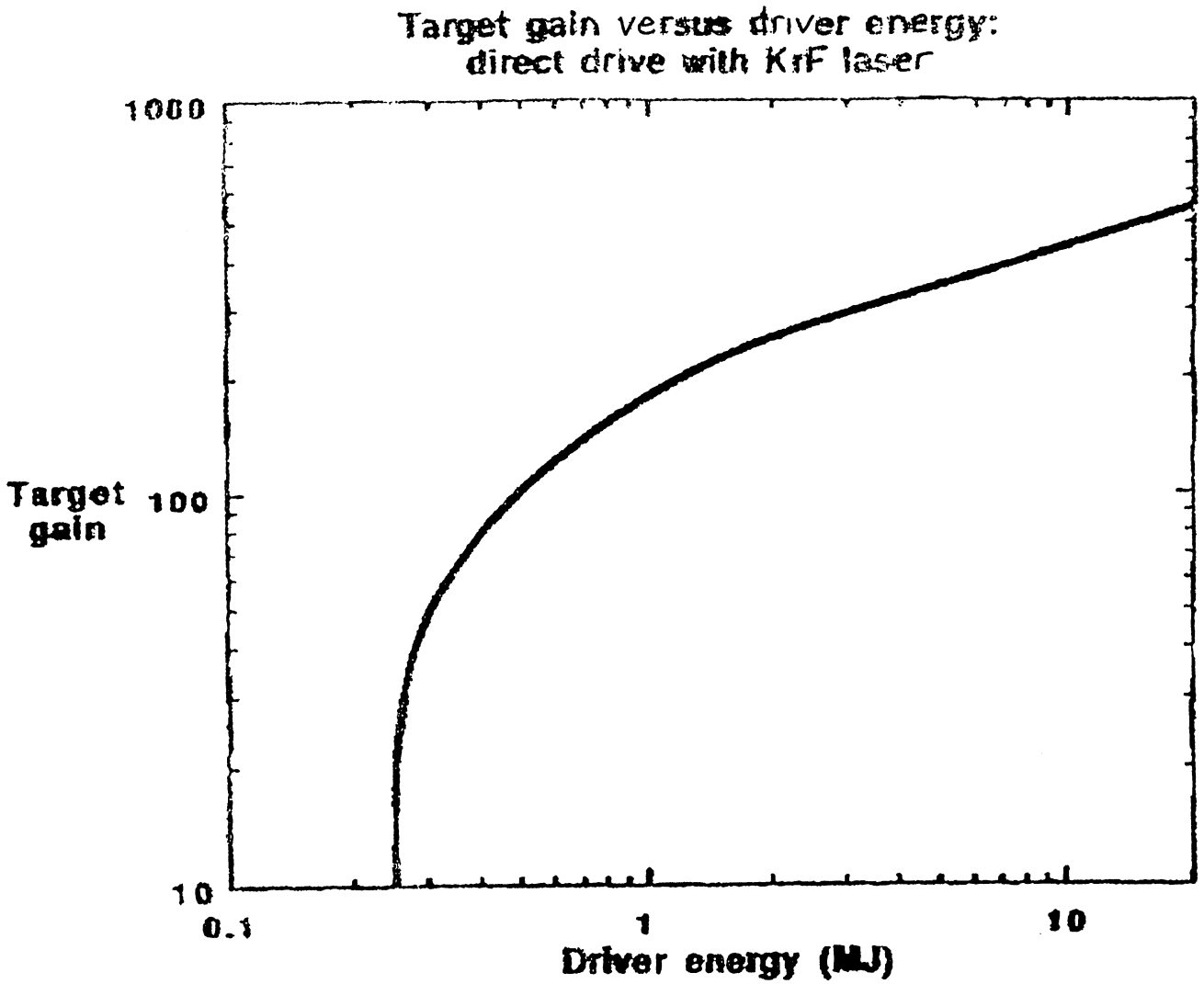

Figure 5 NRL gain curve for directly driven laser targets.

Appendix B

Reactor Concept Selection Process

CONTENTS

B.1 RATING REACTOR CONCEPTS
B.2 CHAMBER CONCEPT SELECTION

W.J. SCHAFER ASSOCIATES • 6140 STONERIDGE MALL ROAD • SUITE 385 • PLEASANTON, CALIFORNIA 94588-3235 • (510) 463-1108

March 8, 1991
WRM-SF91-024

M E M O R A N D U M

To: Reactor Studies Team
From: Wayne Meier
Subject: Rating Reactor Concepts

As you know, it is time to make a decision and proceed with the design phase of the study. We would like input on how you rate the various reactor concepts. We will use the same procedure that we used at the review meeting in Berkeley.

Evaluation Criteria

Recall that we reduced the number of evaluation criteria to three:

• Technical Issues (includes Technical Credibility and Technology Development)	50%
• Environmental and Safety	30%
• Economics (Operability effects economics)	20%

Rating Scale

We will us a simple rating based on the following scale:

• Very good	5
• Good	4
• OK	3
• Poor	2
• Very Poor	1

Reactor Concepts for KrF Driver - Uniform Illumination Target

1) Onion with Flibe breeder/coolant and a gas protected first wall (CVI SiC)

2) SBMB with a Li_2O breeder/coolant and a gas protected first wall (C/C composite)

3) Higher pressure SBMB

We completed preliminary evaluations of the first two concepts for the KrF driver at the LBL meeting. Based on the input of 7 individuals at the LBL meeting, the two concepts were rated nearly equal, with Onion slightly favored (26.4 to 25). However, we still need one more evaluation from UW. I have enclosed a copy of the rating you did at LBL in case you want to change your mind.

Most of the concern with the SBMB concept seemed to focus on the pressure isolators. Therefore, please rate option 3 listed above which is a higher pressure version of SBMB. In this case the chamber would run at a pressure closer to the pressure of the gas stream used to lift the breeder to the top of the chamber (~3-4 atm, which is about the same as Onion's hydrostatic head). This would reduce or maybe illuminate the need for the pressure isolators. A higher pressure design could also incorporate an onion-type cooling scheme. Cold Li_2O could be injected and fluidized up along the first wall to remove first wall heating. The material would then flow down and out of the reactor in a slower moving outer region that absorbs the bulk of the neutron heating.

Reactor Concepts for HIB Driver - Indirect Drive Target

1) Cascade with Be coated $LiAlO_2$ breeder/coolant

2) LIFE reactor with PbLi coolant/breeder

3) Onion with PbLi breeder/coolant and a PbLi wetted first wall (V or ferritic steel)

4) Osiris with PbLi breeder/coolant filling SiC fabric blinds and neutron blanket modules

5) SBMB same as above, but at a larger radius

Note that the Flibe versus PbLi choice is still open for all concepts. Reviewers seemed to prefer Flibe, but the pressure-propagation limit is not yet firm.

Please fill out a rating sheet for each of the seven concepts. If any criteria is given a very poor or poor rating (1 or 2), please add a brief comment explaining your concern. I would like input from two people at each institution.

Your input is due on Thursday, March 14.

W.J. SCHAFER ASSOCIATES • 6140 STONERIDGE MALL ROAD • SUITE 385 • PLEASANTON, CALIFORNIA 94588-3235 • (510) 463-1108

March 29, 1991
MJM-SF91-035

MEMORANDUM

To: ICF Reactor Studies Team
From: M. Monsler and W. Meier
Subject: Chamber Concept Selection

Introduction: Well, the votes are in, we are back in town, and it's time to announce the Oscar winners. Before we begin, I want to tell you that we briefed Bob Price at DOE/Germantown on March 21, 1991 on the progress of our study. Our 2-hour briefing, attended by about 8 people (not including Ann Davies, Bob Dowling, or Dave Bixler, unfortunately), was well received. DOE has not been briefed by the other team. Now on to the results—

As you recall, individual scores ranging from 1 (very poor) to 5 (very good) were assigned to three aspects of each concept [technical credibility (50%), environment and safety (30%), and economics (20%)] and weighted appropriately. Combined scores were calculated for each concept for each driver. These are the scores given in the following figures. Each institution was allowed two votes; University of Wisconsin chose to combine the views of four people into one rating sheet, which counted twice.

Chamber Selection for KrF Driver: The scores for the KrF chamber concept are given in Fig. 1. As you recall, the Solid Breeder Moving Bed concept has two embodiments: a low-pressure version requiring pressure isolators and a high-pressure version not needing isolators. The Onion concept uses a Flibe breeder/coolant and a carbon first wall. All KrF driver concepts use gas protection and uniform illumination.

Fig. 1 Scores for Chamber Concepts with KrF Driver

	Onion	SBMB	HP - SBMB
Bechtel	3.70	3.60	3.60
Bechtel	3.54	3.50	3.60
GA	4.00	2.80	3.30
GA	4.10	3.10	3.60
WJSA	3.55	4.10	4.20
WJSA	3.90	3.85	3.95
UW	2.50	4.30	4.30
UW	2.50	4.30	4.30
Average score	3.47	3.69	3.86
Avg w/o Hi and Low	3.53	3.74	3.88

Our team apparently has a preference for the higher pressure SBMB over the other concepts. If you take the average of all scores, or if you drop the high and low scores and average the remaining six, the result is the same. The relative ranking also holds if you consider the rankings shown in Fig. 2, rather than the scores. Notice that HP-SBMB took 5 firsts and 8 firsts or seconds, compared to Onion's 3 firsts and 5 firsts or seconds. If you look at Wayne's scoresheet, you will see that he was consistent in his method of handling ties for rankings, so that if there were two ties for first place, the next ranking was a third place.

Fig. 2 Ranking of Chamber Concepts with KrF Driver

	Onion	SBMB	HP - SBMB
Bechtel	1	2	2
Bechtel	2	3	1
GA	1	3	2
GA	1	3	2
WJSA	3	2	1
WJSA	2	3	1
UW	3	1	1
UW	3	1	1

I interpret the slight preference of the higher pressure version of SBMB over the original as dissatisfaction with current concepts for pressure isolation, not with a desire to operate blankets at higher pressure. Note that the average scores for all three concepts spanned the range from good to very good. From the sparse comments that were offered, Onion did not lose because of any fatal flaws; in fact, it is certainly more conventional in appearance and operation. The concerns mentioned were the effects of isochoric heating from neutron deposition, the use of CVI carbon as unnecessarily exotic, concern over Be, and heat transfer. Instead, I read into the results the desire to look at something different from MFE that may have advantages.

We shall now begin to work on the SBMB concept for a KrF driver, attempting to solve the pressure isolation issue by clever fluidized engineering. I would like suggestions for a brilliant name for this concept. More careful heat transfer calculations must be done to understand the operational trade-off between trying ot operate the carbon first wall as hot as possible while limiting the maximum temperature of Li_2O. Finally, there is plenty of concern over the heat exchanger design. Can this concept also avoid an intermediate loop?

Chamber Selection for HIB Driver: The chamber selection for the HIB driver is more complicated. The average scores fell into two groupings. From Fig. 3, we see that Onion and OSIRIS are clustered together at the top, with the SBMB and rotating chambers ranked lower.

Fig. 3 Scores for Chamber Concepts with HIB Driver

	Cascade	LIFE	Onion	Osiris	SBMB
Bechtel	3.40	3.30	3.70	3.50	3.60
Bechtel	3.10	3.55	3.45	3.75	3.64
GA	2.50	2.90	3.90	2.70	2.80
GA	5.00	3.60	3.60	2.50	3.60
WJSA	2.20	2.45	3.40	4.25	2.70
WJSA	3.00	2.75	3.25	3.85	2.60
UW	2.80	3.00	3.40	3.45	3.10
UW	2.80	3.00	3.40	3.45	3.10
Average	3.10	3.07	3.51	3.43	3.14
Avg w/o Hi and Low	2.93	3.08	3.49	3.45	3.15

In our view, and from the comments given, it seems there are solid reasons for not selecting the bottom three. The HIB-SBMB, having a wall radius over 10 meters, was a great concern for HIB propagation. The Cascade and LIFE concepts have a rotation problem, and I don't think it is just a superficial image problem. The amount of stored mechanical energy is enormous. Monsler calculated that for LIFE spinning at 36 RPM, the energy of rotation is 300 MJ. While this is not a high thermal energy (we handle it at 10 Hz in normal operation), it is enough mechanical energy to throw a two-ton automobile 15 kilometers vertically into the air. This is a seismic and accident safety issue, which I believe was intuitively avoided by many on the team.

Of the two remaining concepts, Onion slightly outscores OSIRIS both on average and when the high/low scores are eliminated. (If only Monsler's and Bourque's scores are eliminated, the scores are equal.) OSIRIS has a much higher standard deviation (not shown) than Onion; apparently, team members either love it or hate it. The picture changes, however, if we look at the rankings shown in Fig. 4.

Fig. 4 Ranking of Chamber Concepts with HIB Driver

	Cascade	LIFE	Onion	Osiris	SBMB
Bechtel	4	5	1	3	2
Bechtel	5	3	4	1	2
GA	5	2	1	4	3
GA	1	2	2	5	2
WJSA	5	4	2	1	3
WJSA	3	4	2	1	5
UW	5	4	2	1	3
UW	5	4	2	1	3

We see that OSIRIS scores 5 firsts compared to 2 for Onion, with Onion the dominant second choice. From the comments, our team liked the more conventional appearance of Onion and potentially higher efficiency, but disliked the metal structure with welds exposed to neutron flux and the need to change out the entire chamber every few years. Our team likes the robust and compact nature of OSIRIS, but was concerned about surface heat transfer. Some ranked OSIRIS very high on chamber clearing, while others were concerned about recondensation times and HIB propagation. All are concerned with the Be and F problems with Flibe and the Po problem with LiPb.

We could live with either of these two reactor concepts for HIB reactor; either has the potential for being engineered into a credible design. As the project manager, I (Monsler) chose the OSIRIS concept, not only because it was selected first by 5 of the 8 votes, but because it shows how the unique features of ICF allow a radically different solution to the engineering problems of fusion than those used in MFE.

My view of ICF reactor design is that, first, the ideal concept has no solid materials: the fusion pellet is simply surrounded by a reestablishable breeding/heat transfer liquid. Given that this is insufficient, one should reluctantly introduce the minimum amount of low-activation solid materials necessary to guide the fluid flow and establish a configuration to accommodate gravity. Second, the configuration should be designed to solve the problems encountered (e.g., HYLIFE jets or HIBALL tubes) rather than living with a simple sphere and trying only to select materials. Third, from the point of view of neutron or mechanical damage and/or lifetime, eliminating the first wall always beats struggling with first wall design. For an HIB reactor, we can follow this philosophy very closely to get the absolute minimum material exposed to neutrons. The only reason we turn to a more conventional first wall/blanket structure for the KrF driver is the dominant geometrical constraint of uniform illumination.

Conclusion:

We now have selected two terrific concepts:

a) A gas protected chamber with a solid-breeder moving-bed blanket, driven by a uniform-illumination KrF laser.

b) A thick liquid wall chamber driven by a heavy ion beam and radiation-driven targets.

This is a great combination to show how we can design for two distinct drivers, two types of targets, two types of reactors, and still have ICF reach its potential and compete favorably with MFE.

Appendix C

Onion Reactor Concept

CONTENTS

C.1 BACKGROUND C-1
C.2 GENERAL DESCRIPTION C-1
C.3 REFERENCE DESIGN C-2
C.4 DESCRIPTION OF REFERENCE DESIGN C-2
C.5 RENEWABLE FIRST WALL COATING C-4
C.6 FIRST WALL STRUCTURE C-7
C.7 FLIBE BLANKET C-7
C.8 BLOWOFF IMPULSE AND CHAMBER RESPONSE C-8
C.9 COMPATIBILITY WITH INDIRECT TARGET SHELL MATERIALS C-8
C.10 ALTERNATE ONION WITH METAL CHAMBER AND LITHIUM-LEAD C-9
C.11 MODIFICATIONS FOR LASER DRIVER C-11
C.12 SUMMARY C-11
C.13 REFERENCES FOR APPENDIX C C-11

APPENDIX C. THE ONION IFE REACTOR CONCEPT

C.1 BACKGROUND

The "Onion" reactor concept described below received about the same overall score as the Osiris concept that was chosen for further analysis. The Onion has a number of features that make it a viable candidate for future study.

C.2 GENERAL DESCRIPTION

To keep reactor costs reasonable and to accommodate heavy ion beam transport, the first wall must be placed close enough that some vaporization does occur. The Onion concept allows controlled vaporization of a very thin surface coating. As discussed below, this vapor very quickly recondenses on the wall with only 1-2 percent lost out the penetrations. This loss is periodically replaced by injecting fresh wall material into the chamber.

The vaporization process generates stress waves that propagate into the wall. Because the initial duration of these waves is so short, 1-3 nanoseconds, attenuation is very rapid. Furthermore, the wall material failure stress tends to be much higher under pulsed loading compared to static. The result of all this is that the wall is likely to survive such repeated pulses. There is a flowing liquid coolant in intimate contact with the wall. This coolant also serves as a mass loader to lower the kinetic energy delivered to the structure by the blowoff impulse, and as a stress wave coupler to carry the stress away from the first wall and dissipate it.

There are a number of issues that must be addressed with this concept such as the amount of material blown off and the time it takes to recondense on the wall. This determines the amount that is lost out the penetrations, mainly the beam lines, and the influences the choice of replacement technique. Another issue is the magnitude and duration of the stress waves generated by x-ray blowoff and the degree of attenuation during propagation. The kinetic energy delivered to the first wall/blanket also generate hoop stresses in this structure. Lastly, the compatibility of the coating with the target debris must be considered.

Carbon is an especially attractive coating because of its high sublimation point and low-Z, which limit the amount blown off, and low activity. There are others also worth considering such as tungsten, tantalum, aluminum, beryllium, lead, lithium lead, and Flibe.

In the following sections, we describe a conceptual design using carbon coating, a unique carbon/SiC composite first wall and blanket structure, and flowing liquid Flibe (Li_2BeF_4) coolant. We also examine a metal chamber with liquid lithium lead coolant. Clearly, there are other combinations that may work just as well or better, and these could be explored in the future. One interesting possibility, particularly for near-term reactors, is ferritic steel with Flibe because the low activity requirement is reduced due to activated indirect target debris. Flibe readily wets metals (it doesn't wet carbon), and is chemically compatible with ferritic steel[C-1] up to at least 600°C.

C.3 REFERENCE DESIGN

The conceptual design is sized for 3000 MW of fusion power, delivered with 300 MJ yield targets at 10 Hz. The neutron power is 2000 MW, with the remainder going to wall surface heating. The chamber is sized to be replaced once a year. We believe that the first wall material chosen, discussed below, can withstand an integrated neutron fluence[C-2] of $4 \cdot 10^{22}$ n/cm^2. With an 80% power factor and an estimated fivefold scattering of the incident fusion neutrons, the required first wall radius is 5.5 m for one year life. With this radius, the neutron wall loading is 5.3 MW/m^2 and the surface power is 2.6 MW/m^2. The surface energy dose per pulse is 0.26 MJ/m^2 (6.3 cal/cm^2) (there is considerable data available at these fluences from underground nuclear tests). The resulting reaction chamber size is small enough to be economical, yet not so compact that high heat fluxes would present engineering difficulties.

C.4 DESCRIPTION OF REFERENCE DESIGN

The reference design is depicted in Fig. C.1 (the "onion" refers to the layers of coolant paths). The first wall consists of a renewable carbon coating 20-50 μm thick on a Vapor Carbon Silicon (VCS) composite wall 0.8 cm thick. VCS is the proposed isotropic composite mentioned above. It consists of annealed vapor-grown carbon fibers in a chemically vapor-infiltrated silicon

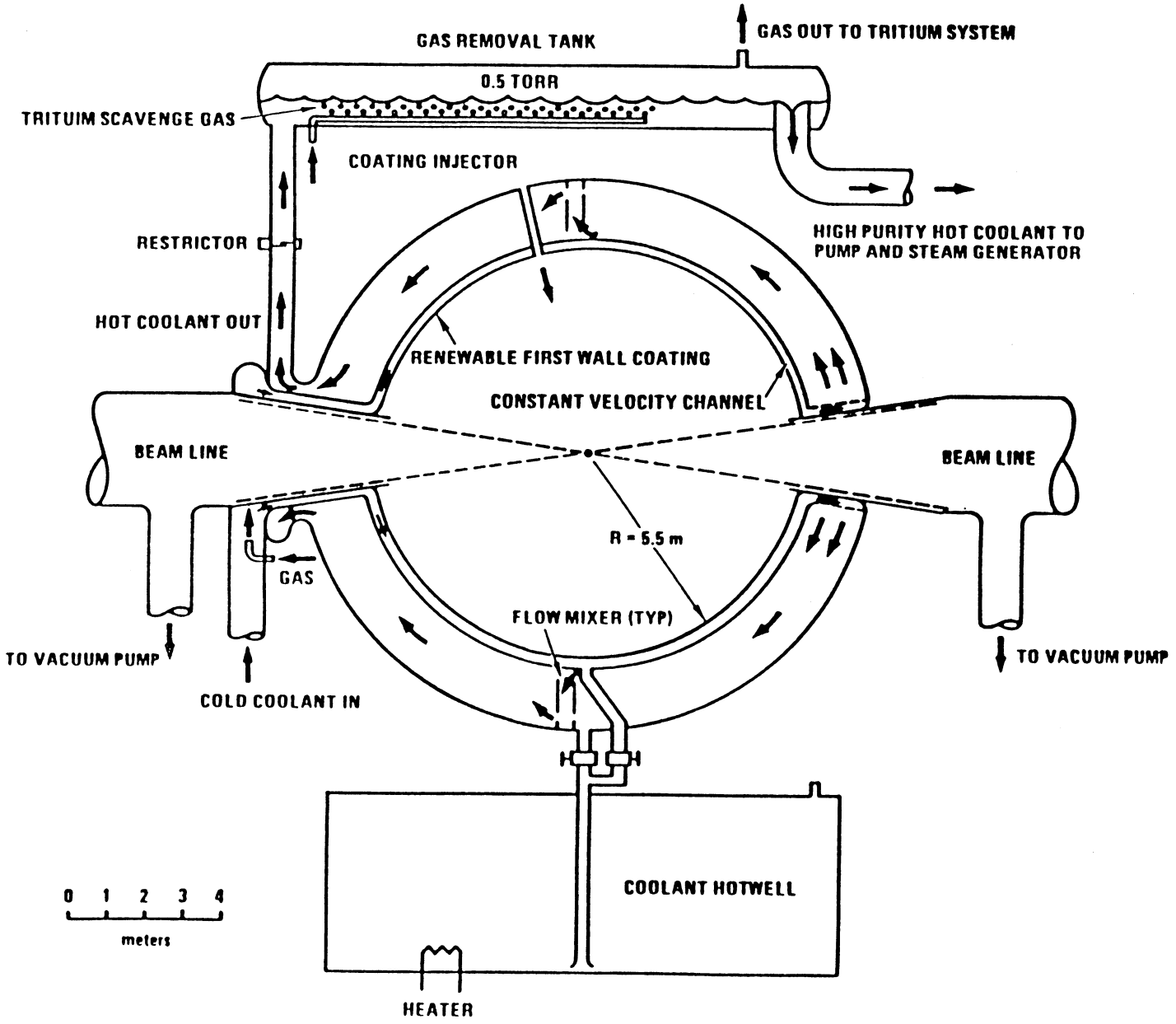

Fig. C.1. The Onion reactor reference design.

carbide matrix. The material has a thermal conductivity approaching copper, very high heat flux and high temperature capability, and neutron damage resistance. It is also resistant to tritium permeation and reducing atmospheres like hydrogen. This material is in the preliminary development stages at General Atomics.

The Flibe coolant removes the first wall heat, absorbs the neutron power, and provides tritium breeding. It makes two passes, one at high velocity along the backside of the first wall and slow return pass to collect the neutron heat. Gas bubbles can be injected in the Flibe in two places: first to dissipate stress waves and second to extract tritium and other gases. Note that the Flibe is reusable and is drained into a hotwell for the annual chamber replacements; only the empty chamber is replaced.

The next sections describe key features of the reference design in more detail.

C.5 RENEWABLE FIRST WALL COATING

We have used the CONRAD hydro code[C-3] to determine the depth of vaporization in the carbon surface layer and the resulting impulse and stress waves. Only about 0.5 μm (370 grams) of carbon are vaporized each shot. All vaporization is due to the soft x-rays, which make up 60 MJ of the fusion yield. The 30 MJ of ions and target debris arrive later and heat the expanding carbon vapor. A small amount of additional carbon is vaporized by radiation from this vapor.

Figure C.2 shows calculated recondensation of the vaporized carbon. Ninety percent of the carbon has recondensed in 3 milliseconds. Fully 99.7% is condensed in 10 msec. However, some 80 msec are needed to get the chamber density down to the level needed for heavy ion beam propagation[C-1] about $4 \cdot 10^{12}$ cm^{-3}. This is compatible with a 10 Hz repetition rate. It is half the interpulse time for the Osiris reference design. A simple pumping calculation shows that only about one percent of the carbon is lost out the beam lines so that only about four grams must be replaced each shot. There are many creative ways to introduce this carbon into the chamber. The one that we prefer at the moment is to mechanically inject carbon soot into the chamber away from the beam axis. This will be vaporized by the fusion energy and condensed on the wall. Subsequent shots will spread out this distribution if it is initially nonuniform.

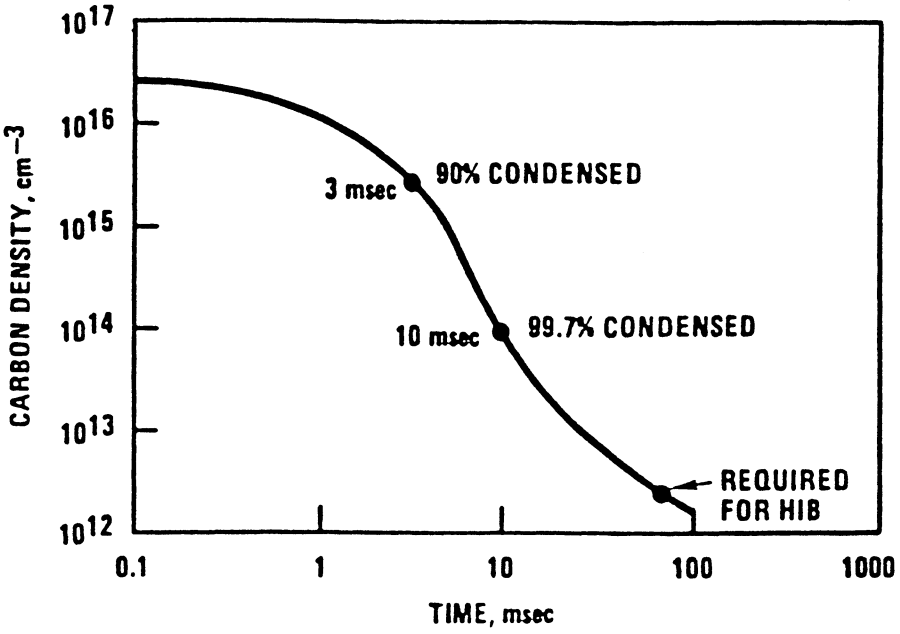

Fig. C.2. Recondensation of vaporized carbon.

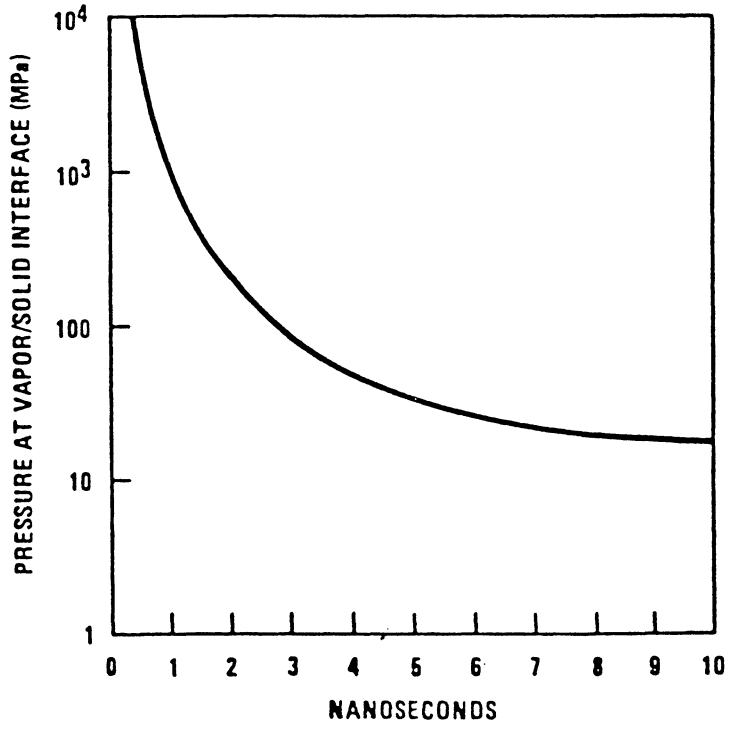

Fig. C.3. Pressure history at vapor/solid interface of carbon layer.

The CONRAD code also calculates the pressure at the vapor/solid interface, and this is shown in Fig. C.3. In one nanosecond, peak stress has fallen to about 1000 MPa; and it is about 200 MPa in 2 nsec. The latter is in the range of the static tensile strength of the carbon layer, and there is data from other materials that indicates the strength under such short-pulse dynamic loading could be as much as 10 times higher. Therefore, the carbon layer may survive because of the brief, nanosecond level duration of the stresses. Figure C.4 shows such data for aluminum.[C-4] Extrapolating back to nanosecond levels suggests a 10-fold increase in tensile strength over static levels.

There are other coating materials that we are also investigating. Aluminum or lead, for example, applied as liquids would not be subject to stress failure. And the higher atomic number would have greater soft x-ray stopping power, resulting in even shallower removal depths and shorter stress duration. Delivered impulse may be higher, however, than carbon. The activation of these materials is also a disadvantage. Lead is interesting because it can be applied from indirect target materials. This was exploited in a previous study[C-5] that could be considered a precursor to the Onion.

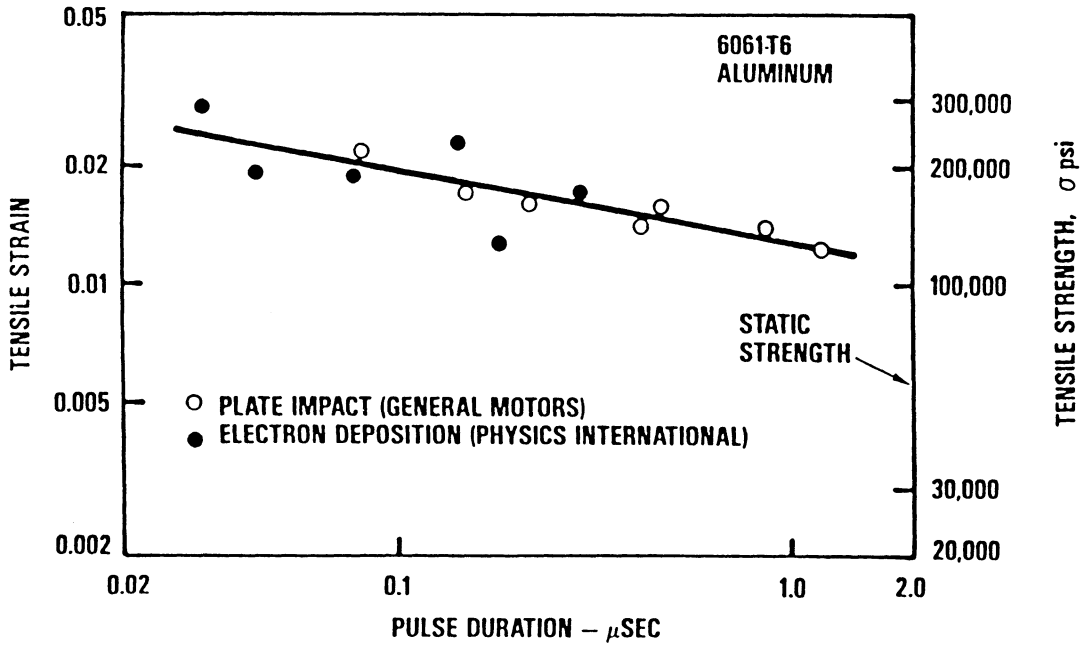

Fig. C.4. Influence of stress duration on tensile strength for aluminum.

C.6 FIRST WALL STRUCTURE

The first wall structure must be capable of high temperature operation, and high heat flux. It must be resistant to neutrons, have minimal tritium absorption, resist reducing atmospheres, and preferably be low activation. We expect the proposed VCS composite to meet these requirements. The composite uses isotropically oriented whiskers of vapor-grown carbon fibers[C-6] 0.5-1.0 mm long and 5-10 μm in diameter in a chemically vapor infiltrated silicon carbide matrix.[C-7] The SiC retards tritium permeation, a significant advantage over carbon-carbon composites. The annealed fibers have an axial thermal conductivity of nearly 2000 W/m-K at room temperature. Ignoring any contribution from the SiC, VCS with 50% carbon fibers randomly oriented should have a conductivity of 330 W/m-K at room temperature. Based on data for other carbons,[C-8] we estimate that VCS irradiated to $4 \cdot 10^{22}$ n/cm^2 would have a conductivity of 83 W/m-K at 1300K operating temperature, well above SiC-SiC composites.

With a low thermal expansion coefficient of about $4 \cdot 10^{-6}$/K, an elastic modulus about that of steel, and an expected tensile strength of 140 MPa, the allowable ΔT across the wall based of thermal stress is 270K. For the design heat flux of 2.6 MW/m^2, the allowable wall thickness is 0.8 cm. This is an acceptable thickness, and the shell should then be able to resist the other loads from the coolant and atmospheric pressure. It would have to reinforced with ribbing, however, to resist buckling. With the use of Flibe coolant, the first wall needs to seal against low pressure liquid leaks, not high pressure gas. Assembly can therefore be with tongue-and-groove panels, perhaps with a silicon sealer.

C.7 FLIBE BLANKET

While Flibe is a poor heat conductor, its low viscosity makes it a tolerable heat *convector*. It works well in this case because of the high temperature capability of the first wall permits high boundary layer ΔT's. The Flibe makes its first pass at a constant 6 m/sec velocity to remove the first wall heating. The Reynolds number is 11,400 and the heat transfer coefficient is an acceptable 12,200 W/m^2-K. The required film temperature rise is 216 K. The maximum VCS temperature is then about 1190 K, well within the capability of the material.

The total residence time of the Flibe in the blanket is about 100 sec during which about 0.5 grams of tritium are bred. The Flibe also dissociates to TF and F_2 during tritium formation, which react with silicon and carbon. To mitigate this, we would add micron-sized silicon and carbon powder to the Flibe to act as scavengers. The resulting SiF_4 and CF_4 are gaseous and could be removed with the tritium gas in the separator tank shown in Fig. C.1.

The flow pressure drops are 0.35 MPa for friction plus 8 kPa for turning. Flibe pumping power for the reactor chamber is then a reasonable 1.5 MW. The maximum Flibe pressure in the chamber is only 0.5 MPa. At \$40/kg[C-9] the estimated cost of the Flibe is a reasonable \$50 million.

C.8 BLOWOFF IMPULSE AND CHAMBER RESPONSE

The vaporization of the carbon gives a blowoff impulse of I = 8 Pa-sec. The resulting kinetic energy E and velocity u of the structure is given by

$$E = \frac{I^2}{2 \rho t}, \qquad u = \frac{I}{\rho t}$$

where ρ and t are the bulk density and thickness of the structure. These equations show why thin, unsupported plates can present problems when there is wall vaporization (At very small t, of course, I drops off because the wall begins moving almost immediately). If the 8 mm VCS wall were not backed by Flibe in intimate contact, it would move away at 0.5 m/s. Because of the Flibe, this is reduced to a negligible 0.005 m/s. The kinetic energy is also reduced, from 2 J/m^2 to 0.02. This energy must be absorbed as hoop strain in the structure. Clearly, this is easier in the latter case.

C.9 COMPATIBILITY WITH INDIRECT TARGET SHELL MATERIALS

While indirect drive targets eliminate the need for uniform illumination, they require high-Z shells around the target to absorb and reradiate x-rays. This material ionizes and is driven to the wall at very high velocity. It interacts with the blowoff vapor, recombines, and condenses and/or reacts chemically with the blowoff.

Many high-Z materials can form carbides with the blowoff carbon. This will complicate recycling because they will plate out on the wall. Carbon may therefore not be the best coating. Ideally, the coating and target material should be the same. Possibilities are tantalum, tungsten, mercury (cryogenic targets), lead, and lithium-lead (especially if this is the blanket material). A molten coating like mercury or lead could be recycled by draining, and is self-healing. However, vapor density limits in the chamber may limit temperatures to unacceptably low levels in some cases.

C.10 ALTERNATE ONION WITH METAL CHAMBER AND LITHIUM-LEAD

We briefly looked at another version of the Onion, shown in Fig. C.5, that has vanadium alloy metal walls and flowing lithium lead coolant. Here the LiPb would serve as the first-wall coating, making the structure very leak-tolerant. The coating would stay liquid and be continuously drained. The blanket inventory could also be used to make the target shells.

Vapor pressure requirements for beam propagation will limit peak coating temperature to ≤600°C. The chamber is therefore larger than the previous case, with R = 6 m, and the wall heat flux is 1.66 MW/m^2. The alloy used is V-15Cr-5Ti, which is a candidate fusion reactor material.[C-9] Thermal stress limits the first wall ΔT to about 170°C, corresponding to a 3 mm wall thickness at this heat flux. This can be built up from welded sections as shown in the figure, with all of the welds hidden from the primary neutrons.

Power conversion issues like pinch point limit the minimum LiPb inlet temperature to above 365°C. The LiPb film drop is 5°C. To keep the coating temperature to 600°C, the bulk LiPb temperature exiting the first wall region is about 425°C. Fusion power energy partitioning them sets the LiPb outlet temperature to 515°C. While this is too low for a conventional steam cycle, it can serve a 400°C multireheat steam cycle, which can deliver 41.5% efficiency. This is not much less than the 45% achieved in conventional steam cycles. This low temperature cycle would have supercritical steam and three reheats. While this requires a lot of steam ducting, costs should not be an issue because the lower temperature permits the use of lower cost materials.

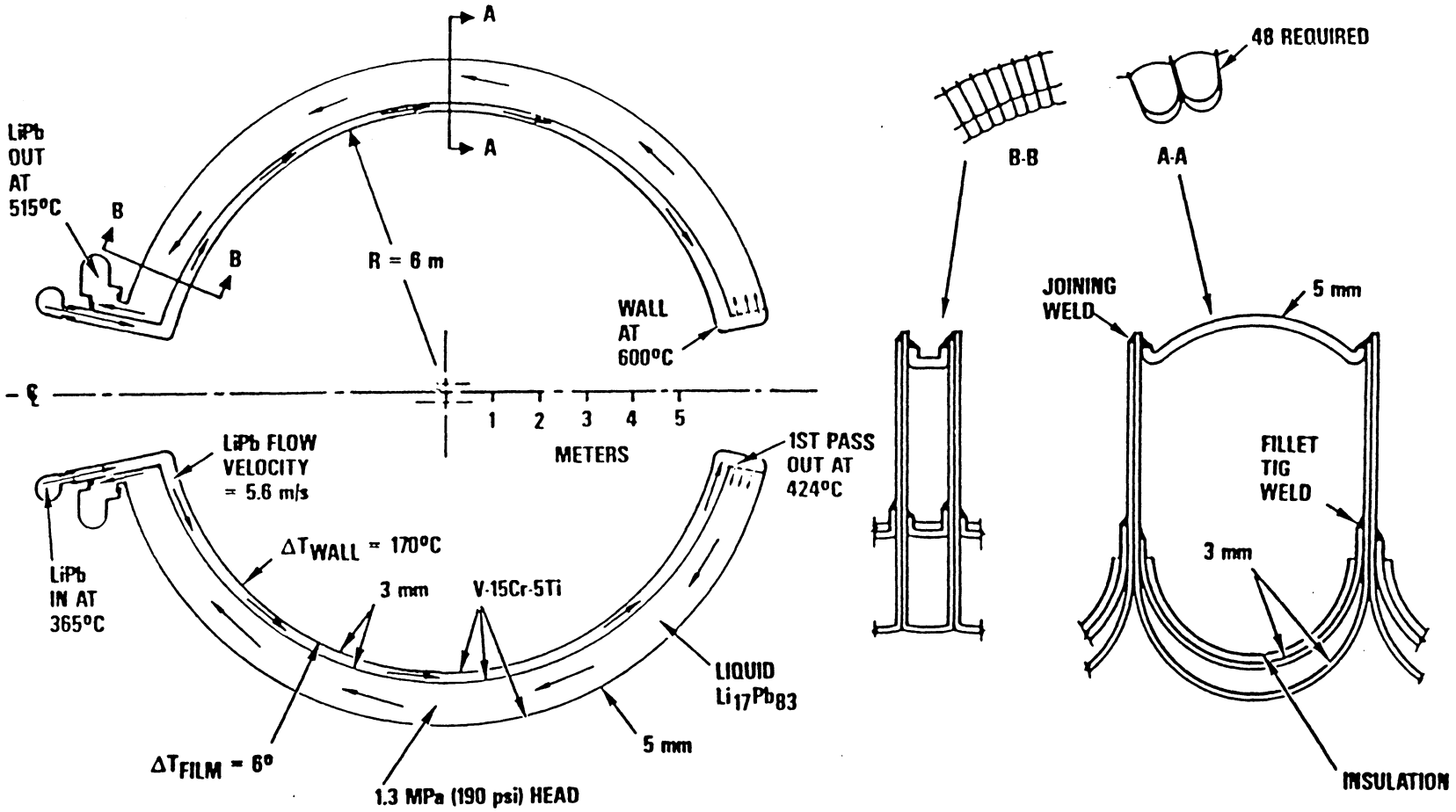

Fig. C.5. Alternative, all-metal version with lithium-lead coolant.

C.11 MODIFICATIONS FOR LASER DRIVER

The Onion reactor concept above is easily modified for laser drivers. Then the first wall vaporization from soft x-rays is eliminated by introducing a 0.5-1.0 torr xenon gas into the chamber, an acceptable level for laser beam propagation.[C.1] Vaporization from harder x-rays that get through the gas is eliminated by retaining the low-Z first wall, which spreads out the energy deposition. The uniformly-distributed beam ports can pass directly through the Flibe blanket. They would be shaped with leading and trailing edges so as to eliminate Flibe stagnation, and vacuum pumping could be done through these ports.

C.12 SUMMARY

The Onion reactor concept with a renewable carbon coating, a carbon fiber/SiC first wall, and a flowing Flibe blanket appears to be a robust, low activation design. Technology development requirements are not unreasonable. Work needs to be done in characterizing stress wave propagation and damage, particularly under repeated pulses. The VCS composite needs to fabricated in large sections and tested. And concepts such as scavenging powders to mitigate Flibe chemistry need to be examined in more detail. Other combinations, such as metal chambers with Flibe or lithium-lead, need further investigation.

C.13 REFERENCES FOR APPENDIX C

C.1 M.J. Monsler, J. Hovingh, D.L. Cook, T.G. Frank, G.A. Moses, "An Overview of Inertial Fusion Reactor Design," *Nucl. Tech./Fusion*, 302-358 (1981).

C.2 G.R. Hopkins, R.J. Price, P.W. Trester, "Radiation Effects on Structural Ceramics in Fusion," presented at the Seventh Topical Mtg. on the Technology of Fusion Energy, Reno, Report GA-A18521, General Atomics, San Diego, CA (1986).

C.3 R.R. Peterson, J.J MacFarlane, G.A. Moses, "CONRAD - A Combined Hydrodynamics-Condensation/Vaporization Computer Code, Report UWFDM-670, Fusion Technology Institute, University of Wisconsin (1986).

C.4 L.D. Webster, "X-Ray Shock Effects on Containment Wall Candidates for the LMF Facility," Kaman Sciences Corporation, presented at Lawrence Livermore National Laboratory, Livermore, CA (1988).

C.5 E.W. Sucov, ed., "Inertial Confinement Fusion Central Station Electric Power Generating Plant Final Report for the Period March 1, 1979 - September 30, 1980," Report WFPS-TME-81-001, Westinghouse Electric Corporation, PA (1981).

C.6 G.G. Tibbets et al., "Carbon Fibers Grown from the Vapor Phase: a Novel Material, SAMPE J. (September/October 1986).

C.7 T.D. Gulden et al., "Forced-Flow Thermal-Gradient Chemical Vapor Infiltration (CVI) of Ceramic Matrix Composites," *Proc. 11th Int. Conf. on Chemical Vapor Infiltration*, Seattle (1990).

C.8 G.R. Hopkins, R.J. Price, R.E. Bullock, J.A. Dalessandro, J. Hovingh, "An Assessment of Carbon and Silicon Carbide as First Wall Materials in Inertial Confinement Fusion Reactors," presented at 3rd ANS Topical Mtg. on Tech. of Controlled Nucl. Fusion, Santa Fe (1978).

C.9 D.L. Smith et al., "Blanket Comparison and Selection Study - Final Report," Rep. ANL/FPP-84-1, Argonne National Laboratory, IL (1984).

Appendix D

Life Reactor Concept

CONTENTS

D.1 INTRODUCTION D-1
D.2 DESCRIPTION OF THE CONCEPT D-1
D.3 STORED ENERGY AND PRESSURE D-3
D.4 FIRST SURFACE BLOWOFF AND CONDENSATION D-4
D.5 VAPOR CONDENSATION D-6
D.6 ROTATING SEAL D-7
D.7 ROUGH COSTING D-7
D.8 SUMMARY D-9
D.9 REFERENCES FOR APPENDIX D D-10

APPENDIX D. THE LIFE IFE REACTOR CONCEPT

D.1 INTRODUCTION

The Cascade IFE reactor concept has received considerable attention because of the potential for very low activation, elimination of replaceable first walls, low cost and high efficiency.[D-1] In Cascade, solid granules flow in a rotating chamber which keeps the granules against the wall and the central region clear for target and beam injection. But using solid granules presents a number of problems: First, the granules will erode due to x-rays motion against each other and against fixed walls. Sudden X-ray deposition also gives rise to stress waves that can fracture the surface layer of granules. Lastly, the impulse from X-ray induced blowoff can cause the surface layer of granules to rebound into the chamber. If those granules are still in flight at the time of the next shot, they will be driven into the rest of the granule bed at very high velocity. There are also issues of granule fabrication, transport through the system, and heat transfer to the working fluid by radiation.

Many of these issues are eliminated by replacing the solid granules with a lithium-bearing flowing liquid. The liquid is self-healing, is easily transported through ducts and heat exchangers, and requires no fabrication facilities. It does, however, introduce a problem of vapor pressure in the chamber. This is a critical issue because the geometry of rotating chambers is suitable only for one or two-sided illumination, limiting drivers to heavy ion beams that require very low chamber pressures for propagation.

The idea of a liquid lithium rotating chamber has been examined before,[D-2] but appears to have been abandoned. As part of this study, we explored rotating chamber concepts using $Li_{17}Pb_{83}$ and Flibe (Li_2BeF_4). The former is especially attractive when it is also used as the target high-Z material. The latter has lower induced activity, but is a poor heat transfer material unless it is highly convective. The concept is called the LIFE reactor (Liner Inertial Fusion Energy).

D.2 DESCRIPTION OF THE CONCEPT

Figure D.1 shows the basic configuration for a lithium-lead blanket. The chamber rotates at 36 rpm, sufficient to provide about 1.5-g at the minimum radius. LiPb enters from fixed

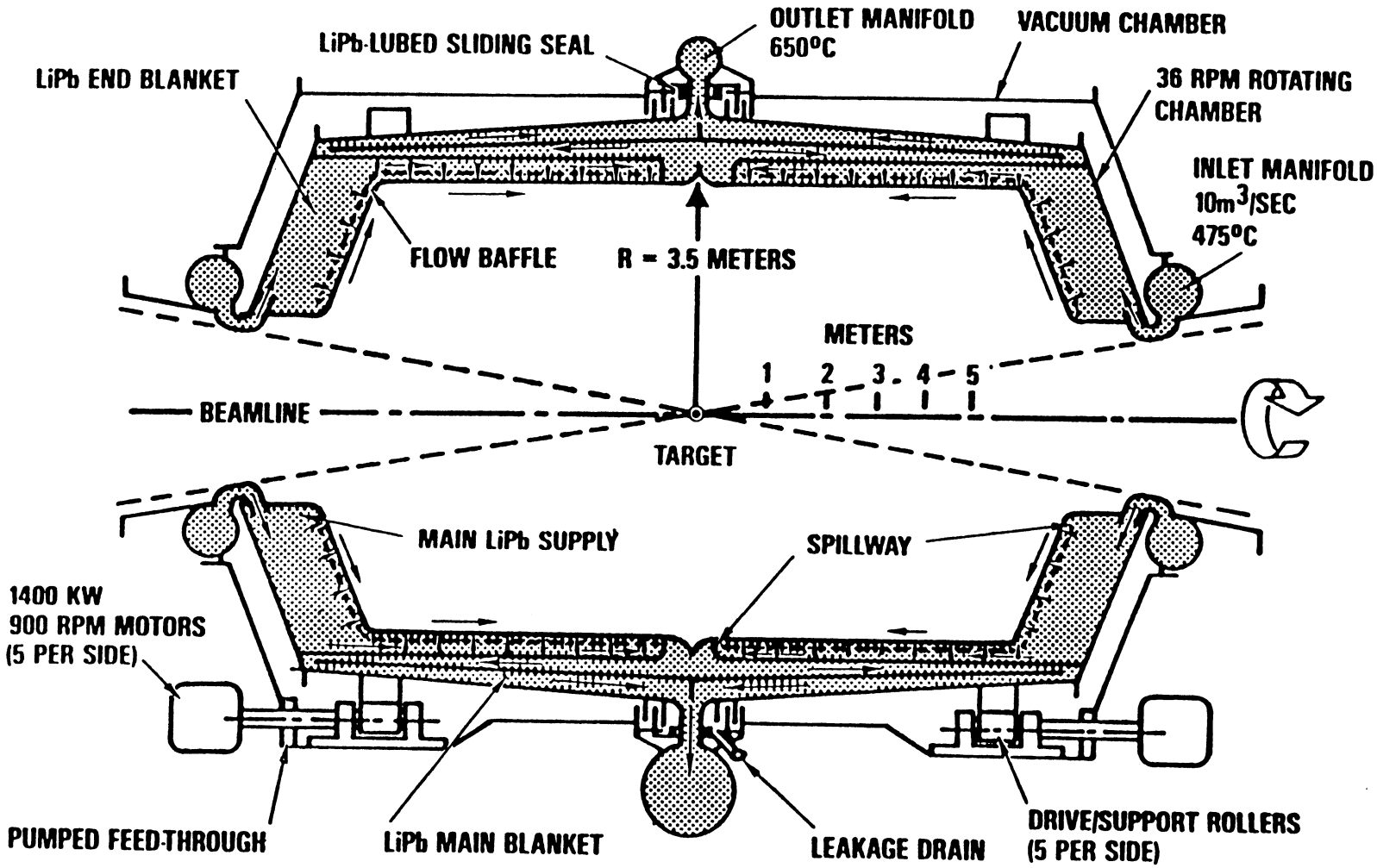

Fig. D.1. Cross section of the LIFE Reactor concept showing rotating blanket, turbulence-generating baffles, exit seal, and vacuum chamber.

manifolds at the ends into open weirs. A portion spills over the edge, protecting the end surfaces, while the rest makes up the end blanket and flows radially outward. Flow baffles allow liquid to jet to the surface, which generates the turbulence needed to prevent overheating (discussed below). All of the flow moves over the surface, picking up the X-ray and debris power, and is then directed radially outward by other baffles where it picks up the neutron heating and exits at the peak temperature. A low-pressure seal couples the rotating exit flange to a fixed outlet manifold. The rotating chamber is surrounded by a fixed chamber pumped down to moderate vacuum. The liquid flowing from the inlet manifold to the free surface of the end blankets seals the reactor chamber from the vacuum chamber. Ten 1400 kW (for LiPb) drive motors rotate the chamber. The chamber radius and aperture openings are scaled so that all of the liquid blanket will remain in the chamber if rotation were stopped.

D.3 STORED ENERGY AND PRESSURE

With a density of 9400 kg/m^3, lithium-lead can generate considerable pressure and stored energy in a rotating system. The pressure at a radius R_2 is easily derived and is given by

$$p_2 = \frac{\rho\omega^2}{3R_2}(R_2^3 - R_1^3) \tag{1}$$

where R_1 and R_2 are the inner and outer radii, respectively, of the liquid layer, ρ is the liquid density, and ω is the angular velocity in radians/s. In the reference design, for example, R_1 = 1.3 m and R_2 = 4.1 m in the ends. With ω = 3.4 rad/s, p_2 = 0.58 MPa (83 psi), which is high but tolerable. Most of this pressure is used up driving the liquid through the flow baffle restrictions. In the center section, R_1 = 3.5 m and R_2 = 4.5 m at the outlet manifold, giving p_2 = 0.4 MPa (55 psi). This pressure can be used to drive the LiPb through the heat exchangers and return ducting; no other pump is needed. The stored energy in the rotating system, which could be a safety concern, is given by

$$KE = \frac{\pi}{4}\rho L\omega^2(R_2^4 - R_1^4) \tag{2}$$

where L is the axial length of the section with radii R_1 to R_2. With 3.4 rad/s, the stored energy is about 270 MJ. This could throw the LiPb up to a height of 9 meters. The dynamic pressure

after thermalization associated with this energy are 0.8 MPa (115 psi) and 0.5°C. These values seem containable over local areas in expected reactor buildings. With Flibe, the stored energy, dynamic pressure, and temperature rise are reduced to 1/5 or less of the LiPb values: 57 MJ of rotational stored energy, 0.17 MPa (24 psi) dynamic pressure, and 0.04°C temperature rise. It is concluded that neither pressures from rotation nor stored energies are critical faults of the concept.

D.4 FIRST SURFACE BLOWOFF AND CONDENSATION

The maximum temperature at which the surface can operate is determined by the driver vacuum requirements. This depends on the vapor pressure of the liquid. Preliminary results from the ICF reactor study indicate that Flibe can operate at a surface temperature of 600°C; lithium-lead is limited to about 500°C.

Although the target explosion imparts a sharp energy pulse to the front surface, blowoff and recondensation convert this to a quasi-steady power flow. With 1000 MW of surface energy (3000 MW total thermal power), at R = 3.5 m the power flux is 6.5 MW/m^2. With 400 MJ yield and 2400 MW fusion power, the interpulse time is 0.167 s. If the surface of the liquid were quiescent, LiPb temperature would rise a prohibitive 630°C in this interval. Turbulent mixing is required, and this can be accomplished with liquid jets created by baffles. This is shown in Figs. D.1 and D.2.

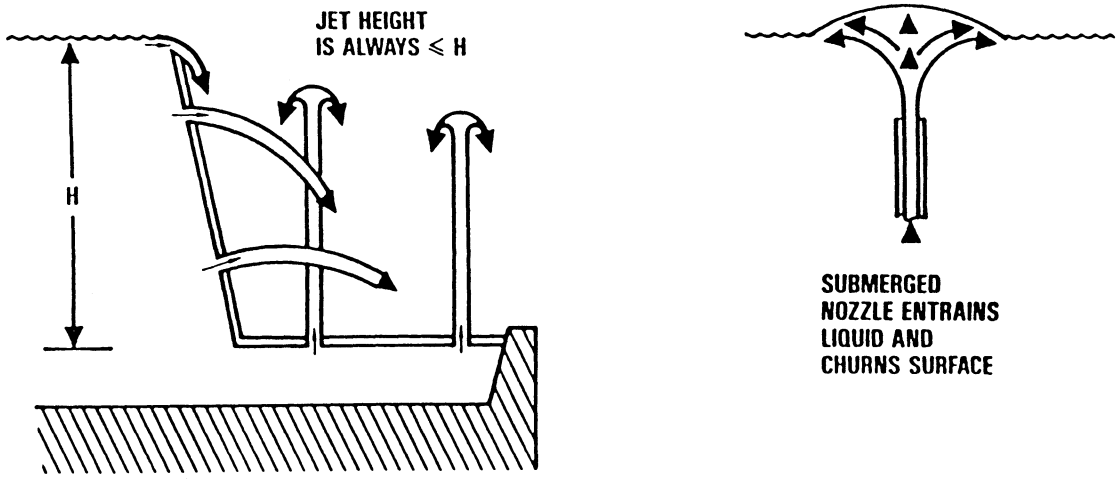

Fig. D.2. Conceptual depiction of turbulence mechanism.

Even though LiPb has a reasonable thermal conductivity, 15.1 W/m-K, turbulence is still needed at the heat fluxes encountered. With Flibe, K = 1.0 W/m-K, and conduction is negligible. However, because its viscosity is fairly low, it can handle these heat fluxes if turbulent. The Nusselt number, Nu, is a measure of the ratio of heat transfer with convection vs. that by conduction alone. To get rough estimates of surface temperature, the conduction equation can be used[D-3] with NuK replacing K:

$$\Delta T_s = 2q_s\sqrt{\frac{\tau}{\pi\rho C_p NuK}} \tag{3}$$

where ΔT_s is the temperature rise in time τ of an element of fluid on the surface when subjected to a steady heat flux q_s. For liquid metals, the Nusselt number is given by[D-4]

$$Nu = 5.6 + 0.165Re^{0.85}Pr^{0.86} \tag{4}$$

where Pr and Re are the Prandtl and Reynolds numbers, respectively. Eq. (4) is valid for liquids metals, which have very low Pr values. Flibe, on the other hand, has a Pr value of 19. Here another expression for Nu is appropriate[D-5]

$$Nu = 0.036Pr^{0.33}Re^{0.8} \tag{5}$$

In order to prevent surface overheating, Nusselt numbers must approach 300 for LiPb and 1000 for Flibe. These can reasonably be achieved in both cases with jet velocities in the 5 m/s range and jet characteristic dimensions of a few cm. Such velocities can be produced by the existing hydrostatic heads. The small, closely-spaced holes can be had with perforated plates of the type shown in Fig. D.1.

While Nusselt analysis can give a fair estimate of surface turbulence, a more detailed approach is to perform an analysis of entrained jets. A jet submerged a distance x below the surface will entrain liquid[D-6] and spread to a radial distance $b = 0.255x$. The jet diameter at x from a nozzle with diameter D is then $2b + D$. The velocity in the center of the jet falls off only linearly with distance:[7]

$$\frac{u}{u_o} = \frac{D}{x} \tag{6}$$

where $u(x)$ is the axial velocity, and u_o is that at the nozzle exit. The turbulent mixing length is $\lambda = 0.068b = 0.017x$. We can define a mixing time τ_m as the time an element of the jet is exposed to the surface heat flux:

$$\tau_m = \frac{\lambda}{u} = \frac{0.017x^2}{u_o D} \tag{7}$$

This time can be used in Eq. (3) to estimate surface temperature rise. Using the jet equations above, one can get a self-consistent design for the flow baffles. This is shown for Flibe in Table D.1.

The table shows a design having jets flowing radially inward toward the surface. There are a number of other possibilities, of course. For example, louvers directing the jets to flow near-tangentially could increase turbulence even more.

Table D.1. Flow Baffle Design for Flibe

Allowable ΔT	75°C
Surface Heat Flux	6.5 MW/m^2
Flibe Volume Flow	4.2 m^3/s
Initial Jet Velocity	8 m/s
Baffle Nozzle Hole Diameter	1.0 mm
Hole C-C Spacing	17.6 mm
Hole Depth Below Surface	23 mm
Number of Holes	710,000
Surface Fluid Mixing Time	0.5 ms

D.5 VAPOR CONDENSATION

As shown above, the cool, turbulent liquid surface can condense hot vapor directed to it up to a heat flux of several MW/m^2. The question remains about the pumping rate of the vapor on to the liquid surface. The analysis below for Flibe, the worst case, shows that pumping is rapid and not a constraint to condensation.

The pumping speed of the vapor is given by[D-8]

$$S = \frac{62.5\ A}{\sqrt{M}}\sqrt{\frac{T}{298}}\quad l/s \tag{8}$$

where A is the liquid surface area in cm^2, $M = 14$ is the average molecular weight for dissociated Flibe, and T is the gas temperature in K, estimated to be 10,000 K. For a volume to be pumped, V, the pumpdown time over a pressure ratio p_1/p_2 is

$$\tau = 2.3\frac{V}{S}\log\frac{p_1}{p_2} \tag{9}$$

Density can be substituted for pressure in Eq. (9) by noting that the remaining vapor expands adiabatically and therefore $p \sim n^{\gamma}$, where $\gamma = 1.67$ for a monatomic gas. With a cylindrical chamber of 3.5 m radius and a length of 10 m, pumping from of 10^{23} m^{-3}, which exists just after a shot, to 10^{18} m^{-3}, needed for beam penetration for the next shot, requires 24 ms, a small fraction of the interpulse time. We conclude that blowoff vapor can be condensed in the time available.

D.6 ROTATING SEAL

A sliding seal is required between the rotating reactor chamber and the outlet manifold (no seal is needed at the inlet manifold because the inlet flow is onto a free surface). Figure D.3 shows the seal concept. The sliding seal is large, about 9 m in diameter, but can be segmented, and some leakage is allowed. The segmented seal slides against the outlet flange and is lubricated by the lithium-lead or Flibe. Metal O-rings, which can roll, seal the housing and allows the segmented seal to wear. Labyrinth seals contain any leakage so that it can be collected at the bottom of the reactor chamber and pumped back into the main f ow.

D.7 ROUGH COSTING

This concept is at a very early stage of development. Nevertheless, some rough costing is in order as part of the evaluation. The rotating chamber and flow baffle material is V-15Cr-5Ti, which is very expensive ($350/kg), but is compatible with hot LiPb. Less critical structures

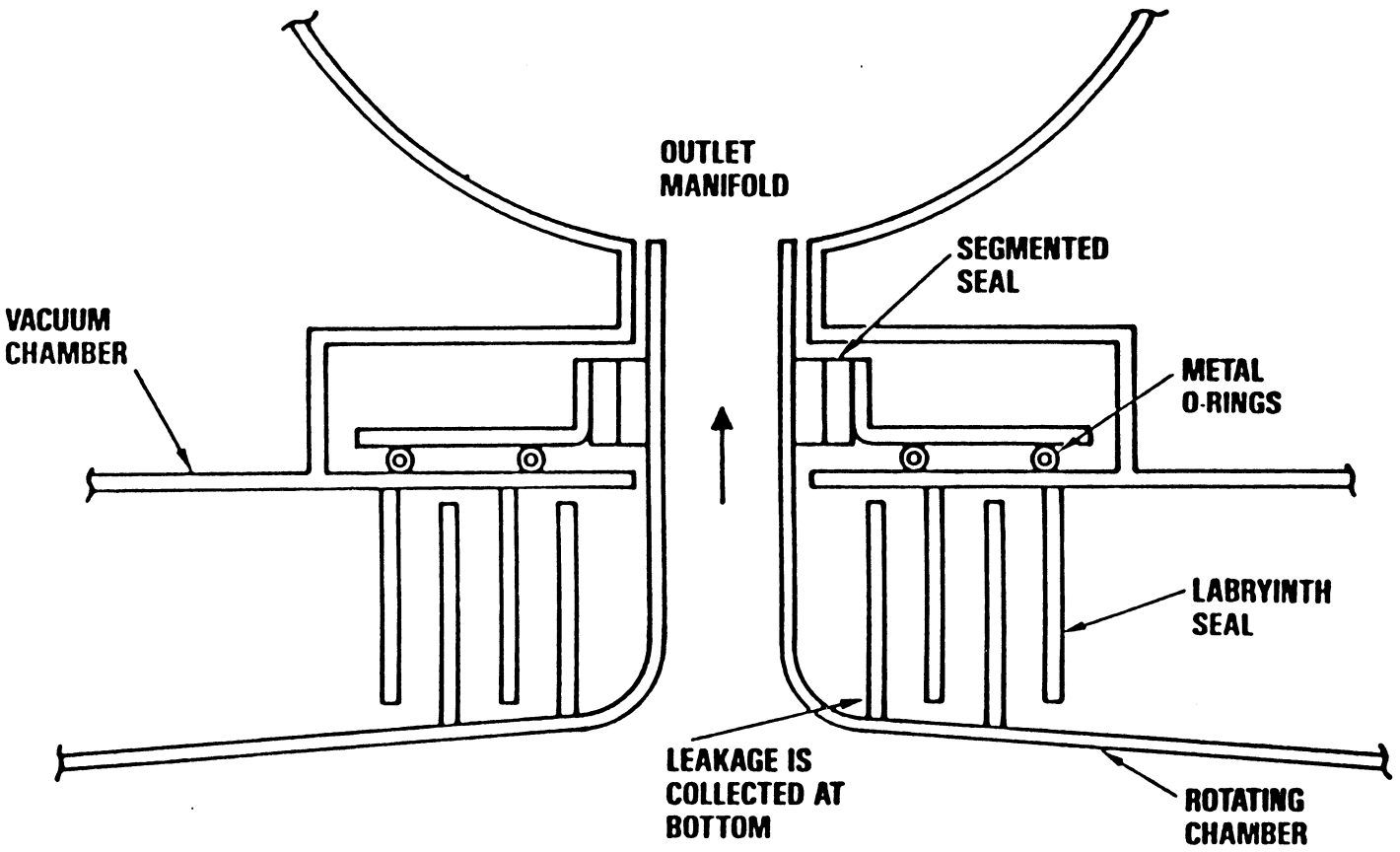

Fig. D.3. Sliding seal concept.

are of stainless steel ($50/kg). The outer shield is an aluminum water tank. The blanket coolant mass is increased 30% to account for that in manifolds and heat exchangers. A hotwell is provided below the reactor to store the molten coolant during service periods. Direct installed costs for the primary components are shown in Table D.2. Although these costs are very inexact, it is seen that large errors could occur and costs would still remain moderate.

Table D.2. Cost Estimate ($ Millions)

	LiPb	Flibe
Rotating Chamber	16	10
Blanket Coolant	17	66
Vacuum Chamber	3	3
End Plates/Manifolds	10	10
IHX	18	24
Water Shield	5	5
Drive Motors	2	1
Hotwell	3	2
Total	74	121

D.8 SUMMARY

This work has shown that a rotating reactor chamber with a liquid blanket can be designed with sufficient turbulence in the free surface to remove the heat generated by target explosions. Because it is viscosity rather than thermal conductivity that limits heat removal, both lithium-lead and Flibe can be used. Although LiPb has a fairly high rotational stored energy, it translates into a moderate dynamic pressure and thermalized temperature rise. The stored energy in Flibe is actually quite low and poses no problem. A rough cost estimate shows that the primary reactor components are not very expensive.

The LIFE reactor concept appears to be an improvement over the Cascade concept in that granule refurbishing is eliminated, the blanket is self-healing, and heat transfer to the power conversion system is by convection rather than radiation. One disadvantage is the lower

operating temperature compared to the ceramic granules in Cascade. However, one can still expect power conversion efficiencies in the 45% range.

The LIFE reactor is but one of several concepts that have been explored in the this study. It was decided not to pursue it further mainly because of concern with large rotating machinery and the large amount of stored energy with lithium-lead. Rotating machines of this scale exist today; therefore this concern is somewhat unfounded. The rotational stored energy issue has been shown above to be a minor one, especially with Flibe. Therefore, this concept can still serve as an important fallback position.

D.9 REFERENCES FOR APPENDIX D

D.1 J.H. Pitts, R.F. Bourque, W.J. Hogan, W.R. Meier, and M.T. Tobin, "The Cascade Inertial Confinement Fusion Reactor Concept," Lawrence Livermore National Laboratory UCRL-LR-104546 (December 23, 1990).

D.2 R. Burke, "Argonne National Laboratory Design Activities," ANL-79-41, *Proc. of the Heavy Ion Fusion Workshop*, Argonne National Laboratory, Argonne, IL, 5-16 (Sept. 19-26, 1978).

D.3 H.S. Carslaw and J.C. Jaeger, *Conduction of Heat in Solids*, 2nd ed., Oxford, Clarendon (1959).

D.4 M.M. El-Wakil, *Nuclear Power Engineering*, McGraw-Hill (1962).

D.5 F. Kreith, *Principles of Heat Transfer*, 2nd ed., International Textbook (1966).

D.6 S.S. Pai, *Fluid Dynamics of Jets*, D. Van Nostrand, NY (1954).

D.7 C.C. Lin, ed., *Turbulent Flow and Heat Transfer*, Princeton University Press (1959).

D.8 A.E. Barrington, *High Vacuum Engineering*, Prentice-Hall, NJ (1963).

Appendix E

Remote Maintenance Equipment Configuration Concepts

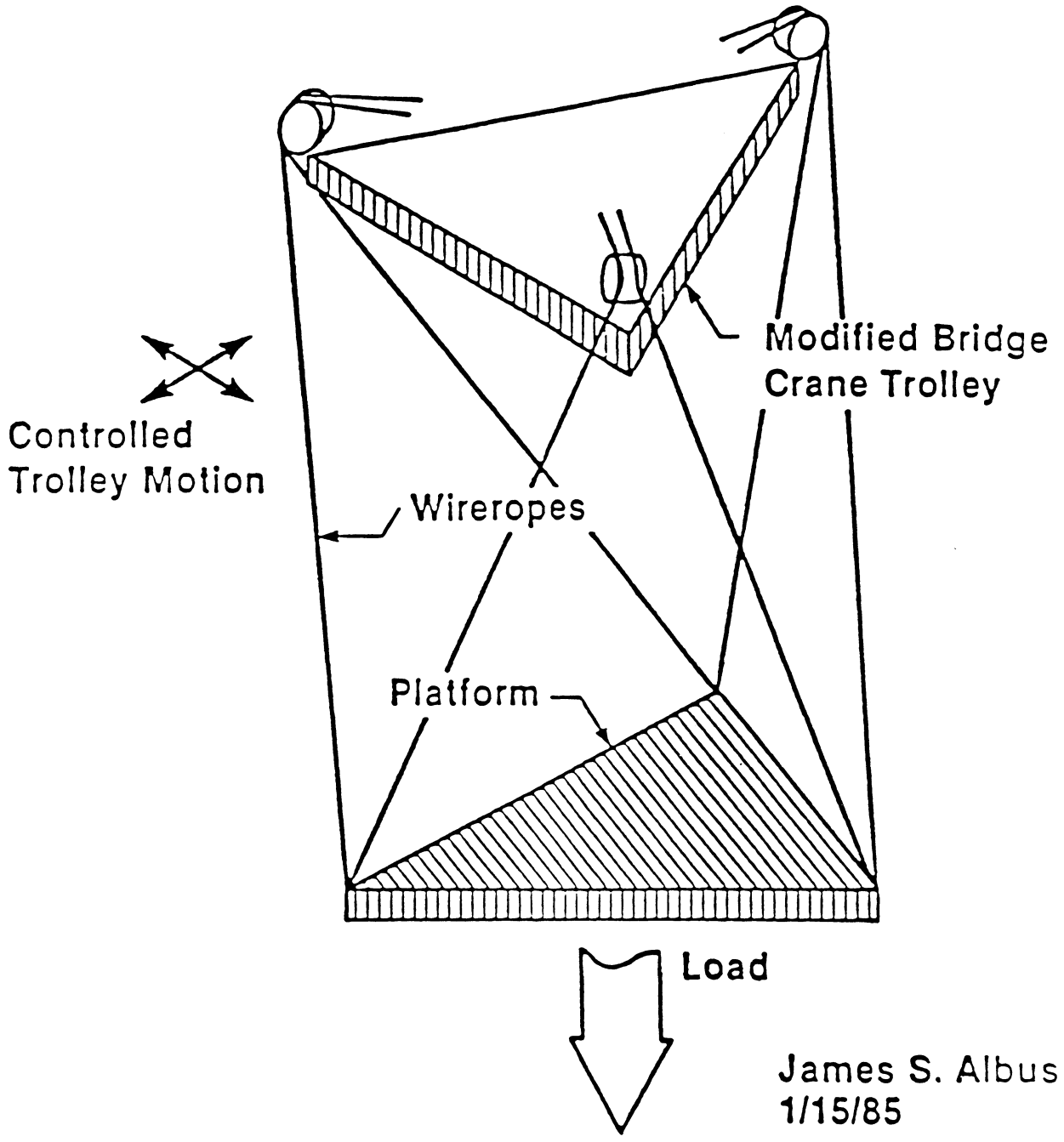

Fig. E.1. Mechanism concept.

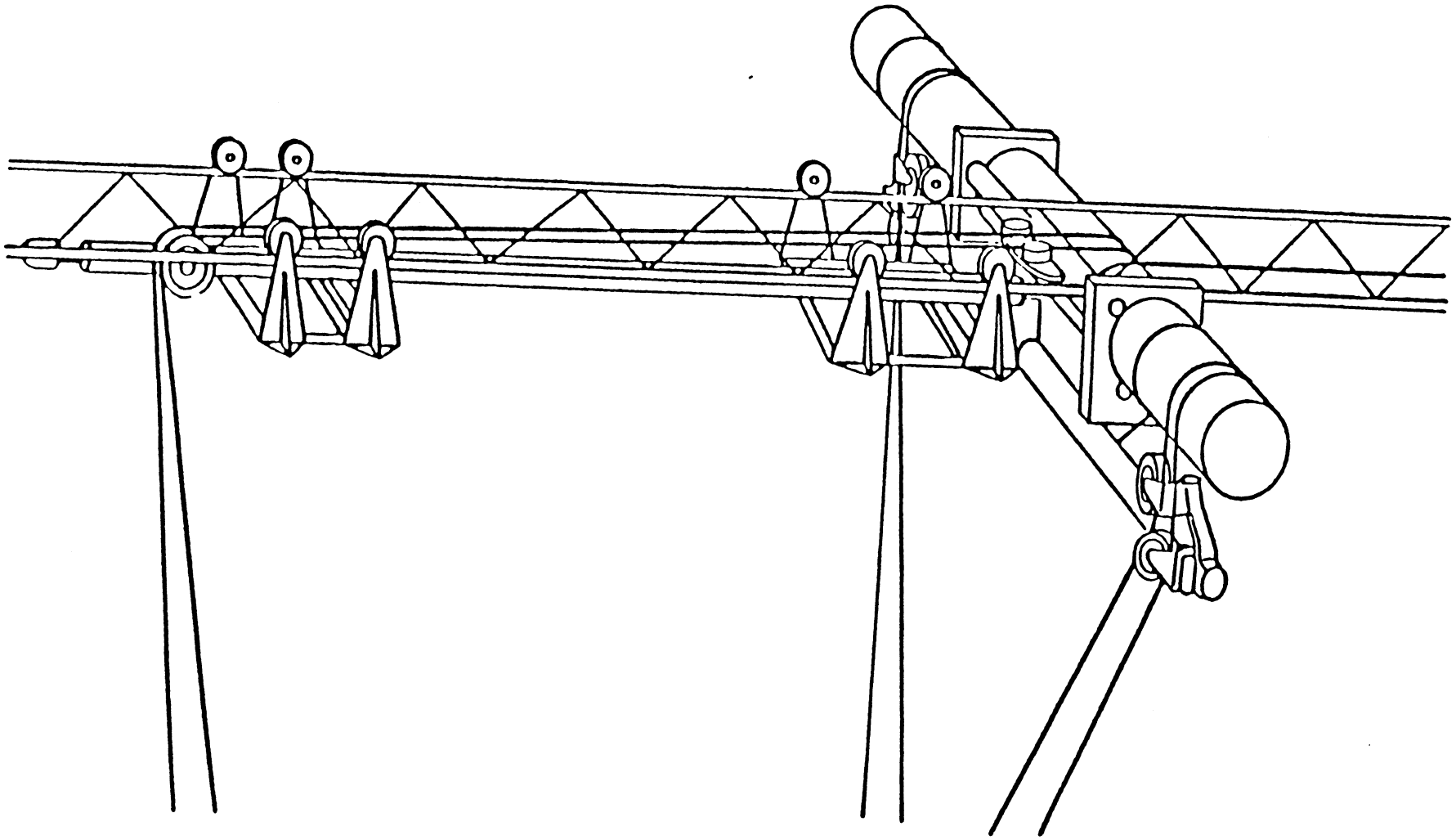

Fig. E.2. Cable suspension carriage with winch.

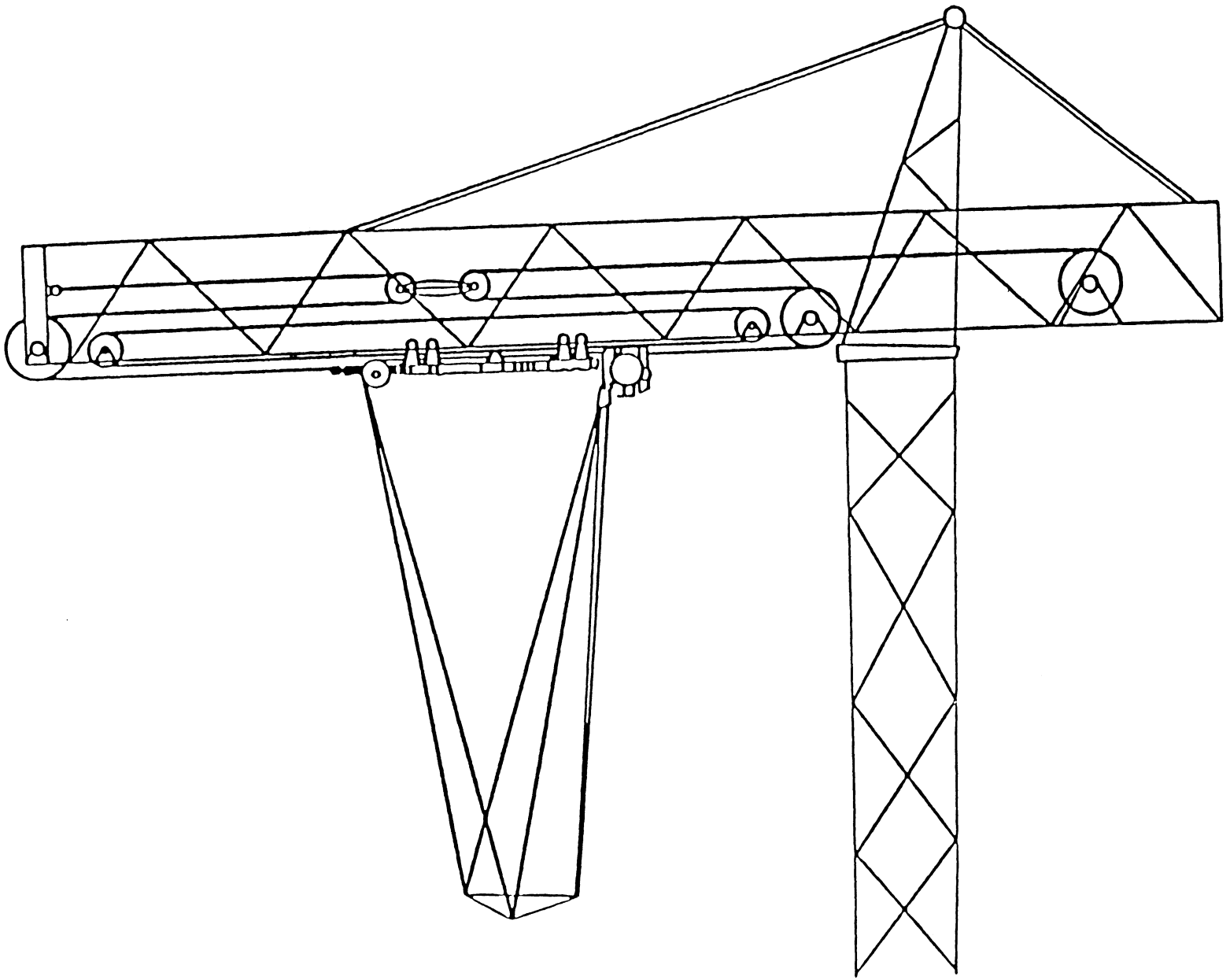

Fig. E.3. Overhead robot crane.

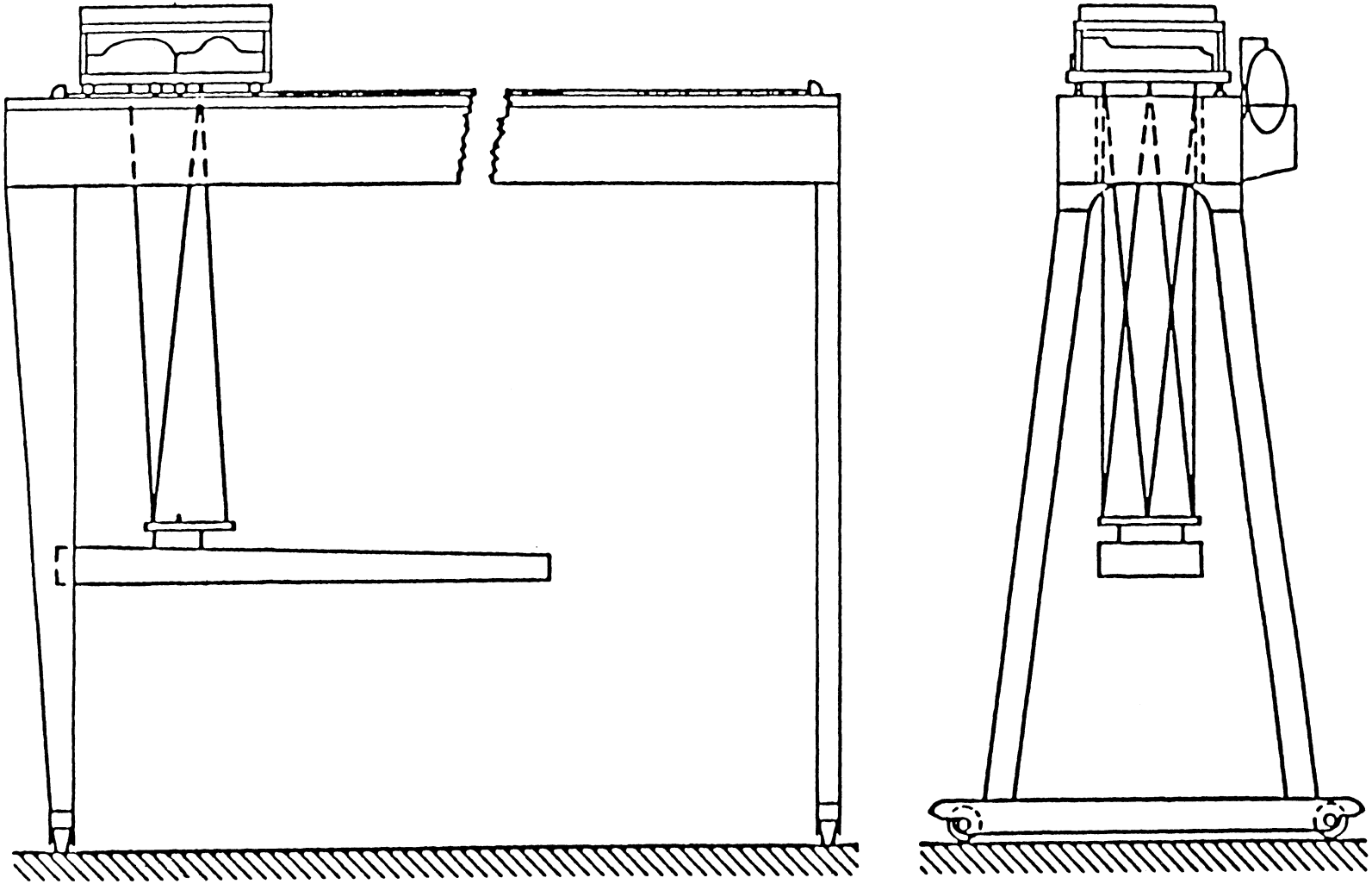

Fig. E.4. Gantry bridge robot crane with extended reach.

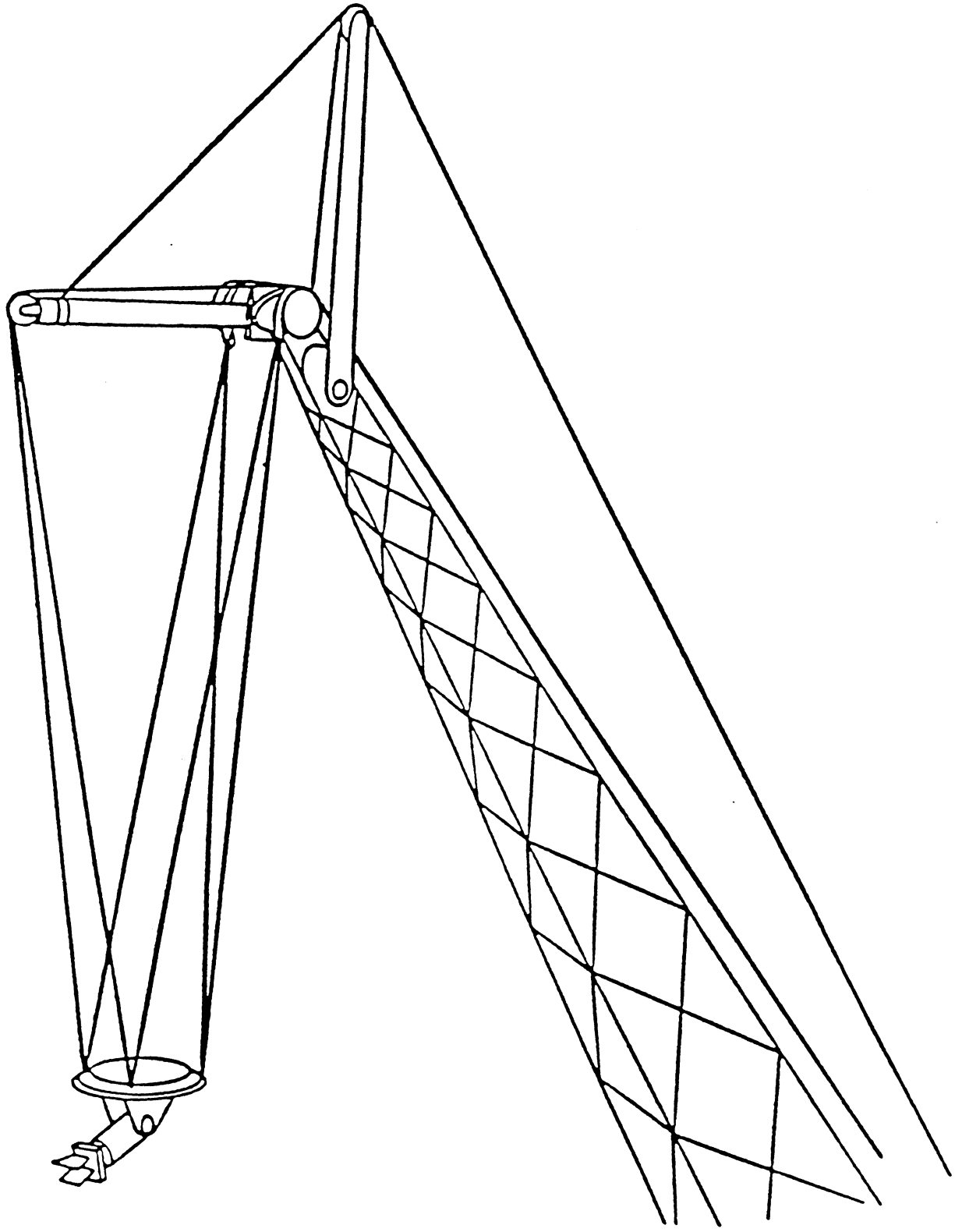

Fig. E.5. Boom robot crane.

Kraft
TeleRobotics, Inc.

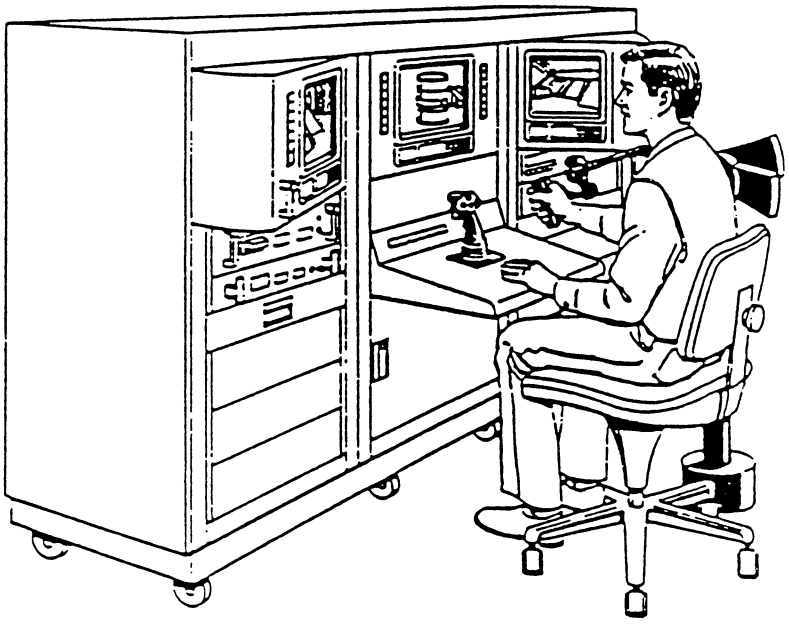

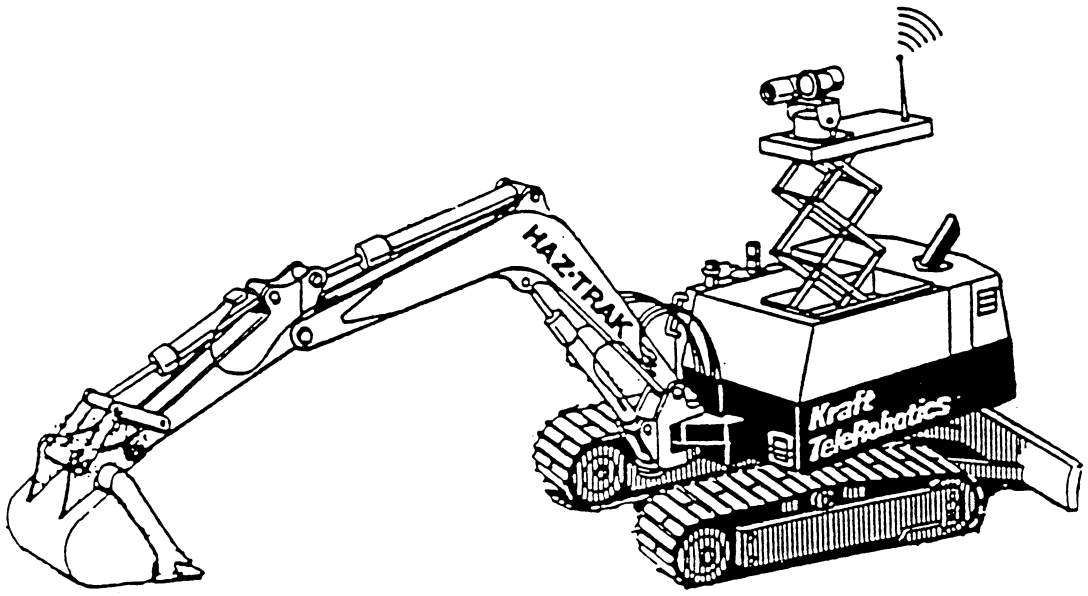

Major components of the HAZ-TRAK system.

Fig. E.6. HAZ-TRAK Vehicle System.

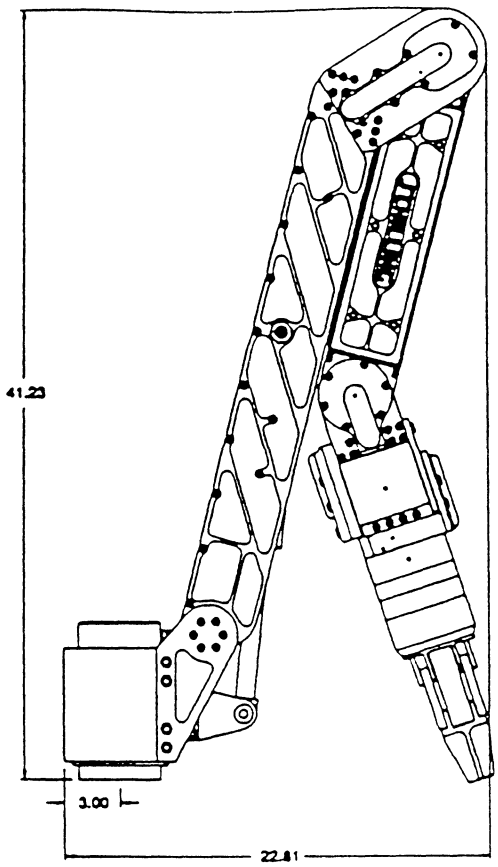

Vertical

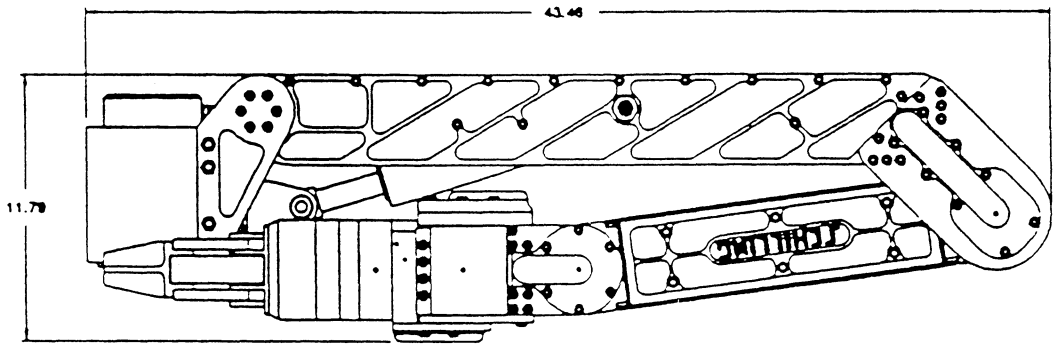

Horizontal

Fig. E.7. Titan-II stow envelops.

Appendix F

Additional Comparisons of Osiris and SOMBRERO

CONTENTS

F.1 PHYSICS COMPARISON F-1
F.2 DRIVER TECHNOLOGY COMPARISON F-4
F.3 REACTOR CHAMBER COMPARISON F-8
F.4 BREEDING MATERIAL COMPARISON F-11
F.5 TARGET AND TARGET DELIVERY COMPARISON F-13
F.6 POWER CONVERSION CYCLE COMPARISON F-15
F.7 SUMMARY OF THE COMPARISON SURVEY F-17

APPENDIX F
ADDITIONAL COMPARISONS OF OSIRIS AND SOMBRERO

In addition to the comparisons presented in Chapter 9, a qualitative comparison of various aspects of the two designs was made by surveying the scientists and engineers involved in the study. Forms requesting qualitative assessment covered the following categories:

- Physics
- Driver technology
- Reaction chamber
- Breeding material
- Targets and target delivery
- Power conversion

Team members were asked to assign each component within a category a measure of confidence level as seen at the present time. The confidence level is an assessment of the current level of understanding and ability to analyze a problem in sufficient detail and/or the ability to design and build a subsystem that would work as envisioned. The measures for confidence level were high, moderately high, moderately low, and low. Although it is generally true that a low confidence level today will correspond to high development needs (i.e., the time and resources required to achieve the required performance or full development the required technology), this is not always true. There are many instances where issues leading to a low confidence level could be addressed in experiments or development programs of modest cost and duration. (Development needs are discussed in Chapter 7.) The following comparisons are based on the responses of the scientists and engineers directly involved in the study. No attempt was made to normalized the relative pessimism and optimism of the respondents.

F.1 PHYSICS COMPARISON

The physics category has been divided into five general areas: the driver, beam propagation, beam/target coupling and x-ray conversion, target gain, fireball calculations and vaporization, and condensation. Figure F.1 summarizes the overall physics comparison.

F.1.1 Driver

The KrF laser design builds on the physics from Nike and Aurora. The Aurora KrF laser has delivered 10 kJ on target while the needed energy in SOMBRERO is 3.4 MJ. The confidence level in the physics is moderately high. Although high current, large induction linacs have not yet been built, the principle of multiple beam transport has been demonstrated in Livermore Berkeley

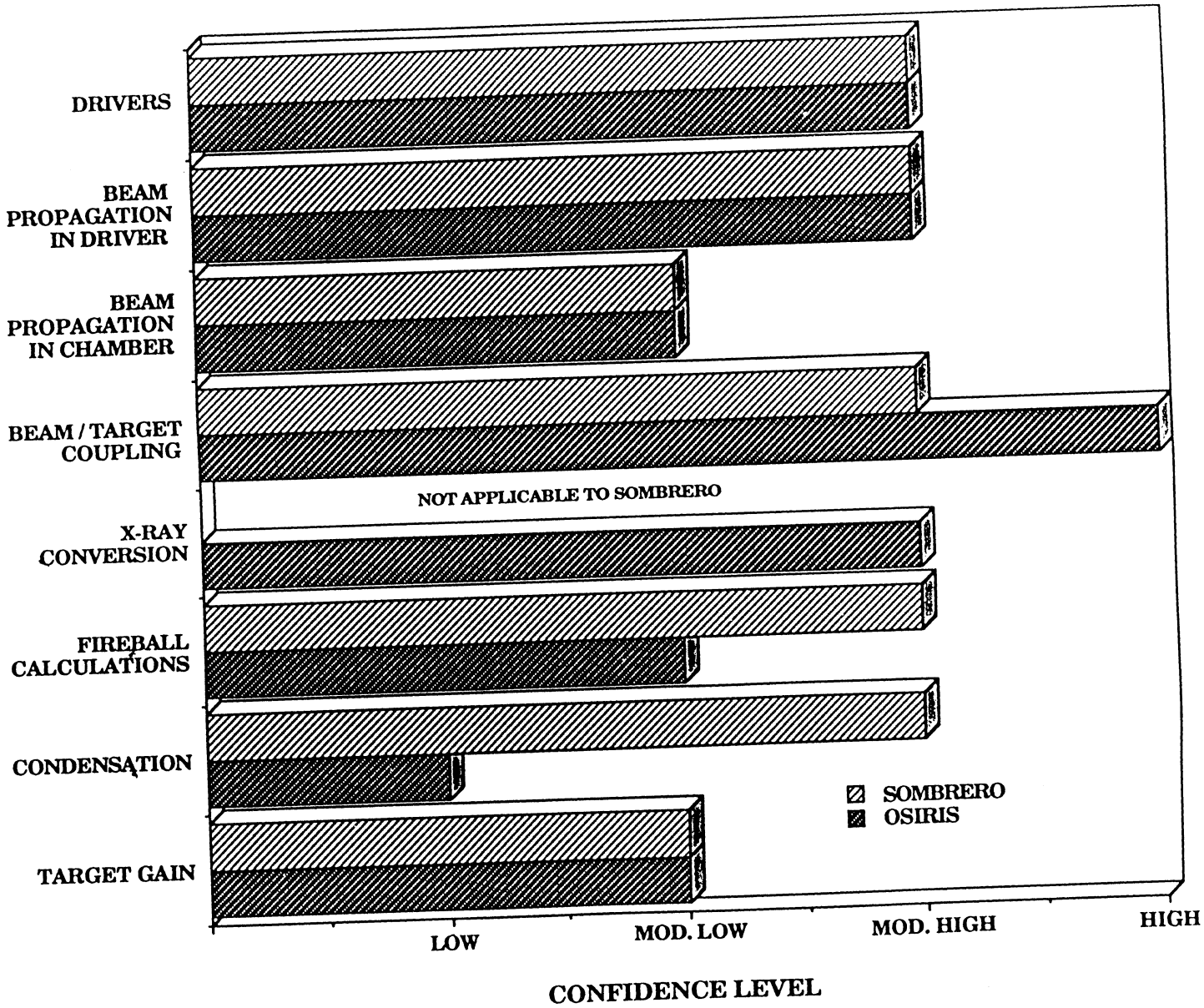

Fig. F.1. Summary of the overall physics comparison.

Laboratory's (LBL) multiple beam experiment (MBE-4). It has a final voltage of 1 MV while the Osiris accelerator will require a voltage of 3.8 GV. Relying on the physics learned from the experiment, the driver has been designed using a conservative approach with singly charged ions and without beam combination or beam separation. Here again, the confidence level in the physics is moderately high.

F.1.2 Beam Propagation

The confidence level for beam propagation through the driver is moderately high for both the HIB driver and the laser. Propagation of the heavy ion beam after it leaves the final optics has a moderately low confidence level. In the case of the laser beam, gas breakdown is an issue of concern, and here the confidence level is moderately low.

F.1.3 Beam Target Coupling and X-ray Conversion

The physics of beam and target coupling is better understood for HIB, rating a high confidence level. Although 1/4 micron wavelength KrF laser light couples to targets better than higher wavelengths, the confidence level is moderately high.

X-ray conversion only applies to the indirect drive targets used by Osiris. Here the confidence level is moderately high.

F.1.4 Fireball Calculations and Vaporization

The confidence level in the Xe gas response to the x-ray and ion deposition in SOMBRERO is moderately high. Ion energy deposition in the Xe gas depends on their in-flight charge state. However, since the initial ions' charge state as they leave the target is not known, this is difficult to determine. The re-radiation of the energy to the SOMBRERO chamber occurs to a large degree in atomic lines, thus, line trapping is a dominant process. The CONRAD code ignores line trapping, but does radiation transport in a multi-group model. It has been found that using many groups in a multi-group model fortuitously gives decent agreement with line trapping calculations. There is a definite need for development of a hydrodynamics code which includes line trapping physics. The reason the confidence level is moderately high is because CONRAD has been benchmarked against shock experiments in Xe gas. Vaporization of the carbon/carbon (C/C) FW is performed with heat transport calculations which have moderately high confidence level, because they rely on the moderately high confidence in the CONRAD simulations. Further, the thermal properties of c/c advanced composites after irradiation are not well known.

The calculations of radiation transport and hydrodynamics in the Flibe cloud vaporized from the Osiris first wall (FW) is rated moderately low confidence, because the chemical kinetics of Flibe at the expected temperatures is uncertain and the optical properties are even more

uncertain, due to molecular effects. The complexity of the Osiris geometry reduces confidence in the one-dimensional calculations. However, the confidence level in the vaporization of Flibe is moderately high, because deposition lengths of x-rays are well known. Volumetric vaporization needs study, however, because it is unclear how material behaves when it is at the boiling temperature but below the vaporization energy.

F.1.5 Condensation

The confidence level for condensation in Osiris is low because of the unusual geometry of the chamber and the very complex chemical issues going on. Vaporization in SOMBRERO is essentially non-existent and, therefore, condensation is not an issue, rating a moderately high confidence level.

F.1.6 Target Gain

Target gain will always have a moderately low confidence level until target experiments are performed at reactor relevant driver energies.

F.2 DRIVER TECHNOLOGY COMPARISON

The drivers have been compared in 11 areas. The first four are meant to be analogous subsystems.

	KrF Laser	Heavy-Ion Driver
1.	Front End	Injector
2.	Intermediate Amplification and Multiplexing	Low Energy Transport and Compression
3.	Final Amplification	Acceleration
4.	Demultiplexing and Beam Delivery	Final Transport and Pulse Compression

The remaining seven features (discussed below) are common to both drivers. Figure F.2 summarizes the driver technology comparison.

F.2.1 Front End / Injector

The non-zooming baseline design can easily build on the front end development for the Nike system at NRL as well as the broad band front end work at Los Alamos in recent years. What is needed is a repetitively pulsed front end with well controlled beam spatial and temporal profiles, but it does not have to be efficient. The confidence level is moderately high. A generic means of achieving stepwise approximation to continuous zooming has been devised for this study. It is likely that a continuous zooming approach can be achieved.

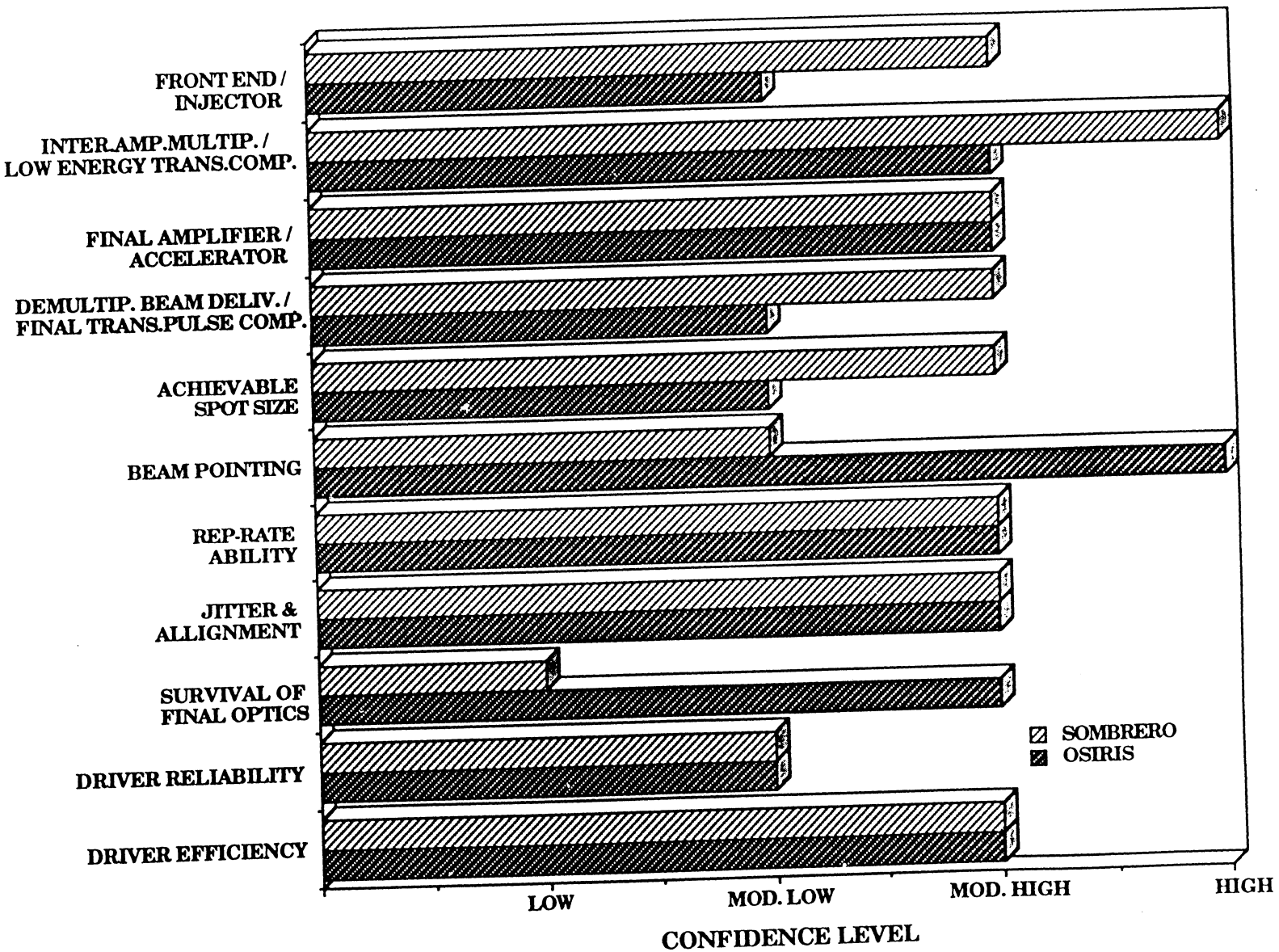

Fig. F.2. Summary of the driver technology comparison.

The needed injector currents in the HIB driver are high. Modeling by the Child-Langmuir law has considerable uncertainties. It may be possible to build injectors with current densities much higher than those given by the Child-Langmuir law, but they will require significant development. Thus the present confidence level is moderately low.

F.2.2 Intermediate Amplification and Multiplexing / Low Energy Transport and Compression

The intermediate amplifier technology for the KrF laser is similar to the final amplifier but less demanding in stress levels, ASE, flow, acoustics, and optics. Multiplexing is a straightforward use of technology developed in Aurora, Nike, and elsewhere. The new element is repetitive operation and for this the confidence level is high.

The low energy transport in the HI driver has two critical issues relating to quadrupole design: 1) How short can a quadrupole be and still have sufficiently high field quality? and 2) How closely can the quadrupoles be packed in the beginning of the driver? The confidence level is moderately high.

F.2.3 Final Amplifier / Accelerator

Much of the KrF final amplifier technology has been demonstrated in key although restricted domains. What remains is the scaling in size and improvement in operating characteristics for the design point selected. The flow and acoustics parameters have been pushed and will require design verification. The confidence level is moderately high.

High rep-rated accelerators have been operating for decades, albeit for significantly different beam parameters, and there are no accelerators that even approach the currents and charge to mass ratio that is needed in Osiris. However, the confidence level is moderately high.

F.2.4 Demultiplexing and Beam Delivery / Final Transport and Pulse Compression

For this stage the requirements are reasonably straight forward and do not require very sophisticated optics development. What is needed is a carefully engineered component design, mounts, beam control between stages and optimized architecture with regard to re-imaging between stages. The confidence level is moderately high.

The critical issues in the HIB final transport and pulse compression are the lack of experimental data. Although sophisticated modeling of final transport and beam compression has been performed, there is no experimental verification. The confidence level is moderately low.

F.2.5 Achievable Spot Size

It is relatively straight forward to achieve the required spot size with the laser since we image an appropriate front end aperture through the amplifier chain, and the beam quality and diffraction requirements are far from the limits. However, care has to be taken in preserving beam spatial and temporal fidelity in the sequence of amplifying stages. The confidence level is moderately high. For the HIB, beam combination is often ignored in calculating the spot size, and expensive experiments will be needed. The confidence level is moderately low.

F.2.6 Beam Pointing

Typically, beam pointing or steering in lasers is achieved by minor adjustments in mirrors located somewhere in the chain in the beam delivery system. The confidence level is moderately low. In the HIB this requirement is not demanding. A two tesla dipole field extending over one meter can steer the beam 10 cm from the chamber center. The confidence level is high.

F.2.7 Rep-Rate Ability

In the laser, having selected a relatively modest 60 kJ size final amplifier cavity and high J/liter input energy, we have a modest size cavity. At rep-rates <10 Hz, pure e-beam pumping allows for a modest flush factor and flow Mach number resulting in a relatively low pressure drop in the flow system. The confidence level is moderately high. Achieving high rep-rate is not a problem for accelerators which have a good track record in this respect. The confidence level is moderately high.

F.2.8 Jitter and Alignment

We did not study jitter and alignment in detail. However, based on development in related systems (e.g., in SDIO and DoD), our confidence level is moderately high. In the case of the HIB, the same is true, and the confidence level is also moderately high.

F.2.9 Final Optics Survival

The lifetime of the grazing incidence metal mirrors (GIMM) is dependent on the degree of radiation damage relief by annealing. This area has a lot of uncertainty due to lack of data. The confidence level is low. In the HIB, the final quadrupoles and steering dipoles are very well shielded, giving a moderately high confidence level.

F.2.10 Driver Reliability

The reliability of the laser as well as the HIB is very difficult to assert because of the simple lack of experience. There is no information on long duration e-beam pumped excimer lasers.

Similarly, accelerators today do not have to push reliability to a level needed for a power reactor. For this reason, the confidence level for both is moderately low.

F.2.11 Driver Efficiency

The laser driver efficiency is based on code calculations that are tied to a rather extensive data base that includes large and small lasers. KrF kinetics and extraction are areas that has been studied at many laboratories around the world for many years and have received continuous peer review. The SOMBRERO design has parameters that are part of this existing data base, but for which not all parameter values have been simultaneously present. Thus, the confidence level is moderately high. The Osiris induction linac efficiency is also based on evaluations performed at LBL and here, too, the confidence level is moderately high.

F.3 REACTOR CHAMBER COMPARISON

The SOMBRERO and Osiris chambers were compared on eight features: materials and construction, leak tightness, heat transfer, fluid dynamics, clearing at rep-rate, nuclear performance, chemistry and erosion, and lifetime assessment. Figure F.3 summarizes the reaction chamber comparison.

F.3.1 Materials and Construction

Both Osiris and SOMBRERO chambers are constructed from carbon based materials. Osiris is made from a very tight weave of graphite fibers with a very carefully controlled diffusion capability. Both the material survival in the corrosive Flibe environment and the ability to construct and maintain a constant weep potential rate a moderately low confidence level. The SOMBRERO chamber is made from a rigidized 4D and 3D weave C/C composite, where the FW is made of 4D and the remaining blanket of 3D. At the present time the confidence level in the materials and chamber construction is moderately low.

F.3.2 First Wall Protection

This is related to the fireball calculation and vaporization, which were covered in F.1.4.

F.3.3 Leak Tightness

Leak tightness is only relevant to SOMBRERO. There is very little information on the leak tightness of C/C composites: however, SiC components have been made vacuum tight. It is assumed that the inside surface of the coolant channels will have a thin coating of SiC as a sealer. Further, it has been shown in Section 3.2.4.2 that a substantial He gas leak rate of ~920 liters/s can

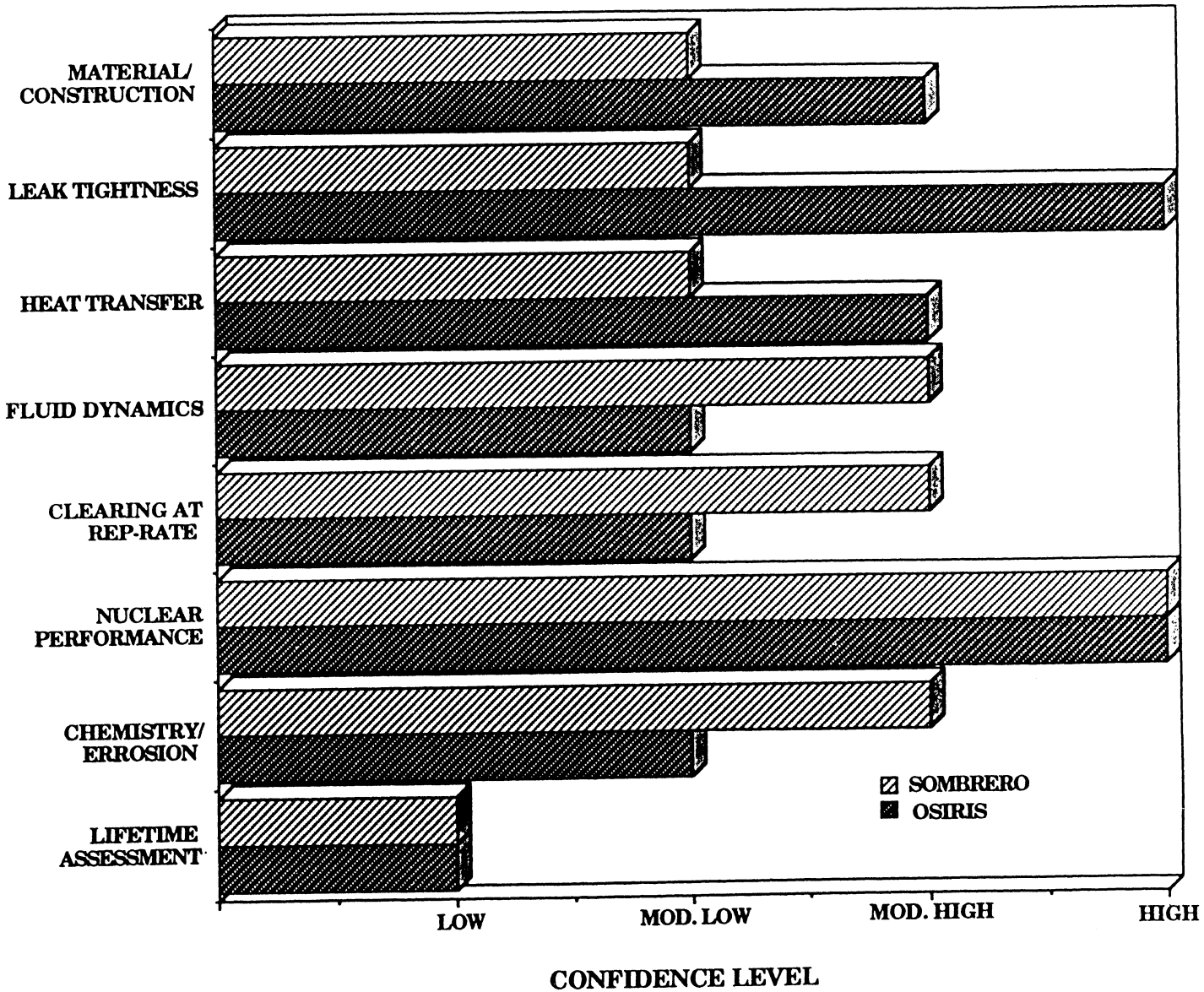

Fig. F.3. Summary of the reactor chamber comparison.

be tolerated without degrading performance. Nevertheless, the confidence level for leak tightness is moderately low.

F.3.4 Heat Transfer

Heat transfer characteristics of Flibe are well known and rate a confidence level of moderately high. There is very scarce information on heat transfer in moving beds. In making use of a continuum in determining heat transfer coefficients, it was necessary to extrapolate effective viscosities to higher values of velocity than are available from experiments. For this reason, heat transfer in SOMBRERO has a moderately low confidence level.

F.3.5 Fluid Dynamics

A critical issue in Osiris is the weeping of Flibe through the FW fabric. Uncertainty about the ability to maintain a uniform layer for the lifetime of the blanket gives this category a moderately low confidence rating. Flow dynamics in SOMBRERO has to do with the movement of the Li_2O particles in the flow channels. These channels are very large, and flow control is at the exit from the channels. Thus the confidence level in this is moderately high.

F.3.6 Clearing at Rep-rate

There is some uncertainty on whether the vapors in Osiris will condense in time between shots, and on this the confidence level is moderately low. SOMBRERO has essentially no evaporation; thus, this is not an issue.

F.3.7 Nuclear Performance

In this area both reactors have a high confidence level.

F.3.8 Chemistry / Erosion

The most detrimental chemical issue in Osiris is the x-ray decomposition of Flibe into the elementary atoms. The recombination of these atoms is difficult to predict without knowing the gaseous reaction rates at high temperatures, but could lead to the formation of LiF, BeF, BeF_2, LiBe and F_2. The chemically reactive fluorine (F_2) formed near the FW would attack the carbon fibers. For this reason, a rating of moderately low is given to the confidence level.

The question of erosion in SOMBRERO is not a concern at the low velocities in the moving bed (115 cm/s), giving a moderately high confidence level.

F.3.9 Lifetime Assessment

The whole area of radiation damage in materials for fusion is in its infancy requiring 14 MeV neutron sources and long development times to accumulate damage rates relevant to power reactors. For this reason, the confidence level for both reactors is low.

F.4 BREEDING MATERIAL COMPARISON

Figure F.4 summarizes the breeding material comparison.

F.4.1 Data Base

The data base for both Flibe and solid Li_2O is pretty well developed, getting a moderately high confidence level and moderately low development needs.

F.4.2 Breeding Potential

Here again the breeding potential for both materials has a high confidence level.

F.4.3 Thermal Performance

Both materials have been proposed for high temperature operation and have excellent thermal characteristics. The confidence level is moderately high for both.

F.4.4 Dissociation/Fragmentation

In the case of Flibe, x-ray dissociation will take place, but the recombination from the elementary atoms is difficult to predict. Thus, the confidence level is low.

Fragmentation in SOMBRERO of the Li_2O is almost certain to occur, but since the material is mobile, the fine fraction will be continuously removed and reprocessed. Just how much fragmentation will occur is hard to predict. Thus the confidence level is moderately low.

F.4.5 Tritium Extraction

Tritium extraction from both Flibe and Li_2O appears to be straightforward getting a moderately high confidence level.

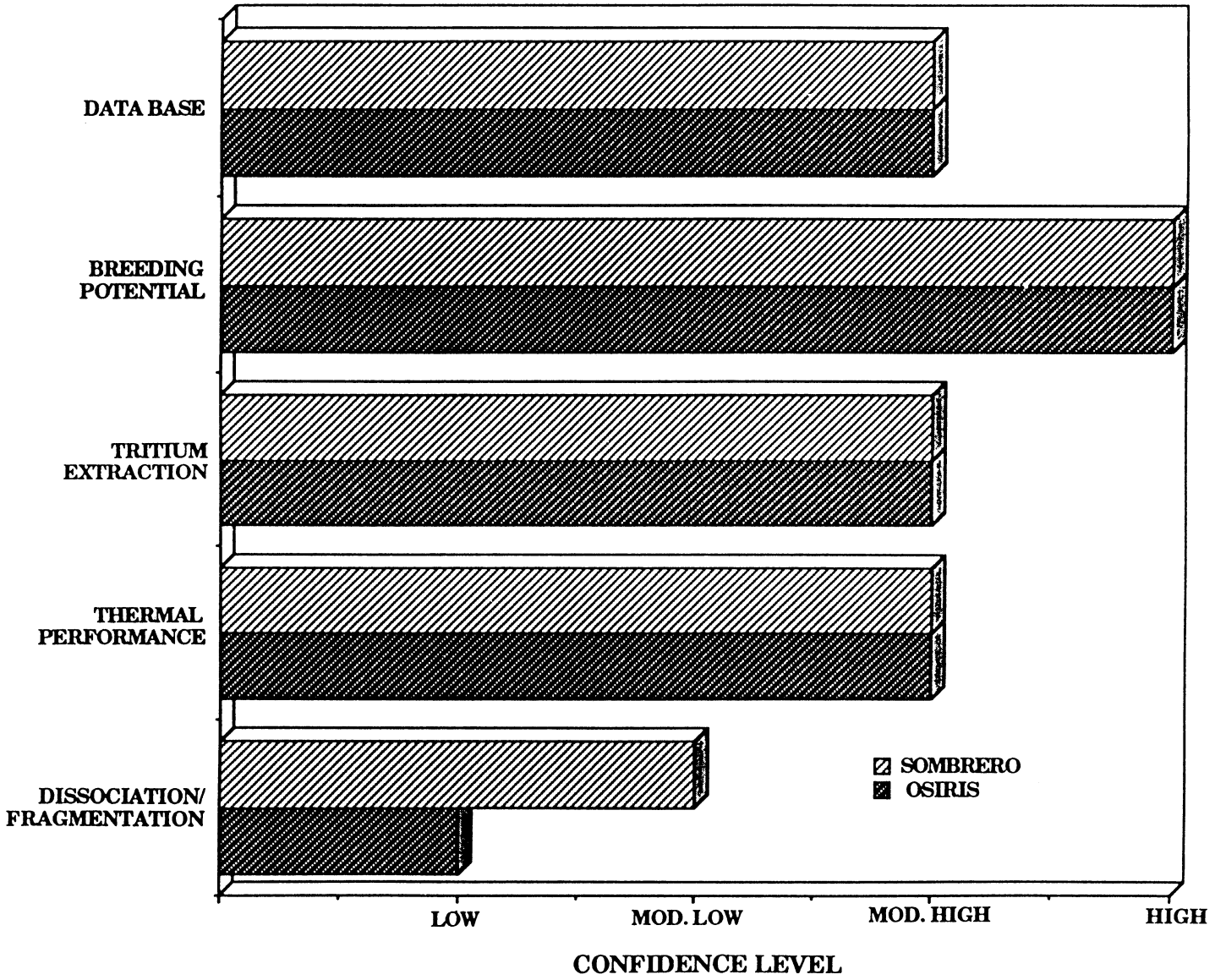

Fig. F.4. Summary of breeding material comparison.

F.5 TARGET AND TARGET DELIVERY COMPARISON

Figure F.5 summarizes the target comparison.

F.5.1 Fabrication at Tolerance

Osiris will be using indirect drive targets, which are generally more complicated than the direct drive targets used by SOMBRERO. It has been demonstrated that very small targets can be fabricated to the required tolerance, but the question still remains on whether they can be mass produced at tolerance. Both targets get a moderately low confidence level.

F.5.2 Tritium Filling

Several schemes for target filling have been demonstrated, but doing it at mass production rates is still very uncertain. Thus the confidence level is low.

F.5.3 Beta or Laser Layering

The confidence level on being able to perform proper layering for thick layers required by reactor scale targets is moderately low.

F.5.4 Alignment on Delivery

Indirect drive targets have to be centered in the chamber and properly oriented with respect to the location of the driver beams. Rifling the injector to provide spin stabilization of the cylindrical target will aid in achieving the proper orientation. The confidence level to do this is moderately high. Direct drive targets do not need a preferred orientation; thus, the confidence level in delivery is moderately high.

F.5.5 Dynamic Survivability

The integrity of cryogenic DT capsules, which are used in both direct and indirect drive targets, under accelerations of >100 g's is untested and uncertain. For indirect drive targets, hohlraum survivability and the ability to keep the capsule precisely within the hohlraum are also issues. The confidence level is low for both direct and indirect designs since there have been no calculations or experiments to address these issue.

F.5.6 Thermal Survivability

The hohlraum gives indirect drive targets a higher thermal inertia than direct drive targets. However, computer calculations indicate that the fuel in both targets can survive without overheating during their flight through the chamber. The ability to maintain a high quality outer

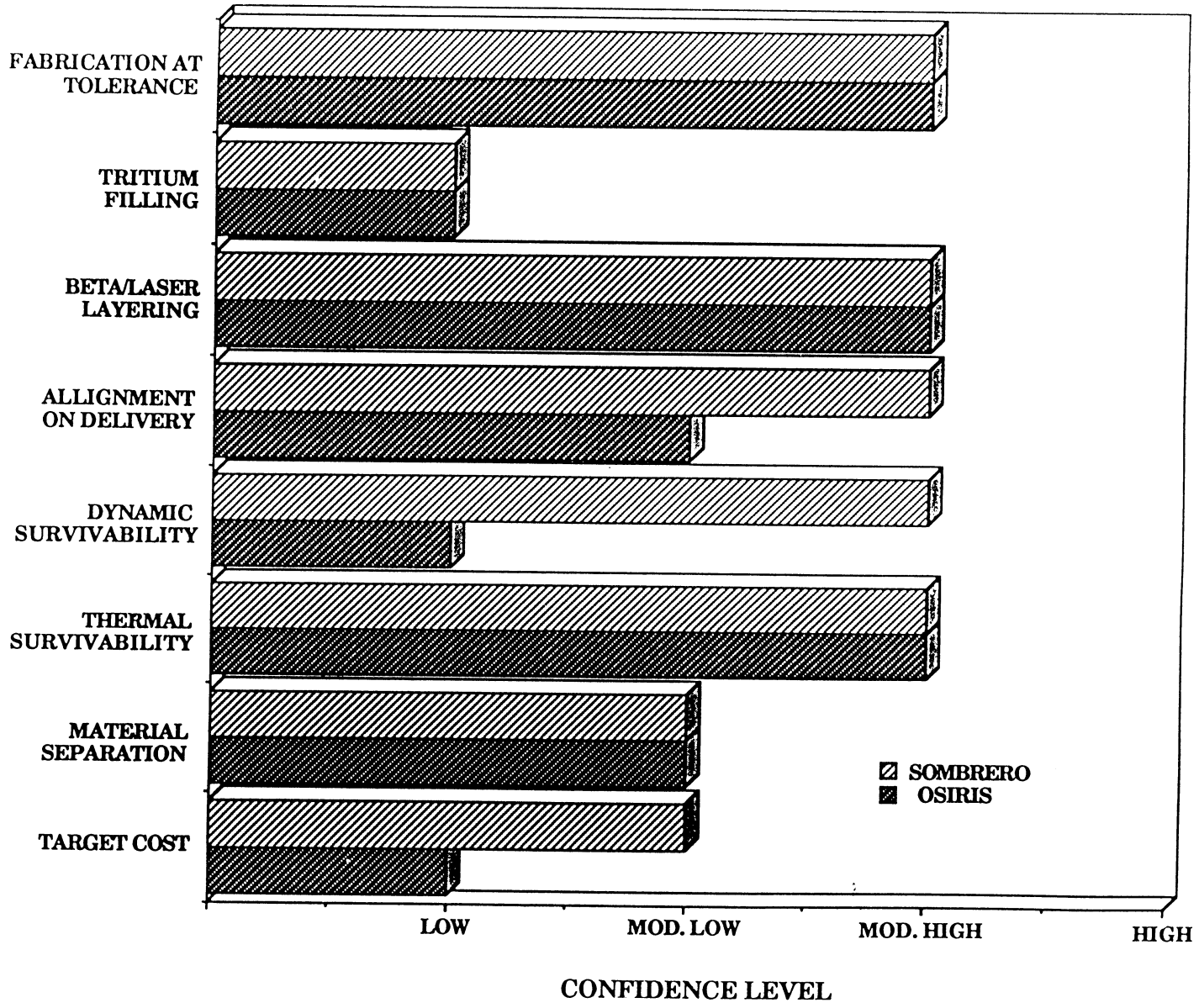

Fig. F.5. Summary of target comparison.

surface of the direct drive capsule is more uncertain. The confidence level in these calculations is moderately high.

F.5.7 Material Separation and Reprocessing

Separating the target materials from the Flibe in the case of Osiris and from the vacuum system in SOMBRERO has a moderately low confidence level.

F.5.8 Target Cost

The confidence level in the cost of mass produced targets at tolerance is low for both direct and indirect drive targets.

F.6 POWER CONVERSION CYCLE COMPARISON

Figure F.6 summarizes the power cycle comparison.

F.6.1 Intermediate Heat Exchangers and Steam Generators

Both Osiris and SOMBRERO utilize an intermediate loop of liquid Pb to minimize T_2 diffusion into the steam cycle and eliminate water/breeding material interaction. The confidence level in the IHX and steam generators for both systems is moderately high.

F.6.2 Maintenance of Power Cycle Equipment

Confidence in the ability to maintain power cycle equipment is moderately high since both systems will have hands-on maintenance capability.

F.6.3 Power Cycle and Conversion Efficiency

Both Osiris and SOMBRERO utilize a supercritical pressure double reheat steam cycle, which is state-of-the-art in many fossil-fired steam power plants. The steam conditions are consistent with the conversion efficiencies currently obtained in these plants. Thus, the confidence level for both systems is high.

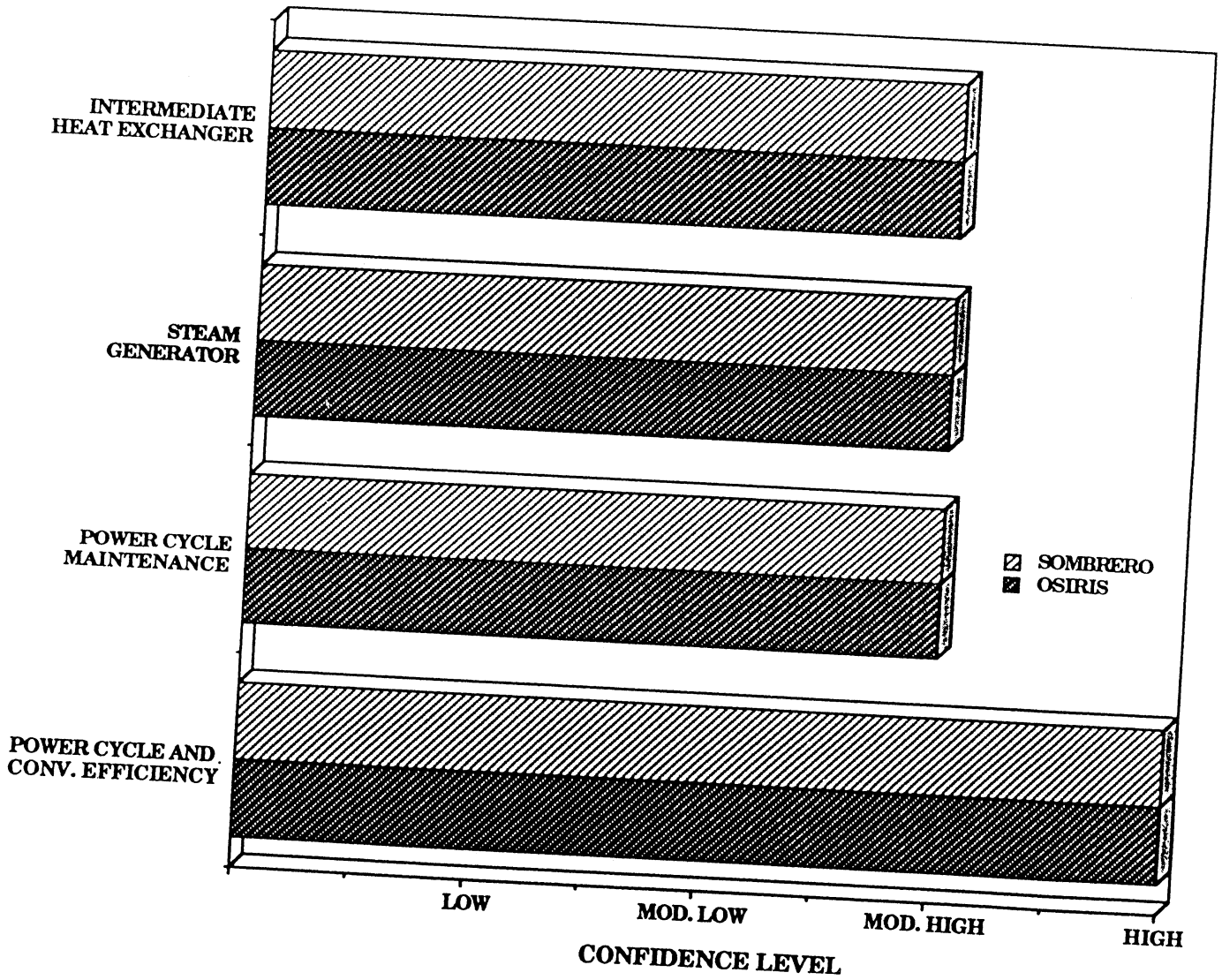

Fig. F.6. Summary of power cycle comparison.

F.7 SUMMARY OF THE COMPARISON SURVEY

In summarizing the major points between the Osiris heavy-ion-driven power plant and the SOMBRERO KrF laser driven power plant, the following can be said:

- Confidence in the driver technology for both systems appears to be even, with the exception of final optics survivability, where Osiris has the definite advantage.

- From the material and construction standpoints, Osiris has advantages of design simplicity and single unit maintenance. However, from the chemical standpoint, Flibe has issues with respect to dissociation and recombination and the potential of the highly reactive fluorine (F_2), formed near the first wall for attacking the graphite fiber.

- First wall protection in SOMBRERO is better understood than in Osiris, although at a price of size and cost. There is considerable uncertainty in the wetting and weeping characteristics of Flibe through the chamber fabric as well as in the rate of condensation.

- The direct drive targets have a slight advantage over indirect drive because there is more uncertainty in the alignment on delivery and dynamic survivability for the indirect drive targets. Indirect drive targets have an advantage in thermal survivability.

- Both reactors have outstanding nuclear performance characteristics.

- Both reactors have excellent safety and environmental characteristics. Osiris, however, has a lower T_2 inventory in the reactor building.

- Although both reactors have a cost of electricity which is competitive with respect to MFE designs, the COE in Osiris is 16% lower than SOMBRERO. The price paid by SOMBRERO for near symmetric illumination and dry wall first wall protection is clearly evident in the economics.

- Finally, it is impossible to say that one design is clearly better than the other. Both designs have definite positive attributes and issues as well. Much more research and development will be needed to confirm the advantages and resolve the issues before a meaningful clear choice can be established.